THE UNIVERSITY
of ADELAIDE

Optimisation and Adaptive Control of Aircraft Propeller Synchrophase Angles

David Mark Blunt

A thesis submitted in fulfilment of the
requirements for the degree of Doctor of Philosophy

January 2012

School of Mechanical Engineering
The University of Adelaide
South Australia 5005

Principal Supervisor: Colin Hansen
Co-supervisor: Anthony Zander
External Supervisor: Brian Rebbechi (Defence Science and Technology Organisation)

© Copyright Commonwealth of Australia 2012
Defence Science and Technology Organisation
506 Lorimer Street, Fishermans Bend, Victoria 3207

For my father
Richard Mark Blunt
24 April 1924 – 24 October 2009

Abstract

This thesis provides a new and detailed examination of how the optimum propeller synchrophase angles for minimum cabin noise and vibration vary with different flight conditions, particularly altitude and airspeed, and how, based on these observations, adaptive control techniques could best be employed to further improve the noise-reducing potential of synchrophasing. This has been done through experimental investigations in one AP-3C Orion and two C-130J-30 Super Hercules aircraft.

It is shown, using propeller signature theory, that synchrophasing has significant effects on the average cabin floor vibration and the average cabin sound pressure levels. In the trial aircraft, these effects range between 4 dB and 12 dB at the blade-pass frequency, depending on the flight condition and the aircraft. The effects at individual sensors locations can, however, sometimes exceed 20 dB.

It is also shown that the effects of altitude and airspeed on the optimum synchrophase angles are significant, and that a fixed set of synchrophase angles cannot be optimal for more than a limited range of flight conditions. For example, over the range of altitudes and airspeeds considered in this investigation, a fixed set of angles is shown to produce results that can vary by more than half of the range from the lowest to the highest predicted average sound pressure level at the blade-pass frequency.

Adaptive control of the synchrophase angles using pre-defined look-up tables or active control algorithms are considered, and the latter recommended for their ability to compensate for unknown and variable influencing factors.

Two ranking strategies are developed and employed to identify the number and placement of error sensors for an active control system. Significantly, both strategies identify that the predicted average sound pressure levels at the blade-pass frequency in the trial aircraft could be maintained within 2 dB of the optimum across all considered flight conditions using as few as 3 to 6 well-placed microphones.

A single-input (master propeller tachometer) multi-output (slave propeller synchrophase angles) feed-forward active control system with multiple error sensors (microphones or accelerometers) is developed using propeller signature theory and the Filtered-x LMS algorithm.

Recommendations for further work are also made.

Acknowledgment

The work presented in this thesis was undertaken through the candidate's employment with the Defence Science and Technology Organisation (DSTO) of the Department of Defence, Australia. It is bound by a PhD Intellectual Property Agreement between DSTO and The University of Adelaide dated 2nd day of September 2008.

The work could not have been completed without the support of the Department of Defence, and the personal encouragement of Mr Brian Rebbechi and Dr David Forrester.

Thesis Declaration

This work contains no material which has been accepted for the award of any other degree or diploma in any university or other tertiary institution to myself and, to the best of my knowledge and belief, contains no material previously published or written by another person, except where due reference has been made in the text.

I give consent to this copy of my thesis, when deposited in the University Library, being made available for loan and photocopying, subject to the provisions of the Copyright Act 1968.

I also give permission for the digital version of my thesis to be made available on the web, via the University's digital research repository, the Library catalogue, and also through web search engines, unless permission has been granted by the University to restrict access for a period of time.

David Mark Blunt

January 2012

Contents

1. Introduction

This chapter establishes the importance of minimising propeller related noise and vibration in aircraft cabins, and introduces how propeller synchrophasing could be better employed to achieve this desired outcome. It also introduces the types of aircraft used in the investigation, and identifies the objectives of the research.

Noise and vibration is a serious problem in all types of aircraft. From a human perspective, noise and vibration are at best annoying and at worst a health hazard. Noise is known to cause problems such as hearing loss, task performance degradation, and speech intelligibility reduction (Powell and Fields, 1991). Prolonged exposure (> 10 years) to high-amplitude (> 90 dB) low-frequency (< 500 Hz) noise, as found in many military propeller aircraft, is also believed to cause vibro-acoustic disease. This disease is associated with damage to vascular and brain tissues (Castelo Branco, 1999a,b; Castelo Branco et al., 1999; Marciniak et al., 1999; Pimenta et al., 1999; Smith, 2002). From an engineering perspective, vibration causes material fatigue and shortens the life of avionics and other airborne equipment. It may also limit the transport of vibration-sensitive cargo such as electronic equipment, medical equipment, and explosive ordnance.

Military propeller aircraft often suffer from very high levels of noise and vibration, as cabin comfort is usually compromised in favour of utility. While commercial propeller aircraft employ more noise and vibration suppression treatments, these often come with significant weight or performance penalties. Hence, any techniques that lower cabin noise and vibration levels by even a few decibels with little or no weight or performance penalties are worth pursuing. Propeller synchrophasing is one such technique that has shown potential in aircraft with two or more propellers; however, it is hypothesised that this technique is not being used to its full potential because the synchrophase angles are typically fixed. This thesis provides a new and detailed examination of how the optimum synchrophase angles in real aircraft vary with different flight conditions, and whether adaptive control techniques could be employed to improve the noise-reducing potential of synchrophasing further.

1.1. Cabin Noise and Vibration in Propeller Aircraft

Cabin noise and vibration in propeller aircraft is dominated by the propeller Blade-Pass Frequency (BPF) and its low-order harmonics (Mixson and Wilby, 1991). This noise enters the cabin through a complex interaction/coupling between the exterior sound field, the airframe vibration, and the enclosed interior sound field (Fuller, 1984a, 1986a,c, 1987). Typical blade-pass frequencies range from 60 Hz to 120 Hz (Table 1.1). Cabin sound pressure levels at these frequencies often exceed 90 dB, and can approach 110 dB or more in military aircraft (Johnston et al., 1981). This tonal droning propeller noise is often considered more unpleasant than the more broadband noise emitted from equivalently sized jet engines.

Blade-pass noise is difficult to control passively because of its relatively low frequencies (< 150 Hz). This often requires a large amount of vibration-absorbing/sound-deadening material and a correspondingly unacceptable weight penalty in typical propeller aircraft (Hansen and Snyder, 1997, §9.13). Active control methods are potentially more attractive for blade-pass noise, although these methods incur additional complexity and cost. They may also incur significant weight penalties depending on the number and type of actuators used.

Active noise and vibration control systems for aircraft cabins typically modify the fuselage vibration with adaptively-tuned vibration absorbers, inertial shakers, or piezo-type actuators, or modify the internal acoustic environment using multiple loudspeakers. There are various examples of such systems in the literature (Borchers et al., 1992; Bullmore et al., 1990; Carme et al., 1997; Coppinger, 2006; Dorling et al., 1989; Elliott et al., 1990; Emborg and Ross, 1993; Emborg et al., 1998; Fuller, 1997; Fuller et al., 1992; Gerner and Sachau, 2003; Gorman et al., 2004; Hinchliffe et al., 2002; Johansson et al., 1999a; Johansson et al., 1999b; Johansson et al., 2000). Some manufacturers have adopted these types of active control techniques in (predominantly commercial) propeller aircraft; e.g., the Bombardier Q-Series aircraft, and the SAAB 340 & 2000 (Bombardier, 2008; Saab, 2004), although Ultra Electronics have also developed a system that can be retro-fitted to the flight deck of the C-130 military aircraft (Ultra, 2009). However, the majority of propeller aircraft still have no active noise or vibration control systems fitted as standard equipment.

Table 1.1 Engines and propellers of several turboprop aircraft (Jane's, 2009c).

Aircraft	Engine	Propeller	Dia. (m)	Dia. (ft)	Blades	100% Np (RPM)	BPF* (Hz)
A400M	TP400-D6	Ratier-Figeac FH 386	5.33	17.5	8	842	112
ATR-42-300 ATR-42-320	PW120 PW121	Hamilton Sundstrand 14SF-5	3.96	13.0	4	1200	80
ATR-42-400 ATR-42-500	PW121A PW127M	Hamilton Sundstrand 568F	3.94	12.9	6	1200	120
AP-3C	T56-A-14	Hamilton Sundstrand 54H60-77	4.11	13.5	4	1020	68
C-130H	T56-A-15	Hamilton Sundstrand 54H60-117	4.11	13.5	4	1020	68
C-130J	AE 2100D3	Dowty Aerospace R391	4.11	13.5	6	1020	102
Fokker 50	PW125B	Dowty Aerospace R352	3.66	12.0	6	1200	120
Q100	PW120A, PW121	Hamilton Sundstrand 14SF-7	3.96	13.0	4	1200	80
Q200 Q300	PW123C/D PW123/B/E	Hamilton Sundstrand 14SF-23	3.96	13.0	4	1200	80
Q400	PW150A	Dowty Aerospace R408	4.11	13.5	6	1020	102
SAAB 2000	AE 2100A	Dowty Aerospace R381	3.81	12.5	6	1100	110

* Propeller speed (N_p), and hence BPF, are sometimes reduced to approximately 85% during cruise, although this does not apply to the AP-3C, C-130H, or C-130J.

1.2. Propeller Synchrophasing

Aircraft with two or more propellers usually have a synchrophaser. A synchrophaser is an electronic device that synchronises the speeds of the propellers and maintains certain relative phase angles between the propeller shafts while they are spinning. These angles are known as the synchrophase angles. They are normally pre-programmed into the synchrophaser and are not varied in flight. In operation, one of the propellers, usually an inboard propeller, is designated the master propeller and the remaining propellers are slaved to this master.

Previous studies in P-3 and C-130 military aircraft (Johnston and Donham, 1981, 1982; Johnston et al., 1980, 1981; Magliozzi, 1983) have shown that optimising the synchrophase angles can potentially reduce the blade-pass noise and vibration in an aircraft cabin, not just redistribute it. This appears to work by finding a set of angles that result in a less efficient coupling between the exterior sound field, the airframe vibration, and the enclosed interior sound field. The reductions quoted in these studies are generally in the order of

10 dB over the worst angle set case. This is a significant reduction in a high noise level environment, and warrants further investigation since it requires absolutely no performance or weight penalty.

Unfortunately, optimising the synchrophase angles is not always an easy task. Analytically modelling the air-airframe-cabin system is difficult for anything other than simple geometries (Hansen and Snyder, 1997, 9.13). Analytical models also need to be validated with at least some experimental data before they can be used with confidence. Empirical methods can also be difficult. While a trial-and-error approach can be adopted if there are two propellers, and hence only one synchrophase angle, this is impractical in an aircraft with four propellers because of the number of potential synchrophase angle combinations required. For example, if synchrophase angle steps of 2° are used in an aircraft with four six-bladed propellers this would require 30 settings for each slave propeller, and a total of 30^3 = 27,000 potential combinations of all three slave propellers. Even 5° steps would still require 1728 combinations.

Fortunately, Johnston et al. (1981) developed a relatively straightforward method for predicting the blade-pass noise and vibration in an aircraft cabin for any combination of synchrophase angles from a limited number of measurements. In this method, the in-flight noise/vibration from a number of sensors within the cabin is measured for a small number of predetermined synchrophase angle sets. These measurements are then used to calculate the influence coefficients, or "Propeller Signatures," for each propeller at each sensor location. The minimum number of synchrophase angle sets required to solve the system of equations is equal to the total number of propellers. However, incorporating more angle sets into the calculation allows the inherent measurement errors to be minimised using a least-squares approach. An optimisation strategy can then be applied to the predictions in order to arrive at the optimum synchrophase angles. Based on their results, this approach has the potential to simplify further investigations and it is extensively used in this thesis.

It can be expected that the optimum synchrophase angles will vary with any parameter that might influence the vibro-acoustic characteristics of the air-airframe-cabin system; e.g., altitude, airspeed, engine power, cabin configuration, and angle-of-attack. For example, it is known that propeller noise changes with thrust and inflow distortion (Magliozzi et al., 1991). It is also known that cabin noise levels in propeller aircraft change with altitude and airspeed (Farrell et al., 2002; Smith, 2004). However, these factors are often ignored in many synchrophase angle optimisation studies. Only one public-domain paper has included synchrophasing results with varying flight conditions. In this paper, Pla et al (1993), found that the optimum synchrophase angle in an OV-10A aircraft depended on the cabin microphone location, engine speed, and weather. This thesis significantly expands on these findings.

The adaptive control of synchrophase angles using cabin mounted microphones or accelerometers as error sensors should be able to compensate for any variation in optimum synchrophase angles that may occur due to various flight conditions. This has the potential to provide optimal propeller-related noise reduction throughout the whole flight envelope of an aircraft, not just over a limited range of flight conditions that may be possible with fixed synchrophase angles. Very little work has been done in this area in comparison to using secondary sound or vibration sources (shakers, piezo-films, loudspeakers etc.). Secondary sources may ultimately provide greater reductions in cabin noise and vibration, but they come with the costs of added complexity and weight; and a large number of sources are typically needed in most aircraft. The adaptive control of synchrophase angles may therefore offer worthwhile reductions with fewer penalties, and be considerably easier to implement and retrofit to existing aircraft. Adaptive synchrophasing may also enhance

the performance of other forms of active noise and vibration control by minimising the noise entering the aircraft cabin.

1.3. Aircraft with Four Propellers

Synchrophasing appears to offer more promise as a noise and vibration reduction tool for four-engined aircraft than two-engined aircraft. In an analysis of data from a P-3 Orion aircraft that eliminated the outboard propellers from consideration, Magliozzi (1983) predicted much lower noise reductions for two propellers (3 dB) than four propellers (10 dB) due to the reduced number of phase angle combinations available. While there may not be many commercial aircraft with four propellers, this configuration is still common in military transport aircraft where the higher thrust available from propellers at low forward airspeed typically allows these aircraft to operate from shorter airstrips than equivalent jet aircraft. The two main aircraft specifically considered in this thesis are the P-3C Orion and C-130J Super Hercules, although the analysis methods used are directly applicable to any aircraft with two or more propellers.

The P-3C Orion is powered by Rolls Royce Allison T56 engines with four-bladed Hamilton Sundstrand 54H60 propellers. Although now out of production, more than 640 P-3 aircraft were delivered from 1962 to 1996 and possibly over 100 of these still remain in service around the world (Lockheed Martin (Lockheed) P-3 Orion, 2009). The Royal Australian Air Force (RAAF) operates 18 AP-3C aircraft (Figure 1.1). This is an upgraded variant of the P-3C with several new avionic systems (Lockheed Martin (Lockheed) P-3 Orion, 2009). However, the propulsion and synchrophasing systems remain the same.

The C-130 Hercules is perhaps the most widely used military transport aircraft around the world. More than 2000 of the original C-130 Hercules were delivered over the period 1955-1998. Approximately 160 of these C-130 Hercules still remain in service with air forces around the world, principally the C-130H version which uses the same engines and four-bladed propellers as the P-3C Orion (Jane's, 2009b). Over 170 of the newer C-130J Super Hercules powered by Rolls Royce AE 2100D3 engines with six-bladed Dowty Aerospace R391 propellers have been delivered since 1994 (Jane's, 2009a). There are two main variants of the C-130J: a short-fuselage variant, and a long-fuselage variant. The RAAF operates 12 C-130J-30 long-fuselage aircraft (Figure 1.2).

Another notable aircraft that may benefit from improved synchrophasing is the A400M (Figure 1.3). This new military transport aircraft is still in development. It is much larger than the C-130, and will have four 10,000+ shaft horsepower (shp) engines (cf. 4500+ shp engines in the AP-3C and C-130J) with eight-bladed propellers. These propellers will have an uncommon counter-rotating configuration (Figure 1.4) for aerodynamic reasons (A400M to have 'handed' propellers, 2004). The more common configuration is where all the propellers rotate in the same direction, as this simplifies gearbox construction (no reversing gear) and only requires a left or right handed version of the propeller instead of both. The A400M will also feature active noise control using 200 electro-mechanical actuators (Coppinger, 2006), indicating that propeller noise is likely to be a significant problem in this aircraft.

Figure 1.1 RAAF AP-3C Orion (A9 Lockheed Orion P3). © Commonwealth of Australia. Reproduced with permission from the RAAF.

Figure 1.2 RAAF C-130J-30 Hercules (A97 Lockheed Hercules). © Commonwealth of Australia. Reproduced with permission from the RAAF.

Figure 1.3 A400M (A400M Photo Gallery). © Airbus Military 2010. Reproduced with permission from Airbus Military.

Figure 1.4 A400M propeller rotation (A400M Photo Gallery). © Airbus Military 2010. Reproduced with permission from Airbus Military.

1.4. Objectives

The objectives of this thesis are to examine the effects of a wide range of flight conditions on the optimum synchrophase angles for cabin noise and cargo-floor vibration reduction in real aircraft, and explore the potential for adaptive control of the synchrophase angles to compensate for these effects. This will be done through analysis of noise and vibration data collected from flight trials in one RAAF AP-3C Orion (A9-660) and two RAAF C-130J-30 Super Hercules aircraft (A97-467 and A97-464).

1.5. Thesis Outline

Following this introduction is a review of the literature in Chapter 2, and an outline of the theory of shell vibration, enclosed sound fields, active control, and propeller signatures in Chapter 3. Chapter 4 introduces the propeller synchrophasing systems in the AP-3C and C-130J-30, and Chapter 5 describes the experimental investigations devised for these aircraft. Next, the measured synchrophase angles, the cabin noise and vibration environment, and the measurement repeatability are analysed in Chapters 6 through to 8. These chapters

provide a better understanding of the system characteristics and constraints in these aircraft. Chapter 9 describes how propeller signature theory was applied and analysed. The effects of different optimisation criteria, and of different altitude and airspeeds, are then individually examined for each aircraft in Chapter 10. A number of new (fixed) candidate synchrophase angle sets are developed during this process. The results of testing the candidate sets for the C-130J-30 in a second aircraft are reported, and the aircraft-to-aircraft differences are considered. Finally, the application of adaptive control to propeller synchrophasing is examined and discussed in Chapter 11, and the outcomes of the investigation are concluded in Chapter 12.

2. Literature Review

This review begins with a brief description of propeller noise. It then moves on to a discussion of the most recently published work about propeller signature theory, analytical models of synchrophasing, and the adaptive control of synchrophase angles. It ends with a summary of the identified research gaps.

2.1. Propeller Noise

Magliozzi et al. (1991) provide a good introduction to propeller noise. Because of its periodic motion, propeller noise is dominated by harmonic components, but it also has some broadband and narrow-band elements.

Propeller harmonic noise occurs at whole multiples of the Blade-Pass Frequency (BPF); i.e., BN, $2\times BN$, $3\times BN$, etc., where B is the number of blades and N is the rotational frequency. It can be split into thickness noise, which is generated by the air displaced by the thickness of the propeller blades, and loading noise, which is generated by the thrust and torque loads on the propeller. The harmonic noise for a single propeller is typically dominated by the fundamental blade-pass frequency component and its low-order harmonics.

Broadband noise typically arises from turbulence, both in the inflow and in the blade boundary layers, but is much less important than harmonic noise. Narrow-band random noise can sometimes be generated when localised distortions to the inflow, such as ingested ground or fuselage vortices, move slowly around the propeller disc causing loading variations that are nearly periodic.

Propeller noise is strongly influenced by operating conditions and installation effects. Examples of these include (Magliozzi et al., 1991):

a) Operation of the propeller in flight where the shaft is at an angle to the inflow. This causes the angle of attack of the blades to vary cyclically with the rotation of the propeller, and generates noise components at harmonics of the BPF.
b) Ground running of the propeller with no forward airspeed. This is associated with severe inflow distortion, and produces noise that is significantly different to that generated in flight.
c) Propellers mounted behind a wing or pylon. Wing or pylon induced distortions produce unsteady loads on the blades that repeat every revolution. These can cause lobes in the circumferential noise directivity pattern of the propeller.

Another installation effect to consider is that the propellers on most multi-engined aircraft all rotate in the same direction.[1] The aircraft will thus have up-going blades immediately adjacent to the fuselage on one side of the aircraft and down-going blades on the other side. This difference could lead to some asymmetry of the cabin noise and vibration patterns.

[1] It is unusual to have both left-handed and right-handed versions of a propeller on an aircraft unless there is a specific (e.g., aerodynamic) reason to over-ride the associated additional engineering costs.

2.2. Propeller Signature Theory

The method of predicting propeller harmonic noise and vibration in aircraft cabins using propeller signatures was first described by Johnston et al. (1980). They also suggested that propeller signatures could be used to determine the various transmission paths into the cabin, although this was more specifically dealt with in a subsequent paper (Johnston and Donham, 1981). Embodiments of the propeller signature method appear in a number of other papers and patents (Magliozzi, 1983, 1995; Pla, 1998).

In propeller signature theory, the harmonic noise or vibration at any particular cabin location is calculated from the vector sum of the contributions (signatures) from each propeller at each blade-pass harmonic. This assumes that the contributions from each propeller do not combine in a non-linear way and appears to be valid based on the results presented in the aforementioned papers, although further confirmation of this may be required. With the propeller speeds synchronised, the harmonic noise or vibration for any combination of synchrophase angles is predicted by changing the phase of each signature in proportion to the change in synchrophase angle, and then recalculating the sum of the resulting contributions.

An example illustrating the method at the BPF is shown in Figure 2.1. Here, the signatures, $S_p\angle\phi_p$, for each propeller, p, at a point inside the cabin are shown in the top half of the figure, and the predicted noise at the same point for a different set of synchrophase angles is shown in the bottom half of the figure. Note that Propeller 2 is the master propeller in this case, and the changes in the synchrophase angles, α_p, are multiplied by the number of blades, B, to give the phase changes at the BPF. The example can be extended to the BPF harmonics by multiplying by nB instead of B, where n = 2, 3, 4, etc.

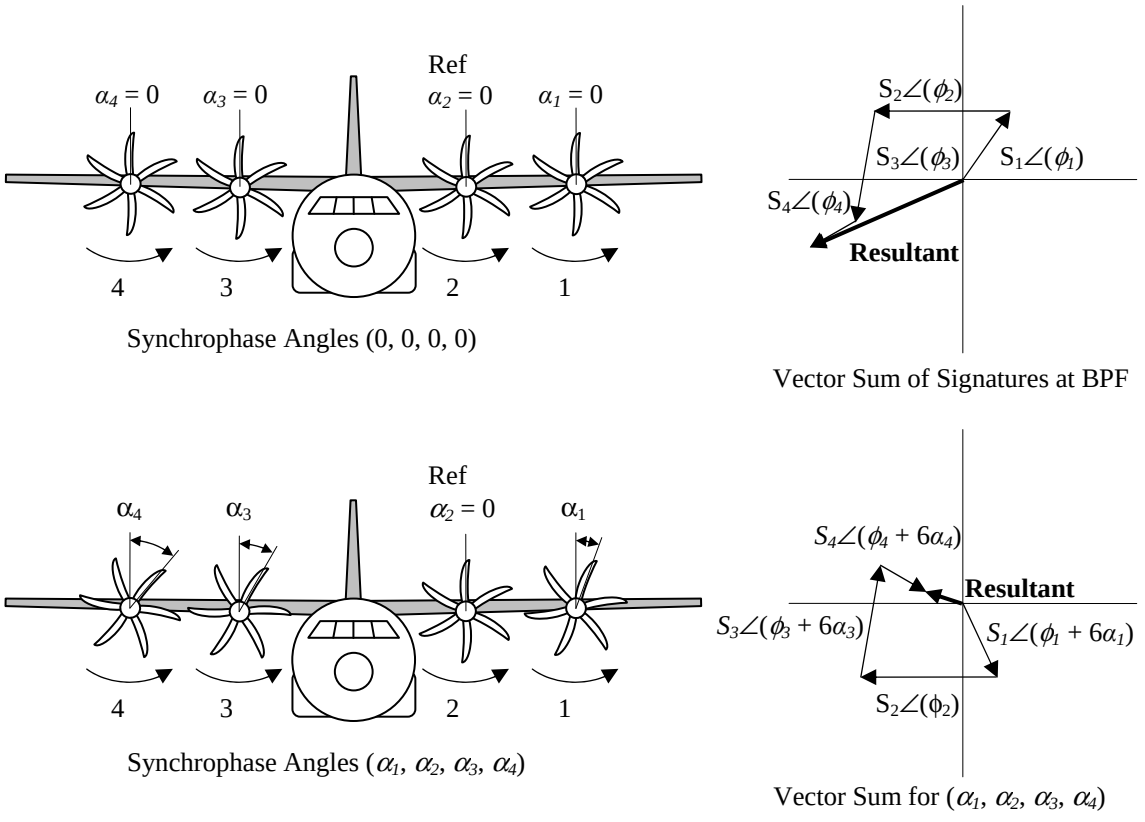

Figure 2.1 Propeller signature theory example adapted from Johnston et al. (1981).

Propeller signature theory uses an influence-coefficient approach to identify the contributions from the individual propellers. This is similar to measuring the influence coefficients in a balancing problem. Instead of a trial weight, a trial synchrophase angle is applied, and the change in the sound or vibration response is measured. The signatures are then calculated by solving the resulting system of linear equations. The minimum number of trial angle sets required is the same as the number of propellers. However, the system of equations can be more generally solved in a least-squares sense to minimise errors; i.e., with data from more angle sets than there are propellers.

Propeller signatures can also be calculated by shutting down an engine and feathering its propeller; i.e., by eliminating its contribution and measuring the change in amplitude and phase of the BPF noise or vibration at the sensor locations. However, this may not be feasible for safety-of-flight reasons, or if the power from the remaining engines needs to increase significantly in order to compensate for the engine that is shut down. Another method is to not synchronise the speeds of the propellers (i.e., to purposefully allow them to have beat frequencies), and to synchronously average the data with respect to the rotational frequency of each propeller in turn, as done by Magliozzi (1983). Essentially, this relies on the data being averaged over a period that is sufficiently long for the contributions from the other propellers to be attenuated to an acceptably low level (i.e., averaged out).

Johnston et al. (1981) applied propeller signature theory to data gathered from flight tests performed on a US Navy Lockheed P-3C Orion aircraft at Patuxent River, Maryland, in 1978. They analysed the noise and vibration signals at 12 different cabin locations (Figure 2.2). The signals were only recorded at one flight condition: straight and level flight at 20,000 ft with an indicated airspeed of 233 knots. The signals were sampled at several different times during a run with the synchrophaser switched off so that the phase relationships between the propellers would vary each time. Fourier analyses of the samples yielded the required data at the BPF (68 Hz) and its first two harmonics (136 Hz & 204 Hz). A software program was used to solve the resulting system of linear equations for the propeller signatures, and to predict the noise and vibration at each location for all combinations of synchrophase angles resulting from 5° steps in the propeller shaft angles; i.e., $(90/5)^3 = 5832$ combinations. The propeller signatures were validated by comparing the predicted levels with the measured levels from a synchrophasing run, and from two other runs in a second flight made three weeks later. The results were within 1 dB to 2 dB at the blade-pass frequency, but got progressively worse at the higher harmonics. The stated reason for this was that the sampling period was not locked to the actual propeller speed and the data at the higher harmonics suffered from frequency smearing. The effect of synchrophasing was found to be different at different locations. The largest effect was at Location 8 where the BPF sound pressure varied by more than 20 dB. This is the

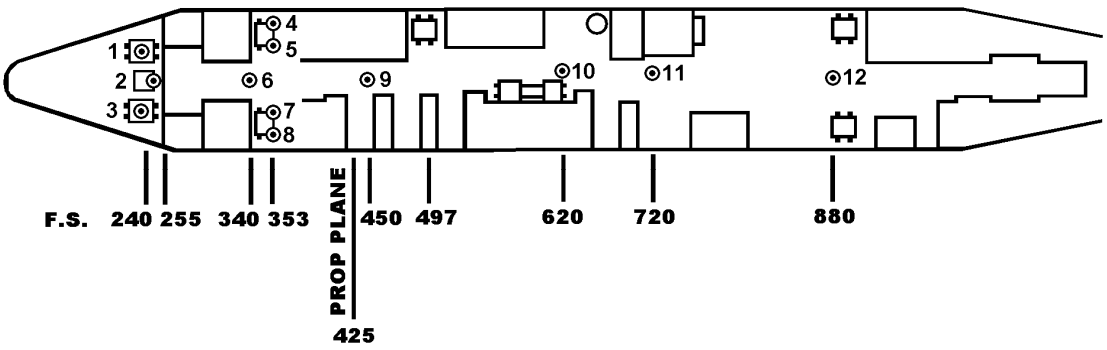

Figure 2.2 US Navy P-3C measurement locations (Johnston et al., 1981).

measurement location nearest to Propeller 2, where the down-going propeller blades are adjacent to the fuselage. The average BPF sound pressures for the best and worst synchrophase angle combinations were 94 dB and 103 dB respectively; i.e., a difference of 9 dB at this frequency. Similar results were found for vibration at the BPF. They concluded that:

a) Propeller synchrophasing varied the total energy inside the cabin; i.e., it did not just redistribute the noise and vibration.
b) The synchrophase angles that minimised the noise at the blade-pass frequency also minimised the vibration at this frequency.
c) The outboard propellers made significant contributions to the cabin noise and vibration.
d) There were setting errors of up to 15° in the existing synchrophasers.
e) The synchrophase angles oscillated by about ± 5° in smooth air, and that a tighter tolerance would achieve a higher noise and vibration reduction.
f) The signatures would have been more accurate if they were calculated from a number of different steady-state synchrophase angle sets rather than from a data set with continuously varying angles.
g) The optimum synchrophase angles were likely to change with changes in equipment and/or changes in the cabin acoustic space.

Magliozzi (1983) also used the propeller signature method to analyse the same P-3C data as Johnston et al. (1981), although he used a different technique to calculate the signatures. The propeller once-per-rev signal was multiplied by 400 to generate an external sampling clock input for an analyser, and the data were synchronously averaged to separate the signatures from each propeller. This approach still relied on the propellers turning at slightly different speeds when the synchrophaser was off. A computer program was used to systematically calculate the noise and vibration at the BPF and its first four harmonics for all combinations of the synchrophase angles resulting from 2° steps in the shaft angles (91,125 combinations). Synchrophasing was found to influence the total harmonic noise at the individual locations by between 15.9 dB (Location 5) and 28.6 dB (Location 1). Two optimisation criteria were used: minimisation of the average noise level over all locations, and minimisation of the noise at the maximum noise location. The calculated reductions were 8 dB and 10 dB respectively. However, the corresponding reductions from a two-engine analysis, in which the contributions from the outboard engines were eliminated, were only 1.5 dB and 3 dB. It was concluded that this was because there were fewer possibilities for the phase angle combinations to cancel over all 12 locations with two sources instead of four sources. Magliozzi also performed a sensitivity analysis and claimed that a synchrophaser accuracy of ± 3° to ± 5° was adequate to achieve this level of noise reduction in conventional propeller installations. However, this ignored any potential errors in the measurement of the propeller signatures, which may have been particularly significant at the higher harmonics, and was only based on the two-engine analysis.

2.3. Analytical Models of Synchrophasing

NASA commissioned an investigation of synchrophasing as a means of reducing aircraft interior noise in 1984. In this work, Fuller (1984a,b, 1986a,c) developed an analytical model of a simple twin-engined propeller aircraft configuration to understand the basic physical mechanism of noise suppression. The fuselage was modelled as an infinite cylindrical shell, and the propellers as dipole sources. The acoustic and structural response of the fluid-shell system was solved in a closed-form solution. The influence of

synchrophasing was assessed by varying the relative phase between the two sources. Fuller found that:

a) Synchrophasing reduced the sound and vibration levels.
b) The optimum synchrophase angle changed with interior location and frequency, and depended on whether the requirement was to suppress the interior acoustic field, the shell response, or the acoustic power flow into the shell.
c) The maximum amount of acoustic attenuation changed with location and frequency, but was greatest in the plane of the propellers.
d) Acoustic energy entered and left the shell in localised hot spots that changed with the synchrophase angle. It was suggested that active acoustic or vibration control could be applied to these hot spots to obtain greater attenuation.
e) The majority of acoustic energy entered the interior of the shell in a length of one shell diameter from the propeller plane and propagated to other locations as interior duct modes.

The coupling of the standing-wave response of the shell with the contained acoustic field was fundamental to the transmission mechanism. However, it should be noted that the coupling in this case would have been more selective than in a real fuselage due to the axisymmetric nature of the model (Hansen and Snyder, 1997, §9.13.12). Depending on its length, the response of a finite shell may also be significantly different to the infinite shell considered in the model.

Complementing the analytical work was an experimental investigation of synchrophasing using a closed cylindrical shell suspended in an anechoic chamber with two monopole sources (Jones, 1987; Jones and Fuller, 1984, 1986a,b). Three microphones were mounted inside the cylinder on a traversing mechanism and the modal response of the cylinder was measured by nine accelerometers mounted around the circumference in the propeller plane. The investigation found that:

a) The interior acoustic field was dominated by the sound levels in the plane of the propellers.
b) The optimum synchrophase angle and the degree of attenuation (10 dB to 34 dB) varied with location, and depended on the modal composition of the cylinder vibration and the coupling of each mode with the interior acoustic field.
c) The transmission of low-frequency sound into the shell was governed by the modal cylinder vibration instead of localised transmission.
d) The transmission of sound was strongly influenced by the near-field characteristics of the propeller sources.

Cylinder asymmetries (due to a joint in the cylinder construction) caused the circumferential modes of vibration to couple, and revealed that any structural modifications (such as the addition of a cabin floor) would affect the transmission of sound.

Predictions from the analytical model were also compared with experimental results from three other investigations in another paper (Fuller, 1986c). One of these was the P-3C synchrophasing study by Magliozzi (1983). Contributions from the outboard propellers were neglected, and the model did not incorporate structural features such as the cabin floor or wings. Results at a single location at the BPF and its first harmonic (68 Hz and 136 Hz) were presented, and Fuller reported that there was “surprisingly good agreement between the prediction of the model and Magliozzi’s results.”

In a later development, Fuller's original analytic model was modified to include a new propeller source model (Mahan and Fuller, 1985). This new source model attempted to replicate the fuselage surface trace velocity and pressure distribution that were observed on an Aero Commander aircraft. The model was deemed to give "adequate agreement" with the measured surface pressure distributions; however, there were still appreciable differences (up to 5 dB in relative SPL) that were attributed to: (a) the non-cylindrical shape of the real fuselage (in the circumferential direction), and (b) the propeller backwash (in the axial direction). The new propeller source model consisted of a pair of equal-strength dipoles that intersected each other at right angles, and were 90° out of phase with each other. This was termed a "virtually rotating dipole." The angular velocity of the rotating dipole was set to match the blade-pass frequency, or a harmonic of this frequency. The new source significantly changed the results predicted by the synchrophasing model. It was concluded that the results were very sensitive to the source model used, and the correct modelling of fuselage surface trace velocities was very important.

2.4. Adaptive Control of Synchrophase Angles

The following organisations have made investigations into the adaptive control of synchrophase angles:

a) United States Air Force Research Laboratory (AFRL)
b) National Aeronautics and Space Administration (NASA)
c) Fokker Aircraft
d) General Electric (GE)
e) United Technologies Corporation (UTC) – Hamilton Sundstrand
f) Institute of Sound and Vibration Research (ISVR), University of Southampton

The first three have developed and flight-tested prototype adaptive synchrophasing systems, while the last three have patented adaptive synchrophasing concepts.

2.4.1. Air Force Research Laboratory

The AFRL contracted Lockheed Martin Control Systems in 1999 to develop a prototype active synchrophasing system for the C-130 Hercules aircraft (Active Synchrophaser Program, 2002; Hammond et al., 1999). This system was designed for the T56-powered variants of the aircraft with four-bladed propellers, not the C-130J, which has Rolls Royce AE 2100D3 engines and six-bladed propellers (McKinley, 2004).

The AFRL C-130 active synchrophaser used the existing engine speed controller and propeller governor in conjunction with a new digital controller that replaced the existing synchrophaser. The new controller operated in two modes: a closed-loop mode, and an open-loop mode. In the closed-loop mode, it adjusted the synchrophase angles to minimise the total noise measured by an array of cabin microphones, although the number of microphones was not stated. In the open-loop mode, the controller maintained specific synchrophase angles between the propellers in order to reduce fly-over noise. However, no further details of the control algorithms, microphone locations, and other particulars of the system were published in the general literature. Flight tests of the system were completed in 2002. It was claimed that interior noise levels were reduced by 10 dB on average (Active Synchrophaser Program, 2002), and up to 22 dB in the cockpit during one phase of the testing (Success story, 2003), and that fly-over noise was reduced by 3 dB to 4 dB (McKinley, 2004). The system could also "move noise from one part of the fuselage to

another" (Active Synchrophaser Program, 2002), presumably by giving more weight to the measurements from microphones in the desired low-noise region.

McKinley (2004) stated that the low bandwidth and hysteresis in the existing hydro-mechanical propeller governor were the limiting factors of the system. He claimed that synchrophase angle tolerances of about 2° to 3° were achieved with the active synchrophaser, but that "0.5° of phase control should realize about 10 dB of flyover noise reduction and potentially 20 dB of cabin noise reduction." While tighter tolerance should improve the ability to stay close to the optimum synchrophase angles, no published work could be found to support this claimed level of additional noise reduction.

Background development for this system included a second-generation phase-locked-loop digital synchrophaser that was flight tested in a NASA Lewis Research Center OV-10A aircraft in 1995 (§2.4.2), and a digital active synchrophaser designed and flight tested in a commercial Beech 1900C aircraft by Lockheed Martin Control Systems (Hammond et al., 1999). Unfortunately, no further details of the Beech 1900C system were given, and no other references to this system could be found.

2.4.2. National Aeronautics and Space Administration

NASA developed a relatively simple adaptive synchrophaser for an OV-10A Bronco (Figure 2.3) twin turboprop aircraft (Pla et al., 1993). This aircraft has particularly high cabin noise levels, up to 130 dB near the passenger location, due to a strong blade-tip shockwave and the lack of any cabin trim (Pla et al., 1993). The system used an engine speed controller with two nested phase-locked loops connected to a single microphone in the cabin. The inner loop matched the speed of the slave engine to the master engine, and the outer loop adjusted the synchrophase angle of the slave propeller to minimise the noise at the microphone location. The microphone was manually moved to achieve the best results. In this approach, the noise contributions from each propeller were assumed to differ in phase only, not amplitude. While this would not matter in this single-dimensional case (i.e., one slave), it would not work well in a multi-dimensional case (i.e., two or more slaves), as some knowledge of the relative contributions from each propeller (e.g., outboard v. inboard) would be required to get the best results. Also, while a single microphone might work well in a relatively small cabin, it is probably less likely to do so in a large one. Both digital and analogue implementations of the controller were built, but only the analogue controller was flight tested. Synchrophasing control was achieved by replacing a fixed mechanical linkage between the power lever and the slave engine with a linear actuator with a limited stroke of 8 mm. This allowed fine control of the engine speed without compromising safety.

The flight tests were conducted at 200 knots at 6000 ft and a propeller speed of 95%.[2] A microphone position behind the passenger seat was found to give good results as measured by a number of additional monitoring microphones distributed throughout the aircraft. The minimised overall noise level behind the passenger seat for the first flight test (in September) was 12 dB (18 dB at the BPF of 95 Hz) lower than the maximised noise level at the same location, and 9.1 dB (15 dB at the BPF) lower than the beat-averaged noise level. The noise reductions at the other three monitoring microphone locations were −0.8 dB, −1 dB and 5 dB lower than the beat-averaged noise levels at these positions respectively, demonstrating that some global reduction was probably achieved. The optimum synchrophase angle was found to vary with the microphone location, and with the

[2] The maximum speed of the three-bladed propeller is 2000 rpm.

engine speed. It was also stated that dissimilar weather conditions in the second part of the trial (in January) caused a difference in the beat amplitude at this same passenger seat location, which was only 8 dB overall (10 dB at the BPF) on this occasion. Beats were said to be “much more pronounced in the OV-10A on a cold day than on a warm day.”

In further work, Goodman et al. (1995) reported using this active synchrophaser with a fixed synchrophaser angle to minimise exterior noise, where the angle was determined through flight tests. No results were reported in this paper, although it appears that the work was funded by the AFRL (Hammond et al., 1999). Hammond et al. (Hammond et al., 1999)claimed reductions of 3 dB to 5 dB in exterior noise levels and 10 dB to 15 dB in cockpit noise levels (§2.4.1).

Although simple, the OV-10A synchrophaser was able to adapt to changing flight conditions. In fact, it was claimed to remain locked-on through a series of transient and steady manoeuvres “well beyond what is encountered in normal commercial flight operation” (Pla et al., 1993). However, the stability of this type of controller would probably be reduced if the number of phase-locked loops was increased to cope with multiple microphones or more than two propellers.

2.4.3. Fokker

An element of adaptive control is incorporated in the Propeller Blade Matching System (PBMS) (Kaptein, 1991, 1992, 1994, 1996) of the Fokker 50 (Figure 2.4). However, the PBMS is designed to reduce the cabin vibration at the propeller rotational frequency instead of the BPF or its harmonics, and the synchrophase angle actually remains fixed. Since six-bladed propellers have six distinct relative shaft angles (separated by 60°) that yield the same synchrophase angle, the PBMS simply searches through these for the one that minimises the once-per-rev vibration in the cabin. The PBMS is claimed to control the propeller shaft speed to within ± 2 rpm and the shaft angle between the propellers to within ± 2° (Kaptein, 1992). A very similar method for minimising vibration at the propeller rotational frequency with a synchrophaser was patented by Magliozzi and Metzger (1992).

Blade-pass noise and vibration in the Fokker 50 are reduced through other means. Fokker claim that cabin noise levels are typically held below 77 dB(A) “using features that include slow-turning, six-bladed propellers and vibration absorbers” and that “no cumbersome active noise control is used” (Fokker 50 Aircraft Overview).

Figure 2.3 OV-10A Bronco. Credit: NASA/Sean Smith. Reproduced with permission.

Figure 2.4 Fokker 50 (Fokker 50). Credit: Ministry of Defence, Netherlands. Reproduced with permission.

2.4.4. General Electric

GE holds two synchrophasing patents (Pla, 1998; Pla and Goodman, 1993). The earlier patent describes the phase-locked loop method used in the NASA OV-10A aircraft (§2.4.2). However, the later patent describes a more sophisticated active synchrophasing concept. It discloses two main methods for noise reduction. Method 1 uses propeller signatures (§2.2), and is expected to lead to lower noise or vibration minimisation than is possible in Method 2. Method 2 uses a simpler gradient-descent approach without identifying the contributions from the individual propellers. It is thus easier to implement, but is not expected to perform as well as Method 1. It is not known whether the AFRL C-130 active synchrophaser uses the ideas in this patent, but it is a possibility given the links between AFRL and NASA, and NASA and GE. If it does, then it is considered more likely to use the approach outlined in Method 2. The two methods can be summarised as follows.

Method 1:

a) Calculate the propeller signatures from cabin noise measurements using any one of the following techniques:
    i) a multiple-phase-sets technique (as per Johnston et al. (1980)),
    ii) a synchronous-averaging technique (as per Magliozzi (1983)), or
    iii) an adaptive-filtering technique (using slightly different speeds to separate the signatures).
b) Use the signatures to predict the cabin noise levels for any desired combination of synchrophase angles.
c) Optimise the synchrophase angles to minimise an appropriate cost function (e.g., the predicted mean square pressure of several cabin microphones) using any one of the following techniques:
    i) a systematic evaluation of the cost function for all synchrophase angle combinations,
    ii) a gradient-descent technique (e.g., Least Mean Square, or Newton’s Method), or
    iii) an exact closed-form solution.
d) Adjust the synchrophase angles of the slave propellers to the optimum values.

Method 2:

a) Estimate the gradient of the noise with respect to each synchrophase angle.
b) Adjust the synchrophase angles by a predetermined small increment down the gradient.
c) Repeat the above steps until each gradient is within a limit.

The patent does not reference any other document that might illustrate the performance of either of these methods in a real aircraft, or provide a detailed comparison of the methods and techniques described within it. It is expected that Method 1 should perform better than Method 2 (i.e., achieve lower noise levels) because it identifies the contributions from each propeller, but the additional computational burden, and the techniques by which it is implemented, could well negate its perceived benefits. For example, Method 1 assumes that the propeller signatures are relatively unchanging and only need to be occasionally updated, but if this is not the case (i.e., they change significantly with varying flight conditions) then it may not be able to keep up and Method 2 may be a better option. Also, using an adaptive-filtering technique to identify the propeller signatures in conjunction with an adaptive gradient-descent technique to optimise the synchrophase angles will run

into the fundamental problem of trying to identify the system characteristics in the presence of a correlated control signal. Off-line identification of the signatures (i.e., with the optimisation switched off) would be the only reliable way around this problem, and would necessarily mean that the noise or vibration could not be continuously minimised. Another issue concerns the behaviour of the cost function. Pla claimed "it can typically be shown that the total mean square pressure is a single-minimum function of a phase function for the slave propellers generating the cancelling sound field." However, no supporting evidence for this was provided. Cost functions that have local minima require special consideration to ensure that the system will actually converge on the true global minimum. Clearly, significant further work is needed before such a system could be implemented reliably.

2.4.5. United Technologies Corporation

A patent assigned to UTC (Magliozzi, 1995) describes a method which basically automates Magliozzi's analysis of the P-3C data set (Magliozzi, 1983). This analysis was previously discussed in §2.2. The method can be summarised as follows:

a) Calculate the propeller signatures using a small set of known synchrophaser angles (at least P sets, where P is the number of propellers).
b) Use the signatures to predict the noise at each cabin microphone (or vibration at each accelerometer) for an extensive number of propeller angle combinations.
c) Search the predicted noise levels for an optimum set of angles that result in the lowest noise level.
d) Send the optimum angles to the synchrophaser.

While this approach can readily incorporate multiple propellers and microphones (or accelerometers), it has a number of limitations:

a) It requires reasonably steady-state flight conditions.
b) It has to be repeated whenever the flight conditions change sufficiently to alter the air-airframe-cabin response of the system. Hence, it may not be able to keep up if the system response changes too quickly.
c) No criteria are given for determining when the flight conditions have changed enough to warrant a new analysis.
d) It is very numerically intensive. For example, using increments of 2°, four four-bladed propellers will have 91,125 possible synchrophase angle combinations.
e) The identification of the propeller signatures necessarily requires the propellers to be operating at non-optimal phase settings for a period during each signature identification stage.

2.4.6. Institute of Sound and Vibration Research

Elliott and Nelson (1987) patented an active synchrophasing concept using multiple cabin microphones, adaptive propeller synchrophaser angles, and adaptive secondary sound sources (loudspeakers) in the aircraft cabin. This system used a gradient-descent algorithm to find the optimum synchrophaser angles, and the active noise control methods described in an earlier patent (Nelson and Elliott, 1985) to find the optimum loudspeaker contributions.

The concept was, however, only tested in a simple numerical simulation, not a real aircraft. This simulation used four microphones, two propellers and two loudspeakers. Simple filters were used to model the cabin acoustics and contributions from each propeller,

although no details were provided about how the filter coefficients were chosen. The simulation found two different optimum synchrophaser angles with the loudspeakers on and off, and predicted significant extra noise reduction with them on.

The lack of detail about the simulation makes it difficult to assess its accuracy. There may have been a connection to work done on a British Aerospace 748 aircraft (Bullmore, 1987; Bullmore et al., 1987), but this is not stated. While it showed some benefit from incorporating active synchrophasing into a more general active noise control system using secondary loudspeaker sources, the results in a real aircraft could be expected to be significantly different.

2.5. Research Gaps

It can be seen from the literature review that there are two sizeable gaps in the knowledge about propeller synchrophasing:

a) There is very little knowledge of how flight conditions, in particular altitude and airspeed, actually influence the ability of synchrophasing to minimise blade-pass noise and vibration in real aircraft cabins.

b) Although some active control techniques have been applied to synchrophasing, there have been no definitive attempts to establish an adaptive control methodology based on knowledge of these flight-condition effects.

These gaps are further explored in this thesis: the first through experimental investigations in the AP-3C and C-130J-30, discussed in Chapters 4–10; and the second through a detailed consideration of adaptive control techniques, including simple look-up tables and more complex error-sensor based approaches, in Chapter 11. However, to begin with, the following chapter provides a more detailed understanding of the problem through a discussion of the underlying theory.

3. Theory

This chapter discusses theory relevant to the transmission of noise into an aircraft cabin (i.e., of shell vibration and enclosed coupled sound fields), how active control can be applied to this problem, and introduces the mathematical basis of propeller signature theory.

Propeller noise is transmitted into an aircraft fuselage along multiple acoustic and structural paths. Acoustically, pressure waves from the propeller blades impinge directly on the fuselage, wing and tailplane surfaces causing them to vibrate. Structurally, propeller vibration passes through the engine mounts into the wing, and the wing and tailplane vibration passes into the fuselage. Finally, the fuselage vibration couples acoustically to the enclosed cabin space. The problem is therefore complex and governed by numerous different sets of equations.

A full analytical model of the way sound is transmitted into the cabin and the effect on synchrophasing on this transmission is not developed here. Others have developed relatively simple analytical models of the process (Fuller, 1984a,b, 1986a,b,c, 1987), as discussed in §2.3. However, a high-fidelity model of a real aircraft would quickly become very complex, as discussed below. The intention of this investigation is therefore to examine experimentally some of the factors affecting this process instead. Notwithstanding this, a review of the underlying theory allows a better understanding of the problem and the parameters that influence noise and vibration transmission in aircraft.

3.1. Shell Vibration

The simplest geometric shell similar to an aircraft fuselage is that of a closed thin circular cylinder. Of course, such a shell can never fully represent the effects of bulkheads and stiffeners found in most fuselages, nor can it account for the influence of a cabin floor, but it is still a representative starting point. Typical fuselage skin thicknesses of pressurised cabins are between 0.9 mm and 1.8 mm (0.036 in. to 0.070 in.).

The vibration of a cylinder is governed by an eighth-order system of partial differential equations. It is more complicated than that of a plate because of the coupling between the displacements in the three coordinate directions (axial, circumferential and radial). Various approximations and simplifications to the equations have been made by many authors over the years to make the problem more tractable. Leissa's (1973) monograph on the subject provides a comprehensive summary and discussion of the differences between the various theories. For unforced (free) vibration in a vacuum, he condensed the equations into the following matrix form

$$[L_{D-M}]\begin{bmatrix} u \\ v \\ w \end{bmatrix} + \frac{h^2}{12R^2}[L_{MOD}]\begin{bmatrix} u \\ v \\ w \end{bmatrix} = 0\,. \tag{3.1}$$

In this equation: the axial, circumferential and radial displacements are u, v and w respectively; h is the thickness, and R is the mid-point radius, of the shell; $[L_{D\text{-}M}]$ is a 3×3 matrix of differential operators for the simplest version of the theory, known as Donell-Mustari theory; and $[L_{MOD}]$ is another 3×3 matrix of differential operators required to modify the system of equations to match a more complicated version of the theory. The coordinate system used by Leissa is shown in Figure 3.1.

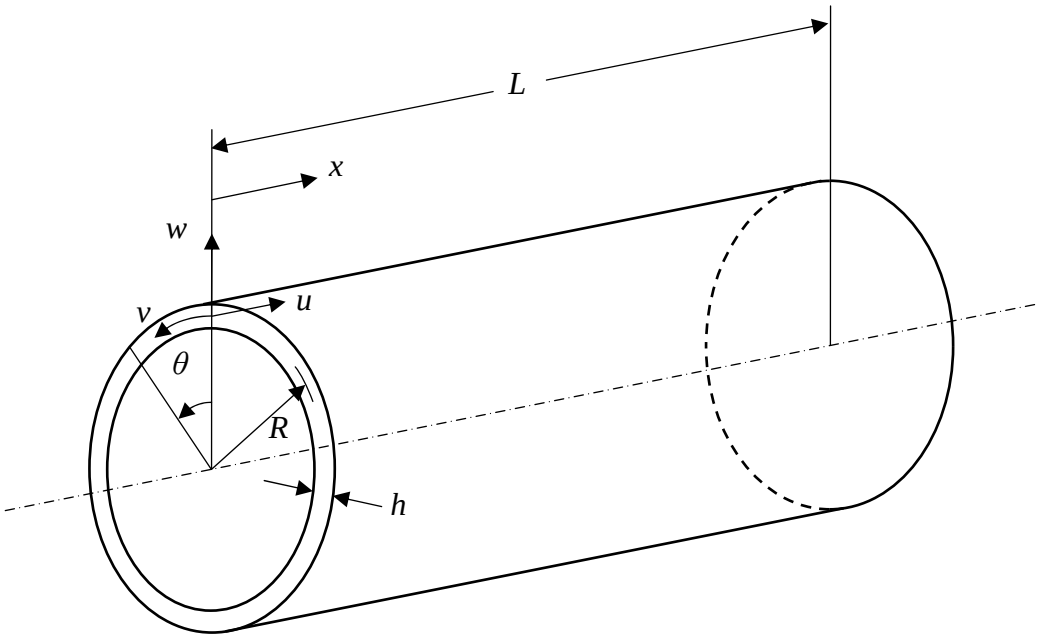

Figure 3.1 The coordinate system for a circular cylindrical shell used by Leissa (1993).

The Donell-Mustari operator (Leissa, 1973) is

$$[L_{D-M}]=\begin{bmatrix} \left(\dfrac{\partial^2}{\partial s^2}+\dfrac{(1-\upsilon)}{2}\dfrac{\partial^2}{\partial\theta^2}-\rho\dfrac{(1-\upsilon^2)R^2}{E}\dfrac{\partial^2}{\partial t^2}\right) & \dfrac{(1+\upsilon)}{2}\dfrac{\partial^2}{\partial s\partial\theta} & \upsilon\dfrac{\partial}{\partial s} \\ \dfrac{(1+\upsilon)}{2}\dfrac{\partial^2}{\partial s\partial\theta} & \left(\dfrac{(1-\upsilon)}{2}\dfrac{\partial^2}{\partial s^2}+\dfrac{\partial^2}{\partial\theta^2}-\rho\dfrac{(1-\upsilon^2)R^2}{E}\dfrac{\partial^2}{\partial t^2}\right) & \dfrac{\partial}{\partial\theta} \\ \upsilon\dfrac{\partial}{\partial s} & \dfrac{\partial}{\partial\theta} & \left(1-\dfrac{h^2}{12R^2}\nabla^4+\rho\dfrac{(1-\upsilon^2)R^2}{E}\dfrac{\partial^2}{\partial t^2}\right) \end{bmatrix}, \qquad (3.2)$$

where s is a non-dimensional axial length/radius ratio

$$s=\frac{x}{R},$$

θ is the cylindrical angle, ρ is the mass density per unit volume, υ is Poisson's ratio, E is Young's modulus, and

$$\nabla^4=\nabla^2\nabla^2,$$

$$\nabla^2=\frac{\partial^2}{\partial s^2}+\frac{\partial^2}{\partial\theta^2}.$$

The more complicated Goldenveizer-Novozhilov theory, which is also equivalent to Arnold-Warburton theory, is recommended for the analysis of sound transmission into

cylindrical enclosures (Hansen and Snyder, 1997, §2.3.5). In this case, the [L_{MOD}] operator is (Leissa, 1973)

$$[L_{MOD}] = \begin{bmatrix} 0 & 0 & 0 \\ 0 & 2(1-\upsilon)\dfrac{\partial^2}{\partial s^2} + \dfrac{\partial^2}{\partial \theta^2} & -(2-\upsilon)\dfrac{\partial^3}{\partial s^2 \partial \theta} - \dfrac{\partial^3}{\partial \theta^3} \\ 0 & -(2-\upsilon)\dfrac{\partial^3}{\partial s^2 \partial \theta} - \dfrac{\partial^3}{\partial \theta^3} & 0 \end{bmatrix}. \tag{3.3}$$

The most frequently discussed solutions to these equations are those for shear diaphragm end conditions; i.e., those where the cylinder can be considered to have thin, flat, circular end plates that support shear forces, preventing motion in the radial and circumferential directions, but not bending moments or axial forces. These boundary conditions can be summarised as

$$v = w = M_x = N_x = 0 \quad \text{at} \quad x = 0, L$$

where M_x is the bending moment, and N_x is the force, in the axial direction.

The solutions for shear diaphragm end conditions take the form (Arnold and Warburton, 1949)

$$\begin{Bmatrix} u = U\cos\left(\dfrac{m\pi x}{L}\right)\cos(n\theta)\cos(\omega t) \\ v = V\sin\left(\dfrac{m\pi x}{L}\right)\sin(n\theta)\cos(\omega t) \\ w = W\sin\left(\dfrac{m\pi x}{L}\right)\cos(n\theta)\cos(\omega t) \end{Bmatrix}, \tag{3.4}$$

where m is the number of axial half-waveforms, n is the number of circumferential waveforms, and ω is the frequency of vibration in radians per second. U, V and W are the respective amplitudes of the vibration in the coordinate directions. Some of the low-order radial mode shapes for these end conditions are shown in Figure 3.2, where the light areas represent bulges in the surface and the dark areas depressions. The $n = 0$ and $n = 1$ modes are sometimes referred to as the axisymmetric and beam-bending modes respectively.

Substituting Equation (3.4) into Equation (3.1) yields a system of equations representing an eigenvalue problem for which the characteristic equation is a cubic in ω^2 (Arnold and Warburton, 1949). This characteristic equation can be written as (Leissa, 1973)

$$\Omega^6 - (K_2 + \kappa\Delta K_2)\Omega^4 + (K_1 + \kappa\Delta K_1)\Omega^2 - (K_0 + \kappa\Delta K_0) = 0, \tag{3.5}$$

where

$$\begin{Bmatrix} K_2 = 1 + \dfrac{1}{2}(3-\upsilon)(n^2+\lambda^2) + \kappa(n^2+\lambda^2)^2 \\ K_1 = \dfrac{1}{2}(1-\upsilon)\left[(3+2\upsilon)\lambda^2 + n^2 + (n^2+\lambda^2)^2 + \dfrac{(3-\upsilon)}{(1-\upsilon)}\kappa(n^2+\lambda^2)^3\right] \\ K_0 = \dfrac{1}{2}(1-\upsilon)\left[(1-\upsilon^2)\lambda^4 + \kappa(n^2+\lambda^2)^4\right] \end{Bmatrix} \tag{3.6}$$

are the constants arising from Donnel-Mushtari theory,

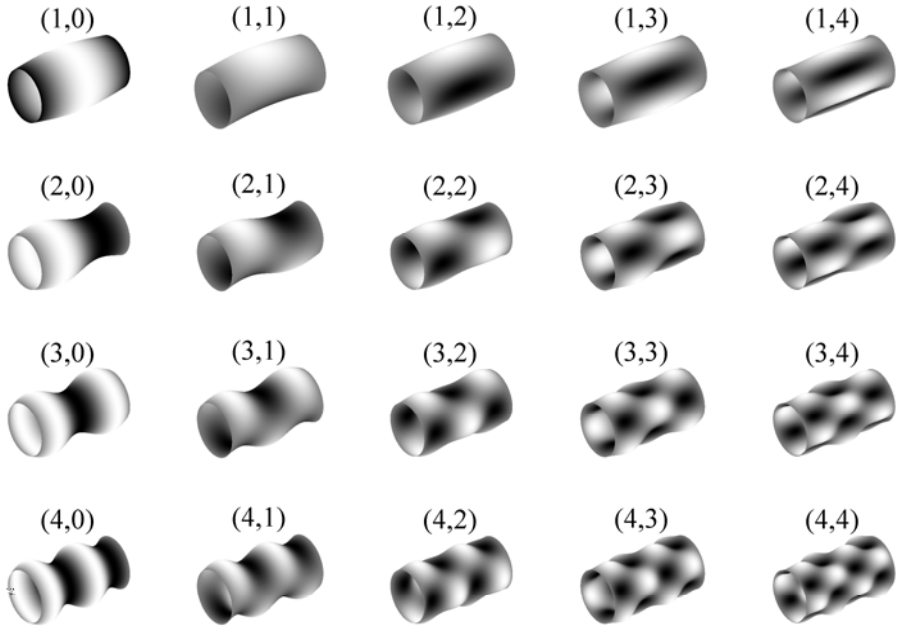

Figure 3.2 Radial mode shapes (m, n) *of a circular cylinder with shear diaphragm end conditions, where* m *is the number of axial half-waveforms, and* n *is the number of circumferential waveforms.*

$$\left\{\begin{aligned}\Delta K_2 &= 2(1-\upsilon)\lambda^2 + n^2 \\ \Delta K_1 &= 2(1-\upsilon)\lambda^2 + n^2 + 2(1-\upsilon)\lambda^4 - (2-\upsilon)\lambda^2 n^2 - \frac{1}{2}(3+\upsilon)n^4 \\ \Delta K_0 &= \frac{1}{2}(1-\upsilon)\left[4\left(1-\upsilon^2\right)\lambda^4 + 4\lambda^2 n^2 + n^4 - 2(2-\upsilon)(2+\upsilon)\lambda^4 n^2 - 8\lambda^2 n^4 - 2n^6\right]\end{aligned}\right\} \tag{3.7}$$

are the modifying constants for Goldenveizer-Novozhilov (Arnold-Warburton) theory, and

$$\Omega^2 = \rho\left(1-\upsilon^2\right)R^2\omega^2/E\,, \tag{3.8}$$

$$\kappa = \frac{h^2}{12R^2}, \tag{3.9}$$

and

$$\lambda = \frac{m\pi R}{L} \tag{3.10}$$

are the non-dimensional frequency, thickness and wavelength parameters respectively. Note that the speed of sound in a two-dimensional solid (i.e., a thin shell) is (Hansen and Snyder, 1997, §2.1.10)

$$c_s = \sqrt{\frac{E}{\rho\left(1-\upsilon^2\right)}}\,, \tag{3.11}$$

so Equation (3.8) can also be written as

$$\Omega = \frac{\omega R}{c_s}. \tag{3.12}$$

The characteristic equation yields three natural frequencies and three ratios of *U/W* and *V/W* for each combination of *m* and *n*. For thin shells, the lowest of these frequencies, referred to as the fundamental frequency, corresponds to the mode shape with the most bending and least stretching of the shell; i.e., the mode shape where the radial displacement is dominant (*U/W*, *V/W* << 1). The other two natural frequencies correspond to mode shapes with considerably more stretching of the shell in the circumferential and axial directions in proportion to the radial direction. These consequently have much higher strain energies and natural frequencies, and are typically beyond the audible range. Because of this, and the reduced radial displacement at these higher natural frequencies, they are not of interest in the sound transmission problem.

It is interesting to note that the ratio of bending to stretching energy is particularly important in shell vibration where there are shear diaphragm (clamped) end conditions, as these force the cylinder to remain circular at the ends. This leads to more stretching of the shell in the vicinity of the ends for modes with a low number of circumferential nodes, and it can cause the fundamental natural frequency of these modes to be significantly higher than those with more circumferential nodes, which is somewhat counterintuitive. This effect is more pronounced as *R/h* increases and *L/(mR)* decreases. A number of graphs illustrating this phenomenon can be found in Arnold and Warburton (1949) and Leissa (1973).

The easiest way to incorporate the effects of longitudinal and circumferential fuselage stiffeners into a cylindrical shell model is to smear the effects of these stiffeners over the entire shell. This is done by modifying the equations of motion to incorporate different stress-strain relationships in the axial and circumferential directions; i.e., by making the shell orthotropic instead of isotropic. However, this approximation is only acceptable if the wavelengths of interest are long compared to the spacing between the stiffeners. If this is not the case, then the stiffeners have to be modelled explicitly, and coupled to the motion of the shell. From this, it can be appreciated that any real aircraft fuselage very quickly becomes exceedingly complex to model as features such as floors, bulkheads, doors, and ramps are added to the basic cylinder.

Kalinins and Dym (1976) provided an overview of the analysis methods that can be used to find the forced response of a shell to a time-dependent load. They divided these methods into two categories: the response to steady-state (i.e., periodic) loads, where the transient vibration has died away to zero, and the response to transient loads. In the former, the solution can be found by representing the load as a Fourier series, separately solving the equations of motion for each Fourier component, and superimposing the results. In the latter case, the transient solutions must be found using methods that incorporate some form of numerical integration, such as a finite-difference method. In both cases, the vibration of the shell can be expressed as a weighted sum of the structural modes determined under free-vibration conditions.

3.2. Enclosed Sound Fields

The transmission of sound from a vibrating aircraft fuselage into the enclosed cabin space is governed by the nature of the coupling that occurs between the structural modes of the fuselage and acoustic modes of the enclosure. Typically, the coupling in regular or symmetrical geometries is far more selective than that in irregular geometries. For example, the coupling in a finite circular cylinder is limited to those modes where the circumferential orders are the same, and the axial orders are an even/odd combination (Li et al., 2002). However, when the cylinder has a single flat partition, representing a cabin

floor, the partition prevents the formation of axisymmetric acoustic modes (Hansen and Snyder, 1997, §9.13.2), and while the coupling in the axial direction remains the same, the coupling in the circumferential direction is no longer limited to those modes with the same circumferential order (Li et al., 2002). This allows a single structural mode to couple with many acoustic modes, and vice versa. The degree of coupling present between any pair of structural and acoustic modes will be dependent on both their geometric alignment and the proximity of their natural frequencies.

There are two mechanisms by which the interior sound level in a coupled enclosure can be reduced: structural modal amplitude control, and structural modal rearrangement control (Hansen and Snyder, 1997, §9.7). Which mechanism can be employed depends on the type of coupling that exists between the acoustic and structural modes. In systems where the acoustic response is dominated by a single structural mode, or where the coupling is limited to pairings between acoustic and structural modes, the amplitudes of the offending structural modes must be reduced in order to reduce the sound level. However, in systems where an acoustic mode is coupled to more than one structural mode, the amplitude of the acoustic mode can also be reduced by changing the relative amplitudes and phases of the associated structural modes without necessarily decreasing the amplitudes of these modes. In fact, the overall structural vibration may increase. From this, it is apparent that modal rearrangement is the most likely mechanism by which synchrophasing can achieve global cabin noise reduction.

Many analytical models of coupled enclosures use modal coupling theory. In this theory, if the enclosure is not too small and the fluid is not too dense, as is generally the case in an aircraft fuselage, the coupling can be considered weak and the model can be simplified by coupling the *in vacuo* vibration modes of the structure to the rigid-walled acoustic modes of the enclosure (Hansen and Snyder, 1997, §9.7). For a finite-length circular cylinder, the *in vacuo* structural mode shapes are given by (Hansen and Snyder, 1997, §9.7)

$$\psi_{m,n}(x,\theta) = \sin\left(\frac{m\pi x}{L}\right)\cos(n\theta), \tag{3.13}$$

where m and n are the axial and circumferential modal indices respectively, and L is the cylinder length. The rigid-walled acoustic mode shapes are given by (Hansen and Snyder, 1997, §9.7)

$$\varphi_{a,b,c}(x,\theta,r) = \cos\left(\frac{a\pi x}{L}\right)J_b\left(\frac{\gamma_{b,c}r}{R}\right)\cos(b\theta), \tag{3.14}$$

where a, b and c are the acoustic axial, circumferential, and radial modal indices respectively, R is the cylinder radius, J_b is a Bessel function of the first kind of order b, and $\gamma_{b,c}$ is the c^{th} zero of the derivative of J_b; i.e.,

$$J_b'(\gamma_{b,c}) = 0. \tag{3.15}$$

Equations (3.13) and (3.14) also have degenerate equivalents where $\cos(n\theta)$ and $\cos(b\theta)$ can be replaced by $\sin(n\theta)$ and $\sin(b\theta)$ respectively. Note that the spatial distribution of the acoustic nodes in the radial direction is dependent on the Bessel function order, b, and thus on the number of circumferential nodes.

The coupling coefficients, $B_{(m,n)(a,b,c)}$, between the (m, n) structural mode and the (a, b, c) acoustic mode are given by (Hansen and Snyder, 1997, §9.7.4)

$$B_{(m,n)(a,b,c)} = \begin{cases} \dfrac{J_b(\gamma_{b,c})}{2L} \dfrac{\varepsilon_b \left(\dfrac{m\pi}{L}\right)\left(1-(-1)^{m+a}\right)}{\left(\dfrac{m\pi}{L}\right)^2 - \left(\dfrac{a\pi}{L}\right)^2} & b = n, \dfrac{m+a}{2} \neq \text{integer} \\ 0 & \text{otherwise} \end{cases}, \tag{3.16}$$

where

$$\varepsilon_a = \varepsilon_b = \begin{cases} 2 & a,b = 0 \\ 1 & a,b > 0 \end{cases}. \tag{3.17}$$

It can be seen from Equation (3.16) that the structural and acoustic modes only couple if the circumferential modal indices *b* and *n* are the same, and the axial modal indices *m* and *a* are an odd-even combination, as previously discussed.

3.3. Active Control

Active noise control in a coupled enclosure, such as an aircraft fuselage, can be achieved using vibration or acoustic control sources, and vibration or acoustic error sensors. Which type of control source has the better ability to control the noise depends largely on whether the system is dominated by structural or acoustic resonances (Hansen and Snyder, 1997, §9.8). Which type of error sensor is best depends mostly on what type of control source is used. In general, acoustic control sources require acoustic error sensors, but vibration control sources can use either. However, using mixed control sources and error sensors is often more difficult because each structural mode usually couples to more than one acoustic mode and vice versa. This cross coupling of vibration and acoustic modes can lead to undesirable spill-over effects; i.e., a decrease in the amplitude of one mode, but an increase in another.

The degree to which an analytical model accurately represents an aircraft cabin is very important when it comes to developing active noise control systems for real aircraft. This is because the performance of the active control system is highly dependent on the location of the control sources and error sensors (Hansen and Snyder, 1997, §9.8). The relationships between these variables and the reduction in cabin acoustic potential energy are non-linear. Hence, the model must be able to predict local fuselage vibration and cabin noise levels very accurately in order to assist in the placement of control sources and error sensors; even moderate simplification of the model may lead to large errors. Effectively, this means that very detailed finite-element models of the *in vacuo* structural vibration and rigid-walled enclosure acoustics must be used (Hansen and Snyder, 1997, §9.13.2) in conjunction with accurate external forcing functions (Mahan and Fuller, 1985).

With adaptive synchrophasing, there is no ability to change the location of the control source. The only decisions to make are what type of error sensors to use and where to place them. Since synchrophasing must rely on modal rearrangement to achieve global noise reductions, and the overall level of structural vibration may therefore not decrease, acoustic error sensors appear to be the better choice. The decision about where to place these sensors is more difficult without prior knowledge of how the internal sound field actually varies with the synchrophase angles. In the absence of a validated analytical model, this must be measured experimentally. Since this is very time, labour, and cost intensive, and as the objective is usually to minimise noise at particular locations, such as the pilot, aircrew, or passenger seats, it makes sense initially to place as many acoustic error sensors at these

locations as possible for system characterisation purposes. The final number and placement of actual sensors can then be refined later.

Overall, the potential for global noise reduction in enclosed sound fields is greatest in systems where the acoustic response can be represented by a small number of acoustic modes; i.e., in systems with a low modal density. Modal density is defined as the average number of resonance frequencies per unit frequency. As the modal density is increased, the potential for global noise reduction is reduced; i.e., good control of a few modes is achieved at the expense of noise spilling over into other modes.

The modal density, *n(f)*, of an aircraft cabin can be roughly estimated using the equation for a rectangular enclosure (Bies and Hansen, 1988):

$$n(f) = \frac{4\pi f^2 V}{c^3} + \frac{\pi f A}{2c^2} + \frac{P}{8c}, \tag{3.18}$$

where V is the volume, A is the total surface area, and P is the total perimeter (length of all edges) of the enclosure, and c is the speed of sound. Using the dimensions of the AP-3C and C-130J-30 cabins shown in Table 3.1, and a speed of sound of 340 m/s, the approximate modal densities of these two aircraft cabins are 0.5 resonances/Hz and 0.8 resonances/Hz at their respective blade-pass frequencies (68 Hz & 102 Hz). These could be considered moderately low modal densities as long as the average 3 dB modal bandwidths, Δf, of any resonances in the vicinity of these frequencies are relatively narrow, and the modal overlap, defined as

$$M(f) = n(f)\Delta f\ , \tag{3.19}$$

is correspondingly low (< 1). Fewer error sensors would be required in this situation.

In systems with a high modal density, only localised noise control is possible. Localised control is characterised by a “zone of quiet” around each error sensor. The diameter of this zone in a diffuse (or modally dense) sound field, when defined as a 10 dB reduction, is approximately one tenth of the wavelength under control (Elliott and Nelson, 1993; Elliott et al., 1988). This makes this form of control only practical for frequencies up to about 100 Hz in a modally dense sound field.

If the modal densities of the sound fields within the AP-3C and C-130J-30 cabins at their respective blade-pass frequencies are not as low as the above estimates, then the zone-of-quiet diameters could be as small as 0.50 m and 0.33 m respectively. These diameters would need to be further divided by 2, 3, 4, etc. at the harmonics of these frequencies. Synchrophasing would have far less potential for global noise and vibration reduction in this situation, particularly at the harmonics of the blade-pass frequencies, and many more error sensors would be required.

Table 3.1 AP-3C and C-130J-30 main cabin dimensions (Jane's, 2009a,b).

	AP-3C	**C-130J-30**
Length (m)	21.06 (from rear of flight deck to rear bulkhead)	16.76 (main cabin excluding flight deck and rear cargo ramp)
Max. Width (m)	3.30	3.12
Max. Height (m)	2.29	2.74

3.4. Propeller Signatures

Propeller signatures identify the contributions of each propeller to the noise or vibration at the BPF (or its harmonics), at particular locations within the aircraft cabin. These contributions are measured experimentally and do not distinguish between transmission paths. The technique is similar to measuring influence coefficients in a balancing problem. Instead of a trial weight, a trial synchrophase angle is applied, and the change in acoustic or vibration response is measured. This circumvents the need to model the system analytically with all its inherent complexity. Based on the published results (Johnston et al., 1981; Magliozzi, 1983), the technique appears to work well but it could bear further verification.

Using propeller signatures, the effect of synchrophasing on the BPF noise at each location can be predicted by changing the phase of the signatures and performing a vector addition. Mathematically, this can be expressed as

$$\hat{A}_k = \sum_{p=1}^{P} \hat{S}_{k,p} e^{iB\alpha_p} \,, \tag{3.20}$$

where $\hat{A}_k$ is a complex number representing the amplitude and phase of the BPF noise at location k, $\hat{S}_{k,p}$ is the signature of propeller p at location k, α_p is the synchrophase angle of propeller p in radians, B is the number of blades on the propeller, and P is the number of propellers. A whole multiple of B can be used for the harmonics of the BPF. In matrix notion this becomes

$$\begin{bmatrix} \hat{A}_1 \\ \hat{A}_2 \\ \vdots \\ \hat{A}_K \end{bmatrix} = \begin{bmatrix} \hat{S}_{1,1} & \hat{S}_{1,2} & \cdots & \hat{S}_{1,P} \\ \hat{S}_{2,1} & \hat{S}_{2,2} & \cdots & \hat{S}_{2,P} \\ \vdots & \vdots & \ddots & \vdots \\ \hat{S}_{K,1} & \hat{S}_{K,1} & \cdots & \hat{S}_{K,P} \end{bmatrix} \times \begin{bmatrix} e^{iB\alpha_1} \\ e^{iB\alpha_2} \\ \vdots \\ e^{iB\alpha_P} \end{bmatrix}$$

or

$$\vec{A} = \mathbf{S} \times \vec{\beta} \,, \tag{3.21}$$

where $\vec{A}$ is a column vector of complex numbers representing the BPF noise at K locations, $\mathbf{S}$ is a $K \times P$ matrix of complex numbers representing the propeller signatures, and $\vec{\beta}$ is a column vector of P complex unit vectors with phase angles equal to $B\alpha_p$.

To solve this equation for $\mathbf{S}$ requires measurements for at least P linearly independent sets of synchrophase angles. When there are measurements for more than P sets, the system is over-determined. In this case, the least-squares solution (Appendix A) for the propeller signatures, $\mathbf{S}_{LS}$, can be obtained from

$$\mathbf{S}_{LS} = \mathbf{A}\,\boldsymbol{\beta}^H \left[\boldsymbol{\beta}\,\boldsymbol{\beta}^H\right]^{-1}, \tag{3.22}$$

where $\mathbf{A}$ is a $K \times Q$ matrix of measurements, $\boldsymbol{\beta}$ is a $P \times Q$ matrix of phase angle vectors, and $\boldsymbol{\beta}^H$ is the Hermitian (or complex conjugate) transpose of $\boldsymbol{\beta}$, and Q is the number of synchrophase angle sets.

3.4.1. Propeller Signature Examples

Two hypothetical examples are presented as follows. The signatures for both are listed in Table 3.2, where the propellers are numbered left to right as viewed from behind the aircraft.

In the first example, the BPF noise at a single cabin location is estimated for a typical military aircraft over a range of synchrophase angle combinations. The signature amplitudes have been chosen so that the outboard propellers (1 & 4) contribute less than the inboard propellers (2 & 3); and the port inboard propeller (2) contributes more than the starboard inboard propeller (3), for the reason outlined in §2.1.

The predicted Sound Pressure Level (SPL) at the BPF for Example 1 is plotted two-dimensionally in Figure 3.3 for 1728 different synchrophase angle combinations of the three slave propellers. In the figure, the phase of each slave propeller is sequentially incremented starting with Propeller 4, then Propeller 3, and finally Propeller 1; i.e., there are 12 steps of Propeller 4 for every increment of Propeller 3, and 144 combinations of Propeller 4 and 3 for every step of Propeller 1. The peak level of 104.7 dB occurs at Combination 1 (0°, 0°, 0°, 0°), and the minimum level of 88.8 dB occurs at phase angle Combination 943 (180°, 0°, 180°, 180°); a difference of 15.9 dB. Note that the signatures have been chosen so that the maximum and minimum levels coincide exactly with the selected step size. This would not generally be the case.

The results for Example 1 are also plotted three-dimensionally in Figure 3.4. Here, the *x*, *y* and *z* axes represent the phase of the contributions from the three slave propellers at the BPF (i.e., $B\alpha_1$, $B\alpha_3$, $B\alpha_4$), and the colour axis represents the sound pressure. Slices through the mid-points of the axes highlight the minimum of 0.55 Pa (88.8 dB) in the centre of the plot, and the maximum of 3.45 Pa (104.7 dB) in the outer corners of the plot.

A feature to note about this example is that the minimum occurs at a unique synchrophase angle combination (180°, 0°, 180°, 180°). This is because the sum of the amplitudes of the three slave propeller signatures (0.35 + 0.75 + 0.35 = 1.45 Pa) is less than the amplitude of the master propeller signature (2 Pa). If this were not the case, a sound pressure of 0 Pa could be achieved with a range of synchrophase angles. This is illustrated in Example 2, where the propeller signatures are all equal. In the three-dimensional view shown in Figure 3.5, it can be seen that the locus of phase angles giving a sound pressure of 0 Pa zigzags its way across the phase-angle space.

Table 3.2 Example propeller signatures.

	Propeller	**1**	**2 (Ref)**	**3**	**4**
Example 1	Sound Pressure (Pa)	0.35	2.00	0.75	0.35
	Sound Pressure Level (dB)	84.9	100	91.5	84.9
	Phase	0°	0°	0°	0°
Example 2	Sound Pressure (Pa)	1.00	1.00	1.00	1.00
	Sound Pressure Level (dB)	94.0	94.0	94.0	94.0
	Phase	0°	0°	0°	0°

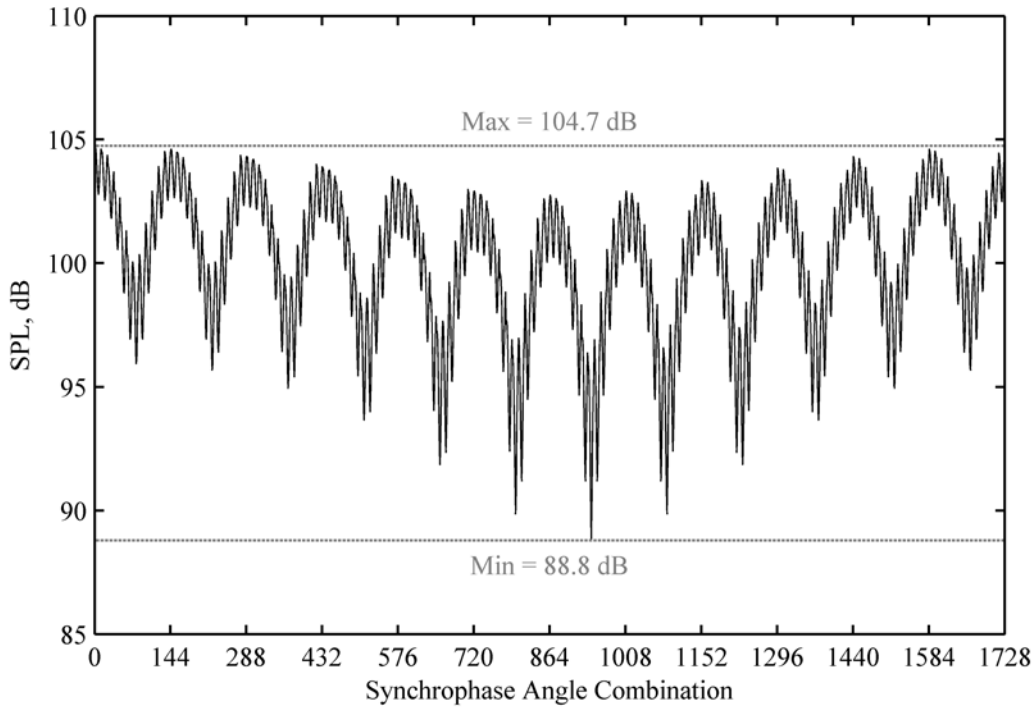

Figure 3.3 Predicted spectrum level at the BPF for Example 1.

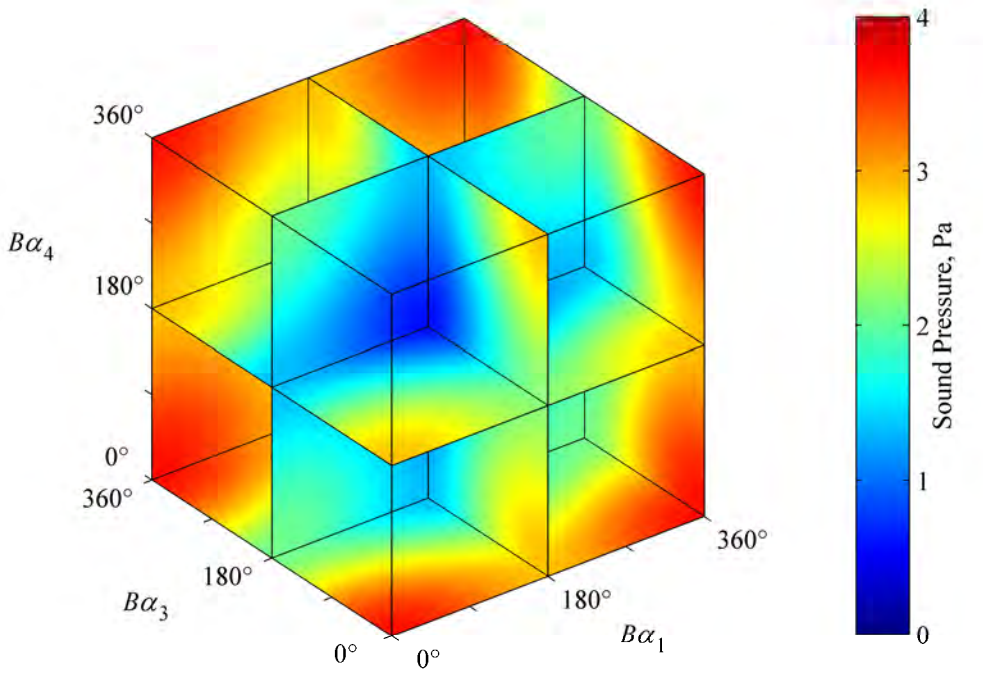

Figure 3.4 Predicted sound pressure at the BPF for Example 1.

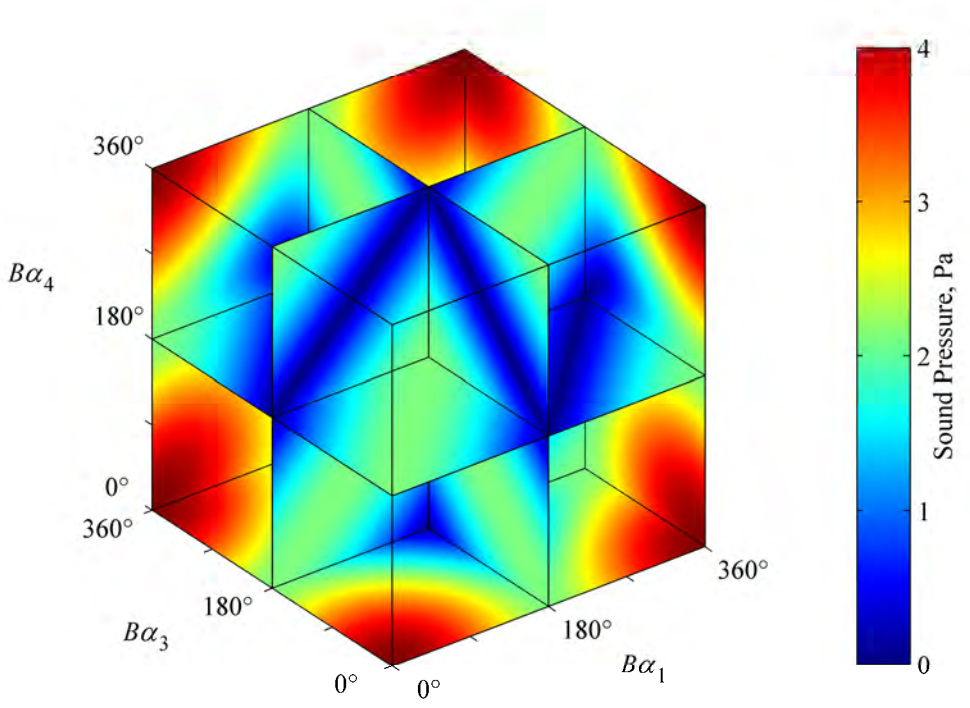

Figure 3.5 Predicted sound pressure at the BPF for Example 2.

4. Synchrophasing Systems

This chapter provides a brief description of the typical synchrophasing systems found in turboprop aircraft, and in particular the systems found the trial aircraft. It also describes the modification to the AP-3C synchrophaser that was made to facilitate changing the synchrophase angles during flight.

Turboprop aircraft are typically fitted with constant-speed variable-pitch propellers; i.e., the rotational speed of the propeller is nominally fixed, and the thrust is varied by changing the pitch of the propeller blades. There may, however, be more than one fixed speed; e.g., a higher speed at take-off, and a lower speed at cruise. Control of the synchrophase angles is typically attained through fine adjustment of the blade pitch. This allows the propeller to speed-up or slow-down within preset limits until the desired synchrophase angle is achieved. It has a minimal effect on thrust since the engine power is not changed.

The following sections provide brief general descriptions of the synchrophasing systems found in the P-3C and C-130J aircraft. While these systems have some attributes that are unique to these aircraft, the underlying principles of operation are similar to many, if not all, turboprop aircraft.

Both the P-3C and C-130J synchrophasing systems use a master-slave relationship; i.e., one of the inboard propellers is designated the master propeller, and the remaining propellers are slaved in speed and shaft angle to this propeller. The main difference between the systems is that the former is analogue and the latter is digital. Digital control is typically claimed to produce faster responses, and tighter speed and synchrophase angle tolerances. A newer digital Electronic Propeller Control System (EPCS) is available for the four-bladed 54H60 propeller found on the P-3C (Adams, 2007), but no RAAF aircraft have been upgraded to this system.

Other differences between the P-3C and C-130J synchrophasing systems include:

a) four-bladed (P-3C) versus six-bladed (C-130J) propellers;
b) the use of once-per-rev (P-3C), or six-per-rev (C-130J) tachometer signals;
c) whether the synchrophase angles are specified as positive and negative angles (P-3C), or just positive angles (C-130J); and
d) the opposite sense of direction of the angles, positive leading the master propeller (P-3C), or positive lagging the master propeller (C-130J).

Note that, due to symmetry, it is theoretically possible for a *B*-bladed propeller to have *B* distinct shaft angles that give the same synchrophase angle. The C-130J synchrophaser can randomly adopt any one of these shaft angles, as shown in Figure 4.1, however it is known that the P-3C cannot (i.e., it always adopts the same shaft angle).

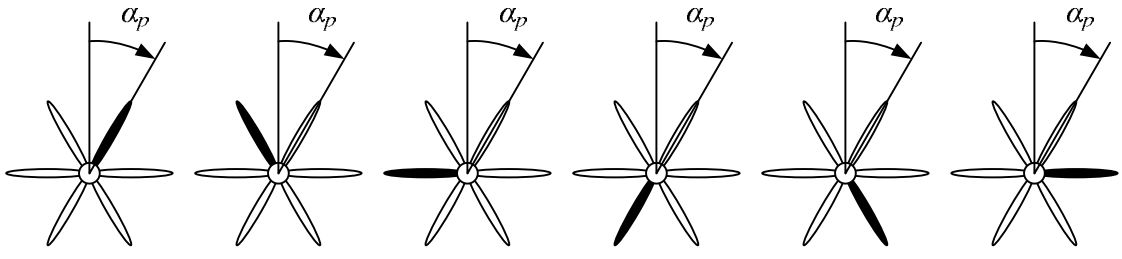

Figure 4.1 Propeller orientations (note the position of the black blade) that give the same synchrophase angle, α_p, for a six-bladed propeller.

4.1. P-3C Synchrophasing System

The P-3C engines and propellers have older-style hydro-mechanical control systems. In normal operation, the propellers automatically adopt a blade pitch, and hence load on the engine, that maintains a propeller rotational speed of 1020 rpm. This pitch varies with airspeed and engine power. Engine power is commanded by mechanical links to the power levers in the cockpit.

The P-3C synchrophaser is a separate electronic device that is mounted in an avionics rack in the main cabin. The synchrophaser provides continuous fine adjustment of the slave propeller blade pitch angles via electrical signals sent to servo-motors in the hydro-mechanical speed governors within the propeller hubs. This allows the slave propellers to speed-up or slow-down within a limited (approximately ± 5%) speed range until the desired synchrophase angles are achieved. The P-3C also features a Master Trim adjustment knob on the synchrophaser control panel that allows the pilots to vary the speed of the master propeller by ±1%.

The synchrophase angles are measured by comparing the once-per-revolution (1P) pulse trains from the master (Propeller 2 or 3) and slave propellers. These signals come from magnetic pick-ups on the propeller hubs. The P-3C synchrophase angle range is [−45°, 45°], where a positive angle means the slave leads the master, and a negative angle means the slave lags the master.

The synchrophase angles are set by trim potentiometers on the circuit boards inside the synchrophaser. These are relatively easy to adjust with a screwdriver during normal synchrophaser maintenance, but impossible to change in flight.

To facilitate the flight test program, a modification was made to a synchrophaser in order to allow the synchrophase angles to be changed in flight with a purpose-built handheld control unit. The modification was designed to only affect the operation of the synchrophaser when Propeller 3 was the master propeller. The modification removed some of the trim potentiometers from within the synchrophaser and replaced them with a breakout connector on the right side of the synchrophaser housing.

The handheld control unit is shown in Figure 4.2. It was connected to the modified synchrophaser with two cables: one to the trim-potentiometer breakout connector, and one to an existing test-point connector at the rear of the synchrophaser assembly. The latter cable allowed access to the internal synchrophaser signals representing the synchrophase angles. The functions of the handheld control unit were:

a) to adjust the synchrophase angles of the slave propellers using three ten-turn lockable potentiometers on the front of the unit,
b) to display the synchrophase angles of the three slave propellers on LCD displays in real-time, and
c) to provide buffered outputs of the measured synchrophase angle signals so that these could be recorded if required.

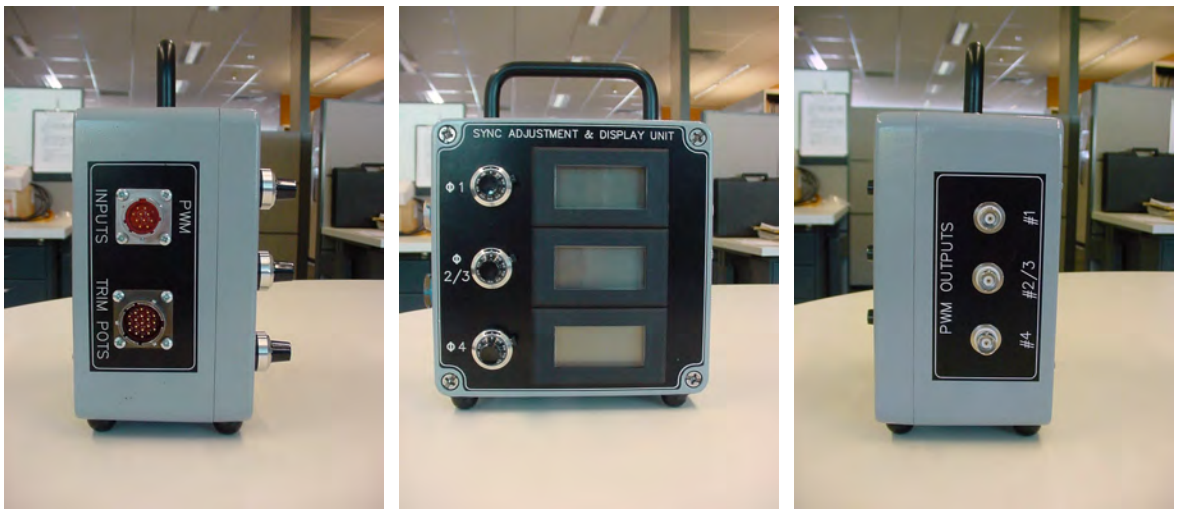

Figure 4.2 Handheld control unit for P-3C synchrophaser – inputs (left), trims potentiometers and displays (centre), and outputs (right).

4.2. C-130J Synchrophasing System

The C-130J has a digital electronic propeller control system that is integrated into the Full Authority Digital Engine Control (FADEC) system of the Rolls Royce AE 2100D3 engine. The FADEC maintains the rotational speed of the propeller at 1020.7 ± 1 rpm and the synchrophase angle within ± 1° (C-130J Advanced Propeller System) by sending signals to a servo-valve in the propeller that varies the blade pitch angle.

Each propeller has two magnetic pickups: a once-per-rev (1P) pickup, and a six-per-rev (6P) pickup. These are mounted on the de-icing brush block bracket at the top of the gearbox output shaft. The 6P pips are on the rim of the de-icing slip ring on the rear of the propeller and are aligned with the propeller blades. The 1P pip is slightly aft of one of the 6P pips. The synchrophasing system uses the 6P signal. It is presumed that FADEC unit calculates the synchrophase angles from the difference in arrival times between the master and slave 6P pulses using a formula similar to Equation (4.1), where N is the number of pulses-per-rev, T_m is the time between successive pulses from the master propeller, and T_s is the time elapsed between the master and slave pulses

$$\alpha_p = \frac{360^\circ}{N} \times \frac{T_s}{T_m}. \tag{4.1}$$

Until recently, the C-130J synchrophasing system could only be turned on or off, and the synchrophase angles defaulted to certain preset values. However, in a recent avionics upgrade, the mission computer software of the aircraft was modified so that the synchrophase angles could be changed in flight by the pilot via a multifunction display integrated into the flight control instruments. This greatly facilitated the flight test program. The mission computer communicates with the engine FADEC units through a MIL-STD-1553 data bus. The synchrophase angles measured by the FADEC units can also be recorded from this bus using a Data Bus Analyser (DBA).

In the C-130J, the synchrophase angles specify how many degrees the slave propellers lag the master. These can be set with a resolution of 1° over the range [0°, 59°]. The master propeller can be selected from either of the two inboard propellers (i.e., Propeller 2 or 3).

5. Experimental Investigations

The design of the experimental investigations and the specific flight trials and data that were collected from the AP-3C and C-103J-30 are described in detail below. The analysis of these data is undertaken in Chapters 6–10.

A number of different flight parameters can potentially influence both the noise generated by the propellers and the vibro-acoustics of the air-fuselage-cabin system. These include: altitude, airspeed, attitude (i.e., roll, pitch, yaw), engine power, propeller speed, propeller blade pitch angle, outside air pressure, temperature and humidity, cargo, fuel loads, time into flight, and cabin air pressure, temperature and humidity.

It was decided to concentrate on the effects of altitude and airspeed in this work, as these were expected to be among the most important and were relatively easy to control. Where possible, all the other parameters were either kept constant, or indirectly specified by the altitude and airspeed: e.g., the aircraft attitude was restricted to straight-and-level flight; propeller speed was maintained at 100%; the engine power and blade pitch angles were functions of, and hence indirectly specified by, the altitudes and airspeeds; and the cabin environment was automatically regulated by the cabin environmental control systems.

Three separate flight trials were designed and conducted in RAAF aircraft: one in an AP-3C, and two in (different) C-130J-30 aircraft. The objectives of these trials were to minimise the propeller-related cabin noise in both aircraft types, and the propeller-related cargo floor vibration in the C-130J-30. The trials utilised propeller signature theory wherever possible in order to minimise the number of measurements, and hence flight time, required at each flight condition; i.e., only a limited number of synchrophase angle sets (seven) were used for most flight conditions. The methodology behind the selection of these synchrophase angle sets is described in §5.1 below. In addition, during the C-130J-30 trials, the synchrophase angles of each slave propeller were individually ‘clocked’ in much finer increments during one altitude-airspeed test point in order to validate this reliance on propeller signature theory. The methodology behind the selection of the sensor locations to gain global coverage of the aircraft cabins is described in §5.2.

The AP-3C and C-130J-30 flight trials are described in §5.3 and §5.4 respectively. Note that all altitudes above 10,000 ft were specified as Flight Levels; i.e., they were not absolute heights above sea level, but constant-pressure altitudes referenced to the International Standard Atmosphere (ISA). These are denoted as FLxxx, where xxx is the pressure altitude in feet divided by 100. Airspeeds were specified in terms of the dynamic air pressure from the Pitot-static probe; i.e., as Knots Indicated Air Speed (KIAS) in the AP-3C, and Knots Calibrated Airspeed (KCAS) in the C-130J-30. Note that calibrated airspeed is the indicated airspeed corrected for instrument errors. True airspeed is the calibrated airspeed corrected for pressure and temperature; i.e., compressibility effects.

5.1. Synchrophase Angle Selection

In propeller signature theory, the contributions from individual propellers add vectorially. Hence, if the synchrophase angle of one propeller is allowed to vary over its full range while the others are held constant, the amplitude and phase of the measured BPF component should describe a circle on a vector diagram. The centre of the circle should be the sum of the contributions from the other three propellers, and the radius of the circle should be the amplitude of the contribution from the propeller in question (Figure 5.1).

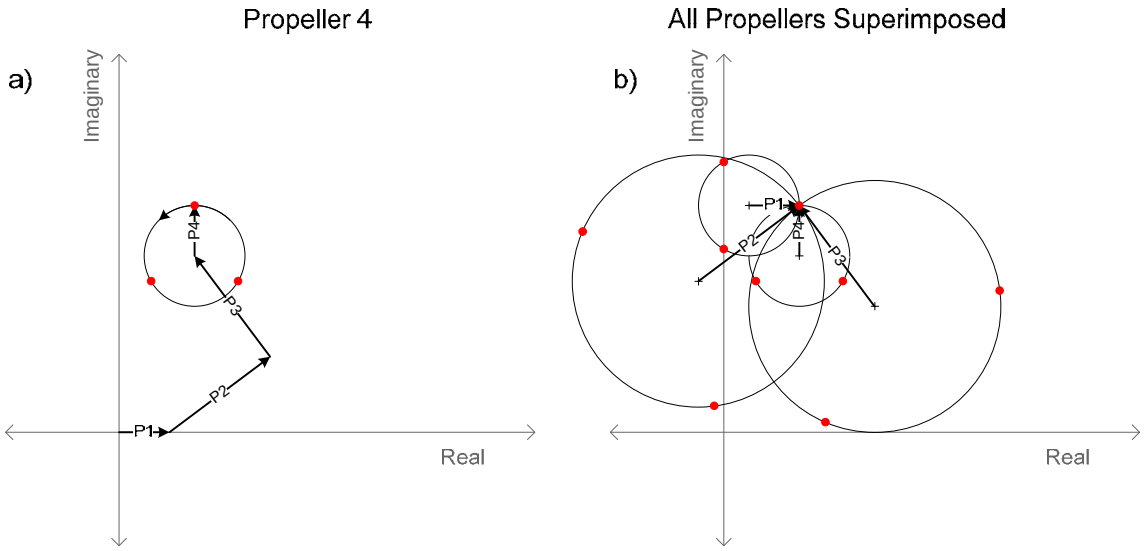

Figure 5.1 Expected effect of varying the synchrophase angle of one propeller at a time: a) Propeller 4 only, b) Propellers 1–4 superimposed.

While it is possible to disable synchrophasing on a single propeller, and effectively allow it to pass through all possible synchrophase angles, such an approach is not easy to control. The rate of change of the synchrophase angle could potentially be too fast for the signatures to be measured accurately (limited by the spectral estimation method), or too slow to complete in a reasonable period (e.g., if the slave speed is very close to the master speed), or not vary systematically or smoothly enough.

The method adopted in the three flight trials was to make a small number of relatively accurate measurements at a limited number of fixed synchrophase angles. With four propellers, a minimum of four linearly independent sets of synchrophase angles are required (§3.4). This could have been achieved by using the default set of synchrophase angles plus one other angle for each slave propeller. However, to reduce the effects of measurement errors, it made sense to use more than four sets of angles. A reasonable, *a priori*, choice seemed to be seven sets of angles; i.e., the default set of angles plus two other angles for each slave propeller. This represented a practical compromise between potentially more accurate estimates of the signatures (a diminishing return) and an arithmetically increasing flight time.

Note that, by definition, changing the synchrophase angle of the master propeller is not possible. However, this can effectively be accomplished by changing the synchrophase angles of all the slave propellers by the same amount in the opposite direction. This was not done in the AP-3C and first C-130J-30 trials because it would have required extra set-up time for these measurements and would have been prone to more error, but it was done during one altitude-airspeed test point in the second C-130J-30 trial.

In theory, the best estimates of the propeller signatures will be obtained when the selected synchrophase angles give the largest phase separations at the frequencies of interest; i.e., at the BPF, and its low-order harmonics. For example, if three synchrophase angles are available for each propeller, the best angles to choose will be those that produce phase changes of ± 120° from the first measurement at these frequencies. These angles should then give groups of three equidistant points when plotted on a vector diagram, as shown by the red dots in Figure 5.1. Simultaneously fitting circles to these groups of points is the graphical equivalent of finding the least-squares solution to Equation (3.22).

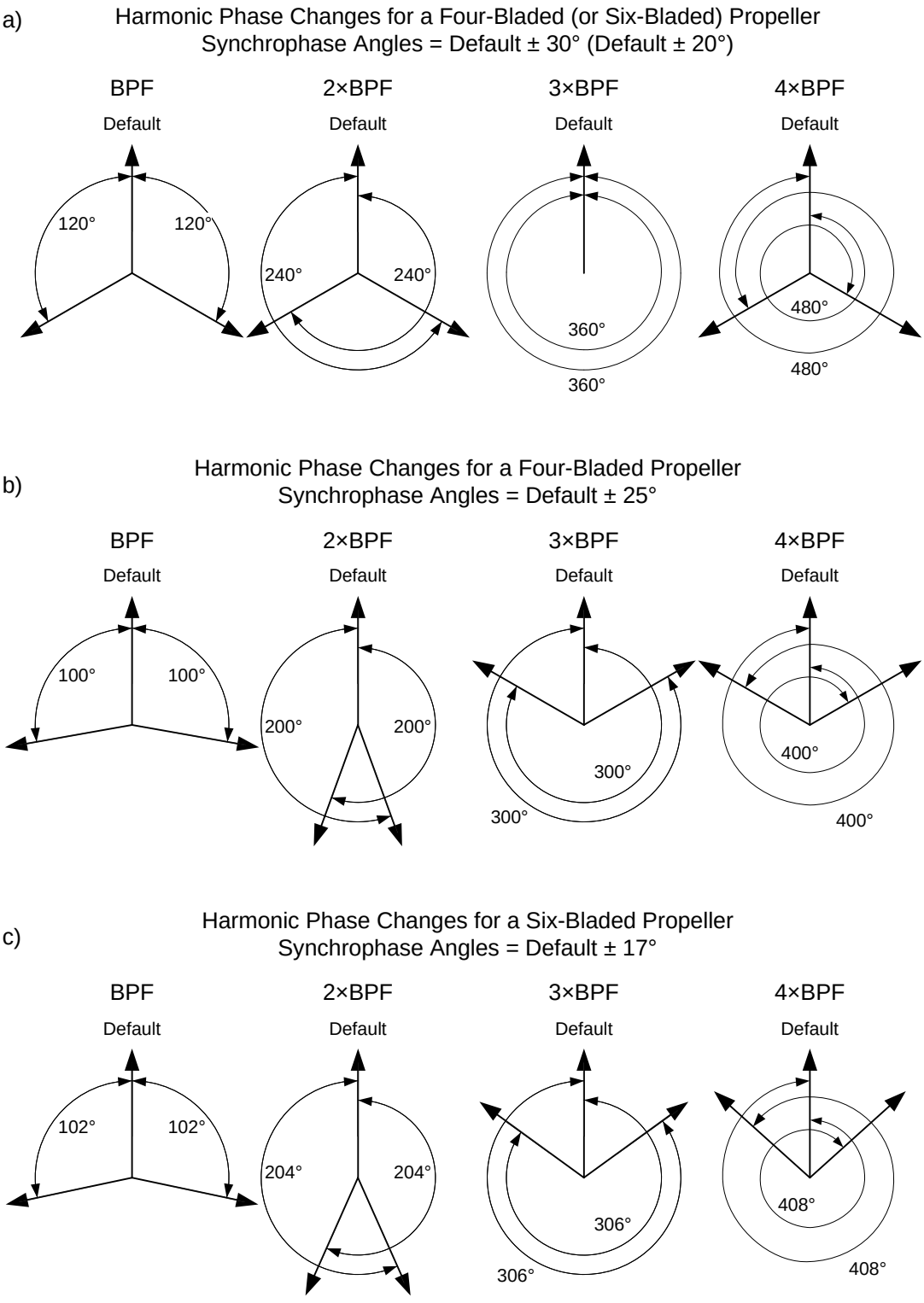

Figure 5.2 Phase changes at the BPF and its low-order harmonics for three different synchrophase angle increment cases: a) increments that produce ± 120° phase changes at 1×, 2×, and 4×BPF, but 0° phase change at 3×BPF; b) compromise selected for AP-3C; c) compromise selected for C-130J-30.

As shown in Figure 5.2a, it is effectively possible to achieve ± 120° phase changes at 1×, 2×, and 4× the BPF simultaneously by using synchrophase angle increments of ± 30° for four-bladed propellers, or ± 20° for six-bladed propellers. However, these increments unfortunately produce no effective phase change at 3× BPF, and the signatures at this frequency would not be not computable; i.e., the columns of matrix **A** in Equation (3.22) would be linearly dependent and **A** would therefore be rank deficient. Since including

additional angle sets for the 3× BPF components at each altitude-airspeed combination would have required significantly more flight time, the selected synchrophase angle increments were instead compromised to allow the signatures to be computed at all four frequencies from the same sets of measurements. The selected increments were ± 25° in the four-bladed AP-3C, and ± 17° in the six-bladed C-130J-30. The effect of these increments on the phase at the BPF and its low-order harmonics are shown in Figure 5.2b and Figure 5.2c respectively. It can be seen that the phase angles are more evenly distributed, and hence likely to produce more-accurate estimates of the signatures, at the two lower frequencies than at the two higher frequencies. This bias to the lower frequencies was intentional, as these were expected to be the higher-amplitude components, and hence more important to predict accurately.

5.2. Sensor Location Selection

The simplest way to minimise cabin noise and vibration in a global sense is to use as many sensors as possible and distribute these as uniformly as possible throughout the cabin (in a three-dimensional sense). This approach has its limitations, though, particularly if the wavelengths of interest are significantly shorter than the sensor spacing, as localised areas of high-amplitude noise or vibration could still exist in such a case. Since the wavelengths at the BPF in the AP-3C and C-130J are approximately 5.0 m and 3.3 m respectively, the sensors should be spaced closer than these distances. However, previous estimates of the modal densities (§3.3) indicate that there are possibly few resonant modes at these frequencies, and that the number of sensors required for global control may be fewer than proposed under this strategy.

The main alternative to this approach is to use a potentially higher spatial density of sensors in a smaller area of the cabin, which is known to always have the highest-amplitude noise and vibration; e.g., the area within, say, one propeller diameter fore and aft of the plane of the propellers. This approach necessarily relies on the assumption that this zone will always have the highest-amplitude noise and vibration regardless of what the synchrophase angles might be at any point in time. The main pitfall of this approach is that it cannot measure what is happening elsewhere in the cabin, and hence may not achieve a true global minimum.

Having little *a priori* knowledge of the noise and vibration in the AP-3C and C-130J-30 cabins, it was decided to adopt the first approach; i.e., to use as many sensors as possible over the widest area of the cabin as possible, even though this may miss some hot spots.

5.3. AP-3C Flight Trial

The AP-3C flight trial occurred over the period 6–10 November 2006 at RAAF Base Edinburgh (AP-3C Propeller Synchrophaser Optimisation Operational Test and Evaluation (OT&E) Plan, 2006). The trial consisted of one ground run and two flights in the same aircraft (A9-660). The sensor locations for this trial (Figure 5.3) included:

- microphones attached to the headrests of all crew seats,
- microphones attached to the overhead grab rail at 3 m (120 in.) intervals – 2 m (80 in.) between last two microphones,
- a microphone above the table (below the bunk) in the rear of the cabin, and
- single-axis (vertical) accelerometers mounted on the seat rails beneath some of the crew seats.

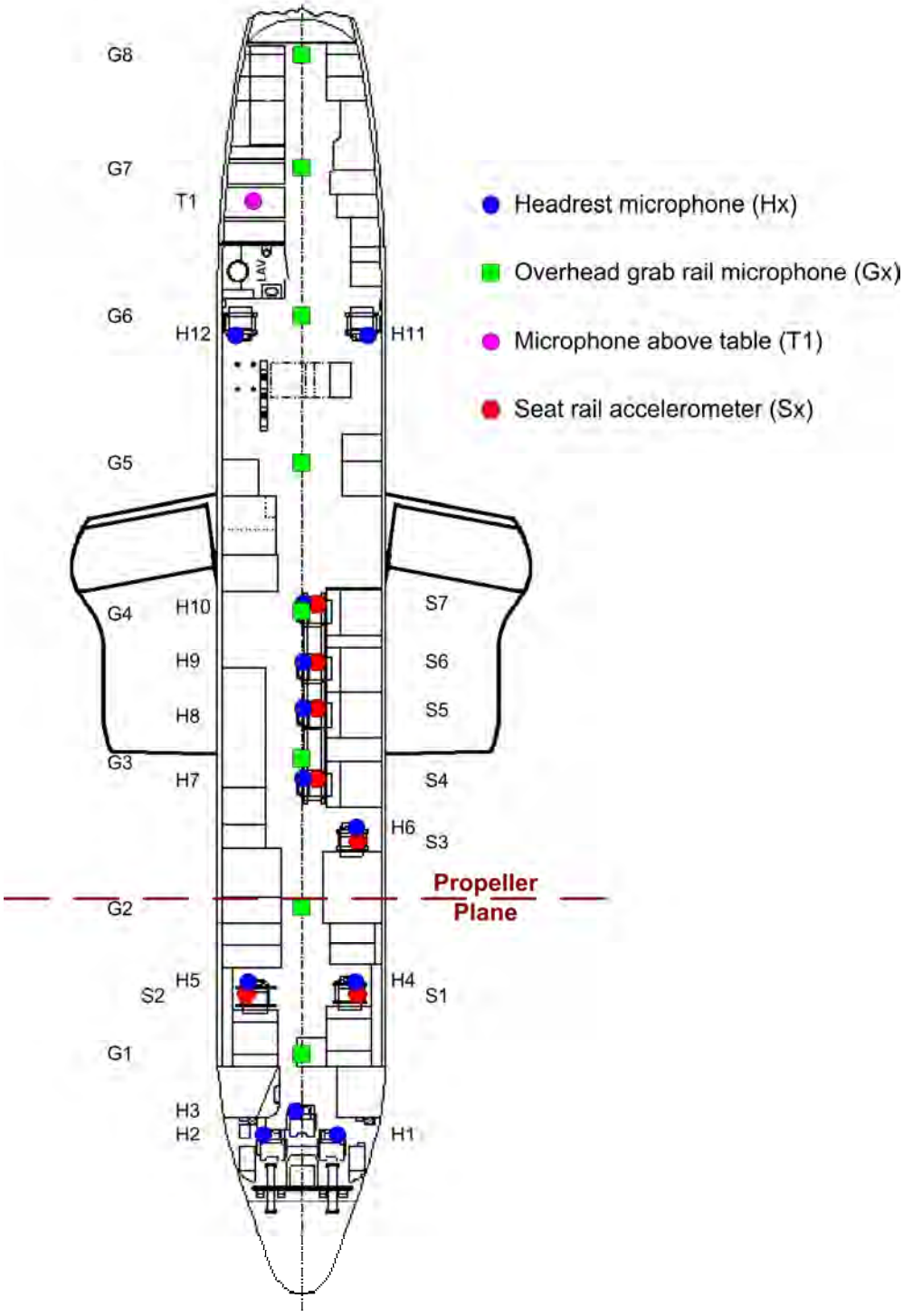

Figure 5.3 AP-3C floor plan overlaid with the sensor locations – figure adapted from (AAP 7215.005-5).

All microphones were held in rubber grips inside butterfly clamps on the end of 20 cm (8 in.) goosenecks. The goosenecks were attached to the headrests and overhead grab rail using rubber-lined P-clamps. The accelerometers were screwed to steel clamps bolted to the seat rails. Once-per-rev (1P) signals for all four propellers were obtained from the break-out connector next to the synchrophaser. All signals were recorded with a bandwidth of 20 kHz using a Heim D120f digital data recorder fitted with four 8-channel ANR20 analogue input modules (32 channels), and a 144 GB hard disk. Sensor details and installation photographs can be found in Appendix B.

The altitude-airspeed combinations flown are listed in Table 5.1. Serials 1–14 were in Flight 1 (08/11/2006), and the remainder were in Flight 2 (09/11/2006). Note that Engine 1 was shut down during Serials 25–28. These serials were included to represent scenarios when one engine is shut down to conserve fuel during extended loitering.

Measurements were made for seven sets of synchrophase angles for Serials 1–24 (Table 5.2), and five sets of synchrophase angles for Serials 25–28 (Table 5.3). Propeller 3 was the designated master propeller for the whole trial.

Table 5.1 AP-3C flight conditions.

Serial[(1)]	**Altitude**	**Indicated Airspeed (KIAS)**	**Engines**
1 2	500 ft	200 220	All
3 4 5	1000 ft	200 220 240	
6 7 8	3000 ft	220 240 260	
9 10 11	10000 ft	220 240 260	
12 13 14 15	FL180	220 240 260 280	
16 17 18	FL200	220 240 260	
19 20 21	FL240	200 220 240	
22 23 24	FL280	180 200 220	
25 26	1000 ft	190 210	2, 3 & 4
27 28	3000 ft	190 210	

(1) Serials 1–14 in Flight 1, and Serials 15–28 in Flight 2.

Table 5.2 AP-3C synchrophase angle sets for Serials 1–24.

Set	**Synchrophase Angles (Prop 1, Prop 2, Prop 3, Prop 4)**	**Description**
a	(α_{def1}, α_{def2}, 0°, α_{def4})	Default angles
b	(α_{def1} + 25°, α_{def2}, 0°, α_{def4})	Prop 1 + 25°
c	(α_{def1} − 25°, α_{def_2}, 0°, α_{def4})	Prop 1 – 25°
d	(α_{def1}, α_{def2} + 25°, 0°, α_{def4})	Prop 2 + 25°
e	(α_{def1}, α_{def2} − 25°, 0°, α_{def4})	Prop 2 – 25°
f	(α_{def1}, α_{def2}, 0°, α_{def4} + 25°)	Prop 4 + 25°
g	(α_{def1}, α_{def2}, 0°, α_{def4} − 25°)	Prop 4 – 25°

Table 5.3 AP-3C synchrophase angle sets for Serials 25–28.

Set	**Synchrophase Angles (Prop 1, Prop 2, Prop 3, Prop 4)**	**Description**
a	(n.a., α_{def2}, 0°, α_{def4})	Default angles
b	n.a.	n.a.
c	n.a.	n.a.
d	(n.a., α_{def2} + 25°, 0°, α_{def4})	Prop 2 + 25°
e	(n.a., α_{def2} − 25°, 0°, α_{def4})	Prop 2 – 25°
f	(n.a., α_{def2}, 0°, α_{def4} + 25°)	Prop 4 + 25°
g	(n.a., α_{def2}, 0°, α_{def4} − 25°)	Prop 4 – 25°

5.4. C-130J-30 Flight Trials

The first C-130J-30 trial occurred over the period 22–30 November 2006 at RAAF Base Richmond (C-130J-30 Trial 1 Plan, 2006). It consisted of one ground run and three flights in the same aircraft (A97-467). The cargo and sensor locations for this trial are shown in Figures 5.4–5.7. Note that the tie-down rings on the cargo floor have a pitch spacing of 20 in. (~0.5 m) and the sensors are therefore approximately half an acoustic wavelength apart at the BPF. The cargo was palletised on standard C-130 pallets (Table 5.4), which

were linked in double and triple pallet configurations for the longer items. The pallets were loaded in the usual manner; i.e., rolled into place on the floor rollers and secured using the restraint rails on either side of the cargo floor. The pallets were rearranged between the first two flights, and removed for the third flight to allow the centre troop seat stanchions and rails to be fitted. The floor rollers were not removed for the third flight due to time constraints.

The sensors used in the first trial included:

- single-axis (vertical) accelerometers mounted in a grid pattern on the cargo floor (in the gap created by the rollers),
- tri-axial accelerometers mounted on each pallet,
- single-axis (vertical & horizontal) accelerometers mounted on some cargo items,
- microphones on the headrests of the pilot and flight engineer seats, and
- microphones on the upper seat rails in the main cabin at seated head height.

The microphones were mounted on 20 cm (8 in.) goosenecks in the same manner as the AP-3C trial. However, the accelerometers were fixed in place using hot-melt glue instead of being bolted down. Sensor details and installation photographs can be found in Appendix C.

The second C-130J-30 trial occurred over 21–24 July 2008 at RAAF Base Richmond (C-130J-30 Trial 2 Plan, 2008). The main purpose of this trial was to test several candidate low-noise and low-vibration synchrophase angle sets predicted from the first trial in a different aircraft (A97-464). A reduced number of sensors was used, as the trial consisted of just one flight and only 40 channels could be simultaneously recorded. The selected sensor locations included most of the higher-amplitude locations in the main cabin from the first trial (Figure 5.8), plus the flight-deck sensors (Figure 5.4). The sensor types and mounting methods were the same as those used in the first trial, although there were probably small differences in the sensor positions (up to ~10 cm). There was no cargo in the second trial.

Laser tachometers were used to generate angular reference signals from the propellers in both trials, as there was no convenient way of tapping into the 1P or 6P signals from the propellers. This was less than ideal, as the magnetic pick-ups would have provided more accurate and reliable signals.

One laser was used in the first trial. It was aimed through a cabin window just behind the propellers at the rear of the Propeller 2 spinner. A piece of reflective tape was placed behind each blade to generate a 6P signal. This made it slightly difficult to identify the same blade from measurement to measurement consistently. However, it was found that this could still be achieved by taking advantage of the small spacing irregularities between the pieces of tape (Appendix D).

Four lasers were used in the second trial, one for each propeller. The lasers for the inboard propellers were mounted and aimed in the same manner as the first trial. However, the lasers for the outboard propellers were aimed through the cabin windows in front of the propellers and targeted at the front of the spinners in order to obtain a direct line of sight. This may have resulted in more trigger-point inaccuracy for the outboard propellers, as the aim reference point for all propellers was a split line in the engine cowling just aft of the spinners; i.e., the reference point was further away from the tape on the outboard propellers. A single piece of tape was positioned on each spinner so that the tachometers would trigger when Blade 1 was pointing vertically downward, as aligned on the ground

with a spirit level placed against the edge of the blade. This positioning was inadvertently different to the first trial, so the absolute phases of the propeller signatures were different between the two trials.

The signals in both trials were recorded with a bandwidth of 20 kHz using a Heim D120f digital data recorder fitted with five 8-channel ANR20 analogue input modules (40 channels), and a 144 GB hard disk. Additionally, a data bus analyser was used to record a set of 1553 data bus parameters associated with the engines and propellers, including the synchrophase angles measured by the engine FADEC units.

The altitudes and airspeeds flown are listed in Table 5.5. The serials common to both trials are underlined. Serials 1, 5.4, 6.4, 7.1, 7.2, and 7.3 were excluded from Trial 2 due to time constraints. The angle sets used in the trials are listed in Tables 5.6–5.9.

Table 5.4 C-130J-30 cargo pallet details for Trial 1.

Pallet	**Mass (kg)**	**Mass (lb)**
Single	980	2160
Double	1450	3200
Triple	4310	9500

Table 5.5 C-130J-30 flight conditions – serials common to both trials are underlined.

Serial	**Altitude**	**Calibrated Airspeed (KCAS)**	**Engines**
1	6000 ft	250	All
2	9000 ft	250	
3	FL150	250	
4.1 4.2 4.3	FL210	205 220 230	
5.1 5.2 5.3 5.4[1]	FL240	195 210 220 235	
6.1 6.2 6.3 6.4[2]	FL280	190 200 205 222	
7.1 7.2 7.3 7.4[3]	FL320	180 185 190 200	
10[4]	FL240	220	

[1] Max Continuous Power, Trial 1 Flights 2 & 3 only. [3] Trial 2 only.
[2] Max Continuous Power, Trial 1 Flight 2 only. [4] Trial 1 Flight 3, and Trial 2 only.

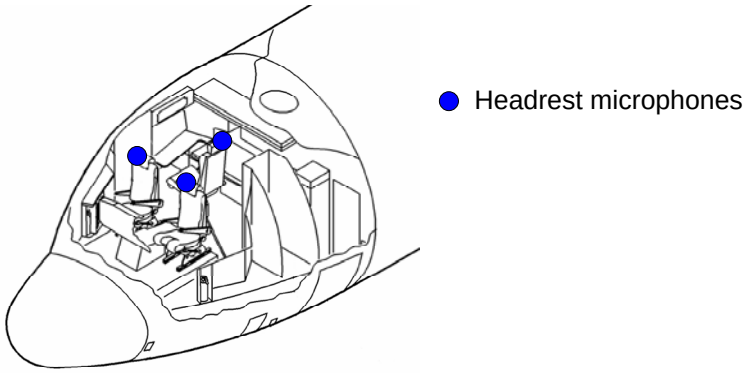

Figure 5.4 C-130J-30 flight deck with sensor locations – figure adapted from (AAP7211.031-1(AM1)) – note the Flight Engineer's seat (at rear) was centred and faced forward, not sideways as shown.

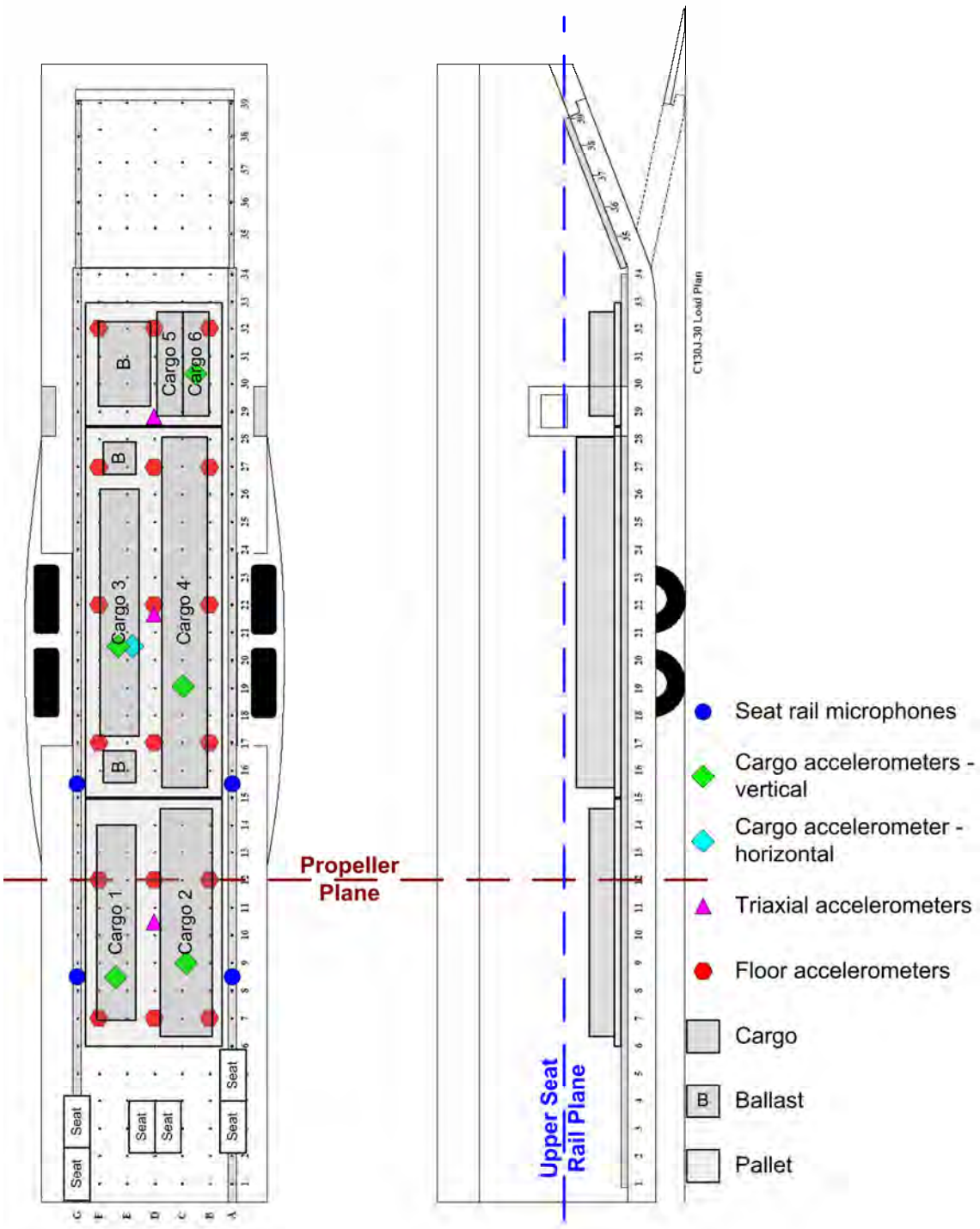

Figure 5.5 C-130J-30 floor plan overlaid with the cargo and sensor locations for Trial 1 Flight 1 (27/11/2006) – figure adapted from (AAP 7211.031-9-2).

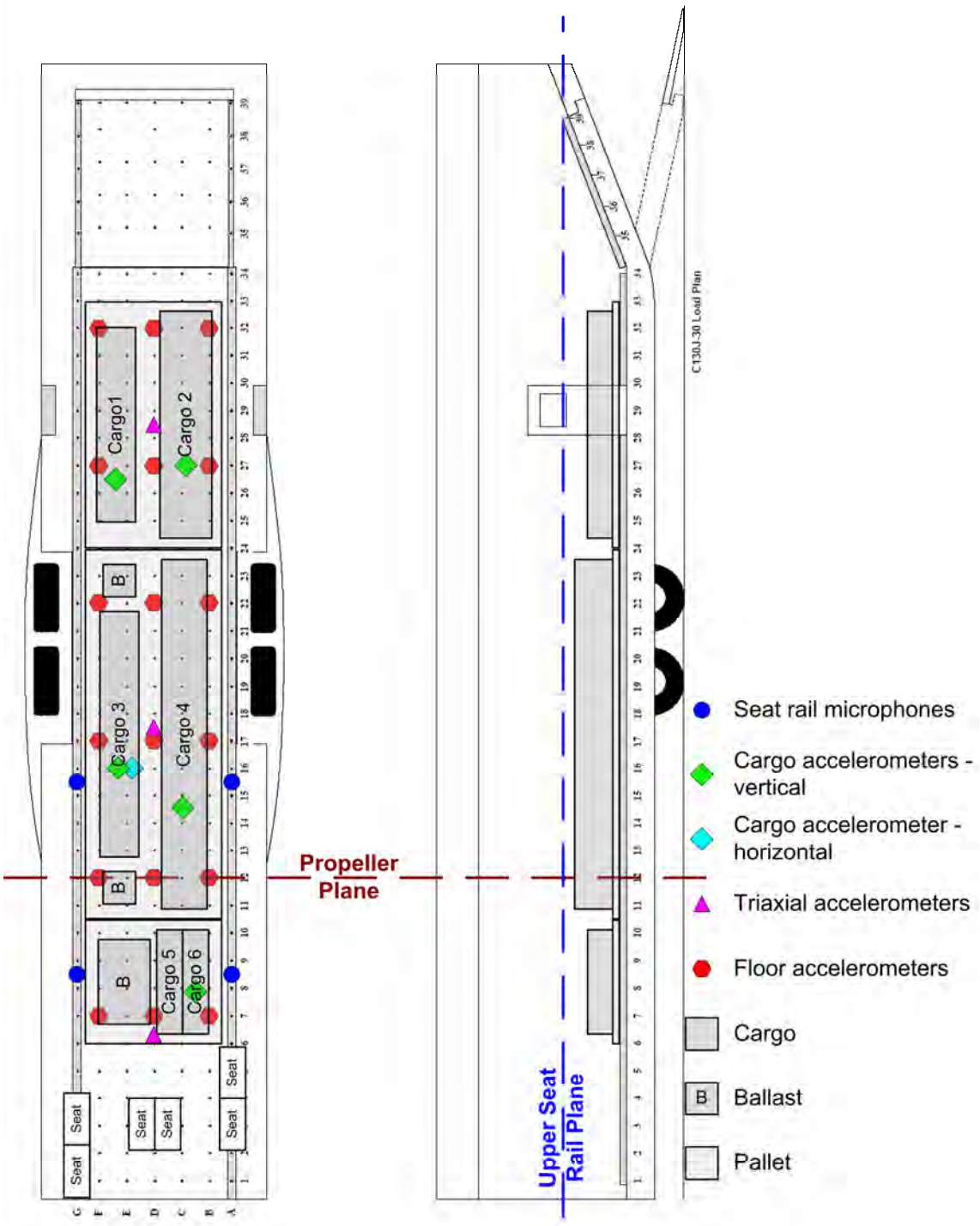

Figure 5.6 C-130J-30 floor plan overlaid with the cargo and sensor locations for Trial 1 Flight 2 (28/11/2006) – figure adapted from (AAP 7211.031-9-2).

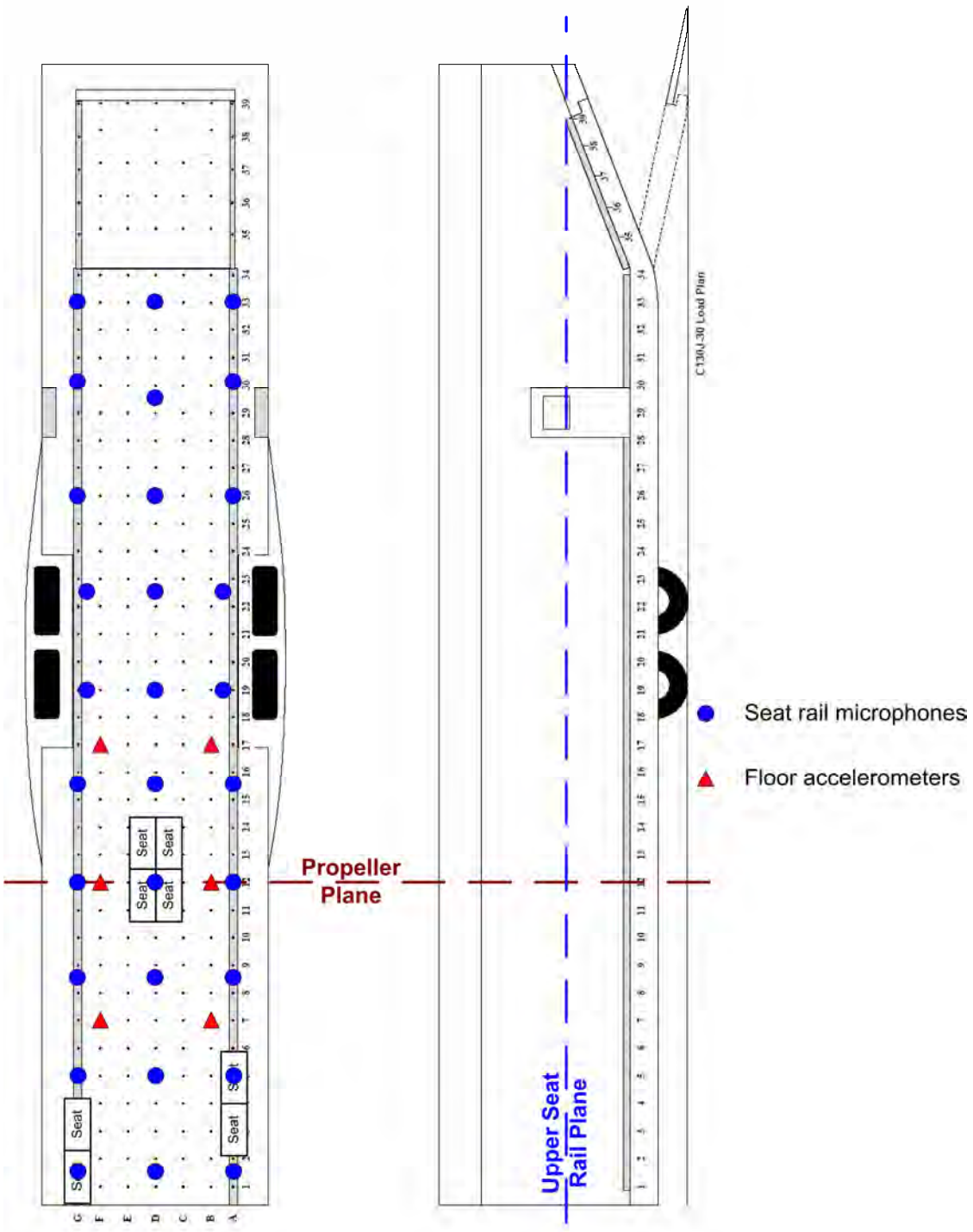

Figure 5.7 C-130J-30 floor plan overlaid with the sensor locations for Trial 1 Flight 3 (29/11/2006) – figure adapted from (AAP 7211.031-9-2).

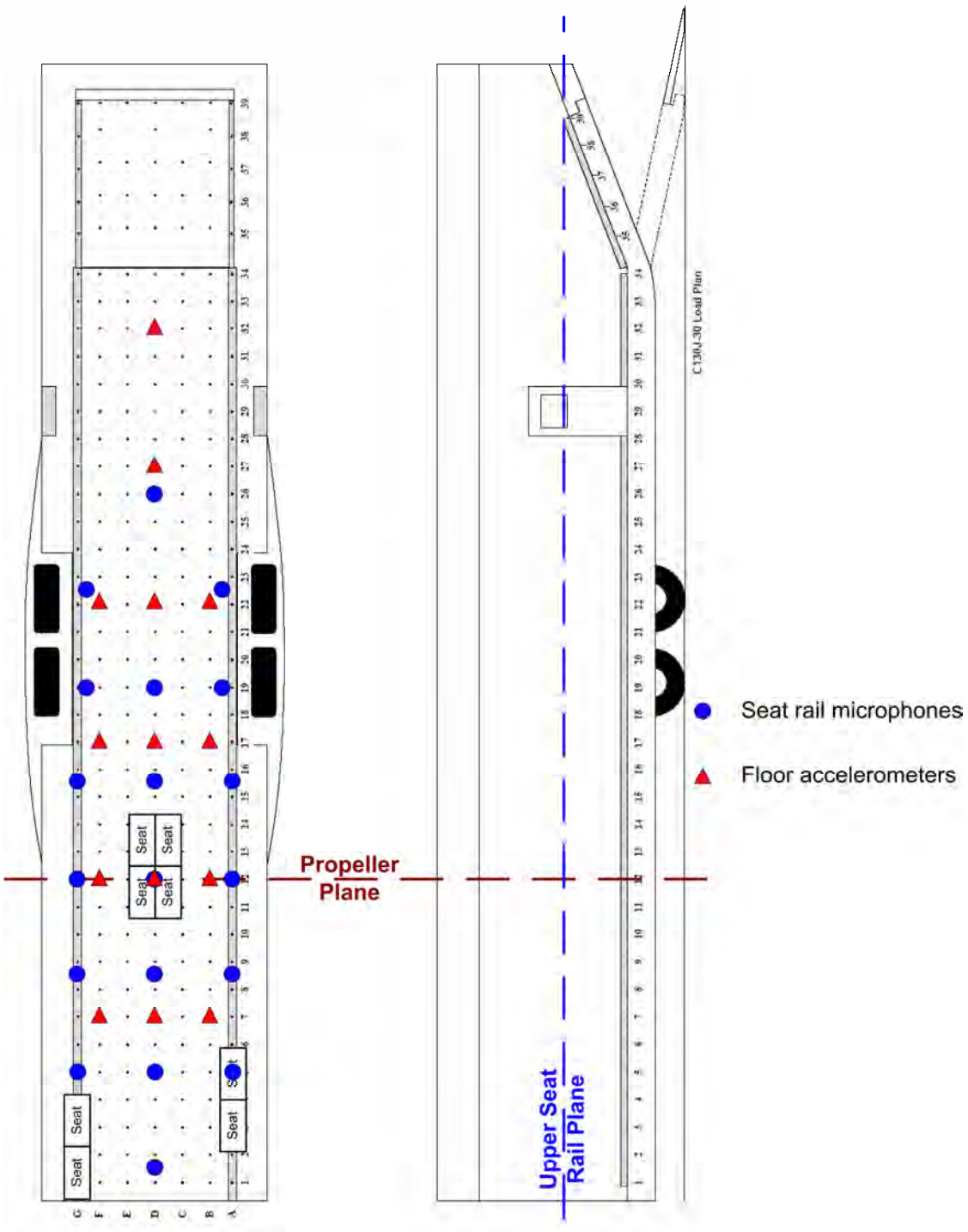

Figure 5.8 C-130J-30 floor plan overlaid with the sensor locations for Trial 2 Flight 1 (23/07/2008) – figure adapted from (AAP 7211.031-9-2).

Table 5.6 C-130J-30 synchrophase angle sets for Trial 1 (except Serial 10).

Set	Angles (P1, P2, P3, P4)	Description	Serials
a	(α_{def1}, 0°, α_{def3}, α_{def4})	Default	All except 10
b	(α_{def1}+17°, 0°, α_{def3}, α_{def4})	Prop 1 + 17°	
c	(α_{def1}−17°, 0°, α_{def3}, α_{def4})	Prop 1 − 17°	
d	(α_{def1}, 0°, α_{def3}+17°, α_{def4})	Prop 3 + 17°	
e	(α_{def1}, 0°, α_{def3}−17°, α_{def4})	Prop 3 − 17°	
f	(α_{def1}, 0°, α_{def3}, α_{def4}+17°)	Prop 4 + 17°	
g	(α_{def1}, 0°, α_{def3}, α_{def4}−17°)	Prop 4 − 17°	

Table 5.7 C-130J-30 synchrophase angle sets for Trial 2 (except Serial 10).

Set	Angles (P1, P2, P3, P4)	Description	Serials
a	(α_{def1}, 0°, α_{def3}, α_{def4})	Default	2.1, 3.1, 4.1, 4.2, 4.3, 5.1, 5.2, 5.3, 6.2, 7.4
b	(6°, 0°, 0°, 34°)	Low vibration candidate set 1	
c	(7°, 0°, 57°, 29°)	Low vibration candidate set 2	
d	(2°, 0°, 12°, 6°)	Low vibration candidate set 3	
e	(57°, 0°, 52°, 22°)	Low sound candidate set 1	
f	(55°, 0°, 48°, 19°)	Low sound candidate set 2	
g	(0°, 0°, 52°, 34°)	Low sound candidate set 3	
h	(50°, 0°, 41°, 5°)	Low sound candidate set 4	
i	(53°, 0°, 32°, 29°)	Low flight-deck sound (FL210–FL240) cand. set	4.2, 5.3, 6.2 only
j	(30°, 0°, 30°, 39°)	High sound (FL210–FL280) candidate set	
k	(40°, 0°, 27°, 32°)	High vibration (all altitudes) candidate set	
l	(0°, 0°, 0°, 40°)	Low sound and vibration measured during Trial 1	

Table 5.8 C-130J-30 synchrophase angle sets for Trial 1 Serial 10.

Set	Angles (P1, P2, P3, P4)	Set	Angles (P1, P2, P3, P4)	Set	Angles (P1, P2, P3, P4)
a	(0°, 0°, 0°, 0°)	h	(0°, 0°, 0°, 0°)	o	(0°, 0°, 0°, 0°)
b	(0°, 0°, 10°, 0°)	i	(10°, 0°, 0°, 0°)	p	(0°, 0°, 0°, 10°)
c	(0°, 0°, 20°, 0°)	j	(20°, 0°, 0°, 0°)	q	(0°, 0°, 0°, 20°)
d	(0°, 0°, 30°, 0°)	k	(30°, 0°, 0°, 0°)	r	(0°, 0°, 0°, 30°)
e	(0°, 0°, 40°, 0°)	l	(40°, 0°, 0°, 0°)	s	(0°, 0°, 0°, 40°)
f	(0°, 0°, 50°, 0°)	m	(50°, 0°, 0°, 0°)	t	(0°, 0°, 0°, 50°)
g	(45°, 0°, 25°, 40°)	n	(45°, 0°, 25°, 40°)	u	(45°, 0°, 25°, 40°)

Table 5.9 C-130J-30 synchrophase angle sets for Trial 2 Serial 10.

Set	Angles (P1, P2, P3, P4)	Set	Angles (P1, P2, P3, P4)	Set	Angles (P1, P2, P3, P4)	Set	Angles (P1, P2, P3, P4)
a1	(0°, 0°, 0°, 0°)	a2	not flown	a3	(0°, 0°, 0°, 0°)	a4	(0°, 0°, 0°, 0°)
b1	(5°, 0°, 0°, 0°)	b2	(5°, 0°, 5°, 5°)	b3	(0°, 0°, 5°, 0°)	b4	(0°, 0°, 0°, 5°)
c1	(10°, 0°, 0°, 0°)	c2	(10°, 0°, 10°, 10°)	c3	(0°, 0°, 10°, 0°)	c4	(0°, 0°, 0°, 10°)
d1	(15°, 0°, 0°, 0°)	d2	(15°, 0°, 15°, 15°)	d3	(0°, 0°, 15°, 0°)	d4	(0°, 0°, 0°, 15°)
e1	(20°, 0°, 0°, 0°)	e2	(20°, 0°, 20°, 20°)	e3	(0°, 0°, 20°, 0°)	e4	(0°, 0°, 0°, 20°)
f1	(25°, 0°, 0°, 0°)	f2	(25°, 0°, 25°, 25°)	f3	(0°, 0°, 25°, 0°)	f4	(0°, 0°, 0°, 25°)
g1	(30°, 0°, 0°, 0°)	g2	(30°, 0°, 30°, 30°)	g3	(0°, 0°, 30°, 0°)	g4	(0°, 0°, 0°, 30°)
h1	(40°, 0°, 0°, 0°)	h2	(40°, 0°, 40°, 40°)	h3	(0°, 0°, 40°, 0°)	h4	(0°, 0°, 0°, 40°)
i1	(50°, 0°, 0°, 0°)	i2	(50°, 0°, 50°, 50°)	i3	(0°, 0°, 50°, 0°)	i4	(0°, 0°, 0°, 50°)

6. Synchrophasing System Performance

The ability of the AP-3C and C-130J-30 synchrophasing systems to maintain a set of desired synchrophase angles was essential to the objectives of this investigation. This chapter describes the checks that were made on these systems, and highlights some issues of importance. In general, it was found that both systems worked effectively, although the digital synchrophasing system of the C-130J-30 responded faster, and maintained tighter angle tolerances than the analogue system of the AP-3C, as expected. These performance differences will be reflected to some extent in the results presented in the subsequent chapters. However, it is not expected that these effects will be any more significant than those generated by other factors affecting the measurement repeatability, which are discussed in Chapter 8.

6.1. Photographic Analysis of the Synchrophase Angles

Both aircraft were photographed during ground runs using a camera mounted on a tripod directly in front of the aircraft. An example of the C-130J-30 is shown in Figure 6.1. Unfortunately, these photographs proved difficult to analyse because:

a) the synchrophase angles were relatively unstable on the ground (due to ground-induced turbulence – §2.1),

b) there were synchronisation problems between the clocks of the cameras and data recorders,

c) the vertical motion of the focal-plane shutter induced distortion (curvature) in the image of the propeller blades (worst for the near-vertical blades), and

d) the measurements were subject to parallax error.

These factors are further discussed in Appendix E where the photographic measurement error is estimated to range from −1° up to +3°.

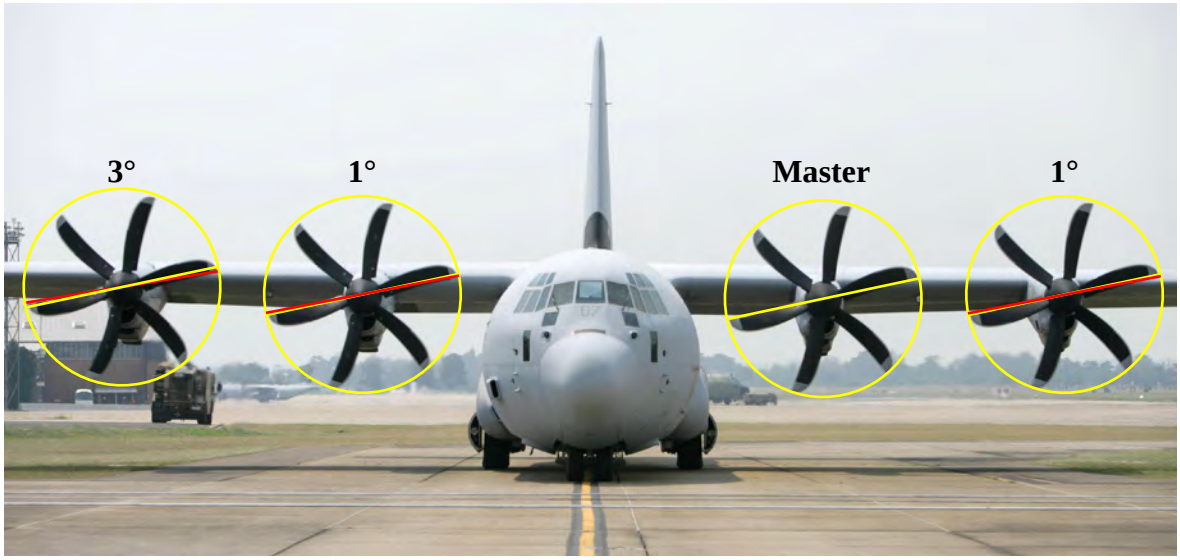

Figure 6.1 Photograph of a C-130J-30 during a ground run with the synchrophase angles set to (0°,0°,0°,0°) and Propeller 2 selected as the master. The angles of the master and slave propellers are represented by the yellow and red lines respectively. The angles measured from this photograph are (1°,0°,1°,3°). © Commonwealth of Australia. Reproduced with permission from the RAAF.

6.2. AP-3C Synchrophase Angle Analysis

The AP-3C synchrophase angles were calculated on a pulse-by-pulse basis from the propeller magnetic pick-up signals, as shown in Figure 6.2. Note that the synchrophase angles in the AP-3C are defined over a [−45°, 45°] range, with 0° occurring when the master and slave pulse are actually 180° apart. The angles specify how many degrees the slave propellers lead the master propeller. This measurement convention is different to that in the C-130J, which is described in §6.3.

Examples of the measured synchrophase angles in moderately turbulent air and in smooth air are shown in Figures 6.3 and 6.4 respectively. It is immediately obvious that the AP-3C synchrophaser performs significantly better in smooth air, as expected. The tolerances for these two cases were estimated by calculating the standard deviations of the angles during the nominally steady-state regions in the figures. A range of ± 3 standard deviations equates to tolerances of about ± 6° in smooth air, and about ± 10° in moderate turbulence.

There are two other features of note in the figures:

a) There was significant overshoot (> 20°) following each adjustment, and it took at least 500 revolutions (~30 s at 1020 rpm) for the propellers to settle on the new angles.

b) Perturbations in the speed of the master propeller (e.g., due to turbulence) caused the synchrophaser to unnecessarily adjust all three slave propellers even though they may not have been similarly perturbed. This is clearly shown near the 16,000-revolution mark in Figure 6.4. This effect could be reduced if the synchrophase angles were calculated in a different way. One way would be to filter out the perturbations in the master propeller signal. Another might be to generate an artificial master signal and to make all the propellers slaves.

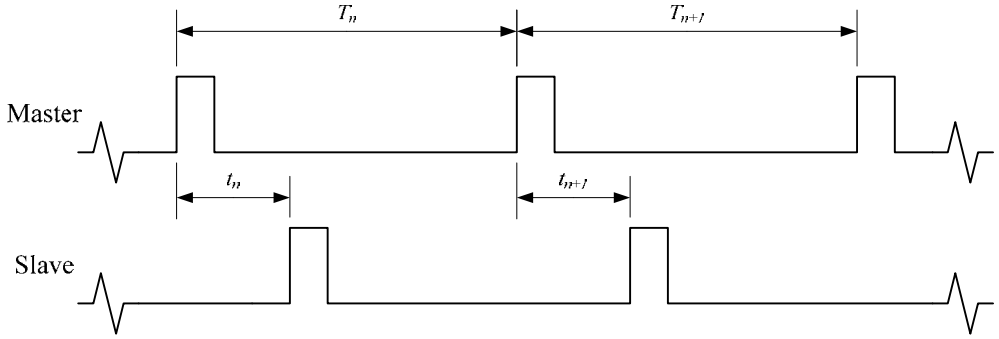

Figure 6.2 Pulse-by-pulse method of calculating the synchrophase angle, α, from the magnetic pick-up signals on the master and slave propellers in the AP-3C. T_n and T_{n+1} represent the elapsed time between pulses from the master propeller, and t_n and t_{n+1} represent the elapsed time between the master and slave pulses.

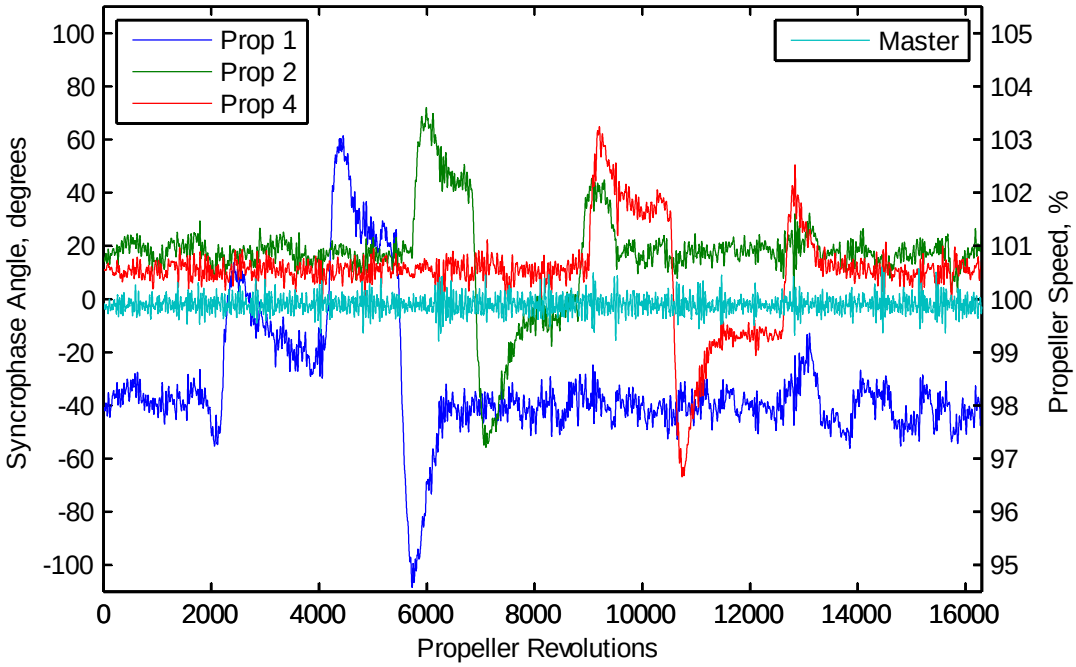

Figure 6.3 AP-3C synchrophase angles (left axis) and master propeller speed (right axis) for Serial 1 (200 KIAS at 500 ft) – moderately turbulent air.

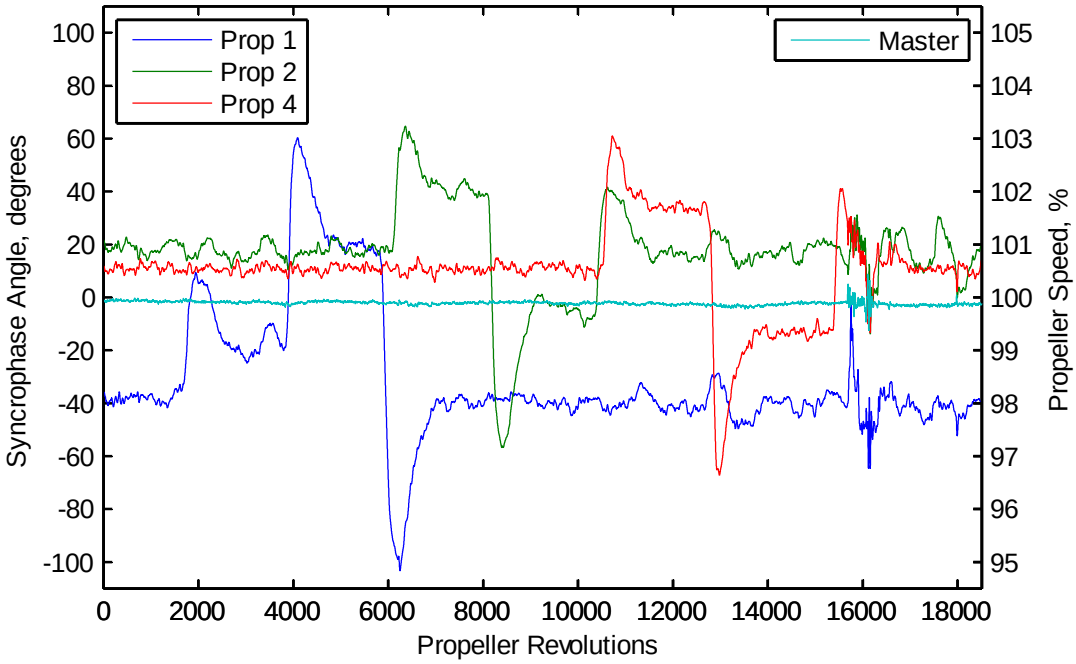

Figure 6.4 AP-3C synchrophase angles (left axis) and master propeller speed (right axis) for Serial 9 (220 KIAS at 10 000 ft) – smooth air.

6.3. C-130J-30 Synchrophase Angle Analysis

The C-130J-30 synchrophase angles were calculated on a pulse-by-pulse basis from the laser-tachometer signals available in Trial 2, as shown in Figure 6.5. Note that the synchrophase angles in the C-130J are defined over a [0°, 60°] range and specify how many degrees the slave propellers lag the master propeller. This measurement convention is different to that in the AP-3C, which is described in §6.2.

A typical smooth-air example of the in-flight FADEC and laser-tachometer synchrophase angles from Trial 2 is shown in Figure 6.6. There were no turbulent-air examples available. It can be seen that the synchrophasing system responded rapidly to changes in the angle settings, only taking ~10 s to settle on the new angles and limiting overshoot to about 5°. Other features of note are:

a) Both sets of synchrophase angles follow each other very closely, but there are small offsets between them. These are most likely due to laser and reflective tape alignment errors, particularly on the outboard propellers (§5.4). The average offsets between the two sets of angles in this figure are (0.7°, 3.0°, 1.8°, 1.7°) for Propellers 1–4 respectively, although the 3.0° offset for Propeller 2 (the master) is probably spurious – the angle of the master propeller is necessarily 0°, so the angle read from the 1553 bus (57° in this case) is unlikely to be correct. All synchrophase angle measurements in the remainder of the investigation were sourced from the FADEC data.

b) The standard deviations of the laser-tachometer angles during steady-state conditions were approximately 0.5°. The angle tolerances in smooth air were therefore estimated to be about ± 1.5°. The FADEC angles appear to have a slightly larger range in the figure, but this is a numerical artefact – the FADEC angles were only recorded as integers from the 1553 bus, while the laser-tachometer angles were calculated as floating-point numbers.

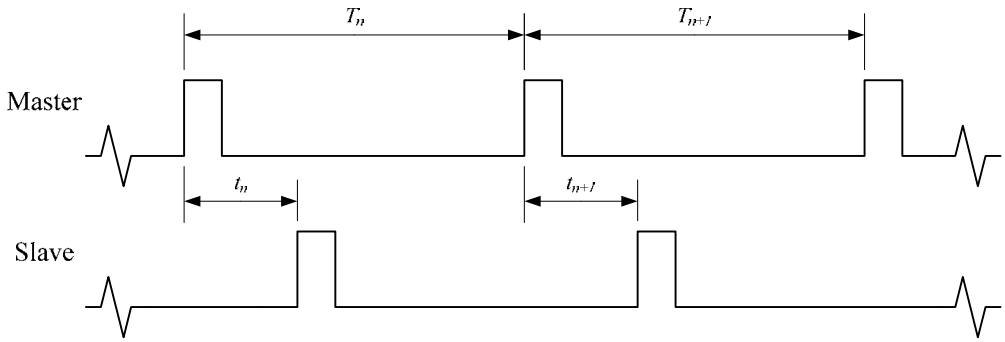

Figure 6.5 Pulse-by-pulse method of calculating the synchrophase angle, α, from the laser-tachometer signals on the master and slave propellers in the C-130J-30 (Trial 2 only). T_n and T_{n+1} represent the elapsed time between pulses from the master propeller, and t_n and t_{n+1} represent the elapsed time between the master and slave pulses. The modulo function is necessary because the synchrophasing system can synchronise on any blade; i.e., there are six possible shaft angles separated by 60° for any one synchrophase angle.

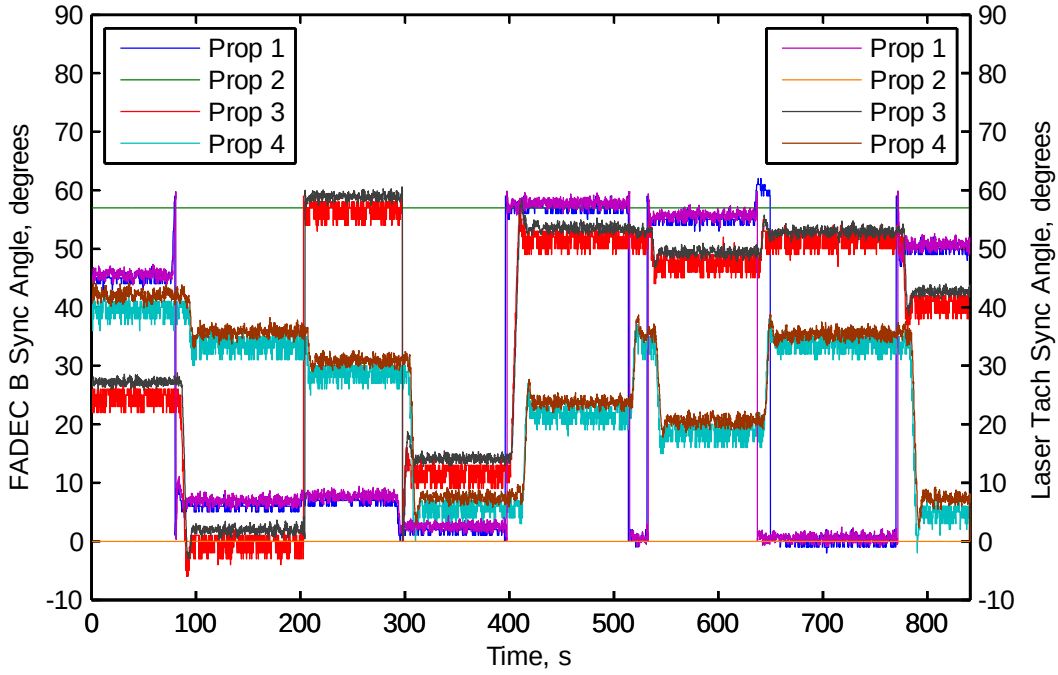

Figure 6.6 C-130J-30 synchrophase angles for Serial 4.3 (230 KCAS at FL210) Trial 2; FADEC B (FADEC in control, left axis) and laser-tachometer synchrophase angles (right axis).

7. Cabin Noise and Vibration Environments

This chapter discusses the existing noise and vibration environments inside the AP-3C and C-130J-30 for the default sets of synchrophase angles in each aircraft only. These results are presented in order to gain an understanding of the cabin environments prior to any optimisation of the synchrophase angles. Further characterisation of these environments, in terms of the measurement variability and repeatability, is discussed in Chapter 8.

Note that the outboard propellers in both these aircraft are somewhat higher than the inboard propellers due to the dihedral angles of the wings. This is slightly more pronounced in the low-wing AP-3C than the high-wing C-130J. The AP-3C outboard propellers are also a few inches to the rear of the inboard propellers, while the C-130J propellers are all in the same plane.

The environments inside these aircraft both have similar characteristics, and can therefore be considered as representative of most other multi-engine propeller aircraft. Both are dominated by the blade-pass frequency and its low-order harmonics (up to about 4× BPF). Higher blade-pass harmonics are present, but the amplitudes of these components taper off as the frequency increases. The main differences between the aircraft are the respective blade-pass frequencies (68 Hz v. 102 Hz), and the relative spectrum levels of these components. The AP-3C is also a little quieter overall than the C-130J-30. This possibly reflects the civil origins of the AP-3C (Lockheed Electra) and a larger amount of sound absorbing material lining its fuselage.

The noise and vibration spectra shown here were all computed using Welch's averaged modified periodogram spectral estimation method. They were calculated from 30-second blocks of data using a Hamming window applied to 1-second segments of data with 75% overlap.

Note that the dynamic range of the instrumentation set an effective measurement floor of ~45 dB (re 20×10^{-6} Pa) for the microphones and ~2×10^{-4} g_{rms} for the accelerometers. This was a consequence of the sensor sensitivities (nominally 5.6 mV/Pa for the B&K Type 4935 microphones, and 100 mV/g for the PCB 353B33 accelerometers), and the minimum input range of the 16-bit recorder (± 1 V).

Also note that the BPF sound pressure levels (90 dB – 105 dB) that are shown in the following sections would have high perceived loudness levels to the human ear (> 70 phons) (ISO 226, 2003). Since A-weighting was originally designed to follow the relatively low 40-phon Fletcher-Munson equal-loudness-level contour (Kinsler et al., 1982, §12.2), and C-weighting would have little effect at the frequencies of interest, no acoustic weighting has been applied to any of the measurements shown here, or elsewhere in this thesis. This is further discussed in Appendix F. If A-weighting was applied to the spectra in the following sections, then there would be significant attenuation of the spectral components at the respective blade-pass frequencies and their low-order harmonics, as shown in Table 7.1.

Table 7.1 Attenuation from A-weighting at the BPF and its low-order harmonics.

	BPF	**2×BPF**	**3×BPF**	**4×BPF**
AP-3C	25.0 dB at 68 Hz	15.1 dB at 136 Hz	10.6 dB at 204 Hz	7.9 dB at 272 Hz
C-130J	18.9 dB at 102 Hz	10.6 dB at 204 Hz	6.9 dB at 306 Hz	4.6 dB at 408 Hz

7.1. AP-3C Cabin Noise and Vibration

7.1.1. Seat Headrest Microphones

The spectra from the seat headrest microphones for a typical serial (Serial 17, 240 KIAS at FL200) are shown in Figure 7.1. It can be seen that the BPF and its harmonics are most prominent near the plane of the propellers (Microphones H4–H6), and gradually diminish towards the rear of the cabin.

The sound pressure level at the BPF ranges from ~95 dB at the front of the cabin (H1–H3), up to 104 dB at the noisiest location just ahead of the propeller plane (H4). It hovers around 100 dB just aft of the propeller plane (H6–H7), then goes down to 90 dB – 95 dB for the other seats in the rear of the cabin. The 2× BPF components at H4, H5, and H6 are also all above 90 dB.

The frequency components near 6 Hz and 12 Hz visible in many of the spectra probably correspond to the fundamental axial resonance frequency of the fuselage (i.e., with a half-wavelength equal to the cabin length) and its first harmonic (i.e., a full wavelength). The propeller rotational frequency (17 Hz) can also be seen in many of the spectra. While these low-frequency components may cause significant vibrations in items with similar resonant frequencies, they are below the human audible frequency range and of little concern here.

Note that the 193 Hz component present in the H1–H3 signals and the 230 Hz component present in the H6–H10 signals are probably generated by avionic devices in these areas of the cabin.

7.1.2. Overhead Grab Rail Microphones

The spectra from the grab rail microphones for the same serial are shown in Figure 7.2. Again, it can be seen that the spectra are dominated by the BPF and its harmonics. The sound pressure level at the BPF is above 90 dB at all but the rear-most microphone, peaking at 105 dB at G3. The 2× BPF components at G1, G2, and G4 are also above 90 dB. The 3× BPF component at the G2 microphone is 101 dB.

7.1.3. Seat Rail Accelerometers

The spectra from the seat rail accelerometers for the same serial are shown in Figure 7.3. These are very similar to the microphone spectra shown in Figure 7.1, although there are no significant components at 6 Hz and 12 Hz. The highest BPF component is 0.125 g_{rms} (0.113 in./s) at S1. Interestingly, the 2× BPF components exceed the amplitudes of the BPF components at S2 and S7.

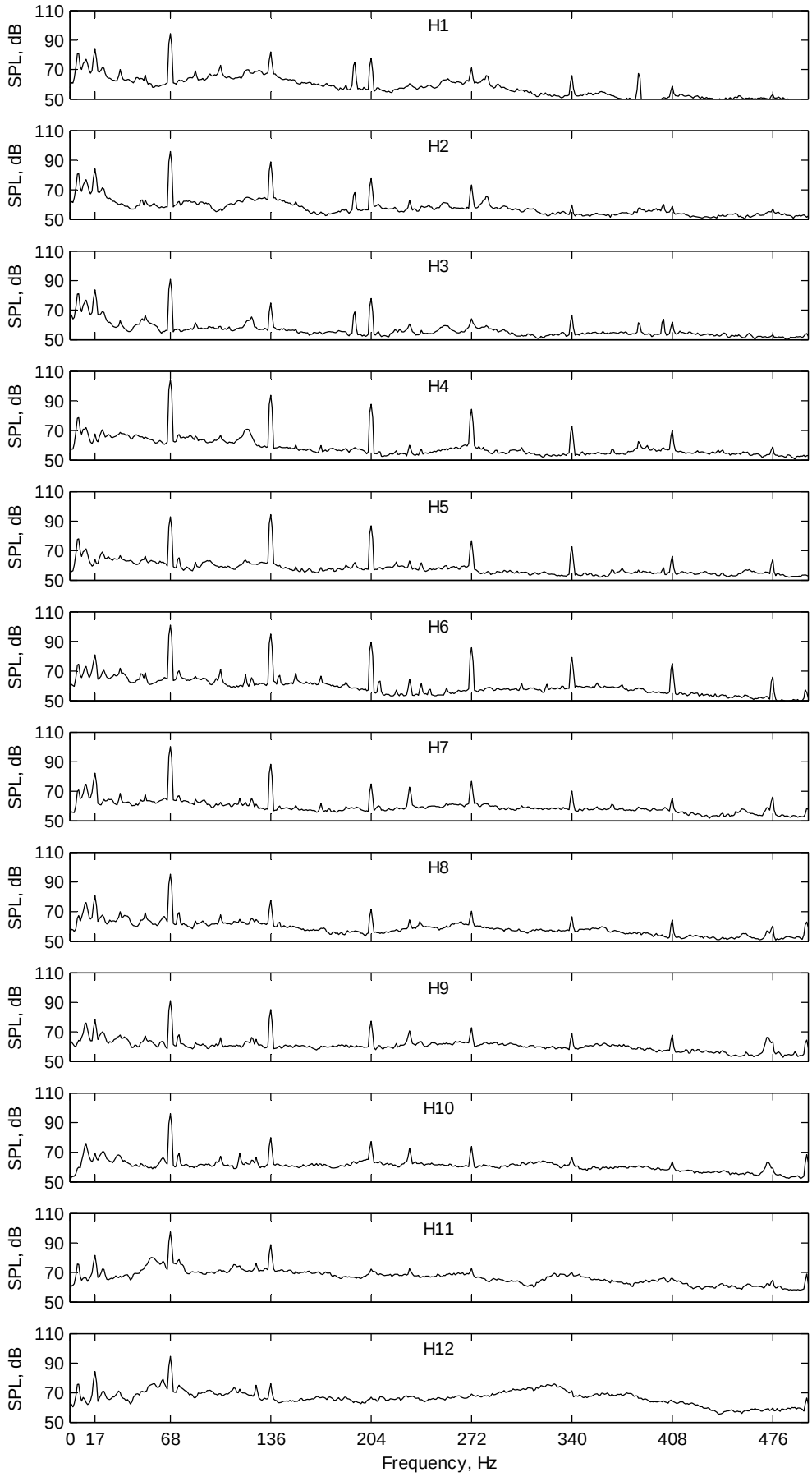

Figure 7.1 Spectra from the microphones on the AP-3C seat headrests, default synchrophase angles, Serial 17a (240 KIAS at FL200).

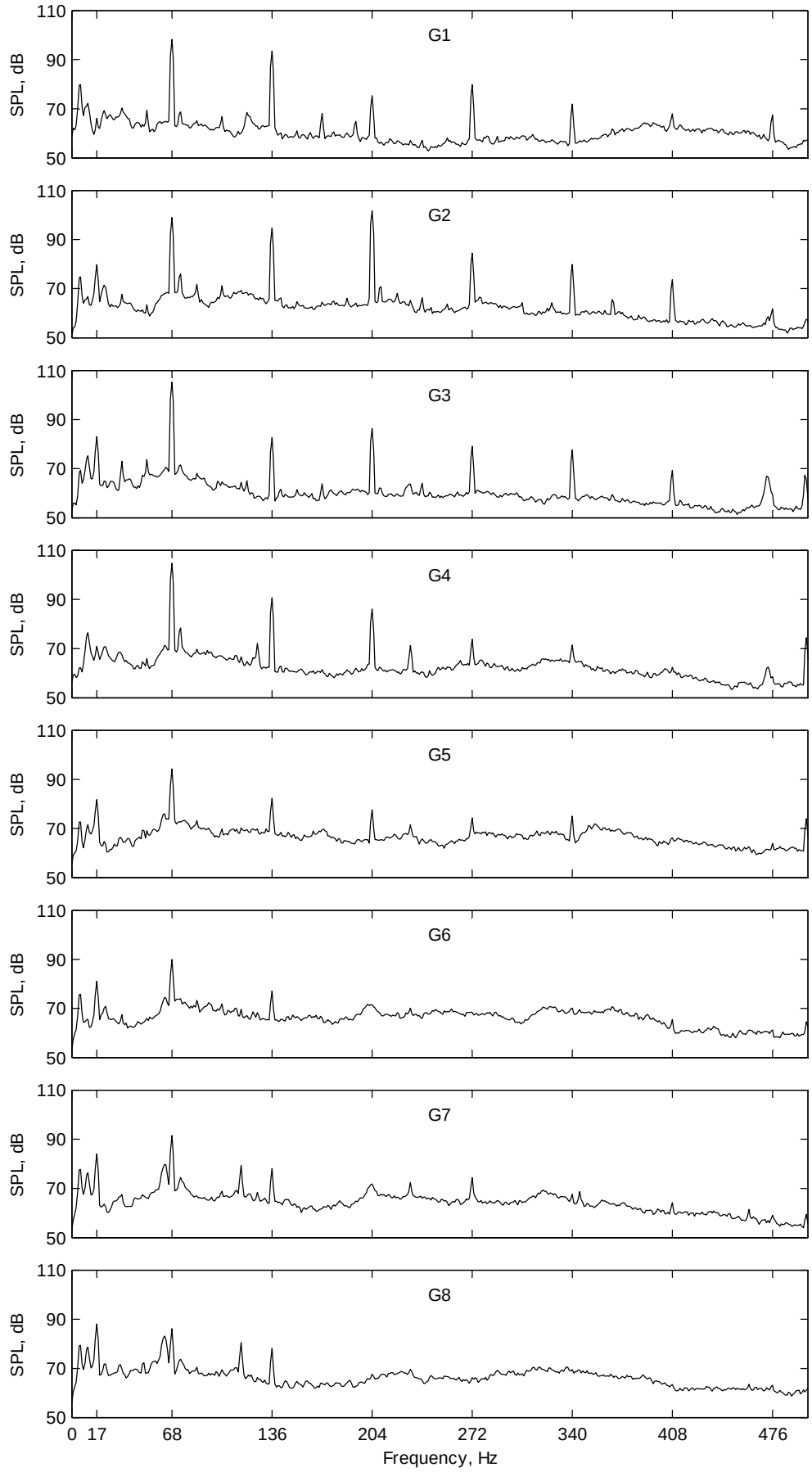

Figure 7.2 Spectra from the microphones on the AP-3C overhead grab rail, default synchrophase angles, Serial 17a (240 KIAS at FL200).

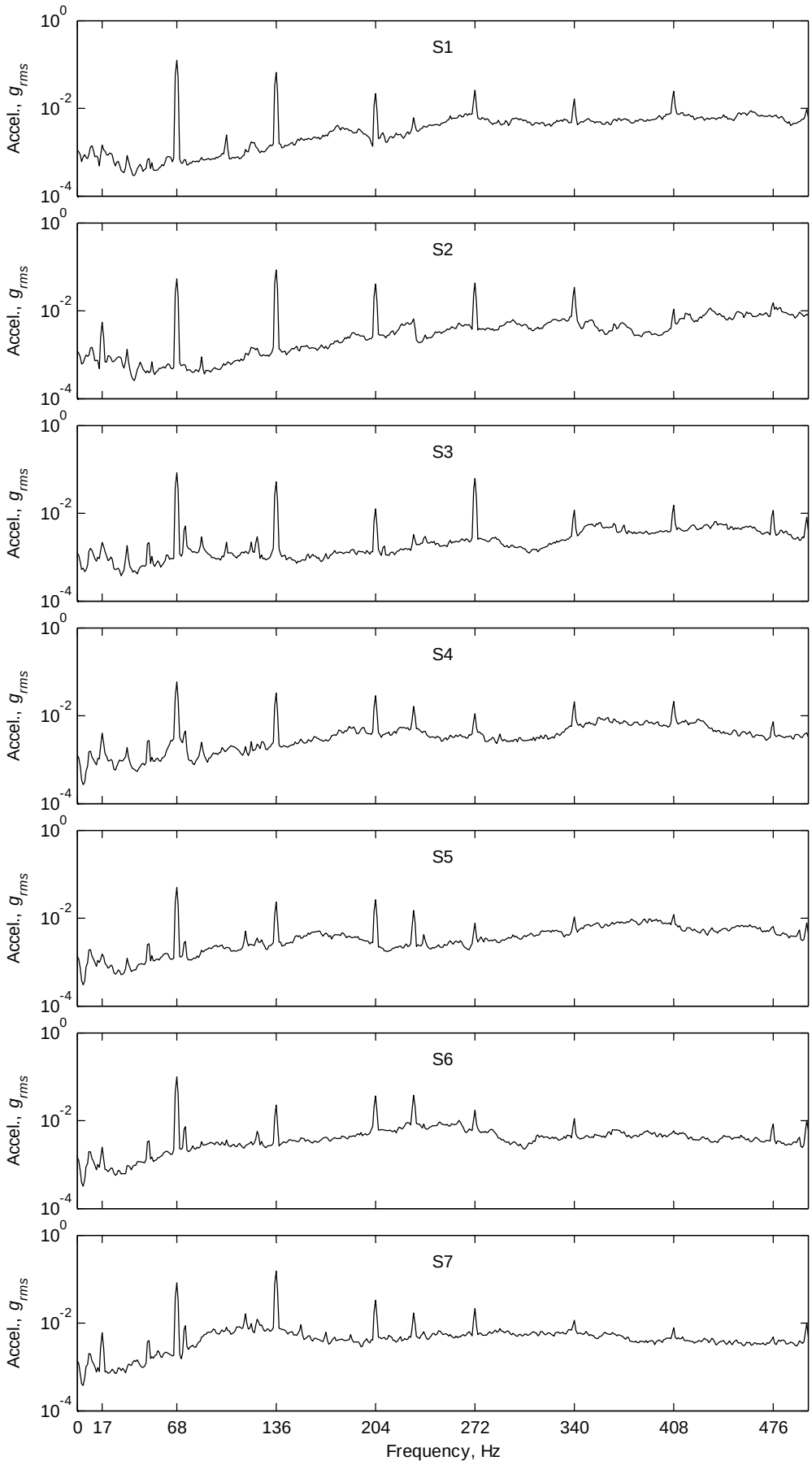

Figure 7.3 Spectra from the accelerometers on the AP-3C seat rails, default synchrophase angles, Serial 17a (240 KIAS at FL200).

7.2. C-130J-30 Cabin Noise and Vibration

7.2.1. Flight Deck Microphones

The spectra from the microphones on the pilot, co-pilot and flight engineer seat headrests during Flight 3 of Trial 1 are shown in Figure 7.4. It can be seen that the first three BPF harmonic components are significant on the flight deck (up to 94 dB at the BPF), although the amplitudes of these components are lower than in the main cabin (§7.2.2).

The flight-deck and main-cabin acoustic spectra (§7.2.2) differ from the cargo-floor vibration spectra (§7.2.3) in the region below 20 Hz, where there are significant acoustic components at 6 Hz, and to a lesser extent 12 Hz, that are not present in the vibration spectra. These are probably the frequencies of the fundamental axial acoustic mode of the fuselage (i.e., with a half-wavelength equal to the cabin length) and its first harmonic (i.e., a full wavelength). It is also possible to see a small 17 Hz component (propeller rotational frequency) in some of the noise spectra, but this is not nearly as significant as in the vibration spectra. While these low-frequency components may cause significant vibrations in items with similar resonant frequencies, they are below the human audible frequency range and of little concern here.

Note that there is a relatively high-amplitude (~82 dB) component at 196 Hz present in these spectra that is not present in the main-cabin spectra. This is probably generated within the flight deck area, as it is not a harmonic of the BPF. Its presence will limit the amount of perceived noise reduction on the flight deck that can be achieved by optimising the synchrophase angles, particularly the 2× BPF component.

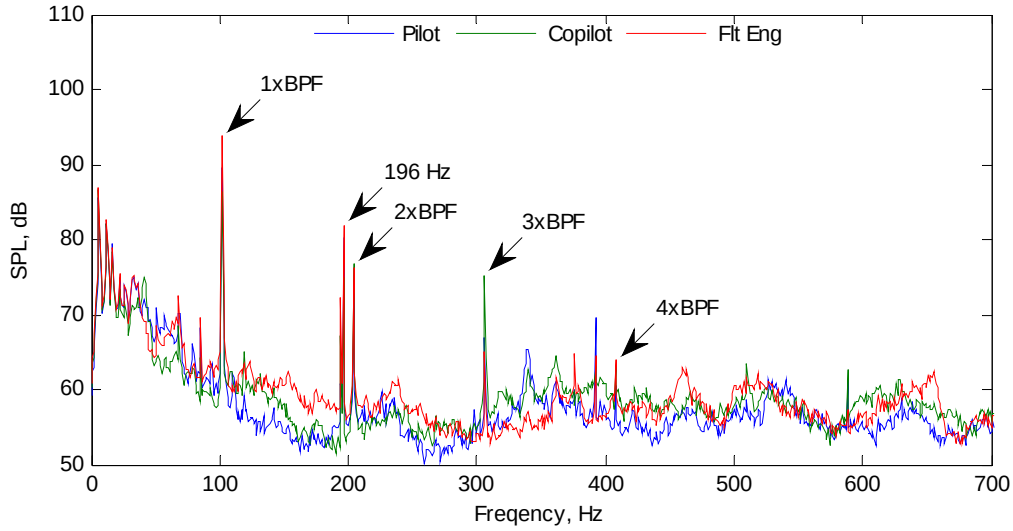

Figure 7.4 Spectra from the microphones on the C-130J-30 flight deck, default synchrophase angles, Trial 1, Flight 3, Serial 6.2a (200 KCAS at FL280).

7.2.2. Main Cabin Microphones

The main-cabin noise spectra for Serials 4.2a, 5.2a, 6.2a and 7.2a from Flight 3 of Trial 1 are shown in Figures 7.5–7.7. It can be seen that the amplitudes of the BPF harmonics are greatest in the front half of the cabin, particularly near the plane of the propellers (near Tie-Down Ring #12), and diminish towards the rear of the cabin. The spectra for the different serials are generally quite similar, overlapping in many regions; however, the amplitudes of the BPF harmonic components vary with the flight conditions. Overall, the results are

very similar to the cargo floor vibration (§7.2.3) showing that the internal acoustic environment contains many of the features of the fuselage vibration.

7.2.3. Cargo Floor Accelerometers

The floor vibration spectra for three different flight conditions (Serials 4.2a, 5.2a and 6.2a) of Flights 1 and 2 (i.e., the cargo flights) of the first trial are shown in Figures 7.8–7.13.

In general, it can be seen that the amplitudes of the BPF harmonics gradually taper off, and the broadband vibration gradually increases, as the frequency rises. Although not shown here, the broadband vibration continues to increase with frequency, peaking at around 3 kHz, after which it gradually decreases. The amplitudes of the BPF harmonics are greatest in the front half of the cabin, particularly near the plane of the propellers (near Tie-down Ring #12), and diminish towards the rear of the cabin. The spectra for the different serials are generally quite similar, overlapping in many regions; however, the amplitudes of the BPF harmonic components vary with the flight conditions.

Looking at the differences between the results for Flights 1 and 2 (i.e., differences caused by different cargo positions), the results for accelerometers F12, and to a lesser extent F17, from Flight 2 (Figure 7.13) stand out. These show frequency components that appear to be propeller-related 17 Hz sidebands of the 3×, 4×, 5×, and 6× BPF harmonics, and hence may have been the result of some localised modulation of the vibration in these regions during Flight 2. The cause of this is unknown.

7.2.4. Pallet Accelerometers

The pallet vibration spectra for both cargo flights from Trial 1 are shown in Figures 7.14–7.19. The acceleration scale is the same as that used for the cargo floor vibration.

Generally, the pallet vibration spectra are very similar to the underlying floor vibration spectra. The pallet vibration is dominated by the BPF harmonics, and the vertical components are similar in magnitude to the floor vibration amplitudes, although there are differences that can be attributed to the disparities in the accelerometer locations, and/or the flexure of the pallets.

Significantly, it can be seen that the X (fore/aft) and Y (lateral) components of the pallet vibration are similar in amplitude to the components in the Z (vertical) direction. Hence, vibration in the X and Y directions should not be ignored when assessing the effects on vibration-sensitive cargo.

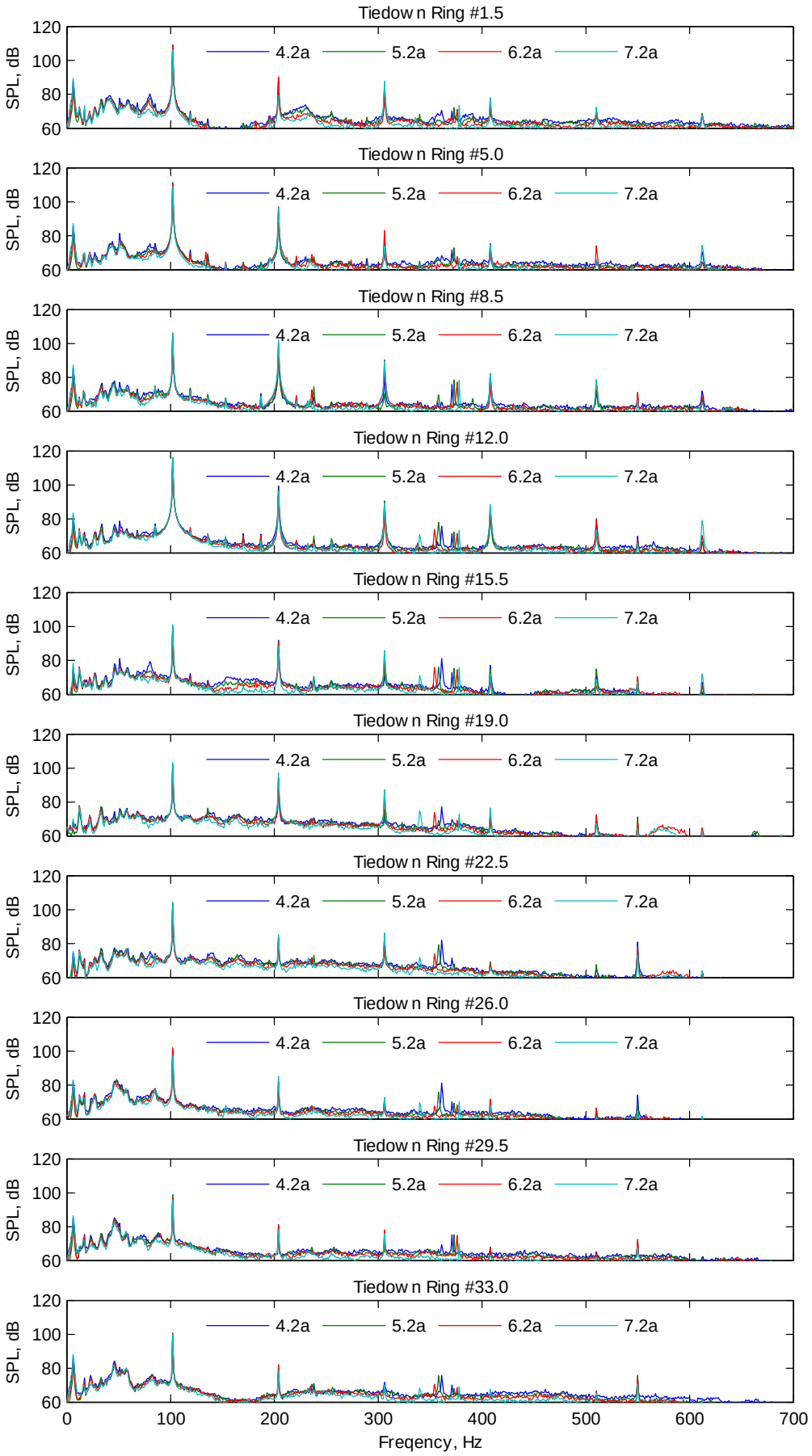

Figure 7.5 Spectra from the microphones along the port side of the C-130J-30 main cabin, default synchrophase angles, Trial 1, Flight 3.

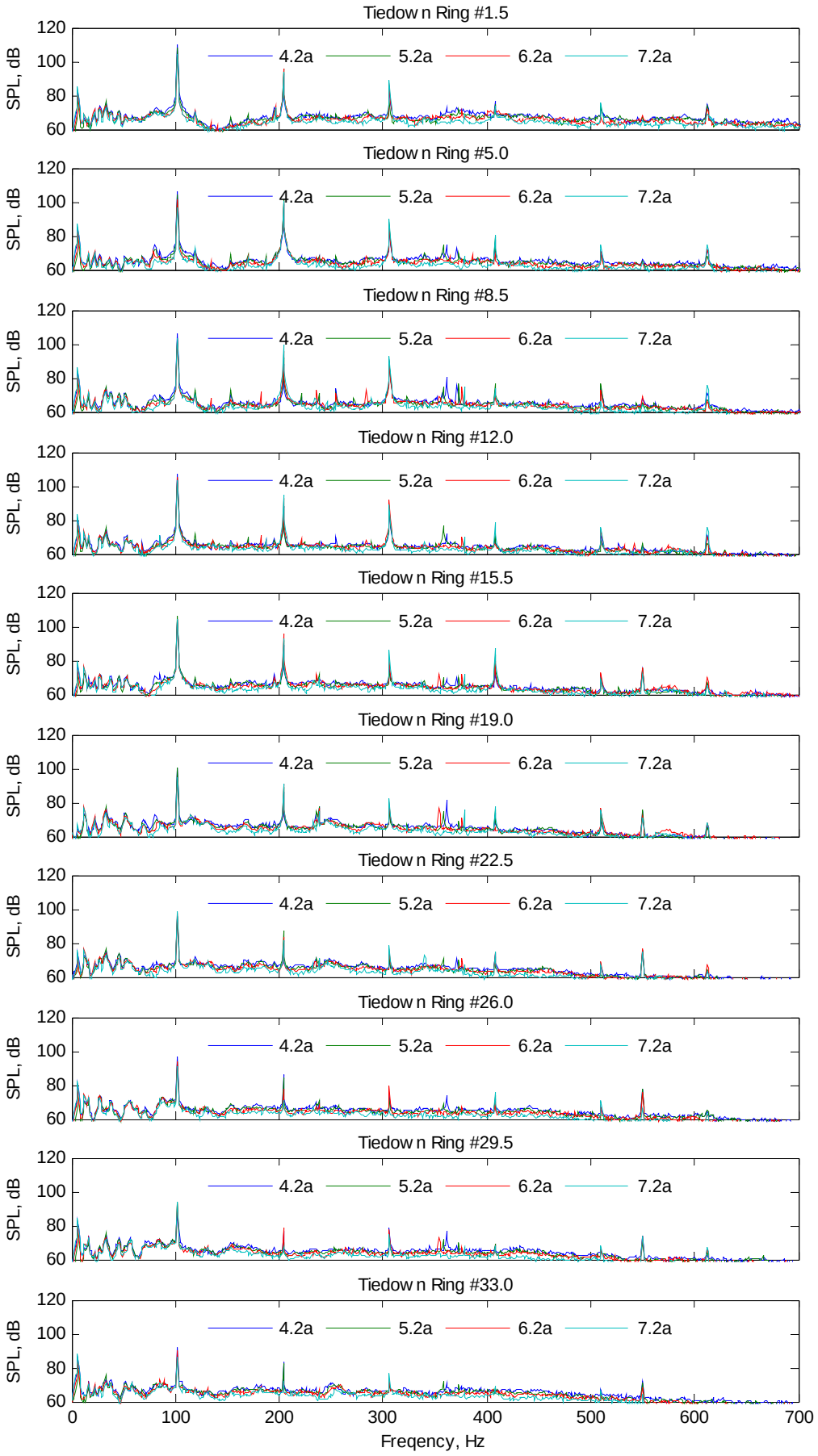

Figure 7.6 Spectra from the microphones along the centre line of the C-130J-30 main cabin, default synchrophase angles, Trial 1, Flight 3.

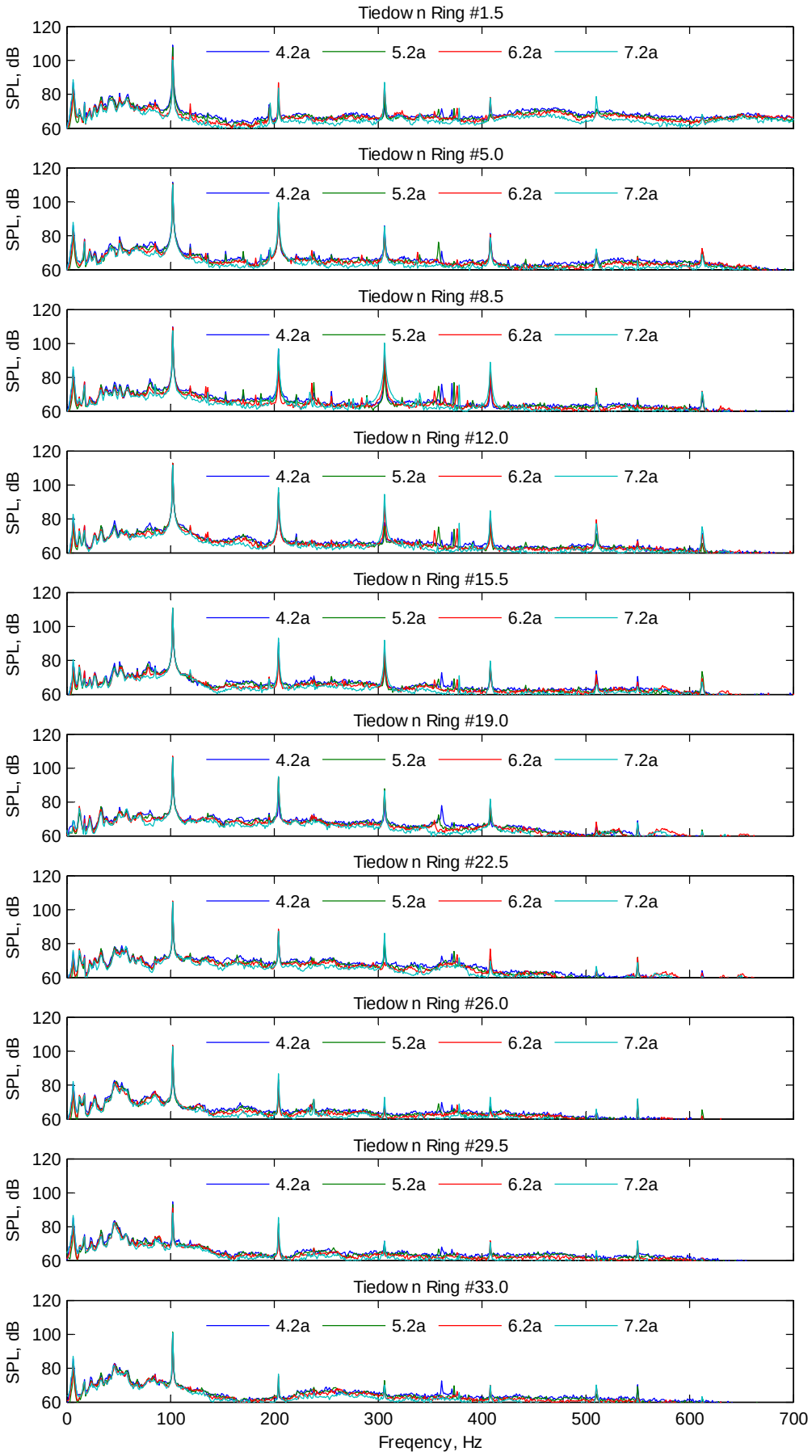

Figure 7.7 Spectra from the microphones along the starboard side of the C-130J-30 main cabin, default synchrophase angles, Trial 1, Flight 3.

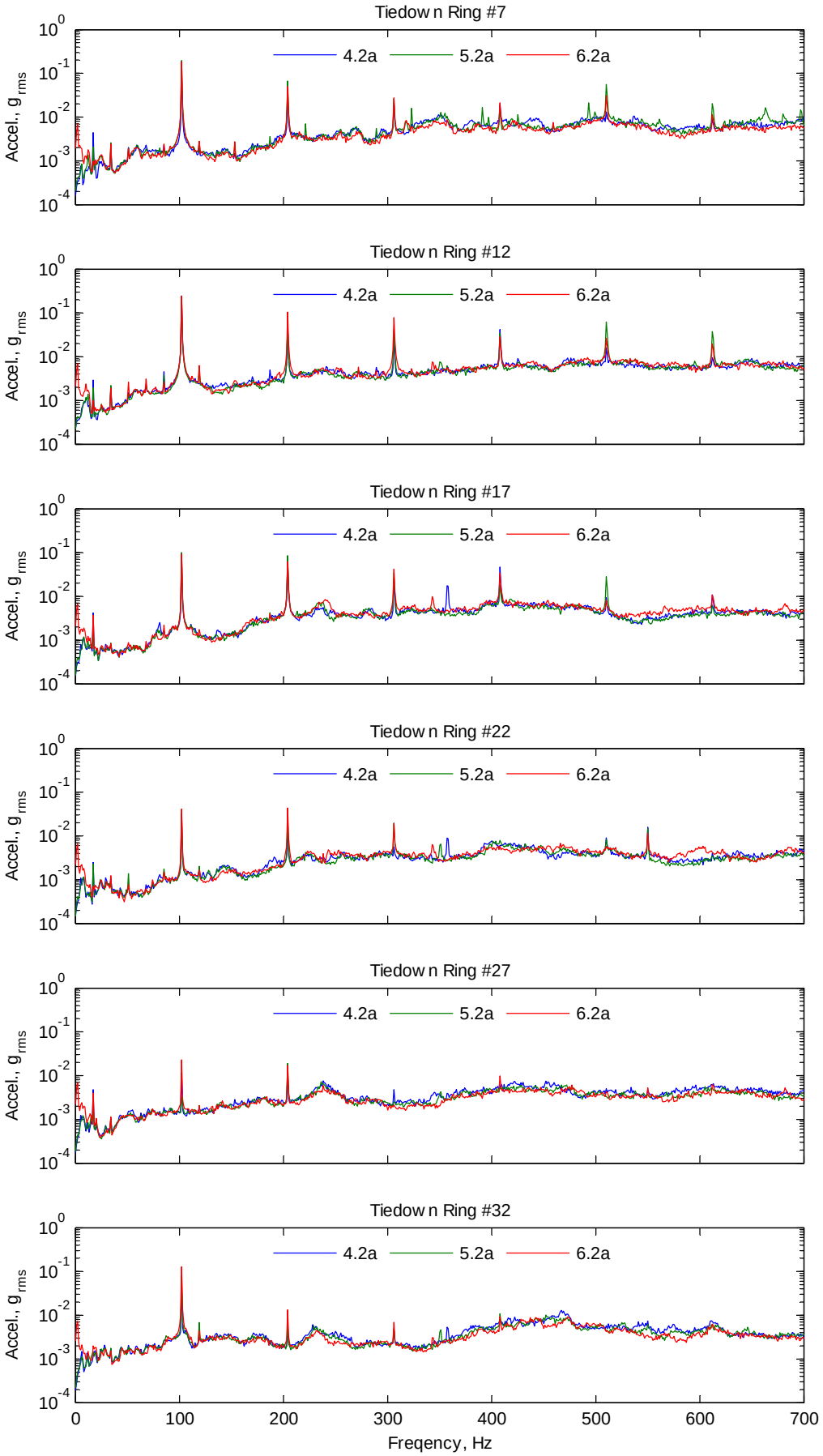

Figure 7.8 Spectra from the accelerometers along the port side of the C-130J-30 cargo floor, default synchrophase angles, Trial 1, Flight 1.

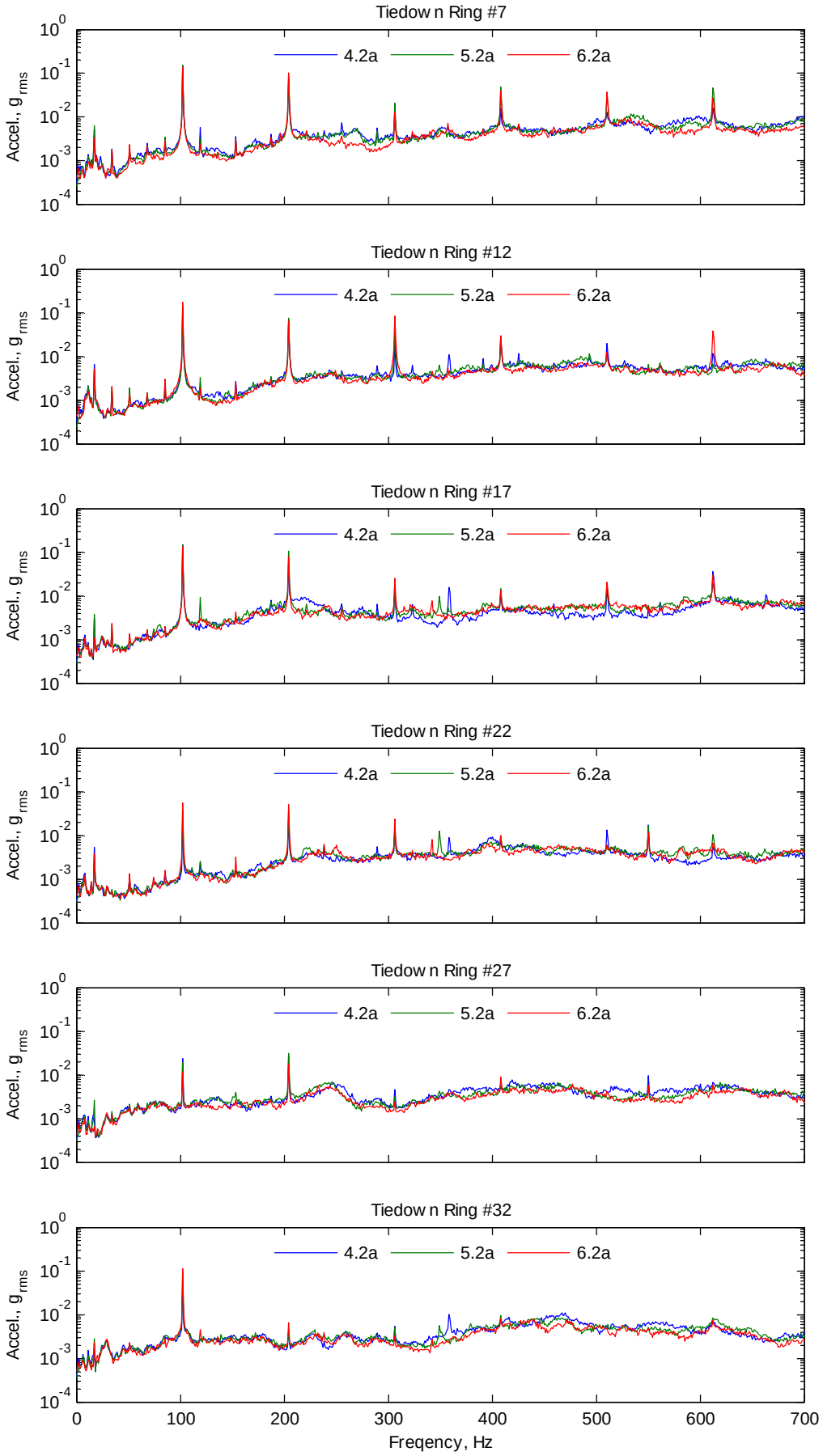

Figure 7.9 Spectra from the accelerometers along the port side of the C-130J-30 cargo floor, default synchrophase angles, Trial 1, Flight 2.

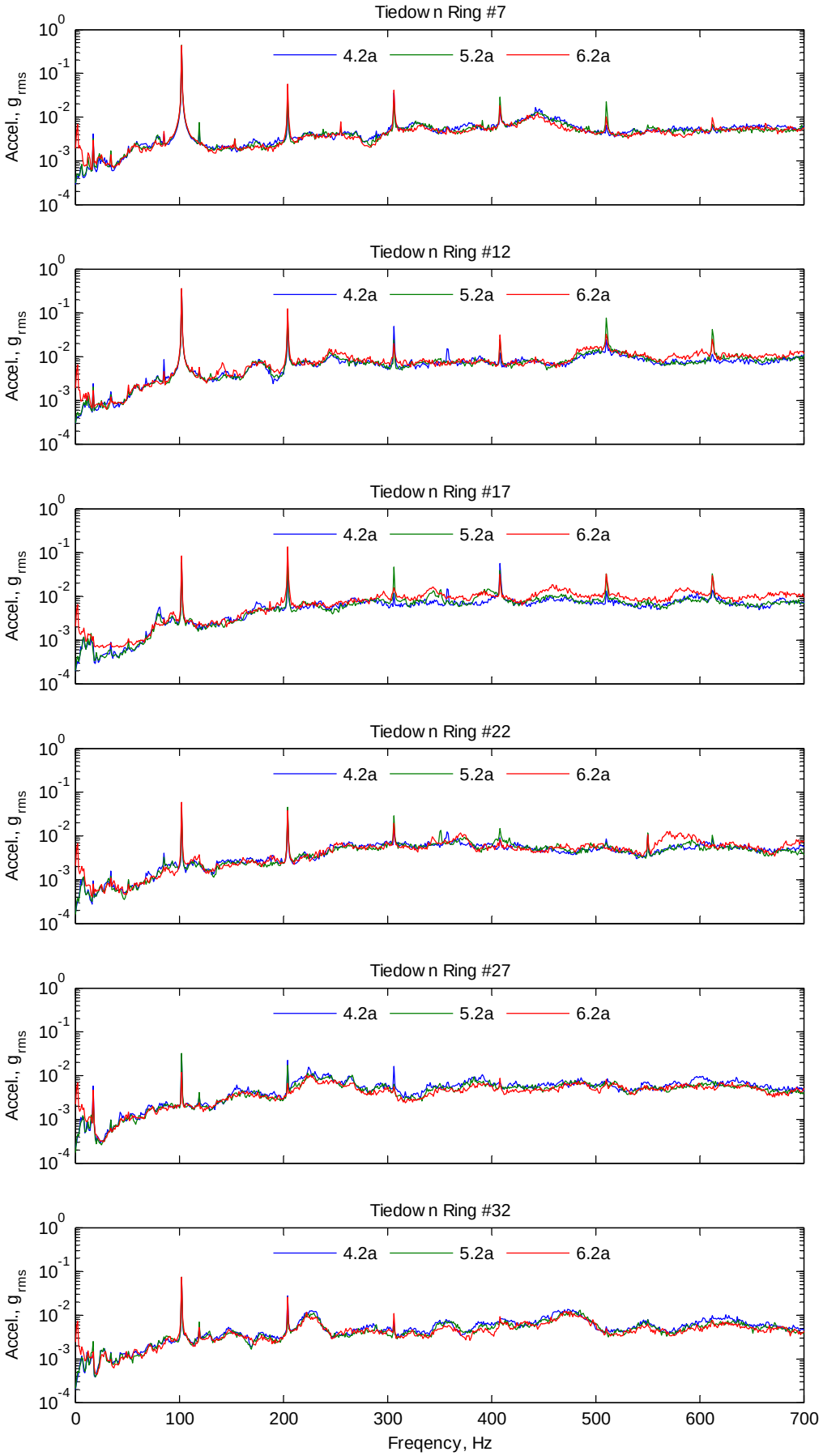

Figure 7.10 Spectra from the accelerometers along the centre line of the C-130J-30 cargo floor, default synchrophase angles, Trial 1, Flight 1.

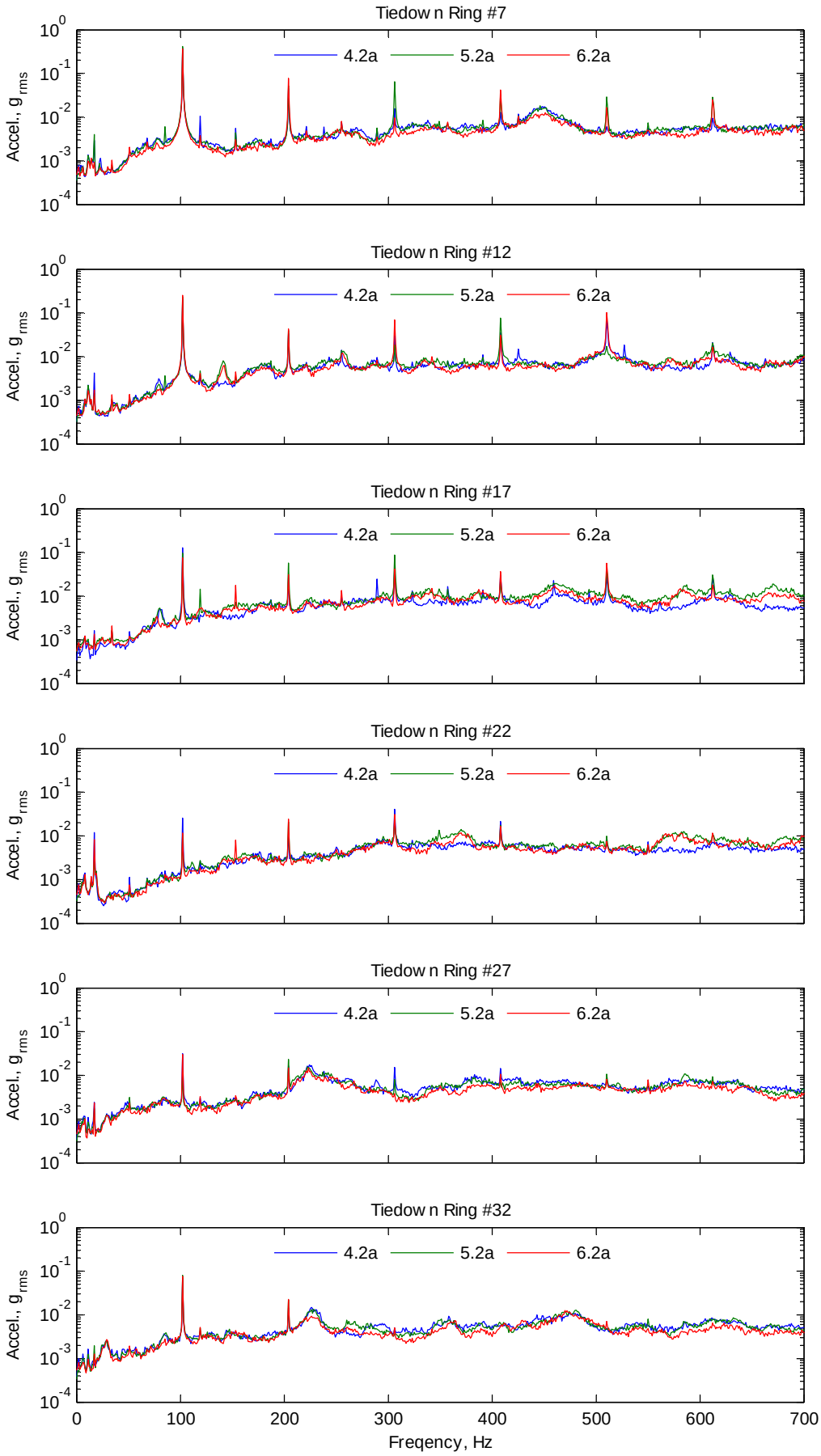

Figure 7.11 Spectra from the accelerometers along the centre line of the C-130J-30 cargo floor, default synchrophase angles, Trial 1, Flight 2.

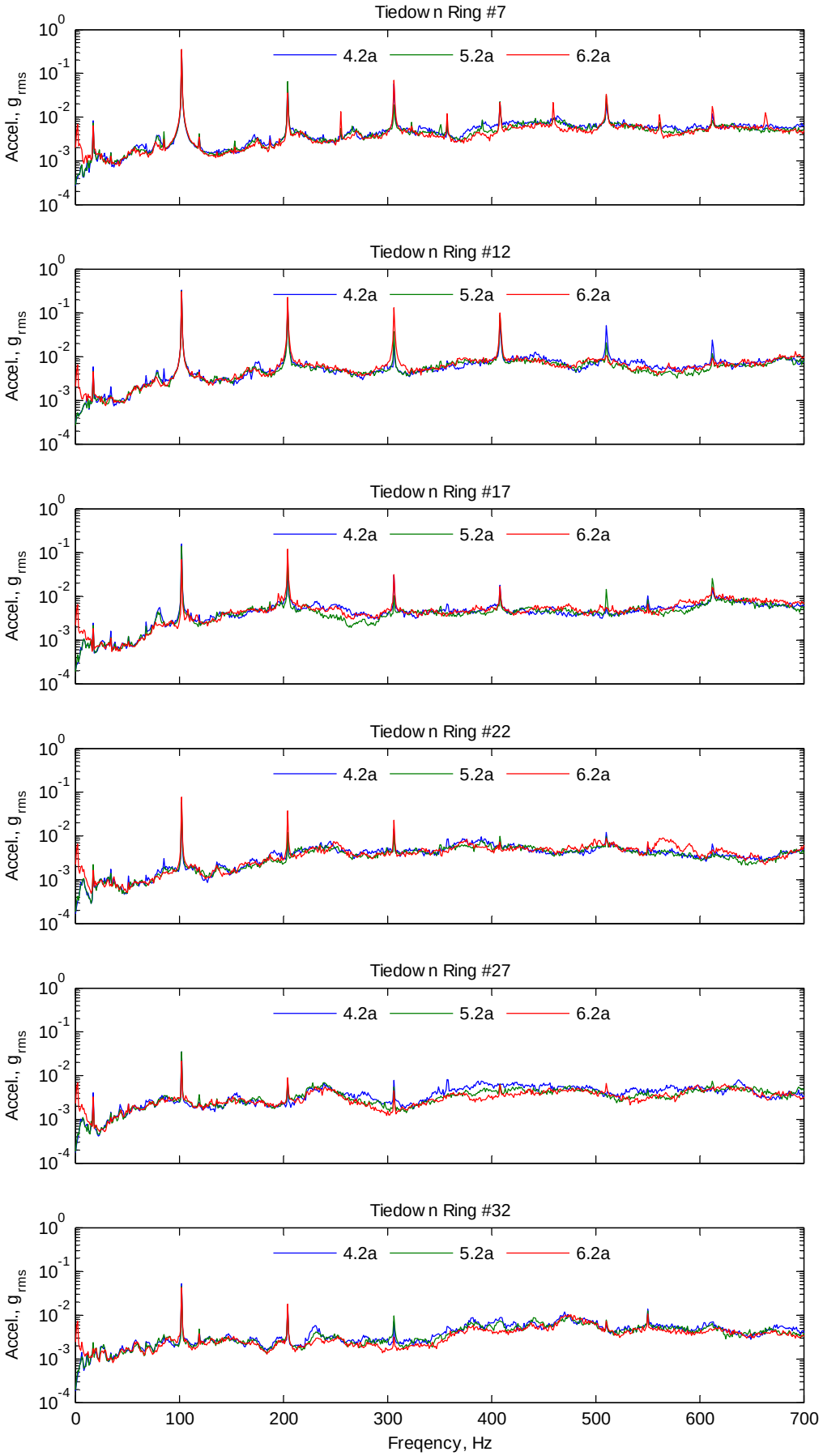

Figure 7.12 Spectra from the accelerometers along the starboard side of the C-130J-30 cargo floor, default synchrophase angles, Trial 1, Flight 1.

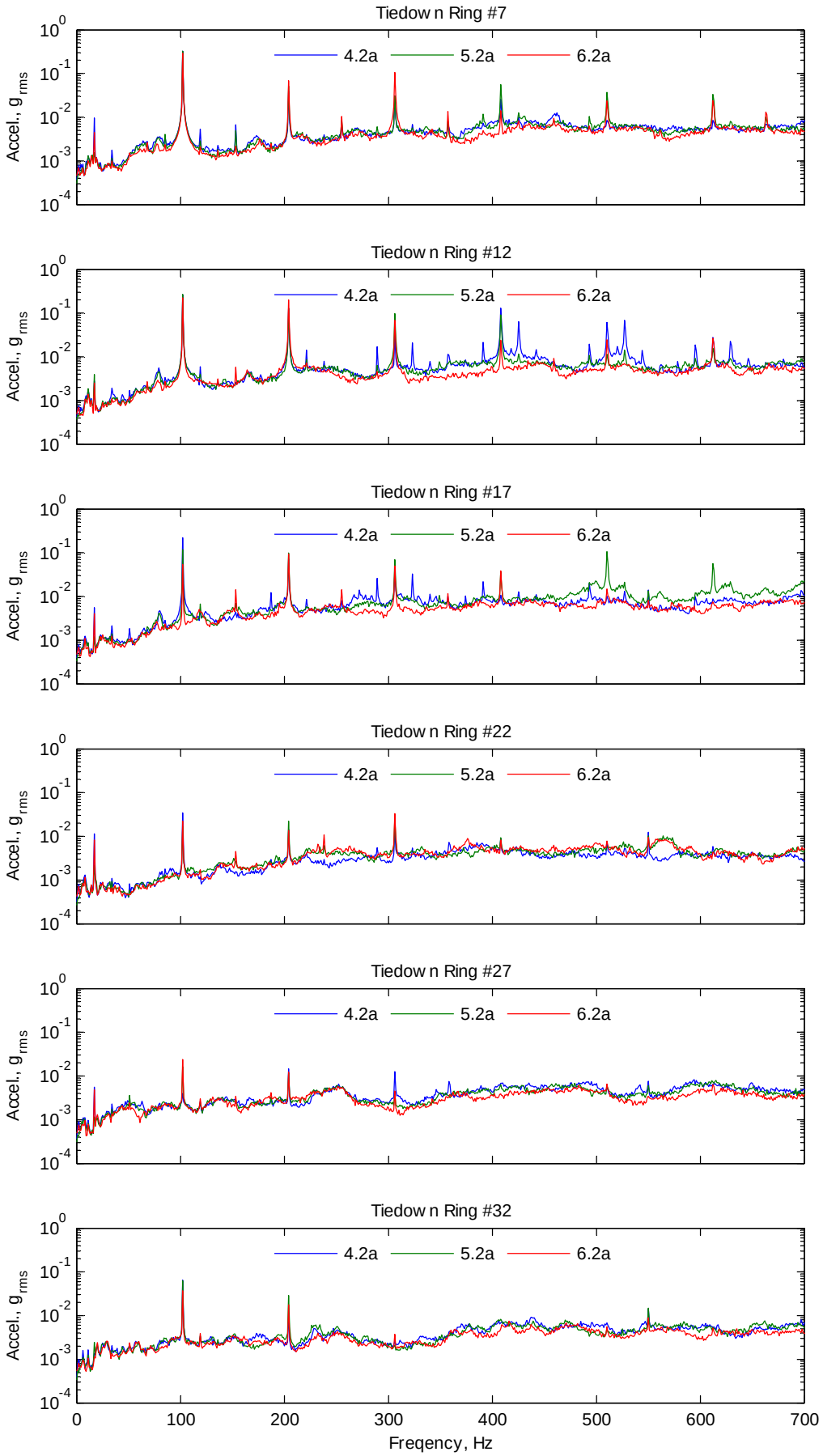

Figure 7.13 Spectra from the accelerometers along the starboard side of the C-130J-30 cargo floor, default synchrophase angles, Trial 1, Flight 2.

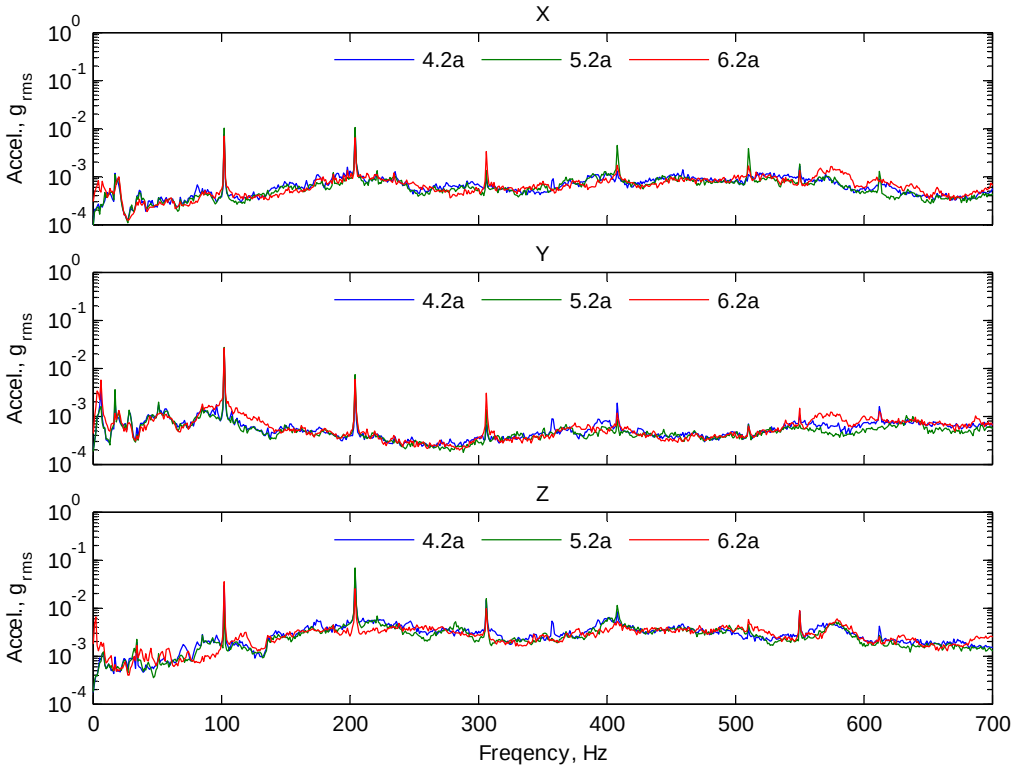

Figure 7.14 Spectra from the tri-axial accelerometer on the single pallet in the C-130J-30, Trial 1, Flight 1.

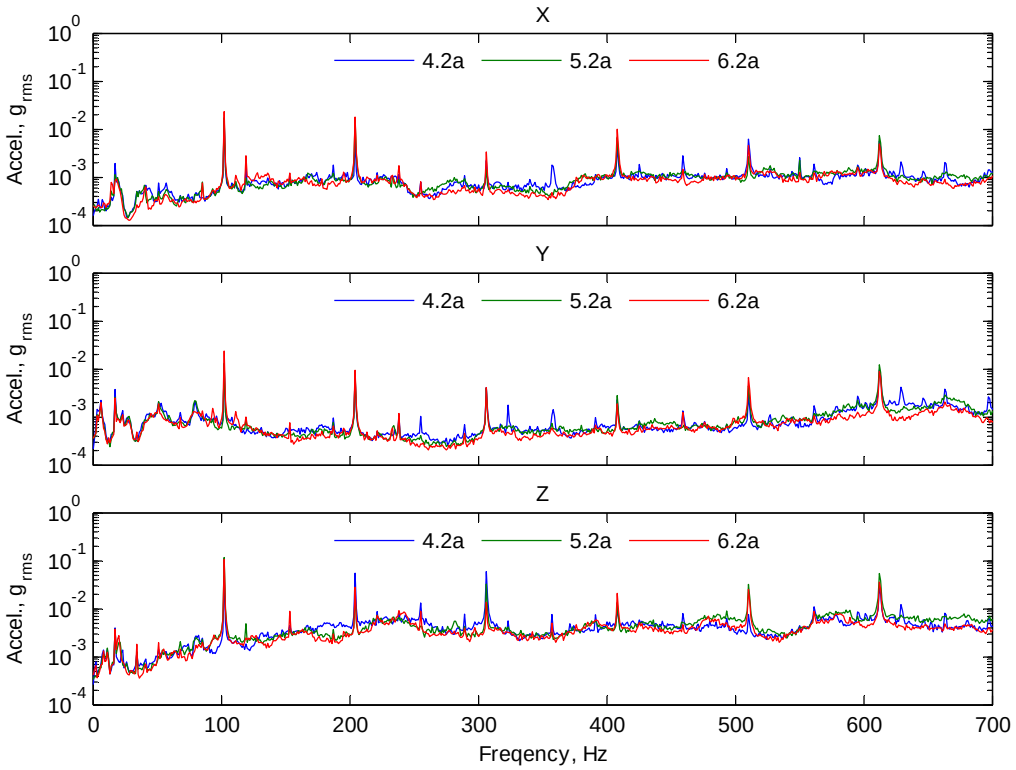

Figure 7.15 Spectra from the tri-axial accelerometer on the single pallet in the C-130J-30, Trial 1, Flight 2.

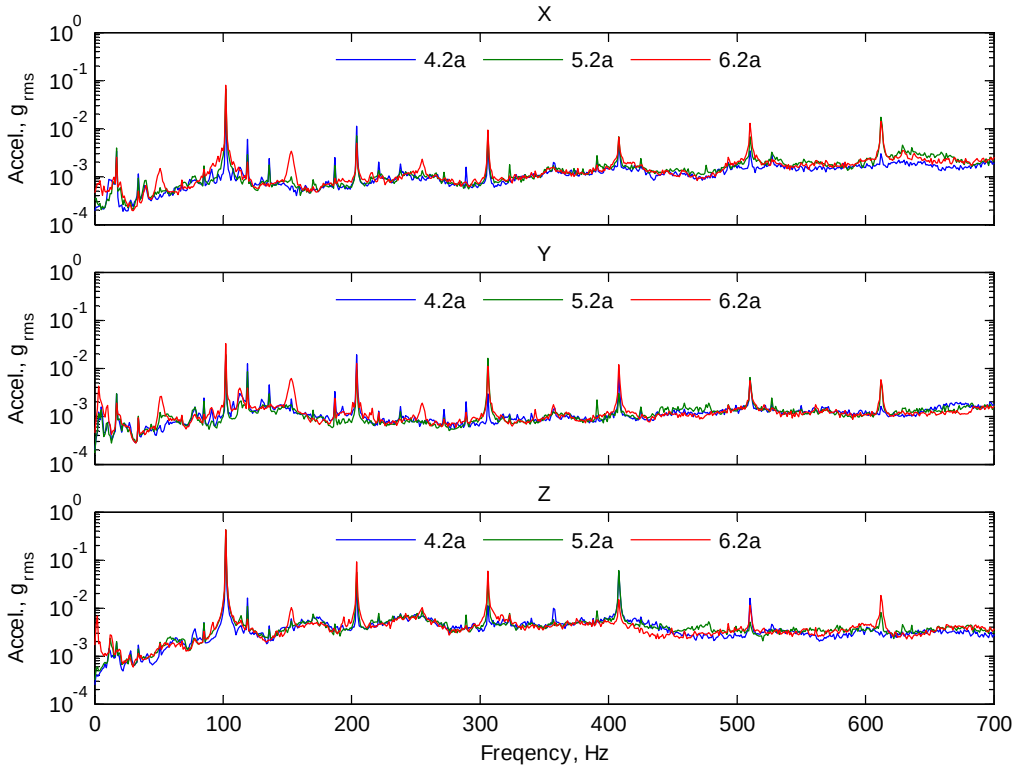

Figure 7.16 Spectra from the tri-axial accelerometer on the double pallet in the C-130J-30, Trial 1, Flight 1.

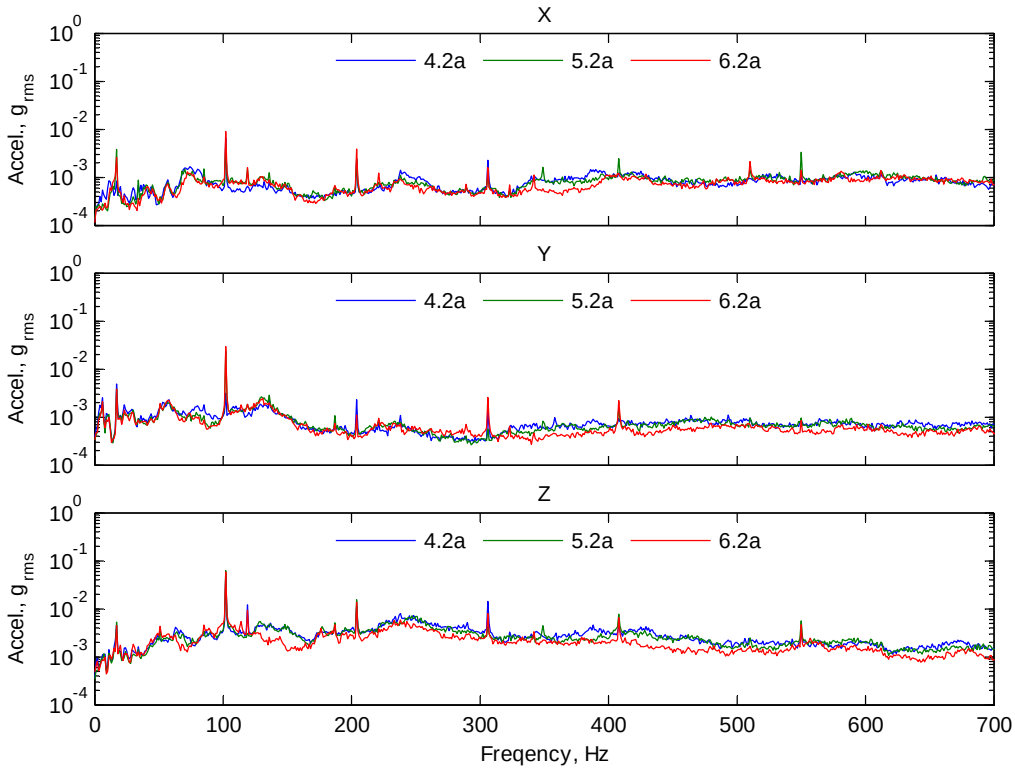

Figure 7.17 Spectra from the tri-axial accelerometer on the double pallet in the C-130J-30, Trial 1, Flight 2.

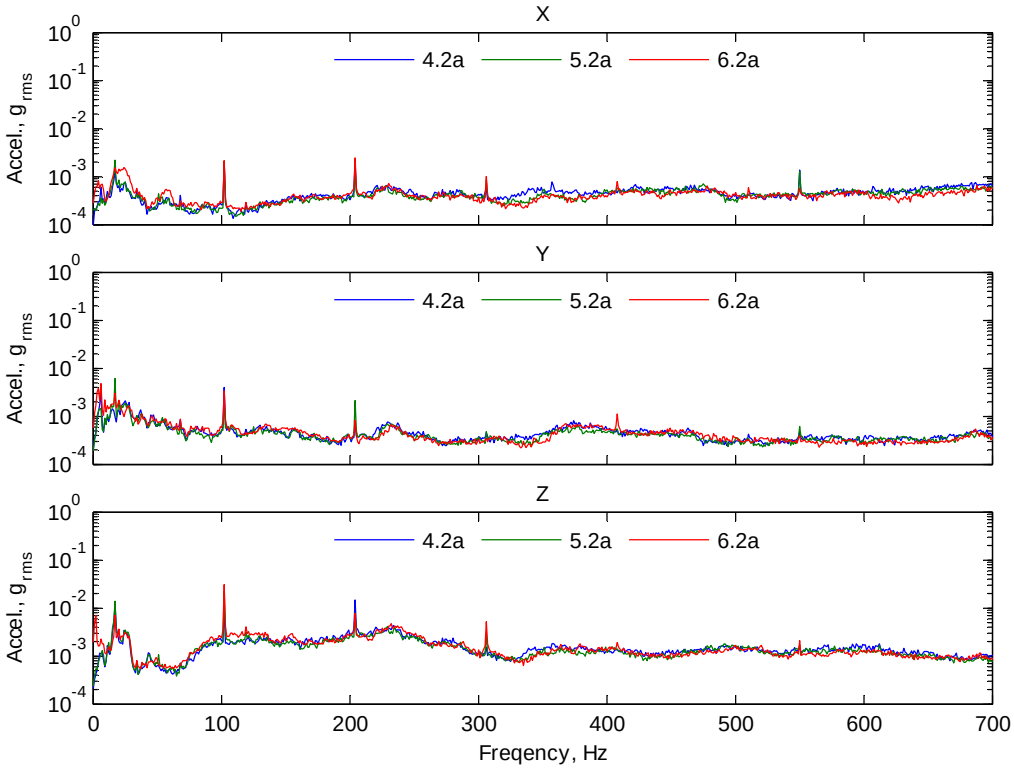

Figure 7.18 Spectra from the tri-axial accelerometer on the triple pallet in the C-130J-30, Trial 1, Flight 1.

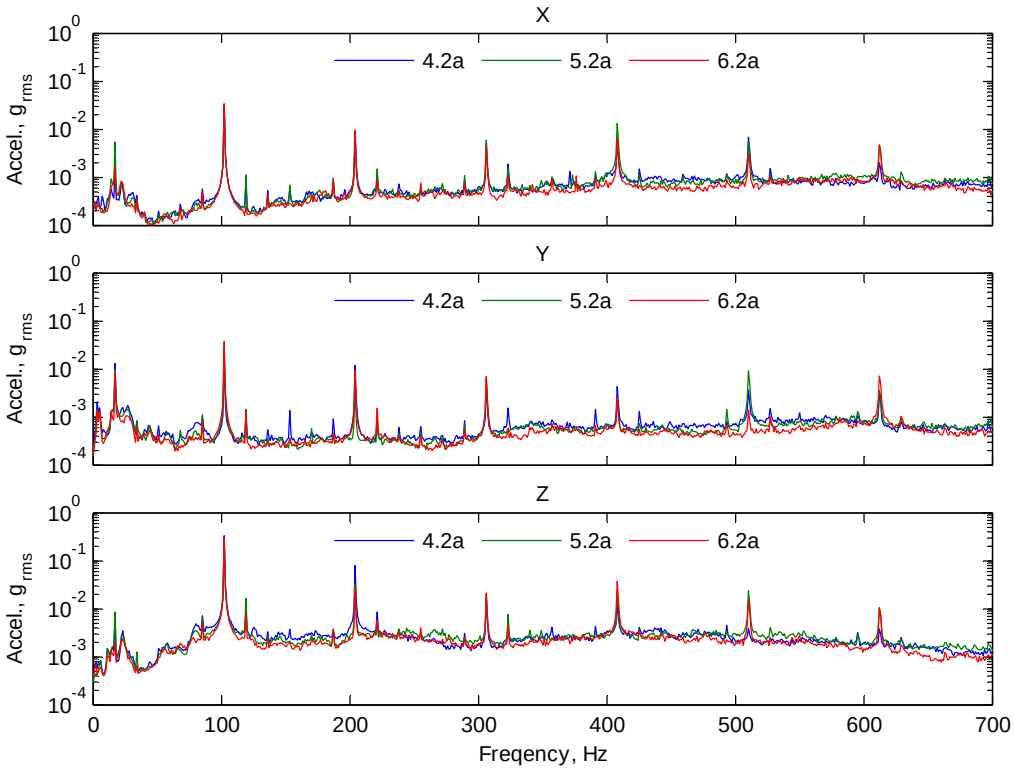

Figure 7.19 Spectra from the tri-axial accelerometer on the triple pallet in the C-130J-30, Trial 1, Flight 2.

8. Measurement Variability and Repeatability

This chapter examines the variability and repeatability of the measured cabin noise and vibration levels at the BPF and its low-order harmonics for fixed synchrophase angles under the same nominal flight conditions. This is done in order to quantify some of the measurement differences between the various flight tests, and to provide some indication about how these differences may affect the accuracy of the propeller signature estimation method, and the subsequent optimisation process. The calculated propeller signatures are, however, analysed in more detail in Chapter 9.

The measurement variability and repeatability is examined here in three contexts:

a) the short-term variability of the signal levels over a continuous 10 s period (§8.1),
b) the repeatability of measurements at 10-minute intervals in the same aircraft (§8.2), and
c) the variation between measurements in two aircraft of the same type (§8.3).

Low variability and high repeatability in contexts a) and b) are both necessary for the effective utilisation of propeller signature theory. If the signal levels are not stable, or if the measurement repeatability over 10-minute intervals (when the flight conditions should nominally be constant) is not good, then the accuracy of the computed signatures, which require a number of separate measurements at different synchrophase angles, will be reduced.

The potential effect of measurement uncertainty on the propeller signature estimation method (§5.1) is shown qualitatively in Figure 8.1. It can be seen that as the uncertainty grows (i.e., as the red circles get bigger), it becomes more difficult to estimate the signatures accurately (i.e., the black circles can grow, shrink or move relative to each other and still fit the measurements). Note that the figure assumes no measurement bias introduced by factors not under experimental control. Any such bias will displace the measurements and further impede the signature estimation process. Variations observed in contexts a) and b) may well imply that such factors are present. Several of these, including specific examples of the effects of synchrophase angle deviations, are discussed in §8.4. It should be noted that these factors do not necessarily invalidate the use of propeller signature theory, but may suggest that the signatures should be estimated from data collected over shorter periods, and be updated more frequently, depending on the timeframes over which the factors operate. The influence exerted by these additional factors also provides further motivation for adopting an adaptive synchrophasing system (i.e., one that can compensate for these influences), compared to an optimised but non-adaptive system (i.e., one that cannot compensate for these influences).

Any variations identified in context c) may be caused by similar factors to those in contexts a) and b). However, they may also be due to differences in sensor positions and/or flight conditions between the two aircraft, or imply the presence of vibro-acoustic differences between aircraft of the same type. These issues are also discussed in §8.4.

Note that the AP-3C trial data could only be used to examine the short-term variation, as no serials were repeated in this trial, and only one aircraft was used. However, all three types of variation could be examined using the C-130J-30 data. In particular, two different sets of synchrophase angles (the default angles, and (0°,0°,0°,0°)) were each repeated three times during Serial 10 of Trial 1, and one of these (0°,0°,0°,0°) was also repeated three times during Serial 10 of Trial 2 (§5.4).

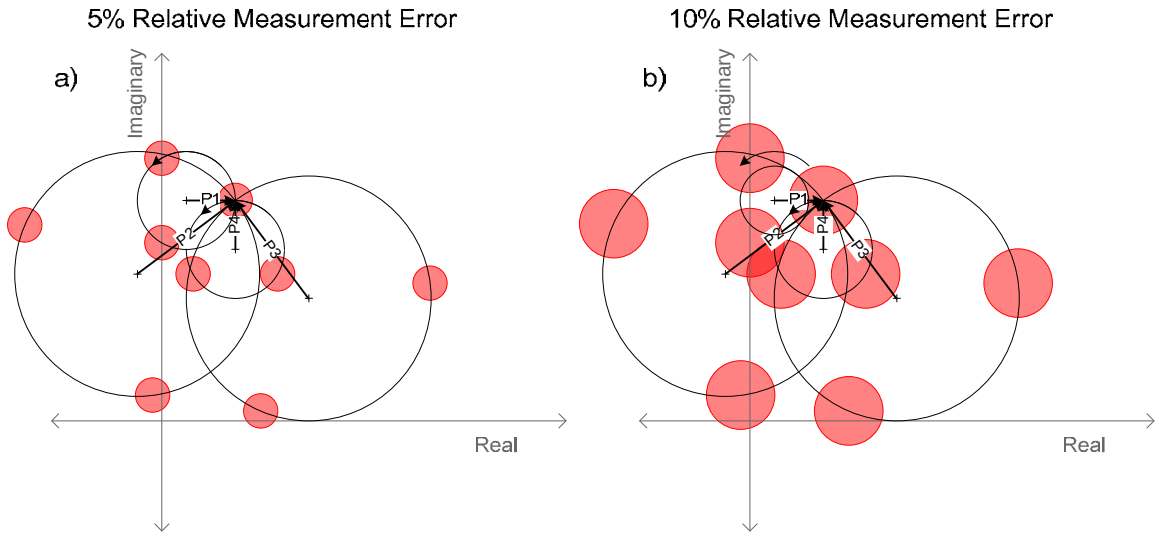

Figure 8.1 The effect of measurement uncertainty (shown as red circles) on the graphical propeller signature estimation method (i.e., fitting the black circles to the measurements), where the three measurements for each propeller have ideal phase-angle spacing of 120° as discussed in §5.1. The measurement error is shown as a percentage of the maximum signal level and assumes no bias from factors not under experimental control.

8.1. Short-Term (10 s) Spectrum Level Variability

In this test, the signals were synchronously re-sampled with respect to the 1P signal from the master propeller (Propeller 3 in the AP-3C, and Propeller 2 in the C-130J-30) so that the frequencies of interest (i.e., 1×, 2×, 3× and 4× BPF) would fall as closely as possible to the midpoints of the Fourier-transform frequency bins and minimise any picket-fence effect. The spectrum levels of these re-sampled signals were computed using a short-time Fourier transform (spectrogram) method using a 17-rev (~1 s) Hamming window sliding over a 187-rev segment of data with 16-rev overlap. This produced 171 averaged spectra over a ~10 s period.

The variability of the spectrum levels with respect to time for a few selected channels from Serial 17a of the AP-3C trial, and Serial 10 of the first C-130J-30 trial, are shown in Figures 8.2 to 8.5, and Figures 8.6 to 8.8 respectively. The C-130J-30 figures include the short-term variation of all three repeated measurements for both sets of synchrophase angles: i.e., the default set of angles, and (0°,0°,0°,0°).

In general, it can be seen that:

a) There are different amounts of variation for different channels during the same measurement periods.

b) There is less variability at the BPF than at its harmonics. This is probably because deviations in the synchrophase angles inherently cause larger variations in the phase of the harmonic components (see §8.4.3).

c) There is more variability in the lower-amplitude, and hence lower signal-to-noise ratio, components, particularly below about 75 dB for acoustic signals and 0.02 g_{rms} for vibration signals (see §8.4.2).

d) Some spectrum levels show small increasing or decreasing trends over time, indicating that some other influencing factor(s) (§8.4) may have been changing during those particular measurements.

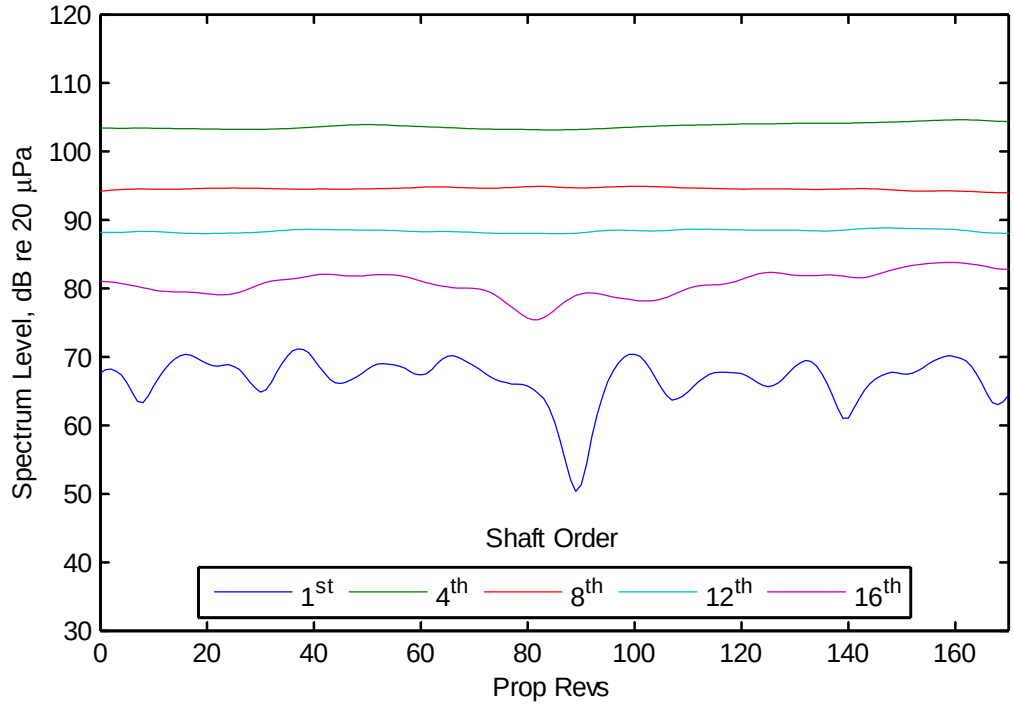

Figure 8.2 Short-term spectrum level variation for AP-3C Microphone H4, default synchrophase angles, Serial 17.

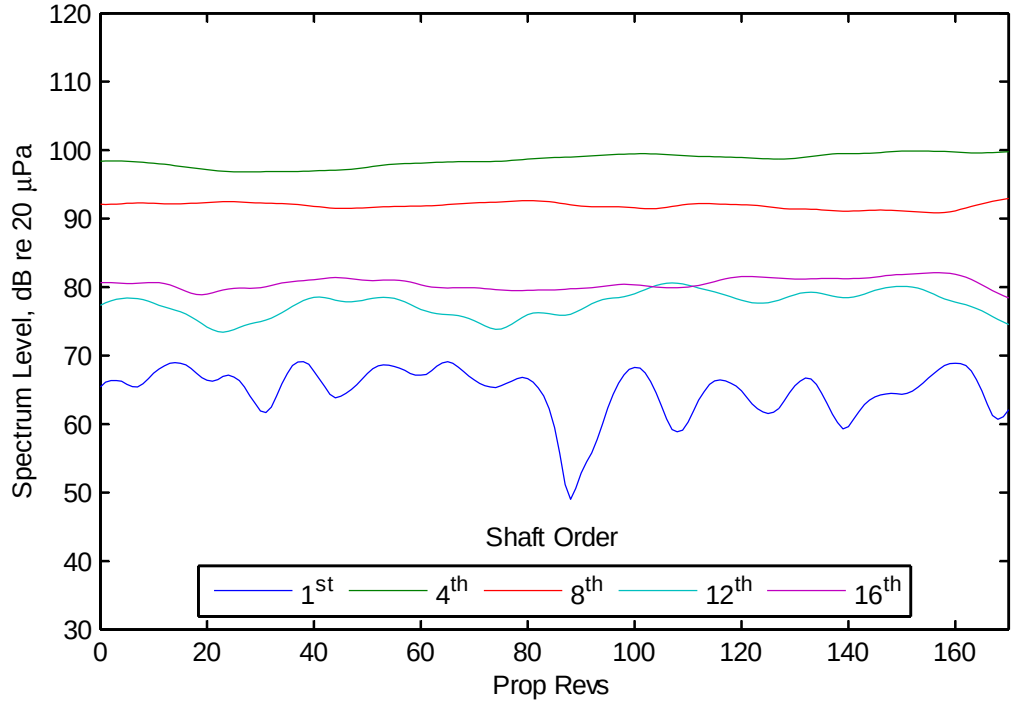

Figure 8.3 Short-term spectrum level variation for AP-3C Microphone G1, default synchrophase angles, Serial 17.

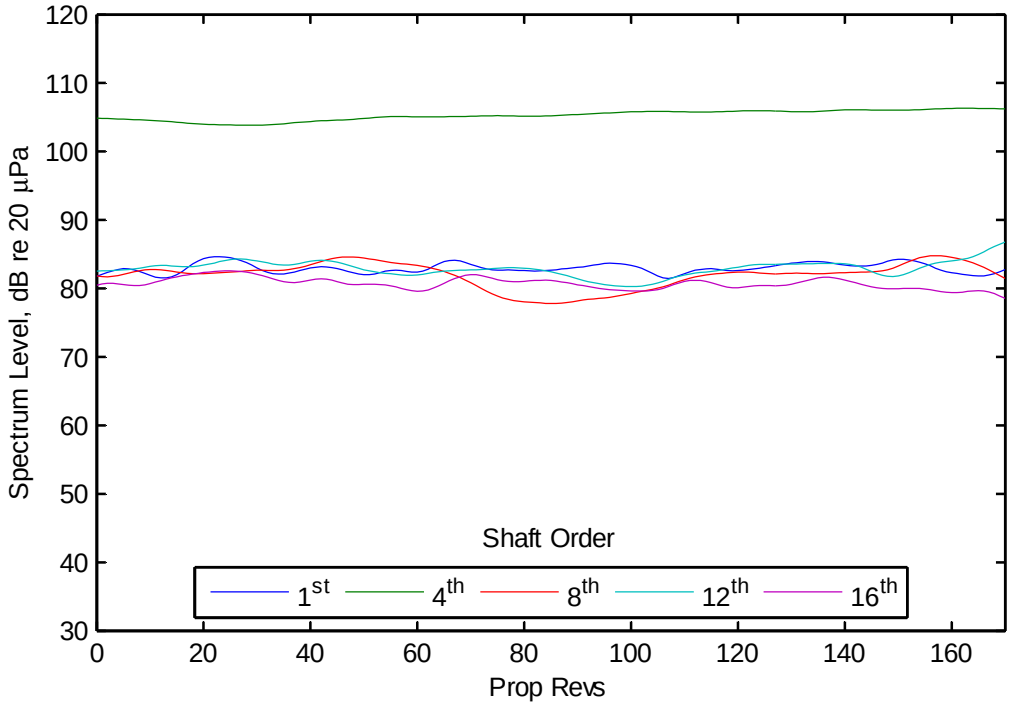

Figure 8.4 Short-term spectrum level variation for AP-3C Microphone G3, default synchrophase angles, Serial 17.

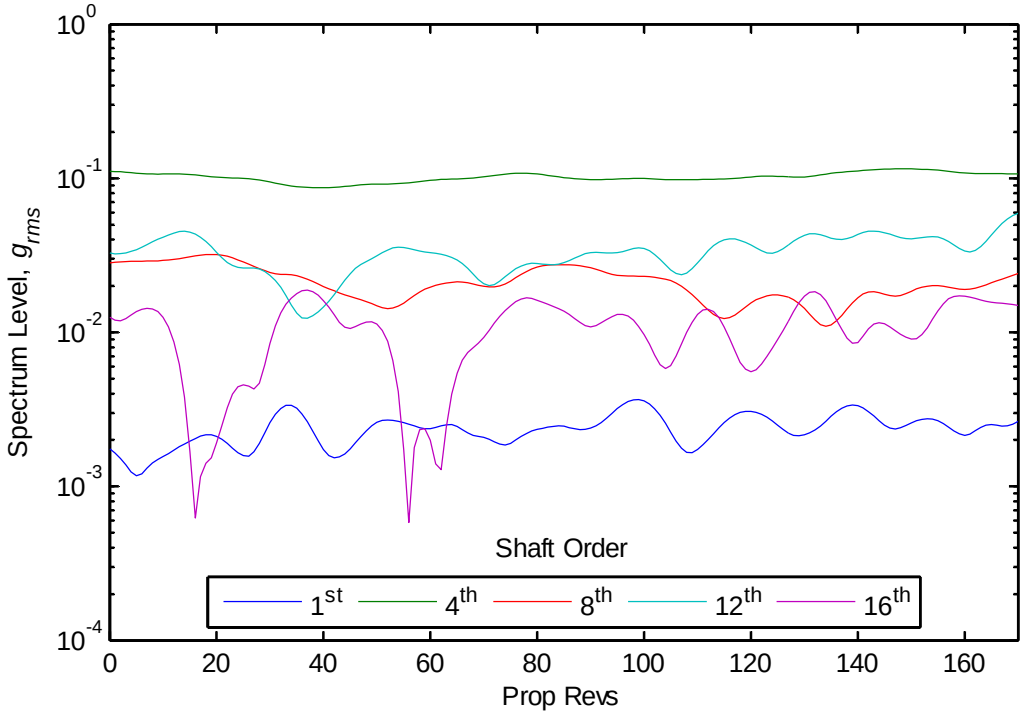

Figure 8.5 Short-term spectrum level variation for AP-3C Accelerometer S6, default synchrophase angles, Serial 17.

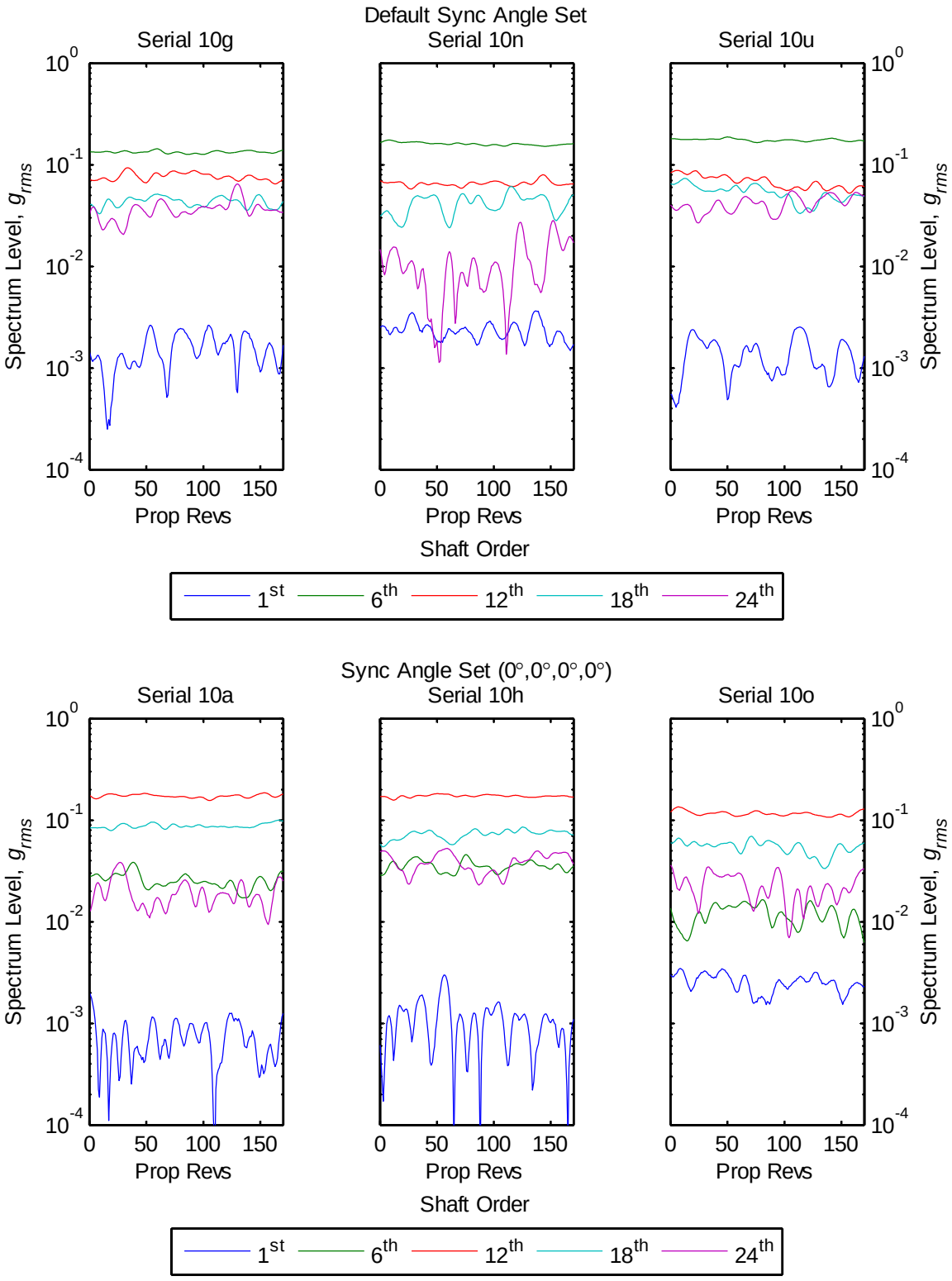

Figure 8.6 Short-term spectrum level variation for C-130J-30 Accelerometer B17, Serial 10, Trial 1. Default synchrophase angles top, (0°,0°,0°,0°) synchrophase angles bottom.

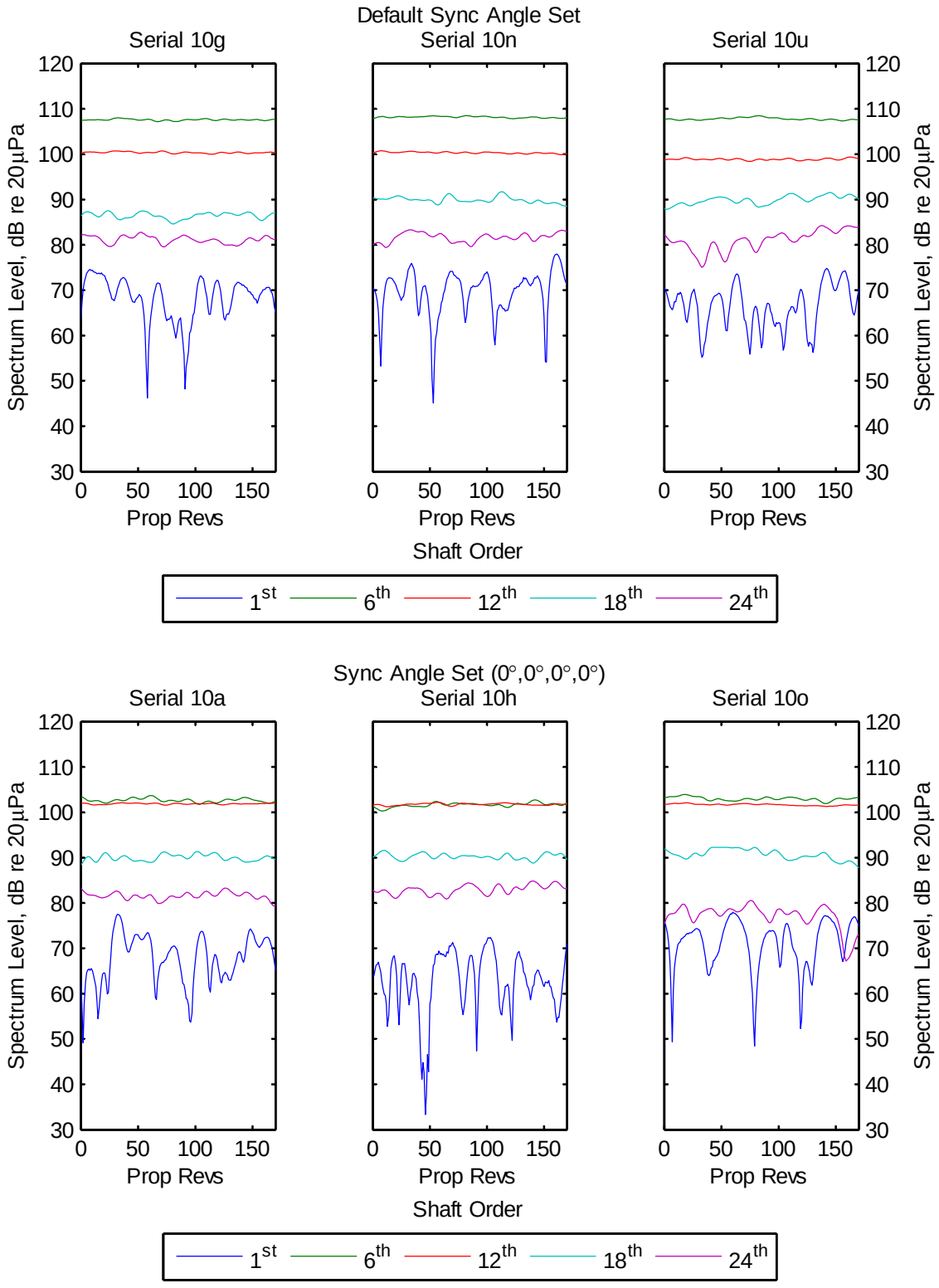

Figure 8.7 Short-term spectrum level variation for C-130J-30 Microphone P8.5, Serial 10, Trial 1. Default synchrophase angles top, (0°,0°,0°,0°) synchrophase angles bottom.

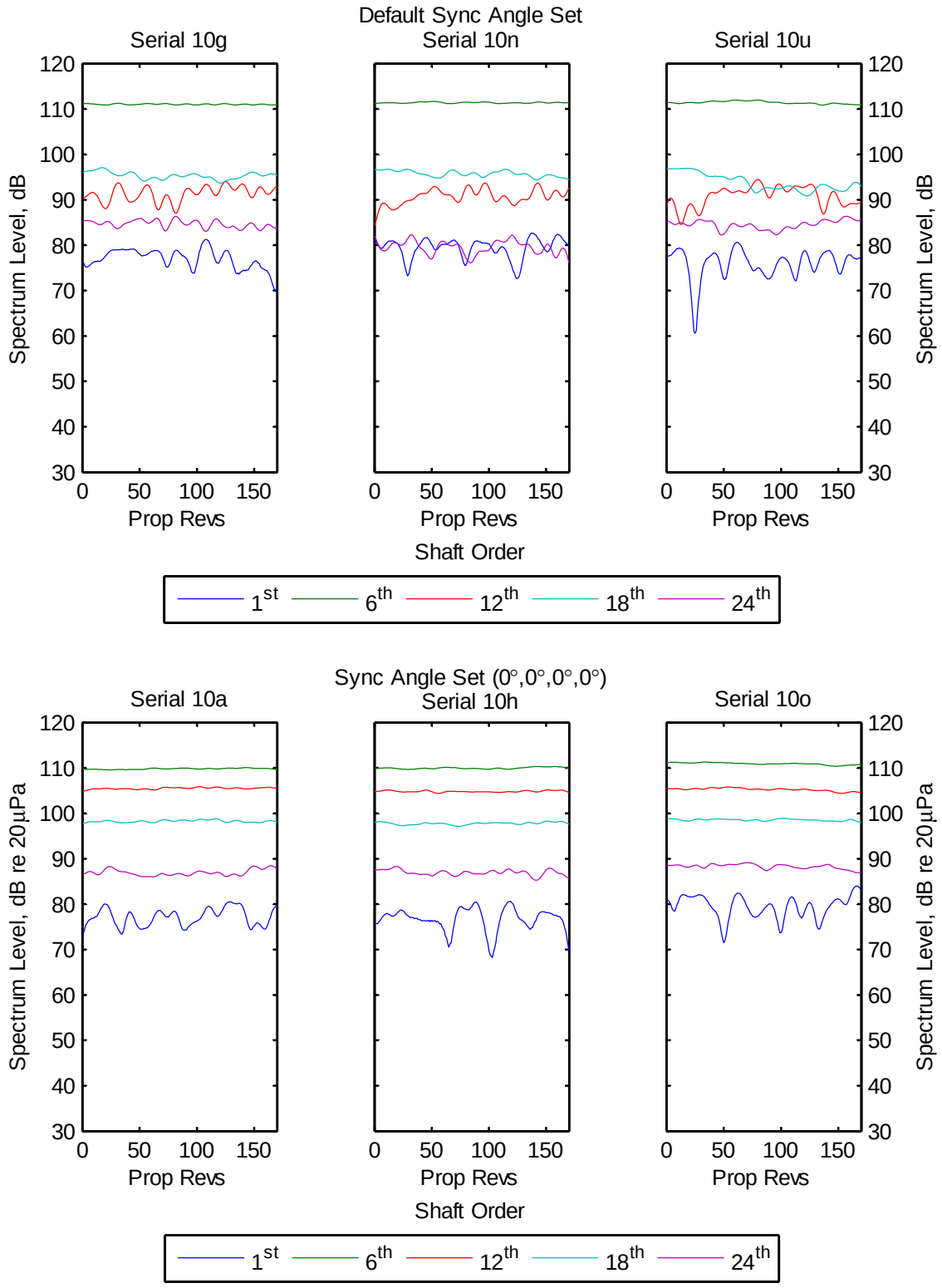

Figure 8.8 Short-term spectrum level variation for C-130J-30 Microphone S8.5, Serial 10, Trial 1. Default synchrophase angles top, (0°,0°,0°,0°) synchrophase angles bottom.

8.2. Longer-Term (20 min) Spectrum Level Variability

In this test, the average spectrum levels at the frequencies of interest (i.e., 1×, 2×, 3× and 4× BPF) were compared for each of the measurements repeated at approximately 10-minute intervals during Serial 10 of the first C-130J-30 trial.

The spectra were calculated from the same synchronously resampled data used in the short-term variability analysis (§8.1). Welch's averaged modified periodogram spectral estimation method was used with the same 17-rev (~1 s) Hamming window sliding over the same 187-rev segment of data with 16-rev overlap. This produced spectrum levels that were essentially 10 s averages of the spectrum levels from the short-term variability analysis.

The longer-term variability of the average spectrum levels are respectively shown in Figures 8.10 and 8.11 for the two different sets of synchrophase angles: default and (0°,0°,0°,0°). Note that Channels 5–7 and 30–32 are vibration signals, and Channel 27 is the 1P signal from the master propeller. All other channels are acoustic signals.

It can be seen that:

a) There is less variability at the BPF than its harmonics. This is probably because deviations in the synchrophase angles inherently cause larger variations in the phase of the harmonic components (see also §8.4.3).

b) The spectrum levels of some components, particularly the harmonics of the BPF, show significant (> 5 dB) variation.

c) The results for the two sets of synchrophase angles are different, indicating that the results are not sensor location dependent.

The estimated signal-to-noise ratios for these signals are shown in Figures 8.12 and 8.13. The background noise levels for each frequency of interest were estimated by averaging two spectral lines either side of a band gap of five lines centred on that frequency. This band gap was chosen to avoid spectral leakage from the frequency of interest (Figure 8.9). The background levels were separately estimated for each of the repeated measurements. It can be seen from the results that, when the short-term levels are averaged over about 10 s, low signal-to-noise ratios do not necessarily translate to significant spectrum level variability; i.e., other factors are probably more important. These are discussed in §8.4.

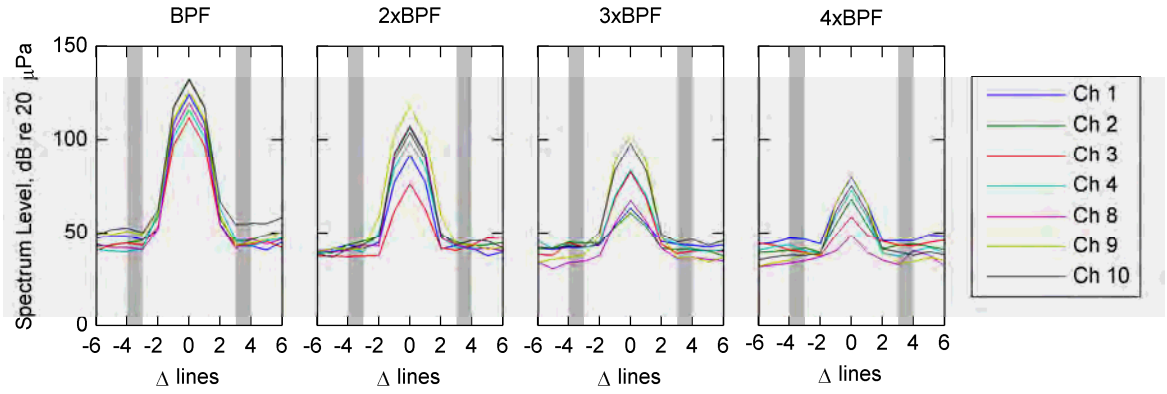

Figure 8.9 Typical microphone spectra around the frequencies of interest for synchrophase angles of (0°,0°,0°,0°). Background noise levels were estimated from the grey regions to avoid spectral leakage.

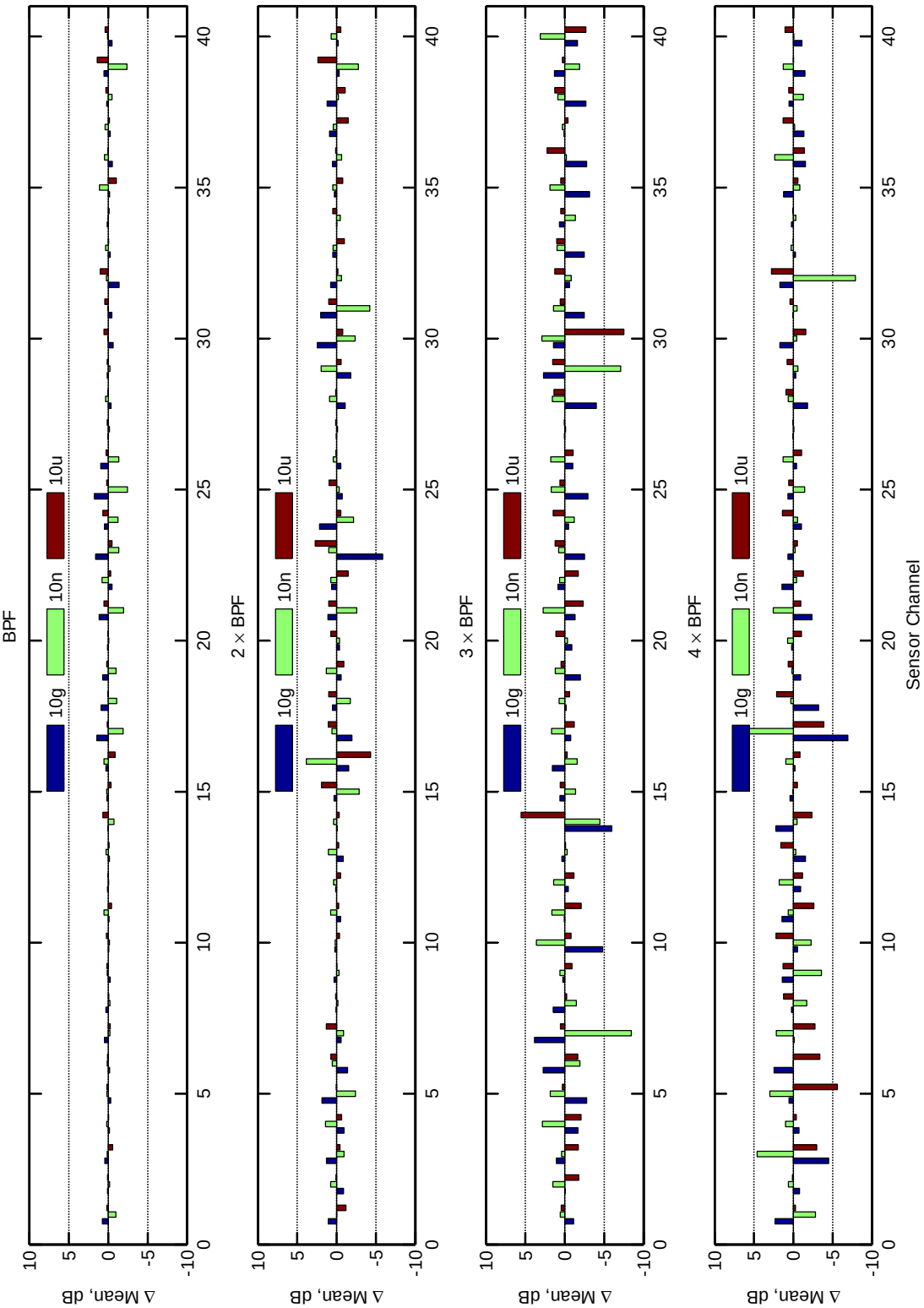

Figure 8.10 Spectrum level differences of C-130J-30 measurements repeated at 10-minute intervals, Serial 10, Trial 1 (def. sync. angles).

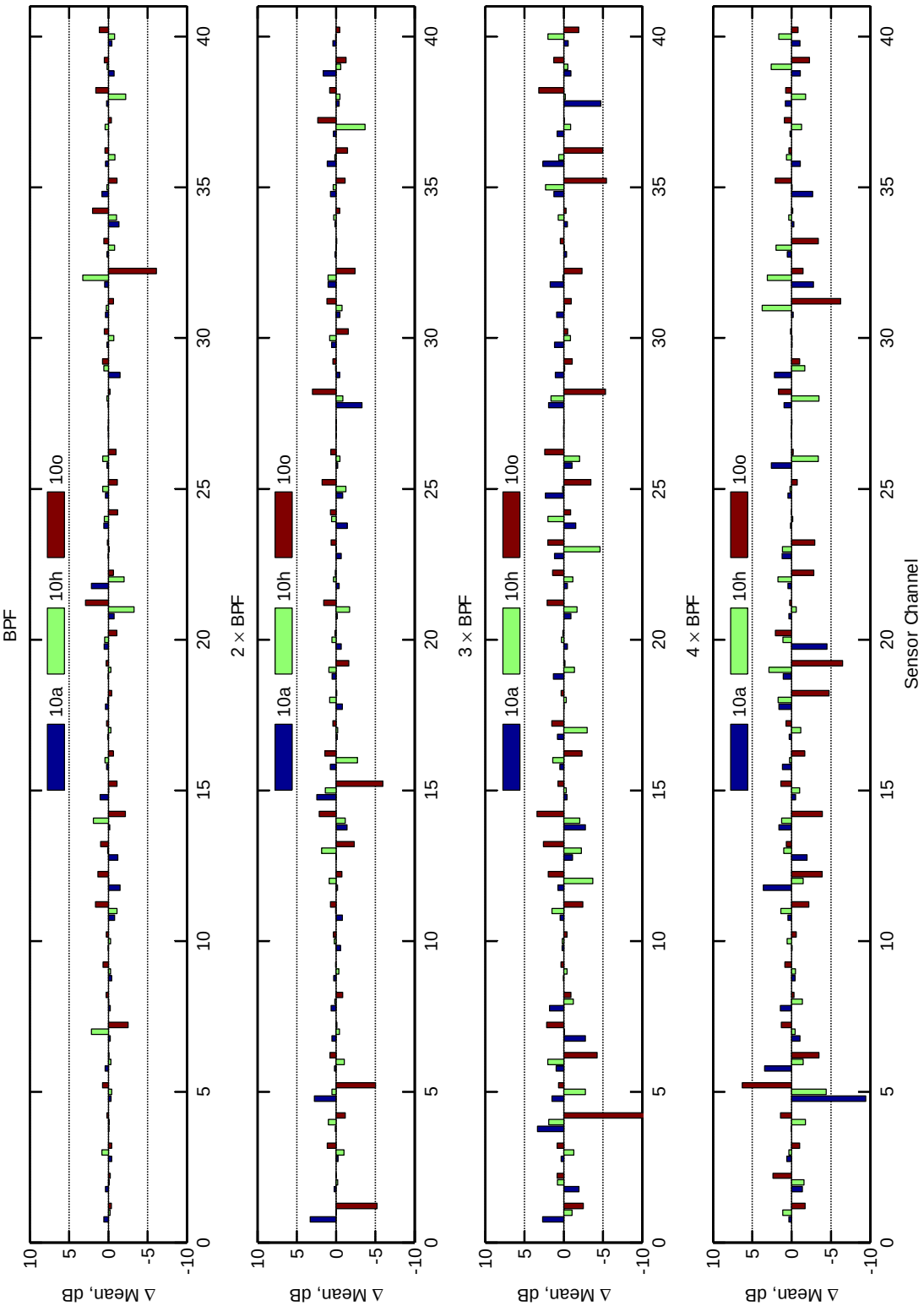

Figure 8.11 Spectrum level differences of C-130J-30 measurements repeated at approx. 10-minute intervals, Serial 10, Trial 1 (0°,0°,0°).

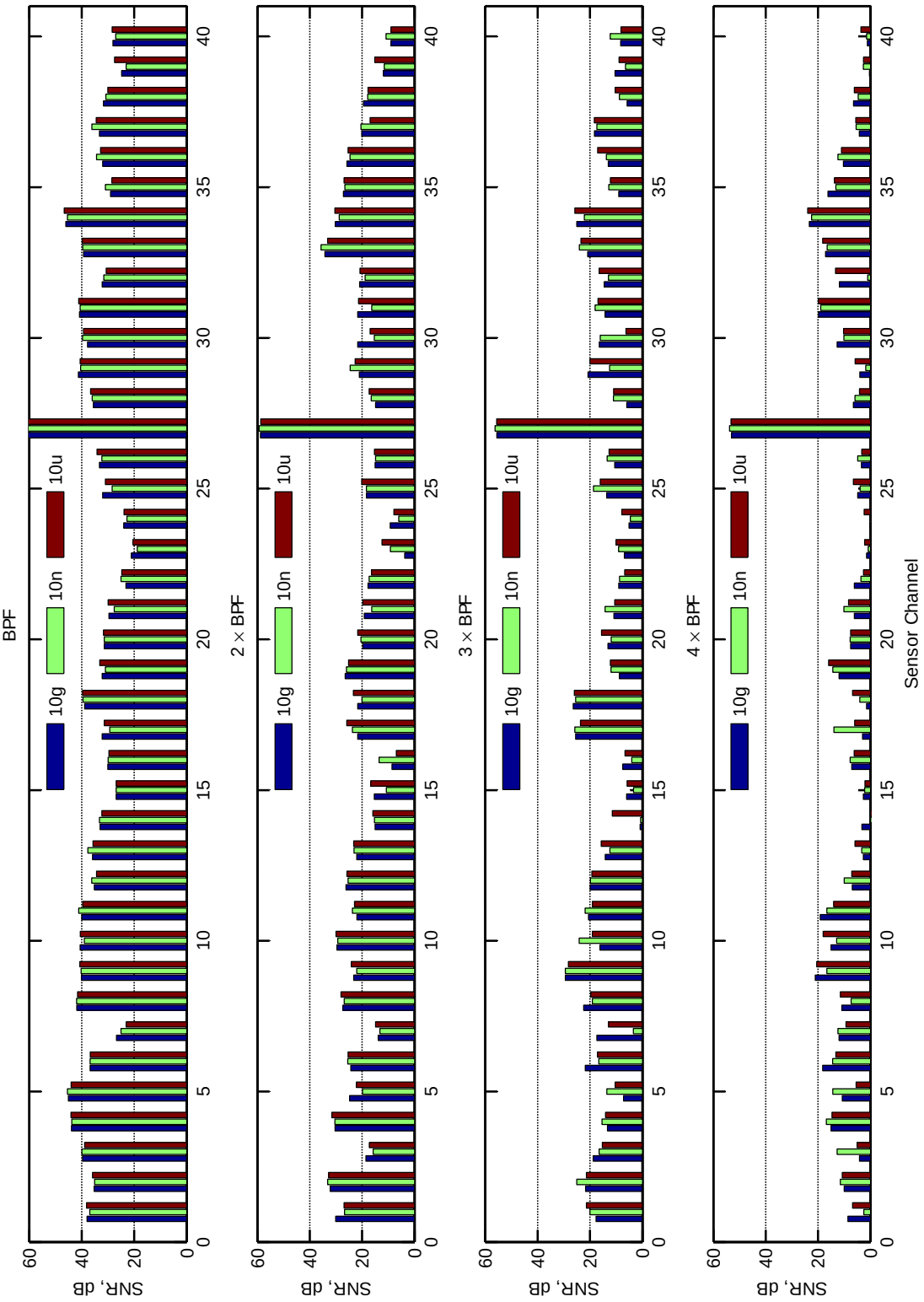

Figure 8.12 Estimated SNR of C-130J-30 measurements repeated at approx. 10-minute intervals, Serial 10, Trial 1 (def. sync. angles).

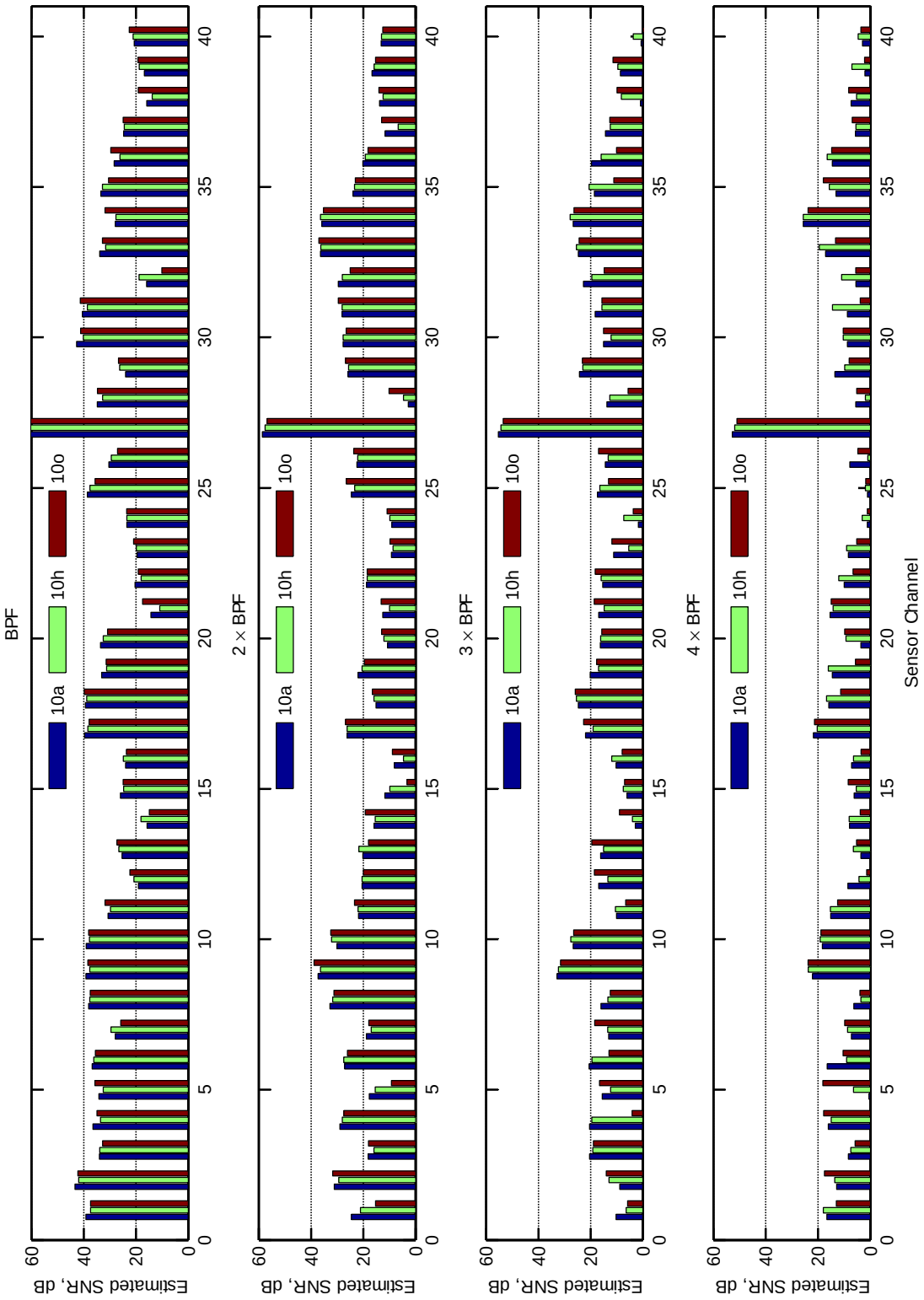

Figure 8.13 Estimated SNR of C-130J-30 measurements repeated at approx. 10-minute intervals, Serial 10, Trial 1 (0°,0°,0°,0°).

8.3. Inter-Aircraft Spectrum Level Variability

The spectrum levels of the three repeated (0°,0°,0°,0°) measurements from Serial 10 of the second trial were compared to the mean levels of the three repeated (0°,0°,0°,0°) measurements from Serial 10 of the first trial. The results for the sensors in common between the trials are shown in Figure 8.14. Note that the channel numbering is the same as in Figures 8.10–8.13 in §8.2; i.e., the channels from the second trial have been re-ordered to match the first trial. The channels that were not measured in the second trial are marked N.A.

It can be seen that there are variations between each of the repeated measurements in the second trial. These are of a similar magnitude to those observed in the first trial (Figures 8.10 and 8.11), and therefore as expected. However, the more important observation is that the spectrum levels vary more significantly between the trials than they do within the same trial. The variation at the BPF for some channels is up to ~12 dB. There are several possible reasons for this:

a) sensor position differences between the trials,
b) flight condition differences between the trials,
c) synchrophase angle differences between the trials, and
d) vibro-acoustic differences between the two airframes.

These are discussed in §8.4 along with other factors that may influence measurement repeatability.

8.4. Factors Affecting Measurement Repeatability

The factors affecting the measurement repeatability are discussed in the following sub-sections. With the limited degree of control available over these factors, some level of measurement variation is inevitable. This will necessarily affect the accuracy of any propeller signatures calculated from these measurements, and the resulting predictions made from those signatures. Obtaining better estimates of these effects would be a good area for future research.

8.4.1. Atmospheric Turbulence

Atmospheric turbulence will be the leading cause of synchrophase angle deviations, which are discussed in more detail in §8.4.3. However, turbulence may also vary the diffraction and scatter of sound from each propeller. This could lead to transient phase differences in the sound reaching the fuselage skin, and hence alter the fuselage vibration and the resulting acoustic response inside the cabin. Turbulence will also place dynamic loads on the wings and fuselage that could alter the structural response of the aircraft in a transient way. These effects can be minimised by averaging over time periods that are several times longer than the timescale of the transients.

8.4.2. Signal-to-Noise Ratio

The variability of the spectrum levels will increase the closer they get to the background noise level; i.e., as the random noise becomes a more significant component of the signal. Longer averages will be required to minimise this effect, but longer averages expose the measurements to other effects such as perturbations in the synchrophase angles and flight conditions.

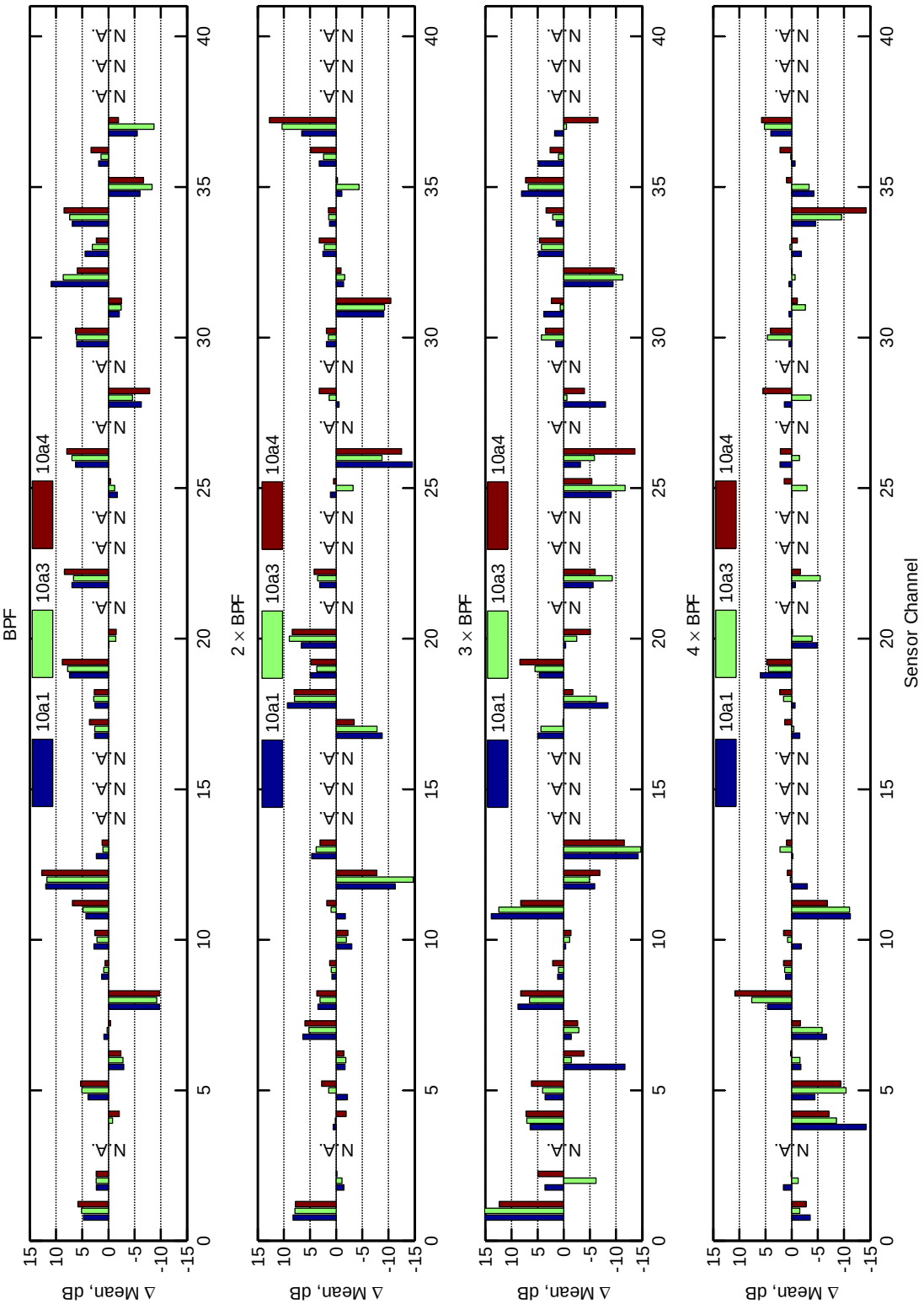

Figure 8.14. Spectrum level differences of Trial 2 measurements to average of Trial 1 measurements for mics in common, Serial 10 (0°,0°,0°,0°).

8.4.3. Propeller Speed Perturbations and Synchrophase Angle Deviations

The rotational speed of each propeller will be perturbed about its mean value by atmospheric turbulence (§8.4.1), and by changes in the flight conditions – manoeuvres, changes in the engine power levels, etc. (§8.4.4). These perturbations will:

a) lead to deviations in the synchrophase angles, and
b) cause variations in the propeller blade-pass frequencies and harmonics.

These two effects can be examined using the AP-3C magnetic pick-up data and C-130J-30 laser-tachometer data from the synchrophase angle analysis examples shown in §6.2 and §6.3.

Deviations in the synchrophase angles are expected to be a major source of measurement variability. The synchrophase angles, when measured with respect to the master propeller, will reflect perturbations of both the master and the slave propellers about their respective mean positions. The synchrophasing system may even interpret perturbations in the speed of the master propeller as deviations of the slave propeller synchrophase angles, and actually amplify the perturbations of the slave propellers, as discussed in §6.2. Synchronously averaging the data with respect to a tachometer signal from the master propeller will effectively transfer the perturbations of the master propeller to the slave propellers; i.e., the master propeller will be treated as if it has no speed perturbations. However, the frequencies will now be measured in terms of rotational orders of the master propeller, not as absolute frequencies. This should not influence the calculation of the propeller signatures unless there are significant differences in the speed settings, and hence the vibro-acoustic response of the aircraft, between the propellers that can be selected as master on one aircraft, or between the master propellers on two aircraft of the same type. This is potentially more of a problem in the analogue controlled AP-3C, where the speed settings are adjusted by trim screws, than the digitally controlled C-130J. The AP-3C also features a Master Trim adjustment knob on the synchrophaser control panel that allows the pilots to vary the speed of the master propeller by ± 1%. These effects were eliminated in this investigation by only using the same master propeller for all test serials, and by keeping the Master Trim control knob at its mid-point (zero) position.

In the synchronously resampled signals, deviations in the synchrophase angles should cause proportional deviations in the phase of the components at the BPF and its harmonics; i.e., a 1° deviation of the synchrophase angle of a four-bladed propeller should cause 4°, 8°, 12°, and 16° deviations in the phase at the 1×, 2×, 3× and 4× BPF frequency components respectively. These phase deviations will be 50% larger in a six-bladed propeller (i.e., 6°, 12°, 18°, and 24°). The effect of these phase deviations on the propeller signature estimation process can be examined by applying typical synchrophase angle deviations to a set of nominal propeller signatures, and calculating a new set of signatures from the phase-distorted signals.

Figure 8.15 shows the effect of applying a 170-revolution (~10 s) period of relatively large synchrophase angle deviations from the AP-3C Serial 1 magnetic pick-up data (i.e., the first 170 propeller revolutions shown in Figure 6.3) to the vector sum of four nominal unit-amplitude zero-phase signatures. The same set of signatures is used for all frequencies of interest (i.e., 1×, 2×, 3× and 4× BPF). It can be seen that these synchrophase angle deviations cause sweeping arcs and loops in the summations of the phase-deviated signatures, particularly at the harmonics of the BPF.

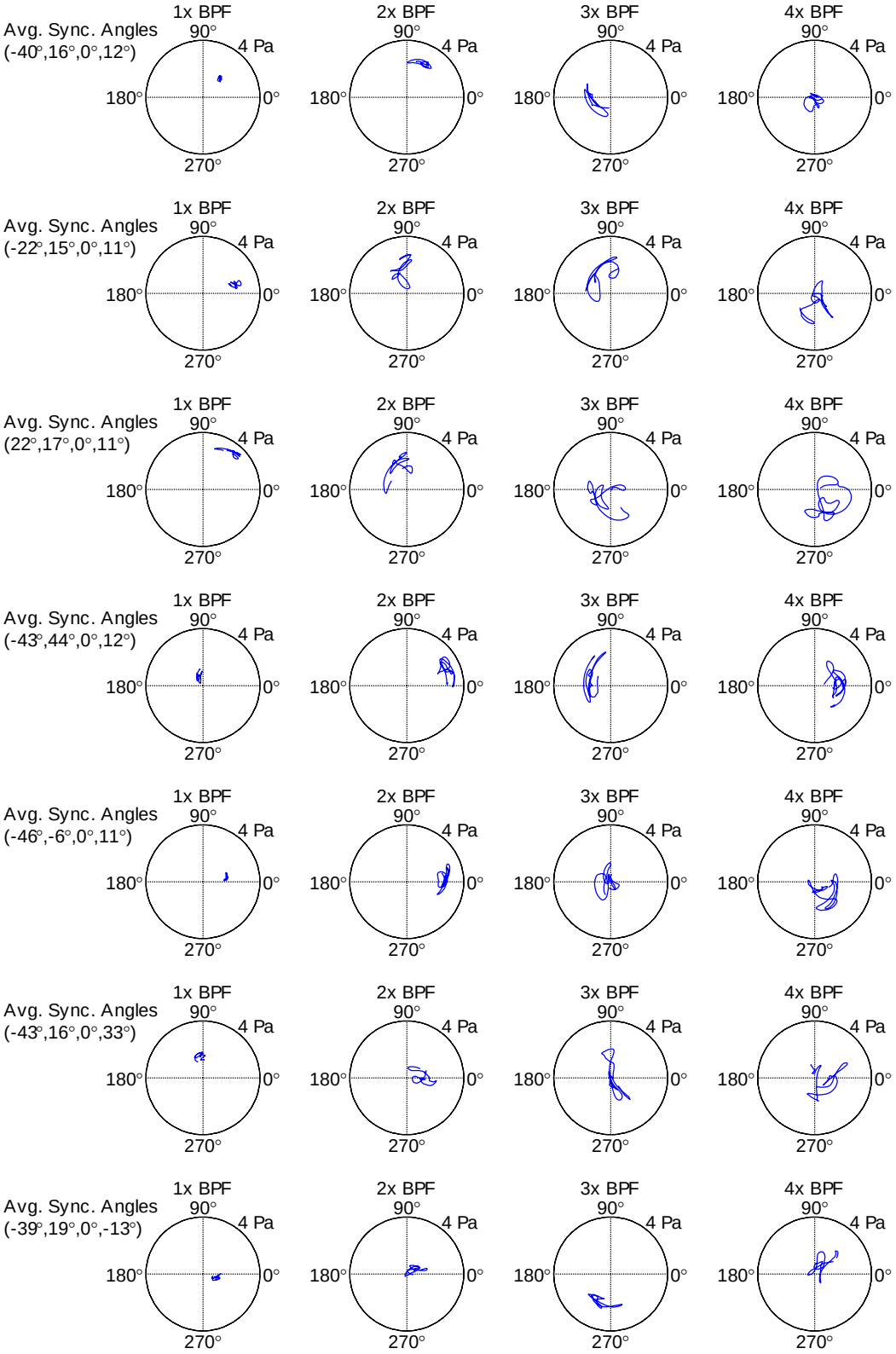

Figure 8.15 Effect of applying a 170-revolution (~10 s) period of relative large synchrophase angle deviations from the AP-3C Serial 1 magnetic pick-up data to the vector sum of four nominal unit-amplitude zero-phase propeller signatures for seven different sets of synchrophase angles.

An enlarged view of one set of synchrophase angles from Figure 8.15 is shown in Figure 8.16. Here, it is easier to see the differences between:

a) the mean value of the vector sum of the phase-deviated signals,

b) the predicted value using the signatures calculated from the phase-deviated signals and the average synchrophase angles, and

c) the predicted value using the original signatures and the average synchrophase angles.

The differences between b) and c) for each set of synchrophase angles are shown in Figure 8.17. These have been termed the phase-deviation-induced errors. The differences between the signatures calculated from the phase-deviated signals and the original signatures are also shown in Figure 8.18. From these figures it can be appreciated that synchrophase angle deviations can introduce significant errors, particularly at the 3× and 4× BPF components. These errors can be reduced by shortening the averaging period, as shown in Figures 8.19 and 8.20 respectively, where the period is only 17 revolutions (~1 s). However, the averaging period cannot be reduced to zero; there will necessarily be a trade-off between reducing the phase-deviation-induced errors, and accurately estimating the spectral components at the frequencies of interest.

Phase-deviation-induced error will impair the optimisation of the synchrophase angles for lower noise and vibration. The overall level of impairment will depend on the relative contribution from each sensor location to the overall cost function, and will also vary with the synchrophase angles. However, as an example, if the phase-deviation-induced error was 10% at all sensor locations, this would produce a level of uncertainty of around 1 dB in a cost function such as the average sound pressure level. Ultimately, no optimisation benefit will be achieved if the overall uncertainty in the cost function (as a result of all errors) equals or surpasses the effect of synchrophasing on the function.

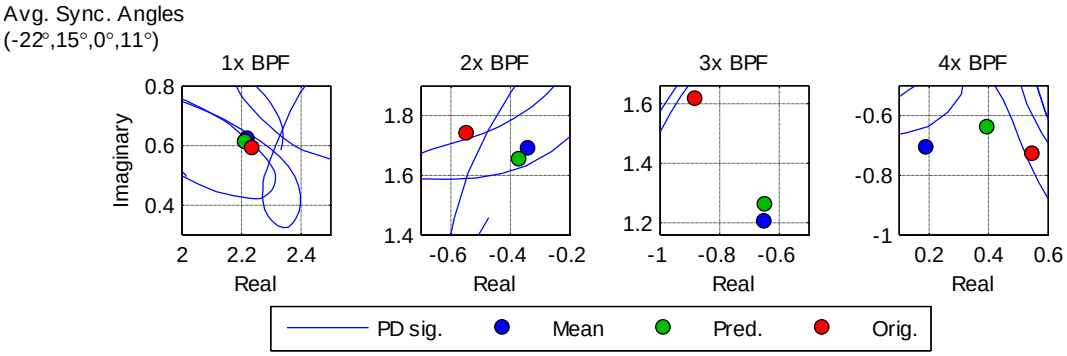

Figure 8.16 Enlarged view of one set of synchrophase angles from Figure 8.15 showing: the mean of the phase-deviated signals (blue dot), the predicted value using the signatures calculated from the phase-deviated signals (green dot), and the predicted value using the original signatures and the average synchrophase angles (red dot). Note, the signature calculation process attempts to find the best fit of the signatures to the averaged data in a least-squares sense (i.e., it tries to get the green dots as close to the blue dots as possible across all seven synchrophase angle sets).

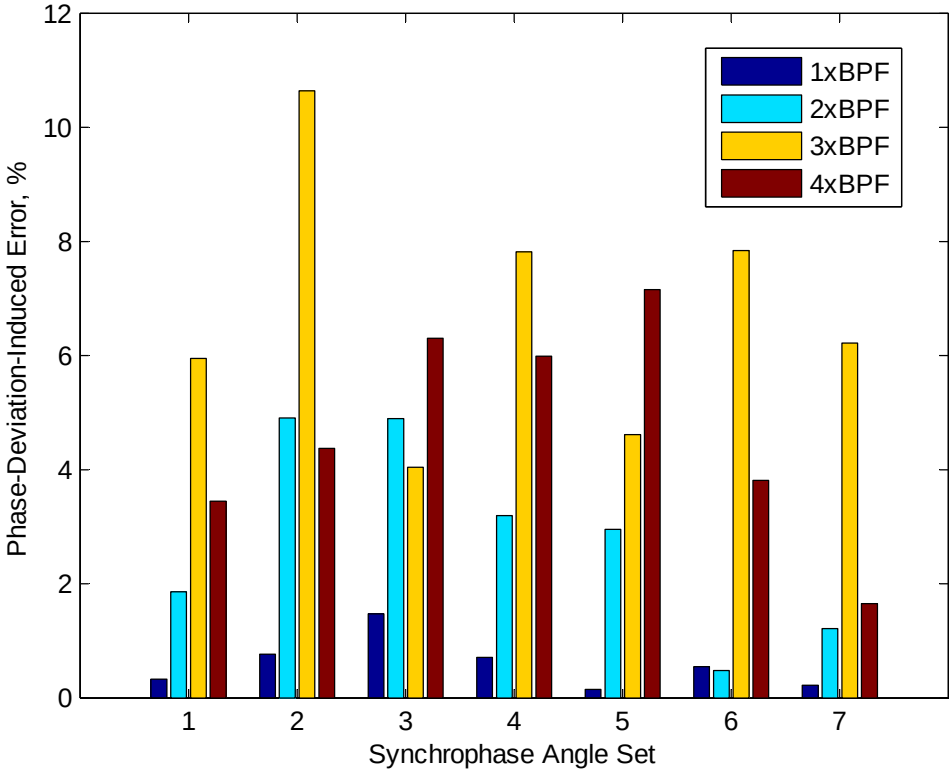

Figure 8.17 Normalised phase-deviation-induced error obtained by comparing the predicted values from the 170-rev phase-deviated signatures and the original signatures at the average synchrophase angles (i.e., the distance between the green and red dots in Figure 8.16 divided by the sum of the original signature amplitudes).

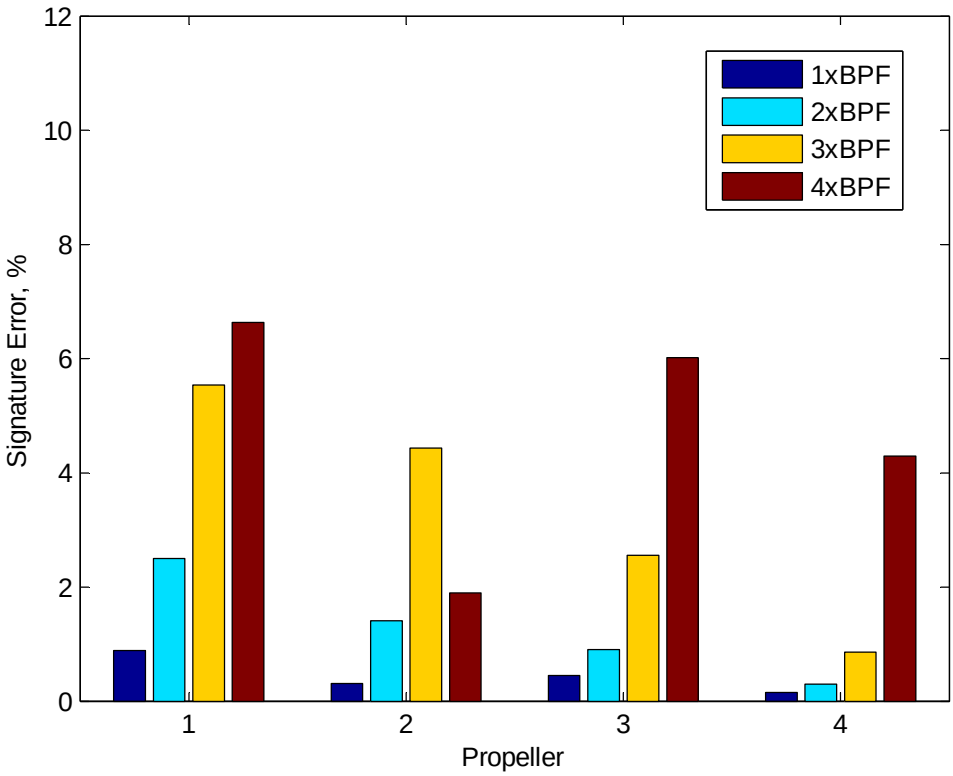

Figure 8.18 Normalised propeller signature error obtained from the 170-rev phase-deviated signals (i.e., the magnitude of the difference in the signatures, divided by the amplitude of the original signature).

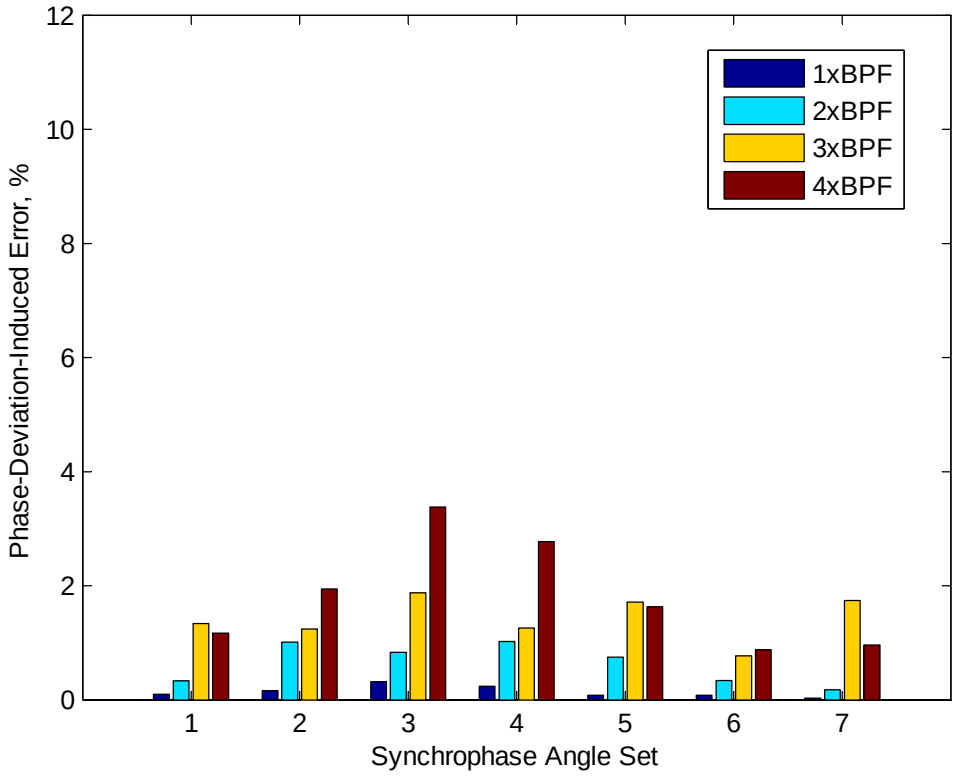

Figure 8.19 Normalised phase-deviation-induced error obtained by comparing the predicted values from the 17-rev phase-deviated signatures and the original signatures at the average synchrophase angles.

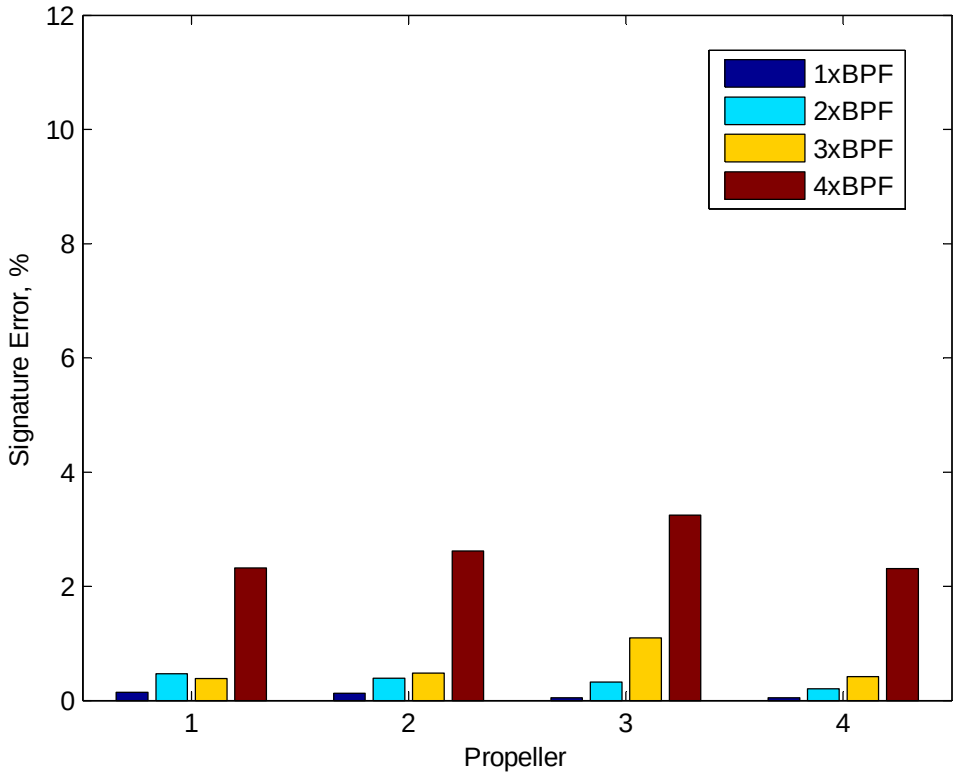

Figure 8.20 Normalised propeller signature error obtained from a 17-rev period of phase-deviated signals (i.e., the magnitude of the difference in the signatures, divided by the amplitude of the original signature).

The variations in the speed of the propellers, and the effect of this on the frequencies of interest, for the examples shown in §6.2 and §6.3 are listed in Tables 8.1 and 8.2 respectively. Note that the speed perturbations are approximately normally distributed (Appendix D), and the maximum, minimum, mean and standard deviations of the speeds have been calculated on a rev-to-rev basis. It can be seen that the frequency variations are relatively minor at the BPF ($\leq$ 0.3 Hz), but steadily increase for each successive harmonic, and get close to 1.0 Hz at 4× BPF. This 'blurring' of the higher excitation frequencies may begin to change the vibro-acoustic response of the aircraft, and hence the accuracy of the propeller signatures at these higher harmonics, particularly when flying through turbulent air. It is difficult to quantify this effect as no data were collected for different propeller speed settings (e.g., 101% N_p), or in both smooth and turbulent air at the same altitude and airspeed. However, given the small frequency spread at the BPF and lower harmonics, the effect is expected to be much less than that from the deviations in the synchrophase angles.

Table 8.1 Typical propeller speed perturbations. [1]

AP-3C Serial 1 (200 KIAS at 500 ft) – Moderately Turbulent Air				
	Propeller 1	Propeller 2	Propeller 3	Propeller 4
Max (rpm)	1021.9	1022.3	1022.7	1022.1
Min (rpm)	1015.7	1015.8	1016.1	1016.1
Mean (rpm)	1018.8	1018.7	1018.8	1018.8
Std Deviation (rpm)	1.0	1.1	1.1	0.9
AP-3C Serial 9 (220 KIAS at 10,000 ft) – Smooth Air [2]				
	Propeller 1	Propeller 2	Propeller 3	Propeller 4
Max (rpm)	1020.0	1019.8	1019.9	1019.9
Min (rpm)	1018.9	1018.9	1019.1	1018.9
Mean (rpm)	1019.4	1019.4	1019.4	1019.4
Std Deviation (rpm)	0.2	0.2	0.1	0.2
C-130J-30 Serial 4.3 (230 KCAS at FL210) Trial 2 – Smooth Air				
	Propeller 1	Propeller 2	Propeller 3	Propeller 4
Max (rpm)	1022.3	1022.2	1022.0	1023.2
Min (rpm)	1019.0	1019.2	1019.6	1018.8
Mean (rpm)	1020.7	1020.7	1020.7	1020.7
Std Deviation (rpm)	0.5	0.5	0.4	0.7

[1] Over 1020 propeller revolutions (~60 s) at the default synchrophase angles.
[2] The propeller speeds and synchrophase angles were particularly steady at start of Serial 9 (Figure 6.4).

Table 8.2 Typical frequency variations at 1×, 2×, 3× and 4× BPF. [1]

AP-3C Serial 1 (200 KIAS at 500 ft) – Moderately Turbulent Air				
	Propeller 1	Propeller 2	Propeller 3	Propeller 4
1×BPF (Hz)	67.9±0.2	67.9±0.2	67.9±0.2	67.9±0.2
2×BPF (Hz)	135.8±0.4	135.8±0.4	135.8±0.4	135.8±0.4
3×BPF (Hz)	203.8±0.6	203.7±0.7	203.8±0.6	203.8±0.5
4×BPF (Hz)	271.7±0.8	271.7±0.9	271.7±0.9	271.7±0.7
AP-3C Serial 9 (220 KIAS at 10,000 ft) – Smooth Air				
	Propeller 1	Propeller 2	Propeller 3	Propeller 4
1×BPF (Hz)	68.0±0.0	68.0±0.0	68.0±0.0	68.0±0.0
2×BPF (Hz)	135.9±0.1	135.9±0.1	135.9±0.1	135.9±0.1
3×BPF (Hz)	203.9±0.1	203.9±0.1	203.9±0.1	203.9±0.1
4×BPF (Hz)	271.8±0.2	271.8±0.1	271.8±0.1	271.8±0.1
C-130J-30 Serial 4.3 (230 KCAS at FL210) Trial 2 – Smooth Air				
	Propeller 1	Propeller 2	Propeller 3	Propeller 4
1×BPF (Hz)	102.1±0.2	102.1±0.1	102.1±0.1	102.1±0.2
2×BPF (Hz)	204.1±0.3	204.1±0.3	204.1±0.2	204.1±0.4
3×BPF (Hz)	306.2±0.5	306.2±0.4	306.2±0.3	306.2±0.6
4×BPF (Hz)	408.3±0.7	408.3±0.6	408.3±0.5	408.3±0.8

[1] Mean ± three standard deviations (from Table 8.1).

8.4.4. Flight Condition Perturbations/Differences

It is inevitable that small variations in the flight conditions (e.g., altitude, airspeed, engine power, etc.) will occur during a measurement. However, it is difficult to quantify how these will affect the measurement, as they are very difficult to eliminate, and no measurements were made where any of the flight condition parameters were deliberately perturbed in order to exaggerate the effects.

An example of the typical perturbations in the flight condition parameters recorded by the Data Bus Analyser in the first C-130J-30 trial is shown in Figure 8.21. Only the data from FADEC A are shown as the data from FADEC B are similar. It can be seen that there were potentially significant variations in both the airspeed and engine power over the course of the serial. It can also be seen that the blade pitch angles closely follow the airspeed and engine power variations; i.e., they are the result of the airspeed and engine power perturbations, not the cause of them. It is thought that the 1°–2° adjustments in the engine power lever angles before 10b, 10c, 10h, 10o, and 10u were probably made in order to maintain the desired airspeed. However, it is not known whether they were the result of pilot or autothrottle[3] inputs or both. The lever adjustments caused engine power changes of ~100 hp, or approximately 4% of the mean engine output (2500 hp) during the serial. As a first approximation, these might be expected to produce similar changes in the sound pressure levels as well, although some frequencies may be more affected than others.

While the pitch, roll and yaw of the aircraft were not directly recorded, notes taken during the trial indicate that there were two banked turns during Serial 10: one just before 10a, and one between 10k and 10l. These are annotated and shaded in the plots. The sound and vibration component amplitudes during these turns were found to be significantly different to those during straight and level flight (Figures 8.22–8.25), so the data near these regions were not included in any further analysis.

8.4.5. Vibro-Acoustic Differences

As discussed in Chapter 3, the transmission of sound from the propellers into the aircraft cabin is the result of a complex interaction between the exterior sound field, the fuselage vibration, and the interior sound field. Anything that affects this interaction (e.g., aircraft-to-aircraft variation in the fuselage panel vibration) will affect the resulting propeller signatures. It is assumed that any vibro-acoustic differences between the aircraft are small. If this is not the case, then the best results for any particular aircraft could only be obtained by measurements on that aircraft. Evidence of potential vibro-acoustic differences between the two C-130J-30 aircraft used in this investigation are further discussed in §10.3.6

8.4.6. Synchrophase Angles

Any systemic measurement error of the synchrophase angles by the synchrophasing system could cause differences in the measured noise and vibration. However, the accuracy of the collected photographic and laser tachometer data described in Chapter 6 were not sufficient to identify any such measurement errors.

---

[3] The autothrottle is part of the automatic flight control system, and can be operated in conjunction with, or separately to, the autopilot. It adjusts the engine power to maintain the aircraft at a constant airspeed.

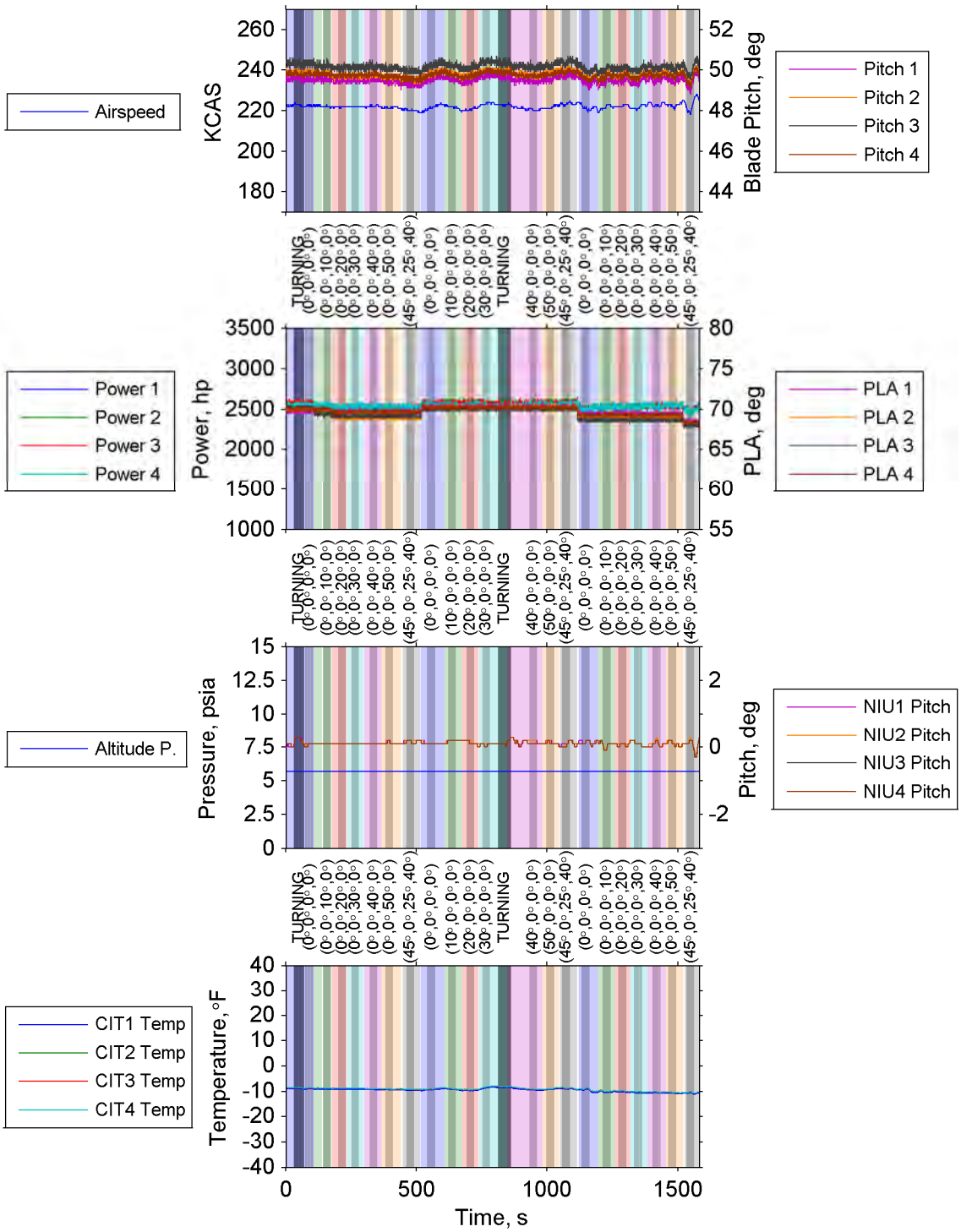

Figure 8.21. C-130J-30 flight condition parameters recorded during Serial 10, Trial 1. The coloured regions indicate where the synchrophase angles were within ± 3° of the desired angles. The shaded regions indicate the periods where the noise and vibration data were analysed. The dark regions indicate banked turns. Pitch refers to propeller blade pitch, Power to engine power, PLA to Power Lever Angle, Altitude P. to Altitude Pressure, NIU Pitch to Nacelle Interface Unit pitch, CIT Temp to Compressor Inlet Temperature.

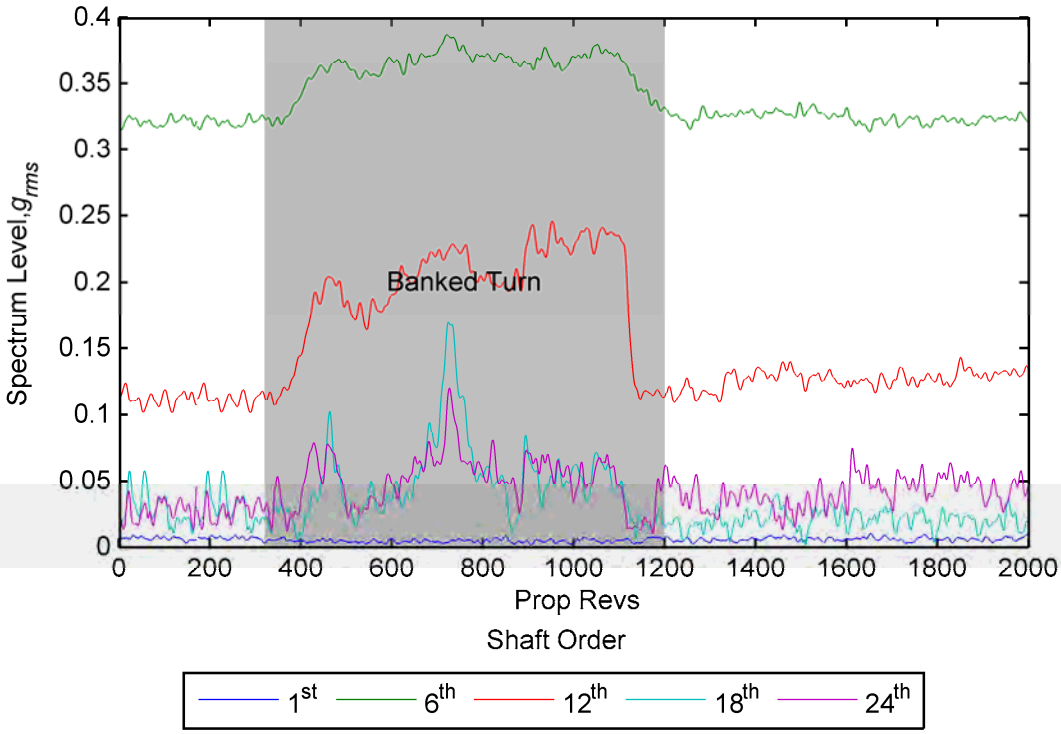

Figure 8.22 Effect of the banked turn (shaded region) between C-130J-30 Trial 1 Serials 10k and 10l on the spectrum levels recorded from Accelerometer B7. The synchrophase angles were (30°, 0°, 0°, 0°) before the turn and (40°, 0°, 0°, 0°) after the turn.

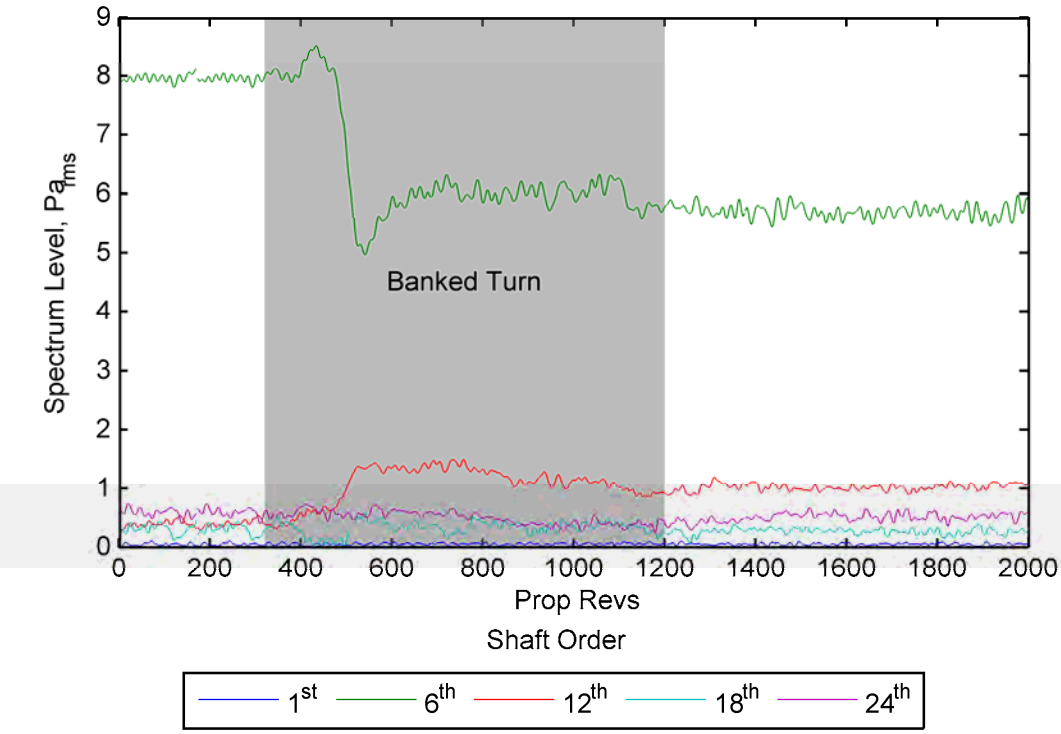

Figure 8.23 Effect of the banked turn (shaded region) between C-130J-30 Trial 1 Serials 10k and 10l on the spectrum levels recorded from Microphone C1.5. The synchrophase angles were (30°, 0°, 0°, 0°) before the turn and (40°, 0°, 0°, 0°) after the turn.

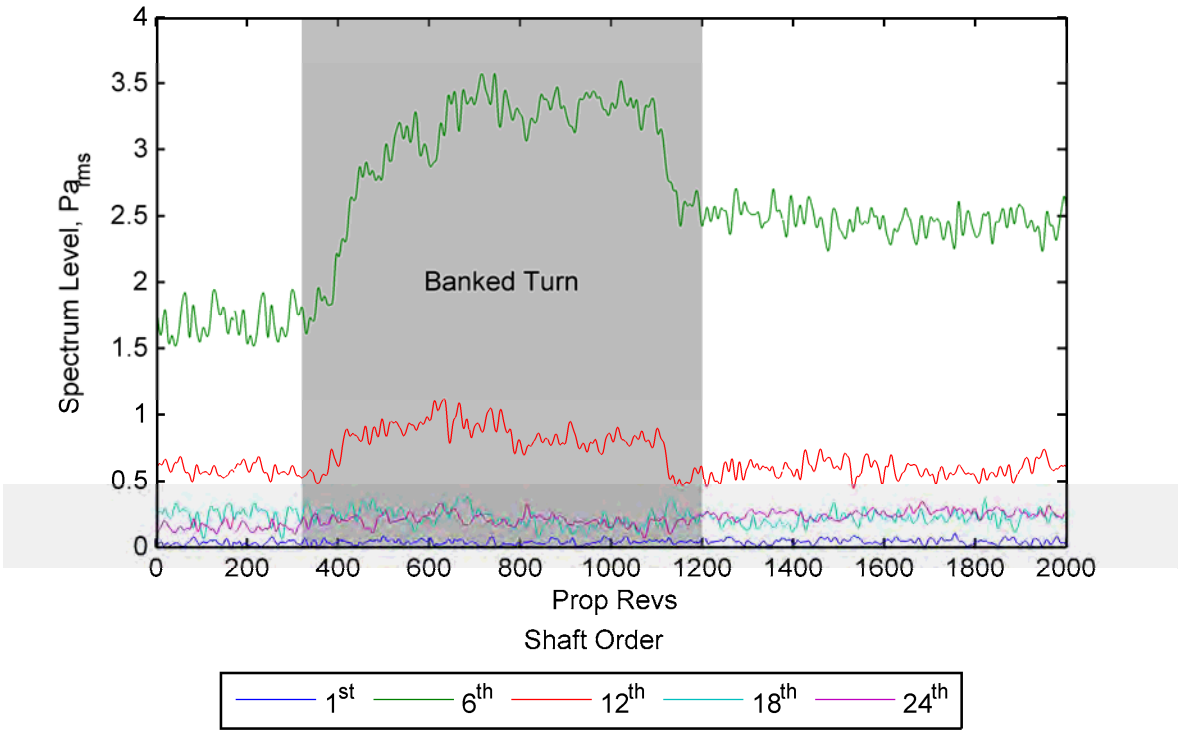

Figure 8.24 Effect of the banked turn (shaded region) between C-130J-30 Trial 1 Serials 10k and 10l on the spectrum levels recorded from Microphone P19. The synchrophase angles were (30°, 0°, 0°, 0°) before the turn and (40°, 0°, 0°, 0°) after the turn.

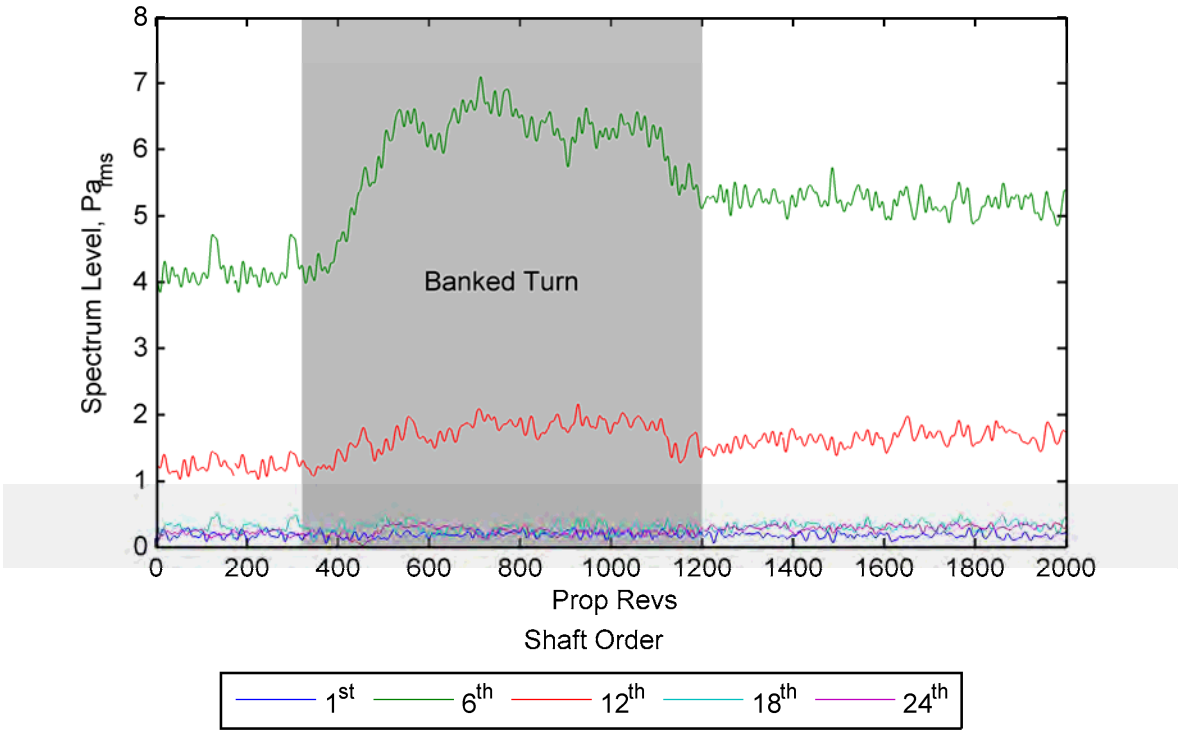

Figure 8.25 Effect of the banked turn (shaded region) between C-130J-30 Trial 1 Serials 10k and 10l on the spectrum levels recorded from Microphone S5. The synchrophase angles were (30°, 0°, 0°, 0°) before the turn and (40°, 0°, 0°, 0°) after the turn.

8.4.7. Synchronising on Different Propeller Blades

Note that this is only relevant to the C-130J, as the analogue synchrophaser in the P-3C always synchronises on the same propeller blade (§4). Differences brought about by the propellers synchronising on different blades should not be evident at the BPF or its harmonics. This is because the aerodynamic noise generated by each blade should be the same (when averaged over a period sufficient to smooth out the effects of turbulence). It is unlikely that there would be enough physical differences between the blades, such as wear or pitch-angle deviation, to cause any significant noise source variation between them. However, differences at the propeller rotational frequency are possible because the relative phases of the propeller unbalance forces will change with respect to one another.

8.4.8. Microphone Movement and Vibration

Unfortunately, due to the use of flexible goosenecks, there was some movement of the microphones throughout the course of each flight. A few were accidentally knocked and repositioned, and others may have moved because of gravity, turbulence or aircraft manoeuvres. While this movement was not recorded, it is estimated that it would have been less than 10 cm (gooseneck length = 20 cm). However, it should be noted that none of the floor accelerometers were moved, and variability was still observed in these sensors.

It is known that there were some differences (possibly up to 20 cm) in the sensor positions between the two C-130J-30 trials (§5.4). These could possibly account for some of the observed signature differences between the trials.

The microphones were also subjected to vibration transmitted along the goosenecks. The microphone specifications state that the sensitivity to vibration is approximately 50 dB in equivalent sound pressure level for a $1\ \mathrm{m\ s^{-2}}$ (~0.1 g) axial acceleration. Typical floor vibration levels at the BPF measured during the trial were ~0.1 g_{rms}, so this may have been a problem. Soft rubber grips were used between the clamps and the microphones in an attempt to minimise this vibration, but it is not known how effective these were.

8.4.9. Cabin Pressure & Temperature

Cabin air pressure is typically automatically controlled and therefore less prone to differences between flights. Cabin air temperature will be subject to more variability, depending on air conditioning settings and the preferences of aircrew and passengers. While the cabin air temperature was not recorded in any of the trials, it is unlikely to have varied by more than a few degrees during the course of each trial, and is therefore unlikely to have been a significant source of variability. The differences in cabin temperatures between the two C-130J-30 trials may, however, have been slightly larger, as these were conducted at different times of the year (December & July).

8.4.10. Movement of Personnel

Given the volume of the cabin relative to the volume occupied by personnel during the flight tests, the movement of personnel within the cabin is only likely to have affected nearby sensors. Since there were only five personnel within the main cabin, and they were mostly occupied with tasks that kept them in one location during measurements, it is unlikely that this was a major cause of variability.

9. Propeller Signature Calculation and Analysis

The methods by which the propeller signatures were calculated and analysed using the experimental data are described in this chapter. In brief, the signatures were calculated by synchronously averaging the measured sound and vibration data with respect to the master propeller, extracting the amplitude and phase information at the frequencies of interest (i.e., 1×, 2×, 3× and 4× the BPF), and finding the least-squares solutions to Equation (3.22) on a frequency-by-frequency basis. Predictions using the propeller signatures were then compared with the measured data in order to assess which of the frequencies of interest should be incorporated into the synchrophase angle optimisation process that follows in Chapter 10.

9.1. Calculation

The amount of synchrophase angle deviation evident in the AP-3C data, as discussed in §6.2 and §8.4.3, posed a significant problem when it came to computing the propeller signatures for this aircraft because of the resulting relatively large phase deviations at the BPF and its harmonics. The approach adopted was to limit the data used from each measurement to only 4 propeller revolutions (~0.24 s). This prevented the synchrophase angles from varying by more than about ± 2° in the worst measured case; i.e., when the aircraft was flying through moderate turbulence.

The variation of the C-130J-30 synchrophase angles was only about a quarter of that in the AP-3C. Hence, phase variation at the BPF and its harmonics was less of a problem, and 170 propeller revolutions (~1.0 s) of data were used for the propeller signature calculations in this aircraft.

The propeller signatures were calculated by solving Equation (3.22) separately for each blade-pass harmonic component; i.e., 1×, 2×, 3× and 4× the BPF. In all cases, the noise and vibration data were synchronously averaged with respect to the master propeller 1P signal.[4] This was done partly to attenuate the non-synchronous components (i.e., components unrelated to the propellers), but also to ensure that the frequency components of interest would fall as close to the middle of the FFT frequency bins as possible, and hence limit any picket-fence effect associated with the measured frequency falling between the bins.

Matrix **A** was populated by:

a) synchronously resampling the data with respect to the master propeller (3000 points per revolution, giving an effect sample rate of ~51,000 Hz compared to the original sample rate of 44,000 Hz),

b) computing synchronous averages of the resampled data for all sensor signals (4-rev averages for the AP-3C, and 170-rev averages for the C-130J-30);

c) transforming the synchronous averages into the frequency (propeller-shaft-order) domain using the FFT; and

[4] The 1P signals were sourced from the magnetic pick-ups or laser tachometers on the master propellers, except for C-130J Trial 2 where a virtual 1P signal for Prop 2 was created due to low battery power on the Prop 2 laser. This was done by adjusting the phase of the Prop 3 signal by the mean FADEC-in-control synchrophase angle of Prop 3 over the averaging period.

d) extracting the amplitude and phase at the frequencies of interest (i.e., 4, 8, 12 & 16 orders for the AP-3C, and 6, 12, 18 & 24 orders for the C-130J-30).

Matrix **β** was populated by:

a) calculating the synchrophase angles from the magnetic pick-up signals (AP-3C), or extracting the FADEC synchrophase angles from the DBA data (C-130J-30);
b) averaging the angles over the period of interest; and
c) converting the average angles to unit-amplitude vectors with the corresponding phase angle.

9.2. Analysis

The predicted and measured sound and vibration levels values were compared at all sensor locations for each frequency of interest (i.e., 1×, 2×, 3× and 4× the BPF). In this comparison, the predicted levels were obtained from the vector sum of the signatures at the average synchrophase angles during the measurements. The consistency between the predicted and measured values was gauged by dividing the distance between the measured and predicted points on a vector diagram (i.e., in the complex plane) by the sum of the propeller signature amplitudes for that sensor (i.e., the maximum predicted sound or vibration level at that sensor location for that particular frequency). This measure of the relative prediction error provided an indication of how well the predictions fitted the measurements in a least-squares sense, and helped to identify where the application of propeller signature theory broke down due to factors affecting measurement repeatability (§8.4). The results for the AP-3C and C-130J-30 are detailed in §9.2.1 and §9.2.2 respectively.

It should be noted that this measure of the relative prediction error does not necessarily provide an accurate indication of the absolute prediction error, and it can only be used as a means of comparison when the number of linearly independent synchrophase angle sets exceeds the minimum required; i.e., when Equation (3.22) is over determined, so that a least-squares fit is required. If the number of synchrophase angle sets equals the minimum required (i.e., four in this case), an exact fit can always be found with the measurements, and the relative prediction error will drop to zero. From this, it can be seen that a better indication of where the theory breaks down will be obtained where there are measurements from many sets of synchrophase angle at the same flight condition. There were more of these available in the C-130J-30 data (up to 35 in one test serial) than the AP-3C data (only 7 for all test serials).

It could be expected that the relative prediction error, as defined above, would approach the absolute prediction error if the propeller signatures were computed using measurements from all possible synchrophase angle combinations. In this case, the least-squares fit would have no bias towards measurements at particular synchrophase angles. However, as the number of measurements within a test serial increases, there is more time/opportunity for factors affecting the repeatability of the measurements, and hence the accuracy of the signatures, to change. The absolute prediction error can also be expected to grow with time from the moment the signatures are estimated for the same reasons. Nevertheless, it can be expected that the measure of the relative prediction error used here will follow the same trends as the absolute prediction error, particularly where there are measurements from many sets of synchrophase angles. Note that an absolute prediction error of 10% could be expected to translate to a level of uncertainty of ~1 dB in the average sound or vibration levels at that frequency.

9.2.1. AP-3C Propeller Signatures

The AP-3C propeller signatures were examined at one typical low-turbulence four-engine serial (Serial 17, 240 KIAS at FL200), and one typical low-turbulence three-engine serial (Serial 26, 210 KIAS at 1000 ft).

The relative prediction errors for all Serial 17 synchrophase angle set measurements at all the frequencies of interest are summarised in Figures 9.1 and 9.2 for the microphone and accelerometer signals respectively. The figures show how well the measurements fit the theory in a least-squares sense when Equation (3.22) is slightly over-determined; i.e., when 7 sets of synchrophase angles are used. It can be seen that the microphone and accelerometer results both follow the same general trend; i.e., as the signal levels increase, the errors fall, and the signatures become more consistent with the measured data. The best results occur at the BPF (68 Hz), where the sound pressures and accelerations are relatively large, and the corresponding relative prediction error drops below 10%. The errors at the harmonics of the BPF are generally above 10%, except for some high-amplitude 2× and 3× BPF components (> ~1 Pa_{rms}, or > ~0.1 g_{rms}) that overlap the BPF results. These high-amplitude harmonic components fall within a region near the plane of the propellers (i.e., ±1 propeller diameters for the 2× BPF components, and ±½ a propeller diameter for the 3× BPF components). The poor predictions for the lower-amplitude signals appear to be the result of poor estimates of the propeller signatures caused by the measurement variability, as discussed in Chapter 8. The two outlying points in Figure 9.1 (Microphones H12 & G6) were probably caused by unusually large signal level variations for these sensors during one, or possibly more, of the 7 synchrophase angle settings used to compute these signatures. These sensors did not consistently produce problems in the other serials.

The relative prediction errors for all Serial 26 synchrophase angle set measurements at all the frequencies of interest are shown in Figures 9.3 and 9.4. It can be seen that the results for three-engine operation are very similar to those for four-engine operation.

The relative prediction errors shown here could be expected to increase for measurements at synchrophase angle sets that are not included in the calculation of the propeller signatures; i.e., the signatures are necessarily biased towards the measurements that are included in the calculation of these signatures. This effect could be estimated by excluding the measurements from one set of synchrophase angles from the propeller signature calculation, and then using the resulting signatures to predict the excluded measurement. This was done with the C-130J-30 data (§9.2.2), but not with the AP-3C data due to the limited number of synchrophase angle sets available.

While the predictive ability of the propeller signatures appears to break down at the harmonics of the BPF, it can be seen that the amplitudes at these frequencies are often an order of magnitude less than at the BPF. These lower-amplitude components will be of less importance to the synchrophase angle optimisation process, and can potentially be excluded from the process at little cost to the achievable reduction in the overall cabin noise and vibration.

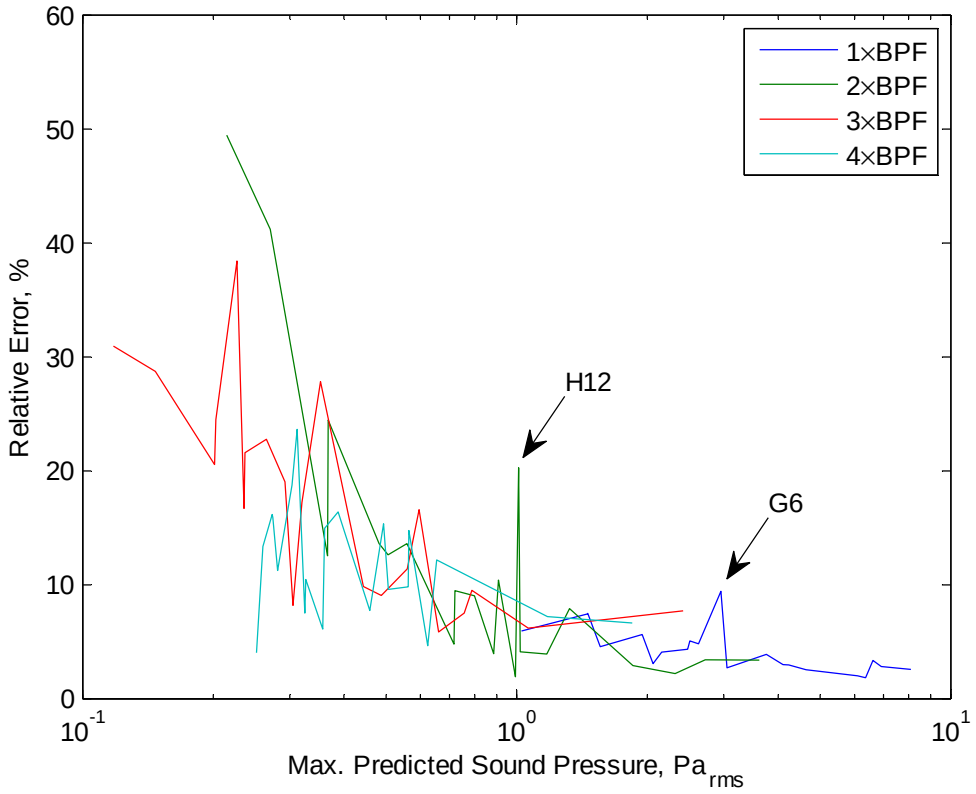

Figure 9.1 Relative prediction error for AP-3C microphones, Serial 17. Outliers correspond to Microphones G6 & H12.

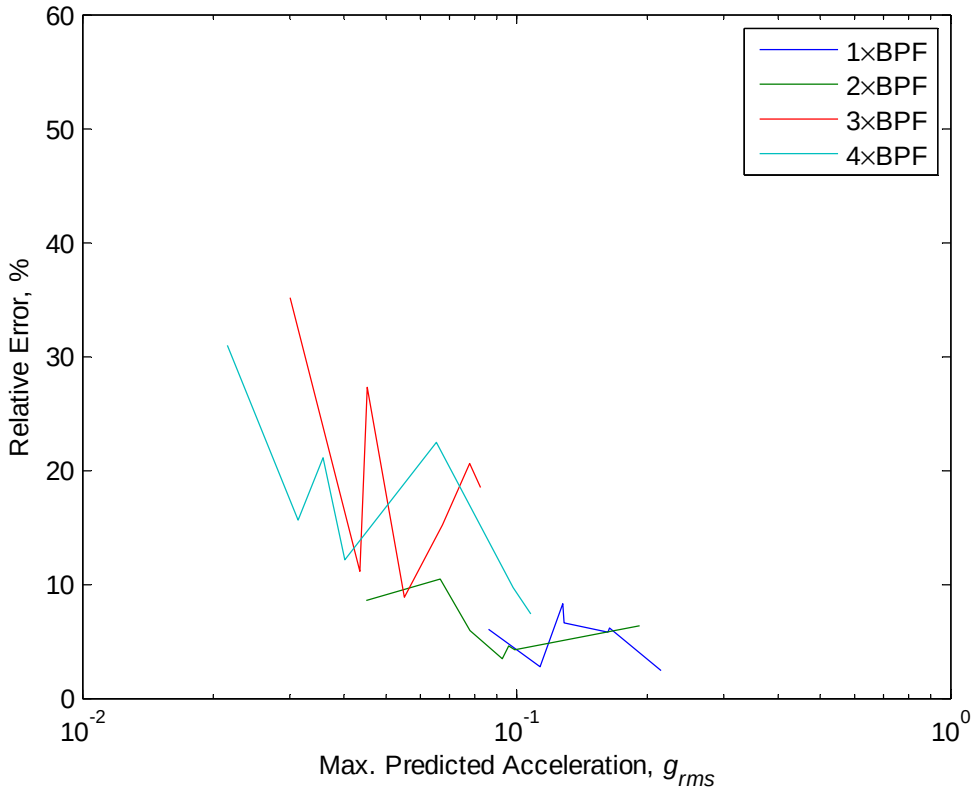

Figure 9.2 Relative prediction error for AP-3C accelerometers, Serial 17.

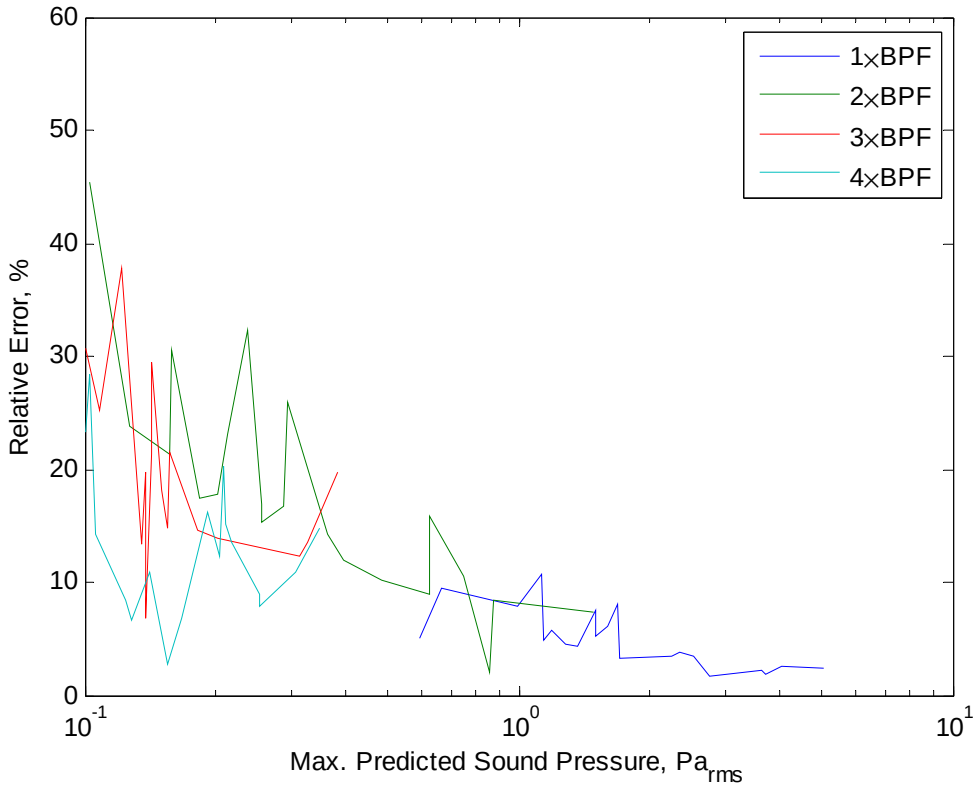

Figure 9.3 Relative prediction error for AP-3C microphones, Serial 26 (three-engine operation).

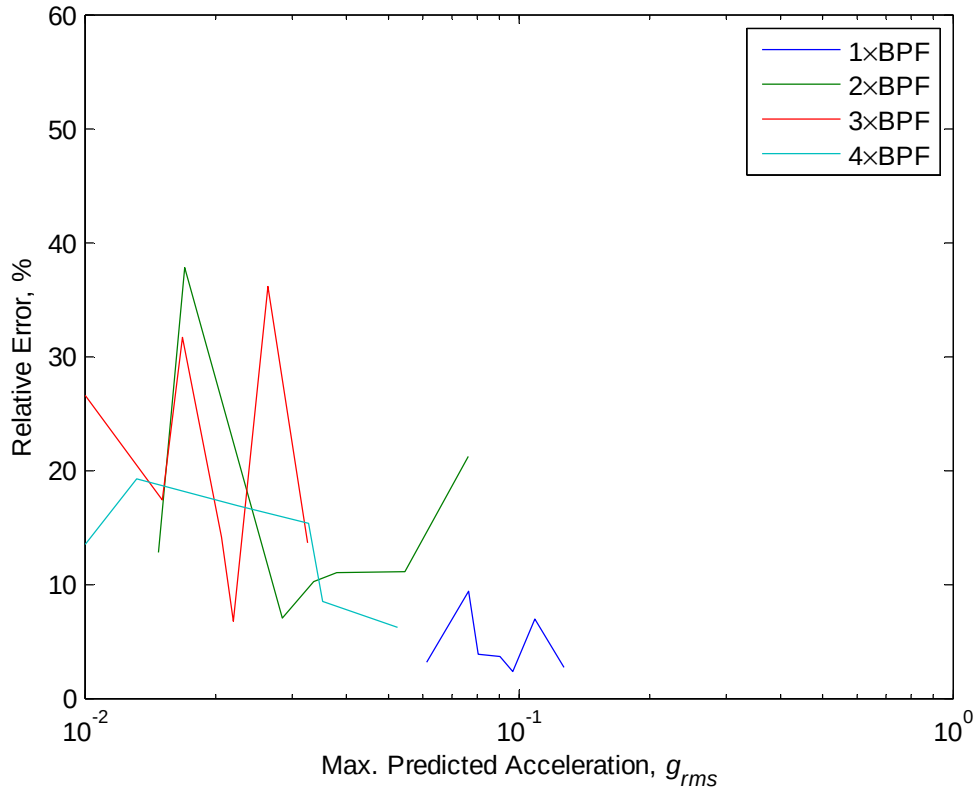

Figure 9.4 Relative prediction error for AP-3C accelerometers, Serial 26 (three-engine operation).

9.2.2. C-130J Propeller Signature Analysis

The C-130J-30 propeller signatures were subjected to more analysis than the AP-3C signatures (§9.2.1), as there were more data available from the C-130J-30 trials. Specifically, the propeller signatures from Serials 5.3 and 10, which were collected under the same nominal flight conditions (220 KCAS at FL 240), were analysed in the following ways:

a) The Serial 10 measurements were compared to the Serial 10 predictions to establish how well the signatures fit the data when Equation (3.22) was highly over-determined; i.e., when using the measurements from a large number of synchrophase angle sets (21 in Trial 1, and 35 in Trial 2).

b) The Serial 5.3 measurements were compared to the Serial 5.3 predictions to establish how well the signatures fit the data when Equation (3.22) was only slightly over-determined; i.e., when using the measurements from only 7 sets of synchrophase angles, as per the AP-3C signatures.

c) The Serial 5.3 measurements were compared to the predictions based on the Serial 10 signatures to establish the prediction error when the measurements are not included in the signature calculation; i.e., when the signatures are not biased towards the measurements in question.

d) The signatures from Serial 5.3 were compared to the signatures from Serial 10 to establish the difference brought about by the number of measurements included in the signature calculation.

The Serial 10 microphone and accelerometer prediction errors for Trials 1 and 2 are shown in Figures 9.5 to 9.8. The figures show how well the measurements fit the theory in a least-squares sense when Equation (3.22) is highly over-determined. It can be seen that the results all follow the same general trend as the AP-3C data; i.e., as the signal level increases, the relative error falls, and the signatures become more accurate. The best results occur at the BPF (102 Hz), where the sound pressures and accelerations are relatively large, and the corresponding relative error drops below 10%. The results for the harmonics of the BPF are generally not that good, except for some high-amplitude 2× BPF microphone components (> ~2 Pa_{rms}) that overlap the BPF results. These high-amplitude 2× BPF microphone components come from a region that extends from about one propeller diameter in front of, to half a propeller diameter behind, the plane of the propellers. The poor predictions for the lower-amplitude signals (i.e., < ~2 Pa_{rms}, or < ~0.2 g_{rms}) appear to be the result of poor estimates of the propeller signatures caused by the measurement variability, as discussed in Chapter 8. The results for Trial 2 are very similar to Trial 1 except for the outliers in the 1×, 2×, and 3× BPF results caused by Accelerometer D7. This indicates that there was probably a problem with this sensor. The vector diagrams for Accelerometer D32 and the Flight Engineer's seat microphone in Trial 2 also showed some irregularities at the BPF. The individual vector diagrams for each sensor and each frequency in Trial 1 can be found in Appendix G.

The Serial 5.3 prediction errors for Trials 1 and 2 are shown in Figures 9.9 to 9.12. It can be seen that the results are very similar to the Serial 10 prediction error results, although the prediction errors do not increase quite as quickly as the signal levels fall. This probably reflects the fact that it is easier to fit the signatures to fewer measurements, than the prediction error being lower in a real sense, as described in §9.2.

The prediction errors for the Serial 5.3 measurements using the Serial 10 signatures are shown in Figures 9.13 to 9.16. It can be seen that results are very similar to the Serial 10

and Serial 5.3 prediction error results, except that the relative error is slightly worse now that the signatures are not biased towards the measurements in question.

The relative differences (measured in the same way as the prediction error) between the Serial 5.3 and Serial 10 signatures are shown in Figures 9.17 to 9.20. It can be seen that the difference decreases as the signal levels increase in much the same way as prediction errors fall as the signal levels increase. This tends to indicate that the signatures based on only 7 sets of synchrophase angle measurements will still be relatively accurate where the signal levels are relatively high; i.e., at the BPF.

The above analysis is consistent with and helps to confirm the results to the AP-3C signature analysis; namely, that the predictive ability of the propeller signatures breaks down at the harmonics of the BPF. However, as with the AP-3C results, these harmonics typically have lower-amplitudes components, and can potentially be excluded from the synchrophase angle optimisation process at little cost to the achievable reduction in the overall cabin noise and vibration.

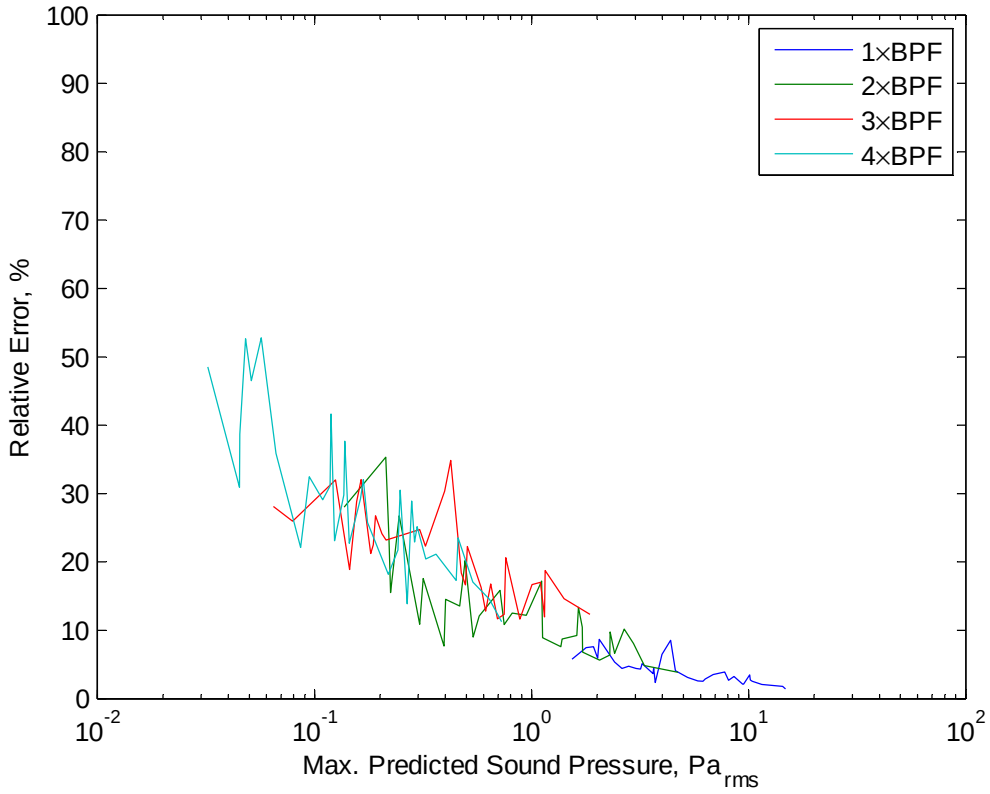

Figure 9.5 Relative prediction error for C-130J-30 microphones, Serial 10, Flight 3, Trial 1.

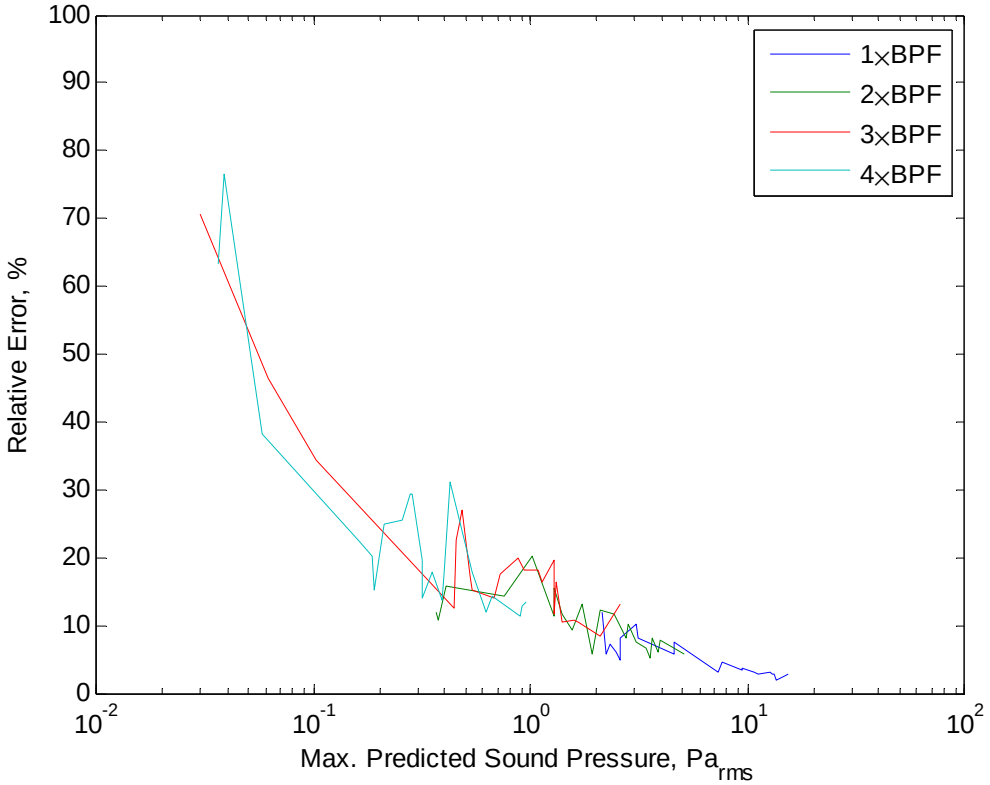

Figure 9.6 Relative prediction error for C-130J-30 microphones, Serial 10, Flight 1, Trial 2.

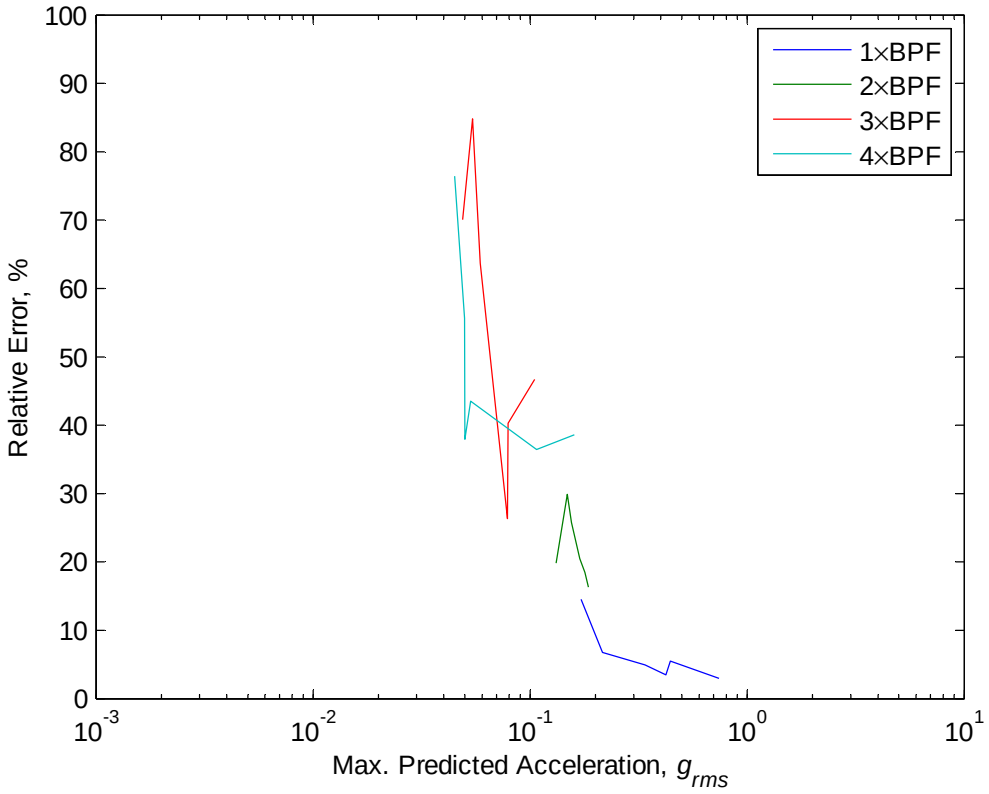

Figure 9.7 Relative prediction error for C-130J-30 accelerometers, Serial 10, Flight 3, Trial 1.

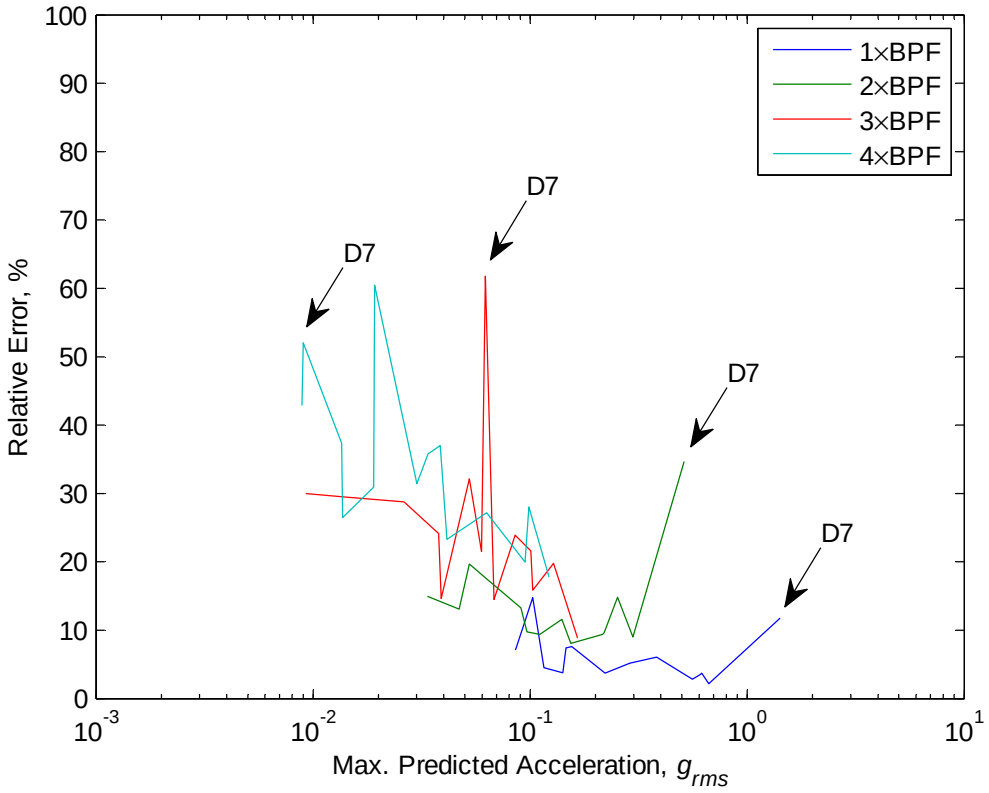

Figure 9.8 Relative prediction error for C-130J-30 accelerometers, Serial 10, Flight 1, Trial 2. Outliers correspond to Accelerometer D7.

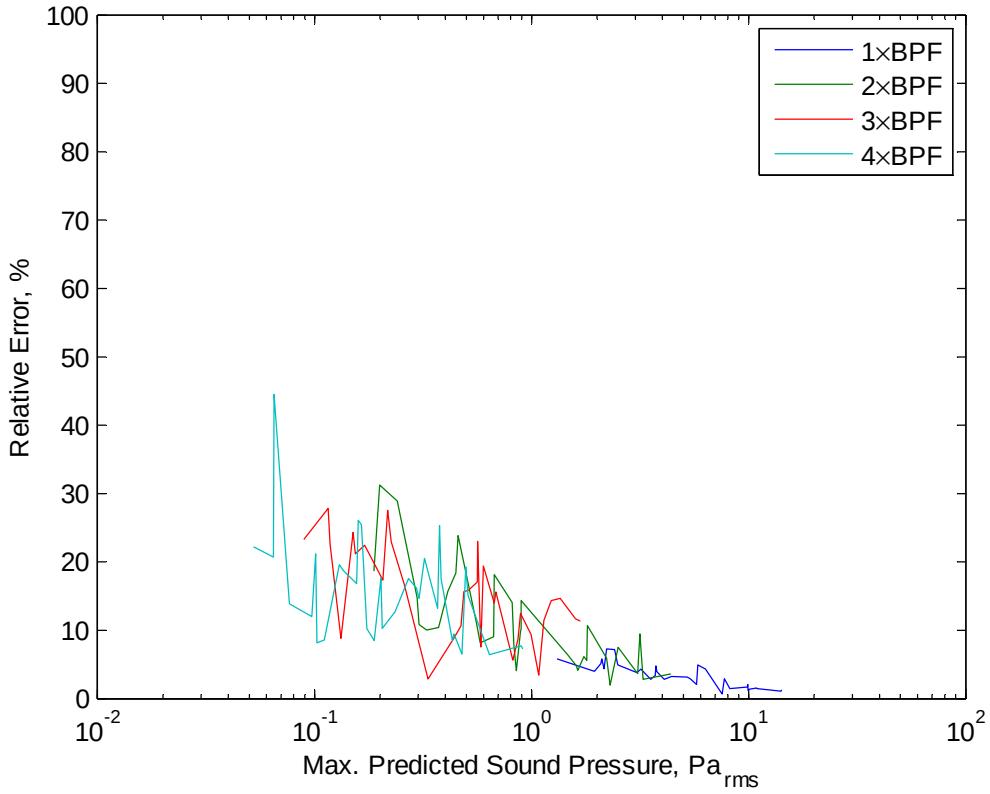

Figure 9.9 Relative prediction error for C-130J-30 microphones, Serial 5.3, Flight 3, Trial 1.

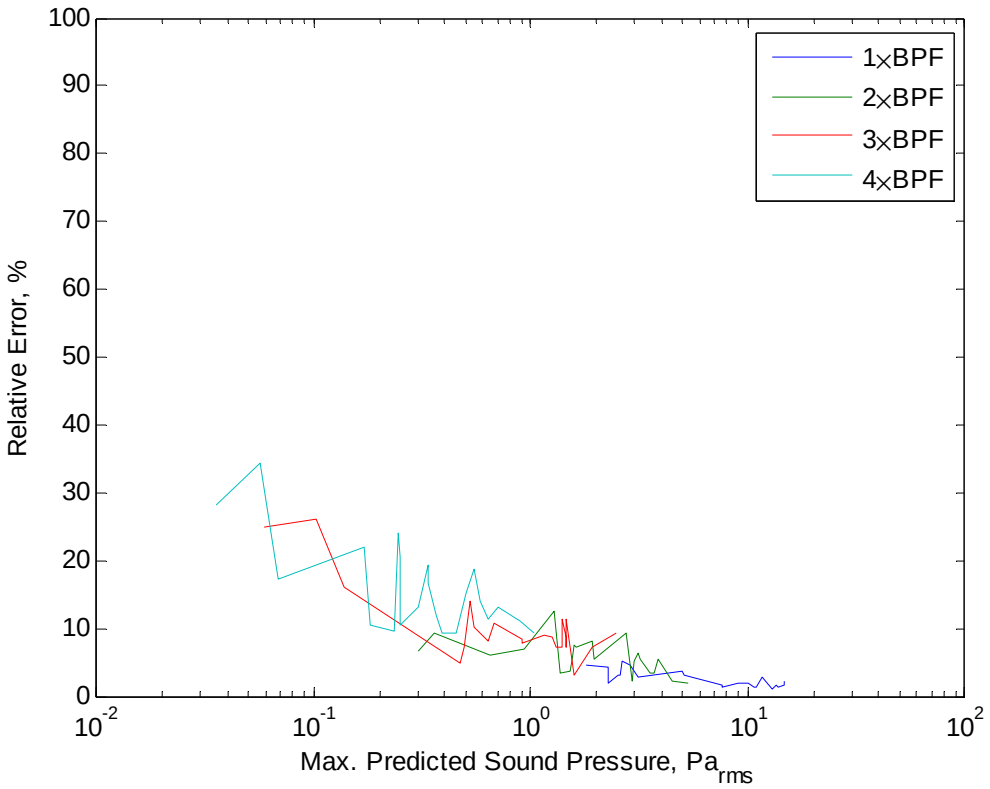

Figure 9.10 Relative prediction error for C-130J-30 microphones, Serial 5.3, Flight 1, Trial 2.

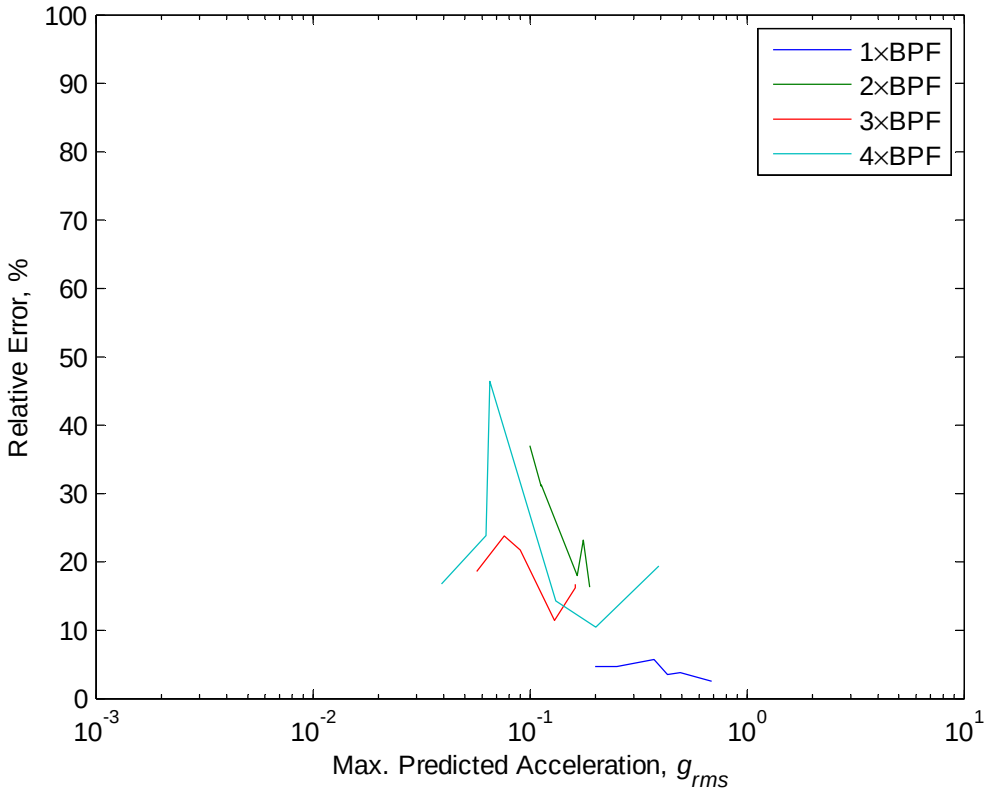

Figure 9.11 Relative prediction error for C-130J-30 accelerometers, Serial 5.3, Flight 3, Trial 1.

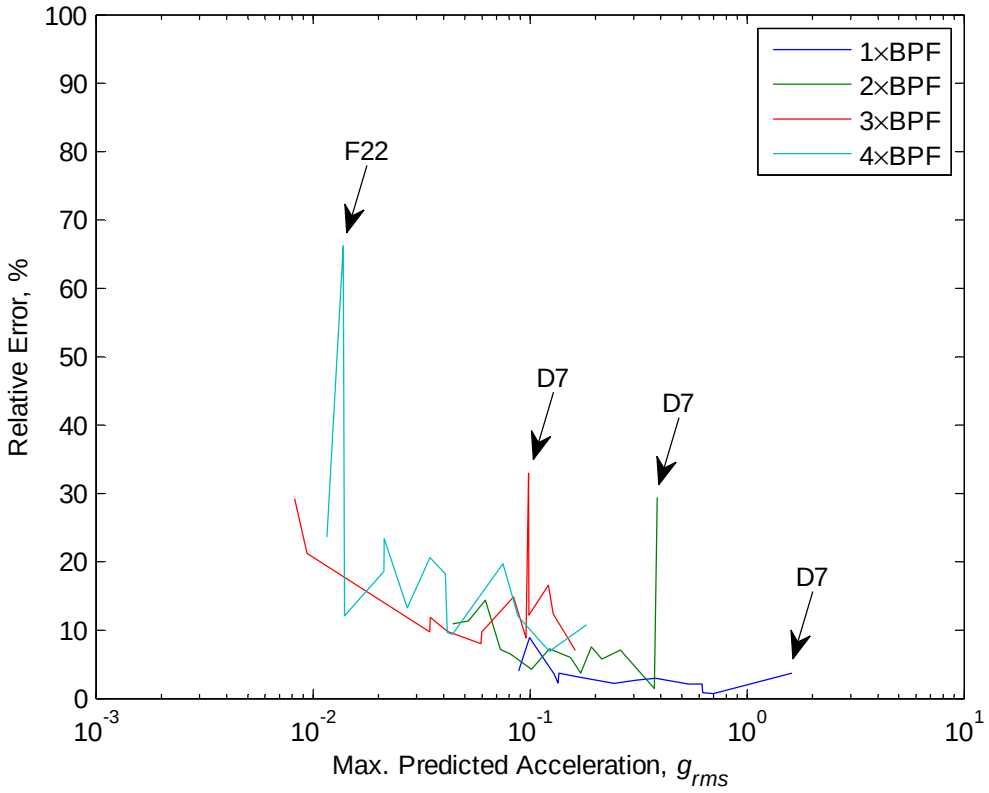

Figure 9.12 Relative prediction error for C-130J-30 accelerometers, Serial 5.3, flight 1, Trial 2. Outliers correspond to Accelerometers D7 & F22.

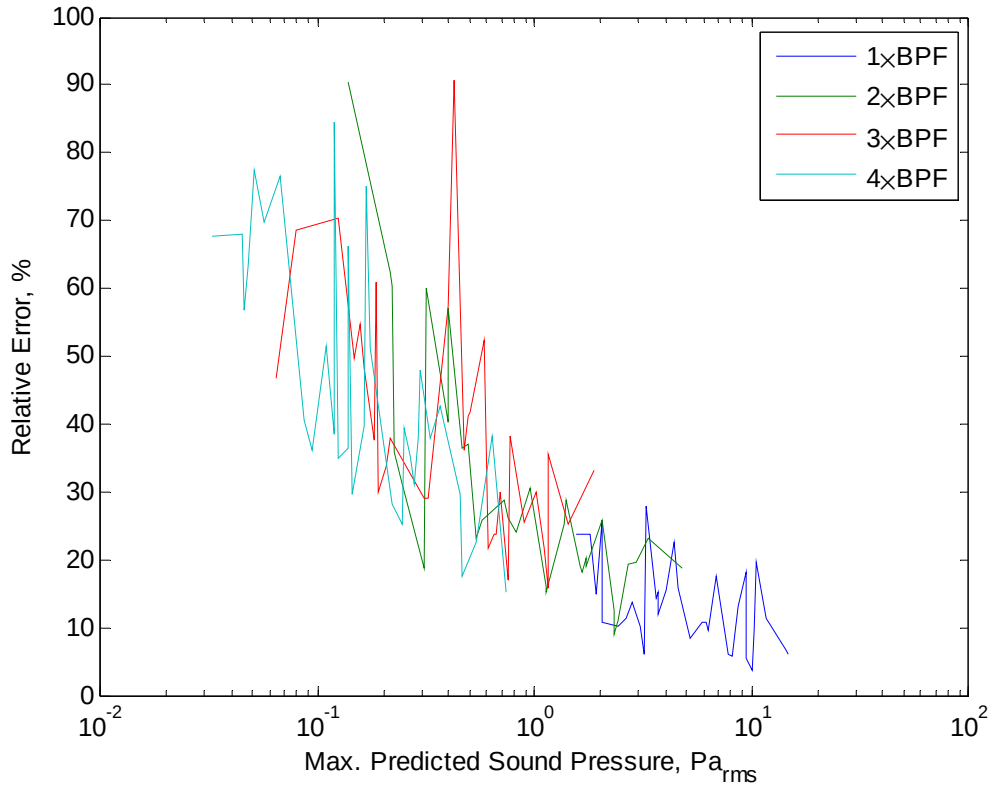

Figure 9.13 Relative prediction error for C-130J-30 microphones, Serial 5.3 using Serial 10 signatures, Flight 3, Trial 1.

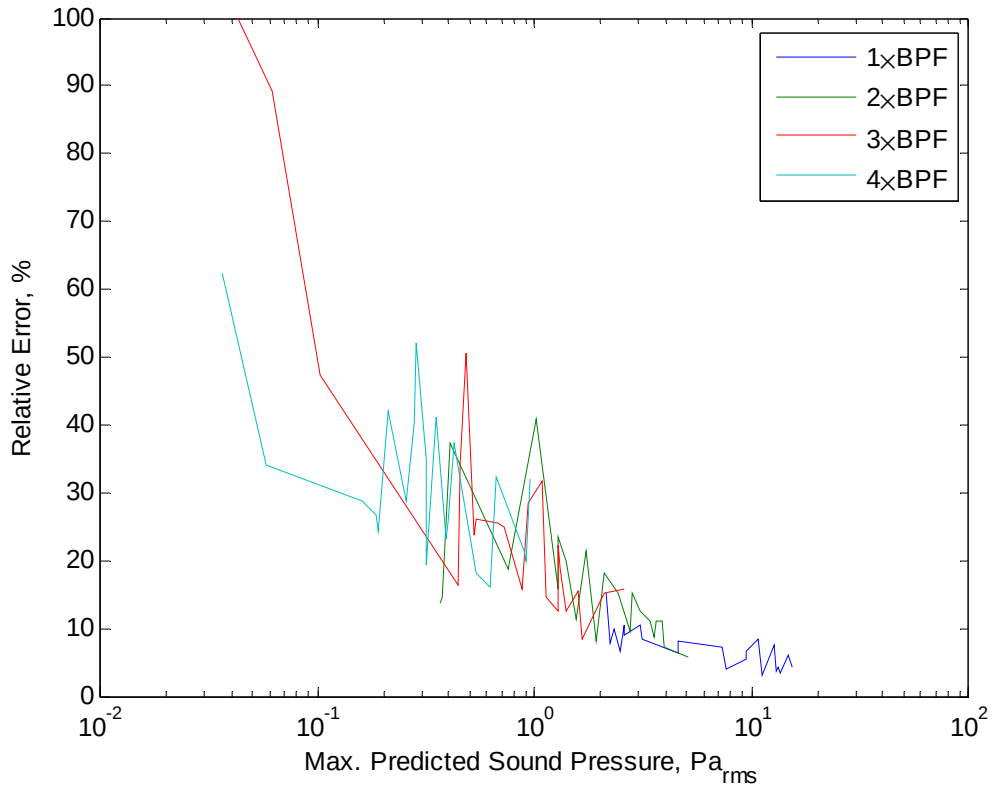

Figure 9.14 Relative prediction error for C-130J-30 microphones, Serial 5.3 using Serial 10 signatures, Flight 1, Trial 2.

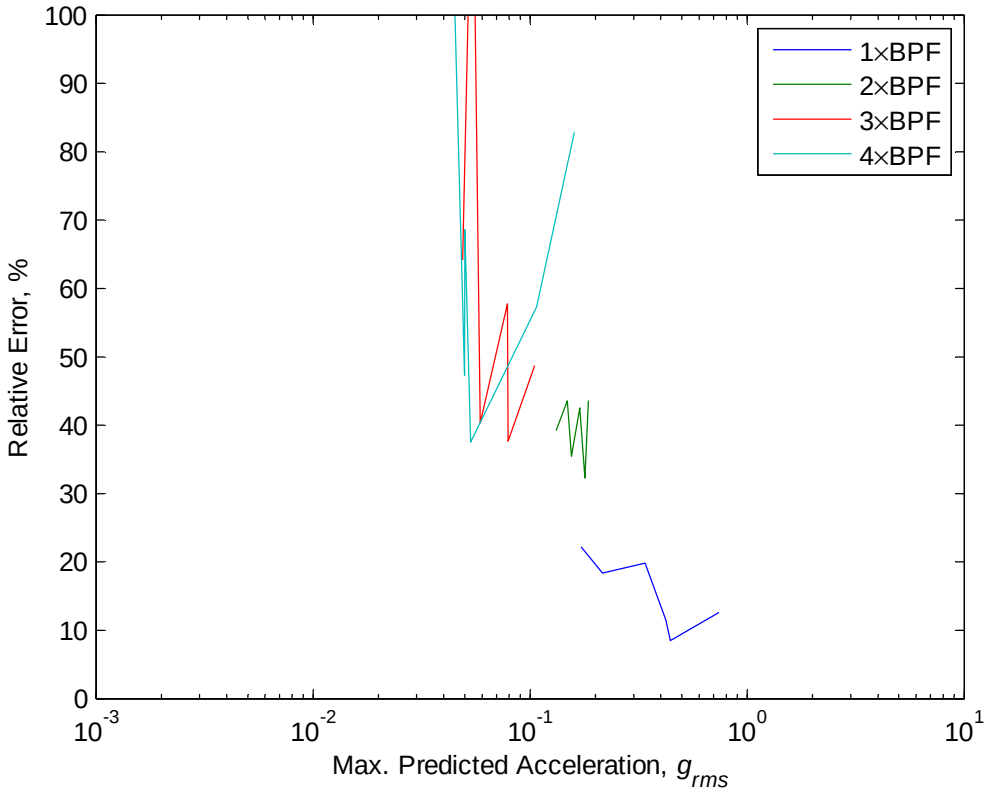

Figure 9.15 Relative prediction error for C-130J-30 accelerometers, Serial 5.3 using Serial 10 signatures, Flight 3, Trial 1.

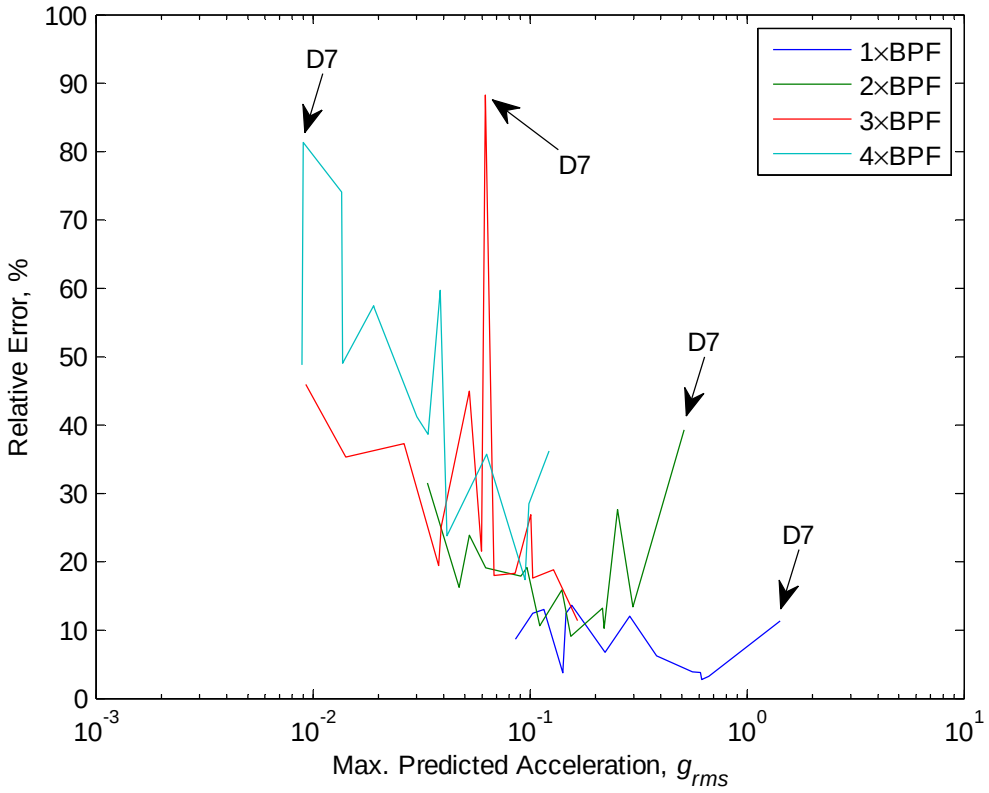

Figure 9.16 Relative prediction error for C-130J-30 accelerometers, Serial 5.3 using Serial 10 signatures, Flight 1, Trial 2. Outliers correspond to Accelerometer D7.

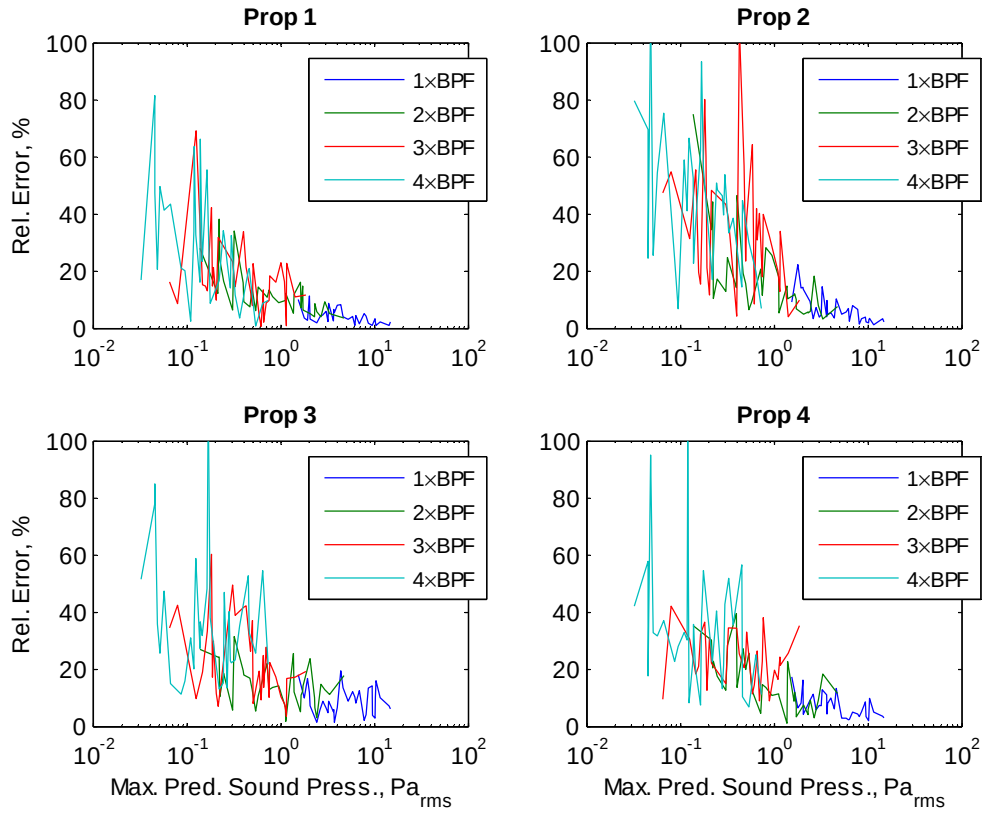

Figure 9.17 Differences between the C-130J-30 microphone signatures for Serial 5.3 and Serial 10, Flight 3, Trial 1.

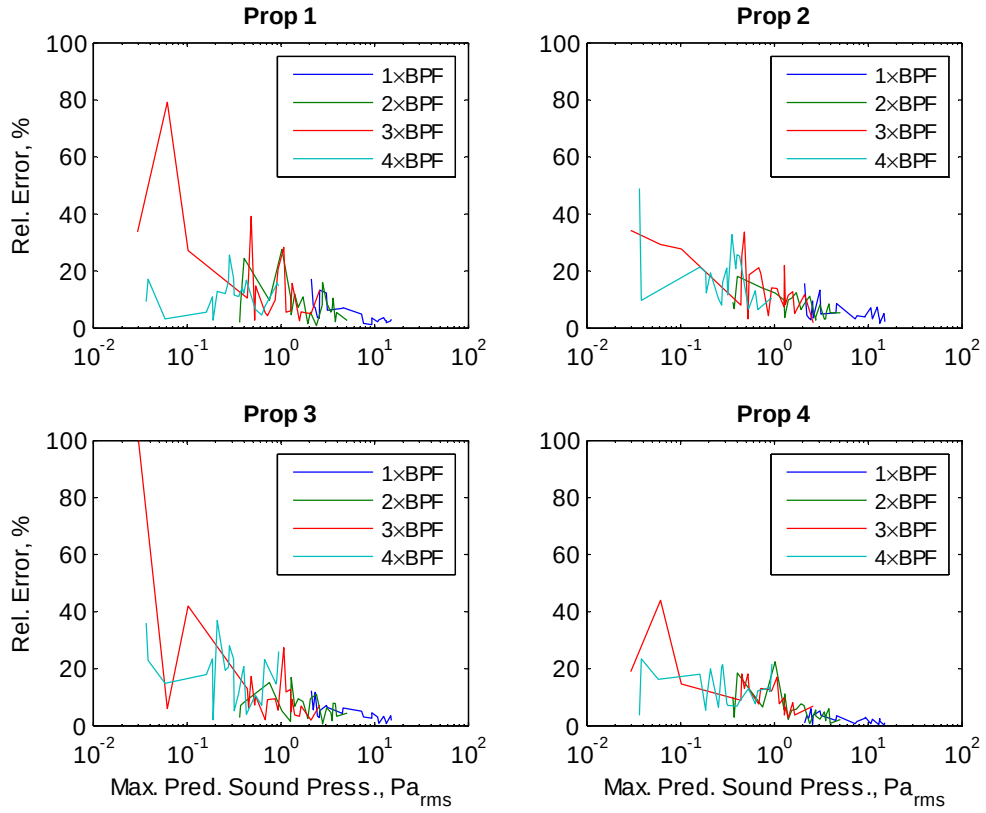

Figure 9.18 Differences between the C-130J-30 microphone signatures for Serial 5.3 and Serial 10, Flight 1, Trial 2.

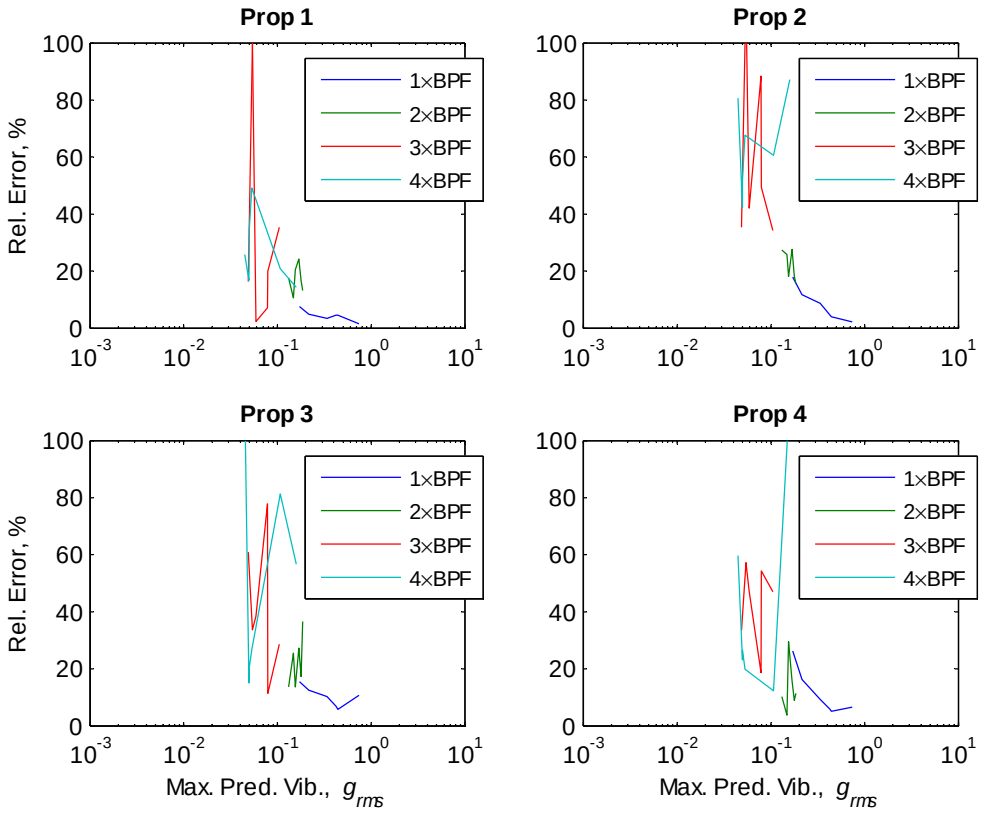

Figure 9.19 Differences between the C-130J-30 accelerometer signatures for Serial 5.3 and Serial 10, Flight 3, Trial 1.

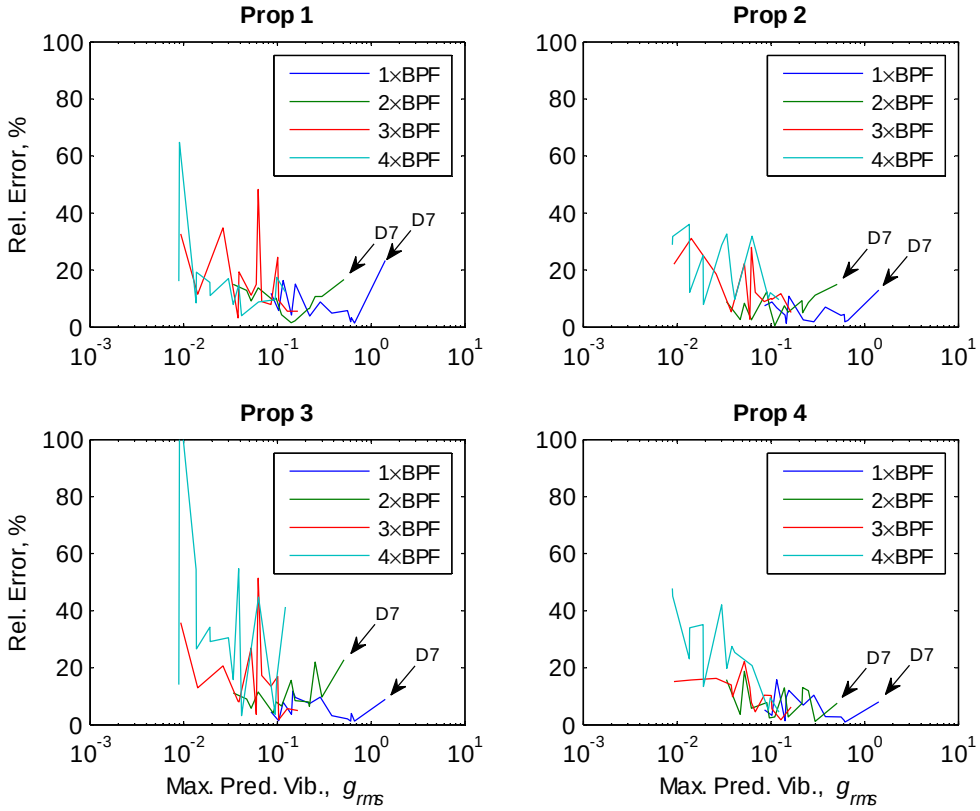

Figure 9.20 Differences between the C-130J-30 accelerometer signatures for Serial 5.3 and Serial 10, Flight 1, Trial 2. Outliers correspond to Accelerometer D7.

10. Synchrophase Angle Optimisation

This chapter details the synchrophase angle optimisation process that was applied to the experimental data. The results for the AP-3C and C-103J-30 are presented in three parts:

a) The effects of different optimisation criteria on the predicted noise and vibration levels are examined at a typical steady-state flight condition. These criteria are principally based on different sensor groupings.
b) The effects of altitude and airspeed on the optimum synchrophase angles are examined for typical optimisation criteria.
c) Several new (fixed) candidate synchrophase angle sets are derived for potential implementation using the existing synchrophasing systems; i.e., without adaptive control. Adaptive synchrophase angle control methods are specifically addressed in Chapter 11.

Additionally, for the C-130J-30, the relative performance of the candidate synchrophase angle sets are assessed in a second C-130J-30 aircraft, and the possible reasons for the observed differences between the two aircraft are discussed.

10.1. Optimisation Process

Since the propeller signature analysis presented in Chapter 9 yielded relatively high prediction errors at the harmonics of the BPF for most sensors, it was decided that the best initial approach would be to ignore these higher frequencies and concentrate on the BPF. This was still expected to produce an overall reduction in the noise and vibration levels because the BPF component amplitudes were significantly higher than those of the harmonics. The effectiveness of this approach was checked using the data from the second C-130J-30 trial, by comparing the measured reductions at the BPF with the combined measured reductions at 1×, 2×, 3× and 4× the BPF.

The optimisation of the propeller synchrophase angles was done using a simple exhaustive search algorithm, and a number of optimisation criteria (cost functions) based on different sensor groupings. These criteria are described in §10.2 and §10.3 for the AP-3C and C-130J-30 respectively. The sound and vibration levels at the BPF for all sensor locations were predicted from the propeller signatures for synchrophase angle combinations based on 2° angle increments (−44° to +44°) for the AP-3C, and 1° angle increments (0° to 60°) for the C-130J-30. These increments were chosen to be slightly finer than the accuracy of the synchrophasing systems in the respective aircraft. The process required 91,125 predictions for each sensor in the AP-3C, and 216,000 predictions for each sensor in the C-130J-30. All sensors within each sensor group were uniformly weighted.

10.2. AP-3C Synchrophase Angle Optimisation

As outlined at the start of this chapter, the synchrophase angle optimisation results for the AP-3C are presented in three parts: the effects of different optimisation criteria on the predicted noise and vibration levels are examined in §10.2.1; the effects of altitude and airspeed on the optimum synchrophase angles are examined in §10.2.2; and several new (fixed) candidate synchrophase angle sets for potential implementation using the existing synchrophaser are derived in §10.2.3.

10.2.1. Effects of Different Optimisation Criteria

The optimisation criteria (cost functions) that were selected for the AP-3C are listed in Table 10.1. Note that Criterion 1 is actually the opposite of Criterion 2, and was included to give an example of what could happen if an adverse set of synchrophase angles are used.

Table 10.1 Optimisation criteria for the AP-3C.

Criterion	Description
0	Default angles; i.e., no optimisation.
1	Highest average over all microphones (H1–H12, G1–G8, T1) of the SPL at the BPF
2	Lowest average over all microphones (H1–H12, G1–G8, T1) of the SPL at the BPF
3	Lowest average over the seat and table microphones (H1–H12, T1) of the SPL at the BPF
4	Lowest average over the grab-rail microphones (G1–G8) of the SPL at the BPF
5	Lowest average over the forward seat microphones (H1–H5) of the SPL at the BPF
6	Lowest average over the middle seat microphones (H6–H10) of the SPL at the BPF
7	Lowest average over the rear seat and table microphones (H11–H12, T1) of the SPL at the BPF
8	Lowest average over the seat-rail accelerometers (S1–S7) of the vibration at the BPF

The effects of these criteria on the noise and vibration levels at the BPF for a typical flight condition (Serial 17: 240 KIAS at FL 200) are shown in Figures 10.1 to 10.9. The left side of each figure shows the BPF levels at each sensor location, and the right side shows two different 3-D visualisations (slices and isosurfaces) of the cost function for that particular case. Note that the axes of the 3-D plots are the synchrophase angles of the three slave propellers, and the rotational symmetry of the synchrophase angles causes the cost functions to wrap around at the limits of each axis (i.e.,$-45° \leftrightarrow +45°$). The sensor maxima, minima and average values at the BPF for all serials are also tabled in Appendix H.

The main features to note from Figures 10.1 to 10.9 are as follows:

a) The default synchrophase angles (Figure 10.1) produce a reasonably good compromise at this particular flight condition. It can be seen that they are relatively close to the optimum synchrophase angles for Criterion 2 (Figure 10.3).

b) When the synchrophase angles are optimised for Criterion 1 they produce significant increases in the BPF amplitudes. The average over the grab-rail microphones increases from 98.3 dB to 106.5 dB, the average over the seat and table microphones increases from 95.7 dB to 102.3 dB, and the average over the seat rail accelerometers increases from −24.9 dB to −20.2 dB.

c) Compared to the default angle case, the optimum synchrophase angles for Criterion 2 (Figure 10.3) lower the (relatively-high) average over the grab-rail microphones (98.3 dB → 95.8 dB) more than the (relatively-low) average over the seat and table microphones (95.7 dB → 94.7 dB), and raise the average over the seat-rail accelerometers slightly (−24.9 dB → −24.1 dB).

d) The optimum synchrophase angles for Criterion 3 (Figure 10.4) produce the lowest average over the seat and table microphones (92.6 dB), but, compared to the default angle case, allow the average over the grab-rail microphones to increase (98.3 dB → 100.4 dB), and the average over the seat-rail accelerometers to increase (−24.9 dB → −21.5 dB).

e) The optimum synchrophase angles for Criterion 4 (Figure 10.5) produce a very similar result to Criterion 2 (Figure 10.3). The decreases in the averages over the grab-rail microphones (98.3 dB → 95.7 dB) and over the seat and table microphones (95.7 dB → 94.9 dB), and the increase in the average over the seat-rail accelerometers (−24.9 dB → −24.1 dB), are all nearly the same. The optimum synchrophase angles are also very similar in both cases, (−24°,22°,0°,30°) and

(−26°,22°,0°,28°), and there are only small differences in the cost function contours. However, the similarity between the results for these two criteria may not extend to other flight conditions.

f) The optimum synchrophase angles for Criterion 5 (Figure 10.6) produce good results at Microphones H1–H4 (80 dB, 85 dB, 82 dB, 76 dB), although H5 remains elevated (91 dB), at the expense of the SPL at the BPF in the rear of the cabin. The averages over the grab-rail microphones (98.3 dB → 99.6 dB), the seat and table microphones (95.7 dB → 95.0 dB), and the seat-rail accelerometers (−24.9 dB → −22.1 dB) do not change significantly.

g) The optimum synchrophase angles for Criterion 6 (Figure 10.7) produce good results in the middle of the cabin, and slightly lower the average over all the seat and table microphones (95.7 dB → 94.8 dB), but allow the average over the grab-rail microphones to increase (98.3 dB → 101.3 dB), and the average over the seat-rail accelerometers to increase (−24.9 dB → −21.8 dB).

h) The optimum synchrophase angles for Criterion 7 (Figure 10.8) produce good results in the rear of the cabin, but increase the average over the seat and table microphones (95.7 dB → 99.1 dB), markedly increase the average over the grab-rail microphones (98.3 dB → 102.7 dB), and also increase the average over the seat-rail accelerometers (−24.9 dB → −21.3 dB). The shape of this cost function is also quite different to the others, with the isosurfaces forming tubes that pass diagonally through the space.

i) The optimum synchrophase angles for Criterion 8 (Figure 10.9) produce the lowest average over the seat-rail accelerometers (−24.9 dB → −26.4 dB), but cause increases in the averages over the grab-rail microphones (98.3 dB → 100.0 dB), and the seat and table microphones (95.7 dB → 96.5 dB).

j) All the cost functions are smooth and have well-defined minima making them amenable to typical gradient-descent search algorithms.

The noise and vibration levels for a typical three-engine flight condition (Serial 26: 210 KIAS at 1000 ft), and its relatively close four-engine counterpart (Serial 4: 220 KIAS at 1000 ft), are shown in Figures 10.10 and 10.11 respectively. It can be seen that the sound and vibration levels have very similar distributions in both cases, and the cost function minima are also very close if the angle for Propeller 1 is ignored. These findings generally hold true for all other 3-engine serials considered in this investigation.

It can be concluded that:

a) Incorporating all the microphones into the cost function generally produces low overall sound pressure levels, but does not necessarily guarantee low sound pressure levels at key (e.g., high-workload) regions of the cabin.

b) Using various sub-sets of sensors in the cost function generally lowers the levels in those respective regions of the aircraft, but allows the levels elsewhere to increase and generally increases the overall levels.

c) The seat-rail vibration levels are generally quite low regardless of the optimisation criteria and therefore of less concern than the sound pressure levels.

d) Shutting down Engine 1 does not lower the cabin noise and vibration significantly. This is probably because the remaining three engines have to work harder, and hence produce more propeller noise, to maintain a similar airspeed.

e) The optimum synchrophase angles for four-engine operation continue to work relatively well when Engine 1 is shut down, but this may not be the case if a different (e.g., inboard) engine is shut down.

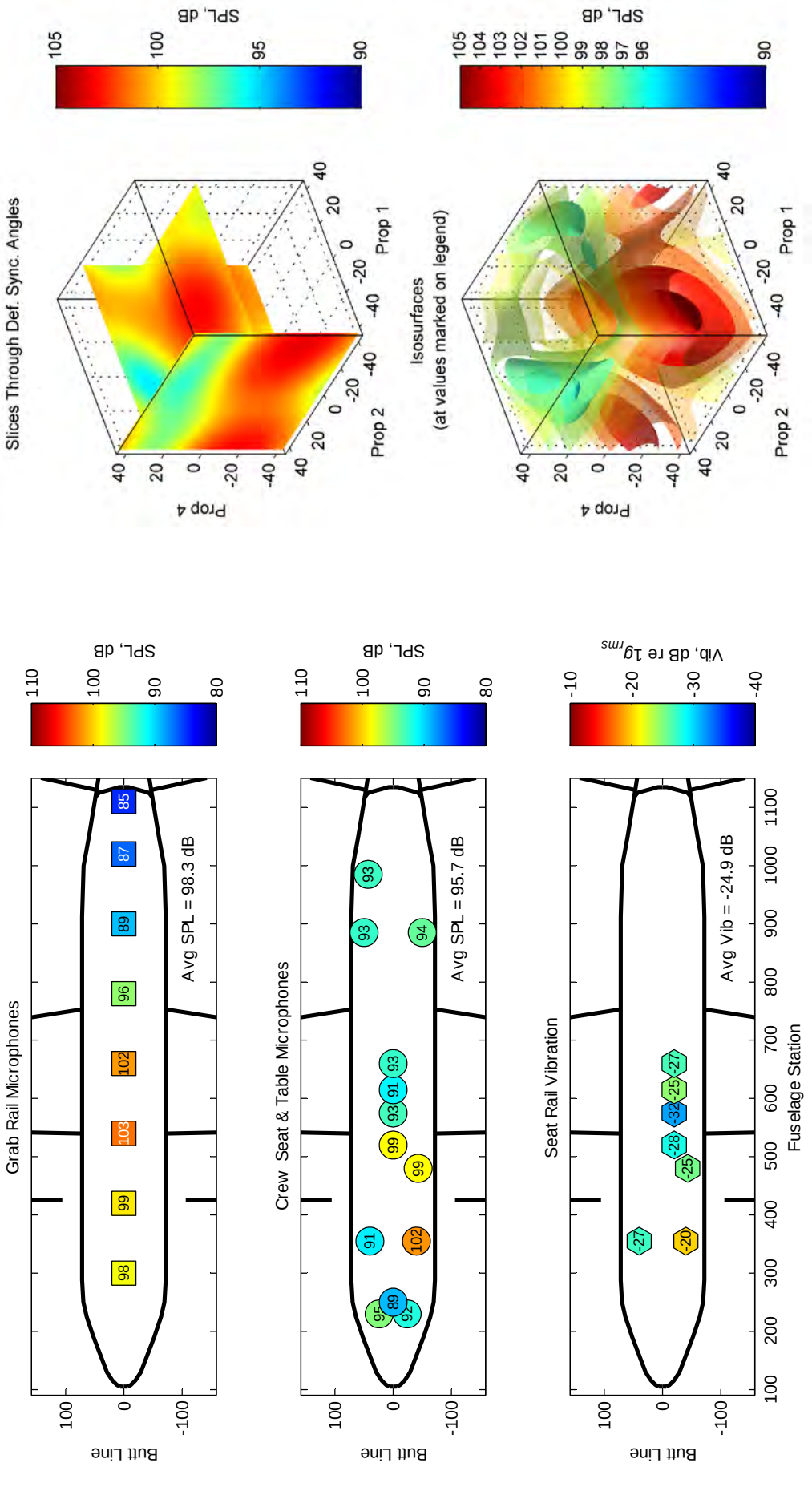

Figure 10.1 AP-3C sensor levels at the BPF for the default synchrophase angles, Serial 17: measured individual levels (left), and the predicted average over all microphones (right).

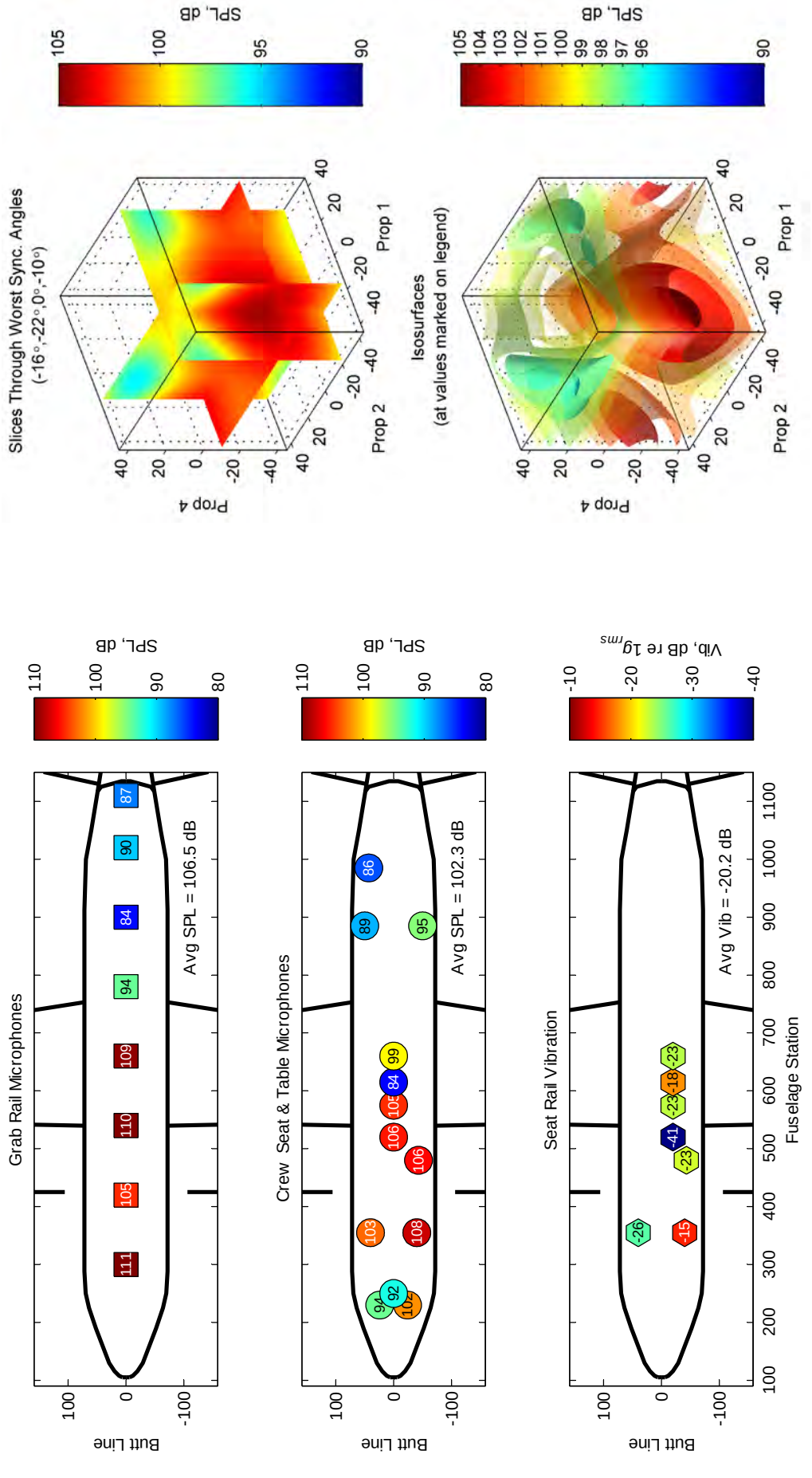

Figure 10.2 AP-3C sensor levels at the BPF for the synchrophase angles giving the highest average over all microphones (-16°,-22°,0°,-10°), Serial 17: predicted individual levels (left), and the predicted average over all microphones (right).

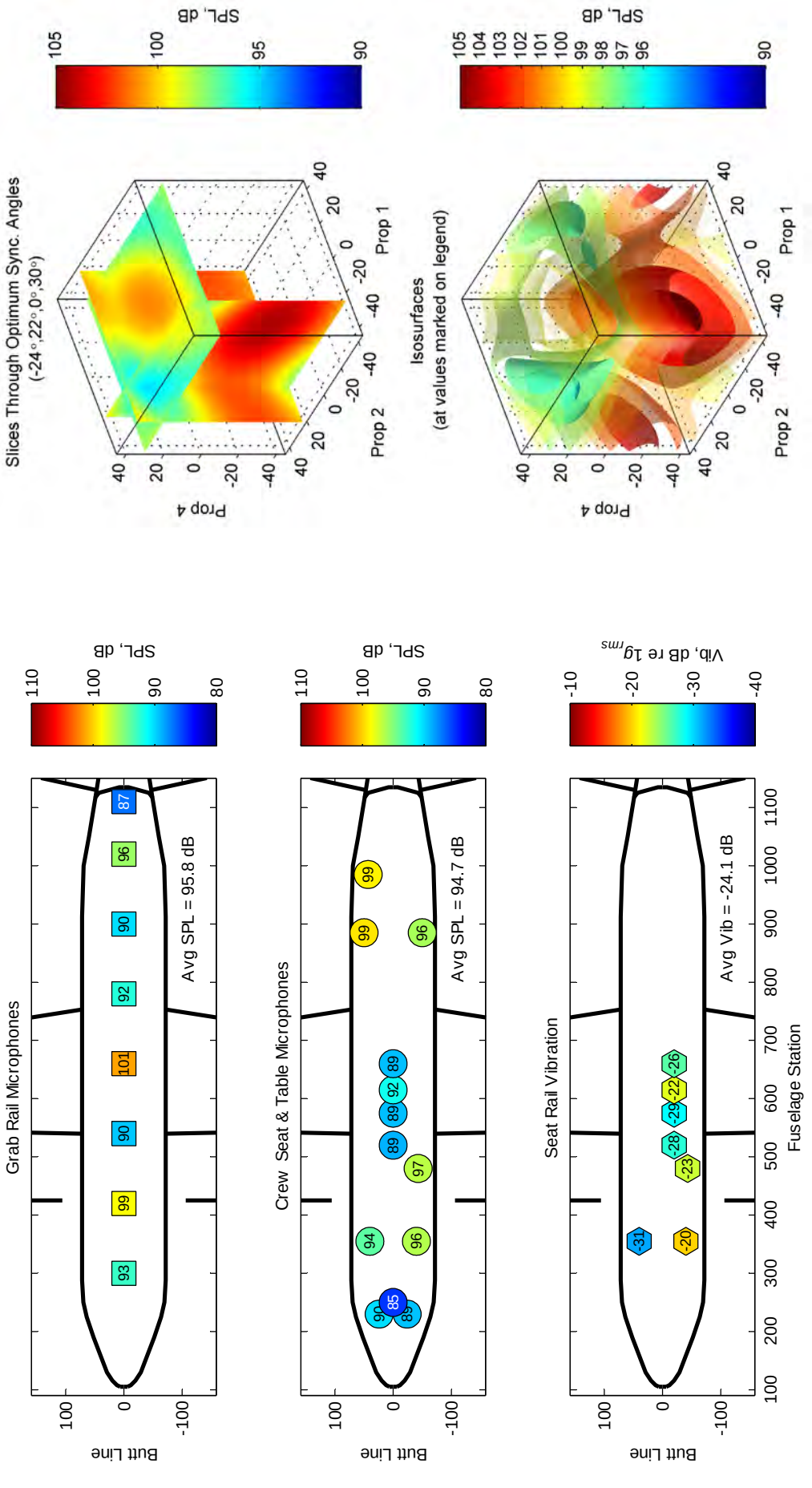

Figure 10.3 AP-3C sensor levels at the BPF for the synchrophase angles giving the lowest average over all microphones (-24°,22°,0°,30°), Serial 17: predicted individual levels (left), and the predicted average over all microphones (right).

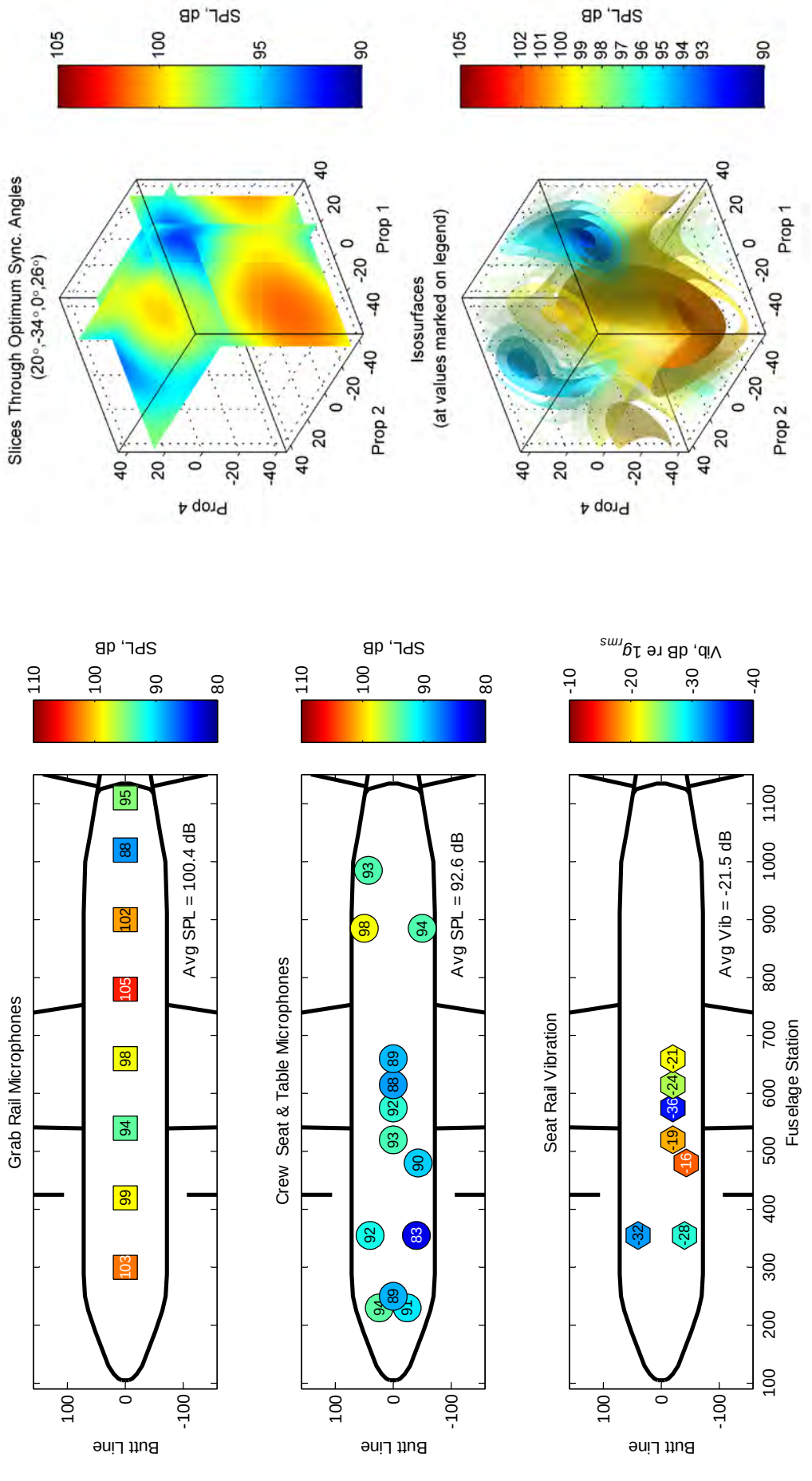

Figure 10.4 AP-3C sensor levels at the BPF for the synchrophase angles giving the lowest average over the seat and table microphones (20°,-34°,0°,26°), Serial 17: predicted individual levels (left), and the predicted average over the seat and table microphones (right).

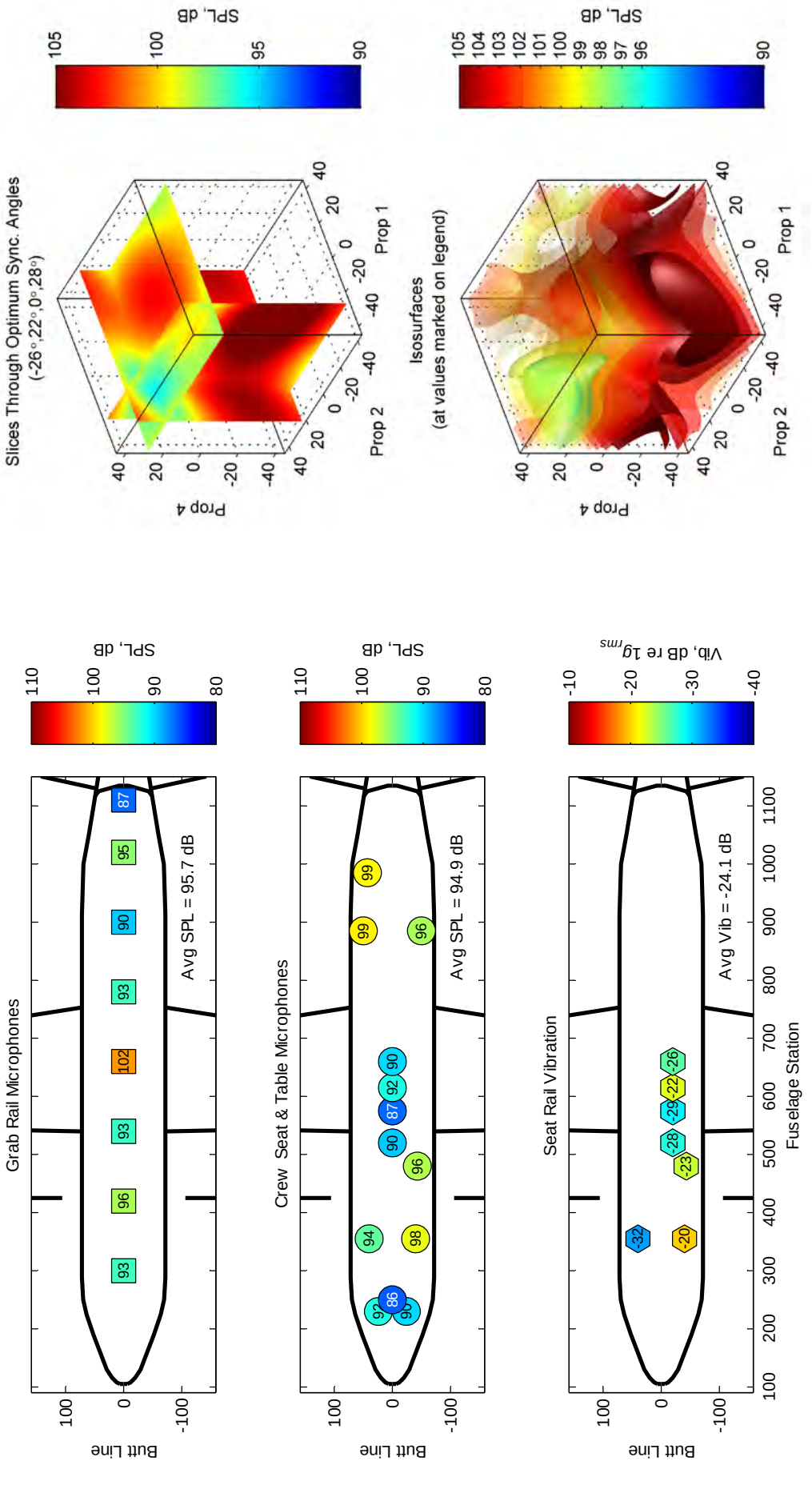

Figure 10.5 AP-3C sensor levels at the BPF for the synchrophase angles giving the lowest average over the grab-rail microphones (-26°,22°,0°,28°), Serial 17: predicted individual levels (left), and the predicted average over the grab-rail microphones (right).

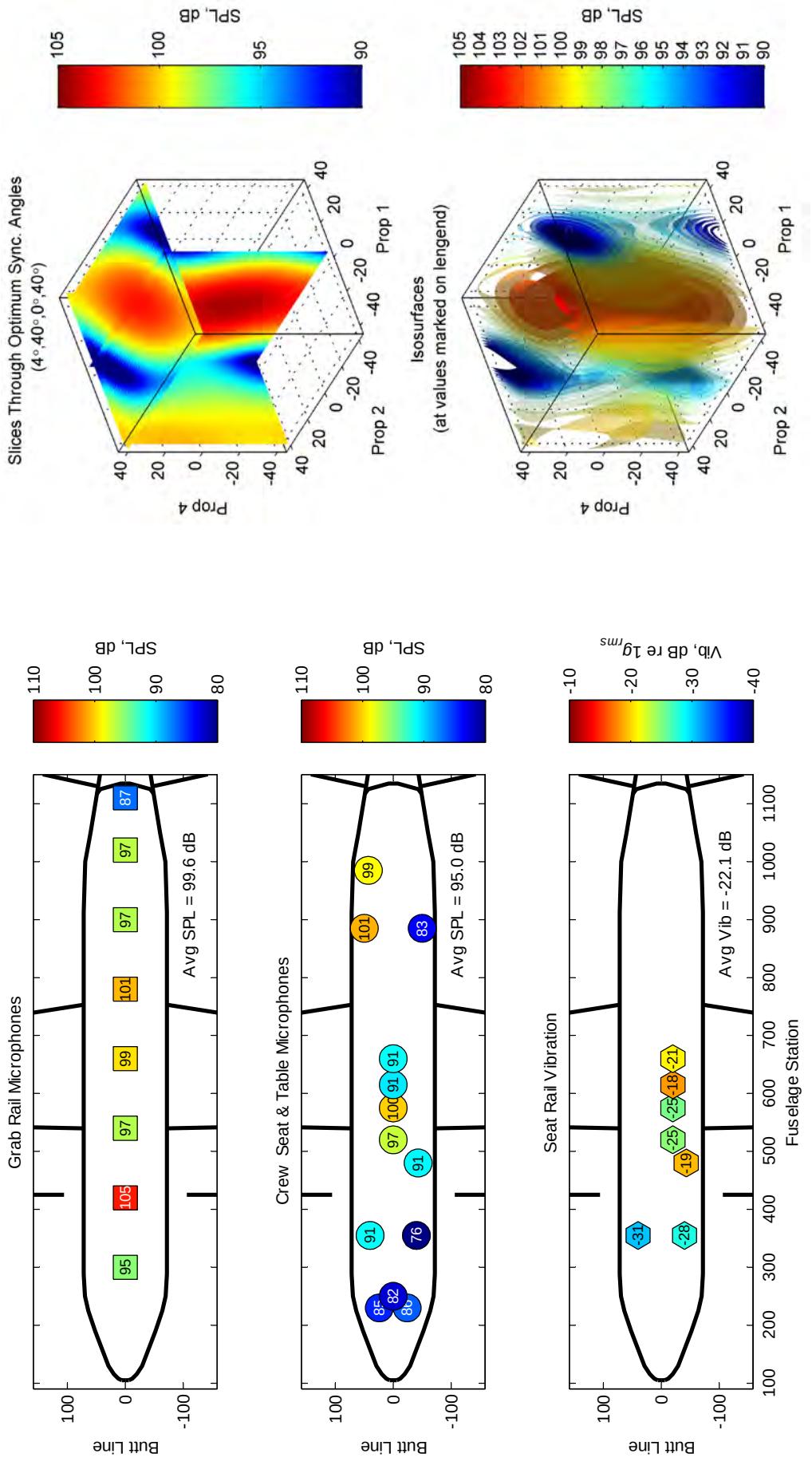

Figure 10.6 AP-3C sensor levels at the BPF for the synchrophase angles giving the lowest average over the H1–H5 microphones (4°,40°,0°,40°), Serial 17: predicted individual levels (left), and the predicted average over the H1–H5 microphones (right).

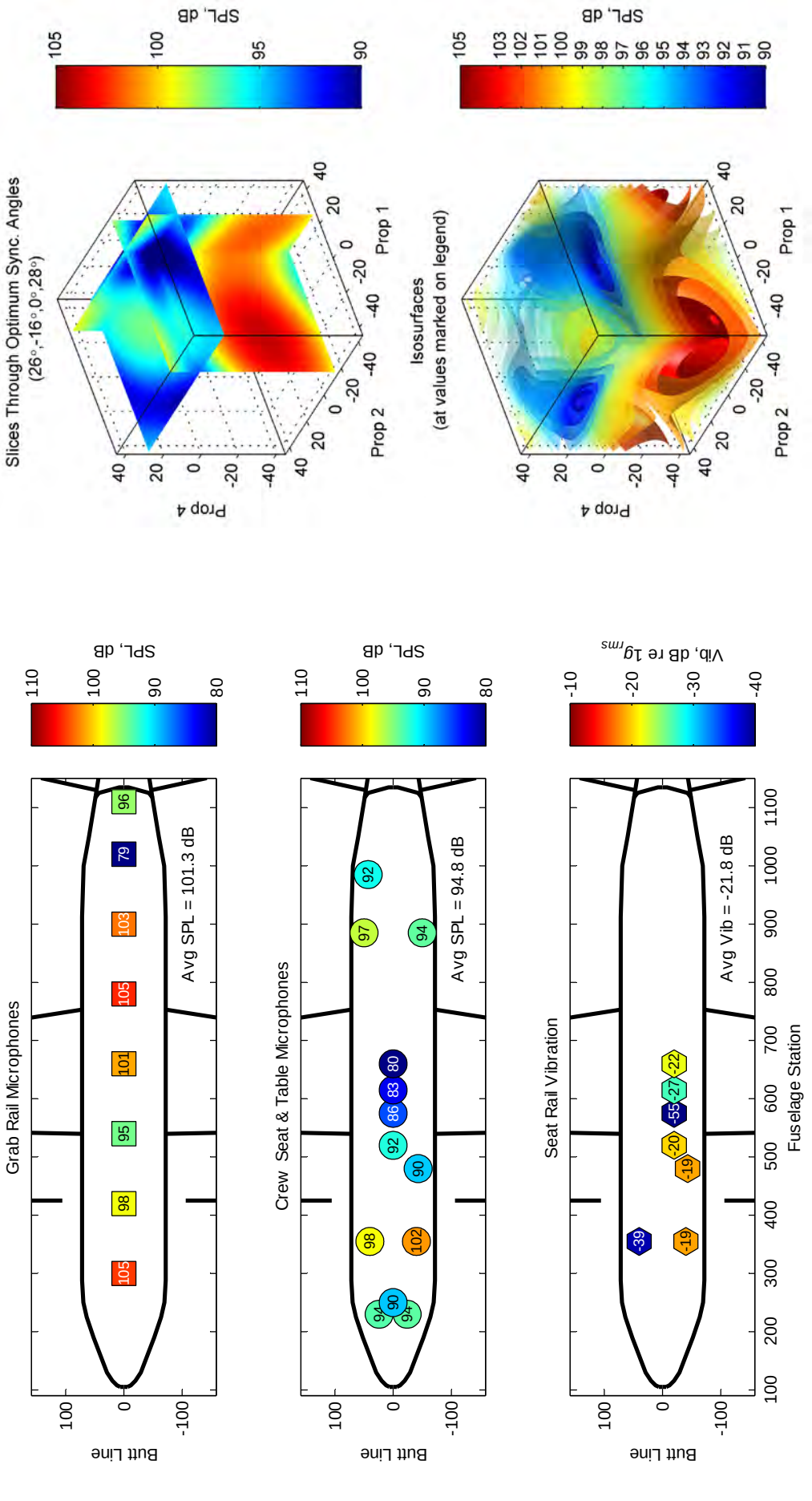

Figure 10.7 AP-3C sensor levels at the BPF for the synchrophase angles giving the lowest average over the H6-H10 microphones (26°,-16°,0°,28°), Serial 17: predicted individual levels (left), and the predicted average over the H6-H10 microphones (right).

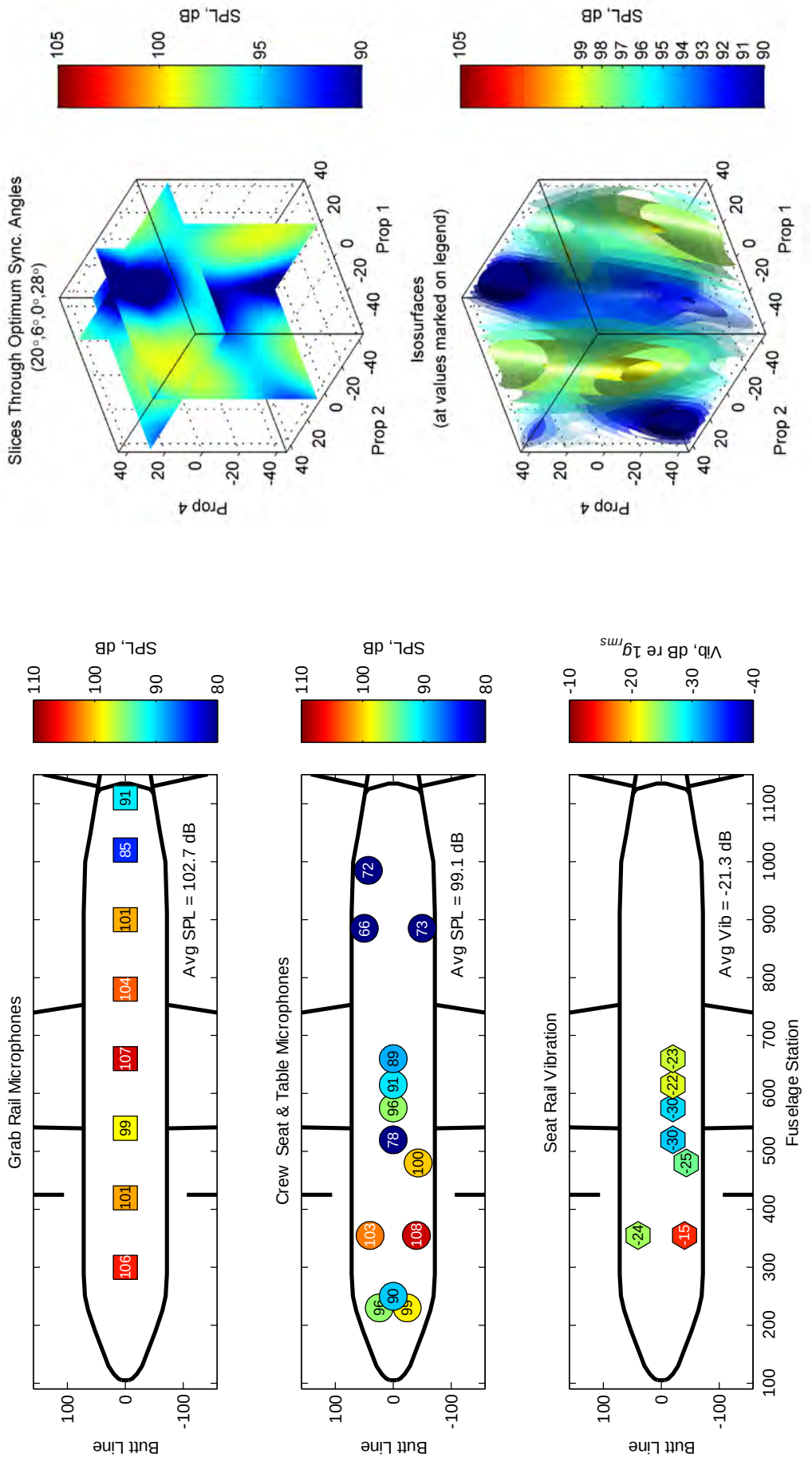

Figure 10.8 AP-3C sensor levels at the BPF for the synchrophase angles giving the lowest average over the H11, H12 & T1 microphones (-20°,6°,0°,28°), Serial 17: predicted individual levels (left), and the predicted average over the H11, H12 & T1 microphones (right).

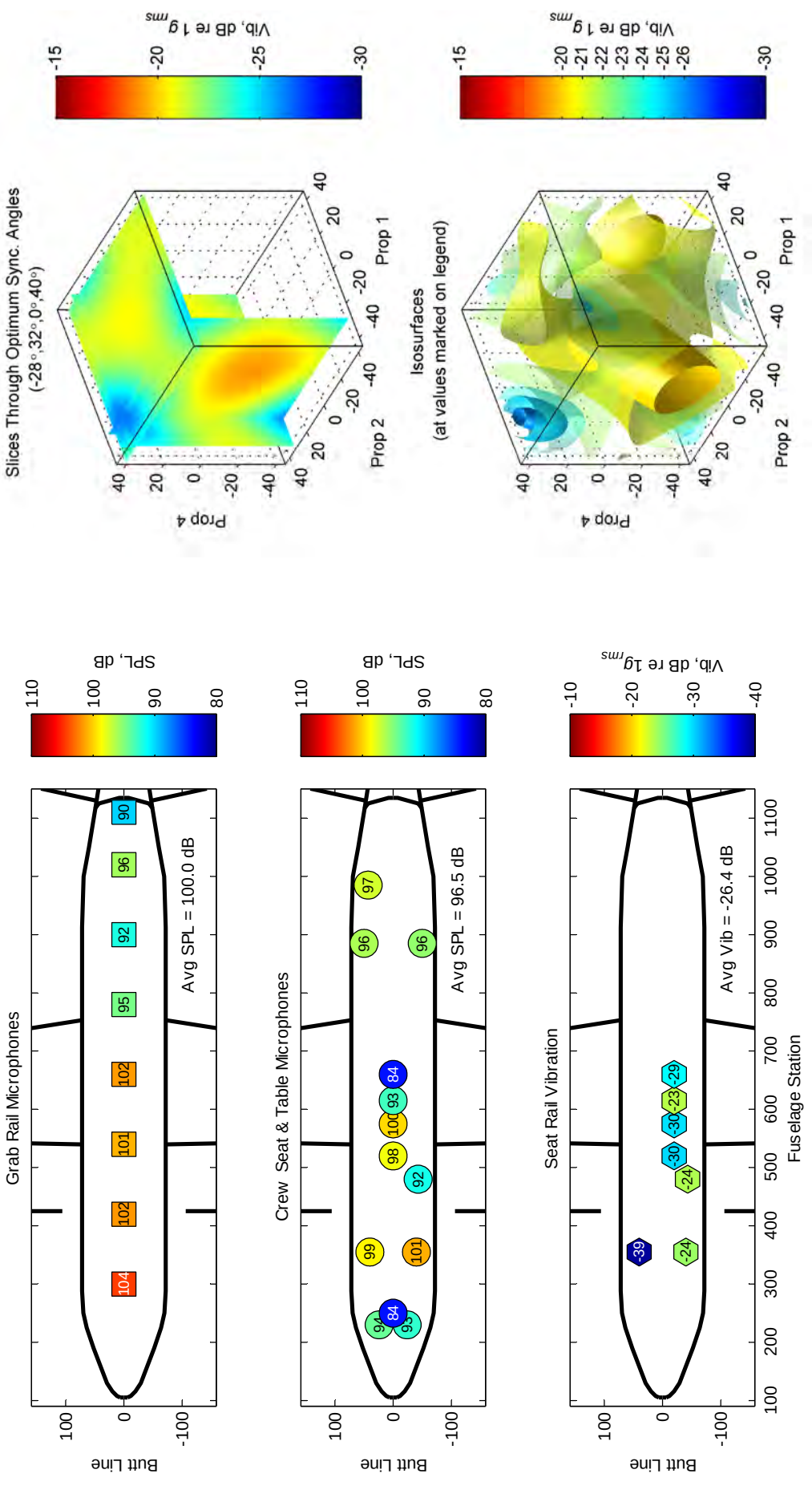

Figure 10.9 AP-3C sensor levels at the BPF for the synchrophase angles giving the lowest average over the seat-rail accelerometers (-28°,32°,0°,40°), Serial 17: predicted individual levels (left), and the predicted average over the seat-rail accelerometers (right).

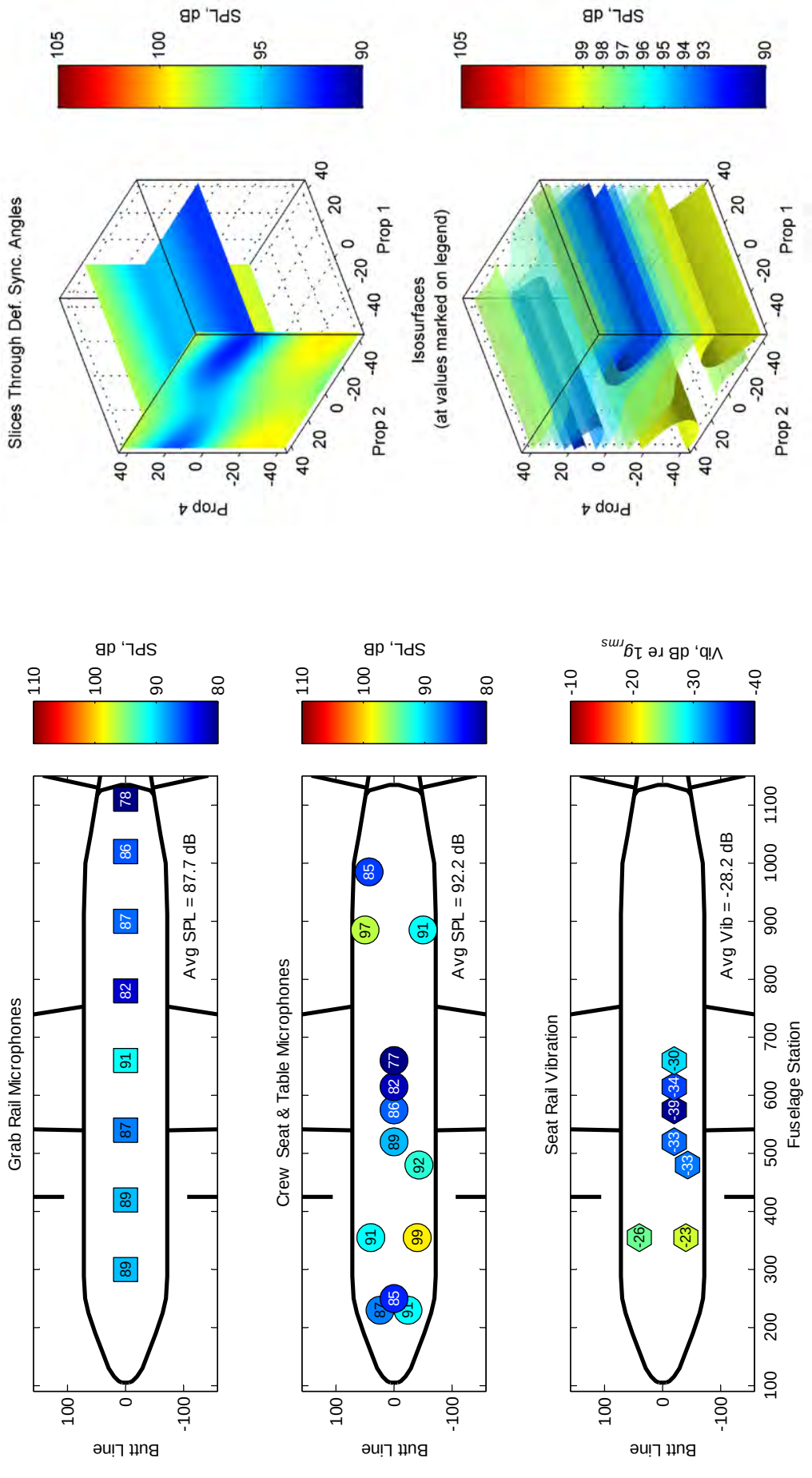

Figure 10.10 AP-3C sensor levels at the BPF for the default synchrophase angles, Serial 26: measured individual levels (left), and the predicted average over all the microphones (right).

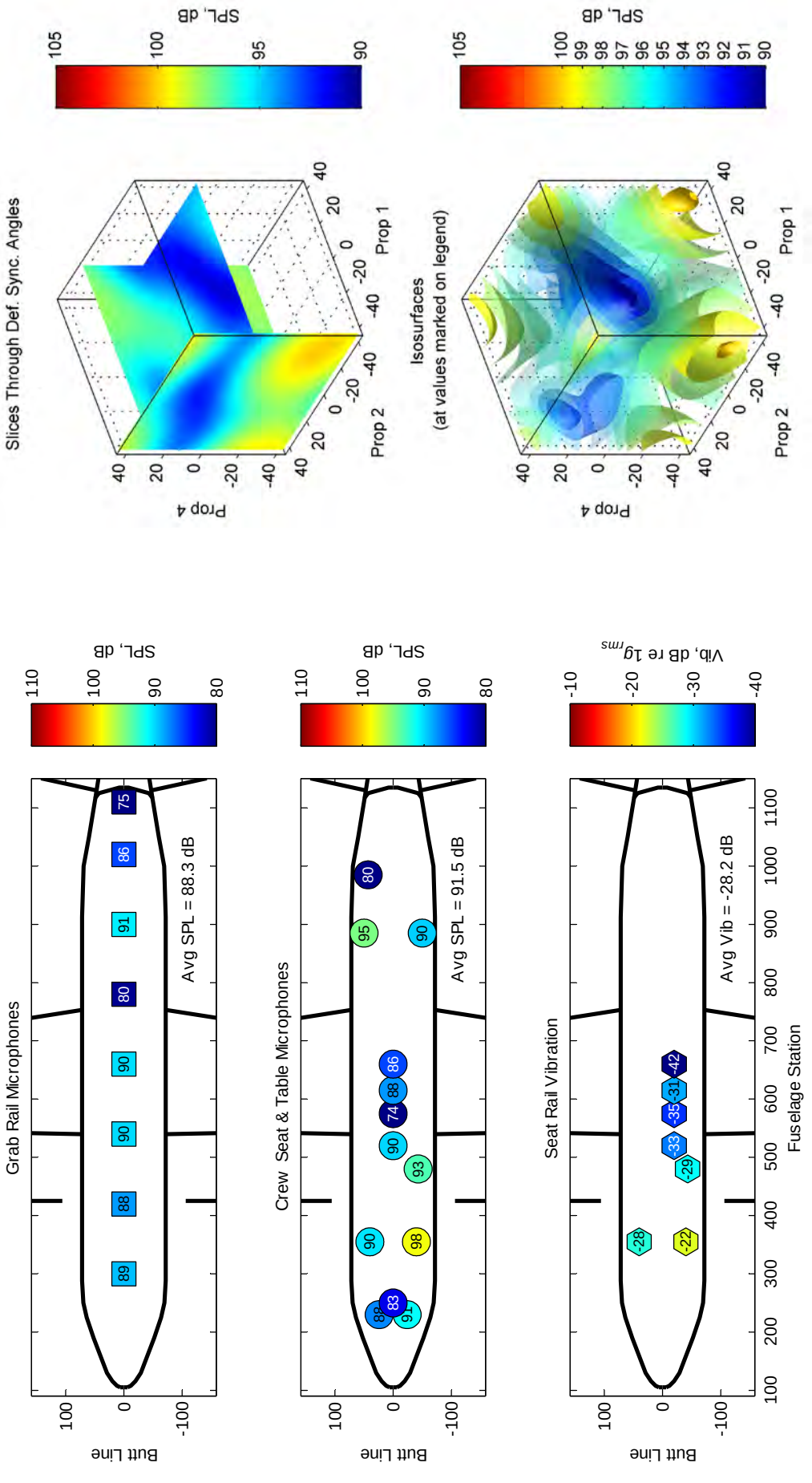

Figure 10.11 AP-3C sensor levels at the BPF for the default synchrophase angles, Serial 4: measured individual levels (left), and the predicted average level over all microphones (right).

10.2.2. Effects of Altitude and Airspeed

To illustrate the effects of altitude and airspeed on the optimum synchrophase angles, a typical cost function (the average over all microphones of the SPL at the BPF; i.e., Criterion 2 from Table 10.1) was calculated for each altitude-airspeed combination. The cost function range, and the value at the default synchrophase angles, are shown for each flight condition serial in Figure 10.12. The individual cost functions are shown in Figures Figure 10.13 to Figure 10.15. The optimum synchrophase angles and the predicted effects on the cost function are listed in Table 10.2. The main features to note from these figures and table are:

a) The default synchrophase angles do not offer the best outcome for all flight conditions (Figure 10.12). They only approach the cost function minimum at one flight condition (Serial 6).

b) The optimum synchrophase angles (Table 10.2) change significantly over the range of flight conditions considered, and a single set of synchrophase angles cannot produce the good results for all conditions.

c) The cost function varies by an amount between 5.6 dB (Serial 25) and 13.7 dB (Serial 8) (Table 10.2 and Figure 10.12).

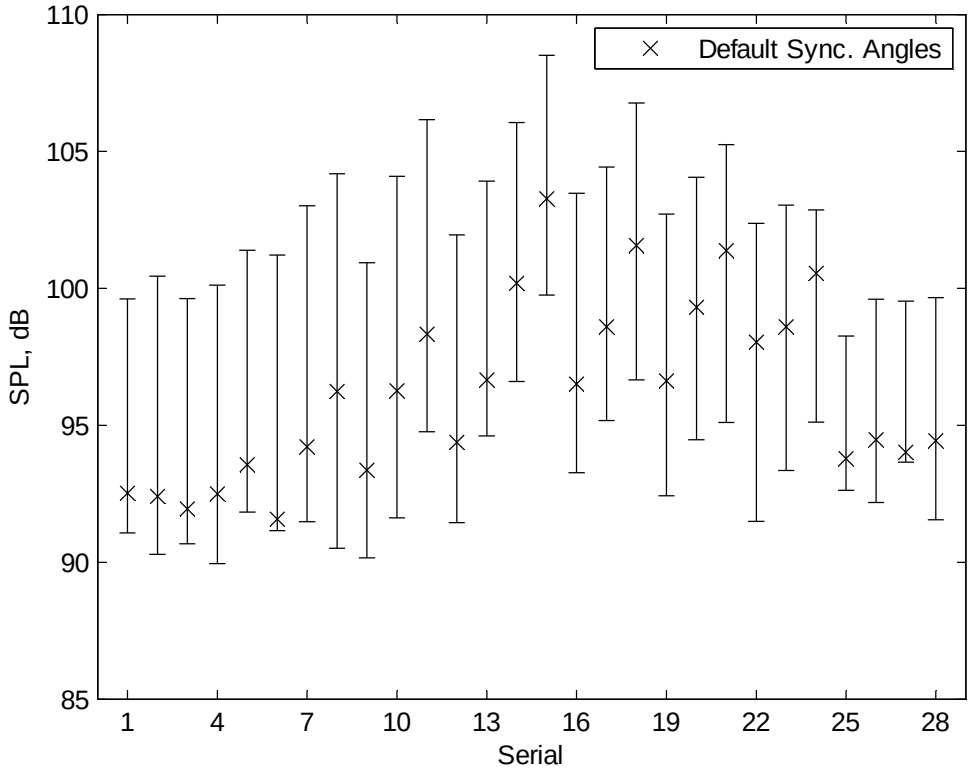

Figure 10.12 AP-3C predicted cost function range (average over all microphones of the SPL at the BPF) for each flight condition serial.

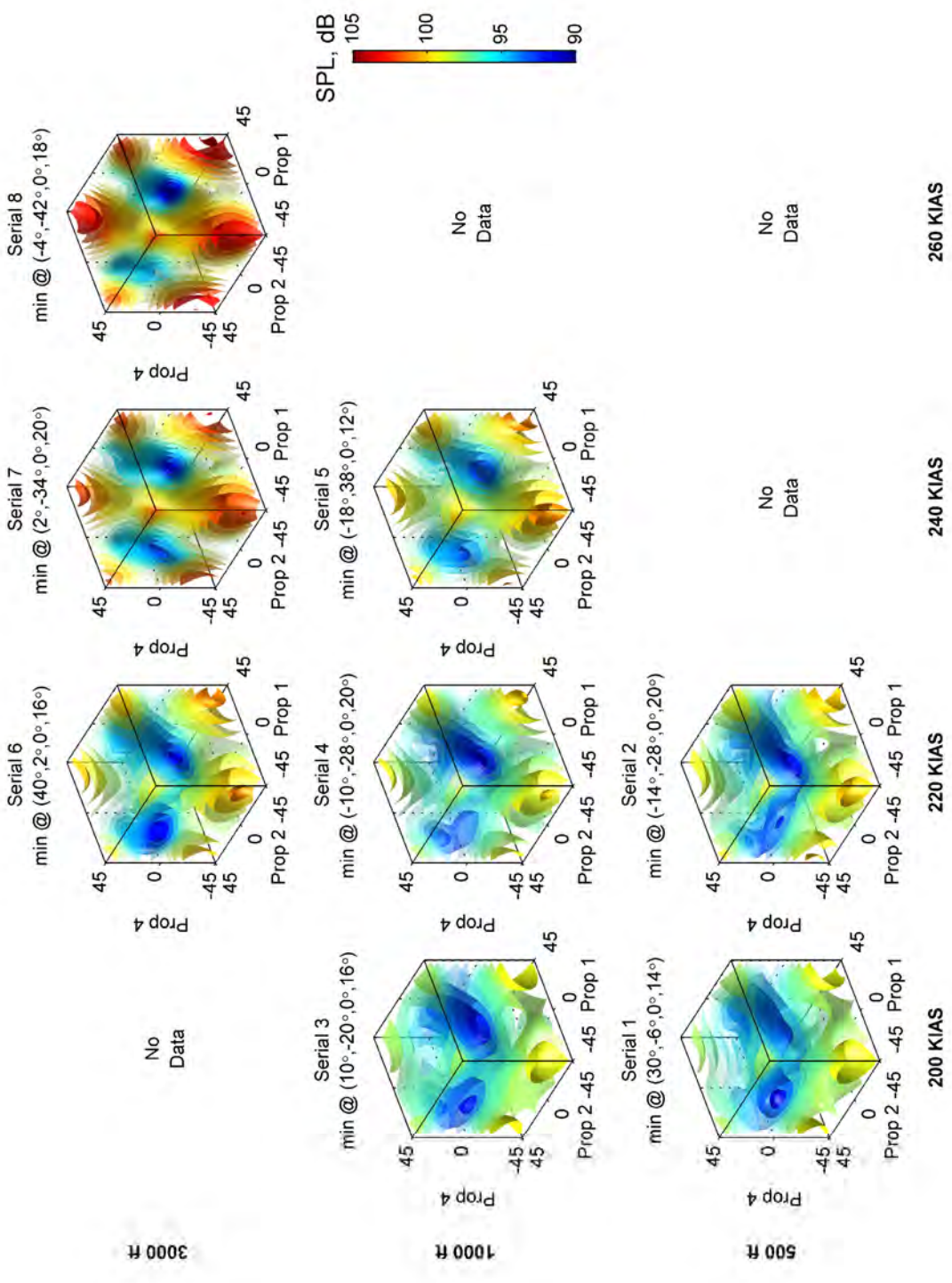

Figure 10.13 AP-3C predicted average over all microphones of the SPL at the BPF, Serials 1-8.

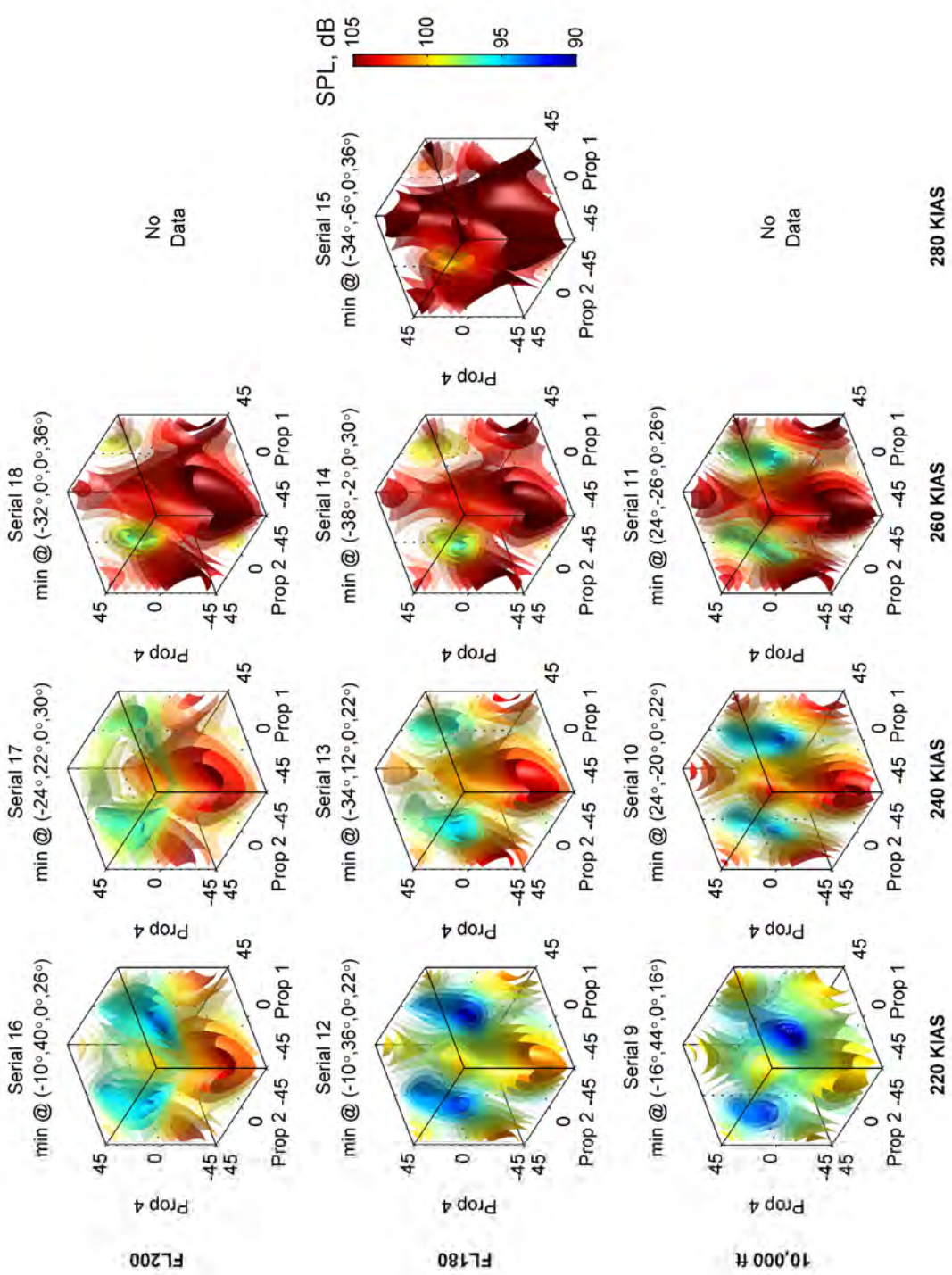

Figure 10.14 AP-3C predicted average over all microphones of the SPL at the BPF, Serials 9-18.

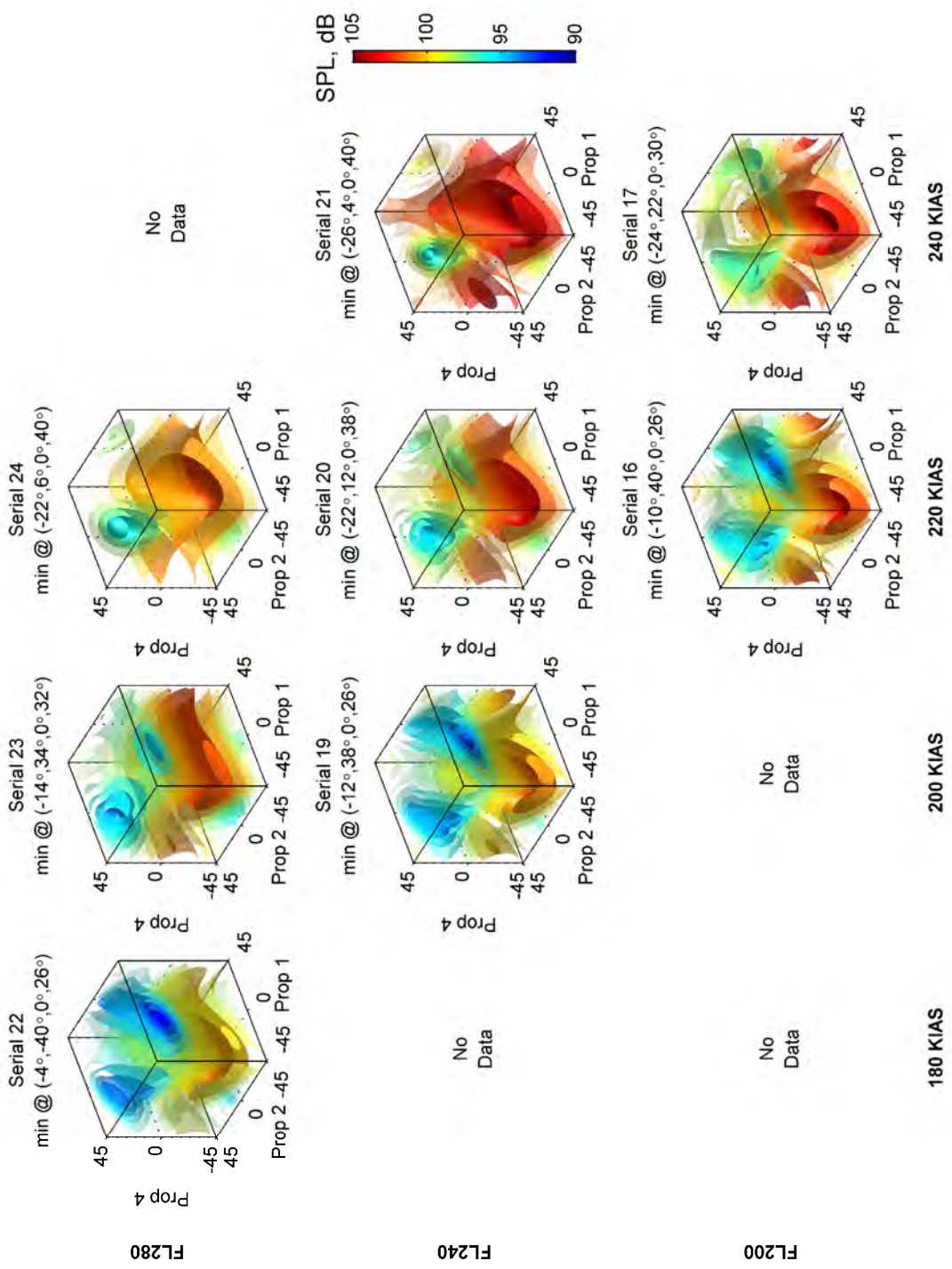

Figure 10.15 AP-3C predicted average over all microphones of the SPL at the BPF, Serials 16-24.

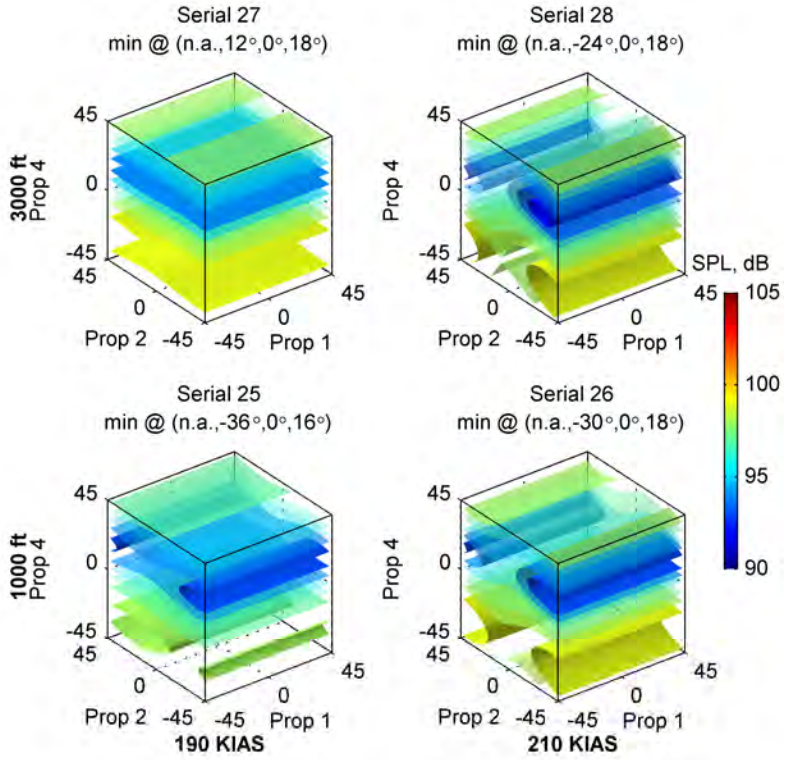

Figure 10.16 AP-3C predicted average over all microphones of the SPL at the BPF, Serials 25-28 (three-engine serials).

Table 10.2 AP-3C optimum synchrophase angles and predicted effects.

Serial	Optimum Synchrophase Angles	Reduction in average SPL at BPF from the default angle set (dB)	Reduction in average SPL at BPF from the worst-case angle set (dB)
1	(30°,−6°,0°,14°)	1.4	8.5
2	(−14°,−28°,0°,20°)	2.1	10.1
3	(10°,−20°,0°,16°)	1.3	9.0
4	(−10°,−28°,0°,20°)	2.5	10.2
5	(−18°,−38°,0°,12°)	1.7	9.6
6	(40°,2°,0°,16°)	0.4	10.1
7	(2°,−34°,0°,20°)	2.7	11.5
8	(−4°,−42°,0°,18°)	5.7	13.7
9	(−16°,44°,0°,16°)	3.2	10.8
10	(24°,−20°,0°,22°)	4.6	12.5
11	(24°,−26°,0°,26°)	3.6	11.4
12	(−10°,36°,0°,22°)	2.9	10.5
13	(−34°,12°,0°,22°)	2.0	9.3
14	(−38°,−2°,0°,30°)	3.6	9.5
15	(−34°,−6°,0°,36°)	3.5	8.8
16	(−10°,40°,0°,26°)	3.2	10.2
17	(−24°,22°,0°,30°)	3.4	9.2
18	(−32°,0°,0°,36°)	4.9	10.1
19	(−12°,38°,0°,26°)	4.2	10.3
20	(−22°,12°,0°,38°)	4.8	9.6
21	(−26°,4°,0°,40°)	6.3	10.1
22	(−4°,−40°,0°,26°)	6.5	10.9
23	(−14°,34°,0°,32°)	5.3	9.7
24	(−22°,6°,0°,40°)	5.4	7.7
25	(n.a.,−36°,0°,16°)	1.2	5.6
26	(n.a.,−30°,0°,18°)	2.3	7.4
27	(n.a.,12°,0°,18°)	0.4	5.9
28	(n.a.,−24°,0°,18°)	2.9	8.1

10.2.3. Candidate Synchrophase Angle Sets

In the absence of an adaptive control system, the existing AP-3C synchrophaser can only be configured with a fixed set of synchrophase angles for each master propeller setting. To realise a relatively small set of synchrophase angles that could be expected to be applied in practice, the many different sets of optimum angles found in §10.2.2 must be reduced down to just a few candidates. Based on the observations from §10.2.2, the most obvious way to do this is to average the results over different altitude ranges, and compare the effects.

The predicted average sound pressure levels at the BPF when averaged over the groups shown in Table 10.3 for the two most promising optimisation criteria (the lowest average over all microphones, and the lowest average over the seat and table microphones) are shown in Tables 10.4 and 10.5 respectively. The relative reductions from the averages at the default synchrophase angles are shown in Tables 10.6 and 10.7 respectively.

Generally, it can be seen that compromises must be made:

a) Averaging the high-altitude results gives a good outcome at the high altitudes (4.7 dB reduction in average over all microphones), but this comes with a significant cost at the low altitudes (−2.7 dB).
b) Averaging the mid-altitude results gives a slightly lower reduction at the mid-to-high altitudes (3.0 to 3.7 dB), but still has a cost at the low altitudes (−1.5 dB).
c) Averaging the low-altitude results gives a small reduction (1.3 dB) at the low altitudes (i.e., the default angles already work reasonably well at these altitudes), and no benefit at the mid-to-high altitudes (−2.2 to 0.0 dB).
d) Averaging over all altitudes for a good all-round result produces a more moderate benefit (2.1 dB), and because there are more mid-to-high altitude serials than low-altitude serials, the results are skewed to providing a better outcome above 10,000 ft than below.
e) Averging over all microphones produces a better outcome than averaging over just the seat and table microphones; i.e., the additional benefit to be had at the seat locations in the latter case is outweighed by the cost paid at the other locations. For example, at the high-altitudes, the additional reduction in the average SPL of the seat and table microphones is 1.6 dB, but the average SPL of all microphones increases by 3.0 dB.

Possibly the best non-adaptive outcome will be achieved if two sets of synchrophase angles are recommended: (−4°,−36°,0°,18°) for low-altitude flight (e.g., anti-submarine warfare, search and rescue, etc.), and (−24°,10°,0°,38°) for high-altitude flight (e.g., high-altitude surveillance). The synchrophaser could then be configured with one set of angles when Propeller 2 is the master and another set when Propeller 3 is the master. The more appropriate set of angles could then be chosen as required. The alternative is to only specify one set of angles (−34°,4°,0°,30°) with a lower overall benefit and more of a bias towards the mid-to-high altitudes than the current default angles. These two options are listed in Table 10.8. The predicted effects of the recommended synchrophase angle sets are shown in Figures 10.17 to 10.19.

It should be noted that these recommendations do not account for any possible aircraft-to-aircraft differences that may exist within the AP-3C fleet. Some differences were found between the two C-130J-30. The possible reasons for these are discussed in §10.3.

Table 10.3 AP-3C altitude groups used for candidate synchrophase angle sets.

Group	Description	Serials	Altitudes
a	High-altitude compromise	19–24	FL240 – FL280
b	Mid-altitude compromise	12–18	FL180 – FL200
c	Low-altitude compromise	1–8	500 ft – 3000 ft
d	All-altitude compromise	1–24	500 ft – FL280

Table 10.4 AP-3C predicted average SPL at the BPF when optimised for the lowest average over all microphones.

Set	Angles (P1, P2, P3, P4)	Predicted average SPL at BPF (dB)							
		High-alt.		Mid-alt.		Low-alt.		All altitudes	
		All mics.	Seat mics.	All mics.	Seat mics.	All mics.	Seat mics.	All mics.	Seat mics.
a	(−24°,10°,0°,38°)	94.7	94.1	97.4	97.0	96.1	95.2	96.4	95.6
b	(−36°,−2°,0°,32°)	95.7	94.0	96.7	96.9	94.9	94.8	95.8	95.5
c	(−4°,−36°,0°,18°)	99.4	96.0	101.9	99.1	92.1	90.8	98.9	96.1
d	(−34°,4°,0°,30°)	95.9	94.5	96.8	97.0	94.4	94.1	95.8	95.3
	default angles	99.4	98.5	99.7	99.4	93.4	93.0	97.9	97.3

Table 10.5 AP-3C predicted average SPL at the BPF when optimised for the lowest average over the seat and table microphones.

Set	Angles (P1, P2, P3, P4)	Predicted average SPL at BPF (dB)							
		High-alt.		Mid-alt.		Low-alt.		All altitudes	
		All mics.	Seat mics.	All mics.	Seat mics.	All mics.	Seat mics.	All mics.	Seat mics.
a	(22°,−32°,0°,28°)	97.7	92.5	98.9	95.4	96.4	95.1	97.6	94.8
b	(14°,−40°,0°,26°)	97.7	92.8	99.3	95.3	96.5	95.1	97.7	94.7
c	(2°,−28°,0°,12°)	101.2	97.7	103.2	100.8	93.1	90.2	100.4	97.6
d	(4°,−42°,0°,24°)	97.7	93.4	99.8	95.9	94.8	93.7	97.5	94.3
	default angles	99.4	98.5	99.7	99.4	93.4	93.0	97.9	97.3

Table 10.6 AP-3C predicted reduction in average SPL at the BPF from the default angle set case when optimised for the lowest average over all microphones.

Set	Angles (P1, P2, P3, P4)	Predicted reduction in the average SPL at BPF (dB)							
		High-alt.		Mid-alt.		Low-alt.		All altitudes	
		All mics.	Seat mics.	All mics.	Seat mics.	All mics.	Seat mics.	All mics.	Seat mics.
a	(−24°,10°,0°,38°)	4.7	4.4	2.3	2.4	−2.7	−2.2	1.5	1.7
b	(−36°,−2°,0°,32°)	3.7	4.5	3.0	2.5	−1.5	−1.8	2.1	1.8
c	(−4°,−36°,0°,18°)	0.0	2.5	−2.2	0.3	1.3	2.2	−1.0	1.2
d	(−34°,4°,0°,30°)	3.5	4.0	2.9	2.4	−1.0	−1.1	2.1	2.0

Table 10.7 AP-3C predicted reduction in average SPL at the BPF from the default angle set case when optimised for lowest average over the seat and table microphones.

Set	Angles (P1, P2, P3, P4)	Predicted reduction in the average SPL at BPF (dB)							
		High-alt.		Mid-alt.		Low-alt.		All altitudes	
		All mics.	Seat mics.	All mics.	Seat mics.	All mics.	Seat mics.	All mics.	Seat mics.
a	(22°,−32°,0°,28°)	1.7	6.0	0.8	4.0	−3.0	−2.1	−0.3	2.5
b	(14°,−40°,0°,26°)	1.7	5.7	0.4	4.1	−3.1	−2.1	0.2	2.6
c	(2°,−28°,0°,12°)	−1.8	0.8	−3.5	−1.4	0.3	2.8	−2.5	−0.3
d	(4°,−42°,0°,24°)	1.7	5.1	−0.1	3.5	−1.4	−0.7	0.4	3.0

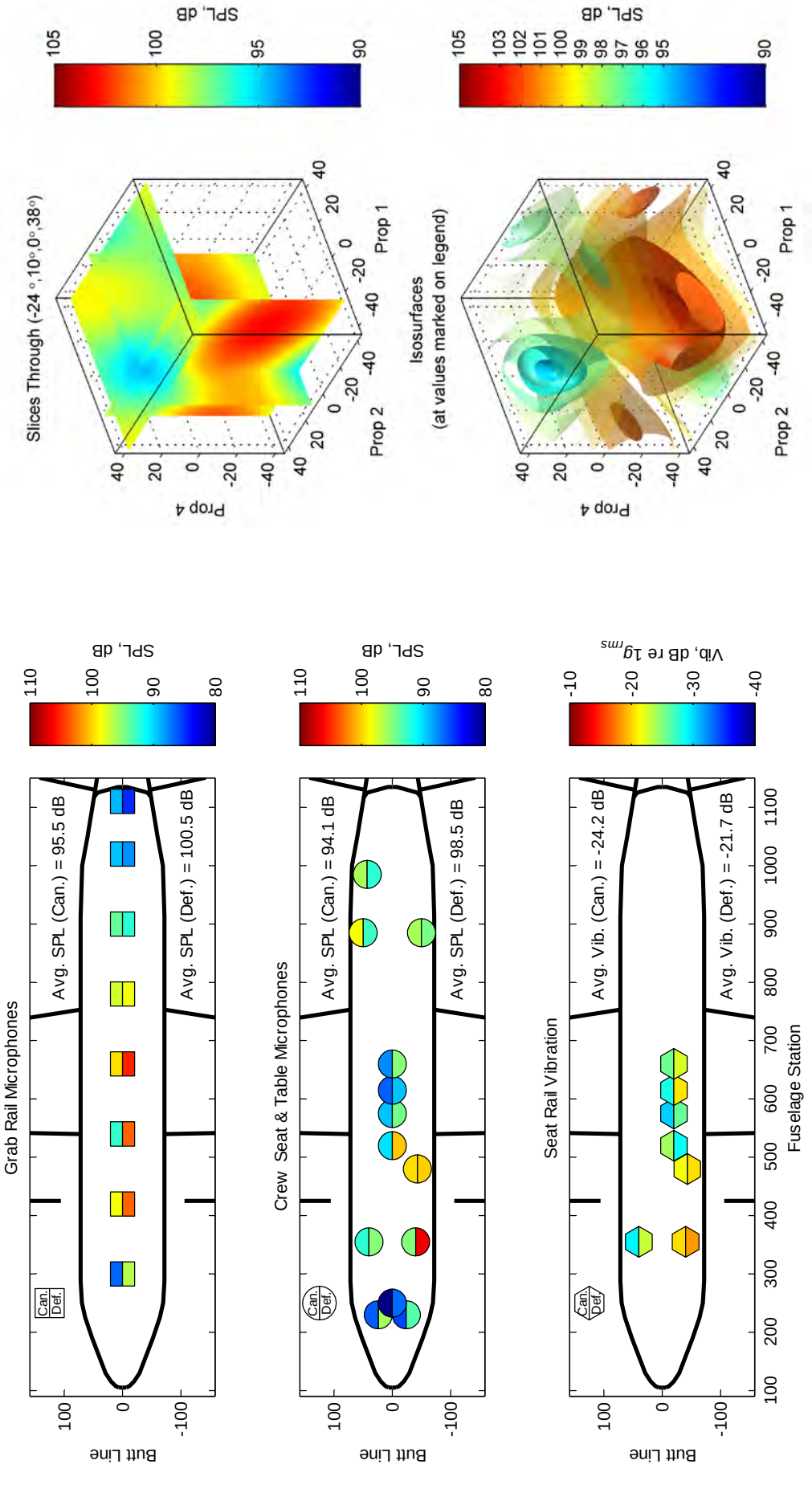

Figure 10.17 AP-3C average sensor levels at the BPF for the high-altitude compromise synchrophase angles (-24°,10°,0°,38°): predicted average sensor levels over the high-altitude serials (left), and predicted average over all microphones (right).

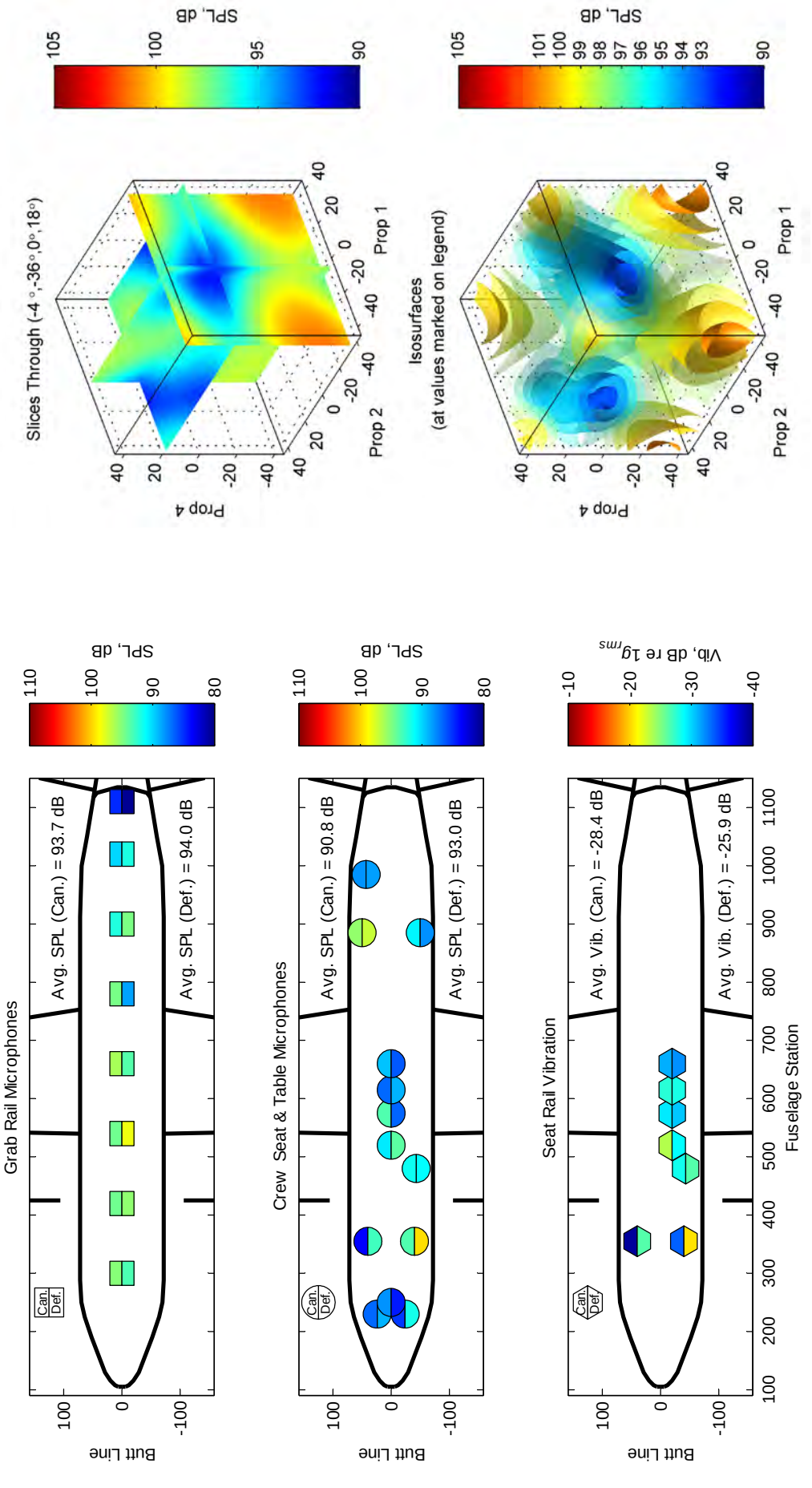

Figure 10.18 AP-3C average sensor levels at the BPF for the low-altitude compromise synchrophase angles (-4°,-36°,0°,18°): predicted average sensor levels over the low-altitude serials (left), and predicted average over all microphones (right).

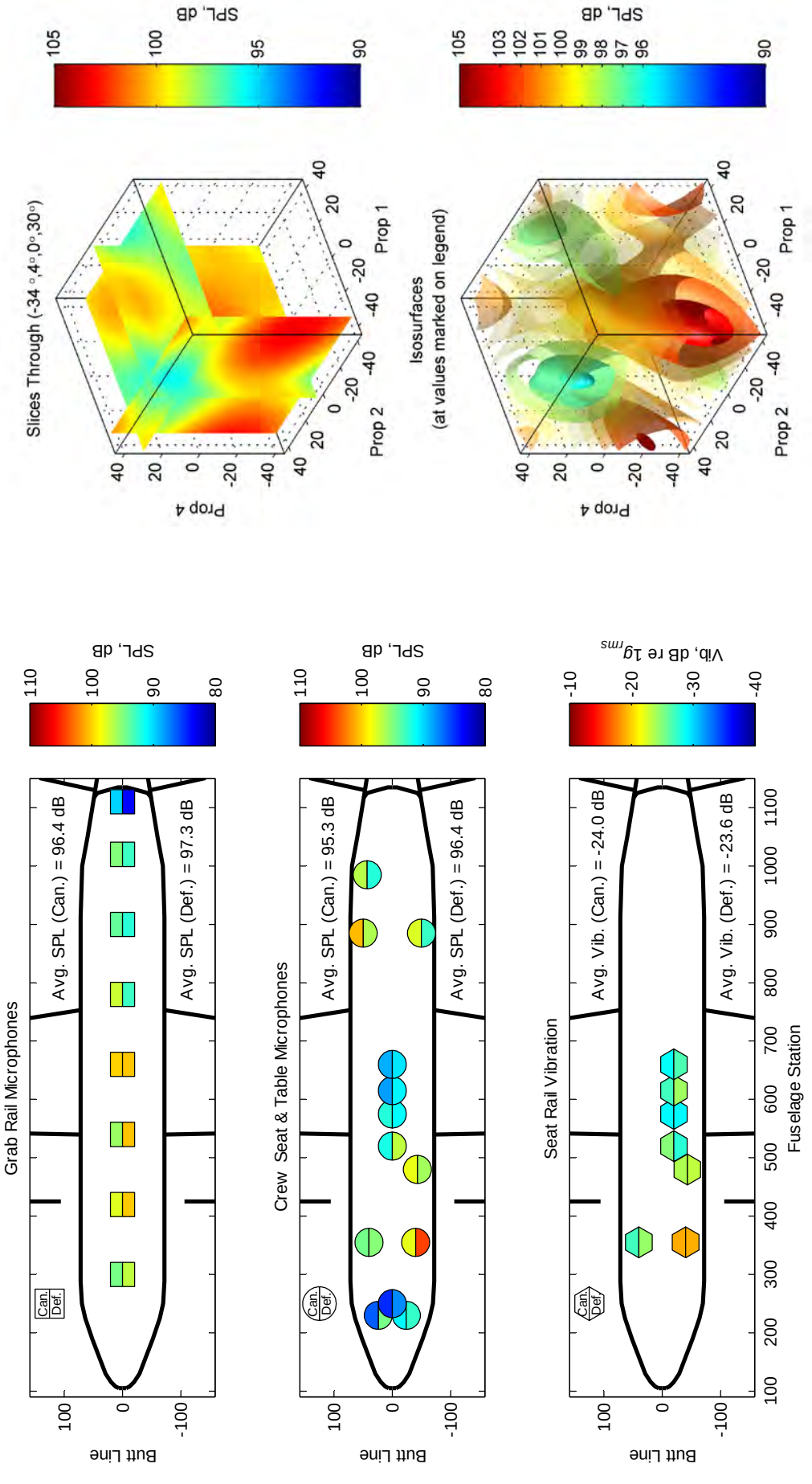

Figure 10.19 AP-3C average sensor levels at the BPF for the all-altitude compromise synchrophase angles (-34°,4°,0°,30°): predicted average sensor levels over all serials (left), and predicted average over all microphones (right).

Table 10.8 Recommended fixed synchrophase angle sets for the AP-3C synchrophaser.

Option	Description	Angles (P1, P2, P3, P4)	Average reduction in the average SPL over all mics. from def. sync. angles*
1	High-altitude set (Prop 3 master) Low-altitude set (Prop 2 master)	(−24°,10°,0°,38°) (32°,0°,36°,−36°)	4–5 dB at mid-to-high alt. 1 dB at low alt.
2	All-altitude set (Prop3 master) All-altitude set (Prop2 master)	(−34°,4°,0°,30°) (−38°,0°,−4°,24°)	2 dB

* Note that these are average reductions; i.e., the reductions will vary depending on the flight condition and the cabin location. Reductions at existing high SPL locations are likely to be more than these values.

10.3. C-130J-30 Synchrophase Angle Optimisation

The synchrophase angle optimisation results for the first C-130J-30 trial are presented in the same way as the AP-3C (§10.2): the effects of different optimisation criteria on the predicted noise and vibration levels are examined in §10.3.1; the effects of altitude and airspeed on the optimum synchrophase angles are examined in §10.3.2; and several new (fixed) candidate synchrophase angle sets for potential implementation using the existing synchrophaser are derived in §10.3.3.

The results from the second C-130J-30 trial are presented in the remaining three sections. First, in §10.3.4, the noise and vibration measurements for each candidate synchrophase angle set are compared with those from the default angle set. This is done to establish the relative performance of each set. Second, in §10.3.5, the measurements for one flight condition (Serial 5.3) are compared with two sets of predictions; one based on the signatures from the first trial, and one based on the signatures from the second trial. This is done in order to determine if there are significant differences in the signatures between the two aircraft. Last, in §10.3.6, a single optimisation search function using only the sensors in common between the two trials is derived for a single (nominally identical) flight condition from each trial (Serial 10). These are compared to highlight the potential effects of any signature differences between the two aircraft on the optimum synchrophase angles for those aircraft.

10.3.1. Effects of Different Optimisation Criteria (Trial 1)

Serial 10 (220 KCAS at FL240) was used for this part of the analysis because the propeller signatures for this serial were based on measurements from 21 sets of synchrophase angles, instead of only 7 sets for all the other serials. These signatures were expected to represent a less-biased fit to the data, and therefore provide more accurate predictions.

The optimisation criteria (cost functions) that were selected for the C-130J-30 are listed in Table 10.9. Note that Criterion 1 is the opposite of Criterion 2, and Criterion 5 is the opposite of Criterion 6. These were included to show the predicted ranges (maximum to minimum) in these respective cases.

Table 10.9 Optimisation criteria for the C-130J-30.

Criterion	Description
0	Default angles
1	Highest average over all microphones of the SPL at the BPF
2	Lowest average over all microphones of the SPL at the BPF
3	Lowest average over the main cabin microphones of the SPL at the BPF
4	Lowest average over the flight deck microphones of the SPL at the BPF
5	Highest average over the cabin floor accelerometers of the vibration at the BPF
6	Lowest average over the cabin floor accelerometers of the vibration at the BPF

The effects of these criteria on the noise and vibration levels at the BPF for Serial 10 are shown in Figures 10.20 to 10.26. The left side of each figure shows the BPF levels at each sensor location, and the right side shows two different 3-D visualisations (slices and isosurfaces) of the cost function for that particular case. Note that the axes of the 3-D plots are the synchrophase angles of the three slave propellers, and the rotational symmetry of the synchrophase angles causes the cost functions to wrap around at the limits of each axis (i.e., 0° ↔ +60°). The sensor maximum, minimum and average values at the BPF for all serials are also tabled in Appendix I.

The main features to note from the figures are as follows:

a) The sensor amplitudes for the default synchrophase angles (Figure 10.20) are close to the highest predicted levels using Criteria 1 and 5 (Figures 10.21 & 10.25), and therefore indicate that there is significant scope for improvement at this flight condition.

b) The results for Criterion 2 (Figure 10.22) and Criterion 3 (Figure 10.23) are the same. This is not surprising given that there were only 3 microphones on the flight deck and 30 in the main cabin. In both cases the average sound pressure levels and floor vibration levels at the BPF are predicted to fall by 7.2 dB and 0.18 g_{rms} (equivalent to 7.1 dB) respectively, over the default angle case. The most significant reduction in the sound pressure level at the BPF occurs in the front half of the main cabin along both sides of the fuselage. This comes at the cost of a small increase in the sound pressure level at the BPF along the centreline in this region. The SPL contours indicate that the results near the global minimum are most sensitive to the synchrophase angle of Propeller 3, and least sensitive to the synchrophase angle of Propeller 1. This generally reflects the relative signature amplitudes of these propellers in the main cabin area (Appendix G).

c) The optimum synchrophase angles for Criterion 4 (Figure 10.24) produce the lowest average sound pressure levels on the flight-deck, but less of an improvement in the main cabin. Also note that the presence of a relatively high-amplitude tonal noise component on the flight deck from another source (75 to 80 dB at 196 Hz, §7.2.1) places an effective limit on how much benefit can be achieved in this region. It can also be seen that the results near the global minimum are more sensitive to the synchrophase angles of Propellers 1 and 4 than Propeller 3, which is very different to the situation in the main cabin, as described previously.

d) The optimum synchrophase angles for Criterion 6 (Figure 10.26) produce a small (0.9 dB) improvement in the average floor vibration at the BPF at the expense of a larger (1.9 dB) increase in the average sound pressure level at the BPF; i.e., it appears better to optimise for sound pressure than floor vibration. However, this result is based on the measurements from only 6 accelerometers and a different outcome might have been achieved if more accelerometers were available in this particular serial. The floor vibration results near the global minimum are most sensitive to the synchrophase angle of Propeller 3 and least sensitive to the synchrophase angle of Propeller 1.

e) There is a degree of asymmetry across the mid-line of the fuselage in all the results; i.e., the sensor levels on one side do not mirror those on the other side exactly. This is could be caused by the propellers rotating in the same direction on both sides of the aircraft (§2.1).

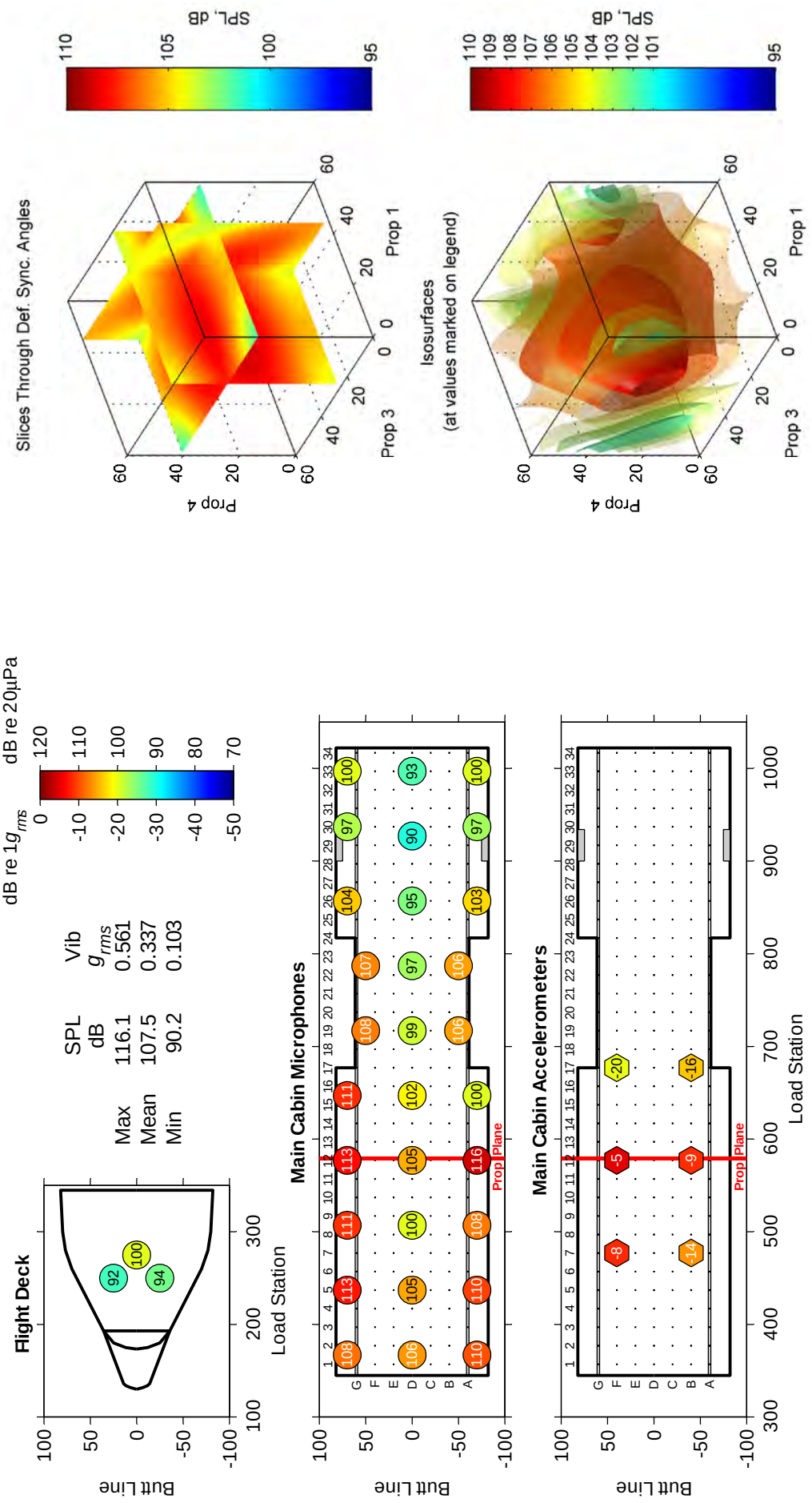

Figure 10.20 C-130J-30 sensor levels at the BPF for the default synchrophase angles, Serial 10, Trial 1: measured individual levels (left), and the predicted average over all microphones (right).

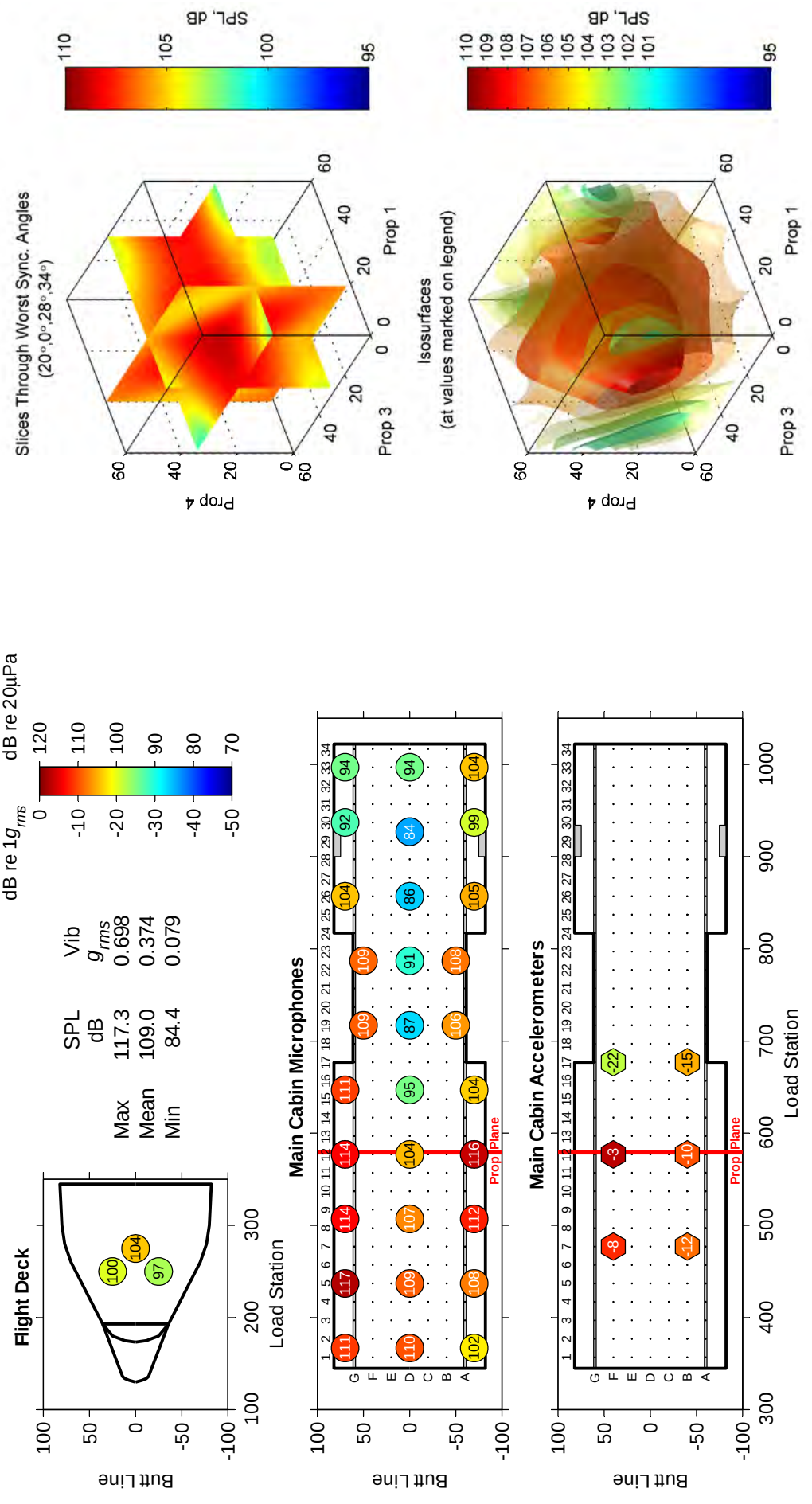

Figure 10.21 C-130J-30 sensor levels at the BPF for the synchrophase angles giving the highest average over all microphones (20°,0°,28°,34°), Serial 10, Trial 1: predicted individual levels (left), and the predicted average over all microphones (right).

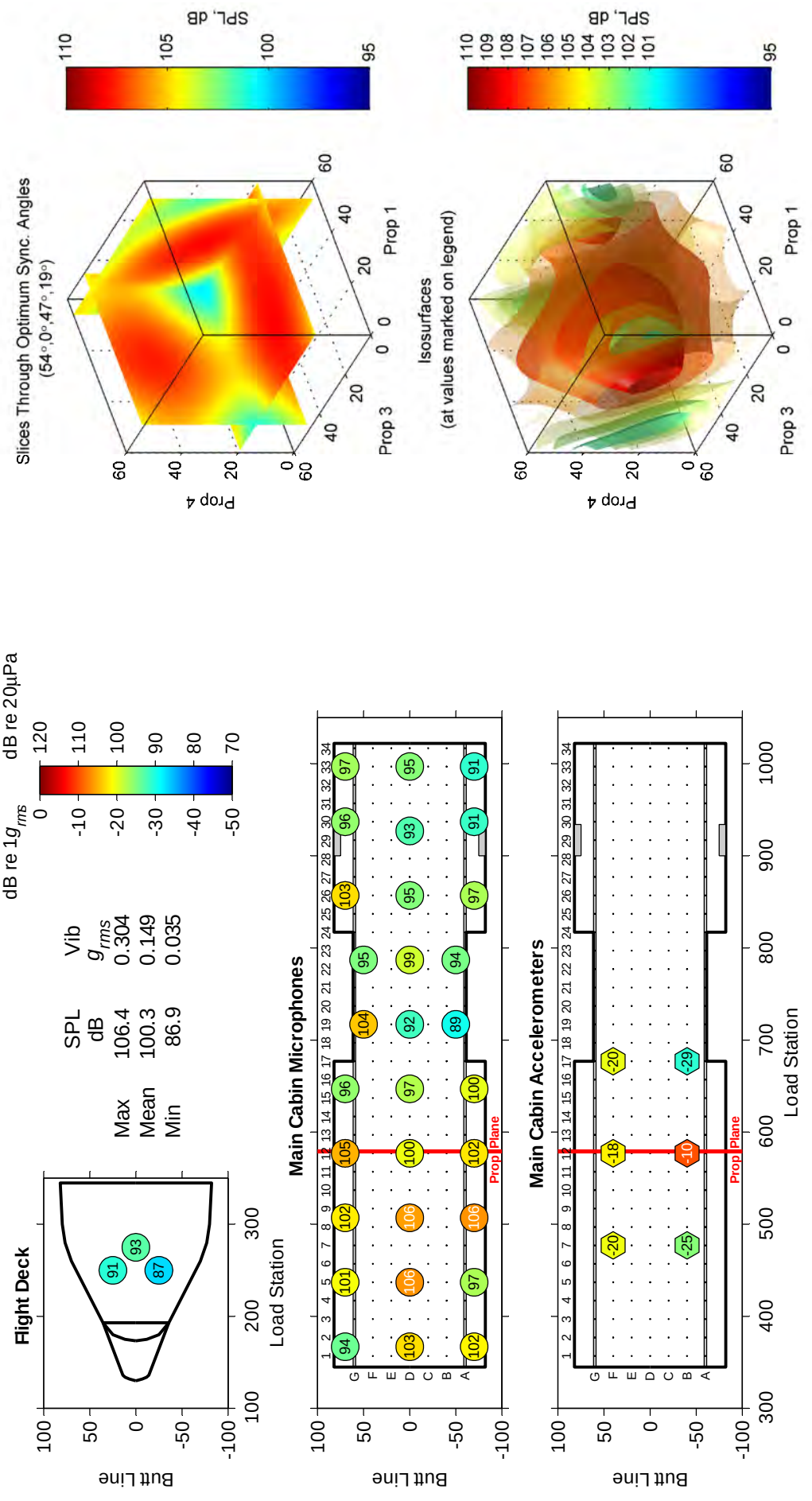

Figure 10.22 C-130J-30 sensor levels at the BPF for the synchrophase angles giving the lowest average over all microphones (54°,0°,47°,19°), Serial 10, Trial 1: predicted individual levels (left), and the predicted average over all microphones (right).

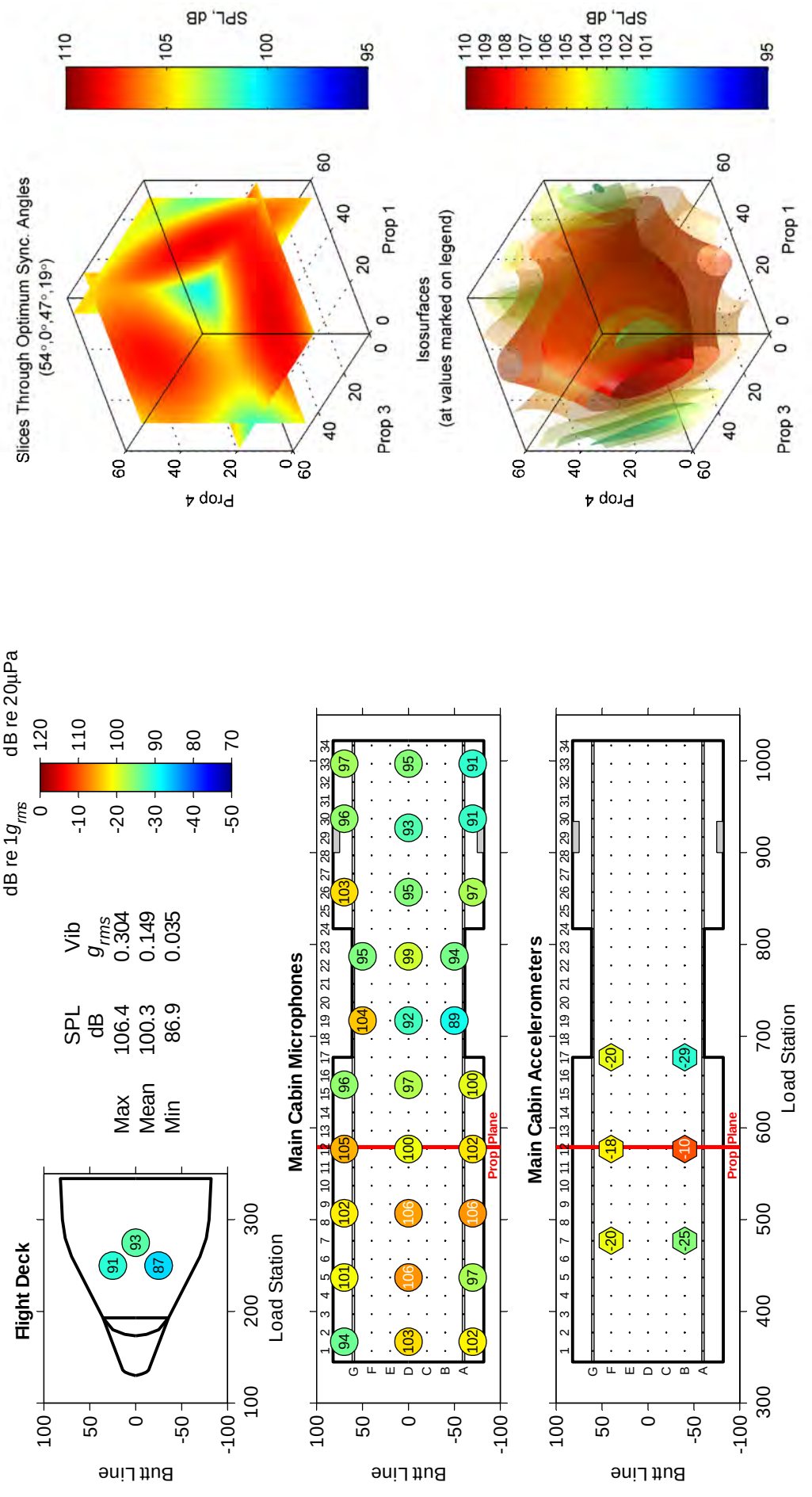

Figure 10.23 C-130J-30 sensor levels at the BPF for the synchrophase angles giving the lowest average over the main cabin microphones (54°,0°,47°,19°), Serial 10, Trial 1: predicted individual levels (left), and the predicted average over the main cabin microphones (right).

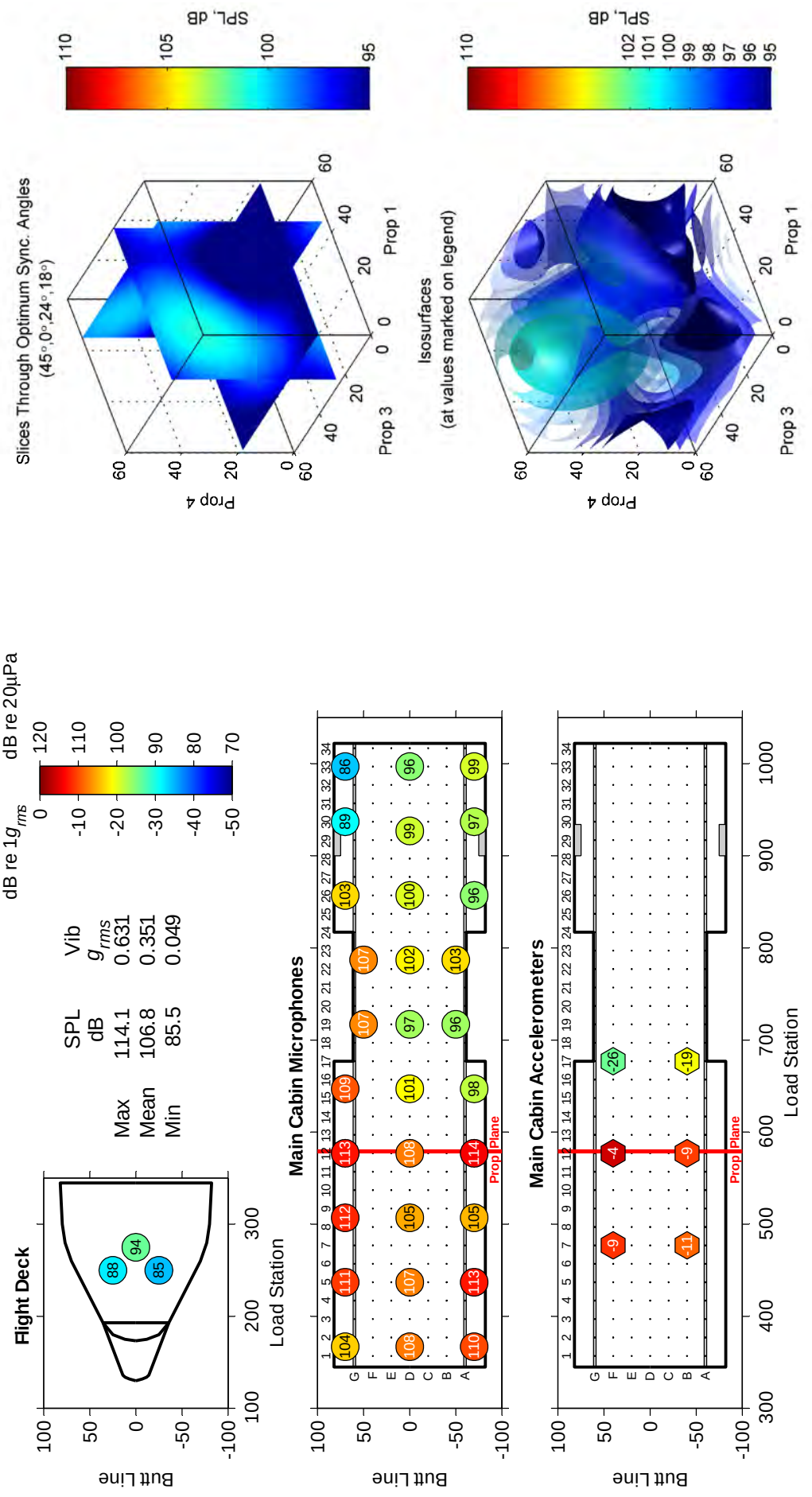

Figure 10.24 C-130J-30 sensor levels at the BPF for the synchrophase angles giving the lowest average over the flight deck microphones (45°,0°,24°,18°), Serial 10, Trial 1: predicted individual levels (left), and the predicted average over the flight deck microphones (right).

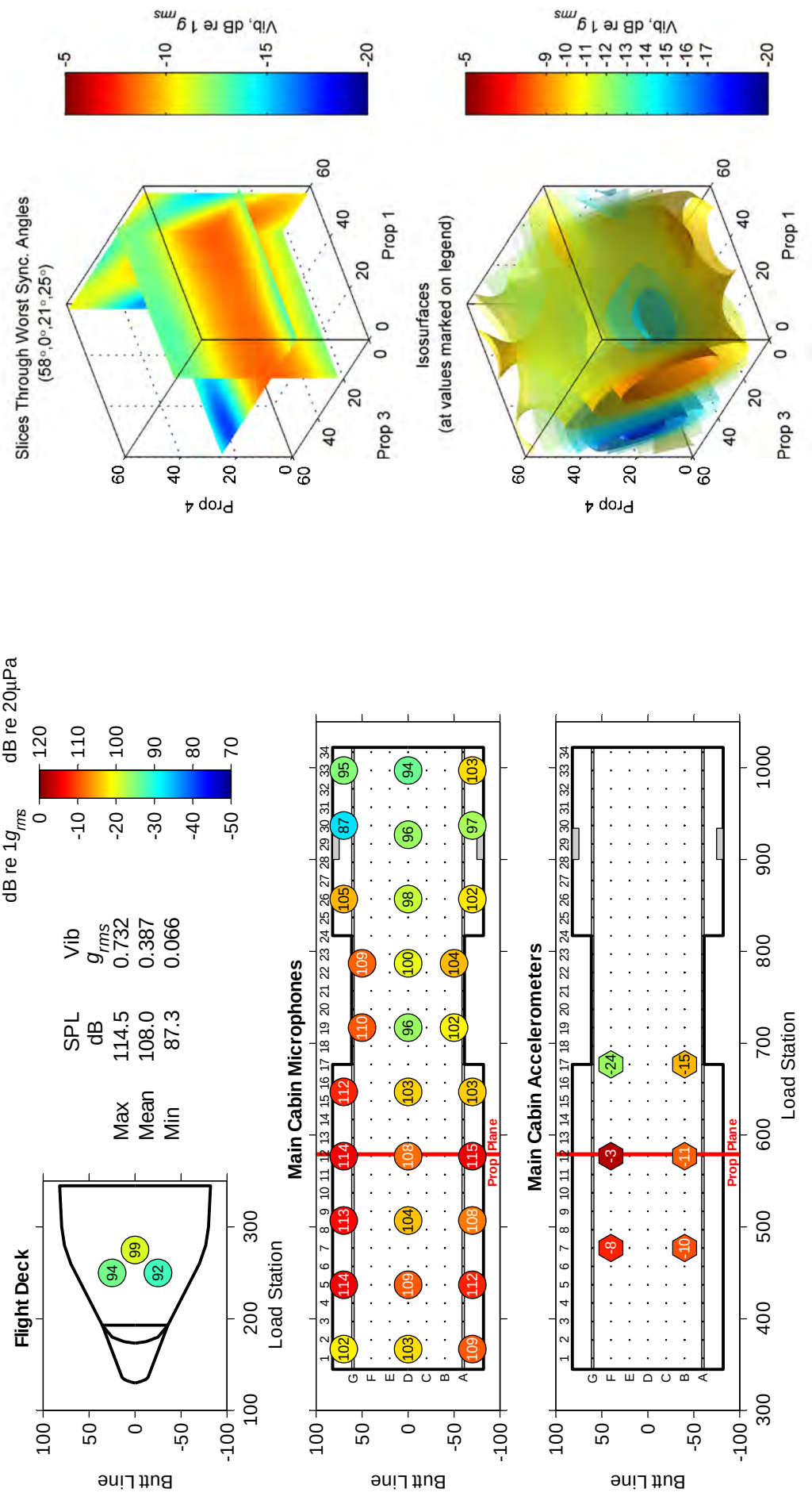

Figure 10.25 C-130J-30 sensor levels at the BPF for the synchrophase angles giving the highest average over the floor accelerometers (58°,0°,21°,25°), Serial 10, Trial 1: predicted individual levels (left), and the predicted average over the floor accelerometers (right).

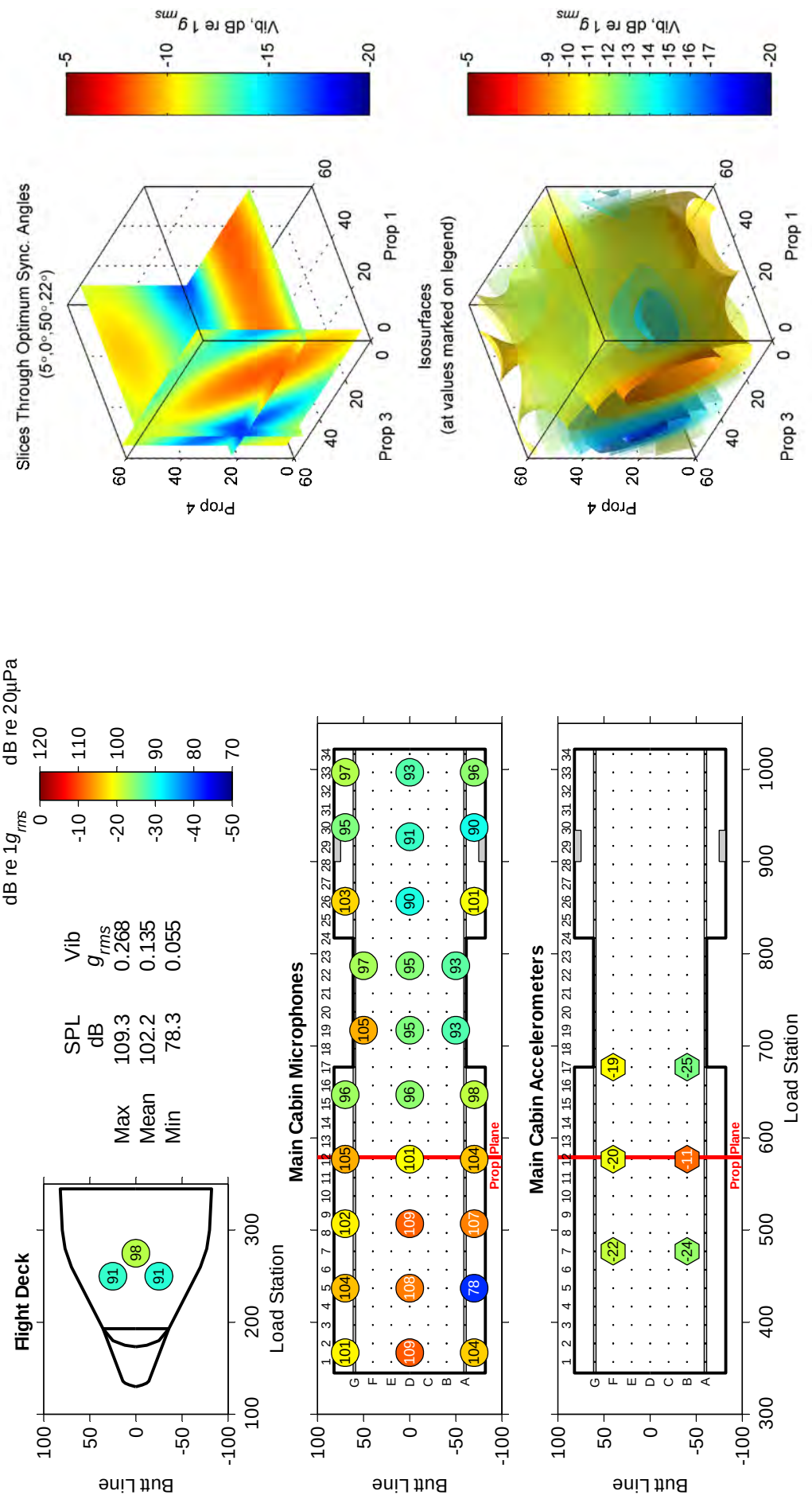

Figure 10.26 C-130J-30 sensor levels at the BPF for the synchrophase angles giving the lowest average over the floor accelerometers (5°,0°,50°,22°), Serial 10, Trial 1: predicted individual levels (left), and the predicted average over the floor accelerometers (right).

10.3.2. Effects of Altitude and Airspeed (Trial 1)

To illustrate the effects of altitude and airspeed on the optimum synchrophase angles, two typical cost functions (the average over all floor accelerometers of the vibration at the BPF for Flights 1 and 2, and the average over all microphones of the SPL at the BPF for Flight 3; i.e., Criteria 6 & 2 respectively from Table 10.9) were calculated for each altitude-airspeed combination. The cost function ranges, and the values at the default synchrophase angles, are shown for each flight condition serial in Figures 10.27 and 10.28. The individual cost functions for each flight are shown in Figures 10.29 to 10.34. The optimum synchrophase angles and the predicted effects on the cost function are listed in Tables 10.10 and 10.11.

The main features to note are very similar to those observed for the AP-3C (§10.2.2):

a) The default synchrophase angles produce values towards the upper ends of the predicted ranges of the selected cost functions (Figures Figure 10.27 and Figure 10.28) showing that there is significant scope for improvement using these optimisation criteria.

b) The optimum synchrophase angles (Table 10.10) vary significantly over the range of flight conditions considered. Hence, a single set of synchrophase angles cannot produce the best results for all conditions.

c) Synchrophasing has a significant effect on both cost functions. It is predicted that the average vibration over all accelerometers (at the BPF) can change by an amount between 7.1 dB and 10.7 dB for the serials in Flights 1 and 2, and the average SPL over all microphones (at the BPF) can change by an amount between 4.6 dB and 8.7 dB for the serials in Flight 3 (Table 10.11). The slightly lower amounts for the variation in the average SPL probably reflect the increased number, and wider spatial distribution, of the microphones compared to the floor accelerometers; i.e., minimising the floor vibration does not necessarily minimise the average SPL within the cabin, and hence a lower average floor vibration can be achieved at the expense of a slightly increased cabin average SPL.

d) There is relatively good agreement between the floor vibration results for Flights 1 and 2. These were conducted on different days, so there appears to be good flight-to-flight repeatability in the same aircraft. Any differences can be attributed to the different positions of the cargo (i.e., different floor loading), and minor variations in the flight conditions between the two flights, as the floor accelerometers were not changed or moved.

e) The variations in the optimum synchrophase angles, and in the shapes of the average vibration and SPL contours, are relatively smooth and gradual. This shows that the synchrophase angles should be readily amenable to some form of adaptive control system. This also implies that, in the absence of an adaptive control system, a single set of synchrophase angles will probably still achieve a relatively good result over a limited range of altitudes and airspeeds.

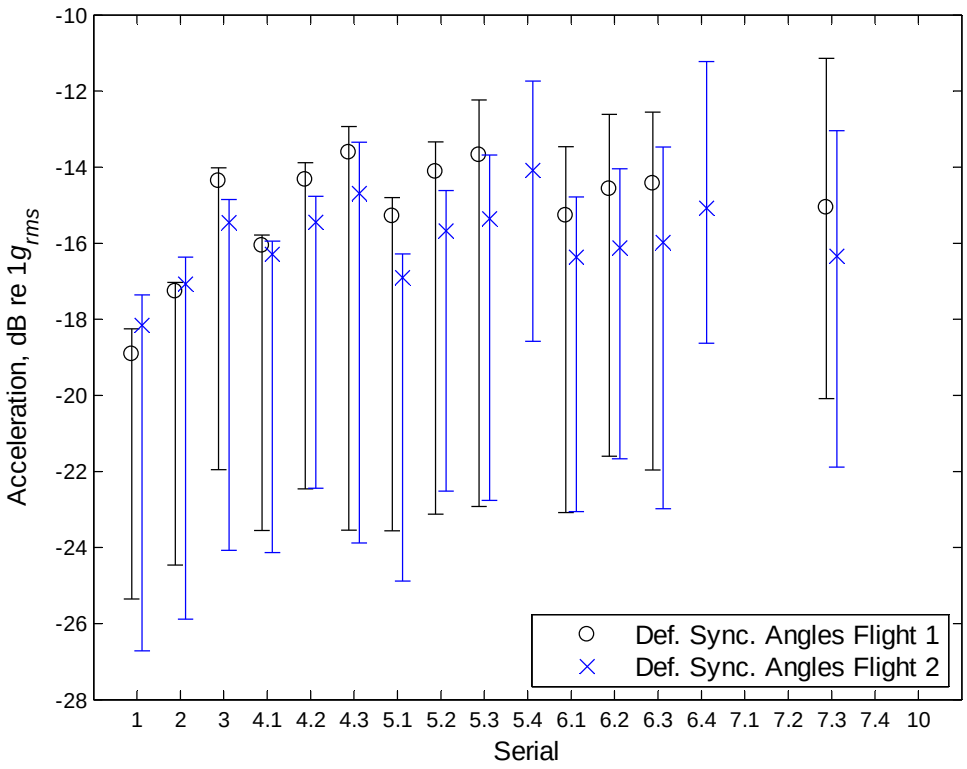

Figure 10.27 C-130J-30 predicted cost function range (average over all floor accelerometers of the vibration at the BPF) for each flight condition serial in Flights 1 and 2, Trial 1.

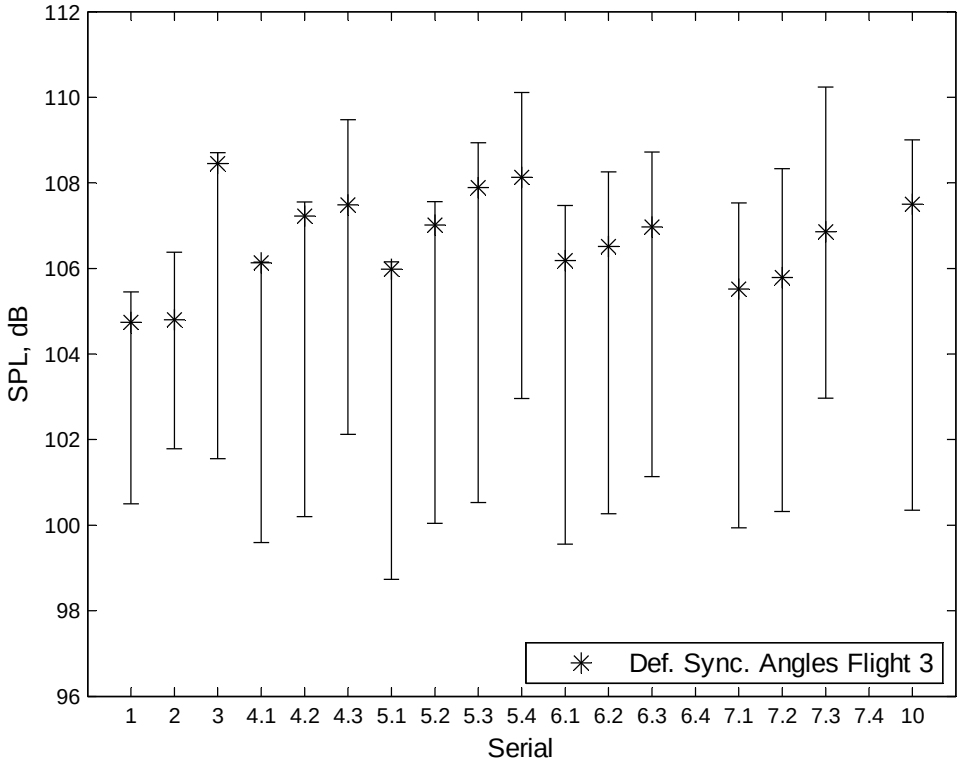

Figure 10.28 C-130J-30 predicted cost function range (average over all microphones of the SPL at the BPF) for each flight condition serial in Flight 3, Trial 1.

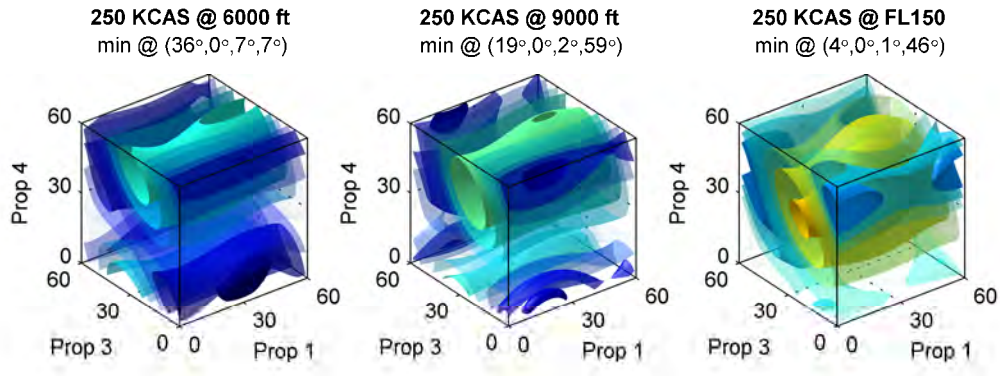

Figure 10.29 C-130J-30 predicted average over all floor accelerometers of the vibration at the BPF, Serials 1–3, Flight 1, Trial 1.

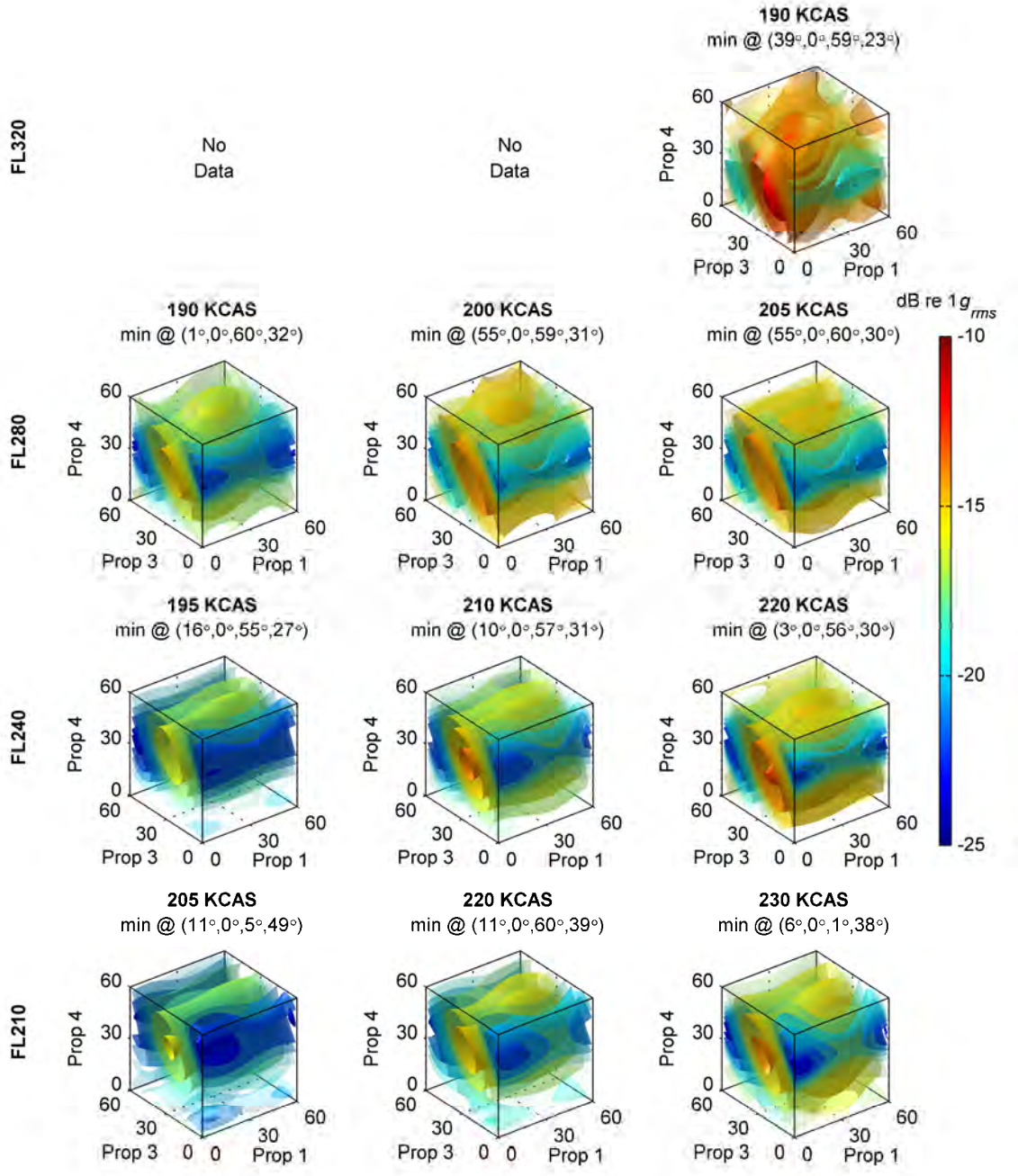

Figure 10.30 C-130J-30 predicted average over all floor accelerometers of the vibration at the BPF, Serials 4.1–4.3, 5.1–5.3, 6.1–6.3, & 7.1–7.3, Flight 1, Trial 1.

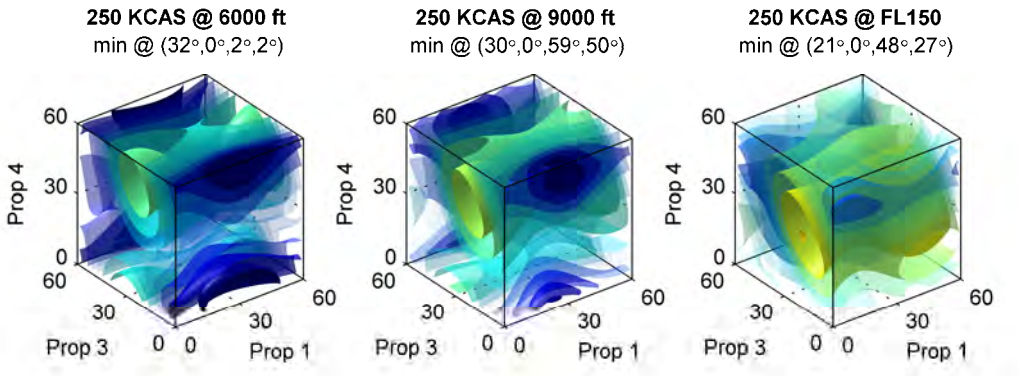

Figure 10.31 C-130J-30 predicted average over all floor accelerometers of the vibration at the BPF, Serials 1–3, Flight 2, Trial 1.

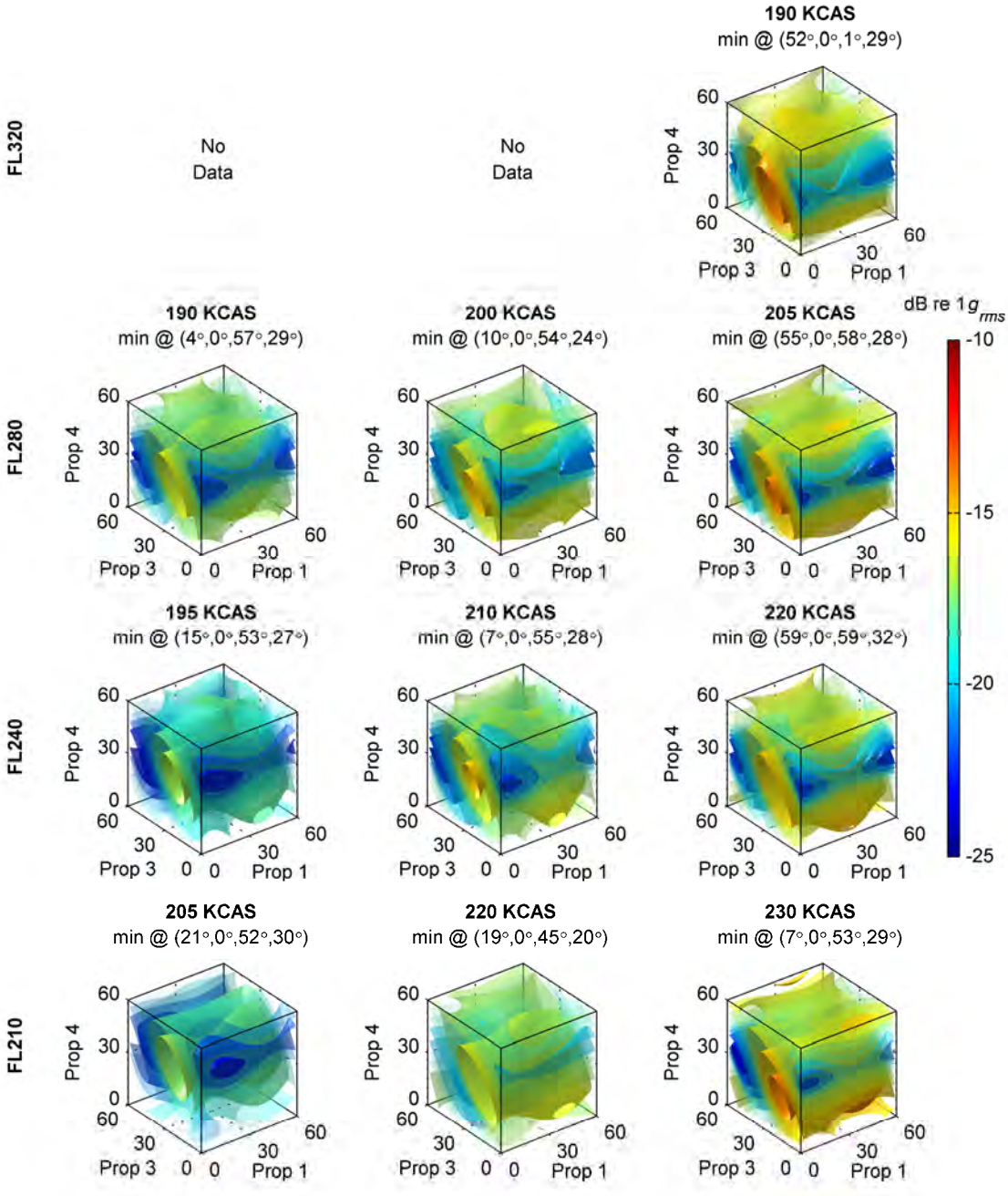

Figure 10.32 C-130J-30 predicted average over all floor accelerometers of the vibration at the BPF, Serials 4.1–4.3, 5.1–5.3, 6.1–6.3, & 7.1–7.3, Flight 2, Trial 1.

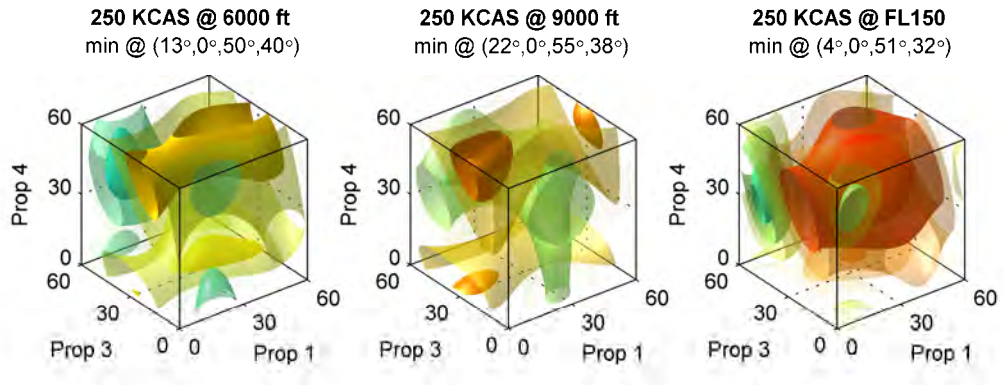

Figure 10.33 C-130J-30 predicted average over all microphones of the SPL at the BPF, Serials 1–3, Flight 3, Trial 1.

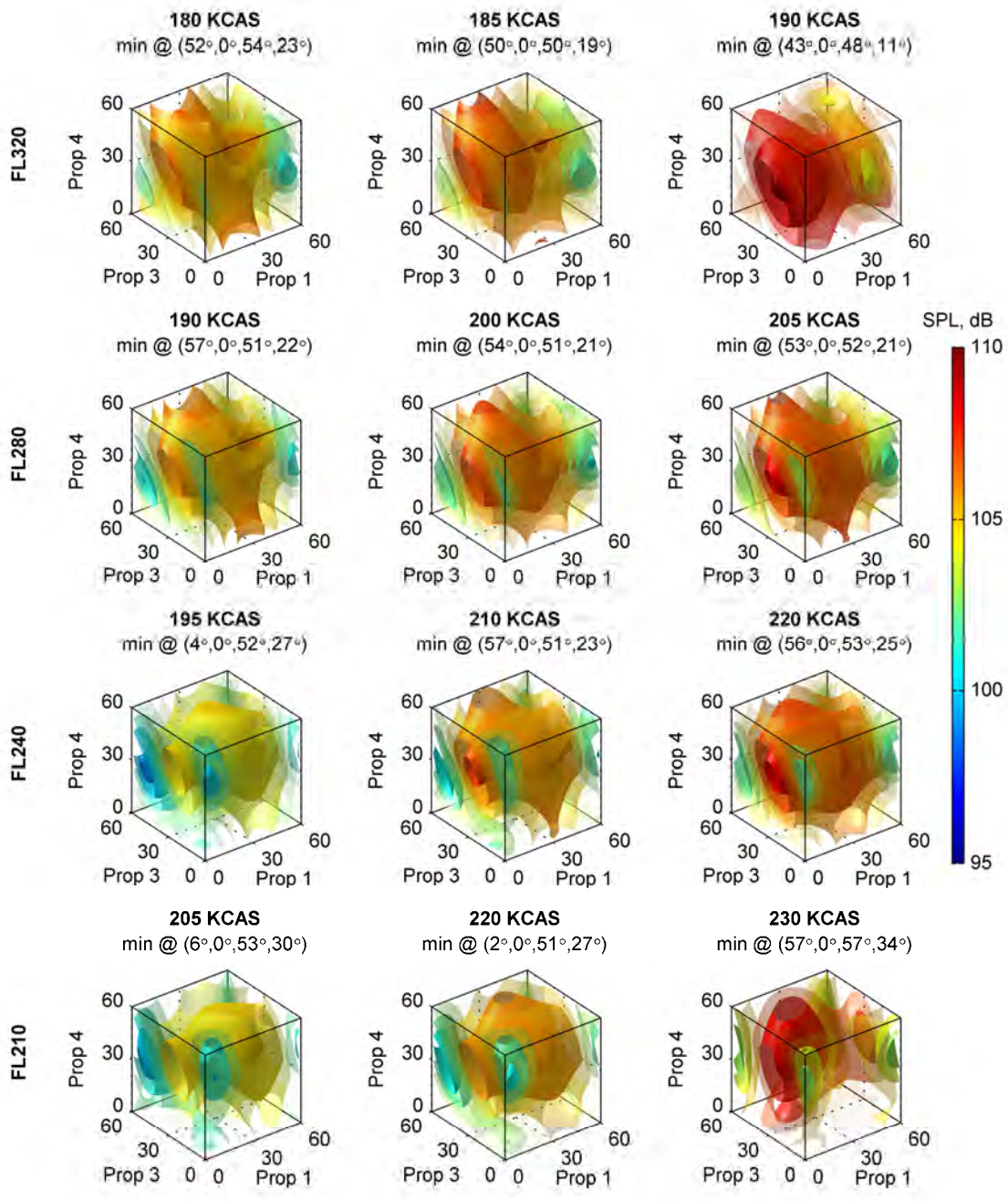

Figure 10.34 C-130J-30 predicted average over all microphones of the SPL at the BPF, Serials 4.1–4.3, 5.1–5.3, 6.1–6.3, & 7.1–7.3, Flight 3, Trial 1.

Table 10.10 C-130J-30 optimum synchrophase angles, Trial 1.

	Flight 1	**Flight 2**	**Flight 3**
Serial	**Synchrophase angles for lowest avg. floor vib. @ BPF**	**Synchrophase angles for lowest avg. floor vib. @ BPF**	**Synchrophase angles for lowest avg. SPL @ BPF**
1	(36°,0°,7°,7°)	(32°,0°,2°,2°)	(13°,0°,50°,40°)
2	(19°,0°,2°,59°)	(30°,0°,59°,50°)	(22°,0°,55°,38°)
3	(4°,0°,1°,46°)	(21°,0°,48°,27°)	(4°,0°,51°,32°)
4.1	(11°,0°,5°,49°)	(21°,0°,52°,30°)	(6°,0°,53°,30°)
4.2	(11°,0°,60°,39°)	(19°,0°,45°,20°)	(2°,0°,51°,27°)
4.3	(6°,0°,1°,38°)	(7°,0°,53°,29°)	(57°,0°,57°,34°)
5.1	(16°,0°,55°,27°)	(15°,0°,53°,27°)	(4°,0°,52°,27°)
5.2	(10°,0°,57°,31°)	(7°,0°,55°,28°)	(57°,0°,51°,23°)
5.3	(3°,0°,56°,30°)	(59°,0°,59°,32°)	(56°,0°,53°,25°)
5.4	Not flown	(57°,0°,59°,31°)	(50°,0°,47°,17°)
6.1	(1°,0°,60°,32°)	(4°,0°,57°,29°)	(57°,0°,51°,22°)
6.2	(55°,0°,59°,31°)	(10°,0°,54°,24°)	(54°,0°,51°,21°)
6.3	(55°,0°,60°,30°)	(55°,0°,58°,28°)	(53°,0°,52°,21°)
6.4	Not flown	(4°,0°,46°,12°)	Not flown
7.1	Not flown	Not flown	(52°,0°,54°,23°)
7.2	Not flown	Not flown	(50°,0°,50°,19°)
7.3	(39°,0°,59°,23°)	(52°,0°,1°,29°)	(43°,0°,48°,11°)
7.4	Not flown	Not flown	Not flown
10.0	Not flown	Not flown	(54°,0°,47°,19°)

Table 10.11 C-130J-30 predicted reductions in average BPF levels, Trial 1.

	Flight 1		**Flight 2**		**Flight 3**	
	Reduction in Avg. Vibration of all 18 Floor Accelerometers.		**Reduction in Avg. Vibration of all 18 Floor Accelerometers.**		**Reduction in Avg. SPL of all 33 Microphones.**	
Serial	**From Default Angle Set Case (dB)**	**From Worst Angle Set Case (dB)**	**From Default Angle Set Case (dB)**	**From Worst Angle Set Case (dB)**	**From Default Angle Set Case (dB)**	**From Worst Angle Set Case (dB)**
1	6.4	7.1	8.6	9.4	4.2	5.0
2	7.2	7.4	8.8	9.5	3.0	4.6
3	7.6	7.9	8.6	9.2	6.9	7.1
4.1	7.5	7.8	7.8	8.2	6.5	6.6
4.2	8.1	8.5	7.0	7.7	7.0	7.4
4.3	9.9	10.6	9.2	10.5	5.4	7.4
5.1	8.3	8.7	8.0	8.6	7.3	7.4
5.2	9.0	9.8	6.8	7.9	7.0	7.5
5.3	9.2	10.7	7.4	9.1	7.4	8.4
5.4	Not flown	Not flown	4.5	6.8	5.2	7.2
6.1	7.8	9.6	6.7	8.3	6.6	7.9
6.2	7.0	9.0	5.5	7.6	6.2	8.0
6.3	7.5	9.4	7.0	9.5	5.8	7.6
6.4	Not flown	Not flown	3.6	7.4	Not flown	Not flown
7.1	Not flown	Not flown	Not flown	Not flown	5.6	7.6
7.2	Not flown	Not flown	Not flown	Not flown	5.5	8.0
7.3	5.0	8.9	5.5	8.8	3.9	7.3
7.4	Not flown	Not flown	Not flown	Not flown	Not flown	Not flown
10	Not flown	Not flown	Not flown	Not flown	7.2	8.7

10.3.3. Candidate Synchrophase Angle Sets (Trial 1)

In the absence of an adaptive control system, the existing C-130J synchrophaser can only be programmed with a limited number of fixed synchrophase angles sets. To realise a relatively small set of synchrophase angles that could be expected to be applied in practice, the many different sets of optimum angles found in §10.3.2 must be reduced down to just a few candidates. The candidates that were selected for Trial 2 and the results they are based on are listed in Table 10.12. The main low-vibration and low-SPL candidate sets are shown in the top part of the table. The bottom part of the table contains four sets of interest that were only used during Serials 4.2, 5.3 and 6.2 of Trial 2.

Table 10.12 C-130J-30 candidate synchrophase angle sets for Trial 2.

Set	Angles (P1, P2, P3, P4)	Description	Based on results from:
a	(α_{def1}, 0°, α_{def3}, α_{def4})	Default Angles	n.a.
b	(6°, 0°, 0°, 34°)	Low Vib. Set 1	Floor acc's, Serials 4.1-4.3, 5.1-5.3, 6.1-6.3, Flight 1,Trial 1
c	(7°, 0°, 57°, 29°)	Low Vib. Set 2	Floor acc's, Serials 4.1-4.3, 5.1-5.3, 6.1-6.3, Flight 1,Trial 1
d	(57°, 0°, 52°, 22°)	Low SPL Set 1	All mics, Serials 4.1-4.3, 5.1-5.3, 6.1-6.3, Flight 3, Trial 1
e	(55°, 0°, 48°, 19°)	Low SPL Set 2	All mics, Serial 10, Flight 3, Trial 1
f	(53°, 0°, 32°, 29°)	Low SPL Flt Deck	Flight deck mics, Serials 4.1-4.3, 5.1-5.3, Flight 3, Trial 1
g	(30°, 0°, 30°, 39°)	High SPL	All mics, Serials 4.1-4.3, 5.1-5.3, 6.1-6.3, Flight 3, Trial 1
h	(40°, 0°, 27°, 32°)	High Vibration	Floor acc's, all serials, Flights 1 & 2, Trial 1
i	(0°, 0°, 0°, 40°)	Low Measured	All sensors, Serial 10, Flight 3, Trial 1

10.3.4. Performance of Candidate Synchrophase Angle Sets (Trial 2)

The candidate synchrophase angle sets developed from Trial 1 (§10.3.3) were tested in Trial 2. The average SPL at the BPF (over all 22 microphones used in Trial 2) and the average floor vibration at the BPF (over all 14 accelerometers used in Trial 2) that were measured for each candidate set are listed in Tables 10.13 and 10.14 respectively.

The relative reductions at the BPF achieved by each candidate set over the default angle set are shown in Figure 10.35. It can be seen that the four main candidate sets generally performed better than the default angle set for nearly every altitude-airspeed combination tested. Interestingly, the Low-SPL sets generally produced slightly lower floor vibration than the Low-Vibration sets. This could reflect the lack of cargo in Trial 2 (i.e., that the Trial 1 signatures were affected by the cargo loading in that trial and therefore not representative of the lack of cargo in Trial 2), or it could be due to aircraft-to-aircraft differences (§10.3.6). As expected, the Low SPL Flight Deck set did not produce a low average SPL over all microphones, and the High Vibration and High SPL sets generally produced slightly higher noise and vibration than the default angle set.

In order to assess whether the reductions at the BPF were offset by increases at the harmonics of the BPF, the measured results were averaged over the low-order harmonics of the BPF (up to 4× BPF). These are shown in Figure 10.36. It can be seen that the average sound pressure and average floor vibration reductions are only fractionally smaller than the BPF-only results, and that the candidate angle sets therefore did not have a significant detrimental effect at these higher frequencies.

The four main candidate angle sets are listed in ranked order for several different altitude groups in Tables 10.15 and 10.16. It can be seen that the Low SPL 2 set produced the lowest average SPL in all but one altitude group, and the lowest average floor vibration in all altitude groups. The Low SPL 1 set performed the next best overall.

These results (Figures 10.35 & 10.36, and Tables 10.15 & 10.16) are not directly comparable to the Trial 1 predictions (Table 10.11) because the sensor sets are not quite the same. Comparisons between the predicted and measured results using only the sensors and flight conditions in common between the two trials are shown in Figures 10.37 and 10.38. Clearly, while the candidate angle sets provided reductions in nearly all cases, they did not perform as well as expected in the second aircraft. This finding is further examined in §10.3.5 and §10.3.6.

Table 10.13 C-130J-30 measured average over all microphones of the SPL at the BPF, Trial 2.

Sync. Angle Set	**Serial**									
	2 (dB)	**3 (dB)**	**4.1 (dB)**	**4.2 (dB)**	**4.3 (dB)**	**5.1 (dB)**	**5.2 (dB)**	**5.3 (dB)**	**6.2 (dB)**	**7.4 (dB)**
Default	106.1	110.2	107.8	108.4	109.1	107.9	107.5	108.8	107.4	108.9
Low vibration 1	104.8	106.1	103.6	105.4	106.8	103.8	104.9	107.1	105.8	109.1
Low vibration 2	104.9	106.2	104.3	105.9	107.2	104.2	105.3	107.2	105.8	109.2
Low SPL 1	105.7	106.5	104.8	105.5	106.3	103.7	104.7	106.0	104.9	108.2
Low SPL 2	105.4	106.4	104.6	105.0	105.9	103.1	104.3	105.3	104.3	108.0
Low SPL Flt Deck	n.a.	n.a.	n.a.	106.8	n.a.	n.a.	n.a.	108.3	107.4	n.a.
High SPL	n.a.	n.a.	n.a.	109.1	n.a.	n.a.	n.a.	109.9	108.5	n.a.
High vibration	n.a.	n.a.	n.a.	108.5	n.a.	n.a.	n.a.	109.4	108.2	n.a.
Low measured Trial 1	n.a.	n.a.	n.a.	104.2	n.a.	n.a.	n.a.	106.5	106.1	n.a.

Table 10.14 C-130J-30 measured average over all floor accelerometers of the vibration at the BPF, Trial 2.

Sync. Angle Set	**Serial**									
	2 (g_{rms})	**3 (g_{rms})**	**4.1 (g_{rms})**	**4.2 (g_{rms})**	**4.3 (g_{rms})**	**5.1 (g_{rms})**	**5.2 (g_{rms})**	**5.3 (g_{rms})**	**6.2 (g_{rms})**	**7.4 (g_{rms})**
Default	0.286	0.324	0.271	0.289	0.307	0.268	0.337	0.368	0.308	0.264
Low vibration 1	0.237	0.234	0.149	0.159	0.158	0.135	0.164	0.201	0.172	0.247
Low vibration 2	0.214	0.238	0.152	0.158	0.167	0.177	0.167	0.197	0.166	0.234
Low SPL 1	0.176	0.238	0.146	0.144	0.160	0.154	0.160	0.179	0.155	0.205
Low SPL 2	0.150	0.218	0.135	0.125	0.148	0.139	0.147	0.158	0.147	0.206
Low SPL Flt Deck	n.a.	n.a.	n.a.	0.263	n.a.	n.a.	n.a.	0.373	0.301	n.a.
High SPL	n.a.	n.a.	n.a.	0.280	n.a.	n.a.	n.a.	0.339	0.293	n.a.
High vibration	n.a.	n.a.	n.a.	0.300	n.a.	n.a.	n.a.	0.420	0.328	n.a.
Low measured Trial 1	n.a.	n.a.	n.a.	0.133	n.a.	n.a.	n.a.	0.208	0.165	n.a.

Table 10.15 Candidate synchrophase angle sets in ranked order for low SPL, Trial 2.

All Serials (Avg. reduction)	**Low-altitude Serials 2 & 3**	**Middle-altitude Serials 4.1–5.3**	**High-altitude Serials 6.2 & 7.4**
Low SPL 2 (3.0 dB)	Low Vib. 1 (2.7 dB)	Low SPL 2 (3.6 dB)	Low SPL 2 (2.0 dB)
Low SPL 1 (2.6 dB)	Low Vib. 2 (2.6 dB)	Low SPL 1 (3.1 dB)	Low SPL 1 (1.6 dB)
Low Vib. 1 (2.5 dB)	Low SPL 2 (2.2 dB)	Low Vib. 1 (3.0 dB)	Low Vib. 1 (0.7 dB)
Low Vib. 2 (2.2 dB)	Low SPL 1 (2.1 dB)	Low Vib. 2 (2.6 dB)	Low Vib. 2 (0.6 dB)

Table 10.16 Candidate synchrophase angle sets in ranked order for low floor vibration, Trial 2.

All Serials (Avg. reduction)	**Low-altitude Serials 2 & 3**	**Middle-altitude Serials 4.1–5.3**	**High-altitude Serials 6.2 & 7.4**
Low SPL 2 (5.7 dB)	Low SPL 2 (4.5 dB)	Low SPL 2 (6.6 dB)	Low SPL 2 (4.3 dB)
Low SPL 1 (5.0 dB)	Low SPL 1 (3.4 dB)	Low SPL 1 (5.8 dB)	Low SPL 1 (4.1 dB)
Low Vib. 1 (4.4 dB)	Low Vib. 2 (2.6 dB)	Low Vib. 1 (5.6 dB)	Low Vib. 2 (3.2 dB)
Low Vib. 2 (4.2 dB)	Low Vib. 1 (2.2 dB)	Low Vib. 2 (5.1 dB)	Low Vib. 1 (2.8 dB)

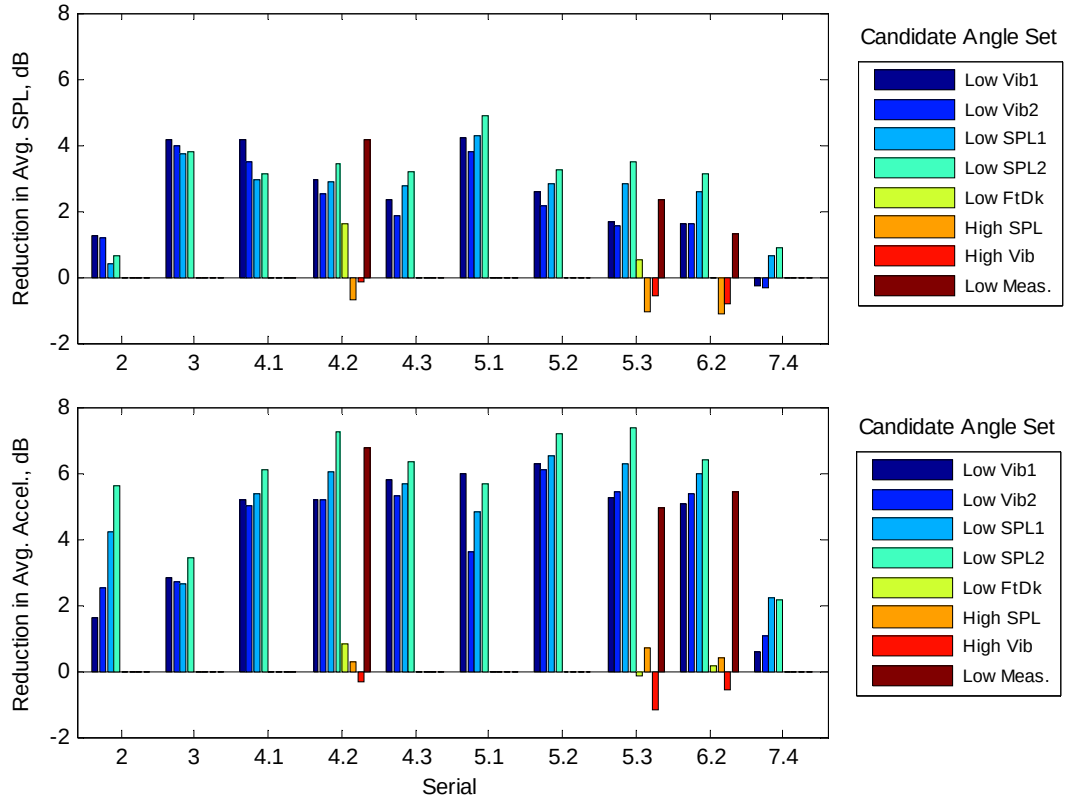

Figure 10.35 C-130J-30 measured reductions at the BPF in the average SPL over all microphones (top), and the average vibration over all floor accelerometers (bottom), compared to the default synchrophase angle set case, Trial 2. The last four angle sets were only measured during Serials 4.2, 5.3 and 6.

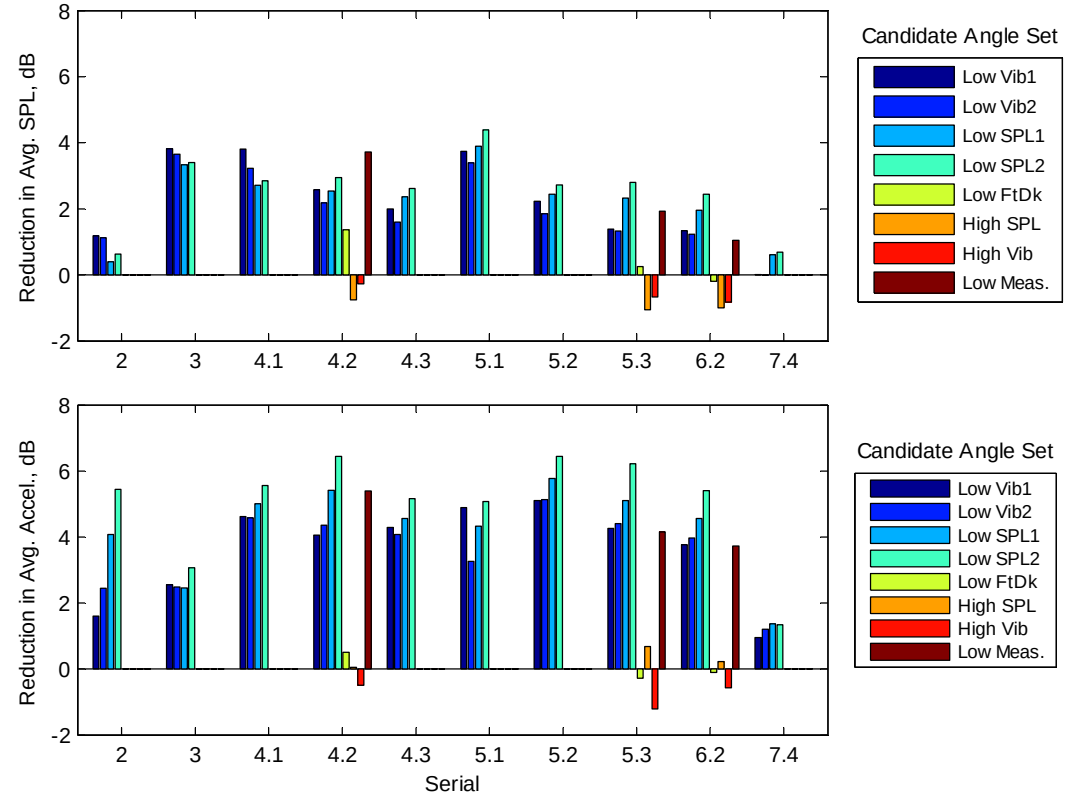

Figure 10.36 C-130J-30 combined measured reductions at 1×, 2×, 3× & 4× BPF in the average SPL over all microphones (top), and the average vibration over all floor accelerometers (bottom) compared to the default synchrophase angle set case, Trial 2. The last four angle sets were only measured during Serials 4.2, 5.3 and 6.

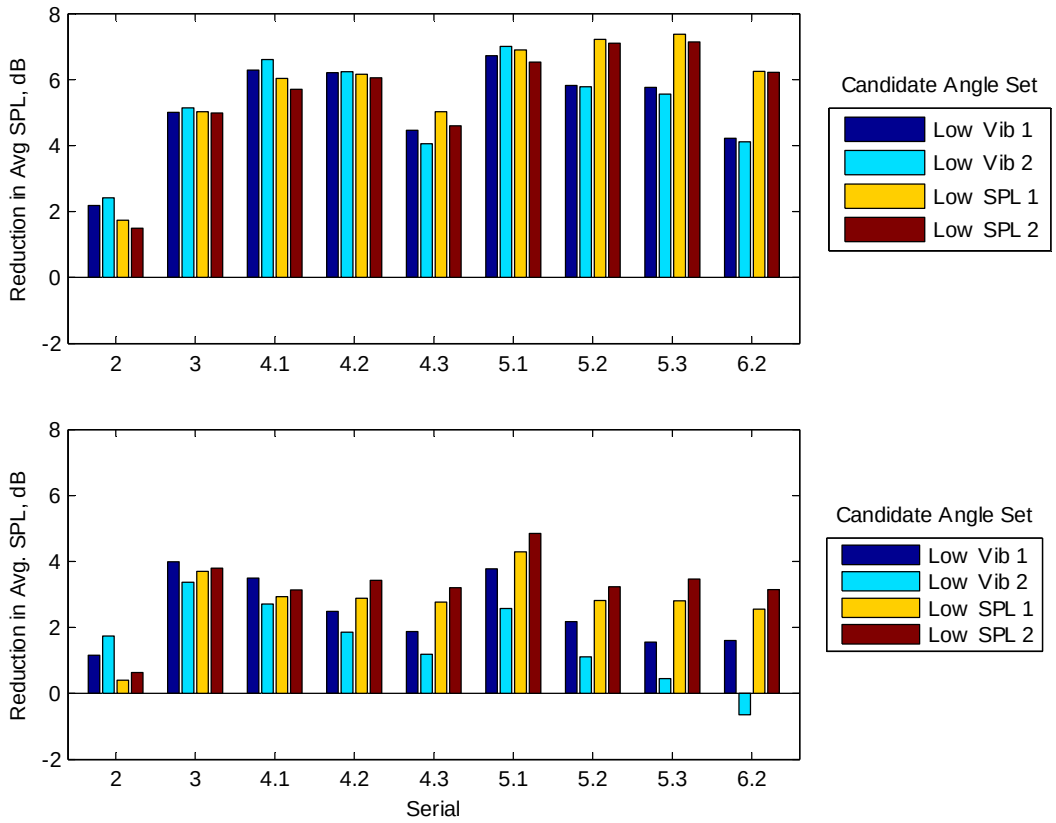

Figure 10.37 C-130J-30 comparison between the Trial 1 predictions (top) and the Trial 2 measurements (bottom) showing the reductions in the average SPL at the BPF from the default angle set using only the sensors and flight conditions in common between the trials.

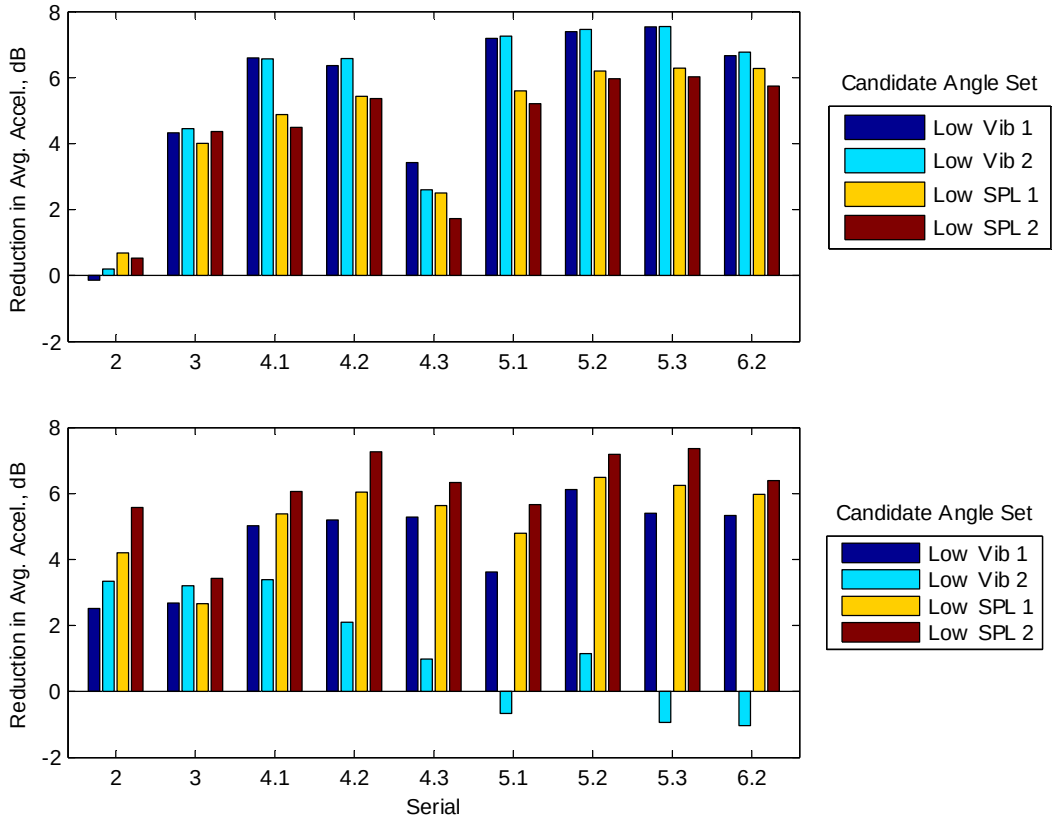

Figure 10.38 C-130J-30 comparison between the Trial 1 predictions (top) and the Trial 2 measurements (bottom) showing the reductions in the average vibration at the BPF from the default angle set using the sensors and flight conditions in common between the trials.

10.3.5. Comparison of Measured and Predicted Levels (Trials 1 & 2)

In order to discover if there were significant differences in the signatures between the aircraft, and where these occurred, the Serial 5.3 measurements from Trial 2 were compared on a sensor-to-sensor basis with two sets of predictions; one based on the Serial 10 signatures derived from Trial 1, and the other based on the Serial 10 signatures derived from Trial 2. Serial 5.3 and Serial 10 were used for this purpose because they shared the same airspeed and altitude (220 KCAS at FL240).

The results are shown in Figures 10.39 to 10.47. In the figures, each sensor circle is split into three equal segments, where the top central segment is the measurement (M), the bottom-left segment is the prediction based on the Trial 1 signatures (P1), and bottom-right segment is the prediction based on the Trial 2 signatures (P2). Note that the P1 predictions for 8 of the 14 floor accelerometers are blank because only 6 accelerometers were measured during this serial.

The results clearly show that the Trial 2 predictions are much closer to the measurements than the Trial 1 predictions in all cases, indicating that there were aircraft-to-aircraft differences in the signatures for many sensors even though the flight conditions were nominally the same. The effect of these differences on the optimum synchrophase angles is discussed in §10.3.6.

10.3.6. Effect of Aircraft-to-Aircraft Signature Differences

In order to establish the typical effect that aircraft-to-aircraft signature differences might have on the predicted optimum synchrophase angles, two typical cost functions (average SPL at the BPF, and average floor vibration level at the BPF) were plotted for the same serial in each trial (Serial 10, 220 KCAS at FL240) using only the sensors in common between the two trials. The results are shown in Figures 10.48 and 10.49. Slices have been taken through the global maxima and minima in each case to reveal the locations of these points and the shape of the contours near these extremes.

It can be seen that, while the contours are very similar for both trials, the Trial 2 levels are slightly higher, and the synchrophase angles of the maxima and minima are different (Table 10.17). This shows that the Trial 1 signatures are not able to produce the best possible results for Trial 2. There are several possible reasons for this:

a) Sensor Positions: It is known that there were some differences in the sensor positions between the trials (§5.4). Even if these were limited to ~10 cm (~3% of the wavelength (~3.2 m) of the sound at the BPF), it is possible that they could still account for a significant proportion of the observed signature differences.

b) Flight Conditions: Inevitably, there would have been minor differences in the serial altitudes and airspeeds between the two trials. However, given the predicted effects of the altitude and airspeed on the optimum synchrophase angles based on the Trial 1 data (§10.3.2), it is considered that these differences would not have been significant.

c) Synchrophase Angles: Any differences in the actual (as opposed to set) synchrophase angles between the trials would necessarily lead to differences in the propeller signatures. The accuracy of the collected photographic and laser tachometer data (Chapter 6) was insufficient to determine whether any such differences may have existed. However, this source of error is considered unlikely since the synchrophasing system is a core function of the Engine FADEC.

d) External Weather Conditions: The first trial was in November, while the second was in July, and differences in the external atmospheric temperature, humidity, etc. may have affected the results. Unfortunately, these were not directly recorded. The closest temperature measurement that would bear some correlation to the external air temperature was the engine compressor inlet temperature. For Serial 10, this varied from −30° C in Trial 1 to −23° C in Trial 2. However, the external air pressures at the altitudes specified in flight levels (i.e., above 10,000 ft) would have been the same between the trials.

e) Vibro-Acoustic Differences: As discussed in Chapter 3, the transmission of sound from the propellers into the aircraft cabin is the result of a complex interaction between the exterior sound field, the fuselage vibration, and the interior sound field. Anything that affects this interaction (e.g., aircraft-to-aircraft variation in the fuselage panel vibration) will affect the resulting propeller signatures. This investigation has necessarily assumed that any vibro-acoustic differences between the aircraft are small. Any differences that do exist between aircraft will necessarily mean that the best results for any particular aircraft can only be obtainable by measurements on that aircraft. However, the performance of the candidate synchrophase angle sets in the second aircraft (§10.3.4) indicate that worthwhile improvements are still likely without resorting to such a detailed examination of every aircraft.

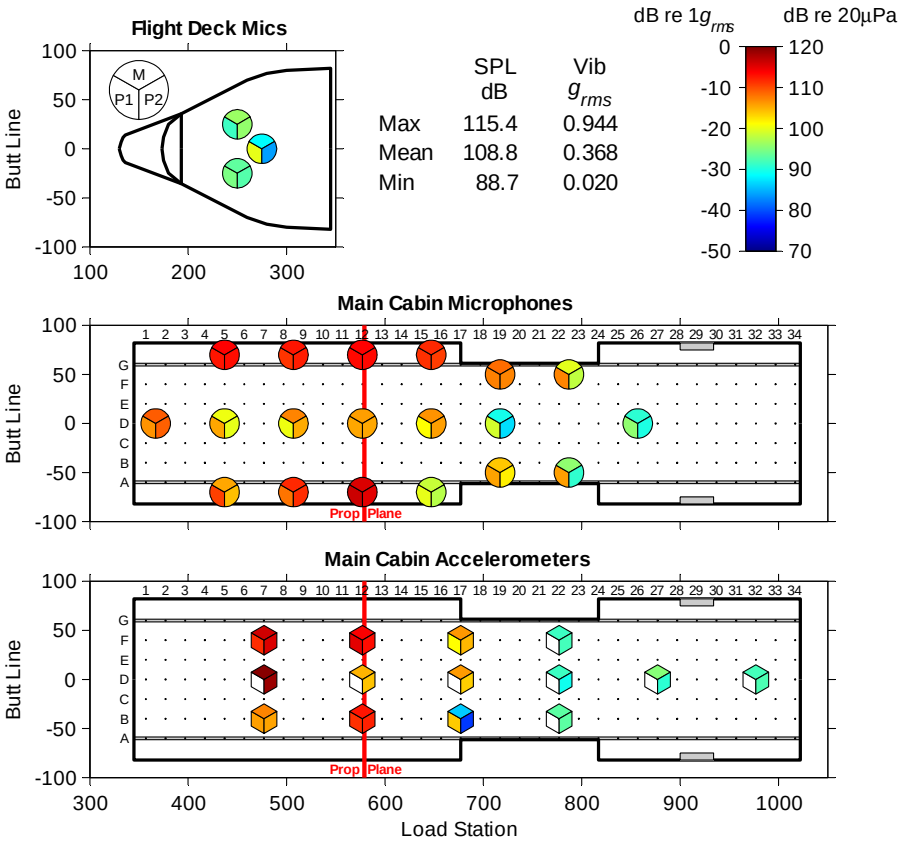

Figure 10.39 C-130J-30 Trial 2 Serial 5.3 measurements v. Trial 1 & Trial 2 predictions, default synchrophase angles.

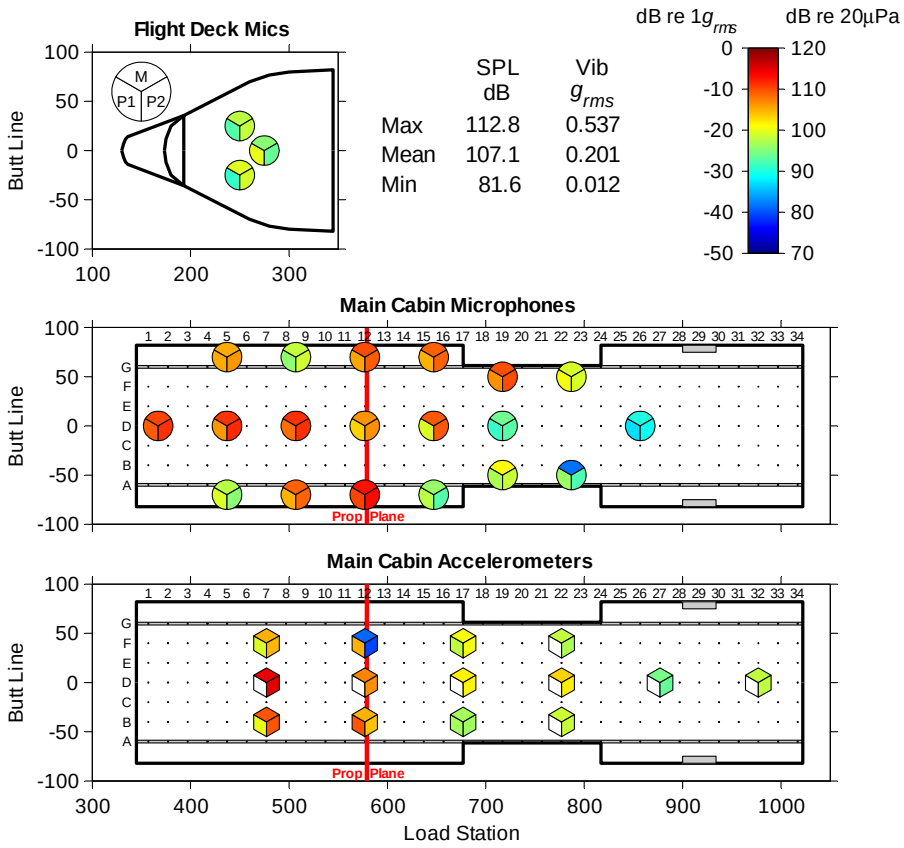

Figure 10.40 C-130J-30 Trial 2 Serial 5.3 measurements v. Trial 1 & Trial 2 predictions, Low Vibration Set 1.

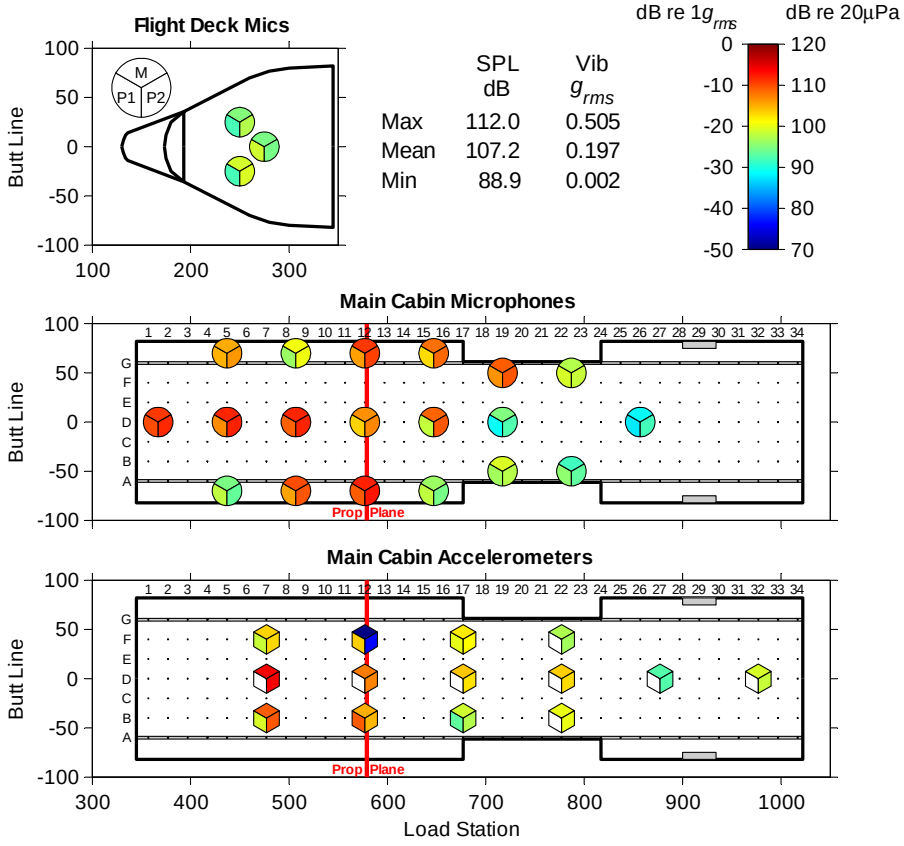

Figure 10.41 C-130J-30 Trial 2 Serial 5.3 measurements vs. Trial 1 & Trial 2 predictions, Low Vibration Set 2.

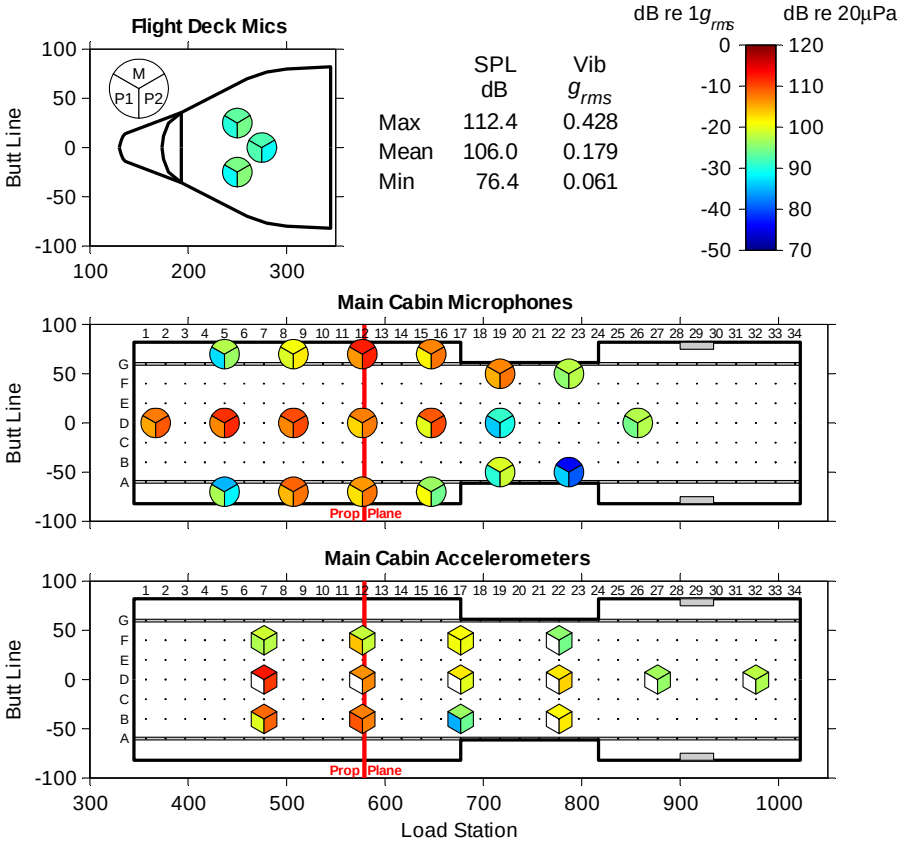

Figure 10.42 C-130J-30 Trial 2 Serial 5.3 measurements vs. Trial 1 & Trial 2 predictions, Low SPL Set 1.

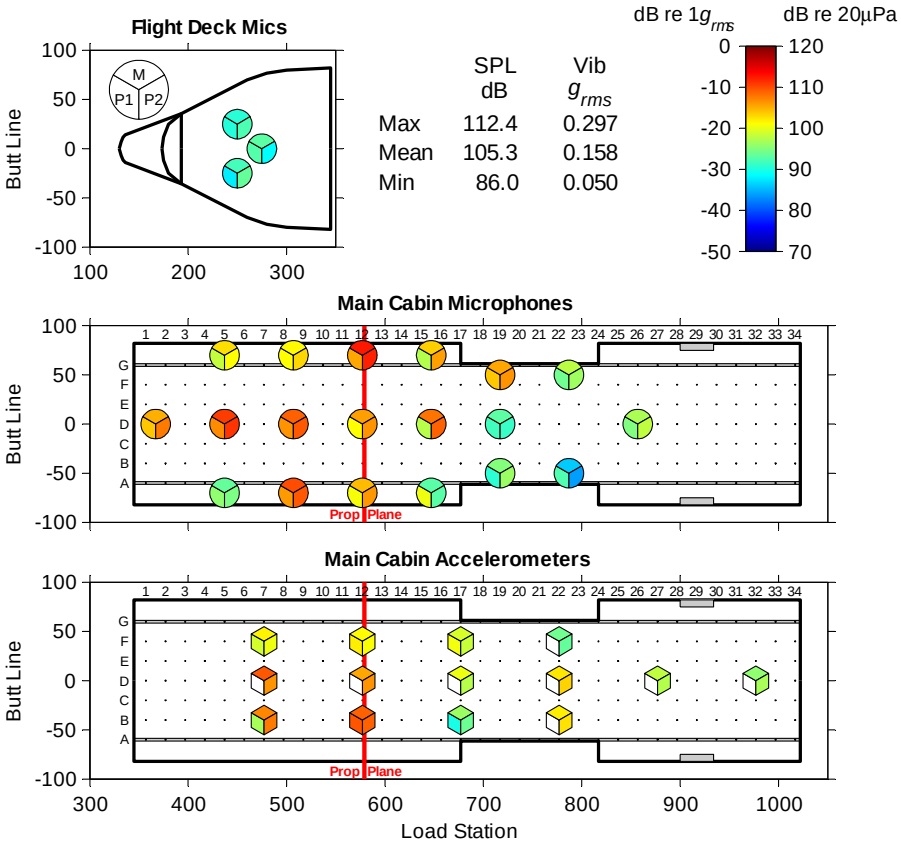

Figure 10.43 C-130J-30 Trial 2 Serial 5.3 measurements vs. Trial 1 & Trial 2 predictions, Low SPL Set 2.

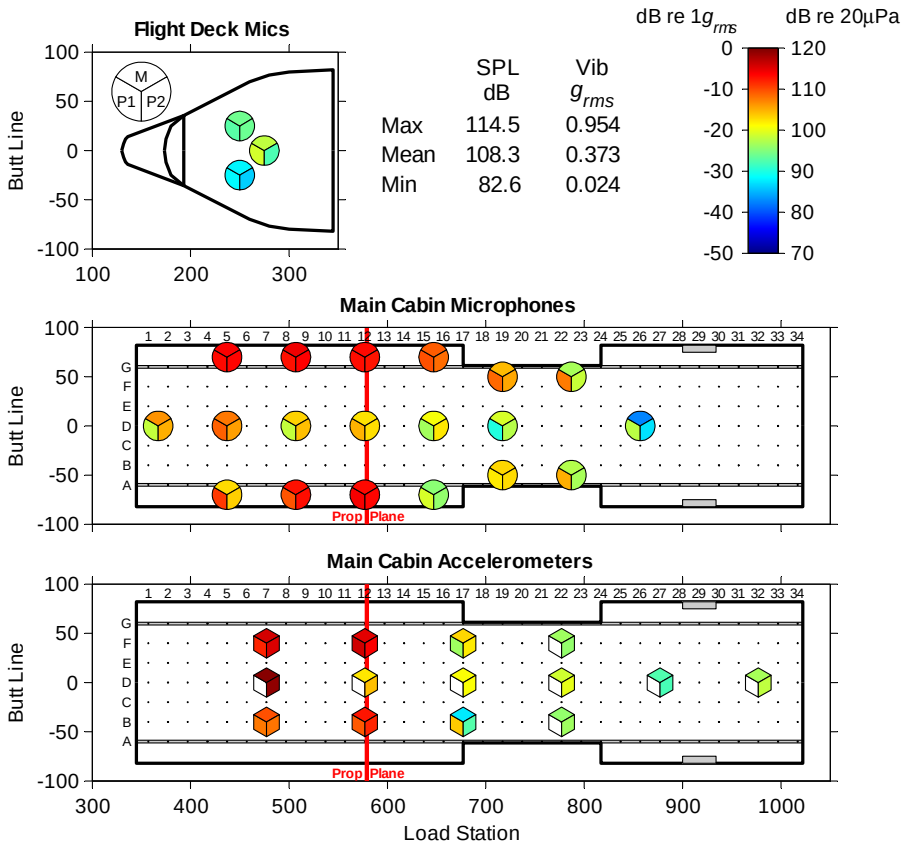

Figure 10.44 C-130J-30 Trial 2 Serial 5.3 measurements vs. Trial 1 & Trial 2 predictions, Low Flight Deck SPL Angle Set.

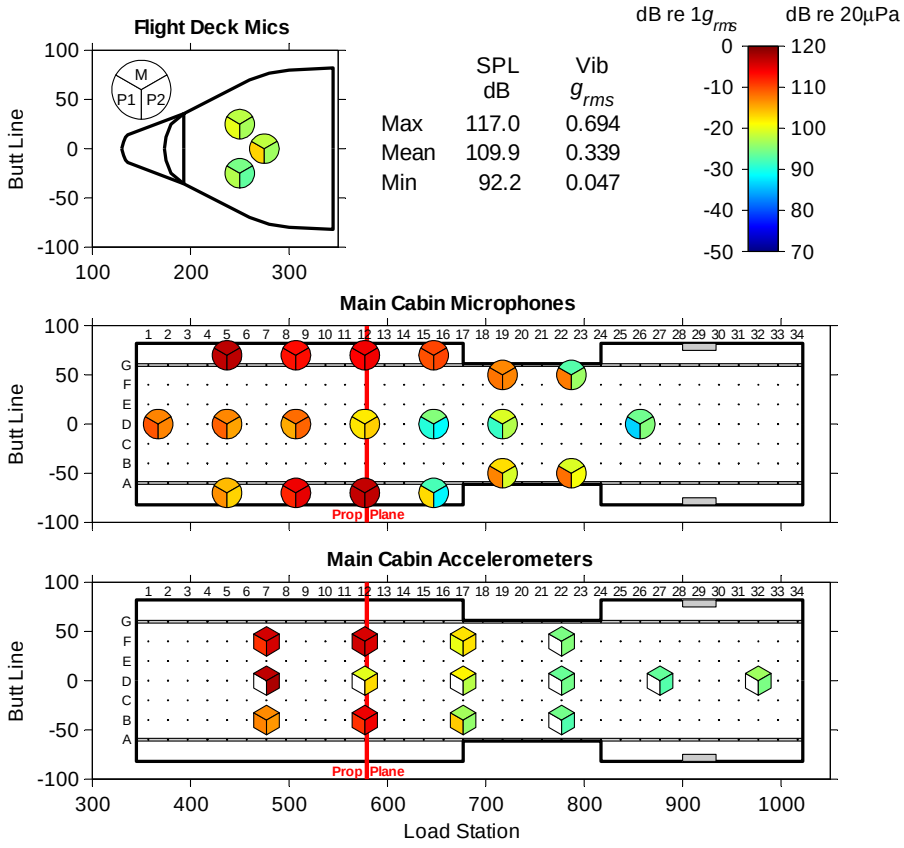

Figure 10.45 C-130J-30 Trial 2 Serial 5.3 measurements vs. Trial 1 & Trial 2 predictions, High SPL Angle Set.

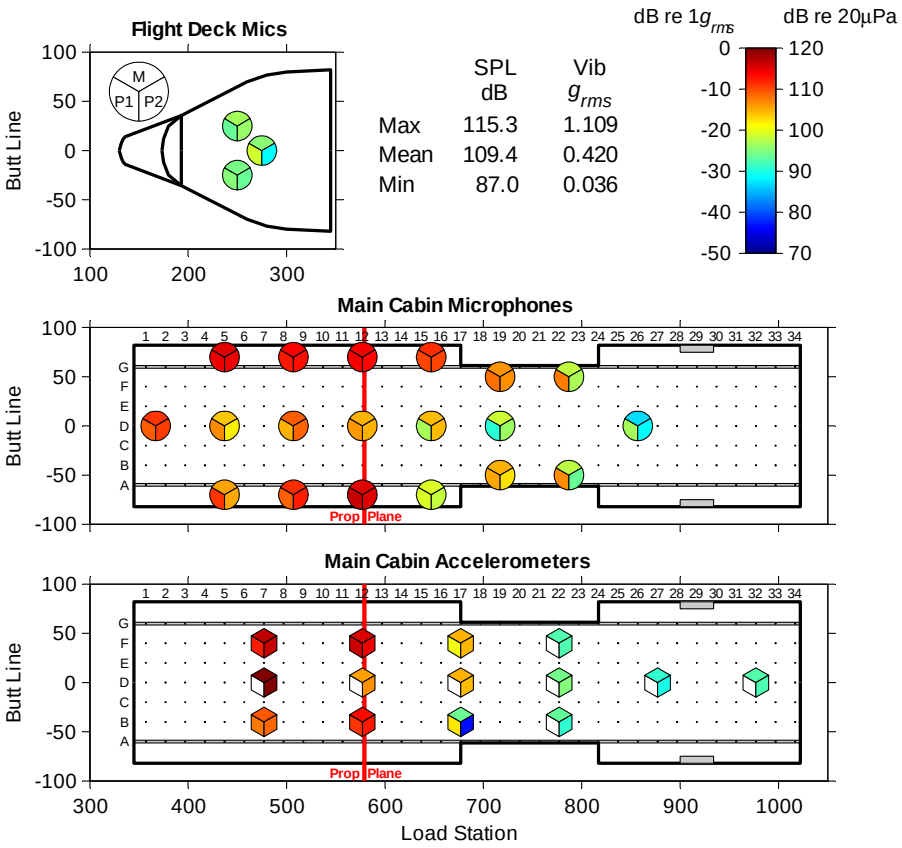

Figure 10.46 C-130J-30 Trial 2 Serial 5.3 measurements vs. Trial 1 & Trial 2 predictions, High Vibration Angle Set.

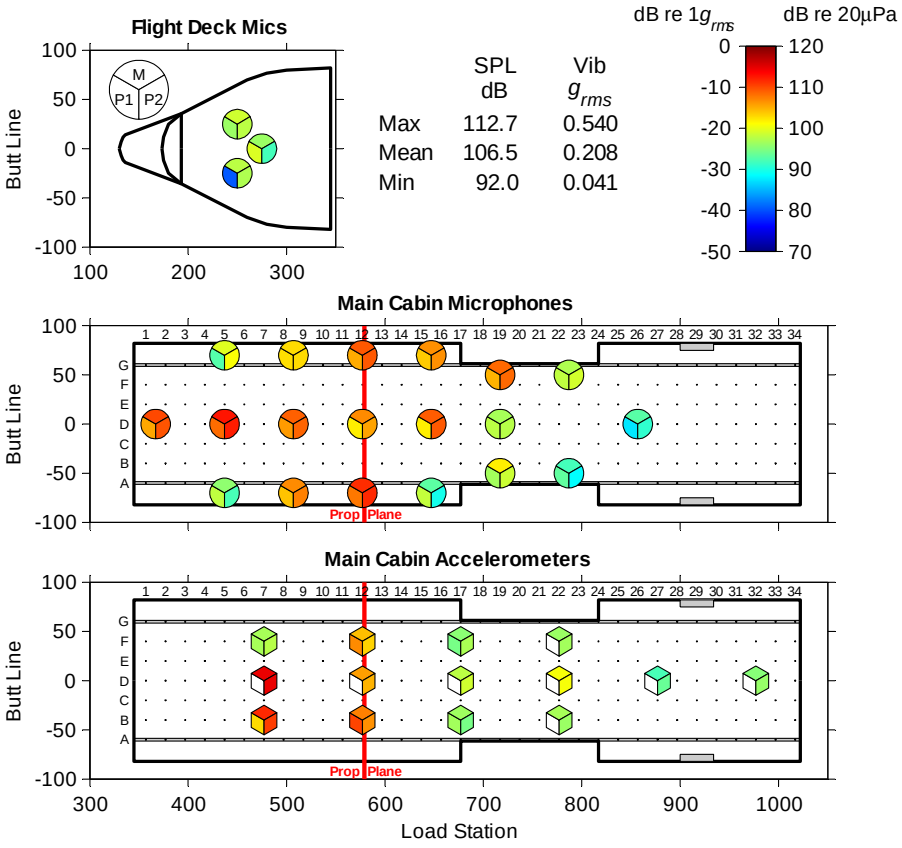

Figure 10.47 C-130J-30 Trial 2 Serial 5.3 measurements vs. Trial 1 & Trial 2 predictions, angle set corresponding to low measured levels in Trial 1.

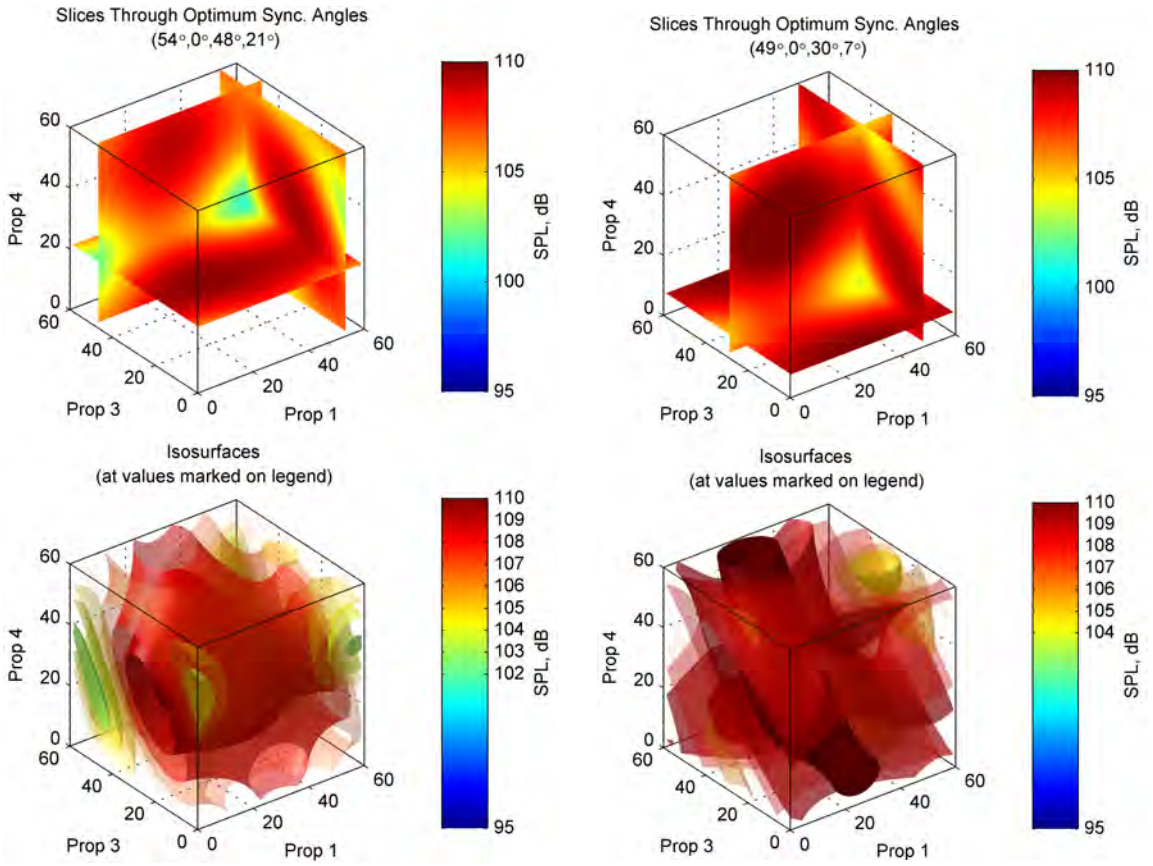

Figure 10.48 C-130J-30 predicted average SPL at the BPF using only the microphones in common for Serial 10 of Trial 1 (left) and Serial 10 of Trial 2 (right).

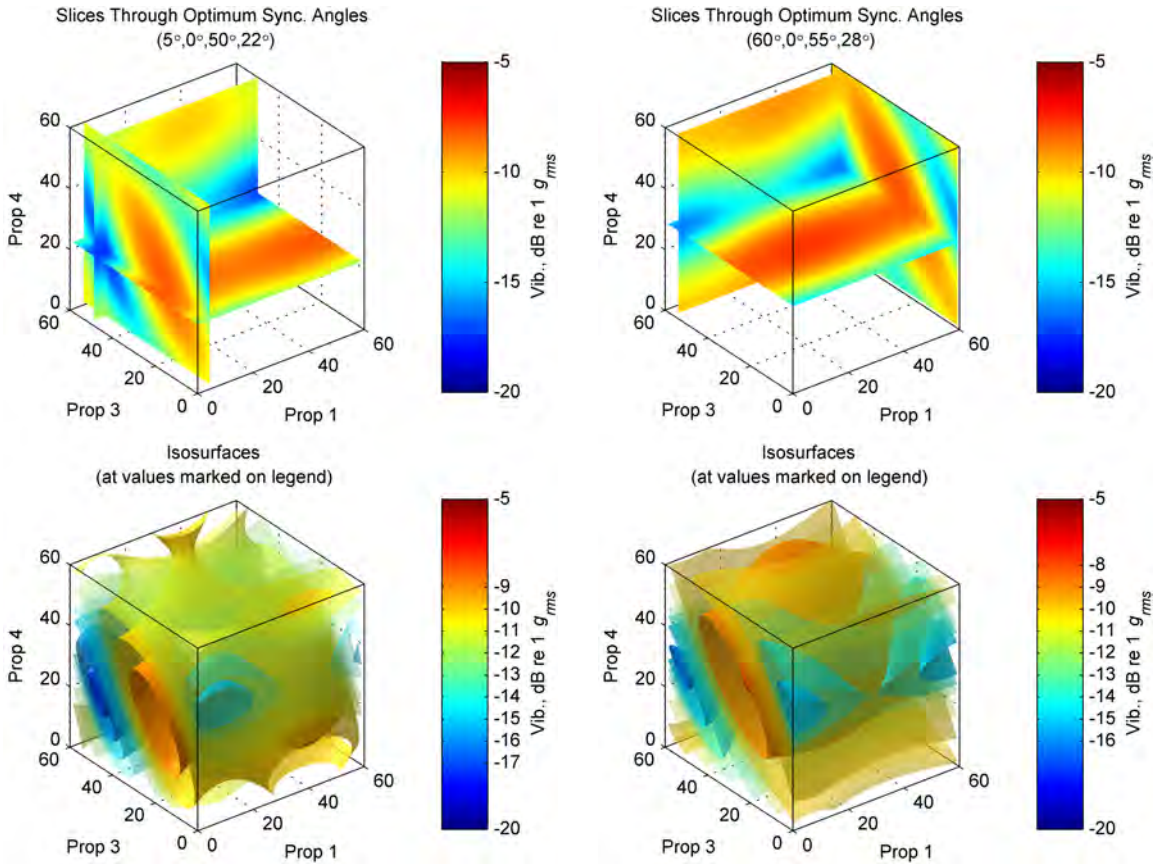

Figure 10.49 C-130J-30 predicted average floor vibration at the BPF using only the accelerometers in common for Serial 10 of Trial 1 (left) and Serial 10 of Trial 2 (right).

Table 10.17 C-130J-30 synchrophase angles and the average SPL and average floor vibration at the BPF at the maxima and minima shown in Figures 10.48 and 10.49.

	Trial	**Average SPL at BPF**	**Average Floor Vibration at BPF**
Max	1	110.5 dB @ (19°, 0°, 28°, 34°)	0.388 g_{rms} @ (58°, 0°, 21°, 25°)
	2	110.7 dB @ (20°, 0°, 34°, 40°)	0.425 g_{rms} @ (27°, 0°, 32°, 37°)
Min	1	101.4 dB @ (54°, 0°, 48°, 21°)	0.135 g_{rms} @ (5°, 0°, 50°, 22°)
	2	103.9 dB @ (49°, 0°, 30°, 7°)	0.155 g_{rms} @ (0°, 0°, 55°, 28°)

11. Adaptive Control of Synchrophase Angles

It has been shown in Chapter 10 that the optimum propeller synchrophase angles for lower cabin noise and vibration change with varying flight conditions. It would be very desirable for a synchrophasing control system to automatically adapt to these changes. Bearing in mind that the control system should be no more complex than it needs to be, there are essentially two different ways this could be implemented.

The first, and perhaps the simplest, method would be to use a look-up table filled with pre-computed optimum synchrophase angles for a comprehensive range of flight conditions. This would require very little in the way of changes to the actual synchrophasing control system, but it would require a highly instrumented series of test flights similar to those described in Chapter 5. The step sizes between the test points would also need to be small enough for the optimum angles for intermediate flight conditions to be interpolated from the table. This method would inherently rely on the assumption that the optimum synchrophase angles for any aircraft of that type are the same as those of the test aircraft (i.e., that there are no aircraft-to-aircraft differences), and that the optimum synchrophase angles are not influenced by the cabin configuration or load. The results presented in §10.3 show that both of these assumptions may not be entirely valid.

The second method would be to implement an active control system with error signals from a number of permanently mounted acoustic and/or vibration sensors distributed throughout the aircraft cabin. The principal advantages of this method would be that the active control system could better adapt to any factors that might influence the optimum synchrophase angles, not just those that might be considered in the first method, and that it could possibly be implemented with less flight testing. The main disadvantages would be the need for a more complex control system, the presence of fragile sensors in potentially awkward places in the cabin, and possibly the need for a relatively large number of sensors in order to guarantee that the system achieves global minimisation of the cabin noise and vibration.

These two approaches are examined in more detail in §11.1 and §11.2 respectively.

11.1. Control using a Look-up Table

The generation of any sort of look-up table of optimum synchrophase angles requires a commitment to at least one instrumented test flight in that type of aircraft. If such a flight is to be conducted then it makes sense to use as many sensors as possible, as these will be relatively inexpensive compared to the cost of flying a large turboprop aircraft. A high spatial density of sensors will also help to ensure that a true global minimum is achieved. However, it is more difficult to ascertain which flight conditions should be measured *a priori*. Based on this investigation, the best answers that can be recommended will be necessarily biased towards the AP-3C and C-130J-30. However, these recommendations may not be the most appropriate for other aircraft types. For example, it may be better to concentrate the measurements around the typical climb, cruise, and decent flight conditions for a passenger aircraft, leaving out those regions of the flight envelope that would seldom be experienced during normal operations.

In general, for a look-up table to work well, the incremental changes in the synchrophase angles between the table entries will also need to be reasonably small compared to the overall range of possible values (say < 10%). If the changes become too large, then the

interpolated values between the table entries may well end up being significantly different from the optimum values, and thus result in unacceptably high sound or vibration levels. Interpolation between the optimum synchrophase angles found in §10.2 for the AP-3C and §10.3 for the C-130J-30 for the lowest average sound pressure level of all microphones are discussed in the following sections.

11.1.1. AP-3C Control using a Look-up Table

The incremental changes in the AP-3C optimum synchrophase angles (for the lowest average SPL at the BPF over all microphones) due to the changes in airspeed and altitude that were made during this investigation are summarised in Tables 11.1 and 11.2 respectively. It can be seen that, while many changes in the optimum synchrophase angles are reasonably small (<9°) compared to the overall range of possible angles (90°), many are also quite large (>30°). This result is a little discouraging as it indicates that intermediate points may be needed between airspeeds as close as 20 KIAS, or altitudes as close as 2000 ft. However, when the 3-D plots of the average sound pressure level for these conditions are examined (Figures 10.13 to 10.15), it can be seen that the low-amplitude regions of this cost function are almost linear. Interpolation between widely-spaced minima will thus be effective in this particular aircraft as long the line of interpolation passes through this low-amplitude region. Unfortunately, this line of interpolation is not always the shortest distance between the two points. Two examples are shown here: one at a constant altitude (Figure 11.1), and one at a constant airspeed (Figure 11.2). Note that the lines of interpolation can wrap around at each axis boundary (−45° ↔ 45°) due to the rotational symmetry of the synchrophase angles. In both cases the most appropriate line of interpolation is not the shortest. For comparison, the lines of interpolation for two more moderate incremental angle change cases are shown in Figures 11.3 and 11.4. Here, it can be seen that the shortest lines of interpolation are the better choices, as expected.

Table 11.1 Incremental changes in the optimum AP-3C synchrophase angles (for the lowest average over all microphones of the SPL at the BPF) due to changes in airspeed.

Altitude	Airspeeds (KIAS)	Prop 1	Prop 2	Prop 3	Prop 4
500 ft	200 → 220	−44°	−22°	Master	6°
1000 ft	200 → 220 → 240	−20° −8°	−8° −10°		4° −8°
3000 ft	220 → 240 → 260	−38° −6°	−36° −8°		4° −2°
10000 ft	220 → 240 → 260	40° 0°	26° −6°		6° 4°
FL180	220 → 240 → 260 → 280	−24° −4° 4°	−24° −14° −4°		0° 8° 6°
FL200	220 → 240 → 260	−14° −8°	−18° −22°		4° 6°
FL240	200 → 220 → 240	−10° −4°	−26° −8°		12° 2°
FL280	180 → 200 → 220	−10° −8°	−16° −28°		6° 8°

Table 11.2 Incremental changes in the optimum AP-3C synchrophase angles (for the lowest average over all microphones of the SPL at the BPF) due to changes in altitude.

Airspeed	Altitudes (ft or FL)	Prop 1	Prop 2	Prop 3	Prop 4
200 KIAS	500 → 1000	−20°	−14°	Master	2°
	FL240→ FL280	−2°	−4°		6°
220 KIAS	500 → 1000 →3000 →10000	4° −30° 24°	0° 30° 42°		0° −4° 0°
	FL180 → FL200 → FL240 → FL280	0° −12° 0°	4° −28° −6°		4° 12° 2°
240 KIAS	1000 →3000 →10000	20° 22°	4° 14°		8° 2°
	FL180 → FL200 → FL240	10° −2°	10° −18°		8° 10°
260 KIAS	3000 →10000	28°	16°		8°
	FL180 → FL200	6°	2°		6°

* Note that, while the indicated airspeed is not changing with altitude, the true airspeed is changing.

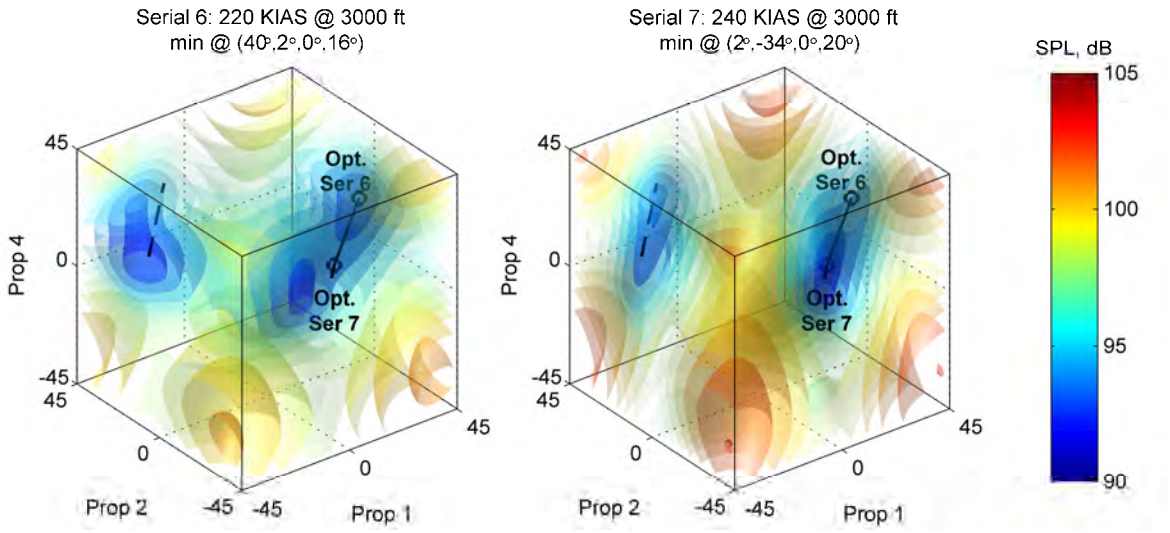

Figure 11.1 AP-3C cost functions (average over all microphones of the SPL at the BPF) showing two potential lines of interpolation between the widely-spaced optimum synchrophase angles for 220 KIAS and 240 KIAS at 3000 ft. Note that the 15% longer dashed line passes through a slightly lower-amplitude region than the shorter solid line.

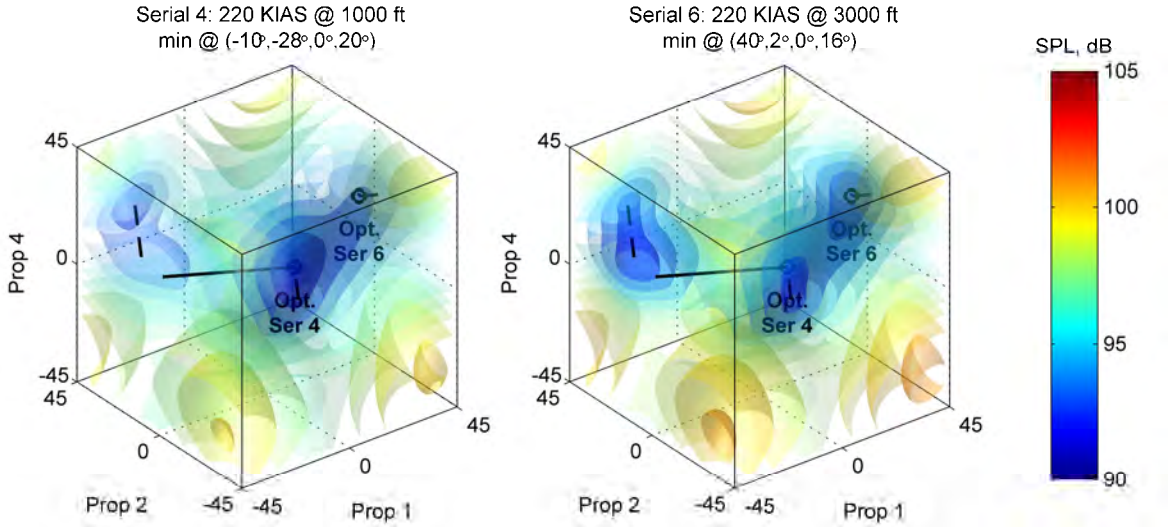

Figure 11.2 AP-3C cost functions (average over all microphones of the SPL at the BPF) showing two potential lines of interpolation between the widely-spaced optimum synchrophase angles for 220 KIAS at 1000 ft & 3000 ft. Note that the 77% longer dashed line passes through a lower-amplitude region than the shorter solid line.

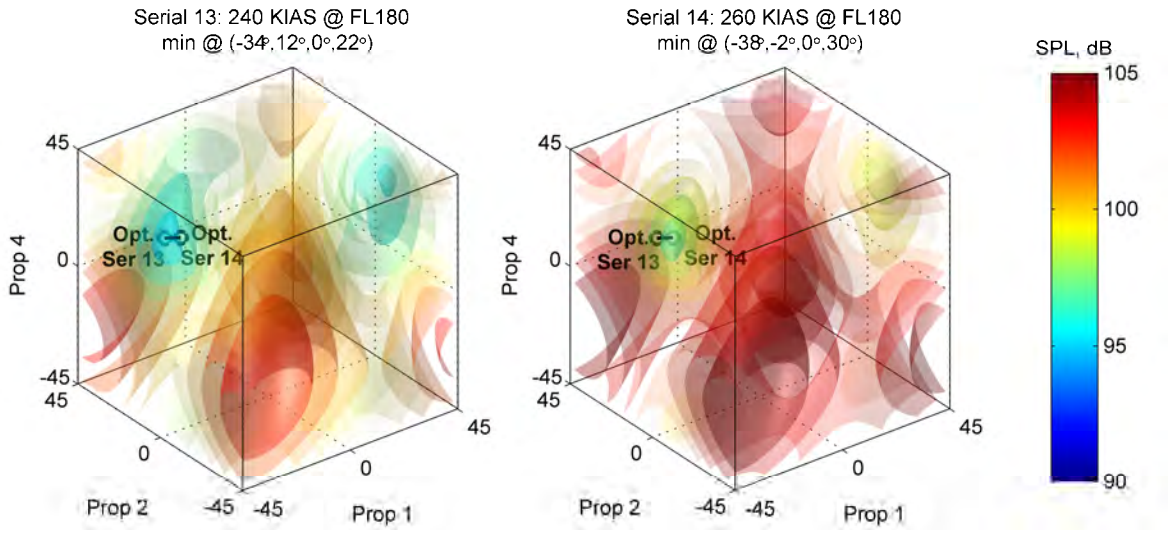

Figure 11.3 AP-3C cost functions (average over all microphones of the SPL at the BPF) showing the shortest line of interpolation between the closely-spaced optimum synchrophase angles for 240 KIAS & 26 KIAS at FL180.

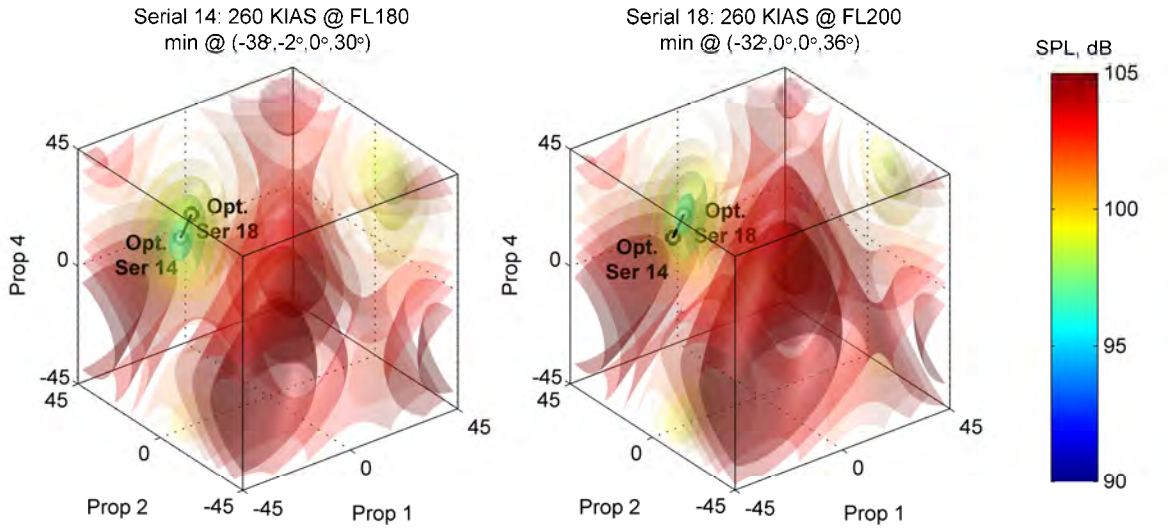

Figure 11.4 AP-3C cost functions (average over all microphones of the SPL at the BPF) showing the shortest line of interpolation between the closely-spaced optimum synchrophase angles for 260 KIAS at FL180 & FL200.

11.1.2. C-130J-30 Control using a Look-up Table

The incremental changes in the C-130J-30 optimum synchrophase angles (for the lowest average over all microphones of the SPL at the BPF) due to the changes in airspeed and altitude that were made during Flight 3 of Trial 1 are summarised in Tables 11.3 and 11.4 respectively. It can be seen that most changes in the optimum synchrophase angles are small (<5°) compared to the overall range of possible angles (60°), and none exceed 20°. Two of the larger changes in optimum angles are shown in Figures 11.5 and 11.6. It can be seen that the shortest line of interpolation would still offer a reasonable compromise for any intermediate flight conditions in these particular cases. For comparison, the lines of interpolation for two smaller incremental angle change cases are shown in Figures 11.7 and 11.8. Here, it can be seen that the shortest lines of interpolation will lead to relatively good estimates of the optimum synchrophase angles for any intermediate flight conditions.

Table 11.3 Incremental changes in the optimum C-130J-30 Trial 1 Flight 3 synchrophase angles (for the lowest average over all microphones of the SPL at the BPF) due to changes in airspeed.

Altitude	Airspeeds (KIAS)	Prop 1	Prop 2	Prop 3	Prop 4
FL210	205 → 220 → 230	−4° −5°	Master	−2° 6°	−3° 7°
FL240	195 → 210 → 220 → 235	−7° −1° −6°		−1° 2° −6°	−4° 2° −8°
FL280	190 → 200 → 205	−3° −1°		0° 1°	−1° 0°
FL320	180 → 185 → 190	−2° −7°		−4° −2°	−4° −8°

Table 11.4 Incremental changes in the optimum C-130J-30 Trial 1 Flight 3 synchrophase angles (for the lowest average over all microphones of the SPL at the BPF) due to changes in altitude.

Airspeed* (KIAS)	Altitudes (ft or FL)	Prop 1	Prop 2	Prop 3	Prop 4
250	6000 ft → 9000 ft → FL150	9° −18°	Master	5° −4°	−2° −6°
190–195	FL240 → FL280 → FL320	−7° −14°		−1° −3°	−5° −11°
200–205	FL210 → FL280	−12°		−3°	−9°
220	FL210 → FL240	−6°		2°	−2°

* Note that, while the indicated airspeed is not changing with altitude, the true airspeed is changing.

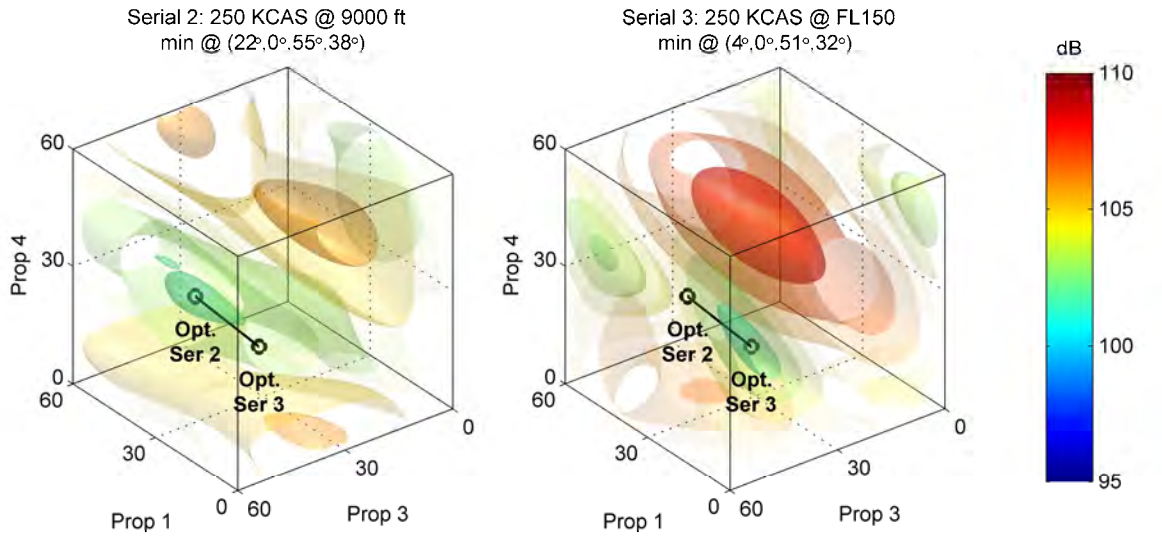

Figure 11.5 C-130J-30 cost functions (average over all microphones of the SPL at the BPF) showing the shortest line of interpolation between the moderately-spaced optimum synchrophase angles for 250 KCAS at 9000 ft and FL150. Note that the plots have been rotated 90° around the vertical axis to give a better view of the optima.

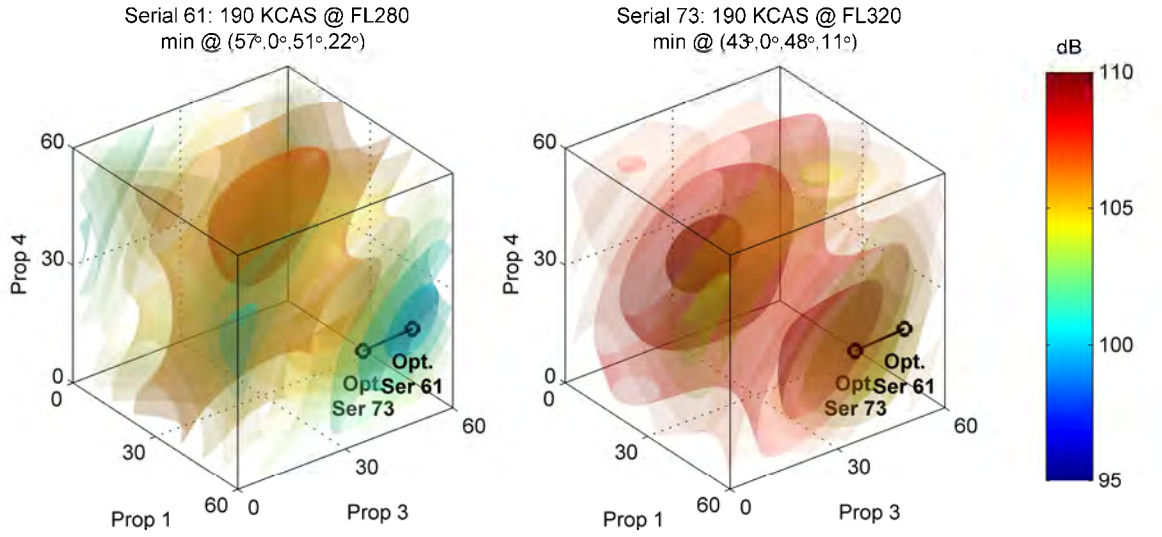

Figure 11.6 C-130J-30 cost functions (average over all microphones of the SPL at the BPF) showing the shortest line of interpolation between the moderately-spaced optimum synchrophase angles for 190 KCAS at FL280 and FL320. Note that the plots have been rotated −90° around the vertical axis to give a better view of the optima.

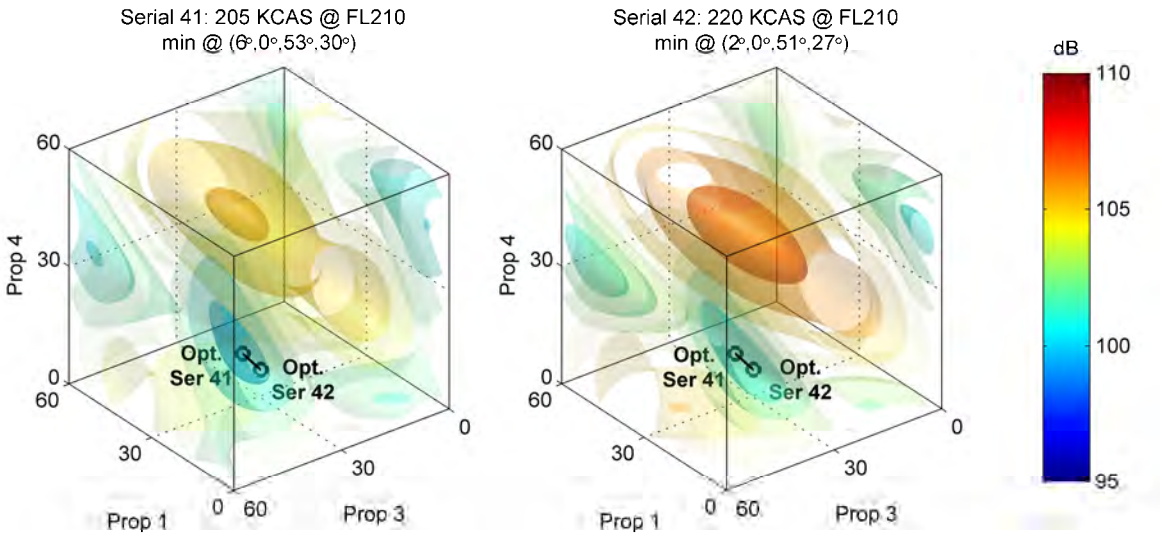

Figure 11.7 C-130J-30 cost functions (average over all microphones of the SPL at the BPF) showing the shortest line of interpolation between the closely-spaced optimum synchrophase angles for 205 KCAS and 220 KCAS at FL210. Note that the plots have been rotated −90° around the vertical axis to give a better view of the optima.

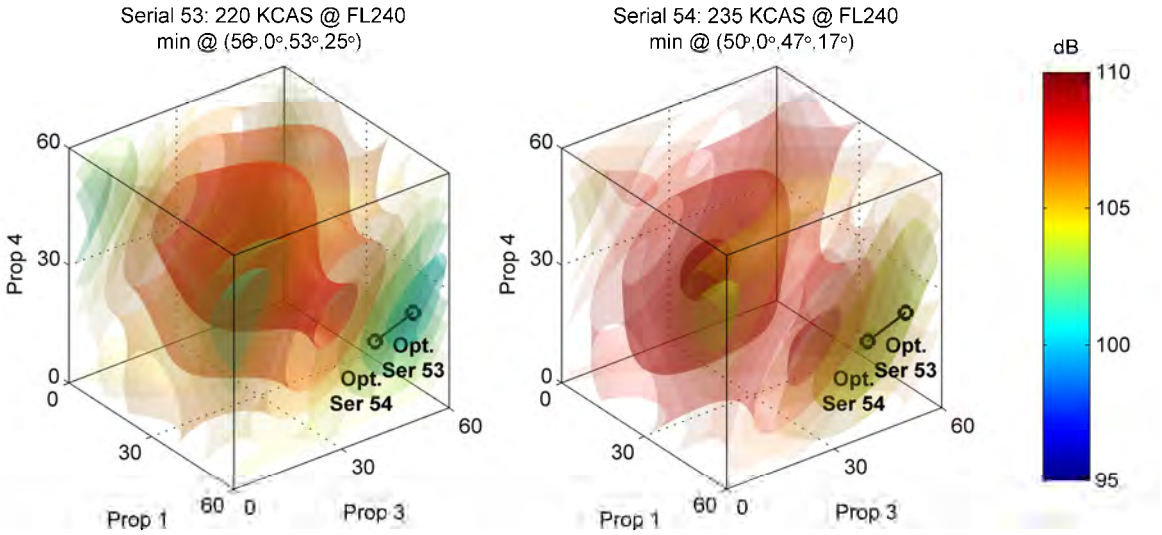

Figure 11.8 C-130J-30 cost functions (average over all microphones of the SPL at the BPF) showing the shortest line of interpolation between the closely-spaced optimum synchrophase angles for 220 KCAS and 235 KCAS at FL240. Note that the plots have been rotated −90° around the vertical axis to give a better view of the optima.

11.2. Active Control using Error Sensors

For an active control system to be implemented using microphone or accelerometer error sensors, four questions need to be answered:

a) What type of sensors should be used?
b) How many sensors are required?
c) Where should the sensors be positioned?
d) What control algorithm should be used?

In the investigation so far, the answers to (a) – (c) have been:

a) to use sensors that directly measure the quantity being minimised,
b) to use as many sensors as possible, and
c) to distribute them as widely as possible.

The previous analysis in Chapter 10 has shown that (a) is an appropriate strategy to maintain. However, it is now possible to look at how reducing the number of sensors will affect the results. This has been done here by examining two different strategies for ranking the relative importance of the sensor positions used (§11.2.1); and by observing the effects on the results as sensors are progressively removed from the optimisation process in these rank orders (§11.2.2). Active control algorithms are considered in §11.2.3.

11.2.1. Sensor Position Ranking Strategies

Two different ranking strategies have been considered:

a) The first is based on the potential for the propeller BPF signatures at each sensor position to cancel each other out; i.e., by the ability of the three weaker signatures to cancel out the strongest signature. Essentially, this assigns more importance to the sensor positions where there is more ‘control’ over the noise or vibration.
b) The second is simply based on the maximum BPF amplitude at each position; i.e., it concentrates on the high-amplitude sensor positions where the noise or vibration reductions will have the most impact.

These strategies have been implemented using rank values calculated from Equations (11.1) and (11.2) respectively, where $\hat{S}_{p,k}$ is the BPF signature of propeller p at location k:

$$R_{cancel} = \sum_{p=1}^{P} \left| \hat{S}_{p,k} \right| - \max\left(\left| \hat{S}_{p,k} \right| \right) \tag{11.1}$$

$$R_{\max} = \sum_{p=1}^{P} \left| \hat{S}_{p,k} \right| \tag{11.2}$$

11.2.2. Effect of Removing Sensors

The results for each aircraft are detailed in §11.2.2.1 and §11.2.2.2 respectively. For each ranking strategy, the results show:

a) the average rank of each sensor across the considered flight condition serials, and
b) the effect on two cost functions (the average over all microphones of the SPL at the BPF, and the average over all accelerometers of the floor vibration at the BPF)

as the sensors are removed in the average rank order (from least to most important).

Note that the average rank has been determined by finding the rank order for each serial, and then averaging the orders across the serials, not by averaging the rank values from Equations (11.1) and (11.2) across the serials and then sorting them into a descending order. Also note that the cost functions are measured using all available microphones (or accelerometers), not just those used in the optimisation process.

11.2.2.1. AP-3C Results

It can be seen in Figures 11.9 and 11.10 that the two ranking strategies produce almost identical results. For the ten most highly ranked microphones (i.e., 1 to 10), only the orders of the second and third, and fourth and fifth, ranked microphones are reversed between the two cases. The accelerometer ranks are also very close, with the orders of the individual accelerometers differing by at most two rank positions.

The most highly ranked microphones are all in the forward half of the fuselage within a region approximately one propeller diameter fore and aft of the plane of the propellers. Not unexpectedly, this corresponds with the previously observed dominance of the propeller tones in this area (§7.1). The asymmetry of the sensor ranking results also matches the asymmetry of the measured BPF amplitudes (§10.2).

Most significantly, it is evident that the predicted average sound pressure levels at the BPF can be maintained within approximately 2 dB of the optimum across all 24 different flight conditions using as few as 3 to 6 microphones instead of all 21 (Figures 11.9 and 11.10). This very interesting result indicates that it is not necessary to have sensors distributed throughout the entire length of the cabin in order to achieve a good global outcome with this particular optimisation criterion. Controlling the average sound pressure of a few well-placed microphones within the zone of the propeller plane will be sufficient. This result can also be demonstrated by plotting the low-amplitude regions of the average sound pressure level at the BPF, as the number of microphones included in the average is progressively increased from one to six. This is shown for Serial 17 (240 KIAS at FL200) in Figures Figure 11.11 to Figure 11.12 for the two different rank orders respectively. While the shape of the contours outlining the low-amplitude regions can be quite extensive and convoluted for one microphone, not unlike the theoretical example shown in Figure 3.5, they converge well to a region very close to the optimum using all 21 microphones that was previously shown in Figure 10.3.

11.2.2.2. C-130J-30 Results

The C-130J-30 results are shown in Figures 11.13 to Figure 11.22. Note that Serial 10 was the only serial where valid propeller signatures were available in Trial 2; the synchrophase angle sets were not sufficiently spaced in the other serials.

For Trial 1 Flights 1 and 2 (cargo configuration) (Figures 11.13 to 11.16), it can be seen that there is little difference between the two ranking strategies for the accelerometers. The top six accelerometers are always in the front two rows (i.e., Tie-Down Rings 7 & 12) in each case. The only accelerometers that change order between the two strategies within these six are the 5^{th} and 6^{th} ranked sensors in Flight 1. These six accelerometers are all that are needed to maintain the average floor (vertical) acceleration within approximately 2 dB of the optimum across the flight conditions considered here. However, the accelerometer at the left rear of the cargo floor (B32) also receives a relatively high ranking (7^{th} to 9^{th}), and

could be worth including in the optimisation process in order to achieve a slightly better result.

For Trial 1 Flight 3 (troop configuration) (Figures 11.17 and 11.18), it can be seen that the highly-ranked microphones are nearly all forward of the propeller plane. This is slightly dissimilar to the AP-3C results, where they are spread fore and aft of the propeller plane, and this may be due to the swept-blade design of the C-130J propeller. However, like the AP-3C, this high-ranked region corresponds with the previously observed dominance of the propeller tones in this area. While there is slightly more variation between the two ranking strategies from the 4th sensor onwards, the highly-ranked microphones exhibit an almost diagonal asymmetric pattern running from the propeller plane on the port side forward and across to the front starboard side of the cabin. Only three microphones are needed to maintain the average sound pressure level at the BPF within 2 dB of the optimum across all the flight conditions considered here, while using 4 to 6 microphones improves the result to within 1 dB of the optimum. It should be noted, however, that the 3rd ranked microphone is in a position that may be difficult to use when the seats are removed. A possible solution to this might be to implement a virtual sensor at this location using a small additional number of microphones around the periphery of the fuselage (Moreau et al., 2008), although this is beyond the scope of this investigation. The microphone at the front centre of the main cabin (ranked 5th and 6th in each strategy respectively) is also on the removable seat stanchions, but it could probably be moved to the forward bulkhead with little impact on the results.

The results for Trial 2 Serial 10 (Figures 11.19 and 11.20) are very similar to the results for Trial 1. The top-ranked accelerometers are again in the first two rows (i.e., Tie-Down Rings 7 & 12). The top six microphones exhibit a little more ranking variation, which can be attributed to the aircraft-to-aircraft variations previously described (§10.3.6). However, it is not difficult to arrive at a compromise ranking that gives low average sound pressure levels for both trials with only small changes to the order of the top six microphones, as shown in Figures 11.21 and 11.22.

Plots of the average sound pressure level at the BPF, as the number of microphones included in the average is progressively increased from one to six, are shown for Serial 10 (220 KCAS at FL240) in Figures Figure 11.23 and Figure 11.24 for the two different trials respectively. Like the AP-3C results (§11.2.2), the shape of the contours outlining the low-amplitude regions are quite convoluted for one microphone, but they converge to a region close to the optimum using all microphones that was previously shown in Figure 10.48. This again demonstrates that controlling the average sound pressure of a few well-placed microphones within a relatively small region of the cabin (in this case forward of the propeller plane) will be sufficient to maintain a good global outcome for this optimisation criterion. It is also reassuring to observe that the contours for the highest-ranked microphone are virtually identical for the two trials, despite the aforementioned aircraft-to-aircraft differences. The contours for 3 to 6 microphones retain very similar shapes between the trials, with the minima falling in slightly different positions within these contours, and indicate that the aircraft-to-aircraft differences may not be as significant as first thought.

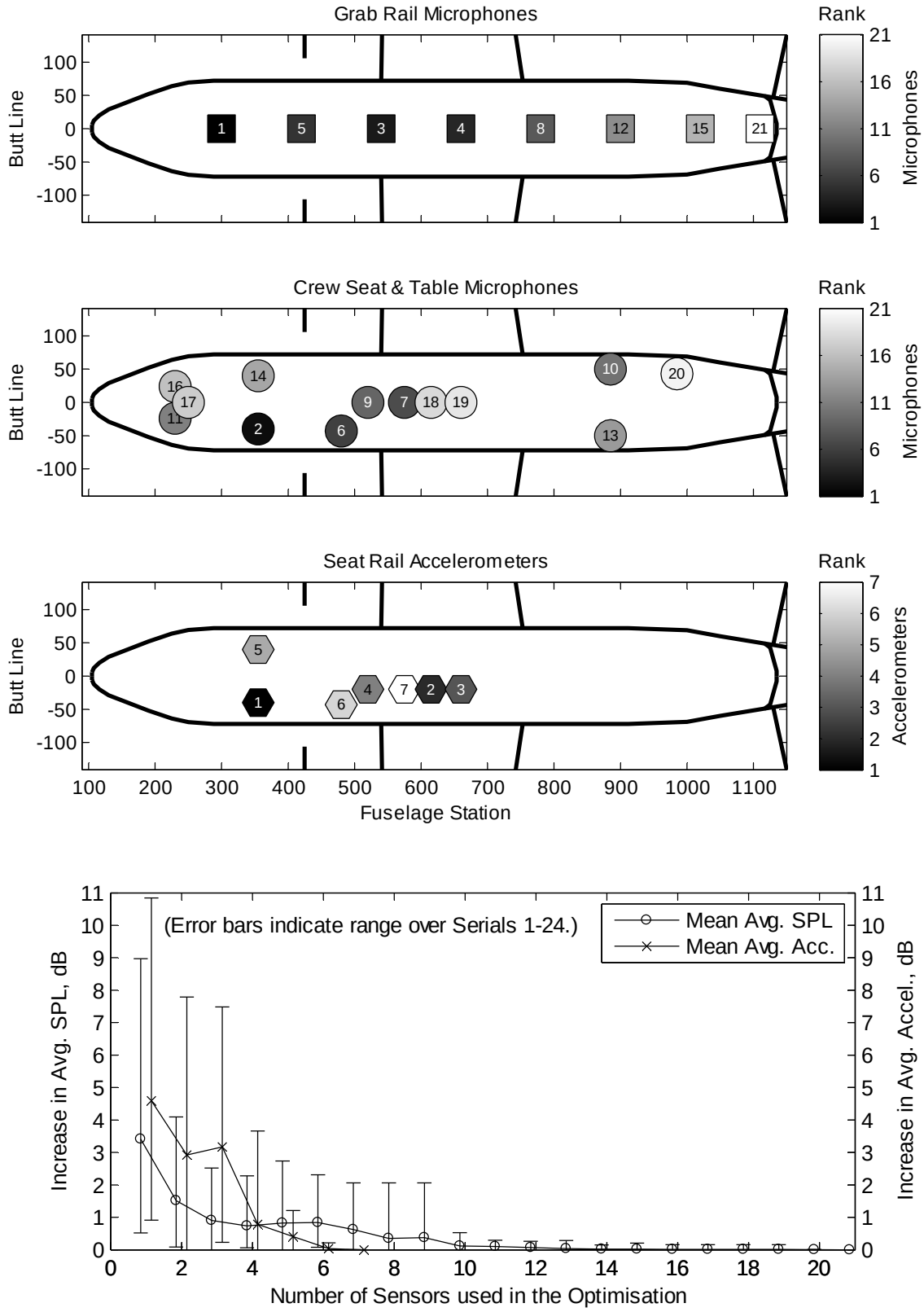

Figure 11.9 AP-3C average microphone and accelerometer ranks (highest rank = 1) for Serials 1–24 based on the potential for signature cancellation at the BPF (top), and the effects of reducing the number of sensors used in the optimisation process based on these ranks (bottom).

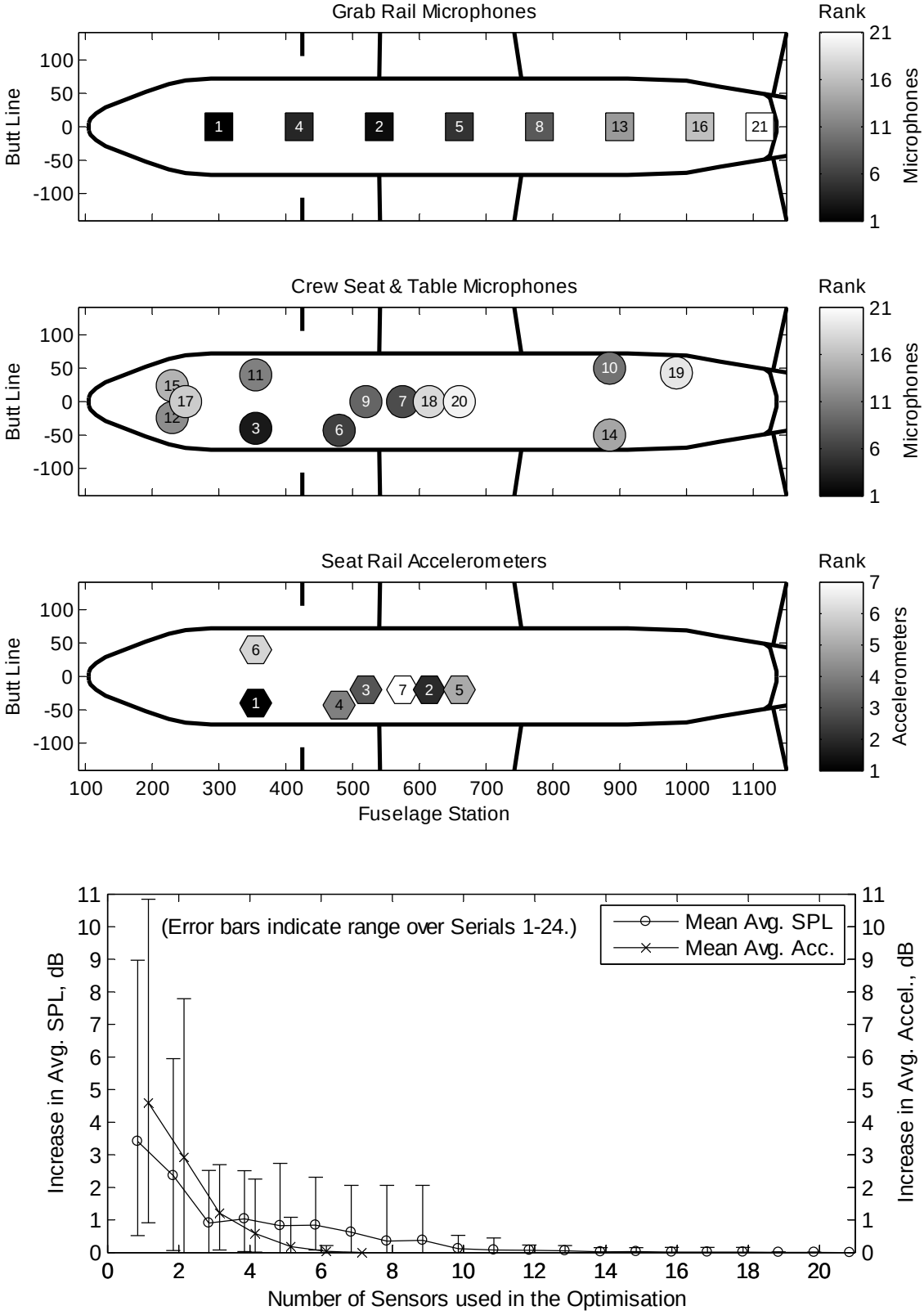

Figure 11.10 AP-3C average microphone and accelerometer ranks (highest rank = 1) for Serials 1–24 based on the maximum amplitudes at the BPF (top), and the effects of reducing the number of sensors used in the optimisation process based on these ranks (bottom).

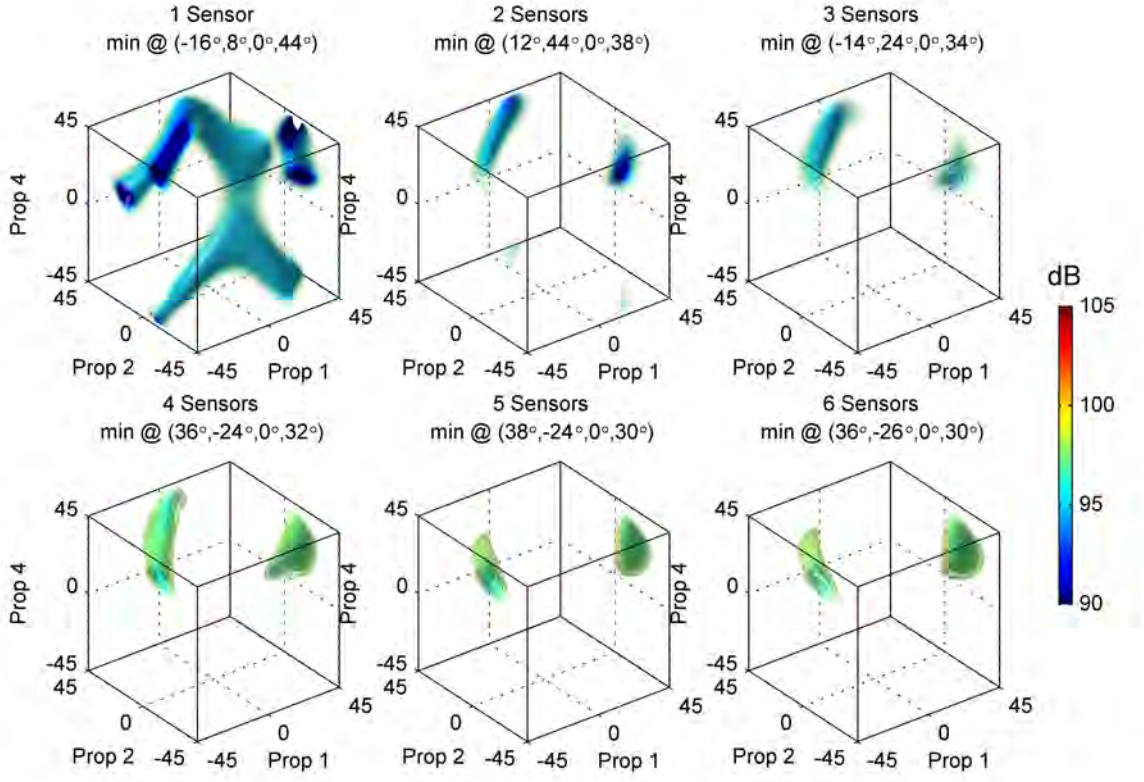

Figure 11.11 AP-3C predicted average over 1 to 6 most highly ranked microphones of the SPL at the BPF for Serial 17 (240 KIAS at FL200) – signature cancellation order.

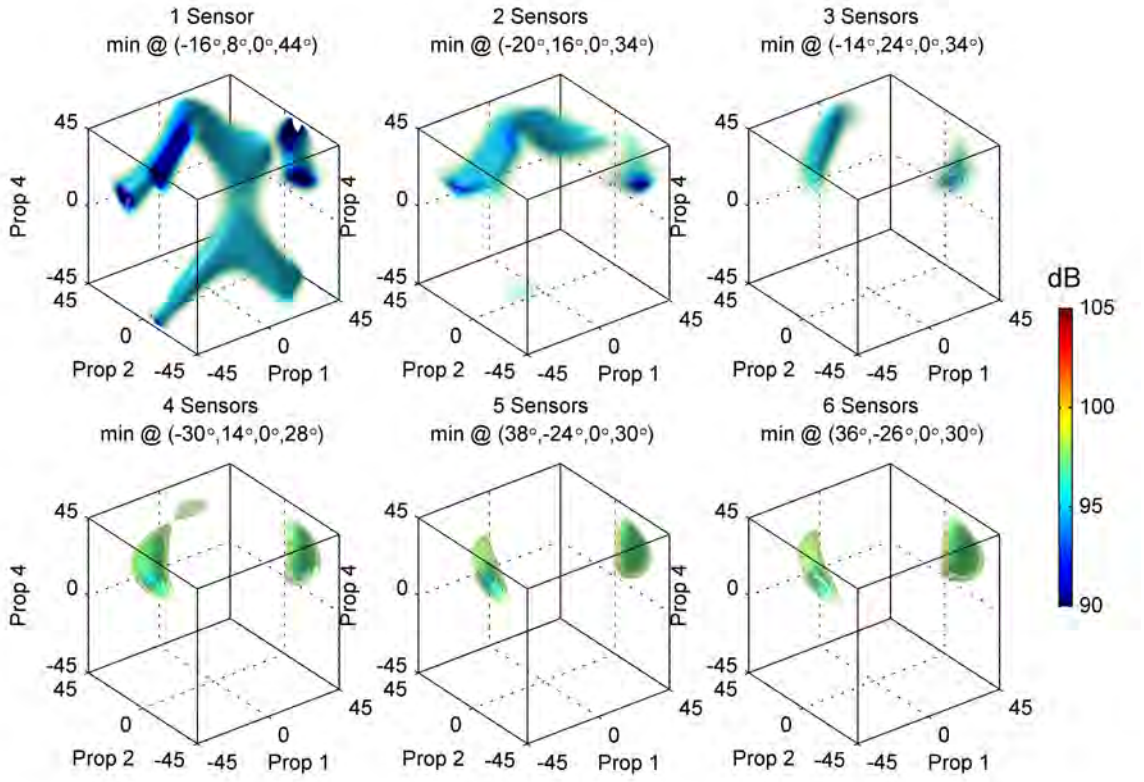

Figure 11.12 AP-3C predicted average over 1 to 6 most highly ranked microphones of the SPL at the BPF for Serial 17 (240 KIAS at FL200) – maximum sound pressure level order.

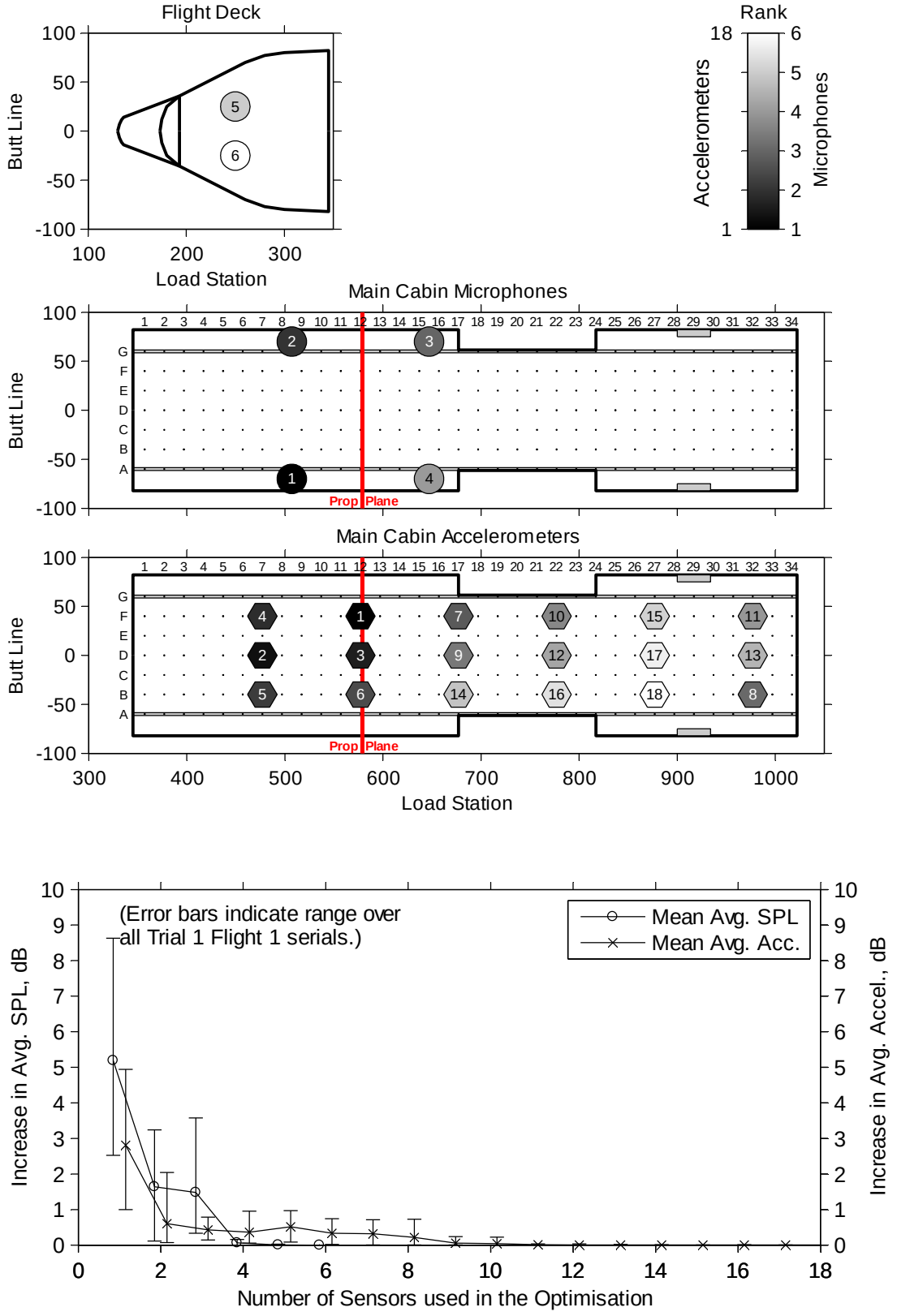

Figure 11.13 C-130J-30 average microphone and accelerometer ranks (highest rank = 1) for all Trial 1 Flight 1 serials based on the potential for signature cancellation at the BPF (top), and the effects of reducing the number of sensors used in the optimisation process based on these ranks (bottom).

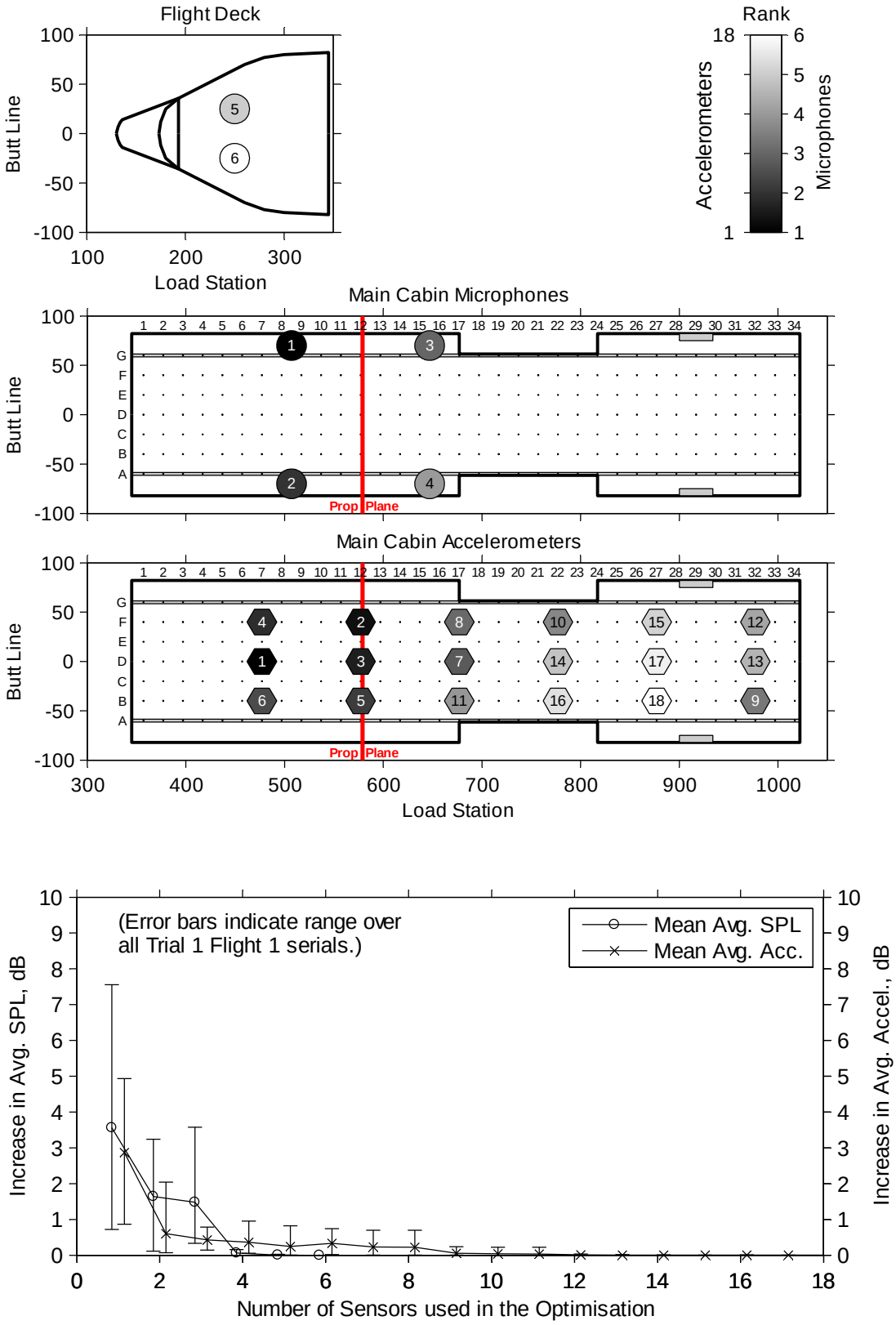

Figure 11.14 C-130J-30 average microphone and accelerometer ranks (highest rank = 1) for all Trial 1 Flight 1 serials based on the maximum amplitudes at the BPF (top), and the effects of reducing the number of sensors used in the optimisation process based on these ranks (bottom).

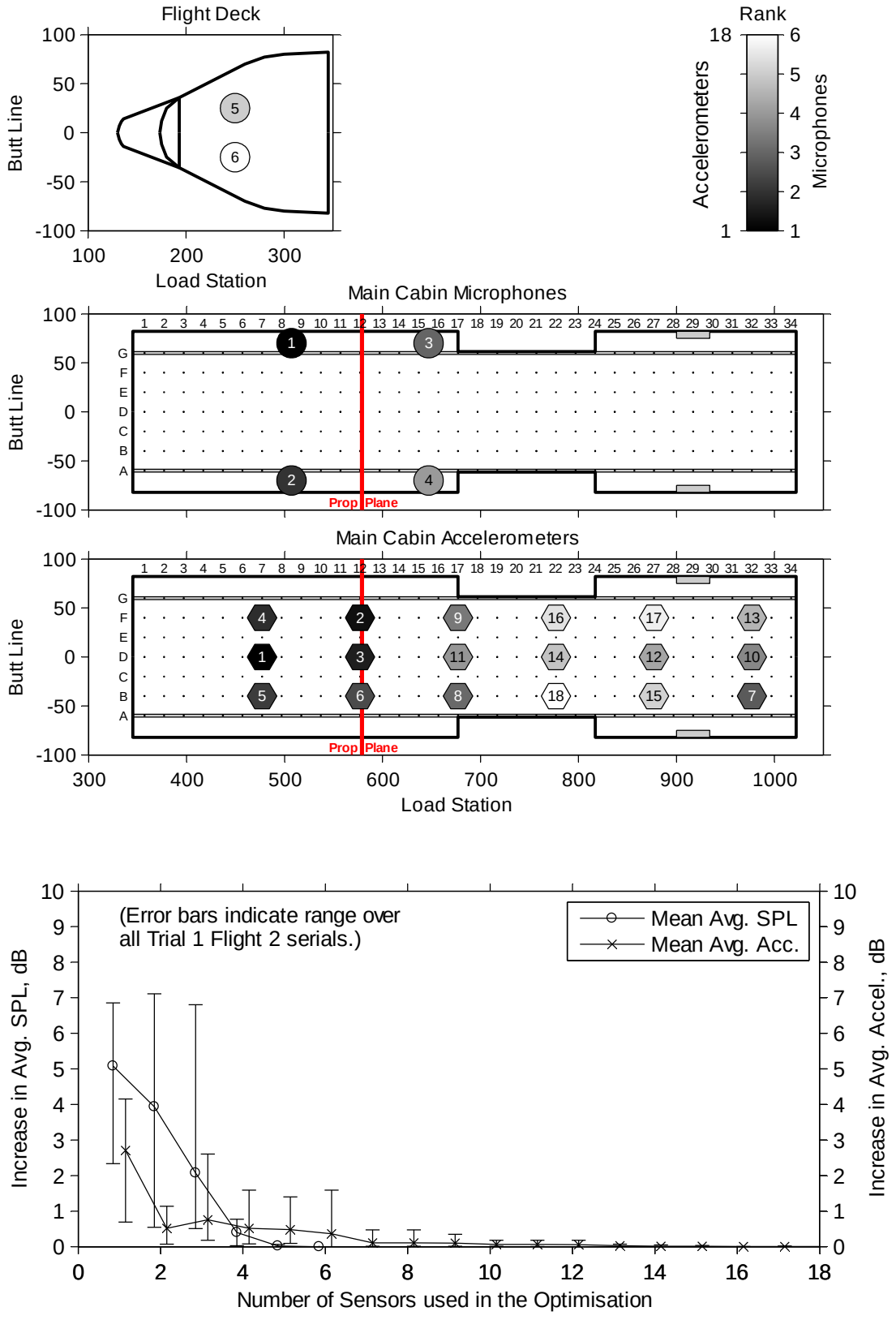

Figure 11.15 C-130J-30 average microphone and accelerometer ranks (highest rank = 1) for all Trial 1 Flight 2 serials based on the potential for signature cancellation at the BPF (top), and the effects of reducing the number of sensors used in the optimisation process based on these ranks (bottom).

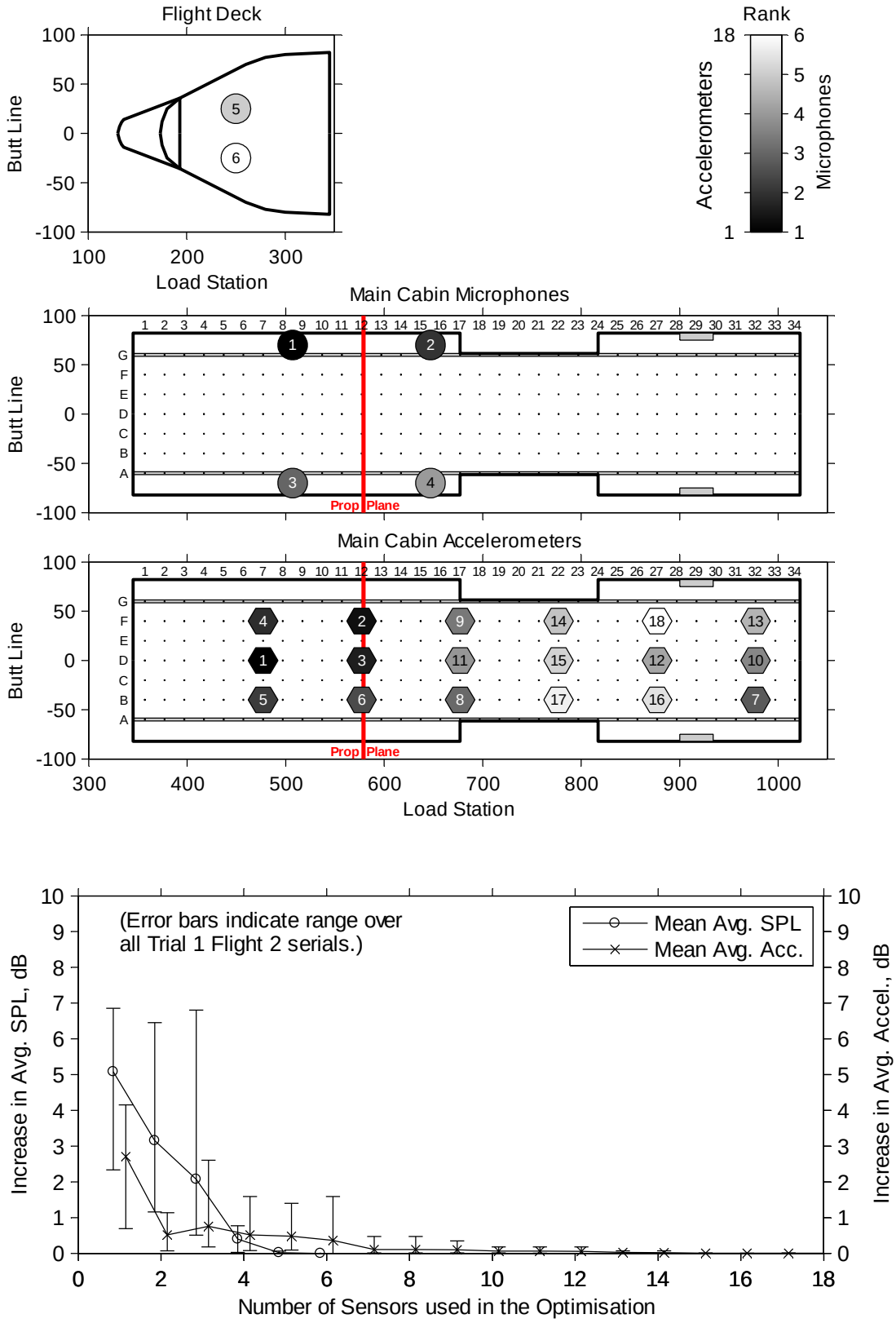

Figure 11.16 C-130J-30 average microphone and accelerometer ranks (highest rank = 1) for all Trial 1 Flight 2 serials based on the maximum amplitudes at the BPF (top), and the effects of reducing the number of sensors used in the optimisation process based on these ranks (bottom).

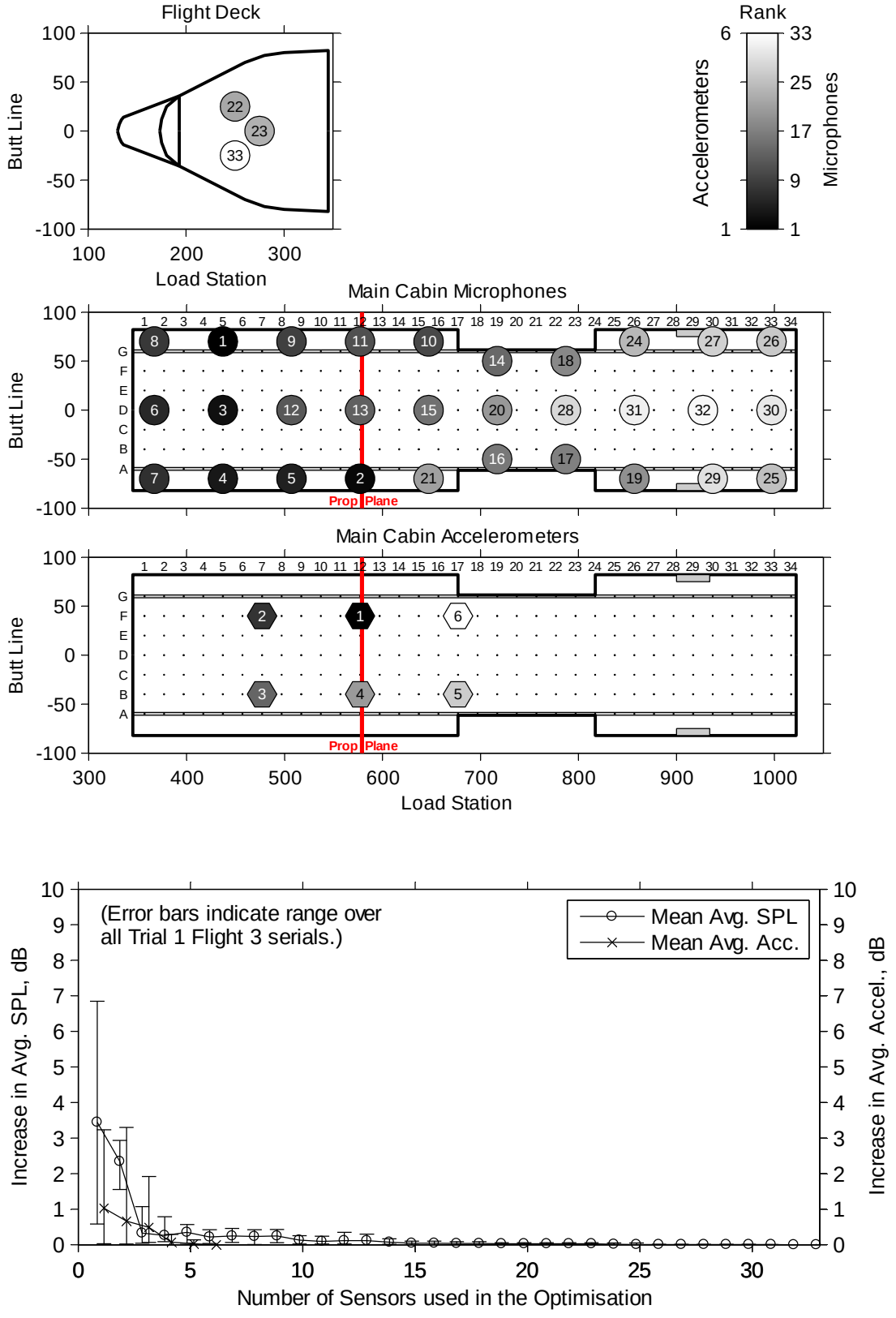

Figure 11.17 C-130J-30 average microphone and accelerometer ranks (highest rank = 1) for all Trial 1 Flight 3 serials based on the potential for signature cancellation at the BPF (top), and the effects of reducing the number of sensors used in the optimisation process based on these ranks (bottom).

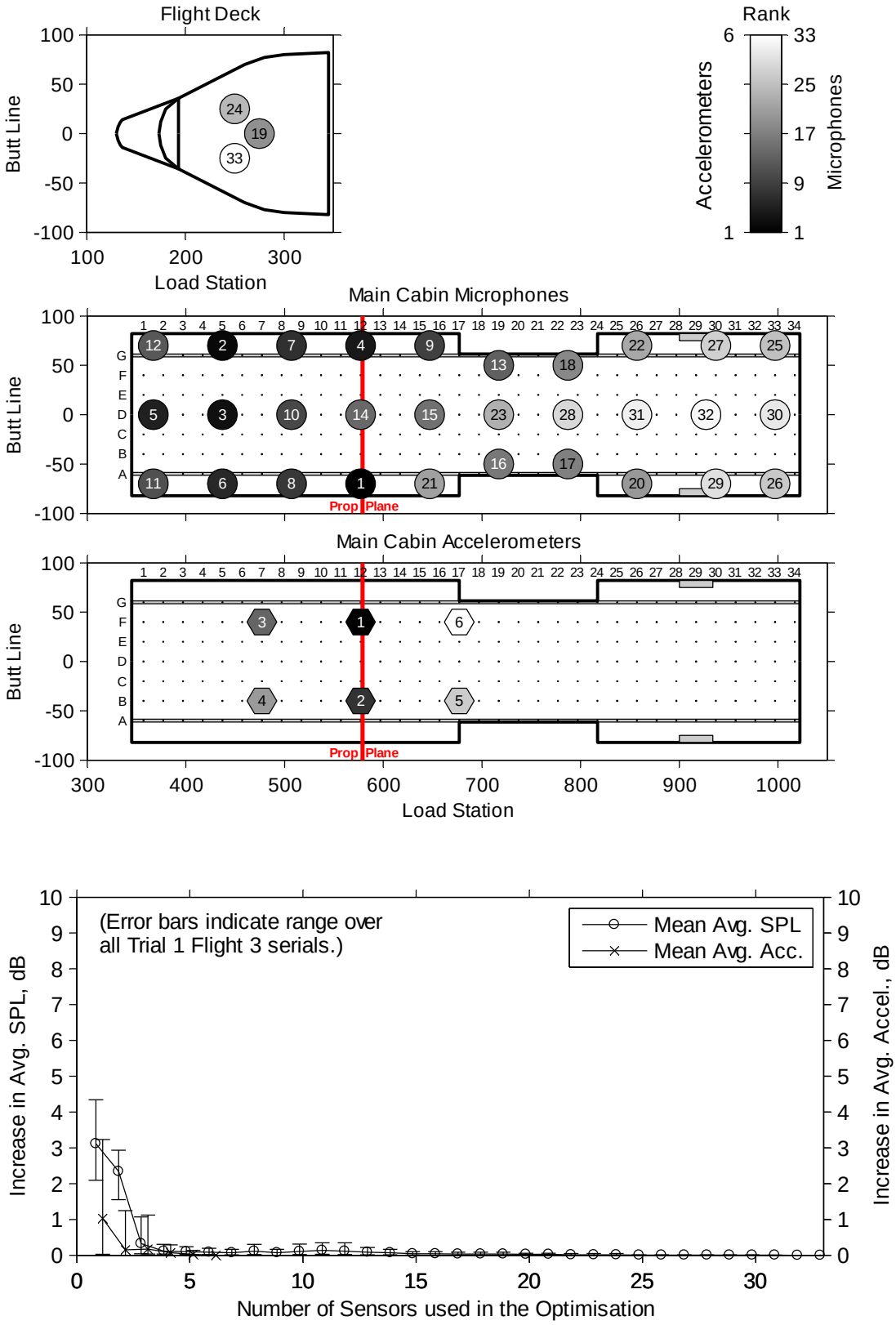

Figure 11.18 C-130J-30 average microphone and accelerometer ranks (highest rank = 1) for all Trial 1 Flight 3 serials based on the maximum amplitudes at the BPF (top), and the effects of reducing the number of sensors used in the optimisation process based on these ranks (bottom).

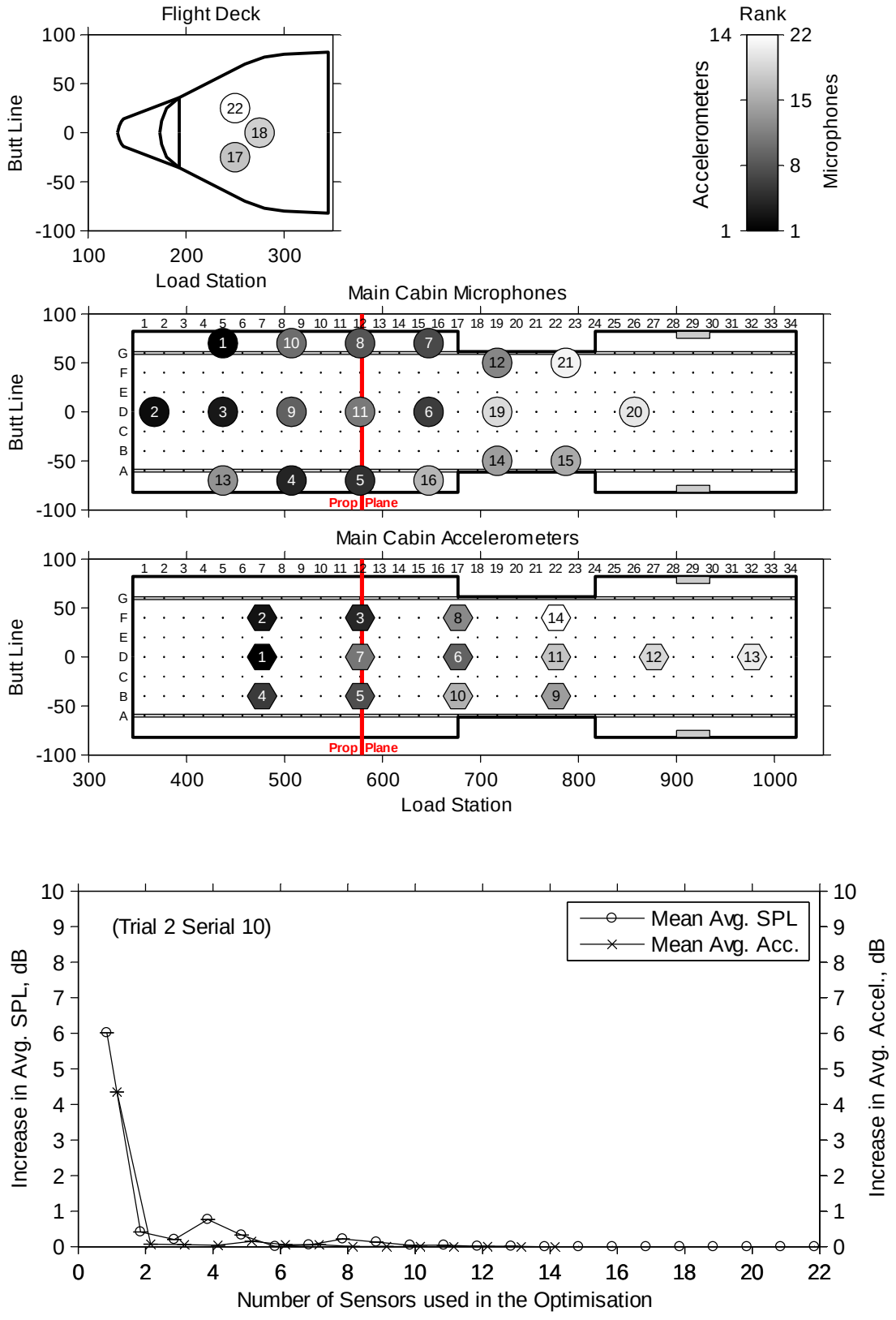

Figure 11.19 C-130J-30 microphone and accelerometer ranks (highest rank = 1) for Trial 2 Serial 10 based on the potential for signature cancellation at the BPF (top), and the effects of reducing the number of sensors used in the optimisation process based on these ranks (bottom).

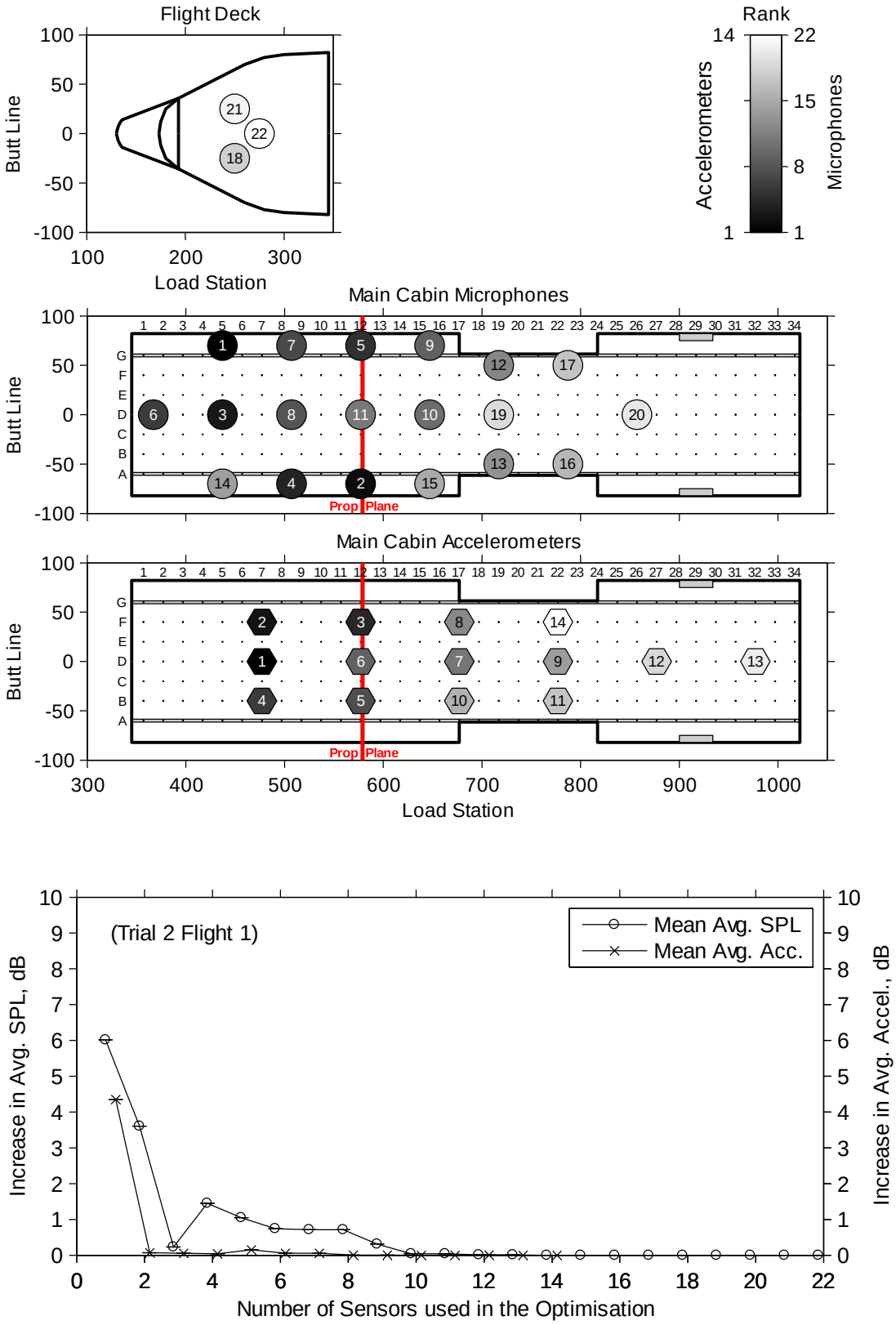

Figure 11.20 C-130J-30 microphone and accelerometer ranks (highest rank = 1) for Trial 2 Serial 10 based on the maximum amplitudes at the BPF (top), and the effects of reducing the number of sensors used in the optimisation process based on these ranks (bottom).

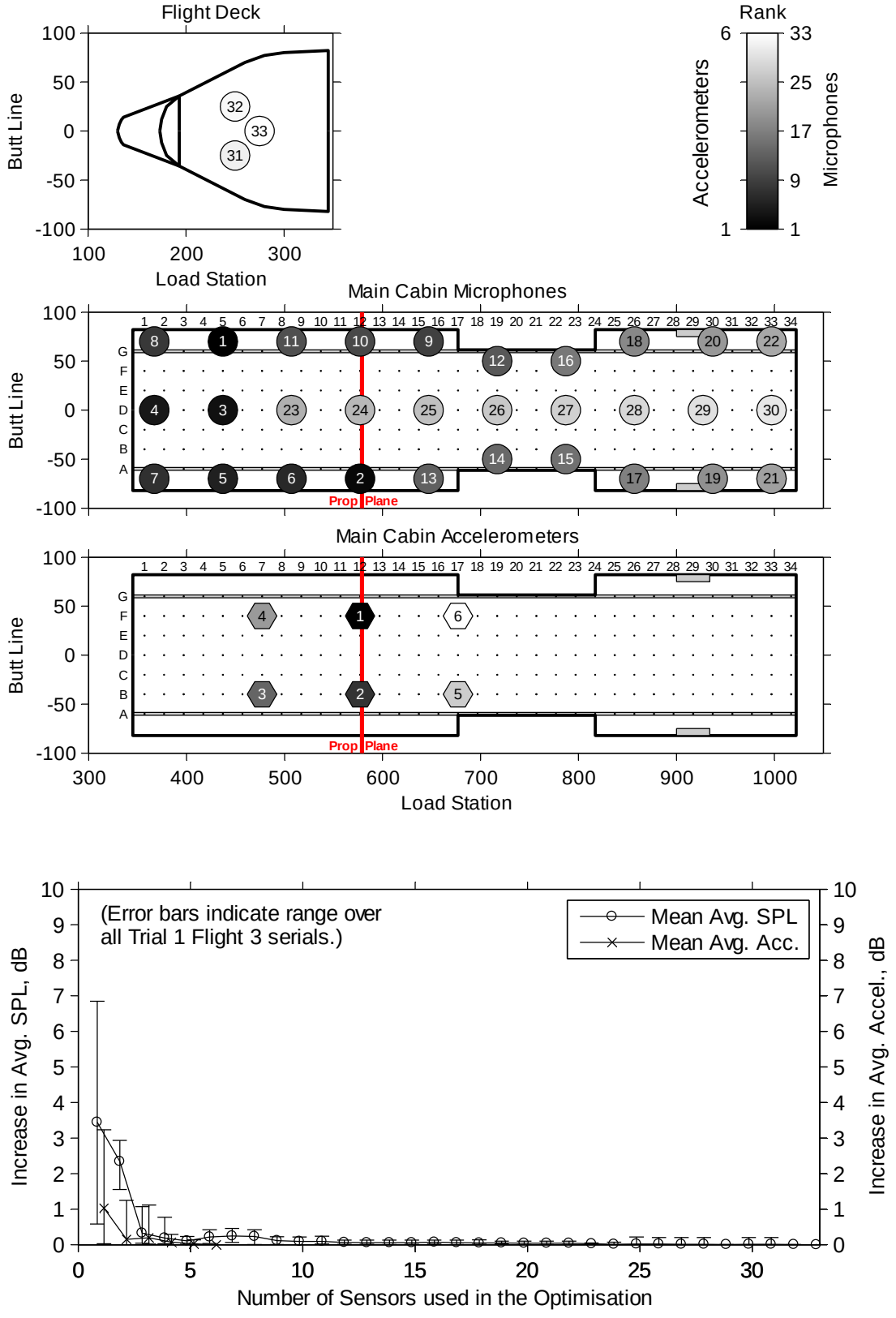

Figure 11.21 C-130J-30 microphone and accelerometer ranks (highest rank = 1) for all Trial 1 Flight 3 serials based on a compromise sensor ranking for Trials 1 & 2 (top), and the effects of reducing the number of sensors used in the optimisation process based on these ranks (bottom).

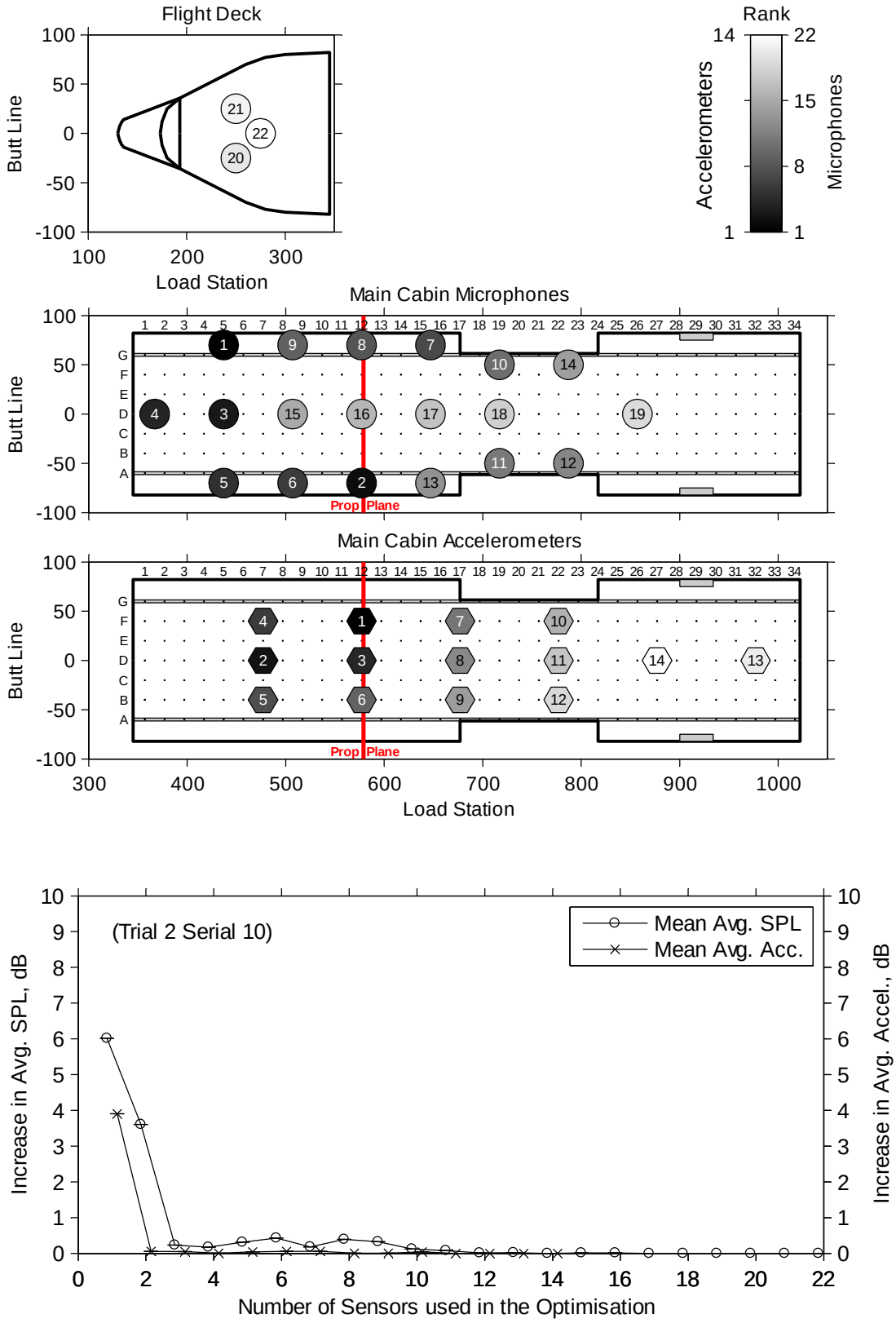

Figure 11.22 C-130J-30 microphone and accelerometer ranks (highest rank = 1) for Trial 2 Serial 10 based on a compromise sensor ranking for Trials 1 & 2 (top), and the effects of reducing the number of sensors used in the optimisation process based on these ranks (bottom).

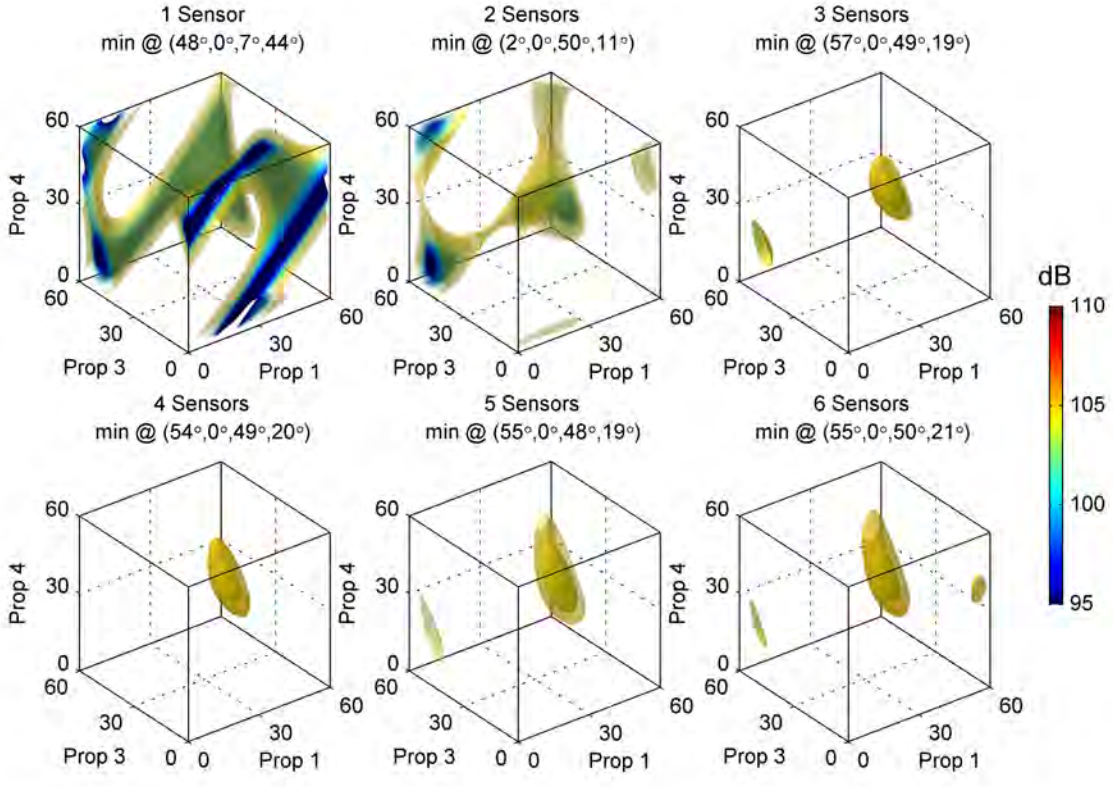

Figure 11.23 C-130J-30 predicted average over 1 to 6 most highly ranked microphones of the SPL at the BPF for Trial 1 Serial 10 (220 KCAS at FL240) – Trial 1 & 2 compromise microphone order.

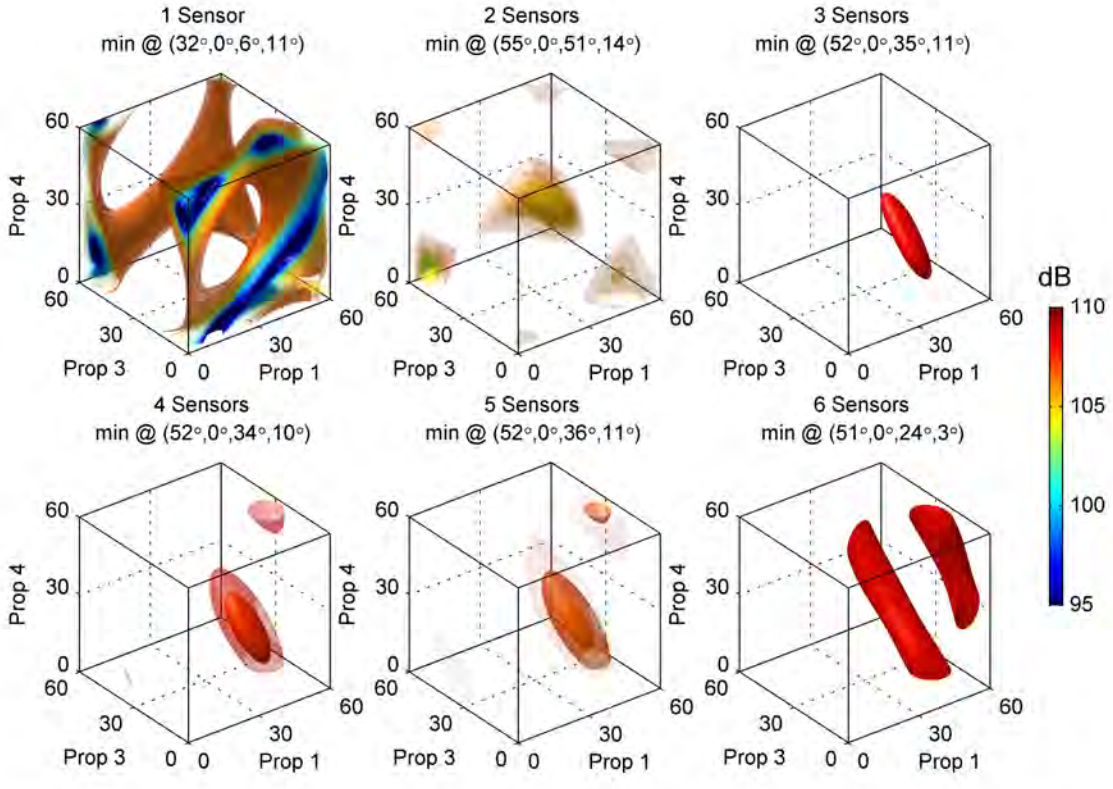

Figure 11.24 C-130J-30 predicted average over 1 to 6 most highly ranked microphones of the SPL at the BPF for Trial 2 Serial 10 (220 KCAS at FL240) – Trial 1 & 2 compromise microphone order.

11.2.3. Active Control Algorithms

As discussed at the start of this chapter, a propeller synchrophasing system utilising an active control algorithm with a number of permanently mounted error sensors distributed throughout the aircraft cabin should be more capable of adapting to any factors that might affect the optimum synchrophase angles than one using a look-up table. However, such a system will be more complex and require sensors in potentially awkward places in the cabin. It is beyond the scope of this investigation to actually develop a fully-functional active-control synchrophasing system. Rather, what follows is a discussion of what is required, and how this might be achieved.

In the analysis presented in Chapter 10, the emphasis was placed on obtaining and visualising the average sound pressure or average floor vibration levels at the BPF over the full range of propeller synchrophase angles; or, in other words, by visualising the entire cost function of the control problem. This was done by identifying the propeller signatures, calculating the individual sensor amplitudes for a large number of synchrophase angle combinations, and then averaging them over all the sensors, as outlined in Figure 11.25. Such an approach could be implemented directly in an active control algorithm. However, it would be computationally intensive and probably less responsive to factors affecting the optimum synchrophase angles (due to the time required to recompute a solution) than other methods.

The complexity of an active control system can be reduced by minimising the number of frequencies incorporated into the cost function. It was shown in §9.2 that the measurement variability was simply too large to consistently predict the amplitudes at the harmonics of the BPF in all but a few sensor positions. One of the underlying reasons for this is that perturbations in the synchrophase angles cause progressively larger phase deviations at the harmonics of the BPF, as discussed in §8.4.3. Unfortunately, as well as limiting the ability to predict the noise or vibration at these frequencies, these phase deviations will also limit the amount of control that can be achieved at these frequencies; i.e., an active control algorithm cannot compensate for the inherent limitations in the ability of the synchrophasing system to maintain the desired synchrophase angles. The multi-dimensional nature of the cost function only accentuates this problem; i.e., in a four-engined aircraft, there are four independent sources of phase deviations. Given the nature of the problem, the typical characteristics of the cabin environment (where the amplitudes at the harmonics get progressively smaller as the frequency increases), and the previous results of this investigation (§9.2), the incorporation of the BPF harmonics into the cost function would seem unlikely to produce further significant reductions in the cabin noise and vibration unless the phase deviations at the harmonic frequencies can be improved beyond current levels (i.e., reduced below ± 24°). Another potential reason not to control the harmonics of the BPF is that they have shorter wavelengths, which could lead to more local control around the sensors and higher amplitudes away from the sensor positions.

The complexity of the active control system can also be reduced by minimising and the number of error sensors used in the cost function. It was previously shown in §11.2.2 that the number of error sensors can be reduced to between 3 to 6 with little impact (< 2 dB) on the achievable reduction in the cabin-wide average sound pressure or vibration at the BPF. Plots of cost functions using reduced numbers of sensors are also shown in Figures 11.11 and 11.12 for the AP-3C, and Figures 11.23 and 11.24 for the C-130J-30. In all cases, it can be seen that the contours are smooth and become relatively well behaved, albeit slightly elongated, once three or more sensors are used. It is only when fewer sensors are used that the functions are seen to bifurcate or abruptly change direction. This result is particularly useful as it means that no special algorithmic approach needs to be taken; i.e.,

a typical gradient-descent algorithm can be used with a relatively high level of confidence in the outcome as long as three or more sensors are used. It is also consistent with whether the least squares solution to finding the minima of these cost functions is under-determined ($L < M$), fully-determined ($L = M$), or over-determined ($L > M$), where L is the number of sensors and M is the number of secondary sources (Nelson and Elliott, 1992). In this case, since there are three slave propellers, $M = 3$, and it makes sense to use at least three sensors to construct the cost function.

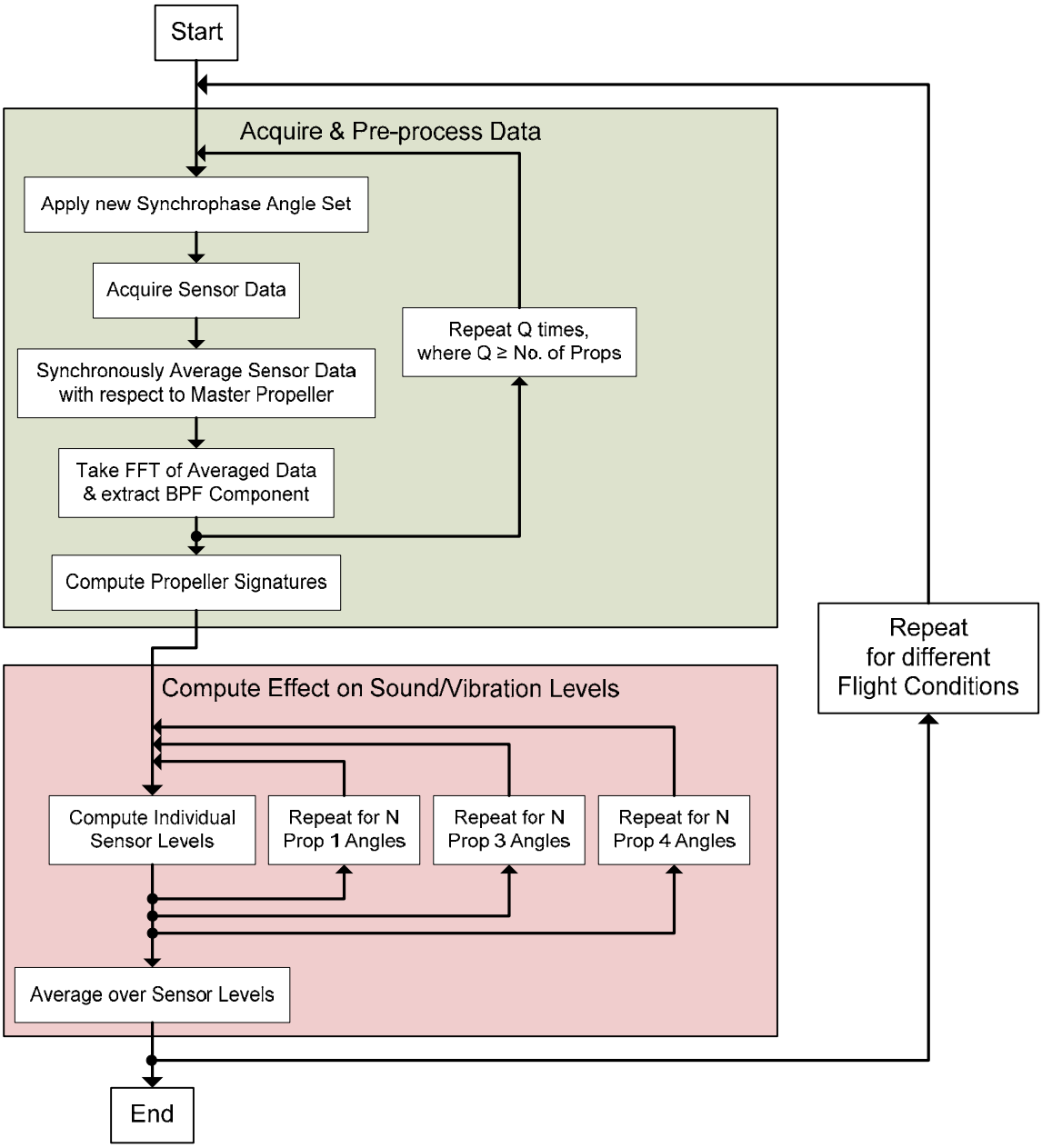

Figure 11.25 Block diagram of the computation process used in the preceding analysis.

A block diagram of the required control system is shown in Figure 11.26, where the adaptive control is shown as a simple extension to the existing synchrophasing system. The figure highlights the three main sources of unreferenced disturbances that the system must be able to manage. The first, and most significant, source is a result of perturbations in the propeller synchrophase angles caused by turbulence or other factors. This type of disturbance will be controlled by the existing synchrophasing system, and should be within acceptable limits at the BPF. However, the performance of the existing synchrophaser may need to be enhanced (i.e., its angle tolerances tightened), if modelling errors induced by

these perturbations reduce the performance of the active control system. The second source of unreferenced disturbance is noise from other external sources such as the engine and fuselage boundary layer. The last is noise from internal sources such as the avionic system or accessories including the air-conditioning. These last two types of unreferenced noise should be significantly lower in amplitude than the propeller noise at the BPF and, because they are not synchronous with the propeller harmonic noise, could be further minimised by synchronously averaging the sensor (error) signals with respect to a reference tachometer signal from the master propeller.

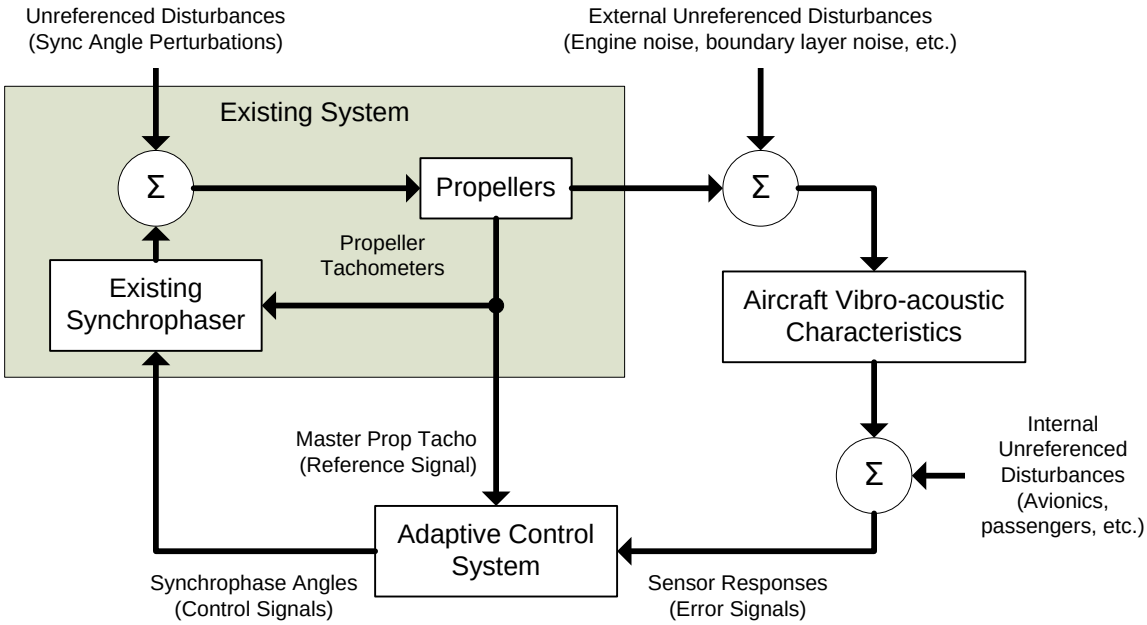

Figure 11.26 Block diagram of an adaptive synchrophase angle control system.

In the absence of a fully-computed cost function, which will be time consuming and computationally expensive to generate, an iterative gradient-descent approach must be taken. There are essentially two ways this can be done: (a) using a trial-and-error method where the synchrophase angle of one slave propeller is adjusted to achieve a minimum in the cost function, and then this is repeated for the next propeller, and so on in a repetitive manner until the global minimum is finally approached; or (b) using a more sophisticated algorithm that uses an estimate of the gradient to adjust the synchrophase angles of all slave propellers simultaneously.

The main advantage of the trial-and-error method is that it is very simple to implement. The transfer functions between the control and the error signals (i.e., the propeller signatures) do not need to be estimated. However, the major disadvantage is a slower convergence on the global minimum. This is because the synchrophase angle value that minimises the cost function for one propeller will change when another propeller is adjusted. Hence, the process of finding the minimum must be repeated multiple times for each propeller in turn in order to get close to the true global minimum. This slower rate of convergence may prevent the system actually reaching the global minimum under conditions where the vibro-acoustic response of the aircraft is not sufficiently stationary; e.g., when the flight conditions are changing too rapidly. Nevertheless, the method may work well under many conditions, particularly if the signature from one slave propeller is consistently larger than the others over all the error sensors, and it should not be discounted.

There are several multi-channel algorithms discussed in the literature that employ a more direct approach to adjusting all control signals simultaneously (Elliott, 2000; Fuller et al., 1996; Kuo and Morgan, 1996; Nelson and Elliott, 1992; Tokhi and Veres, 2002): e.g., LMS (stochastic gradient algorithm), Modified LMS, Filtered-x LMS, Recursive Least-Squares, etc. The respective advantages and disadvantages of these algorithms will not be discussed here. They are well covered by the literature, particularly by Elliott (2000) and Kuo and Morgan (1996). Instead, one of these, the well-known Filtered-x LMS algorithm, is adopted here as the basis for a discussion on how an active control algorithm could be applied to the synchrophase angle control problem using the propeller signature model.

Note that the quadratic function approach of the LMS algorithm necessarily requires that the cost function has a smooth and continuous gradient with respect to the control variables, and a single global minimum. Smooth in this sense also implies that the gradient should not change direction within the time required for each algorithm step unless the step spans the global minimum. If these conditions cannot be met, an alternative algorithm must be devised. While the preceding analysis has not shown that a single minimum can be guaranteed for the chosen cost functions, it has demonstrated (Figures 11.11 and 11.12, and Figures 11.23 and 11.24) that this condition will be met in the aircraft under investigation if there are at least as many error sensors (microphones/accelerometers) as control variables (synchrophase angles of the slave propellers). Hence, this is likely to hold true for other similar aircraft. However, due to the periodic nature of the cost function, implementation of the LMS algorithm would still require care to ensure that the step change in each control variable remains significantly smaller than the period of the function with respect to that variable; i.e., at each step of the algorithm, the change in each synchrophase angle should remain at least an order of magnitude smaller than the full-scale range of the available synchrophase angles. This could be accomplished through the selection of an appropriate convergence coefficient based on the maximum expected gradient of the cost function.

The adaptive synchrophase angle control problem can be reduced down to the single-reference (master propeller tachometer signal) multi-output (slave propeller synchrophase angles) feed-forward control system with multiple error sensors (microphones or accelerometers) that is shown in Figure 11.27. Here, the master propeller is the primary source, and the slave propellers are the secondary sources. The diagram shows a Filtered-x LMS arrangement, but other algorithms could be substituted as desired. In this case, the reference signal is a sine wave at the BPF generated by the master propeller as discussed on the next page. The vibro-acoustic responses represent the transfer functions from the synchrophase angles to the error sensor signals; i.e., they combine the physical noise and vibration sources (the propellers), the plant responses (the vibro-acoustic response of the aircraft), and the error sensor characteristics (microphones/accelerometers and associated signal conditioning) together into one function. In this way, the transfer functions represent the propeller signatures used in the preceding analysis. Note that the synchrophase angle of the master propeller is included in the diagram to show similarity with the slave propellers, but is in fact fixed at 0° by definition. Also, if the adaptive control system is implemented as an extension of the existing synchrophaser, then the control filter $w_p(n)$ does not need to be explicitly implemented, as this is effectively part of the existing synchrophaser. The LMS algorithm only needs to generate the synchrophase angles α_p and send them to the existing synchrophaser.

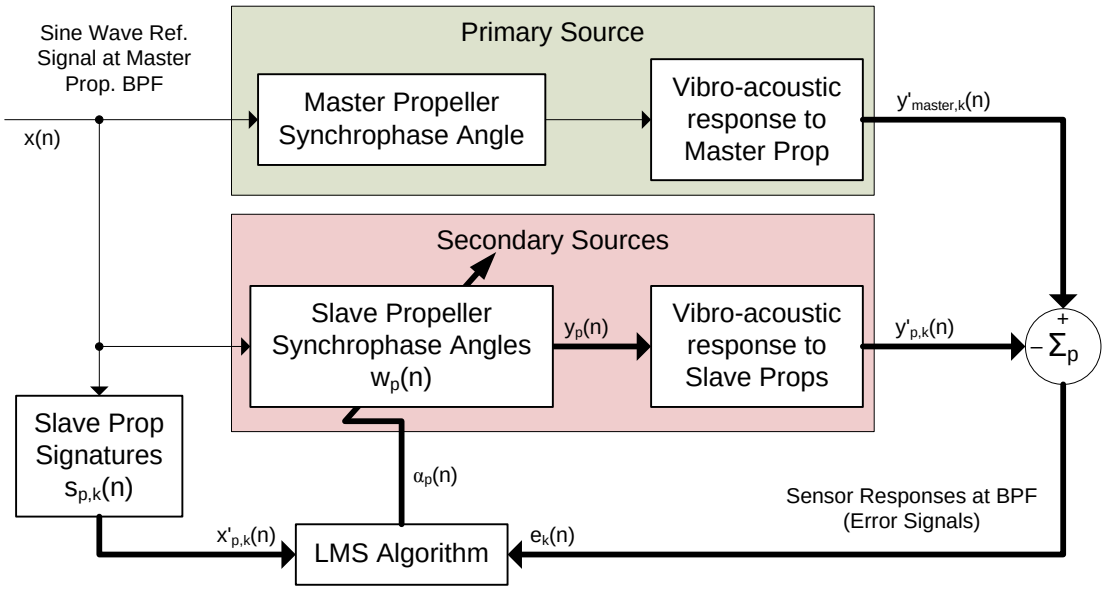

Figure 11.27 A single-reference/multiple-output adaptive synchrophase angle control system for an aircraft with P propellers and K error sensors using the Filtered-x LMS algorithm. Bold lines indicate vectors. Adapted from Kuo and Morgan (1996, Fig. 5.5).

The active control system could be implemented in the time domain or the frequency domain. In the time-domain, filtering consists of a convolution of the signal with the impulse response of the filter. In the frequency domain, it consists of a multiplication of the Fourier transforms of the signal and the impulse response of the filter. Both methods are discussed as follows.

In the time domain, the reference signal $x(n)$ would be a discrete sinusoid that is synchronous with the BPF of the master propeller.[5] This could be generated by an encoder on the propeller shaft, or from a frequency multiplier circuit applied to the once-per-revolution signal. If there were, say, N samples per revolution of the master propeller, there would be B signal cycles of this signal over a period of N samples, where B is the number of blades on the propeller. As the synchrophase angles represent phase changes to the reference signal, the control filters $w_p(n)$ would be simple time (phase) delays associated with the synchrophase angles of each propeller p. The propeller signature filters $s_{p,k}(n)$ would consist of a gain and a time delay corresponding to the amplitude and phase of the signature for propeller p at sensor k. If the filters were implemented in the usual Finite Impulse Response (FIR) transversal form, the filter lengths would need to be $L = N \div B$, where B is the number of blades on each propeller. N would then obviously need to be chosen so that L was a whole number. If N was equal to 360, then the filter lengths would be $L = 90$ in the AP-3C and $L = 60$ in the C-130J, and a synchrophase angle resolution of 1° would be achieved. This would require a sample rate of approximately 6120 Hz in both aircraft, as they both have propeller speeds of 1020 rpm (17 Hz). Note, however, that since all the signals are periodic, and there is only one non-zero filter coefficient in each filter, the filters could easily be implemented as pointers into a circular memory buffer instead of the usual FIR filter form. This would considerably reduce the computational burden. The memory buffer would only need to be L samples long in order to contain one complete cycle of a sine wave. The pointers would then increment by one sample around the loop

[5] With synchronous sampling at the propeller rotational frequency, the time domain really becomes the synchrophase-angle domain.

every sample clock period, and the relative spacing between the pointers would reflect the synchrophase angles.

The reference signal vector at time n would thus be

$$\mathbf{x}(n) = \begin{bmatrix} x(n) & x(n-1) & \dots & x(n-L+1) \end{bmatrix}^T, \tag{11.3}$$

where L is the length of the FIR filters, and

$$x(n) = \cos\left(\frac{2\pi}{L} n\right). \tag{11.4}$$

The control filter vector for propeller p would take the form

$$\mathbf{w}_p(n) = \begin{bmatrix} w_0(n) & w_1(n) & \dots & w_{L-1}(n) \end{bmatrix}, \tag{11.5}$$

where the elements of this vector are defined by

$$w_l(n) = \begin{cases} 0 & l \neq \text{round}\left(\frac{L}{2\pi} B\alpha_p(n)\right) \\ 1 & l = \text{round}\left(\frac{L}{2\pi} B\alpha_p(n)\right) \end{cases}, \tag{11.6}$$

and B is the number of blades on the propeller, and $\alpha_p(n)$ is the lagging synchrophase angle of propeller p at time n.

The reference filter vector for propeller p would take the form

$$\mathbf{s}_{p,k}(n) = \begin{bmatrix} s_0(n) & s_1(n) & \dots & s_{L-1}(n) \end{bmatrix}, \tag{11.7}$$

where the elements of this vector are defined by

$$s_l(n) = \begin{cases} 0 & l \neq \text{round}\left(\frac{L}{2\pi} \angle\hat{S}_{p,k}(n)\right) \\ \left|\hat{S}_{p,k}(n)\right| & l = \text{round}\left(\frac{L}{2\pi} \angle\hat{S}_{p,k}(n)\right) \end{cases}, \tag{11.8}$$

and $|\hat{S}_{p,k}(n)|$ and $\angle\hat{S}_{p,k}(n)$ denote the amplitude and phase of the signature of propeller p at sensor k at time n.

The control filter output $y_p(n)$ and filtered reference $x'_{p,k}(n)$ signals would thus be

$$\mathbf{y}_p(n) = \mathbf{w}_p(n) * \mathbf{x}(n) = \cos\left(\frac{2\pi}{L} n + B\alpha_p(n)\right) \tag{11.9}$$

and

$$\mathbf{x}'_{p,k}(n) = \mathbf{s}_{p,k}(n) * \mathbf{x}(n) = \left|\hat{S}_{p,k}(n)\right| \cos\left(\frac{2\pi B}{N} n + \angle\hat{S}_{p,k}(n)\right) \tag{11.10}$$

respectively, where $*$ denotes convolution. The control filters $w_p(n)$ would be updated using (Kuo and Morgan, 1996, §5.3.1)

$$\mathbf{w}_p(n+1) = \mathbf{w}_p(n) + \mu \sum_{k=1}^{K} \mathbf{x}'_{p,k}(n) e_k(n), \tag{11.11}$$

where μ is a convergence coefficient, and $e_k(n)$ is the error signal at sensor k.

In the frequency domain, the reference signal and filters would be

$$X(f)=\begin{cases}0 & f \neq f_{BPF}\\ 1 & f = f_{BPF}\end{cases}, \tag{11.12}$$

$$W_p(f)=\begin{cases}1 & f \neq f_{BPF}\\ e^{iB\alpha_p} & f = f_{BPF}\end{cases} \tag{11.13}$$

and

$$S_{p,k}(f)=\begin{cases}1 & f \neq f_{BPF}\\ \hat{S}_{p,k} & f = f_{BPF}\end{cases}; \tag{11.14}$$

i.e., each signal can be represented by a single complex number at the BPF. The output and filtered reference signals would thus be

$$Y_p(f_{BPF}) = X(f_{BPF})W_p(f_{BPF}) = e^{iB\alpha_p} \tag{11.15}$$

and

$$X'_{p,k}(f_{BPF}) = X(f_{BPF})S_{p,k}(f_{BPF}) = \hat{S}_{p,k}. \tag{11.16}$$

The error signals $e_k(n)$ would need to be transformed into the frequency domain to arrive at $E_k(f)$. However, only the BPF is required and this could be obtained efficiently using a single-frequency variant of the discrete Fourier transform; i.e.,

$$E_k(f_{BPF}) = \sum_{n=0}^{L-1} e(n)e^{-i\frac{2\pi}{L}n}. \tag{11.17}$$

There would be no need for a windowing function, as the signals would necessarily be periodic with the sampling period. The control filters W_p would be updated every L samples using (Kuo and Morgan, 1996, §8.2.2)

$$\begin{aligned} W_p(n+L) &= W_p(n) + \mu\sum_{k=1}^{K} X'^{*}_{p,k}(n)E_k(n)\\ &= W_p(n) + \mu\sum_{k=1}^{K} \hat{S}^{*}_{p,k}(n)E_k(n)\end{aligned}, \tag{11.18}$$

where μ is a convergence coefficient and * denotes the complex conjugate. The transformation into the frequency domain means that the filter update will be delayed by L points compared to the time-domain implementation. However, this is probably tolerable given the periodic nature of the signals.

From the analysis presented here, it can be seen that there is little computational difference between the time and frequency domain methods. However, given the simplicity of the equations, and the closer match with the propeller signature model, the frequency-domain method would appear to be the better choice.

Estimates of the propeller signatures are obviously required for the control system to function. There are two ways to obtain these: off-line or on-line (i.e., with the active control disabled or enabled). The former is simpler, and potentially more accurate depending on the process used, but means that the system must go off-line to re-model the signatures every time the system dynamics change; i.e., the sound or vibration must

necessarily increase during this system identification phase. The latter is far more attractive, but runs into the fundamental problem of using the control signals both to control and to identify the system simultaneously. The only way to do this reliably is to add an uncorrelated identification signal to the control signal (Elliott, 2000, §3.6.2); i.e., to perturb the synchrophase angles away from their optima in a pre-defined manner. This will again increase the sound or vibration, albeit by smaller amounts depending on the amplitude of the identification signal. Kuo and Morgan (1996, §7.4) suggested an overall modelling algorithm as a potential way around this problem, but the algorithm necessarily relies on an off-line initialisation period, plus any changes in the primary and secondary transfer functions then occurring at a different rates, which will not generally be the case here.

Based on the results shown in Chapter 9 and Appendix G, obtaining accurate propeller signature estimates using a small-amplitude on-line identification signal could be difficult, and off-line modelling would be a more conservative approach for an initial prototype. This could be accomplished by applying several sets of widely-spaced synchrophase angles and solving the signature equations in a least-squares sense, as described in Chapter 5. This could be accomplished in a relatively short period of time, as part of an automated process, although there would still be some ‘dead-time’ following each adjustment to the angles while the propellers settle on the new settings. Another, possibly shorter and better, method would be to separately drive the synchrophase angle of each propeller through its entire range of angles at a fixed rate and average the data over this same time period. This would, in effect, average out the contribution from the propeller in question, and its signature could then be obtained by subtracting the average obtained while the propeller was being ‘clocked’ with another that was obtained when it was not. If the slew rate were, say, 3.6° per-revolution (i.e., a 1% increase or decrease in propeller speed) this would require an average over 100 propeller revolutions (taking < 6 seconds in the AP-3C and C-130J), and would also provide significant attenuation of any non-synchronous components. The 100-revolution averaging period could actually be shortened to as little as $100 \div B$ propeller revolutions, as the phase cycle will repeat B times at the BPF. This would equate to periods of approximately 1.5 s and 1.0 s in the AP-3C and C-130J aircraft respectively. A 1% increase or decrease in propeller speed would be well within allowable propeller speed variations. However, shorter averaging periods could be achieved using faster slew rates.

Off-line modelling of the propeller signatures necessarily requires some determination of when these signatures need to be updated. The simplest approach would be to re-model the signatures after a fixed time interval, although this would be inefficient. Another would be to re-model the signatures whenever there are significant changes to the measured altitude and airspeed, and/or aircraft flight controls (e.g., power levers, control column, pedals, etc.). However, some work would need to be expended to define what ‘significant’ actually means in order to prevent excessive re-modelling of the signatures, and this definition could change from aircraft type to aircraft type. Hence, an approach that does not rely on external control signals would be preferable. One possible way, similar to that suggested by Pla (1998) (§2.4.4), would be to periodically perturb all the synchrophase angles by a small amount, say 1° or 2°, and measure if the cost function increases or decreases. A re-modelling event could then be triggered if a significant decrease, say more than 1 dB, was measured.

12. Conclusions

This thesis has examined the effect of propeller synchrophasing on aircraft cabin noise and vibration in the following ways:

a) how different flight conditions, in particular altitude and airspeed, actually affect the optimum synchrophase angles in real aircraft cabins; and
b) how to develop an adaptive control methodology based on knowledge of these flight-condition effects.

This has been done through experimental investigation in one AP-3C Orion and two C-130J-30 Super Hercules aircraft.

The optimisation of propeller synchrophase angles necessarily relies on the ability of the synchrophaser to maintain the propellers at the desired angles. Both the AP-3C and C-130J synchrophasing systems use a master-slave relationship; i.e., one of the inboard propellers is designated the master propeller, and the remaining propellers are slaved in speed and shaft angle to this propeller. The main difference between the systems is that the former is analogue and the latter is digital. Digital control is typically claimed to produce faster responses, and tighter speed and synchrophase angle tolerances, and this was clearly demonstrated in the results. Hence, it is recommended that digital control should be used in preference to analogue control wherever possible. Additionally, it was recognised that, in a master-slave relationship, turbulence-induced perturbations of the master propeller speed can cause significant, and unnecessary, synchrophase angle perturbations in all the slave propellers. This effect could be reduced if the synchrophase angles were calculated in a different way. One way would be to filter out the perturbations in the master propeller signal. Another might be to generate an artificial master signal and to make all the propellers slaves.

The cabin noise and vibration environments inside the AP-3C and C-130J-30 were found to have similar characteristics, and can therefore be considered as representative of most other multi-engine propeller aircraft. Both are dominated by the blade-pass frequency and its low-order harmonics (up to about 4× BPF). Higher blade-pass harmonics are present, but the amplitudes of these components taper off as the frequency increases. Generally, the BPF and its low-order harmonics are most prominent near the plane of the propellers, and gradually diminish towards the rear of the cabin. However, it was noted that the prominence of these components is slightly further forward in the cabin of the C-130J-30 than the AP-3C. This may be due to the different noise propagation patterns of the propellers of the respective aircraft, or the slightly more rearward positioning of the outboard propellers in the AP-3C, which has a more swept wing than the C-130J.

Cabin noise and vibration measurement repeatability at the BPF and its low-order harmonics was examined over short periods (10 second), medium (10 minute) intervals, and between two different aircraft of the same type. In general, it was found that:

a) It was difficult to isolate all possible causes of spectrum level variability; i.e., some level of measurement variation is inevitable and must be accommodated.
b) There is significantly less variability at the BPF than at its harmonics. This is probably because turbulence-induced perturbations in the synchrophase angles inherently cause larger variations in the phase of the harmonic components.
c) The spectrum levels varied more significantly between two aircraft of the same type than they did within each aircraft individually. The observed variation at the BPF for some channels was up to ~12 dB.

Important factors that may have influenced the observed measurement repeatability included: perturbations/differences in the flight conditions during/between measurements, vibro-acoustic differences between aircraft of the same type, and differences in sensor placement between the measurements.

Propeller signature theory was used extensively in the investigation to reduce the amount of flight time required. The propeller signatures were calculated in a least-squares sense by taking more measurements than were strictly necessary to solve the governing system of equations. The predicted noise and vibration levels were then compared to the measured levels in order to assess predictive ability of the theory and determine which of the frequencies of interest should be incorporated into the optimisation process. It was found that the relative prediction error falls as the signal levels increase. The best results occurred at the BPF, where the sound pressures and accelerations were relatively large, and the corresponding relative prediction errors dropped below 10%. The relative prediction errors for the harmonics of the BPF were generally significantly larger than 10%, except for some high-amplitude 2× and 3× BPF components. These high-amplitude harmonic components fall within a region very near the plane of the propellers. The poor predictions for the lower-amplitude signals appear to be the result of poor estimates of the propeller signatures caused by measurement variability. The main underlying reason for this is that perturbations in the synchrophase angles cause progressively larger phase deviations at each successive harmonic of the BPF. Unfortunately, these phase deviations also limit the amount of control that can be achieved at these frequencies. For example, a synchrophase angle tolerance of ± 5° on a four-bladed propeller allows phase deviations of ± 20°, ± 40°, ± 60° and ± 80° at 1×, 2×, 3× and 4× the BPF respectively. These phase deviations can be reduced, and control at the harmonic frequencies improved, if the synchrophase angle tolerance is tightened.[6] However, given the nature of the problem, and the diminishing importance of the harmonic frequencies to the cabin noise and vibration, further analysis of the data was restricted the BPF only. It was shown that this approach still produced significant reductions in the cabin noise and vibration.

Optimisation of the synchrophase angles at the BPF was studied in three ways:

a) First, the effects of different optimisation criteria on the predicted noise and vibration levels were examined for a single (fixed) flight condition.
b) Second, the effects of altitude and airspeed on the optimum synchrophase angles were examined for a single optimisation criterion.
c) Third, several new candidate synchrophase angle sets were derived and, in the case of the C-130J-30, subsequently tested.

It was found that:

a) For a fixed flight condition, optimising over all microphones (or all accelerometers) is generally a good strategy for low overall noise (or vibration), but it does not necessarily guarantee low levels in particular areas of the cabin. Optimising over various sub-sets of sensors generally lowers the levels in these respective areas, but allows the levels elsewhere to increase, and results in higher overall average levels.
b) Synchrophasing has significant effects on the average cabin floor vibration and the average cabin sound pressure levels. These effects can be expected to range

[6] A synchrophase tolerance of ± 2° on a six-bladed propeller allows phase deviations of ± 12°, ± 24°, ± 36° and ± 48° at 1×, 2×, 3× and 4× the BPF respectively.

between 4 dB and 12 dB at the BPF, depending on the flight condition and the aircraft.

c) Altitude and airspeed both have significant effects on the optimum synchrophase angles. A fixed set of synchrophase angles cannot produce consistently low average sound pressure or vibration levels over all flight conditions.

d) There was relatively good agreement between the optimisation results for the lowest average floor vibration in the same C-130J-30 aircraft on consecutive days. Any differences can be attributed to the different positions of the cargo (i.e., different floor loading), and minor variations in the flight conditions between the two flights, as the floor accelerometers were not changed or moved. This indicates good flight-to-flight repeatability in a single aircraft, at least over the short term.

e) The variations in the optimum synchrophase angles, and in the shapes of the average vibration and SPL contours at the BPF, were relatively smooth and gradual and thus readily amenable to some form of adaptive control system.

f) The candidate angle sets derived from the first C-130J-30 aircraft generally performed well in the second C-130J-30 aircraft; i.e., they recorded lower measured noise and vibration. No significant detrimental effects were observed at the low-order harmonics of the BPF despite the candidate sets being only based on the measurements at the BPF.

g) The results for the candidate angle sets in the second C-130J-30 aircraft were not as good as predicted, and were reflected by changes in the propeller signatures between the two aircraft. Possible reasons for this include slightly different sensor positions, slightly different flight conditions, different external weather conditions (the first trial was in November, while the second was in July), and slightly different vibro-acoustic responses between the two aircraft.

Two methods of adaptive control were investigated: a) using a pre-determined look-up table of optimum synchrophase angles, and b) using a single-input (master propeller tachometer) multi-output (slave propeller synchrophase angles) feed-forward active control system with multiple error sensors.

Look-up tables, while easy to implement or retrofit to existing synchrophasing systems, particularly to aircraft with digital data buses where information about the aircraft's flight conditions would already be available on the bus, were seen as having problems that could well override any advantages. Chief among these were difficulty in determining in advance the size of the flight condition intervals that would be needed to generate a table that could be interpolated with minimal error (for flight test design purposes), and the inability to adapt to other factors such as aircraft-to-aircraft differences and variable cabin configuration or loading.

The active control system design elements that were considered included:

a) What type of sensors should be used?

b) How many sensors are required?

c) Where should the sensors be positioned?

d) What control algorithm should be used?

It is recommended that the type of sensors used should reflect whether the objective is to minimise the cabin noise or vibration; i.e., to use microphones for the former and accelerometers for the latter. However, it was noted that minimising the cabin noise generally had a beneficial, although not necessarily optimal, impact on the cabin floor

vibration, and thus minimising noise could generally be considered a better choice unless vibration was particularly critical.

The number of sensors required and where they should be positioned was examined in some detail by giving the sensors used in the experimental trials ranks based on: a) the potential for the propeller BPF signatures at each sensor position to cancel each other out, and b) the maximum potential BPF amplitude at each sensor position. The results for the two ranking strategies were very similar; i.e., one strategy could not be considered better than the other. Significantly, both strategies identified that the predicted average sound pressure levels at the BPF could be maintained within 2 dB of the optimum across all considered flight conditions using as few as 3 to 6 microphones. This very interesting result indicates that it is not necessary to have sensors distributed throughout the entire length of the cabin in order to achieve a relatively good global outcome, at least when the objective is to minimise the average noise or vibration rather than some other optimisation criterion. Controlling the average sound pressure of a few well-placed microphones within a zone near or slightly forward of the plane of the propellers should be sufficient. It was also demonstrated that, while the shape of the average sound pressure contours outlining the low-amplitude regions can be quite extensive and convoluted for only one microphone, these regions converge relatively well, once 3 to 6 microphones are used, to one very close to that found using all the trial microphones.

The suitability of any active control algorithm to a particular problem depends largely on the behaviour of the cost function. In all cases, it was found that the contours of the average sound pressure or vibration at the BPF are smooth and become relatively well behaved, albeit slightly elongated, once three or more sensors are used. It is only when fewer sensors are used that the functions can be seen to bifurcate or abruptly change direction. This result is particularly useful as it means that no special algortihmic approach needs to be taken; i.e., a typical gradient-descent algorithm can be used with a relatively high level of confidence in the outcome as long as three or more sensors are used. This is entirely consistent with whether the least squares solution to finding the minima of these cost functions is under-determined, fully-determined, or over-determined. In this case, since there are three slave propellers, it makes sense to use at least three sensors to construct the cost function.

Two types of algorithm were specifically considered:

a) a simple trial-and-error algorithm where the synchrophase angle of one slave propeller is adjusted to achieve a minimum in the cost function, and then this is repeated for the next propeller, and so on in a repetitive manner until the global minimum is finally approached; and
b) a Filtered-x algorithm.

The main advantage of the trial-and-error method is that it is very easy to implement. The transfer functions between the control and the error signals (i.e., the propeller signatures) do not need to be estimated. However, the major disadvantage is a slower convergence on the global minimum. This slower rate of convergence may prevent the system actually reaching the global minimum under conditions where the vibro-acoustic response of the aircraft is not sufficiently stationary; e.g., when the flight conditions are changing too rapidly. Nevertheless, the method may work well under many conditions, particularly if the signature from one slave propeller is consistently larger than the others over all the error sensors, and is worth further investigation.

The well-known Filtered-x LMS algorithm was adopted as the basis for a discussion on how an active control system could be applied to the synchrophase angle control problem

using the propeller signature model. In this case, the reference signal is a sine wave at the BPF generated by the master propeller that is filtered by the propeller signature transfer functions before these signals are passed to the usual LMS gradient descent algorithm. Such an active control system could be implemented equally well in the time domain or the frequency domain. The equations become simpler in the latter, although conversion to the frequency domain effectively implies some averaging/delay compared to the time-domain implementation. Estimates of the propeller signatures could be obtained off-line or on-line (i.e., with the active control disabled or enabled). However, obtaining accurate propeller signature estimates using a small-amplitude on-line identification signal was identified as being difficult, and off-line modelling would be a more conservative approach for an initial prototype. A quick and simple method for off-line modelling was suggested where each slave propeller is driven through its full range of synchrophase angles at a constant rate. If, for example, this was undertaken using a slew rate of 3.6° per revolution (i.e., a 1% increase or decrease in propeller speed), it would require an average over $100 \div B$ revolutions, where B is the number of propeller blades. This would equate to periods of approximately 1.5 s and 1.0 s in the AP-3C and C-130J aircraft respectively. Shorter periods could be achieved using faster slew rates. An update to the off-line model of the propeller signatures could be triggered by periodically perturbing all the synchrophase angles by a small amount, say 1° or 2°, and measuring if the cost function decreases by a significant amount, say by more than 1 dB.

In summary, this thesis has made significant contributions to the body of knowledge in the following areas:

a) the performance of aircraft propeller synchrophasing systems;
b) the cabin noise and vibration environment in multi-engined propeller aircraft in general, and the AP-3C and C-130J aircraft in particular;
c) the variability of aircraft cabin noise and vibration measurement,
d) the ability of propeller signature theory to accurately predict cabin noise and vibration at the blade-pass frequency and its low-order harmonics,
e) strategies for optimising the propeller synchrophase angles,
f) the visualisation of cost functions for propeller synchrophase angle optimisation,
g) the nature and extent of variation in the optimum synchrophase angles with changes in flight conditions, and
h) the adaptive control of propeller synchrophase angles.

Other publications resulting from this work can be found in Appendix J.

12.1. Recommendations for Further Work

The following suggestions could be considered for further work on adaptive synchrophase angle control systems:

- Build a synchrophasing rig consisting of a mock fuselage with external model aircraft propellers and an internal array of microphones.
- Test the rig in an anechoic chamber to determine whether it exhibits the same sort of behaviour as a real aircraft.
- Use the rig to investigate how aircraft-to-aircraft vibro-acoustic differences may be caused.
- Investigate how virtual sensing could be used to replace sensors in awkward positions.

- Develop and build a prototype adaptive synchrophase angle control system that can implement the active control algorithms suggested in this thesis.
- Investigate the performance of the suggested active control algorithms using the synchrophasing rig.
- Investigate improvements to the suggested active control algorithms, and/or the benefits of using alternative algorithms.
- Test the prototype on a real aircraft (starting with ground tests and moving on to flight tests), and further refine the control system based on the measured results.

References

A9 Lockheed Orion P3. *Image Gallery of the RAAF*, Retrieved 17 July 2009 from <http://defweb.cbr.defence.gov.au/airforceimages/3a9.htm>

A97 Lockheed Hercules. *Image Gallery of the RAAF*, Retrieved 17 July 2009 from <http://defweb.cbr.defence.gov.au/airforceimages/2a97.htm>

A400M Photo Gallery. *Airbus Military*, Retrieved 23 February 2011 from <http://www.airbusmilitary.com/Multimedia/Gallery/AlbumView.aspx?AlbumId=137>

A400M to have 'handed' propellers (2004). *Flight International*, 18-24 May.

Active Synchrophaser Program Helps Quiet the Mighty Air Force C-130 (2002). *BAE Systems Controls*, Retrieved 16 September 2004 from <http://platformsolutions.na.baesystems.com:8080/news/>

Adams, G. (2007) Propeller Modernization, Retrieved 3 August 2009 from <http://www.lockheedmartin.com/data/assets/ams/2007_HOC_Presentations/Wed_1430_PropellerModernization-HamSundstrand.pdf>

AP-3C Propeller Synchrophaser Optimisation Operational Test and Evaluation (OT&E) Plan (2006), HQ Surveillance and Response Group, RAAF.

Arnold, R. N. & Warburton, G. B. (1949) Flexural vibrations of the walls of thin cylindrical shells having freely supported ends. In Kalinins, A. & Dym, C. L. (Eds.) *Vibration: Beams, Plates and Shells*, Vol. 8 (1976), Benchmark Papers in Acoustics. Stroudsburg, Pennsylvania, Dowden, Hutchison & Ross, Inc.

AS IEC 61672.1 (2004) Electroacoustics - Sound level meters Part 1: Specifications, Standards Australia.

Australian Air Publication 7211.031-1(AM1)B2 Flight Manual C-130J-30 (Book 2 of 2), Royal Australian Air Force.

Australian Air Publication 7211.031-9-2 Loading and Lashing Diagrams Hercules C-130J-30 Aircraft, Royal Australian Air Force.

Australian Air Publication 7215.005-5(AM1) P-3 Orion Aircraft Weight and Balance Manual, Australian Defence Force.

Bies, D. A. & Hansen, C. H. (1988) *Engineering Noise Control*, London, Unwin Hyman.

Bombardier (2008) "Q" Means Quiet, Retrieved 15 July 2009 from <http://www.q400.com/q400/en/quiet.jsp>

Borchers, I. U., Emborg, U., Sollo, A., Waterman, E. H., Paillard, J., Larson, P. N., Venet, G., Göransson, P. & Martin, V. (1992) Advanced Study for Active Noise Control in Aircraft (ASANCA). Paper presented at *NASA/SAE/DLR Fourth Aircraft Interior Noise Workshop*, Friedrichshafen, Germany, 19-20 May.

Bullmore, A. J. (1987) The Active Minimisation of Harmonic Enclosed Sound Fields with Particular Application to Propeller Induced Cabin Noise. Ph.D. Thesis. University of Southampton (United Kingdom).

Bullmore, A. J., Nelson, P. A. & Elliott, S. J. (1990) Theoretical studies of the active control of propeller-induced cabin noise. *Journal of Sound and Vibration,* 140(2), pp 191-217.

Bullmore, A. J., Nelson, P. A., Elliott, S. J., Evers, J. F. & Chidley, B. (1987) Models for evaluating the performance of propeller aircraft active noise control systems. Paper presented at *11th AIAA Aeroacoustics Conference*, Sunnyvale, CA, October 19-21.

C-130J-30 Propeller Synchrophaser Optimisation Technical Trial Plan (2006) HQALG/2006/1164142 Pt 2 (53), HQ Air Lift Group, RAAF.

C-130J-30 Propeller Synchrophaser Optimisation Validation Technical Trial Plan (2008) HQALG/2006/1164142 Pt 3 (44) HQ Air Lift Group, RAAF.

C-130J Advanced Propeller System [Pamphlet]. GE Aviation (Dowty Propellers). Retrieved from <http://www.geaviationsystems.com/Products--

/Propellers/Manufacture/Advanced-Propeller-System-C130J/Literature/APS_C-130J_data_sheet_mid.pdf>

Carme, C., Derrien, D. & Valentin, G. (1997) The ANCAS Seat: Extension and Industrial Applications. Paper presented at *ACTIVE 97: EAA International Symposium on Active Control of Sound and Vibration*, Budapest, Hungary.

Castelo Branco, N. A. (1999a) The clinical stages of vibroacoustic disease. *Aviation Space & Evironmental Medicine,* 70(3 Pt 2), pp A32-9.

Castelo Branco, N. A. (1999b) A unique case of vibracoustic disease: a tribute to an extraordinary patient. *Aviation Space & Environmental Medicine,* 70(3 Pt 2), pp A27-31.

Castelo Branco, N. A., Rodriguez, E., Alves-Pereira, M. & Jones, D. R. (1999) Vibroacoustic disease: some forensic aspects. *Aviation Space & Environmental Medicine,* 70(3 Pt 2), pp A145-51.

Coppinger, R. (2006) Ultra Electronics to reduce A400M's four-engine roar. *Flight International,* 17 Jan.

Dorling, C. M., Eatwell, G. P., Hutchins, S. M., Ross, C. F. & Sutcliffe, S. G. C. (1989) Demonstration of active noise reduction in an aircraft cabin. *Journal of Sound and Vibration,* 128(2), pp 358-360.

Elliott, S. J. (2000) *Signal Processing for Active Control*. Signal Processing and its Applications, Green, R. & Nguyen, T. (Series Eds.), London, Academic Press.

Elliott, S. J. & Nelson, P. A. (1987) Aircraft Cabin Noise Control Apparatus. International Patent WO 87/07974.

Elliott, S. J. & Nelson, P. A. (1993) Active Noise Control. *Signal Processing Magazine, IEEE,* October.

Elliott, S. J., Joseph, P., Bullmore, A. J. & Nelson, P. A. (1988) Active Cancellation at a Point in a Pure Tone Diffuse Sound Field. *Journal of Sound and Vibration,* 120(1), pp 183-189.

Elliott, S. J., Nelson, P. A., Stothers, I. M. & Boucher, C. C. (1990) In-flight experiments on the active control of propeller-induced cabin noise. *Journal of Sound and Vibration,* 140(2), pp 219-238.

Emborg, U. & Ross, C. F. (1993) Active control in the Saab 340. Paper presented at *Proceedings of the Recent Advances in Active Control of Sound and Vibration*, Blacksburg, VA, April.

Emborg, U., Samuelsson, F., Holmgren, J. & Leth, S. (1998) Active and passive noise control in practice on the Saab 2000 high speed turboprop. Paper presented at *4th AIAA/CEAS Aeroacoustics Conference*, Toulouse, France, June 2-4.

Farrell, P. A., Mouser, C. R., Conser, D. P. & Rider, C. D. (2002) C-130J-30 Cargo Vibration Flight Test DSTO-TR-1310, Defence Science and Technology Organisation, Department of Defence, Australia.

Fletcher, H. & Munson, W. A. (1933) Loudness, Its Definition, Measurement and Calculation. *Journal of the Acoustical Society of America,* 5, pp 82-108.

Fletcher, H. & Munson, W. A. (1937) Relation Between Loudness and Masking. *Journal of the Acoustical Society of America,* 9(1), pp 1-10.

Fokker 50 (1997). *Ministry of Defence, The Netherlands*, Retrieved 23 July 2009 from <http://www.defensie.nl/onderwerpen/materieel/vliegtuigen_en_helikopters/transportvliegtuigen/f-50>

Fokker 50 Aircraft Overview [Pamphlet]. Stork Fokker. Retrieved 23 July 2009 from <http://www.fokker.com/downloads/Aerospace/FS/Fokker%2050%20Leaflet.pdf>

Fuller, C. R. (1984a) Analytical Investigation of Synchrophasing as a Means of Reducing Aircraft Interior Noise. Contractor 3823, NASA.

Fuller, C. R. (1984b) Noise Control Characteristics of Synchrophasing - an Analytical Investigation. Paper presented at *AIAA/NASA 9th Aeroacoustics Conference*, Williamsburg, VA, Oct 15-17.

Fuller, C. R. (1986a) Noise Control Characteristics of Synchrophasing, Part 1: Analytical Investigation. *AIAA Journal,* 24(7), pp 1063-8.

Fuller, C. R. (1986b) Structural Influence of a Cabin Floor on Sound Transmission into Propeller Aircraft - Analytical Investigations. Paper presented at *AIAA 10th Aeroacoustics Conference*, Seattle, July 9-11.

Fuller, C. R. (1986c) Analytical model for investigation of interior noise characteristics in aircraft with multiple propellers including synchrophasing. *Journal of Sound and Vibration,* 109(1), pp 141-56.

Fuller, C. R. (1987) Structural influence of the cabin floor on sound transmission into aircraft - Analytical investigations. *Journal of Aircraft,* 24(10), pp 731-736.

Fuller, C. R. (1997) Active Control of Cabin Noise - Lessons Learned? Paper presented at *Fifth International Congress on Sound and Vibration*, University of Adelaide, South Australia, December 15-18.

Fuller, C. R., Elliott, S. J. & Nelson, P. A. (1996) *Active Control of Vibration*, London, Academic Press.

Fuller, C. R., Snyder, S. D., Hansen, C. H. & Silcox, R. J. (1992) Active control of interior noise in model aircraft fuselages using piezoceramic actuators. *AIAA Journal,* 30(11), pp 2613-2617.

Gerner, C. & Sachau, D. (2003) Active Noise Control in a Semi-Enclosure Within an Aircraft Cabin. Paper presented at *Tenth International Congress on Sound and Vibration*, Stockholm, Sweden, 7-10 July.

Goodman, G. C., Pla, F. G. & Reddy, S. B. (1995) Phase locked loop control of turboprop aircraft engines for cancellation of interior or exterior noise. Paper presented at *4th IEEE Conference on Control Applications*, Albany, NY, USA.

Gorman, J., Hinchliffe, R. & Stothers, I. M. (2004) Active Sound Control on the Flight Deck of a C-130 Hercules. Paper presented at *Active 2004: The 2004 International Symposium on Active Control of Sound and Vibration*, Williamsburg, Virgina, USA, September 20-22.

Hammond, D., McKinley, R. & Hale, B. (1999) Noise reduction efforts for special operations C-130 aircraft using active synchrophaser control. *Air Force Research Laboratory*, Retrieved 1 July 2004 from <http://www.hec.afrl.af.mil/publications/FocusFinal.pdf>

Hansen, C. H. & Snyder, S. D. (1997) *Active Control of Noise and Vibration*, London, E & FN Spon (an imprint of Chapman & Hall).

Haughton, P. (2002) *Acoustics for Audiologists*, London, Academic Press.

Hinchliffe, R., Scott, I., Purver, M. & Stothers, I. M. (2002) Tonal Active Control in Production on a Large Turboprop Aircraft. Paper presented at *Active 2002: The 2002 International Symposium on Active Control of Sound and Vibration*, University of Southampton, UK, July 15-17.

ISO 226 (2003) Acoustics - Normal equal-loudness-level contours, International Organization for Standardization (ISO).

Jane's (2009a) Lockheed Martin 382U/V Super Hercules, Retrieved 15 July 2009 from <http://www.janes.com>

Jane's (2009b) Lockheed Martin (Lockheed) C-130 Hercules, Retrieved 15 July 2009 from <http://www.janes.com/>

Jane's (2009c), Retrieved 15 July 2009 from <http://www.janes.com>

Johansson, S., Persson, P. & Claesson, I. (1999a) Active control of propeller-induced noise in aircraft mock-up. Paper presented at *1999 International Symposium on Active Control of Sound and Vibration (ACTIVE 99)*, Fort Lauderdale, Florida, Dec 2-4.

Johansson, S., Claesson, I., Nordebo, S. & Sjösten, P. (1999b) Evaluation of Multiple Reference Active Noise Control Algorithms on Dornier 328 Aircraft Data. *IEEE Transactions on Speech and Audio Processing,* 7(4), pp 473-477.

Johansson, S., Persson, P., Claesson, I. & Lagö, T. L. (2000) Evaluation of the Performance of an Active Noise Control System in an Aircraft Mock-up. Paper presented at *7th International Congress on Sound and Vibration*, Garmisch-Partenkirchen, Germany, 4-7 July.

Johnston, J. F. & Donham, R. E. (1981) Attenuation of propeller related vibration and noise. Paper presented at *AIAA/ASME/ASCE/AHS 22nd. Structures, Structural Dynamics and Materials Conference*, Atlanta, Ga., April 6-8.

Johnston, J. F. & Donham, R. E. (1982) Attenuation of propeller-related vibration and noise. *AIAA Journal of Aircraft,* 19(10).

Johnston, J. F., Donham, R. E. & Guinn, W. A. (1980) Propeller signatures and their use. Paper presented at *AIAA 6th Aeroacoustics Conference*, Hartford, CT.

Johnston, J. F., Donham, R. E. & Guinn, W. A. (1981) Propeller signatures and their use. *AIAA Journal of Aircraft,* 18(11).

Jones, J. D. (1987) A study of active control techniques for noise reduction in an aircraft fuselage model. Ph.D. Thesis. Virginia Polytechnic Institute and State University, Blacksburg, Virginia.

Jones, J. D. & Fuller, C. R. (1984) Noise Control Characteristics of Synchrophasing - an Experimental Investigation. Paper presented at *AIAA/NASA 9th Aeroacoustics Conference*, Williamsburg, VA.

Jones, J. D. & Fuller, C. R. (1986a) An Experimental Investigation of the Interior Noise Control Effects of Propeller Synchrophasing CR-178185, NASA.

Jones, J. D. & Fuller, C. R. (1986b) Noise Control Characteristics of Synchrophasing, Part 2: Experimental Investigation. *AIAA Journal,* 24(8), pp 1271-6.

Kalinins, A. & Dym, C. L. (Eds.) (1976) *Vibration: Beams, Plates, and Shells*. Benchmark Papers in Acoustics, Lindsay, R. B. (Series Ed.), Stroudsburg, Pennsylvania, Dowden, Hutchison & Ross, Inc.

Kaptein, D. (1991) Propeller Blade Synchrophasing. UK Patent GB 2 237 415 A.

Kaptein, D. (1992) Active Synchrophasing of Propeller Unbalance. Paper presented at *NASA/SAE/DLR Fourth Aircraft Interior Noise Workshop*, Friedrichshafen, Germany, Jul.

Kaptein, D. (1994) Propeller Blade Position Controller. United States Patent 5,295,641.

Kaptein, D. (1996) Propeller Blade Position Controller. United States Patent 5,551,649.

Kinsler, L. E., Frey, A. R., Coppens, A. B. & Sanders, J. V. (1982) *Fundamentals of Acoustics*, New York, John Wiley & Sons.

Kuo, S. M. & Morgan, D. R. (1996) *Active Noise Control Systems: Algorithms and DSP Implementations*. Wiley Series in Telecommunications and Signal Processing, New York, John Wiley & Sons Inc.

Leissa, A. (1973) Vibration of Shells NASA SP-288, Reprinted by the Acoustical Society of America, 1993.

Leissa, A. (1993) *Vibration of Shells*, Acoustical Society of America.

Li, D. S., Cheng, L. & Gosselin, C. M. (2002) Analysis of structural acoustic coupling of a cylindrical shell with an internal floor partition. *Journal of Sound and Vibration,* 250(5), pp 903-921.

Lockheed Martin (Lockheed) P-3 Orion (2009). *Jane's Aircraft Upgrades*, Retrieved 15 July 2009 from <http://www.janes.com>

Magliozzi, B. (1983) Synchrophasing for cabin noise reduction of propeller-driven airplanes. Paper presented at *8th AIAA Aeroacoustics Conference*, Atlanta, GA, Apr. 11-13.

Magliozzi, B. (1995) Adaptive Synchrophaser for Reducing Aircraft Cabin Noise and Vibration. United States Patent 5,453,943.

Magliozzi, B. & Metzger, F. B. (1992) Method for Reducing Aircraft Cabin Noise and Vibration. United States Patent 5,148,402.

Magliozzi, B., Hanson, D. B. & Amiet, R. K. (1991) Propeller and Propfan Noise. In Hubbard, H. H. (Ed.) *Aeroacoustics of Flight Vehicles: Theory and Practice*, Vol. 1: Noise Sources, NASA Reference Publication 1258, WRDC Technical Report 90-3052. NASA.

Mahan, J. R. & Fuller, C. R. (1985) An Improved Source Model for Aircraft Interior Noise Studies. Paper presented at *Collection of Technical Papers - AIAA/ASME/ASCE/AHS Structures, Structural Dynamics & Materials Conference 26th*.

Marciniak, W., Rodriguez, E., Olszowska, K., Atkov, O., Botvin, I., Araujo, A., Pais, F., Soares Ribeiro, C., Bordalo, A., Loureiro, J., Prazeres De Sa, E., Ferreira, D., Castelo Branco, M. S. & Castelo Branco, N. A. (1999) Echocardiographic evaluation in 485 aeronautical workers exposed to different noise environments. *Aviation Space & Environmental Medicine,* 70(3 Pt 2), pp A46-53.

McKinley, R. (2004) Active Synchrophaser Project [e-mail]. Personal Communication to Blunt, D. M., 21 July.

Mixson, J. S. & Wilby, J. F. (1991) Interior Noise. In Hubbard, H. H. (Ed.) *Aeroacoustics of Flight Vehicles: Theory and Practice*, Vol. 2: Noise Control, NASA Reference Publication 1258, WRDC Technical Report 90-3052.

Moreau, D., Cazzolato, B., Zander, A. & Petersen, C. (2008) A Review of Virtual Sensing Algorithms for Active Noise Control. *Algorithms,* 1, pp 69-99.

Nelson, P. A. & Elliott, S. J. (1985) Active noise reduction apparatus. UK Patent 2149614A.

Nelson, P. A. & Elliott, S. J. (1992) *Active Control of Sound*, London, Academic Press.

Pimenta, M. G., Martinho Pimenta, A. J., Castelo Branco, M. S., Silva Simoes, J. M. & Castelo Branco, N. A. (1999) ERP P300 and brain magnetic resonance imaging in patients with vibroacoustic disease. *Aviation Space & Environmental Medicine,* 70(3 Pt 2), pp A107-14.

Pla, F. G. (1998) Method for Reducing Noise and/or Vibration from Multiple Rotating Machines. United States Patent 5,789,678.

Pla, F. G. & Goodman, G. C. (1993) Method and Apparatus for Synchronizing Rotating Machinery to Reduce Noise. U.S. Patent 5,221,185.

Pla, F. G., Goodman, G., Ranaudo, R. & Silcox, R. J. (1993) Cabin noise cancellation using active RPM control OV-10A flight test results. Paper presented at *15th AIAA Aeroacoustics Conference*, Long Beach, CA, October 25-27.

Powell, C. A. & Fields, J. M. (1991) Human Response to Aircraft Noise. In Hubbard, H. H. (Ed.) *Aeroacoustics of Flight Vehicles: Theory and Practice*, Vol. 2: Noise Control, NASA Reference Publication 1258, WRDC Technical Report 90-3052.

Robinson, D. W. & Dadson, R. S. (1956) A re-determination of the equal-loudness relations for pure tones. *British Journal of Applied Physics,* 7, pp 166-181.

Saab (2004) Saab 2000 Aircraft Specifications, Retrieved 15 July 2009 from <http://www.saabaircraftleasing.com/prod/pictures.asp?Mod=2000>

Smith, D. H. (2004) Wavelet Multi-Resolution Analysis of C-130J Vibration Data - Steps Towards Environment Characterisation DSTO-TR-1626, Defence Science and Technology Organisation, Department of Defence, Australia.

Smith, S. (2009) OV-10A. *NASA*, Retrieved 20 Feb 2011 from <http://www.nasa.gov/centers/langley/images/content/449066main_OV_10_904.jpg>

Smith, S. D. (2002) Characterizing the effects of airborne vibration on human body vibration response. *Aviation Space & Environmental Medicine,* 739(1), pp 36-45.

Strang, G. (1980) *Linear Algebra and its Applications*, Harcourt Brace Jovanovich, Publishers.

Success Story: Active Synchrophaser Lowers C-130 Interior Noise Levels (2003). *Air Force Research Laboratory*, Retrieved 1 July 2004 from <http://www.afrl.af.mil/successstories/2003/support_to_the_warfighter/03-he-07.pdf>

Tokhi, O. & Veres, S. (Eds.) (2002) *Active Sound and Vibration Control: Theory and Applications*. IEE Control Engineering Series, Atherton, D. P., Irwin, G. W. & Spurgeon, S. (Series Eds.), London, The Institution of Electrical Engineers.

Ultra (2009) Active Noise and Vibration Control. *Ultra Electronics*, Retrieved 16 July 2009 from <http://www.ultra-controls.com/productdetails.php?productID=15>

Appendix A. Least-Squares Solutions

The least-squares solution to an over-determined system of linear equations

$$\mathbf{Ax} = \mathbf{b} \tag{A.1}$$

where A is an $m \times n$ matrix, and $m > n$, is found by minimising the length of the error vector

$$\left\| \mathbf{Ax} - \mathbf{b} \right\|. \tag{A.2}$$

This is geometrically equivalent to finding the point $\mathbf{p} = \mathbf{A}\bar{\mathbf{x}}$ in the column space of **A** that is closer to **b** that any other point; i.e., the perpendicular projection of **b** onto the column space of **A**. An example where **A** is a 3×2 matrix is shown in Figure A.1 (Strang, 1980, §3.2).

Since $\mathbf{A}\bar{\mathbf{x}} - \mathbf{b}$ must be orthogonal to every vector in the column space of **A**, the inner-product of $\mathbf{A}\bar{\mathbf{x}} - \mathbf{b}$ and **Ax** must be zero for all **x** (Strang, 1980, §2.5). This condition can be written in matrix notation as:

$$\begin{aligned} (\mathbf{Ax})^T (\mathbf{A}\bar{\mathbf{x}} - \mathbf{b}) &= 0 \\ \mathbf{x}^T \mathbf{A}^T (\mathbf{A}\bar{\mathbf{x}} - \mathbf{b}) &= 0 \\ \mathbf{x}^T \left(\mathbf{A}^T \mathbf{A}\bar{\mathbf{x}} - \mathbf{A}^T \mathbf{b} \right) &= 0. \end{aligned} \tag{A.3}$$

It can be seen by inspection that Equation (A.3) can only be true for all **x** if

$$\mathbf{A}^T \mathbf{A}\bar{\mathbf{x}} = \mathbf{A}^T \mathbf{b}. \tag{A.4}$$

Note that the matrix $\mathbf{A}^T \mathbf{A}$ is square and will always be invertible as long as the columns of **A** are independent (Strang, 1980, §3.1). Hence, the least-squares solution $\bar{\mathbf{x}}$ is found by pre-multiplying both sides of Equation (A.4) by

$$\left(\mathbf{A}^T \mathbf{A} \right)^{-1},$$

giving

$$\bar{\mathbf{x}} = \left(\mathbf{A}^T \mathbf{A} \right)^{-1} \mathbf{A}^T \mathbf{b}. \tag{A.5}$$

Similarly, the least-squares solution to an alternative system of linear equations

$$\mathbf{xA} = \mathbf{b} \tag{A.6}$$

is given by

$$\bar{\mathbf{x}} = \mathbf{b}\mathbf{A}^T \left(\mathbf{A}\mathbf{A}^T \right)^{-1}. \tag{A.7}$$

By simple expansion, it can be seen that the above results also apply to the case where $\bar{\mathbf{x}}$ and **b** are extended to arrays of vectors (i.e., 2D matrices), as long as $\bar{\mathbf{x}}$ and **b** have the same dimensions.

If A is complex then

$$\bar{\mathbf{x}} = \mathbf{b}\mathbf{A}^H \left(\mathbf{A}\mathbf{A}^H\right)^{-1} \tag{A.8}$$

where $\mathbf{A}^H$ is the Hermitian (complex conjugate) transpose of $\mathbf{A}$.

In Matlab, the least-squares solution to $\mathbf{A}\mathbf{x} = \mathbf{b}$ is achieved with left matrix division (i.e., $\bar{\mathbf{x}} = \mathbf{A} \setminus \mathbf{b}$), and the least-squares solution to $\mathbf{x}\mathbf{A} = \mathbf{b}$ is achieved with right matrix division (i.e., $\bar{\mathbf{x}} = \mathbf{A} / \mathbf{b}$).

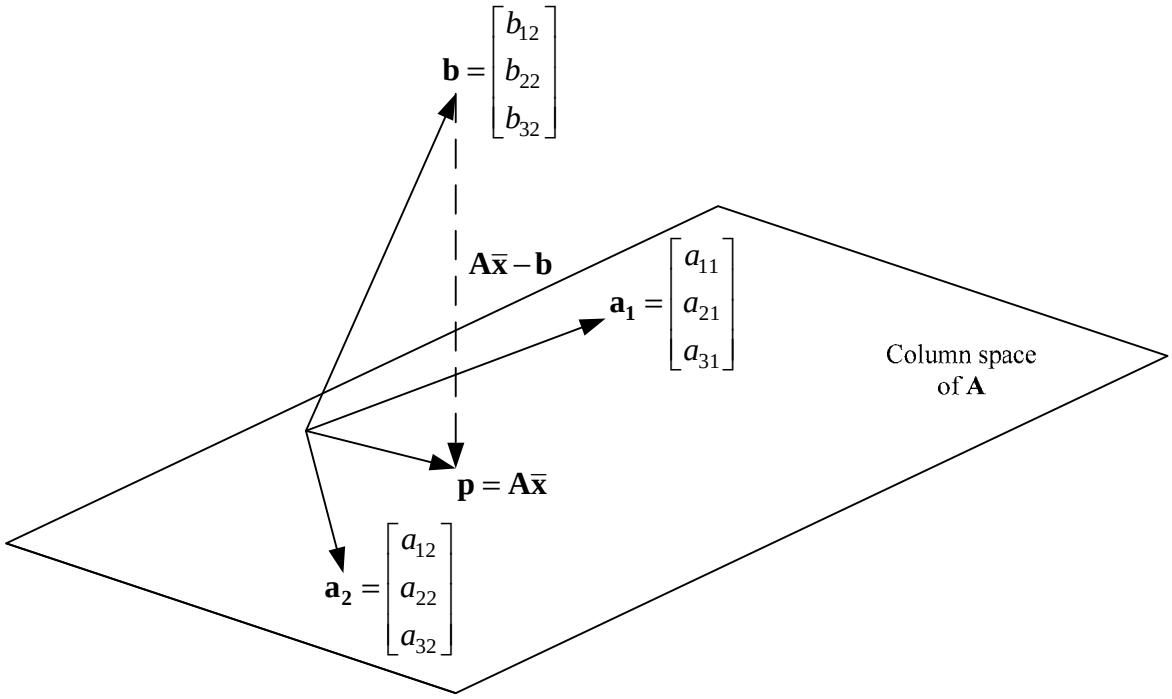

Figure A.1 Perpendicular projection of **b** *onto the column space of a 3× 2 matrix* **A** *(Strang, 1980, Fig 3.4).*

Appendix B. AP-3C Flight Trial

The following tables and figures provide details specific to the AP-3C flight trial that occurred in aircraft A9-660 over the period 6–10 November 2006 at RAAF Base Edinburgh.

Table B.1 AP-3C sensor details.

D120f Channel	Description	OEM	Type	Serial No.	Accel. Sens. (mV/g)	Mic. Sens. (mV/Pa)	Fuselage Station
1	Pilot seat mic.	B&K	4935	2436870	n.a.	5.7650	230
2	Copilot seat mic.	B&K	4935	2436871	n.a.	5.6431	230
3	Flight engineer seat mic.	B&K	4935	2436869	n.a.	5.9026	250
4	Tacco seat mic.	B&K	4935	2436872	n.a.	6.0591	350
5	Navigator seat mic.	B&K	4935	2436873	n.a.	6.1345	350
6	Fwd grab rail mic.	B&K	4935	2436874	n.a.	6.1020	300
7	Navigator seat rail accel.	PCB	353B33	107329	98.7	n.a.	350
8	Tacco seat rail accel.	PCB	353B33	107598	98.7	n.a.	350
9	Prop 1 magnetic pick-up	n.a.	n.a.	n.a.	n.a.	n.a.	n.a.
10	Prop 2 magnetic pick-up	n.a.	n.a.	n.a.	n.a.	n.a.	n.a.
11	Prop 3 magnetic pick-up	n.a.	n.a.	n.a.	n.a.	n.a.	n.a.
12	Prop 4 magnetic pick-up	n.a.	n.a.	n.a.	n.a.	n.a.	n.a.
13	Grab rail above synchro box mic.	B&K	4935	2436863	n.a.	6.4856	420
14	Sensor 4 seat mic.	B&K	4935	2436864	n.a.	5.9652	480
15	Sensor 4 seat rail accel.	PCB	353B33	107599	102.9	n.a.	480
16	Grab rail above SEM mic.	B&K	4935	2436177	n.a.	5.7325	540
17	Sensor 3 seat mic.	B&K	4935	2436865	n.a.	6.0308	515
18	Sensor 3 seat rail accel.	PCB	353B33	107330	99.2	n.a.	515
19	SEM seat mic.	B&K	4935	2436866	n.a.	5.7488	575
20	SEM seat rail accel.	PCB	353B33	108036	99.7	n.a.	575
21	SS2 seat mic.	B&K	4935	2436867	n.a.	6.1740	615
22	SS2 seat rail accel.	PCB	353B33	108039	102.3	n.a.	615
23	SS1 seat mic.	B&K	4935	2436868	n.a.	6.1956	660
24	SS1 seat rail accel.	PCB	353B33	108034	101.8	n.a.	660
25	Grab rail above SS1 mic.	B&K	4935	2436146	n.a.	5.8932	660
26	Grab rail above G2 rack mic.	B&K	4935	2436120	n.a.	5.8420	780
27	Grab rail above observer stations mic.	B&K	4935	2436875	n.a.	5.4751	900
28	Grab rail above galley mic.	B&K	4935	2436876	n.a.	6.3754	1020
29	Bottom of bunk (above table) mic.	B&K	4935	2436855	n.a.	5.9432	990
30	Stbd observer seat mic.	B&K	4935	2436853	n.a.	6.2238	880
31	Port observer seat mic.	B&K	4935	2436852	n.a.	6.3218	880
32	Grab rail above rear bunk mic.	B&K	4935	2436854	n.a.	6.9125	1100

Table B.2 AP-3C aircraft weights.

	Flight 1		Flight 2	
	Take-off	**Landing**	**Take-off**	**Landing**
Total (lbs)	104 000	79 000	108 000	85 000
Payload (lbs)	nil	nil	nil	nil
Fuel (lbs)	35 000	10 000	40 000	17 000
CoG (% MAC)	26.4	not recorded	26.3	not recorded

Table B.3 AP-3C aircrew-recorded flight parameters.

Flight	Serial	Altitude (ft ±50 ft)	Airspeed (KIAS ±5 KIAS)	Cabin Altitude (ft)	Altimeter Setting* (mBar)	OAT (°C)	Engine Power (hp ±50 hp)			
							Eng 1	Eng 2	Eng 3	Eng 4
1	1	500	200	20	1026 (QNH)	11 (ISA −3°)	1200	1200	1230	1220
	2	500	220	20	1026 (QNH)	12 (ISA −2°)	1330	1340	1340	1380
	3	1000	200	130	1026 (QNH)	12 (ISA −1°)	1200	1200	1200	1200
	4	1000	220	160	1026 (QNH)	12 (ISA −1°)	1440	1400	1420	1400
	5	1000	240	180	1025 (QNH)	12 (ISA −1°)	1580	1500	1650	1600
	6	3000	220	330	1025 (QNH)	5 (ISA −4°)	1440	1480	1420	1450
	7	3000	240	330	1025 (QNH)	5 (ISA −4°)	1650	1720	1750	1750
	8	3000	260	350	1025 (QNH)	5 (ISA −4°)	1850	1850	1850	1850
	9	10000	220	310	1025 (QNH)	2 (ISA −7°)	1490	1480	1540	1480
	10	10000	240	280	1025 (QNH)	2 (ISA −7°)	1820	1820	1850	1850
	11	10000	260	280	1025 (QNH)	3 (ISA −8°)	2180	2300	2230	2150
	12	FL180	220	2000	1013 (QNE)	−13 (ISA −8°)	1650	1650	1620	1620
	13	FL180	240	2040	1013 (QNE)	−13 (ISA −8°)	2000	2000	2000	2000
	14	FL180	260	2040	1013 (QNE)	−12 (ISA −7°)	2350	2370	2380	2380
2	15	FL180	282	2040	1013 (QNE)	−12 (ISA +9°)	3000	3000	3000	3000
	16	FL200	220	2950	1013 (QNE)	−18 (ISA +7°)	1900	1900	1900	1900
	17	FL200	240	2980	1013 (QNE)	−18 (ISA +7°)	2150	2130	2120	2120
	18	FL200	260	2980	1013 (QNE)	−18 (ISA +7°)	2550	2550	2550	2550
	19	FL240	200	4920	1013 (QNE)	−25 (ISA +8°)	1750	1750	1750	1750
	20	FL240	220	4920	1013 (QNE)	−25 (ISA +8°)	2000	2000	2000	2000
	21	FL240	240	4920	1013 (QNE)	−26 (ISA +7°)	2300	2300	2300	2300
	22	FL280	180	6960	1013 (QNE)	−37 (ISA +4°)	1600	1600	1600	1600
	23	FL280	200	6940	1013 (QNE)	−38 (ISA +5°)	1800	1800	1800	1800
	24	FL280	220	6940	1013 (QNE)	−38 (ISA +5°)	2000	2000	2000	2000
	25	1000	190	250	1021 (QNH)	15 (ISA +2°)	off	1550	1550	1550
	26	1000	210	200	1021 (QNH)	15 (ISA +2°)	off	1650	1650	1650
	27	3000	190	330	1021 (QNH)	13 (ISA +4°)	off	1550	1550	1550
	28	3000	210	380	1021 (QNH)	13 (ISA +4°)	off	1750	1750	1750

* QNH means the barometric altimeter was adjusted to read altitude relative to the mean sea level air pressure of the day. It was used up to the transition altitude (10 000 ft). QNE means the barometric altimeter was adjusted to read altitude relative to the International Standard Atmosphere mean seal level air pressure of 1013.25 hPa. It was used above 10 000 ft.

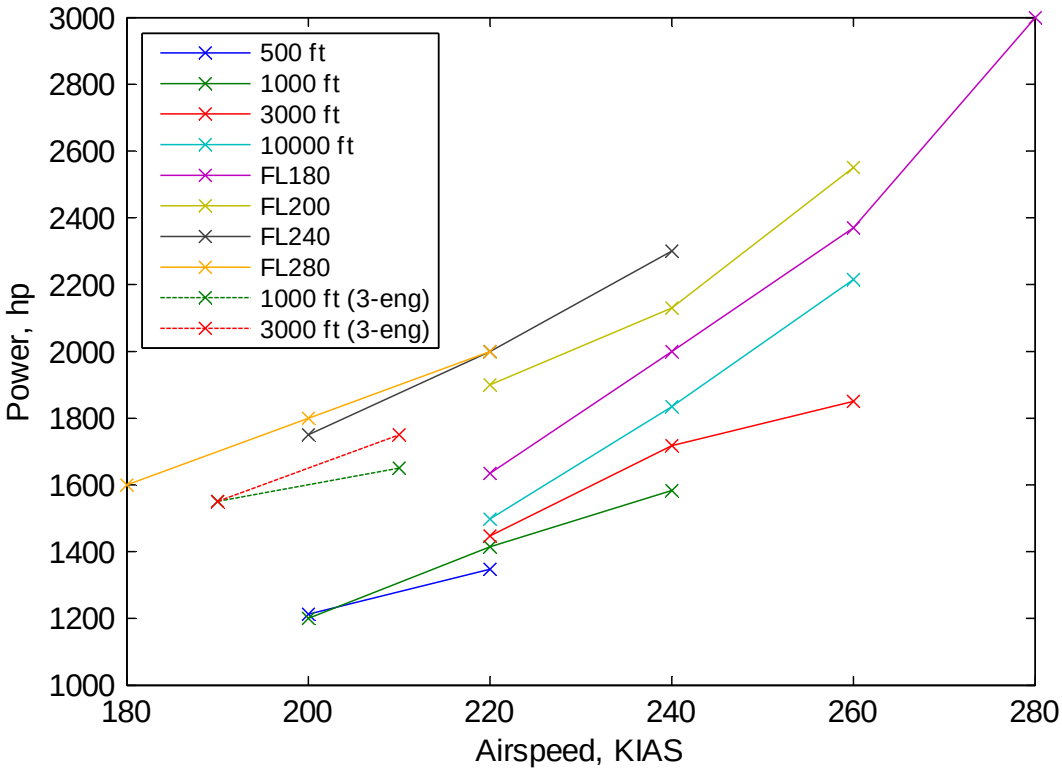

Figure B.1 AP-3C mean engine power.

Figure B.2 AP-3C typical crew seat headrest microphone installation on a 20 cm (8 in.) gooseneck.

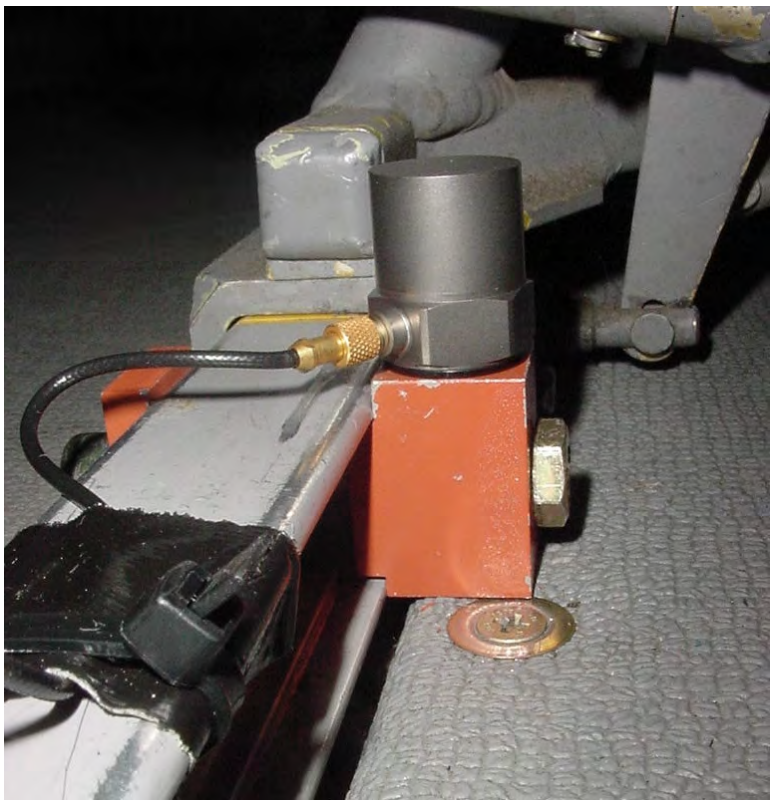

Figure B.3 AP-3C typical seat rail accelerometer installation on a purpose-made bracket bolted through a hole in the seat rail.

Figure B.4 AP-3C typical overhead grab rail microphone installation on a 20 cm (8 in.) gooseneck – the rail is offset to starboard and the microphone is close to the centreline.

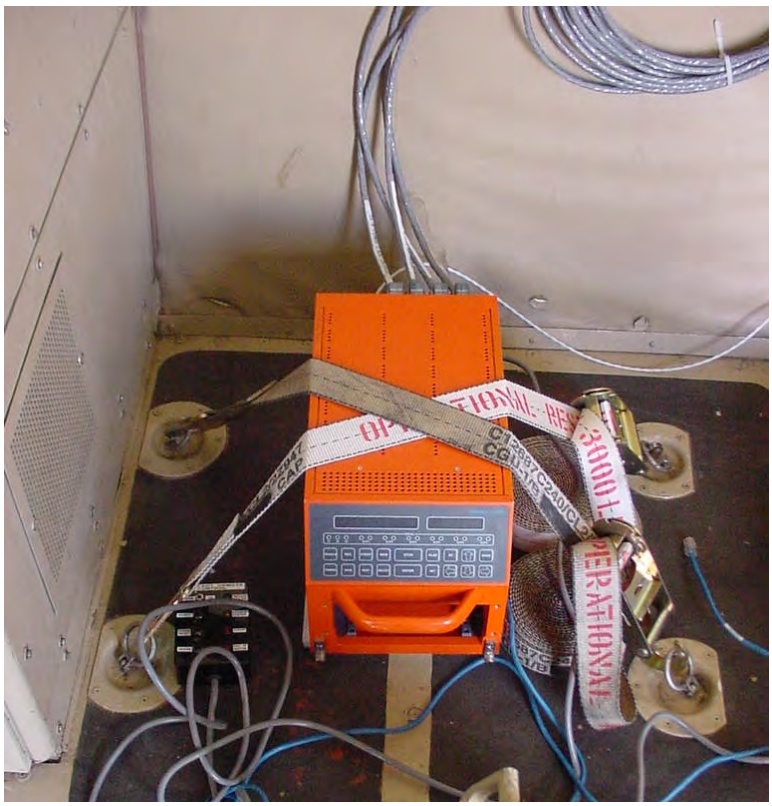

Figure B.5 Heim D120f digital data recorder (hard disk drive removed) strapped to the AP-3C cabin floor.

Appendix C. C-130J-30 Flight Trials

The following tables and figures provide details specific to the two flight trials that took place at RAAF Base Richmond:

a) over the period 22–30 November 2006 in aircraft A97-467 (Trial 1), and

b) over the period 21–24 July 2008 in aircraft A97-464 (Trial 2).

Table C.1 C-130J-30 aircraft weights.

Weights	**Trial 1**						**Trial 2**	
	Flight 1		Flight 2		Flight 3		Flight 1	
	Take-off	Landing	Take-off	Landing	Take-off	Landing	Take-off	Landing
Total (lbs)	136 000	116 500	135 400	117 400	121 000	Not recorded	129 000	Not recorded
Payload (lbs)	15 000	15 000	15 000	15 000	Nil	Nil	Nil	Nil
Fuel (lbs)	32 900	13 400	32 000	14 000	32 000	Not recorded	39 800	10 730
CoG (% MAC)	27.2	28.9	24.1	20.9	25.4	22.3	26.5	Not recorded

Table C.2 C-130J-30 FADEC in control.

Trial	**Description**	**FADEC in Control**
1	Ground Run All Flights	Unknown Unknown
2	Ground Run All flight serials except Serial 2 Serial 2	A B B (Props 1–3), A (Prop 4)

C.1. Trial 1

The average engine power levels, as recorded by the DBA, for all flights and serials in Trial 1 are shown in Table C.3 and Figure C.1. There are a number of interesting features:

a) Although there is some scatter evident, there appears to be a reasonably linear relationship between the calibrated airspeed and engine power over the range shown. The average slope is approximately 24 hp/KCAS.

b) The lines for the two cargo flights (Flights 1 & 2) are very close, except at FL280, where they diverge above 200 KCAS.

c) For the same altitude and airspeed, the engine power is appreciably lower in the troop configuration (Flight 3) than the cargo configurations (Flights 1 & 2) presumably because the aircraft was essentially empty. A more realistic passenger load (e.g., 90–120 troops) may even exceed the payload of the cargo flights and require more engine power.

Table C.3 C-130J-30 average engine power for Trial 1.

Serial	Engine Power (hp)											
	Flight 1				Flight 2				Flight 3			
	Eng 1	Eng 2	Eng 3	Eng 4	Eng 1	Eng 2	Eng 3	Eng 4	Eng 1	Eng 2	Eng 3	Eng 4
1	2705	2772	2724	2708	2736	2732	2770	2757	2742	2736	2720	2707
2	2779	2786	2792	2769	2820	2817	2843	2833	2733	2715	2757	2722
3	3126	3123	3126	3100	3069	3065	3073	3046	3077	3057	3106	3070
4.1	2202	2201	2210	2190	2214	2225	2233	2214	2022	2031	2050	2027
4.2	2514	2518	2523	2513	2547	2560	2558	2548	2407	2421	2422	2402
4.3	2758	2776	2755	2756	2779	2791	2792	2782	2763	2772	2789	2767
5.1	2055	2080	2122	2088	2014	2046	2062	2051	1974	1986	1983	1958
5.2	2357	2394	2411	2382	2349	2370	2382	2369	2284	2316	2330	2269
5.3	2587	2616	2638	2604	2597	2649	2635	2629	2518	2522	2524	2519
6.1	2078	2104	2122	2092	2118	2126	2120	2086	2027	2022	2037	2002
6.2	2253	2289	2289	2261	2260	2275	2272	2261	2217	2224	2230	2219
6.3	2305	2338	2345	2315	2404	2419	2410	2405	2299	2305	2309	2292
7.1	n.a.	n.a.	n.a.	n.a.	n.a.	n.a.	n.a.	n.a.	1837	1865	1885	1858
7.2	n.a.	n.a.	n.a.	n.a.	n.a.	n.a.	n.a.	n.a.	1968	1998	1996	1972
7.3	2323	2366	2341	2333	2261	2304	2280	2270	2325	2366	2346	2322
8	n.a.	n.a.	n.a.	n.a.	2729	2792	2766	2754	n.a.	n.a.	n.a.	n.a.
9	n.a.	n.a.	n.a.	n.a.	3063	3105	3084	3073	2950	2998	2980	2966
10	n.a.	n.a.	n.a.	n.a.	n.a.	n.a.	n.a.	n.a.	2520	2539	2542	2537

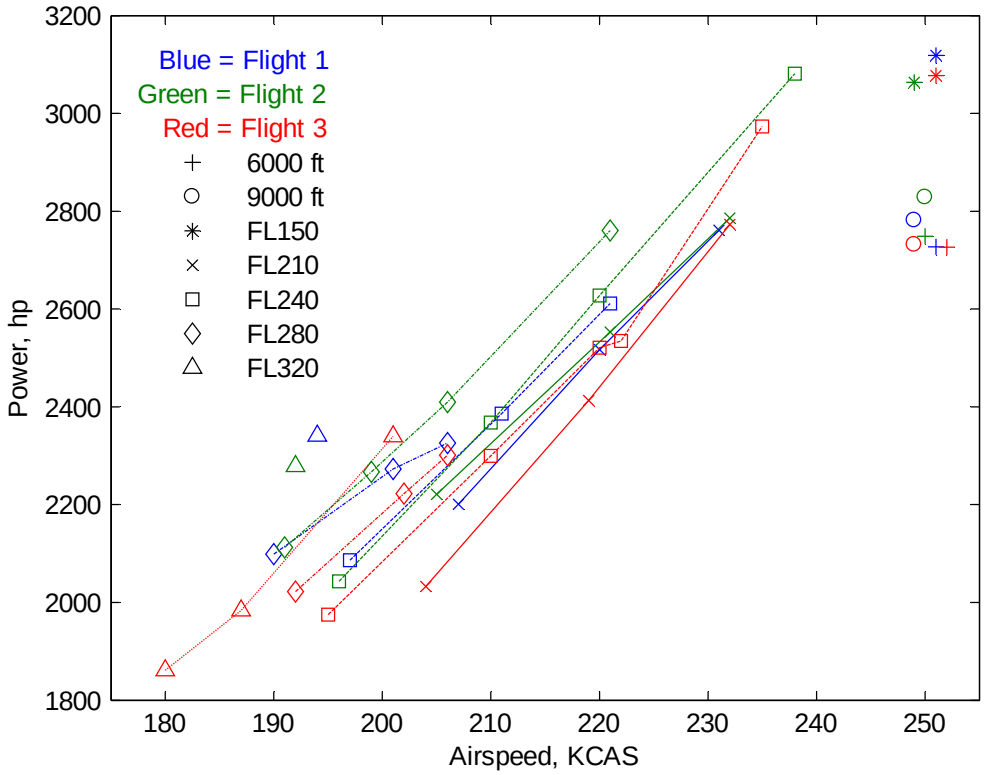

Figure C.1 C-130J-30 average engine power for Trial 1 – the lines connect points of equal altitude during each flight: solid = FL210, dashed = FL240, dash-dot = FL280, and dotted = FL320.

Table C.4 C-130J-30 Trial 1 accelerometers.

Accelerometers					**OEM Cal**	**DSTO Cal**	**Cal Diff**	**D120f Channel**		
Location	OEM	Type	Serial #	Source	mV/g	mV/g	%	Gnd/Flt 1	Flight 2	Flight 3
Floor B7	PCB	J353B33	39614	MPD	102.7	103.8	1.1%	33	33	30
Floor B12	PCB	J353B33	108035	New	101.2	n.a.	n.a.	34	34	31
Floor B17	PCB	J353B33	108037	New	102.4	n.a.	n.a.	35	35	32
Floor B22	PCB	J353B33	107329	New	98.7	n.a.	n.a.	36	36	n.a.
Floor B27	PCB	J353B33	111868	New	100.3	n.a.	n.a.	37	37	n.a.
Floor B32	PCB	J353B33	110267	New	97.9	98.2	0.3%	38	38	n.a.
Floor D7	PCB	J353B33	65549	MPD	100.4	n.a.	n.a.	1	1	n.a.
Floor D12	PCB	J353B33	39210	MPD	102.2	103.3	1.1%	2	2	n.a.
Floor D17	PCB	J353B33	39213	MPD	101.7	102.5	0.8%	3	3	n.a.
Floor D22	PCB	J353B33	39215	MPD	101.5	102.4	0.9%	4	4	n.a.
Floor D27	PCB	J353B33	111867	New	98.1	n.a.	n.a.	5	5	n.a.
Floor D32	PCB	J353B33	107599	New	102.9	n.a.	n.a.	6	6	n.a.
Floor F7	PCB	J353B33	108036	New	99.7	n.a.	n.a.	9	9	5
Floor F12	PCB	J353B33	107597	New	98.5	n.a.	n.a.	10	10	6
Floor F17	PCB	J353B33	108039	New	102.3	n.a.	n.a.	11	11	7
Floor F22	PCB	J353B33	108034	New	101.8	n.a.	n.a.	12	12	n.a.
Floor F27	PCB	J353B33	107598	New	98.7	n.a.	n.a.	13	13	n.a.
Floor F32	PCB	J353B33	107330	New	99.2	n.a.	n.a.	14	14	n.a.
Cargo 1 Vertical	PCB	J353B33	39211	MPD	n.a.	101.7	n.a.	28	20	n.a.
Cargo 2 Vertical	PCB	J353B33	65557	MPD	n.a.	101.0	n.a.	32	24	n.a.
Cargo 4 Vertical	PCB	J353B33	39209	MPD	n.a.	102.1	n.a.	24	32	n.a.
Cargo 5	PCB	302A02	16444	MPD	n.a.	9.7	n.a.			n.a.
Cargo 6	Dytran	3041A2	546	MPD	n.a.	104.5	n.a.	20	28	n.a.
Cargo 3 Vertical	Dytran	3041A2	556	MPD	n.a.	103.5	n.a.	8	8	n.a.
Cargo 3 Horizontal	Dytran	3041A2	549	MPD	n.a.	103.5	n.a.	7	7	n.a.
Triple Pallet	Endevco	2258A-100	11548	X	104.6	103.4	−1.1%	17	17	n.a.
				Y	103.2	102.7	−0.5%	18	18	n.a.
				Z	100.2	99.6	−0.6%	19	19	n.a.
Double Pallet	Endevco	2258A-100	11549	X	102.6	103.3	0.7%	29	21	n.a.
				Y	104.2	104.5	0.3%	30	22	n.a.
				Z	102.5	102.3	−0.2%	31	23	n.a.
Single Pallet	Endevco	2258A-100	11402	X	104.4	104.9	0.5%	21	29	n.a.
				Y	101.5	102.6	1.1%	22	30	n.a.
				Z	102.3	102.2	−0.1%	23	31	n.a.

Notes:
1. Underlined text indicates the sensitivity used.
2. Locations refer to the C-130J-30 load plan diagrams (e.g., B22 is tie-down ring B 22)
3. Tri-axial orientation (X – nose, Y – port, Z – up).

Table C.5 C-130J-30 Trial 1 microphones.

Microphones				**Flt 2 Cal**	**Flt 3 Cal**	**D120f Channel**			
Location	OEM	Type	Serial #	mV/Pa	mV/Pa	Ground	Flight 1	Flight 2	Flight 3
Port 1.5	B&K	4935	n.a.	n.a.	5.890	n.a.	n.a.	n.a.	29
Port 5	B&K	4935	n.a.	n.a.	6.837	n.a.	n.a.	n.a.	8
Port 8.5	B&K	4935	2436870	6.252	6.002	39	39	39	33
Port 12	B&K	4935	2436852	n.a.	6.599	n.a.	n.a.	n.a.	34
Port 15.5	B&K	4935	2436855	6.439	6.139	40	40	40	35
Port 19	B&K	4935	2534982	n.a.	6.247	n.a.	n.a.	n.a.	36
Port 22.5	B&K	4935	2534983	n.a.	6.708	n.a.	n.a.	n.a.	37
Port 26	B&K	4935	2436853	n.a.	6.121	n.a.	n.a.	n.a.	38
Port 30	B&K	4935	2436871	n.a.	5.820	n.a.	n.a.	n.a.	39
Port 33	B&K	4935	2436874	n.a.	6.240	n.a.	n.a.	n.a.	40
Centre 1.5	B&K	4188A021	2472088	n.a.	28.249	n.a.	n.a.	n.a.	1
Centre 5	B&K	4935	2436856	n.a.	6.423	n.a.	n.a.	n.a.	2
Centre 8.5	B&K	4935	2436177	n.a.	5.848	n.a.	n.a.	n.a.	17
Centre 12	B&K	4935	2436872	n.a.	6.225	n.a.	n.a.	n.a.	18
Centre 15.5	B&K	4935	2436865	n.a.	6.049	n.a.	n.a.	n.a.	19
Centre 19	B&K	4935	2436864	n.a.	6.157	n.a.	n.a.	n.a.	20
Centre 22.5	B&K	4935	2484887	n.a.	5.869	n.a.	n.a.	n.a.	21
Centre 26	B&K	4935	2436866	n.a.	5.829	n.a.	n.a.	n.a.	22
Centre 29.5	B&K	4935	2484886	n.a.	6.755	n.a.	n.a.	n.a.	23
Centre 33	B&K	4935	2484885	n.a.	6.098	n.a.	n.a.	n.a.	24
Stbd 1.5	B&K	4935	2484892	n.a.	5.852	n.a.	n.a.	n.a.	3
Stbd 5	B&K	4935	2484891	n.a.	6.540	n.a.	n.a.	n.a.	4
Stbd 8.5	B&K	4935	2436873	6.429	6.217	15	15	15	9
Stbd 12	B&K	4935	2436863	n.a.	6.609	n.a.	n.a.	n.a.	10
Stbd 15.5	B&K	4935	2436854	7.498	7.176	16	16	16	11
Stbd 19	B&K	4935	2484890	n.a.	6.453	n.a.	n.a.	n.a.	12
Stbd 22.5	B&K	4935	2436146	n.a.	6.019	n.a.	n.a.	n.a.	13
Stbd 26	B&K	4935	2436867	n.a.	6.235	n.a.	n.a.	n.a.	14
Stbd 30	B&K	4935	2436869	n.a.	6.133	n.a.	n.a.	n.a.	15
Stbd 33	B&K	4935	2436876	n.a.	6.535	n.a.	n.a.	n.a.	16
Pilot	B&K	4935	2436868	6.384	5.523	26	26	26	26
Co-pilot	B&K	4935	2436120	6.017	6.184	25	25	25	25
Engineer	B&K	4935	2436875	n.a.	5.884	27	n.a.	n.a.	28

Note:
Locations refer to the C-130J-30 load plan diagram
(e.g., Port 1.5 is midway between tie-down rings 1 and 2 on the port side).

Figure C.2 Cargo installation for Flight 1, C-130J-30 Trial 1.

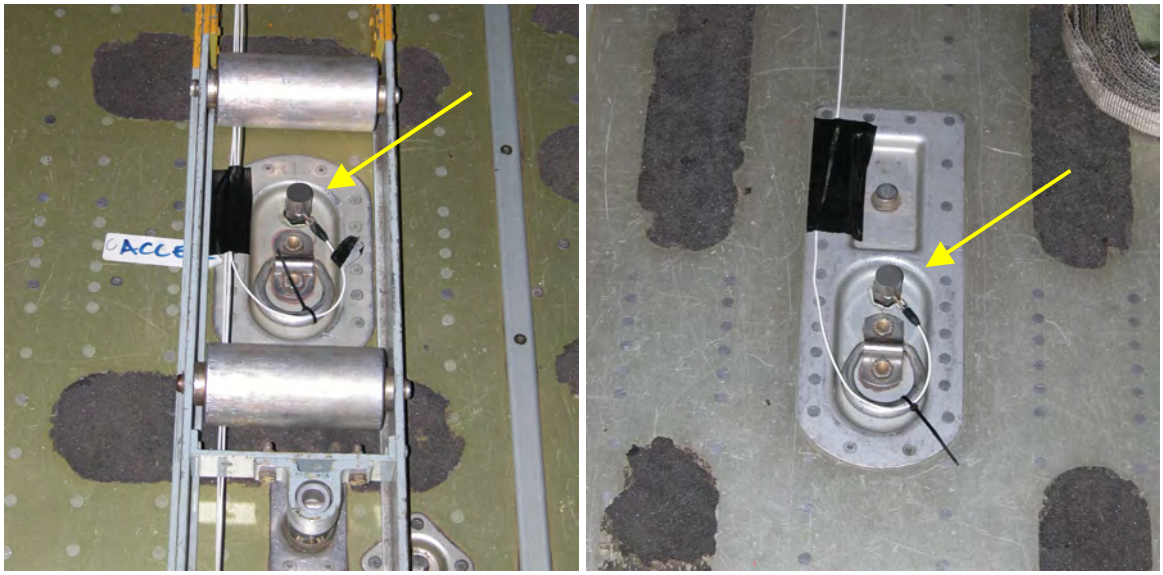

Figure C.3 Typical floor accelerometer installations in the tie-down ring wells for C-130J-30 Trial 1, Rows B & F directly under the outboard floor rollers (left) and Row D in the centre of the floor (right).

Figure C.4 Tri-axial accelerometer on the single pallet (front), C-130J-30 Trial 1.

Figure C.5 Tri-axial Accelerometer on the triple pallet (centre of middle pallet), C-130J-30 Trial 1.

Figure C.6 Main cabin configuration for Flight 3, C-130J-30 Trial 1.

Figure C.7 Typical troop seat microphone installations, C-130J-30 Trial 1.

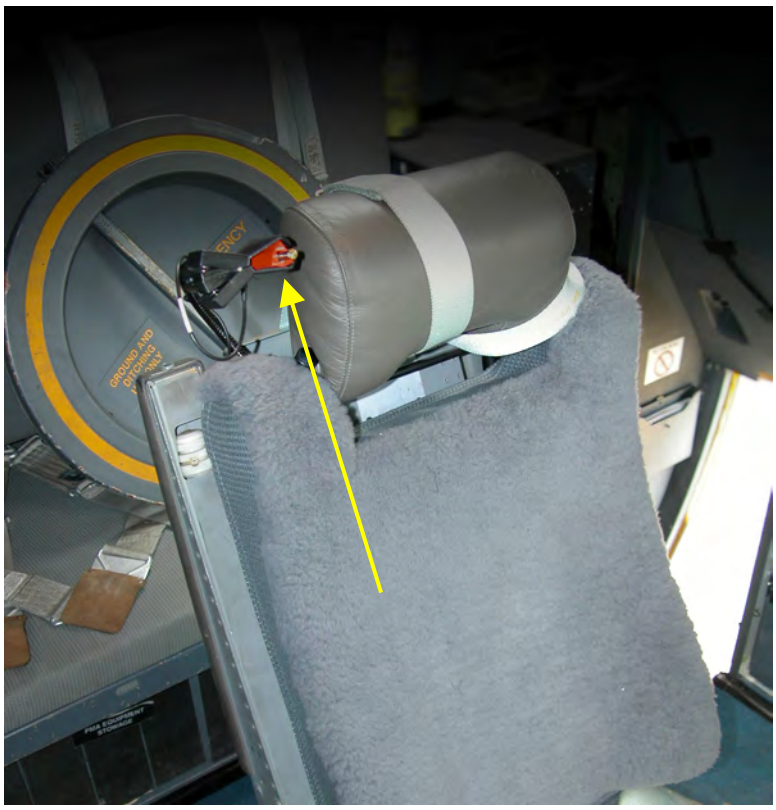

Figure C.8 Flight Engineer seat microphone, C-130J-30 Trial 1.

Figure C.9 Laser tachometer aim point, C-130J-30 Trial 1.

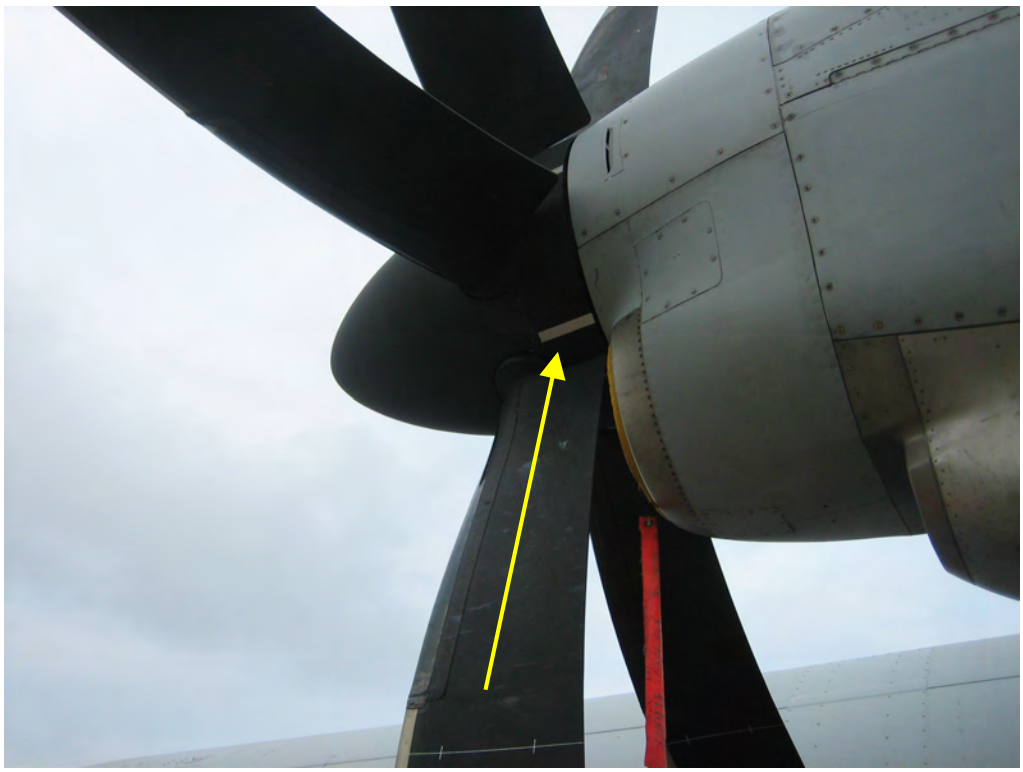

Figure C.10 Reflective tape on Propeller 2, C-130J-30 Trial 1.

Figure C.11 Heim D120f recorder, C-130J-30 Trial 1.

C.2. Trial 2

Table C.6 C-130J-30 Trial 2 accelerometers.

Accelerometers				**OEM Cal**	**D120f Channel**
Location	OEM	Type	Serial #	mV/g	Gnd/Flt 1
Floor B7	PCB	J353B33	112683	100.6	8
Floor B12	PCB	J353B33	112357	98.0	22
Floor B17	PCB	J353B33	112359	99.4	23
Floor B22	PCB	J353B33	108036	99.7	33
Floor D7	PCB	J353B33	107597	98.5	10
Floor D12	PCB	J353B33	112358	100.7	9
Floor D17	PCB	J353B33	112684	100.7	24
Floor D22	PCB	J353B33	108035	101.2	34
Floor D27	PCB	J353B33	112682	99.5	36
Floor D32	PCB	J353B33	111867	98.1	37
Floor F7	PCB	J353B33	112685	102.4	32
Floor F12	PCB	J353B33	112356	100.1	30
Floor F17	PCB	J353B33	112360	101.3	31
Floor F22	PCB	J353B33	108034	101.8	35

Table C.7 C-130J-30 Trial 2 microphones.

Microphones				**Cal**	**D120f Channel**
Location	OEM	Type	Serial #	mV/Pa	Gnd/Flt 1
Port 5	B&K	4935	2484887	5.7435	20
Port 8.5	B&K	4935	2484889	6.6382	19
Port 12	B&K	4935	2484888	5.7804	18
Port 15.5	B&K	4935	2484886	6.5805	17
Port 19	B&K	4935	2436874	6.0970	21
Port 22.5	B&K	4935	2436873	6.1605	38
Centre 1.5	B&K	4935	2484890	6.3523	12
Centre 5	B&K	4935	2484885	6.0293	16
Centre 8.5	B&K	4935	2436177	5.7843	15
Centre 12	B&K	4935	2436875	5.4454	11
Centre 15.5	B&K	4935	2436146	5.9187	14
Centre 19	B&K	4935	2436120	5.8575	13
Centre 26	B&K	4935	n.a.	6.4516	40
Stbd 5	B&K	4935	2436876	6.0809	25
Stbd 8.5	B&K	4935	2436864	5.8732	26
Stbd 12	B&K	4935	2436863	6.5311	27
Stbd 15.5	B&K	4935	2436868	6.2010	28
Stbd 19	B&K	4935	2436866	5.7127	29
Stbd 22.5	B&K	4935	2436865	5.9640	39
Pilot	B&K	4935	2436869	5.9387	7
Co-pilot	B&K	4935	2436871	5.7158	5
Engineer	B&K	4935	2436870	5.8680	6

Figure C.12 Main cabin configuration (looking forward), C-130J-30 Trial 2.

Figure C.13 Main cabin configuration (looking aft), C-130J-30 Trial 2.

Figure C.14 Microphone mounted to flight deck seat headrest, C-130J-30 Trial 2.

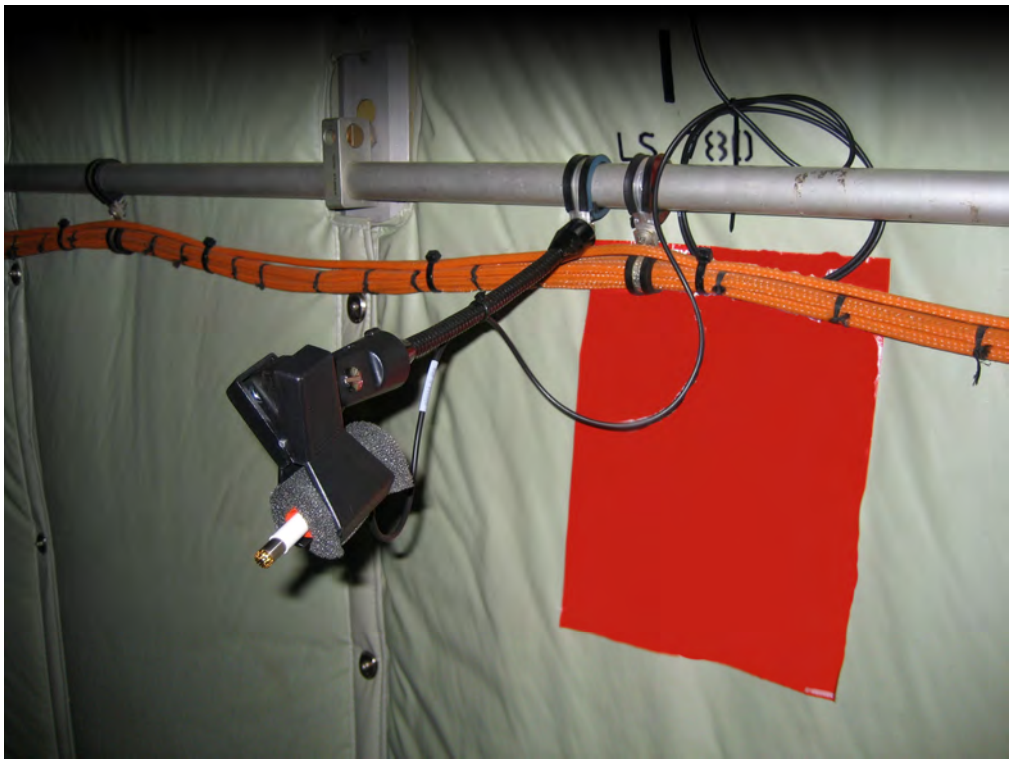

Figure C.15 Microphone mounted to troop seat rail (starboard side), C-130J-30 Trial 2.

Figure C.16 Microphone mounted to centre troop seat rail, C-130J-30 Trial 2.

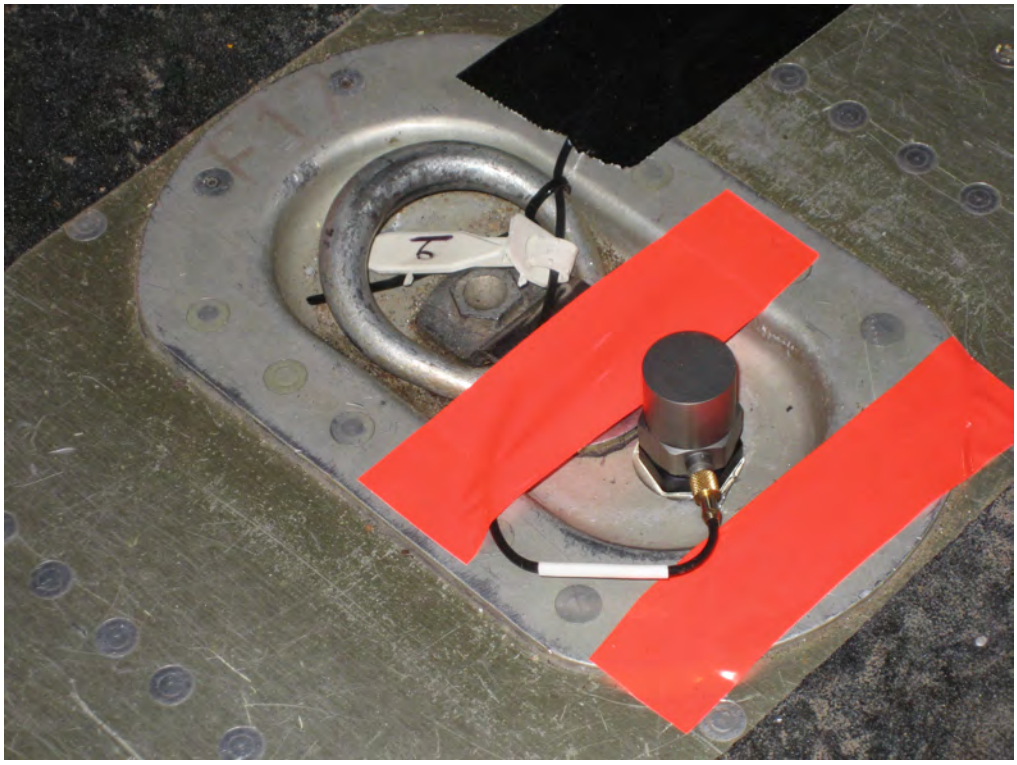

Figure C.17 Accelerometer mounted on cargo floor, C-130J-30 Trial 2.

Figure C.18 Laser tachometer (Propeller 1) mounted to troop seat rails, C-130J-30 Trial 2.

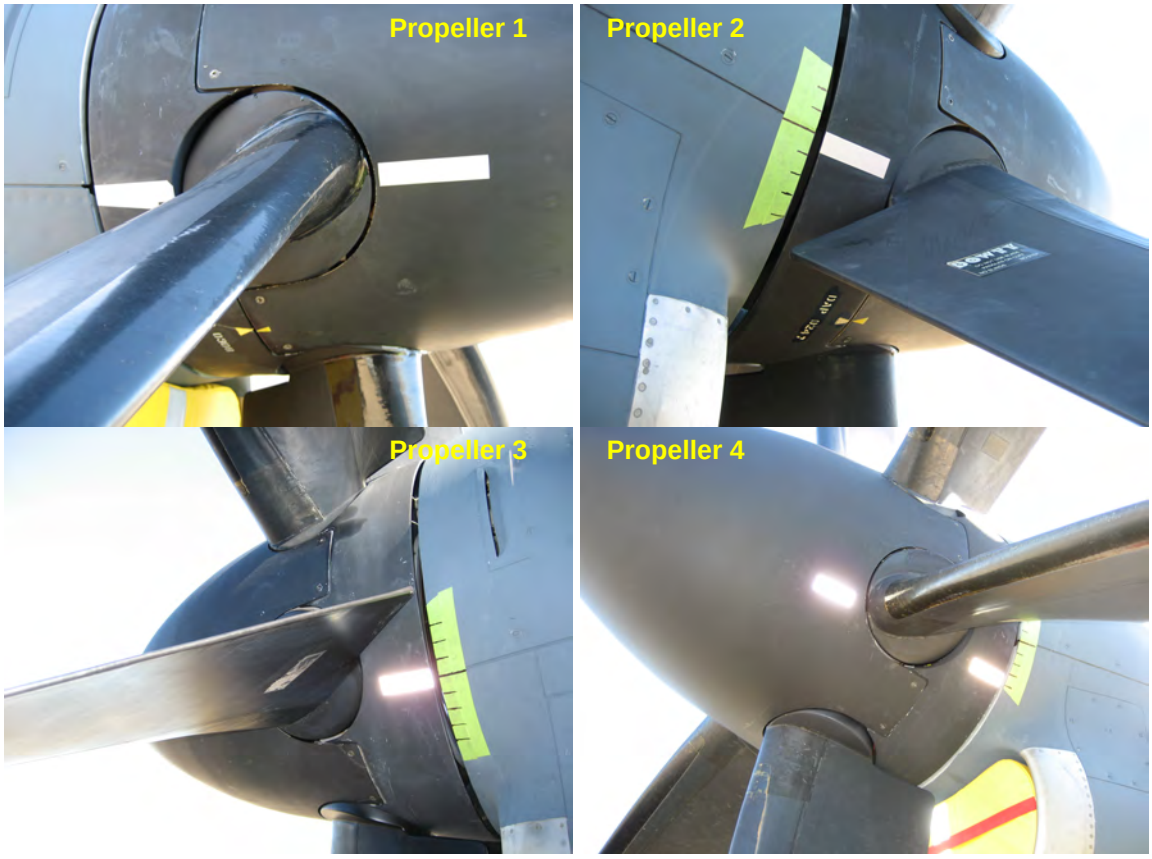

Figure C.19 Reflective tape for laser tachometers, C-130J-30 Trial 2.

Appendix D. C-130J-30 Laser Tachometer Signal

A typical signal from the laser tachometer on the master propeller in the first C-130J-30 trial is shown in Figure D.1. The same type of laser tachometer was used in the second trial so the signals from this trial would be similar.

Variations in the propeller speed were found to be small, as shown in Figure D.2. The spacing of the reflective tape on the propeller hub was found to be slightly uneven. An analysis of the tachometer data from all flights revealed a consistent angular pattern (Table D.1). This pattern was used to find the pulses from the same propeller blade throughout the analysis.

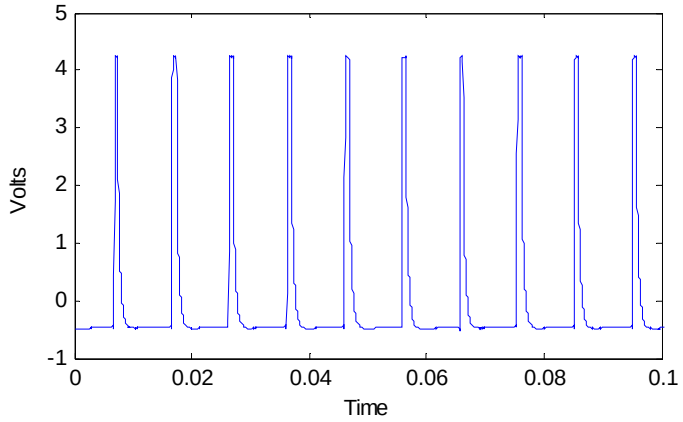

Figure D.1 Typical laser tachometer signal from Propeller 2, C-130J-30 Trial 1.

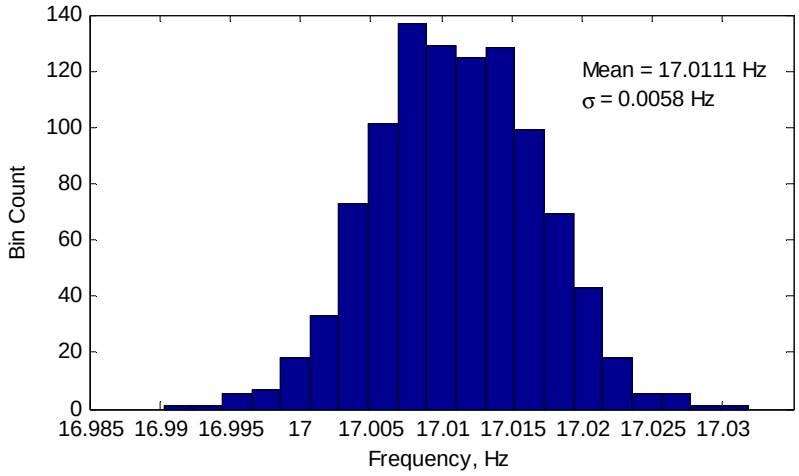

Figure D.2 Typical histogram of Propeller 2 speed over 1000 revolutions, C-130J-30 Trial 1.

Table D.1 Angular spacing between successive pulses from Propeller 2, C-130J-30 Trial 1.

Blade 1	Blade 2	Blade 3	Blade 4	Blade 5	Blade 6
59.0°	60.7°	60.0°	59.7°	60.3°	60.3°

Appendix E. C-130J-30 Ground Run Photographs

The ground run photographs were taken with:

- a Canon EOS-1Ds Mk II in the first trial, and
- a Canon EOS-1D Mk III in the second trial.

E.1. Measurement Error

The overall error associated with measuring the synchrophase angles from the photographs is a combination of:

- image blur due to the motion of the propeller,
- image distortion caused by the motion of the focal-plane shutter, and
- parallax error.

E.1.1. Propeller Motion

All the images were taken with a very high shutter speed in order to minimise the propeller motion blur: 1/4000 s in Trial 1, and 1/8000 s in Trial 2. This limited the rotation of the propellers during each exposure to about:

- 1.5° in Trial 1, and
- 0.8° in Trial 2.

E.1.2. Image Distortion

When the shutter speed is greater than the flash-sync shutter speed, cameras with focal-plane shutters actually record different parts of the image at slightly different times; i.e., the whole image is not exposed all at once, the shutter curtains actually form a narrow slit that travels (in this case vertically) across the focal, or image, plane. This will distort (curve) the image of the propeller blades. The amount of distortion will be equal to the angle that the propeller rotates during the time it takes for the shutter curtains to travel from the tip of one blade to the tip of the opposite blade. This can be estimated from the following three equations.

The angle that the propeller rotates during time t is

$$\varphi(t) = 2\pi f t\,, \tag{E.9}$$

where f is the rotational frequency of the propeller (17 Hz).

The vertical distance from the tip of one blade in the bottom half of the image to the tip of the opposite blade in the top half of the image is

$$y(t) = \frac{D}{2}\left(\sin(\theta + \varphi(t)) - \sin(\theta)\right), \tag{E.10}$$

where D is the diameter of the propeller in the image (~24% of the image height in Trial 1, & ~22% in Trial 2), and θ is the tip angle of the lower propeller blade with respect to the horizontal.

The distance travelled by the shutter curtains can be estimated from

$$y(t) = \frac{H}{S} t \,, \tag{E.11}$$

where H is the height of the image, S is the flash-sync shutter speed of the camera (1/250 s for EOS-1Ds Mk II, & 1/300 s for EOS-1D Mk III), and t is time.

The angular distortion with respect to the axis of the propeller can therefore be determined by substituting (E.9) into (E.10) and then finding the simultaneous solution of the resulting equation with (E.11). The result is shown in Figure E.1.

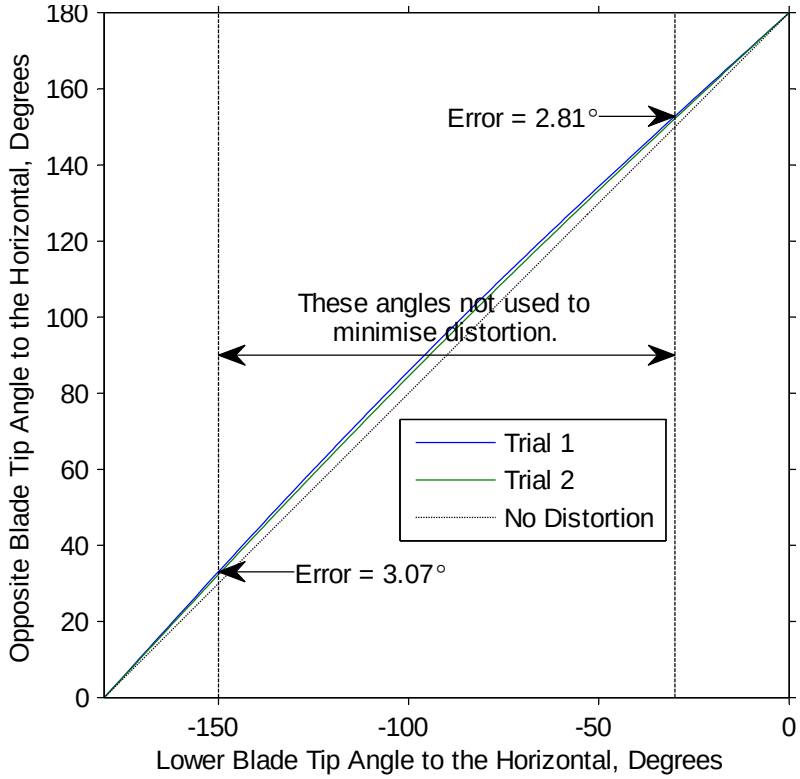

Figure E.1 Distortion induced by motion of the focal-plane shutter.

It can be seen that the distortion is zero for a pair of horizontal blades, because the curtain slit passes both blades simultaneously, and has a maximum of ~6° when the blades are close to vertical. Also, the distortion is approximately the same in both trials despite the differences in flash-sync shutter speed. The distortion is always positive; i.e., it introduces a positive bias to the measurements.

The distortion can be minimised by measuring the synchrophase angles using the blades that are closest to the horizontal (i.e., with the lower blade in the range [−180°, −150°] or [−30°, 0°]). If this is done, the angular distortion is limited to ~3° with respect to the centre of the propeller. However, since it is more practical to measure the angle by drawing a straight line from the tip of one blade to the tip of the opposite blade instead of through the centre of the propeller, the maximum error due to distortion will be about half this value, or 1.5°, using small-angle approximations; i.e., the distortion error will lie in the range [0°, 1.5°].

E.1.3. Parallax Error

Parallax error will occur if the angles of the blades are measured with respect to the tip of the propeller spinner. This is because the tip of the spinner is an appreciable distance in front of the plane of the propeller blades. Hence, parallax error can be minimised by measuring the angles with respect a circle fitted to the propeller blade tips instead of the tip of the spinner.

The residual error, after fitting a circle to the blade tips, is estimated to be approximately ±0.5°.

E.1.4. Combined Measurement Error

Combining the error estimates (blur + distortion + parallax) gives the following overall error estimates.

Trial 1:
$$\begin{Bmatrix} +0.75 & +1.5 & +0.5 \\ -0.75 & -0 & -0.5 \end{Bmatrix} = \begin{Bmatrix} +2.75 \\ -1.25 \end{Bmatrix}$$

Trial 2:
$$\begin{Bmatrix} +0.4 & +1.5 & +0.5 \\ -0.4 & -0 & -0.5 \end{Bmatrix} = \begin{Bmatrix} +2.4 \\ -0.9 \end{Bmatrix}$$

E.2. Synchrophase Angle Measurement Procedure

Examples from both trials are shown in Figure E.2and Figure E.3 below. In each photograph:

- Circles were fitted to the blade tips of each propeller.
- The yellow diameter was rotated to line up with the master propeller blades closest to the horizontal. This was then copied to all slave propellers.
- The red diameters were rotated to line up with the slave propeller blades closest to the horizontal.
- The angles between the red and yellow diameters were measured to the nearest degree.

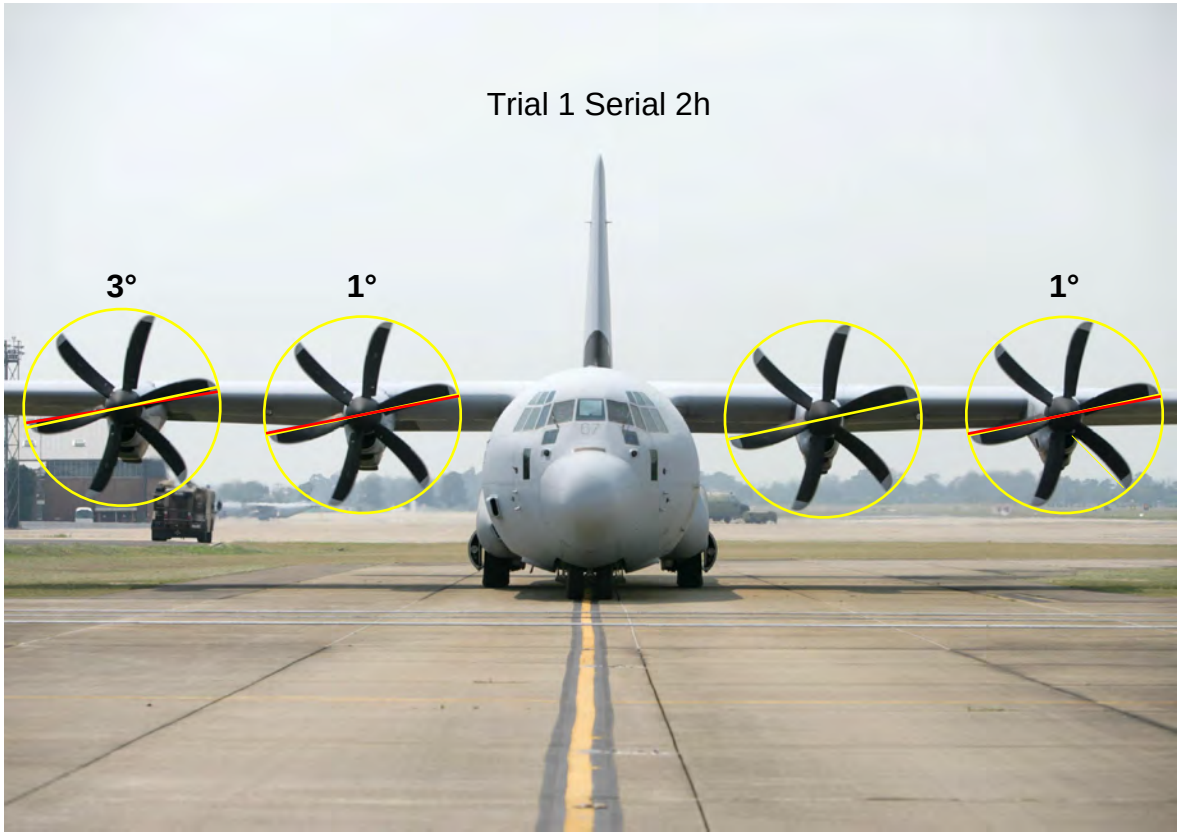

Figure E.2 Ground run photograph from Trial 1 – angles set to (0°,0°,0°,0°), angles measured as (1°,0°,1°,3°).

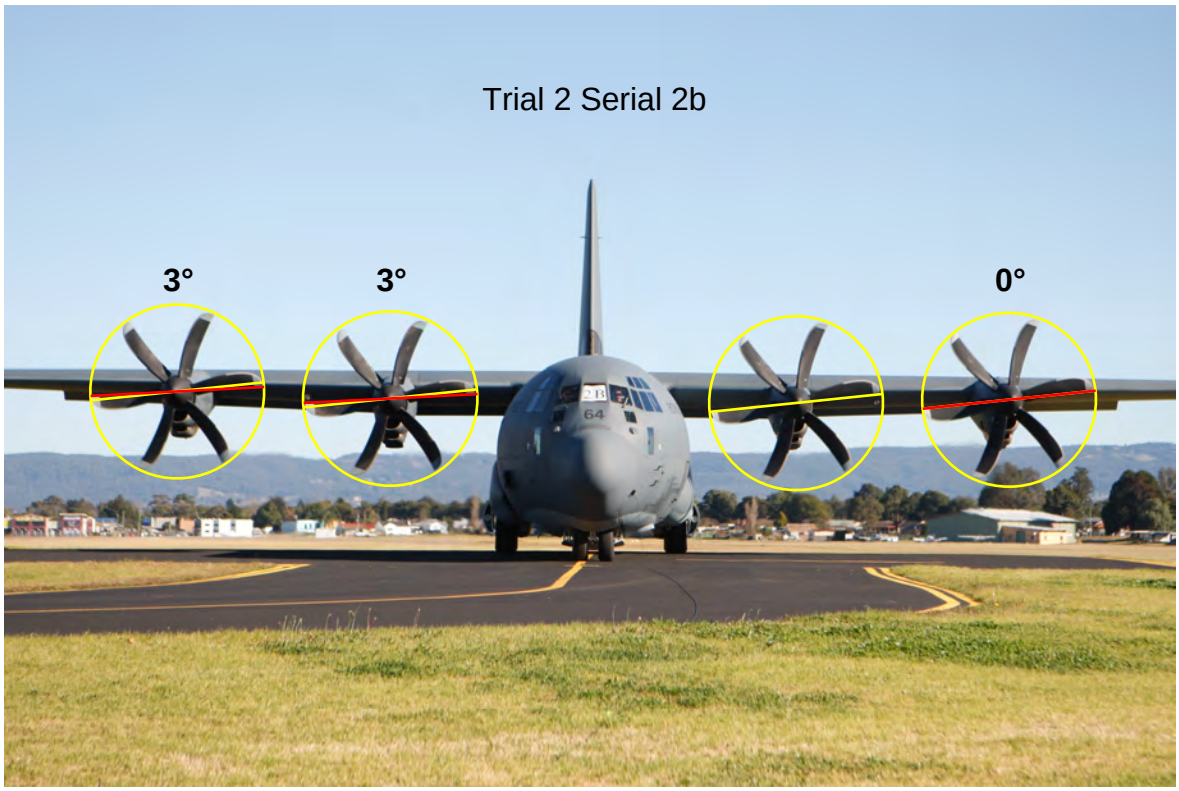

Figure E.3 Ground run photograph from Trial 2 – angles set to (0°,0°,0°,0°), angles measured as (0°,0°,3°,3°).

E.3. Trial 1 Measurements

The synchrophase angle sets used for each serial are listed in Table E.1. The synchrophase angle measurements obtained from the photographs are shown in Table E.2 and Table E.3. The results are listed in the order the photographs were taken. In the tables, “unstable” means the synchrophase angles of the propellers were wandering; i.e., not in sync.

The camera time was found to be 00:44:32 behind local time (Eastern Daylight Saving Time, GMT + 11:00), so 10:15:28 needs to be subtracted from the camera time to convert it to UTC.

The camera EXIF data included the following information: shutter speed 1/4000 s, aperture f 4.0, focal length 95 mm.

Table E.1 Synchrophase angle settings for Trial 1 ground run.

Set	Prop 1	Prop 2	Prop 3	Prop 4
a	α_{def1}	Master	α_{def3}	α_{def4}
b	$\alpha_{def1} + 17°$	Master	α_{def3}	α_{def4}
c	$\alpha_{def1} - 17°$	Master	α_{def3}	α_{def4}
d	α_{def1}	Master	$\alpha_{def3} + 17°$	α_{def4}
e	α_{def1}	Master	$\alpha_{def3} - 17°$	α_{def4}
f	α_{def1}	Master	α_{def3}	$\alpha_{def4} + 17°$
g	α_{def1}	Master	α_{def3}	$\alpha_{def4} - 17°$
h	0°	Master	0°	0°

Table E.2 Difference between the synchrophase angles measured from the Trial 1 photographs, Master = Propeller 2.

Serial	Photograph	Camera Time	Prop 1	Prop 2	Prop 3	Prop 4
2d	20061123raaf8208022_0004_2D.jpg	10:39:36	unstable	Master	+1°	unstable
2e	20061123raaf8208022_0005_2E.jpg	10:40:58	unstable	Master	unstable	unstable
2f	20061123raaf8208022_0006_2F.jpg	10:42:30	unstable	Master	+2°	unstable
2g	20061123raaf8208022_0007_2G.jpg	10:43:58	+2°	Master	+2°	unstable
2h	20061123raaf8208022_0008_2H.jpg	10:46:01	+1°	Master	+1°	+3°
2a	20061123raaf8208022_0009_2A.jpg	10:47:27	unstable	Master	+3°	unstable
2b	20061123raaf8208022_0010_2B.jpg	10:49:04	unstable	Master	+3°	unstable
2c	20061123raaf8208022_0012_2C.jpg	10:50:50	unstable	Master	unstable	unstable

Table E.3 Difference between the synchrophase angles measured from the Trial 1 photographs, Master = Propeller 3.

Serial	Photograph	Camera Time	Prop 1	Prop 2	Prop 3	Prop 4
3a	20061123raaf8208022_0013_3A.jpg	10:59:13	+3°	+5°	Master	unstable
3b	20061123raaf8208022_0014_3B.jpg	11:00:31	+5°	+6°	Master	unstable
3c	20061123raaf8208022_0015_3C.jpg	11:02:14	unstable	unstable	Master	unstable
3d	20061123raaf8208022_0016_3D.jpg	11:03:49	+4°	+6°	Master	unstable
3e	20061123raaf8208022_0017_3E.jpg	11:05:32	unstable	unstable	Master	unstable
3f	20061123raaf8208022_0018_3F.jpg	11:07:10	+5°	+6°	Master	unstable
3g	20061123raaf8208022_0019_3G.jpg	11:08:51	unstable	+6°	Master	unstable
3h	20061123raaf8208022_0020_3H.jpg	11:10:59	+3°	+5°	Master	unstable

E.4. Trial 2 Measurements

The synchrophase angle sets used for each serial are listed in Table E.. Table E. and Table E. list the synchrophase angle measurements from Trial 2 that were obtained from the first and last photographs taken during each serial, plus one or two photographs in between these. The results are listed in the order the photographs were taken.

The camera was connected to a GPS receiver, and the images were tagged with a GPS timestamp. However, as the photographs were taken in motor-drive bursts (at approximately 10 frames per second), and the timestamp was only updated every second (despite being recorded to 3 decimal places), many photographs received identical timestamps.

The camera EXIF data included the following information: shutter speed 1/8000 s, aperture f 3.5, focal length 67 mm.

Table E.4 Synchrophase angle settings for Trial 2 ground run.

Set	Prop 1	Prop 2	Prop 3	Prop 4
a	α_{def1}	Master	α_{def3}	α_{def4}
b	0°	Master	0°	0°
c	15°	Master	0°	0°
d	45°	Master	45°	45°
e	0°	Master	15°	0°
f	0°	Master	0°	15°

Table E.5 Difference between the synchrophase angles measured from the Trail 2 photographs and the set angles, Master = Propeller 2.

Serial	Photograph	GPS Timestamp	Prop 1	Prop 2	Prop 3	Prop 4
2f	20080722raaf8100122_0242.JPG	23:33:23.994	+1°	Master	+3°	+3°
	20080722raaf8100122_0258.JPG	23:33:24.994	+2°		+3°	+3°
	20080722raaf8100122_0274.JPG	23:33:28.994	0°		+2°	+3°
2a	20080722raaf8100122_0275.JPG	23:37:42.994	+1°	Master	+3°	+3°
	20080722raaf8100122_0308.JPG	23:37:44.994	+1°		+3°	+4°
	20080722raaf8100122_0340.JPG	23:37:48.994	+1°		+4°	+4°
2b	20080722raaf8100122_0341.JPG	23:39:55.994	0°	Master	+3°	+3°
	20080722raaf8100122_0349.JPG	23:39:55.994	0°		+3°	+3°
	20080722raaf8100122_0357.JPG	23:39:59.994	+1°		+3°	+3°
	20080722raaf8100122_0372.JPG	23:40:01.994	+1°		+2°	+3°
2c	20080722raaf8100122_0373.JPG	23:41:52.994	+1°	Master	+3°	+3°
	20080722raaf8100122_0387.JPG	23:41:53.994	0°		+2°	+2°
	20080722raaf8100122_0401.JPG	23:41:57.994	+1°		+3°	+3°
2d	20080722raaf8100122_0402.JPG	23:43:31.994	0°	Master	+3°	+3°
	20080722raaf8100122_0417.JPG	23:43:35.994	0°		+3°	+3°
	20080722raaf8100122_0432.JPG	23:43:36.994	+1°		+3°	+3°
2e	20080722raaf8100122_0433.JPG	23:45:15.994	+1°	Master	+4°	+3°
	20080722raaf8100122_0449.JPG	23:45:19.994	0°		+3°	+3°
	20080722raaf8100122_0464.JPG	23:45:20.994	0°		+3°	+3°

Table E.6 Difference between the synchrophase angles measured from the Trail 2 photographs and the set angles, Master = Propeller 3.

Serial	Photo	GPS Timestamp	Prop 1	Prop 2	Prop 3	Prop 4
3a	20080722raaf8100122_0465.JPG	23:47:23.994	+2°	+4°	Master	+3°
	20080722raaf8100122_0472.JPG	23:47:24.994	+1°	+2°		+4°
	20080722raaf8100122_0481.JPG	23:47:28.994	+1°	+3°		+3°
	20080722raaf8100122_0489.JPG	23:47:28.994	+1°	+4°		+4°
	20080722raaf8100122_0496.JPG	23:47:29.994	+2°	+3°		+4°
3b	20080722raaf8100122_0497.JPG	23:49:03.994	+1°	+3°	Master	+3°
	20080722raaf8100122_0512.JPG	23:49:07.994	0°	+3°		+3°
	20080722raaf8100122_0527.JPG	23:49:08.994	0°	+3°		+3°
3c	20080722raaf8100122_0528.JPG	23:50:30.994	+1°	+3°	Master	+4°
	20080722raaf8100122_0543.JPG	23:50:34.994	+0°	+3°		+3°
	20080722raaf8100122_0550.JPG	23:50:34.994	+1°	+3°		+4°
	20080722raaf8100122_0558.JPG	23:50:35.994	+1°	+3°		+4°
3d	20080722raaf8100122_0559.JPG	23:52:18.994	+1°	+3°	Master	+3°
	20080722raaf8100122_0575.JPG	23:52:20.994	0°	+3°		+4°
	20080722raaf8100122_0591.JPG	23:52:24.994	+1°	+2°		+3°
3e	20080722raaf8100122_0626.JPG	23:54:30.994	+1°	+3°	Master	+3°
	20080722raaf8100122_0641.JPG	23:54:32.994	+1°	+3°		+3°
	20080722raaf8100122_0656.JPG	23:54:36.994	0°	+3°		+3°
3f	20080722raaf8100122_0657.JPG	23:56:50.994	+1°	+3°	Master	+3°
	20080722raaf8100122_0674.JPG	23:56:52.994	+1°	+3°		+4°
	20080722raaf8100122_0690.JPG	23:56:55.994	+1°	+4°		+4°

Appendix F. Loudness and Acoustic Weighting

F.1. Loudness

The loudness of a sound perceived by a human ear depends on both its frequency and its sound pressure level. Many historical studies of this characteristic of human hearing have been conducted; most notably those of Fletcher and Munson (1933), and Robinson and Dadson (1956). The most currently accepted equal-loudness-level contours for pure tones are those specified in ISO 226:2003 (ISO 226, 2003). This version of the standard incorporates work from twelve more recent independent experimental investigations compared to the previous 1987 version of the standard. It should be noted that these contours are for pure tones only and do not accurately represent how the human ear perceives sounds consisting of multiple tones or tones in the presence of masking background random noise. Further relations are needed to adequately represent these factors (Fletcher and Munson, 1933, 1937).

The equal-loudness-level contours from ISO 226:2003 are reproduced in Figure F.1. The loudness level, in phons, is experimentally determined by adjusting the sound pressure level of the test tone until it is perceived to be as loud as a reference tone at 1000 Hz. Thus, at 1000 Hz, the loudness in phons is always numerically the same as the sound pressure level of the reference tone in decibels. It can be seen that the ear is most sensitive to frequencies between 3 kHz and 4 kHz, and progressively less sensitive to frequencies below 1 kHz. The contours in this figure are different to those in the 1987 version of the standard, and are also different to those derived by Fletcher and Munson. For comparison, the 40-phon and 100-phon Fletcher-Munson contours are overlaid on the figure.

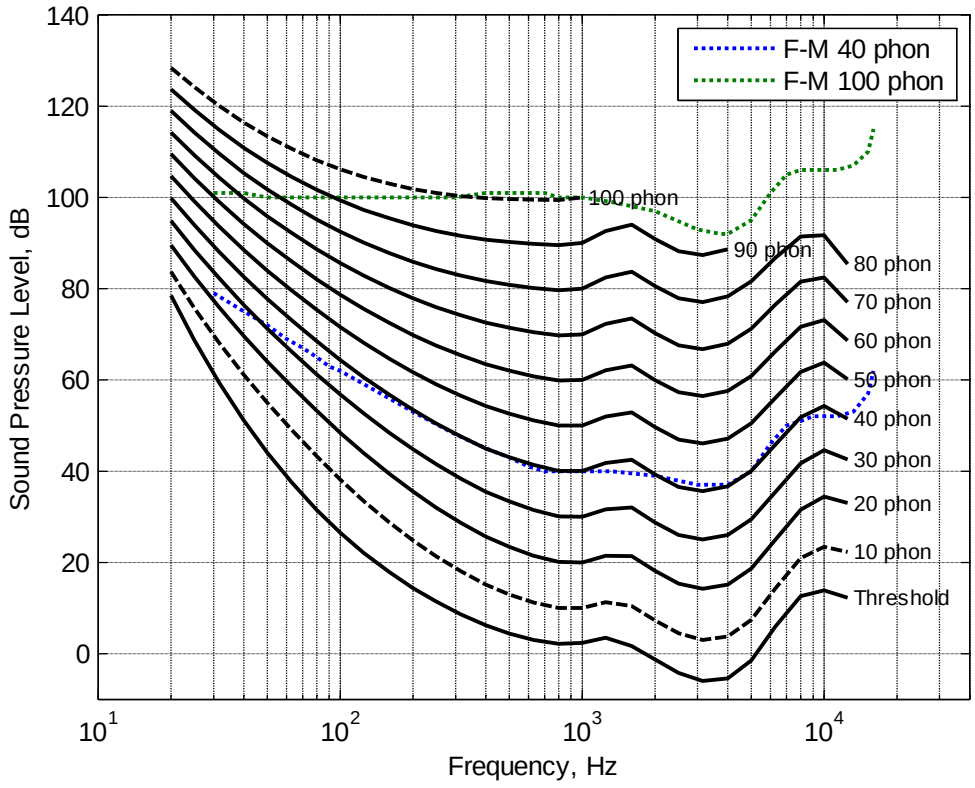

Figure F.1 ISO226:2003 equal-loudness contours (10-phon and 100-phon contours are indicative only) overlaid with Fletcher-Munson 40-phon and 100-phon contours.

F.2. Acoustic Weighting

The A, B and C acoustic frequency weighting functions were historically developed to approximate the inverted 40, 70 and 100 phon Fletcher-Munson equal-loudness contours (Haughton, 2002); i.e., to represent how the human ear perceives low, medium and loud sounds. The A and C weighting functions are still specified for use in sound level meters (AS IEC 61672.1, 2004), but the B frequency weighting function has fallen out of use.

The A and C weighting functions and the inverted and normalised (@ 1000 Hz) 40-phon and 100-phon ISO226:2003 and Fletcher-Munson equal-loudness contours are shown in Figure F.2. For frequencies less than 1000 Hz, it can be seen that the A-weighting and C-weighting curves closely match the inverted Fletcher-Munson 40-phon and 100-phon contours respectively. However, the C-weighting function departs from the newer inverted ISO226:2003 100-phon contour, and neither function is a good approximation of the inverted contours above 1000 Hz. The latter probably reflects the (historical) difficulty of implementing these functions with simple analogue electronic components.

It is shown in this thesis that cabin sound pressure levels in military propeller aircraft are typically high (> 100 dB). The C-weighting function would therefore seem to be more appropriate than the A-weighting function. However, the C-weighting function does not correlate well with the current ISO226:2003 standard, and would actually have very little effect (−0.66 dB to 0.03 dB) over the frequency range represented by the blade-pass frequency and its low-order harmonics (70–500 Hz). Hence, there seems little reason to use it. It should also be noted that the application of any weighting function that attenuates the blade-pass frequency or its harmonics would detrimentally affect the performance of any adaptive control system aimed at minimising these frequencies.

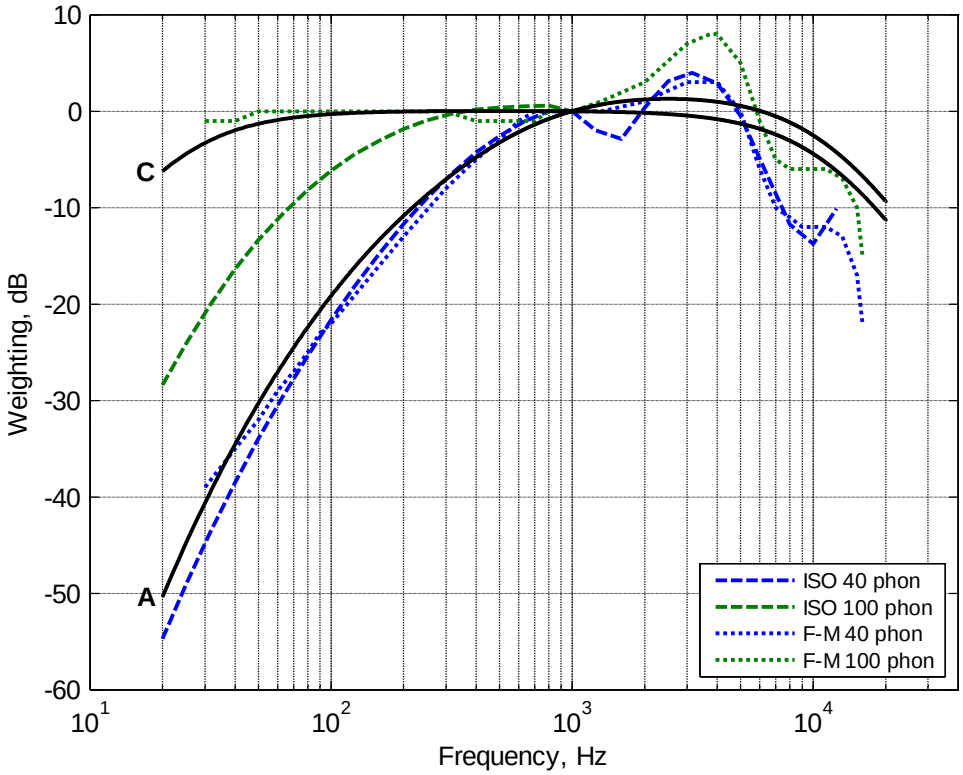

Figure F.2 IEC61672.1 A and C weighting functions overlaid with inverted and normalised ISO226:2003 and Fletcher-Munson 40-phon and 100-phon equal-loudness contours.

Appendix G. Vector Diagrams for C-130J-30 Trial 1 Serial 10

According to propeller signature theory, clocking the synchrophase angle of one propeller at a time should cause the resultant amplitude and phase of the measured BPF component at any sensor location to describe points on a circle when plotted on a vector diagram. The centre of this circle should be the vector sum of the contributions from the other three propellers, which should not change, and the radius of the circle should equal the amplitude of the contribution from the propeller in question. The points should be spaced by the synchrophase angle step size multiplied by the number of blades on the propeller for the BPF component, or at whole multiples of this for the harmonics of the BPF. This principle is shown schematically in Figure G.1. Note that the phase of the BPF component must always be measured with respect to the master propeller, but this can be accomplished by synchronising the sample rate with laser tachometer signal from the master propeller. The measurements made during Serial 10, where the synchrophase angles were clocked in such a manner, therefore provide a convenient test of propeller signature theory.

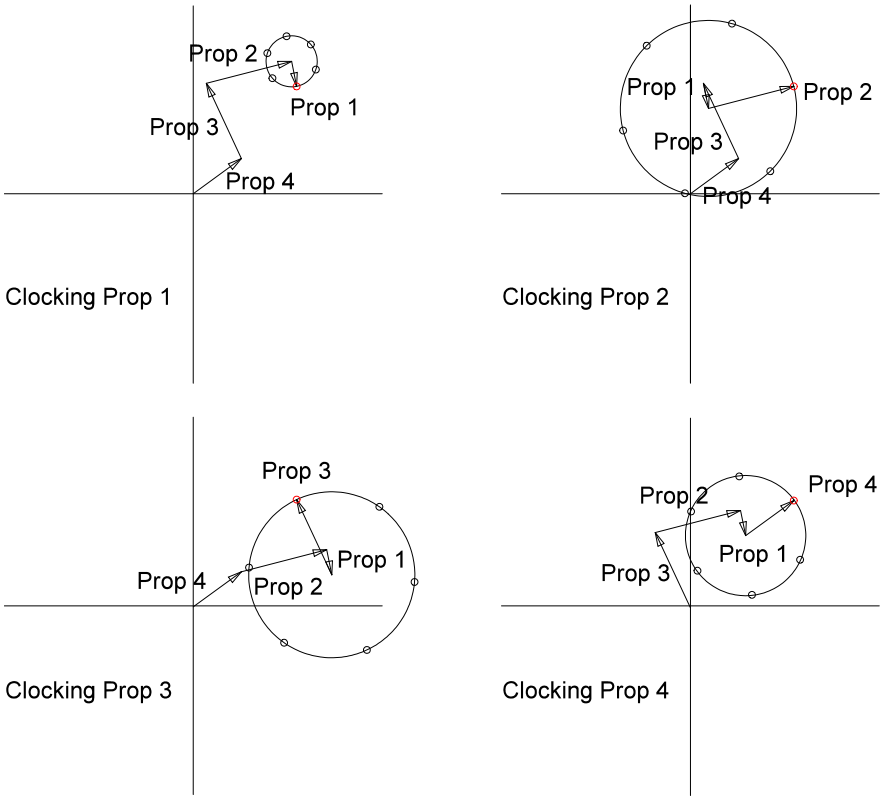

Figure G.1 Theoretical effect of clocking the synchrophase angle of each propeller by 10° at a time on the amplitude and phase of the measured BPF component – the red point indicates the common point of intersection of all four circles.

In Figures G.2 to G.40, the amplitude and phase of the BPF and its harmonics have been extracted from the sensor signals at intervals of one propeller revolution over a period of 10 seconds from the data collected for each set of synchrophase angles. This was done by synchronously re-sampling the data with respect to the tachometer signal of the master propeller (2600 points-per-rev), computing (44,200-point) overlapped spectra with a

Hanning window, and extracting the amplitude and phase of the frequency components of interest. Note that the re-sampling should cause the frequencies of interest to lie at the midpoints of window filter shape thus minimising the picket-fence effect.

In the figures:

- The results are split into a 4×4 grid, with the frequencies shown in separate rows, and the propellers in separate columns.
- The coloured traces show the amplitude and phase of each frequency component over the respective 10 second periods, where the colour indicates the synchrophase angle of the propeller in question (blue = 0°, green = 10°, etc.). All three measurements made with the (0°,0°,0°,0°) setting (i.e., Serials 10a, 10h and 10o) are shown for each propeller so there are three overlapping blue traces in each plot. The blue traces consequently exhibit more variability than the other colours.
- The black circles show the loci of the predicted amplitude and phase obtained from the propeller signature calculations. The signatures were calculated using all 21 data sets (i.e., Serials 10a–10u) so the circles shown for each propeller have actually been fitted to all the data at that frequency, not just the data shown in each plot.
- The circular grey region in the centre of each plot indicates the estimated noise floor of the signals at these frequencies. The estimates were obtained from the average magnitude of the frequency components ±2 Hz (i.e., 2 frequency lines) away from the component of interest plus three standard deviations.

Since the synchrophase angles of the slave propellers were individually clocked with 10° increments during this serial, the amplitude and phase of the resultant BPF components should describe points 60° apart on the signature circles. These circles should intersect at the common point where the synchrophase angles were (0°,0°,0°,0°). Although the master propeller was not clocked, the circle that would have occurred if this had happened can be predicted from the theory and will also intersect the other circles at the same common point. The harmonic components (2×, 3×, 4× BPF) should also describe points on a circle, but these should be 120°, 180°, and 240° apart for 2×, 3×, and 4× BPF components respectively.

It can be seen that the fit between the signature circles and the measured amplitude and phase data is good for all sensors at the fundamental BPF. However, the results at the higher harmonics are not as good. A few sensors still show good agreement with the measurements at 2× and sometimes even 3× the BPF, but these only occur where the amplitudes of these components are relatively large (> 0.35 Pa_{rms}). Generally, this occurs in the region from about one propeller diameter forward of the propellers to about half a diameter aft of the propellers. The poor agreement for the remaining results can be attributed to the measurement variability.

The largest BPF noise signature is 7.00 Pa_{rms} for Propeller 2 at location P 12; i.e., the microphone closest to Propeller 2. The largest BPF floor vibration signature is 0.42 g_{rms} for Propeller 3 at location F12; i.e., the accelerometer closest to Propeller 3. The inboard propellers generally produce larger signatures than the outboard propellers at each sensor location, but there are exceptions (e.g., Propeller 1 at microphones C 22.5, C 33, S 1.5, and Propeller 4 at microphones P 19, P 26, C 22.5, and C 33).

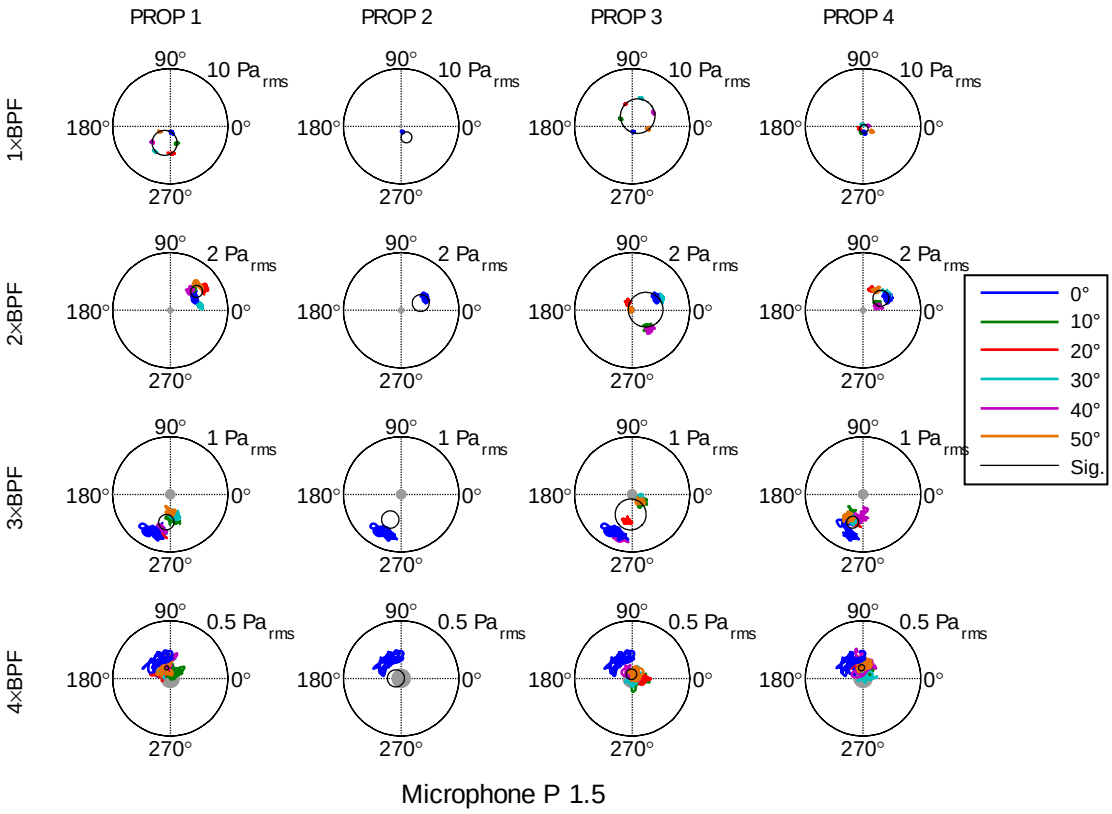

Figure G.2 Effect of separately clocking the synchrophase angle of each propeller on the amplitude and phase of the harmonic components measured with Mic. P 1.5.

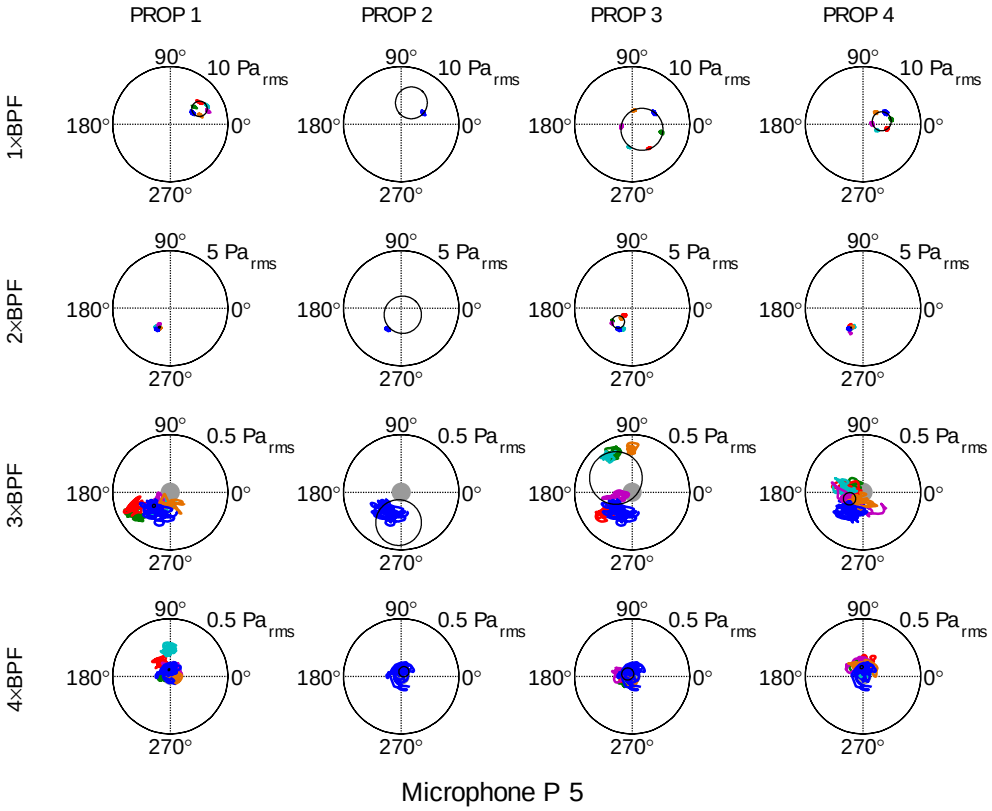

Figure G.3 Effect of separately clocking the synchrophase angle of each propeller on the amplitude and phase of the harmonic components measured with Mic. P 5.

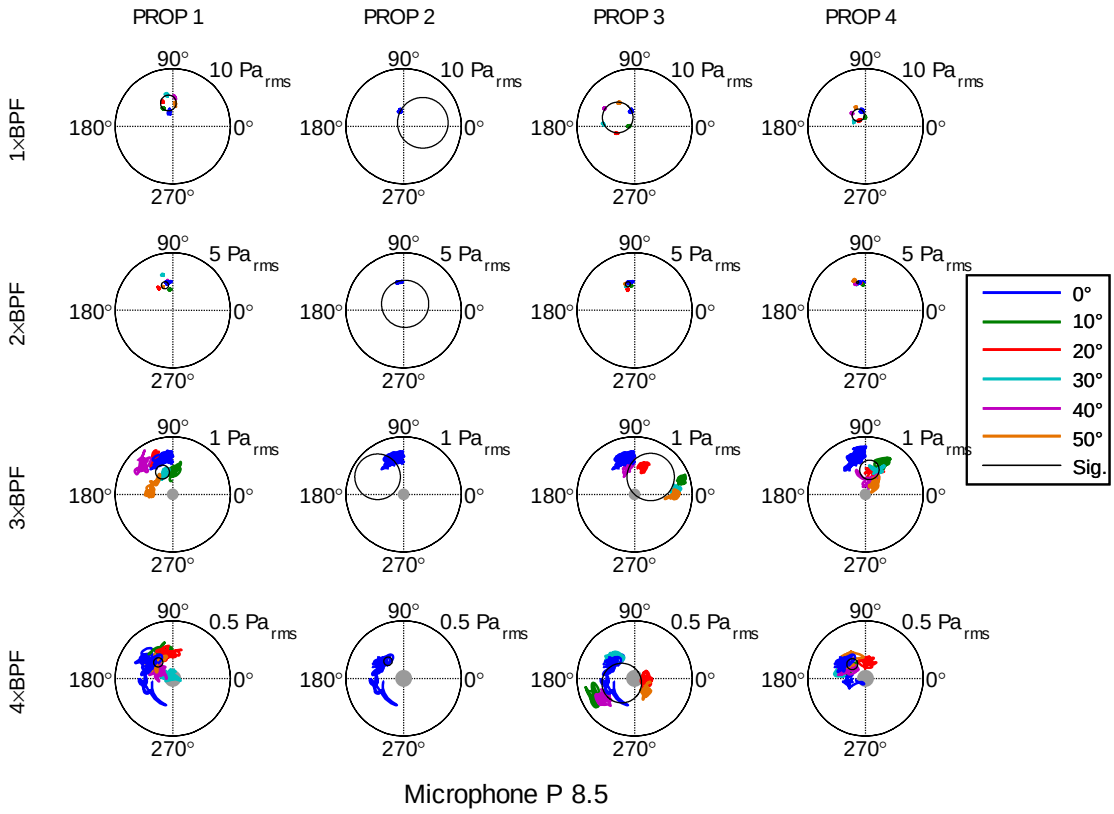

Figure G.4 Effect of separately clocking the synchrophase angle of each propeller on the amplitude and phase of the harmonic components measured with Mic. P 8.5.

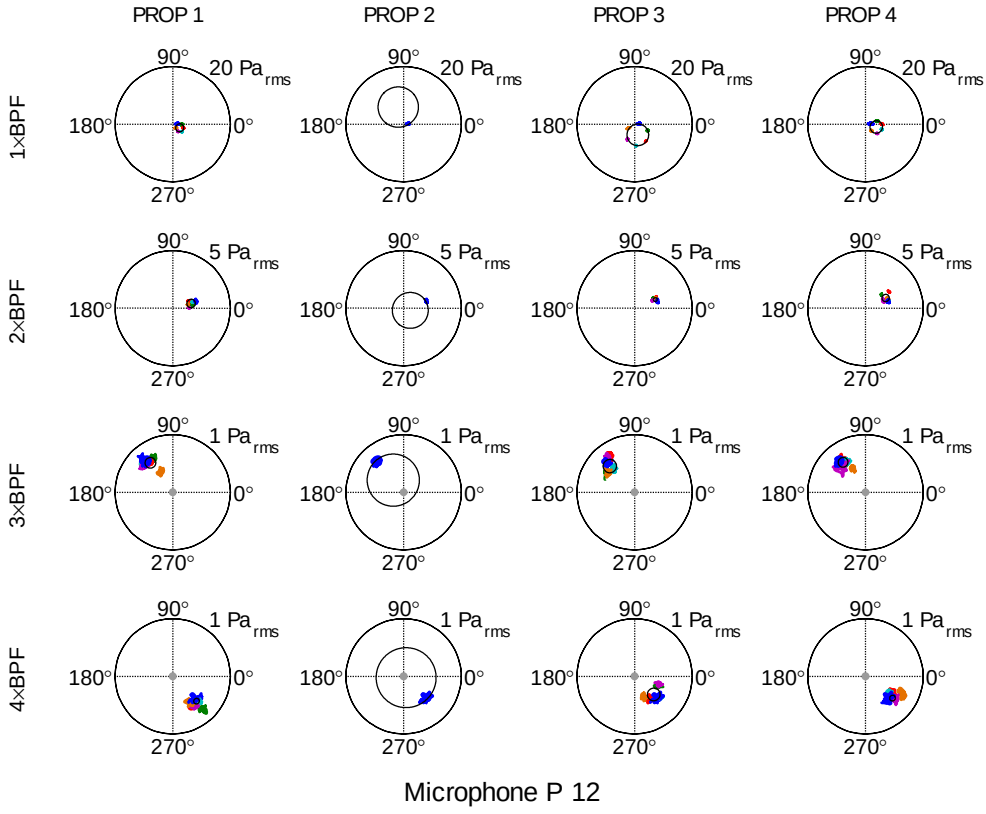

Figure G.5 Effect of separately clocking the synchrophase angle of each propeller on the amplitude and phase of the harmonic components measured with Mic. P 12.

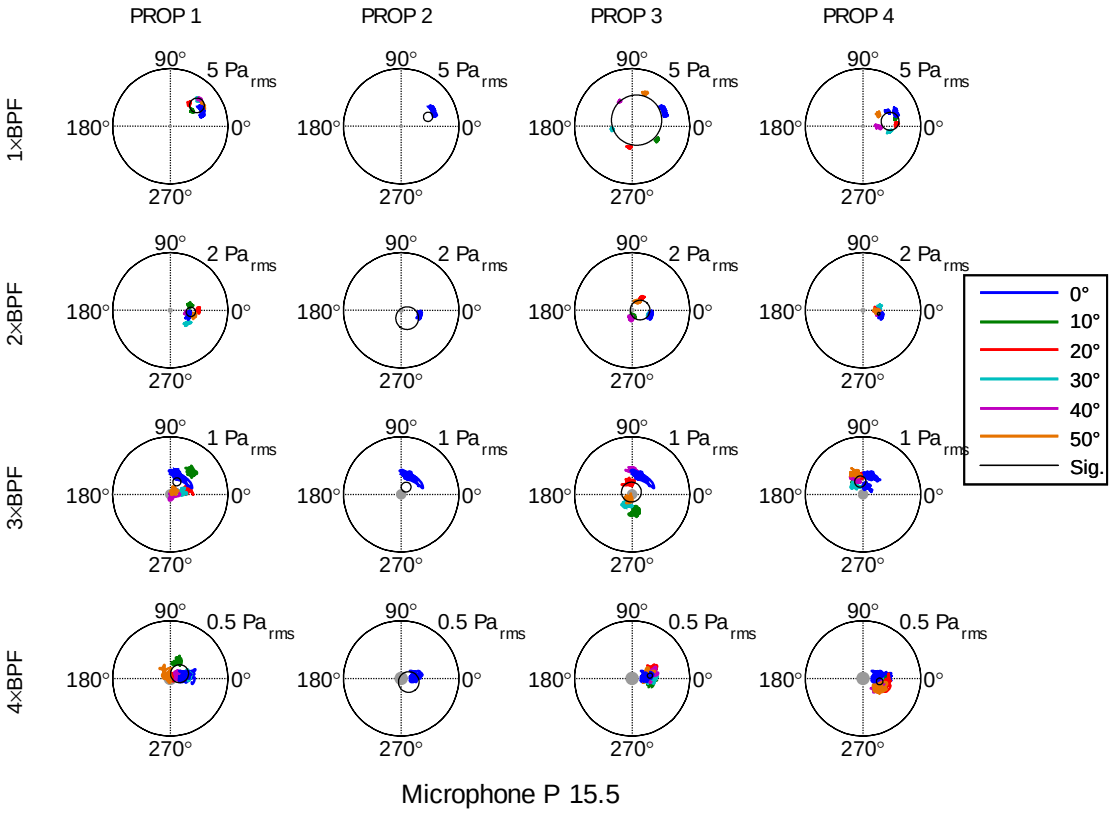

Figure G.6 Effect of separately clocking the synchrophase angle of each propeller on the amplitude and phase of the harmonic components measured with Mic. P 15.5, Trial 1.

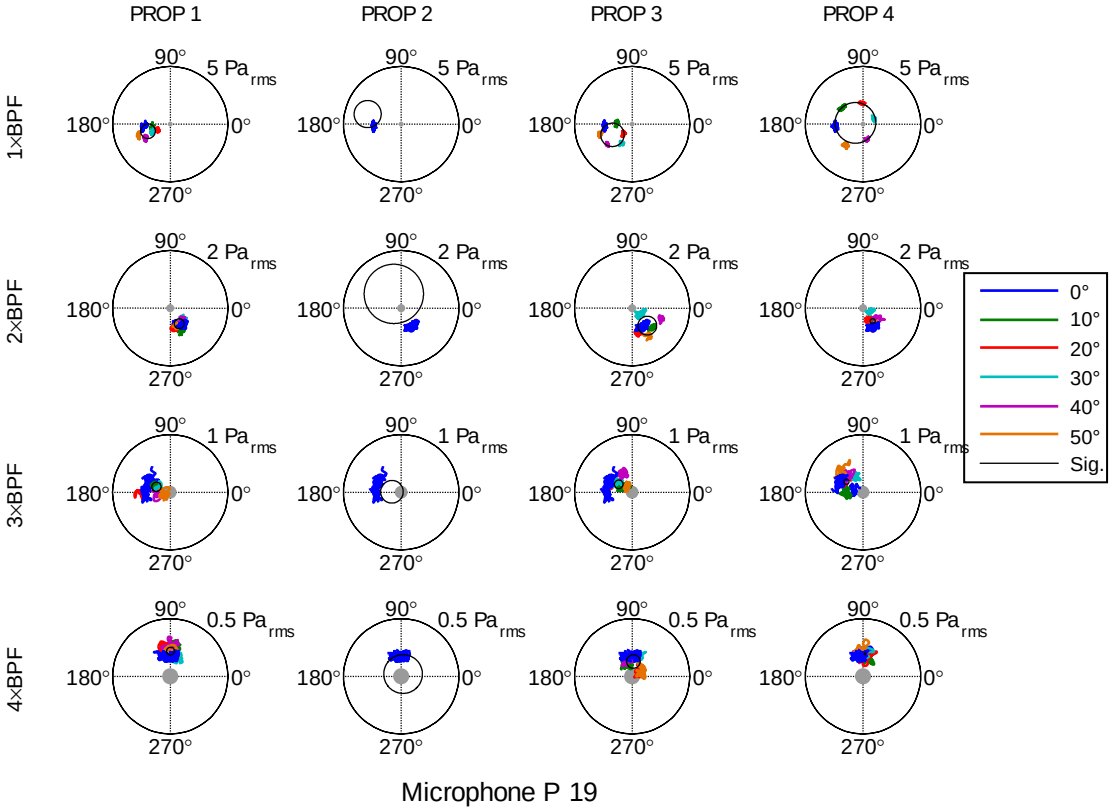

Figure G.7 Effect of separately clocking the synchrophase angle of each propeller on the amplitude and phase of the harmonic components measured with Mic. P 19.

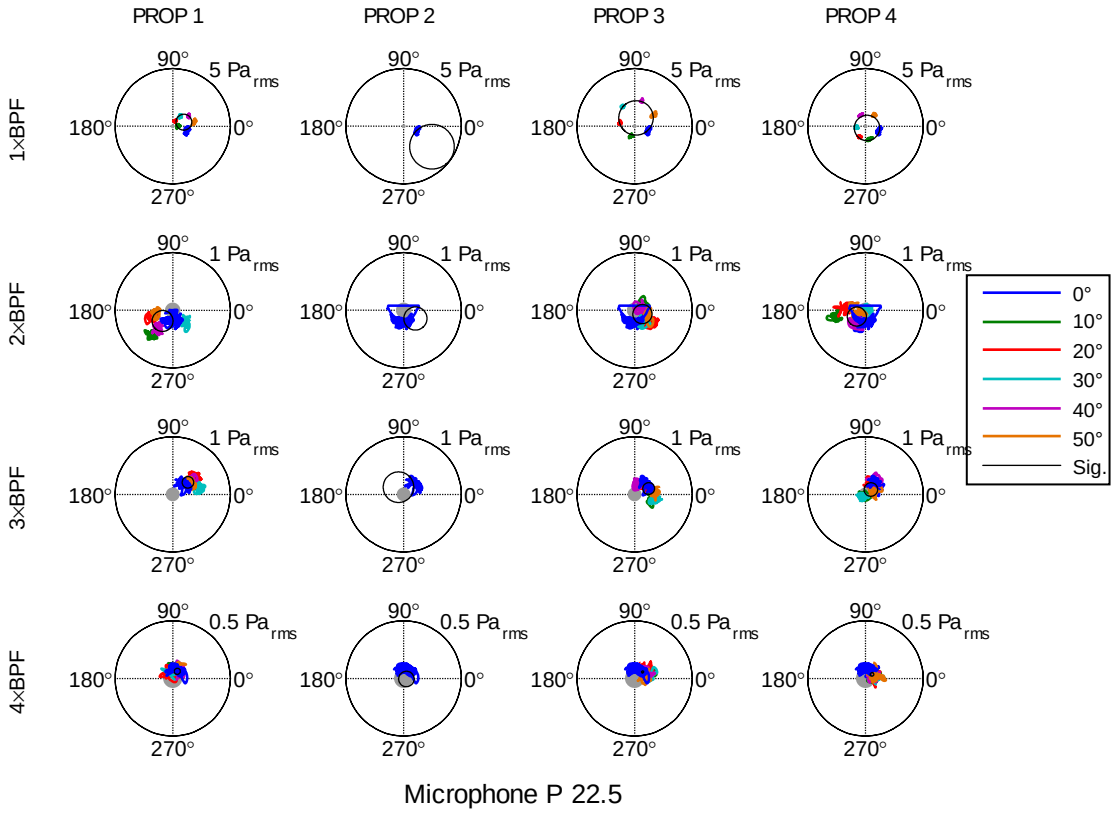

Figure G.8 Effect of separately clocking the synchrophase angle of each propeller on the amplitude and phase of the harmonic components measured with Mic. P 22.5, Trial 1.

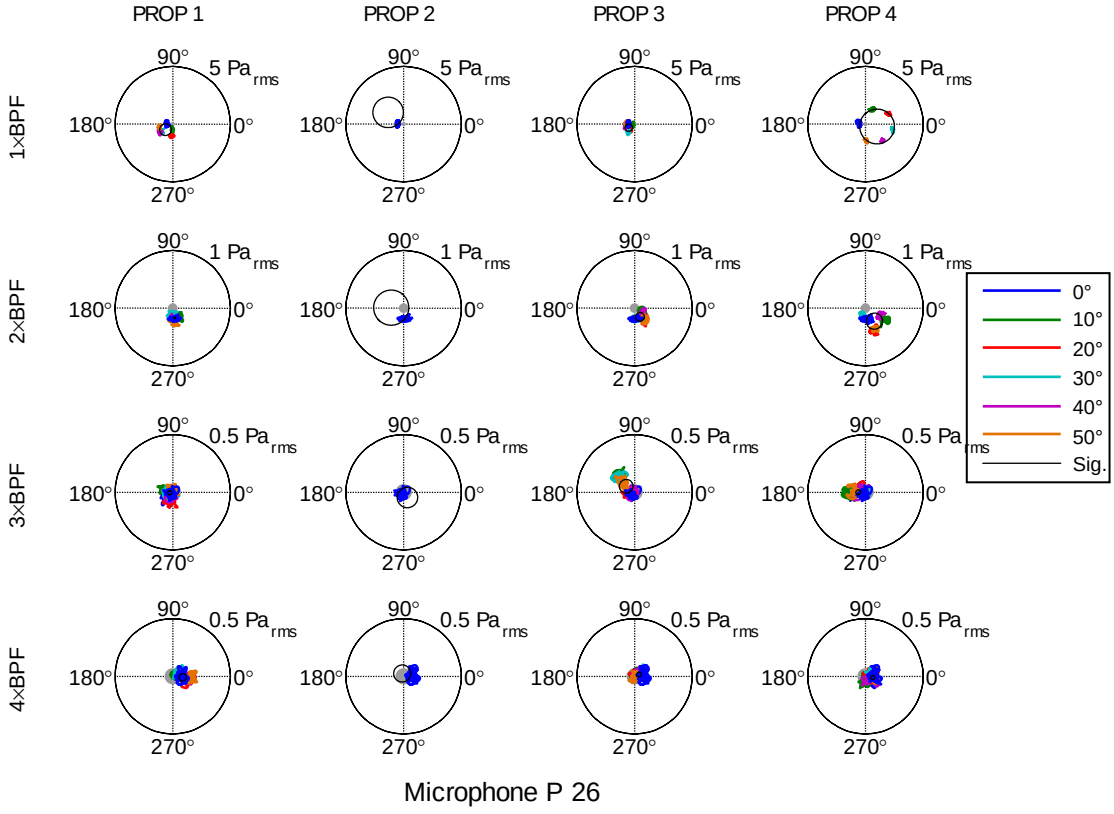

Figure G.9 Effect of separately clocking the synchrophase angle of each propeller on the amplitude and phase of the harmonic components measured with Mic. P 26.

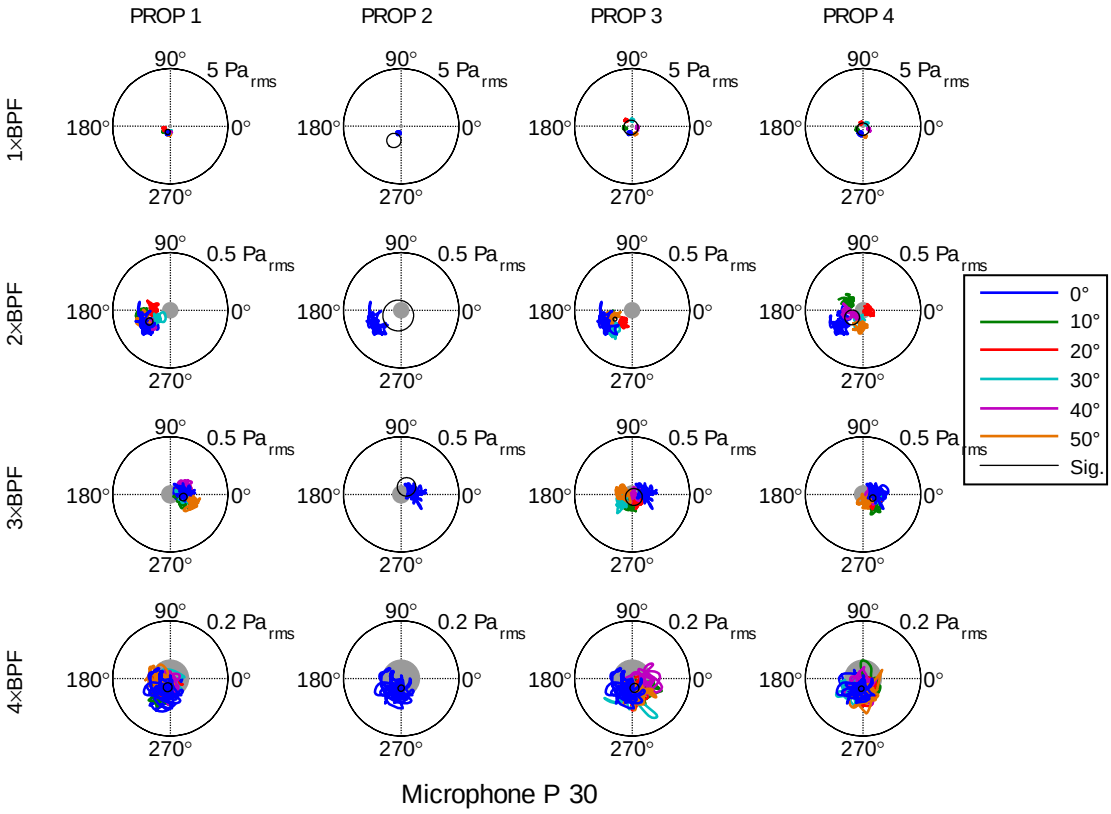

Figure G.10 Effect of separately clocking the synchrophase angle of each propeller on the amplitude and phase of the harmonic components measured with Mic. P 30, Trial 1.

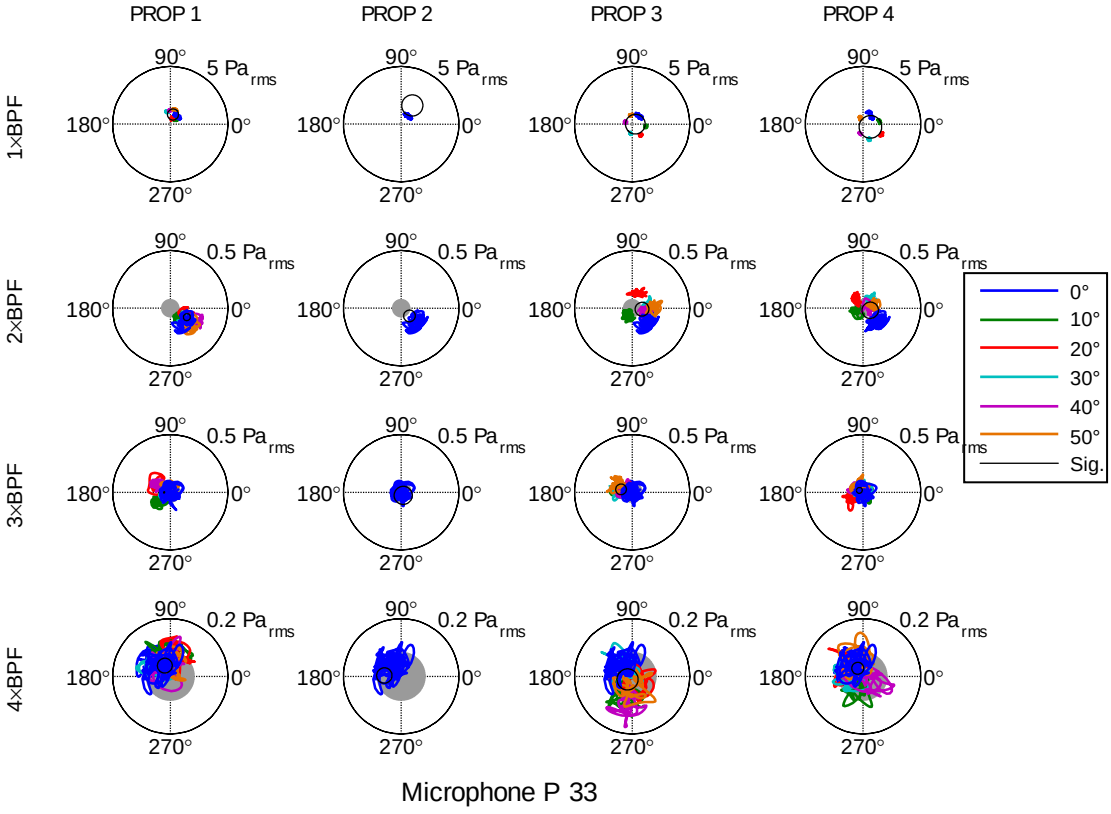

Figure G.11 Effect of separately clocking the synchrophase angle of each propeller on the amplitude and phase of the harmonic components measured with Mic. P 33.

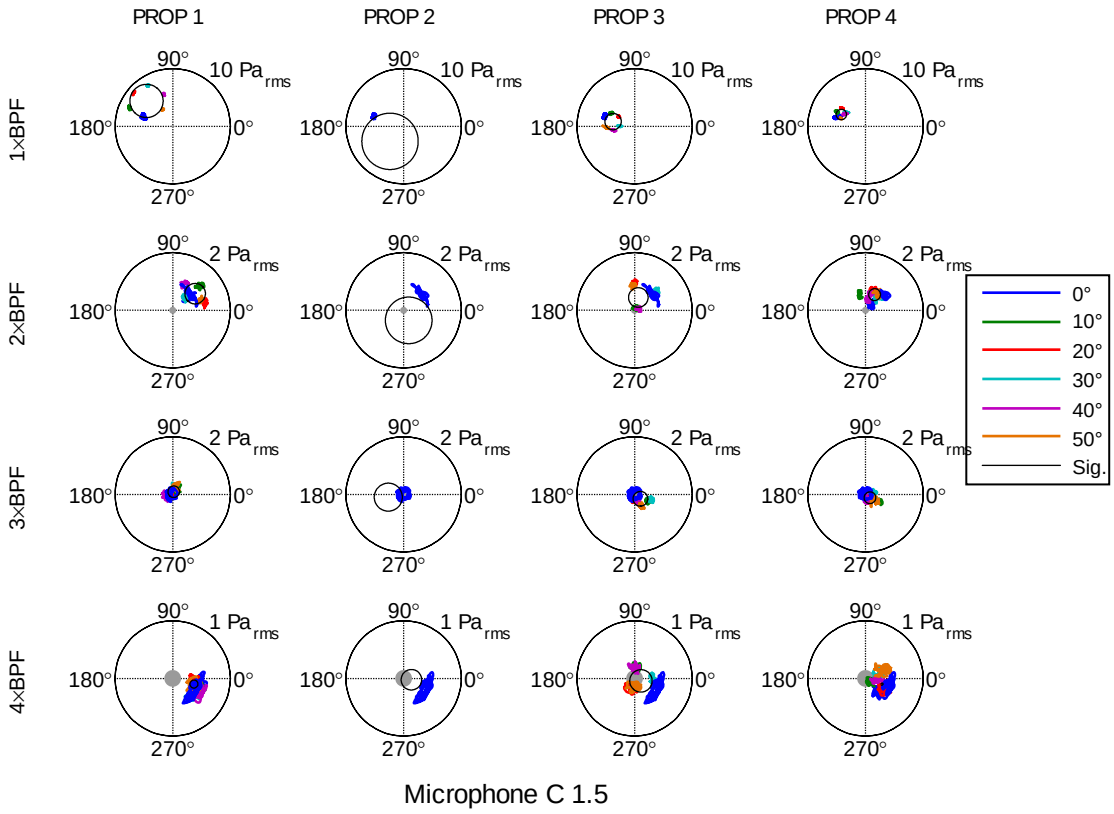

Figure G.12 Effect of separately clocking the synchrophase angle of each propeller on the amplitude and phase of the harmonic components measured with Mic. C 1.5, Trial 1.

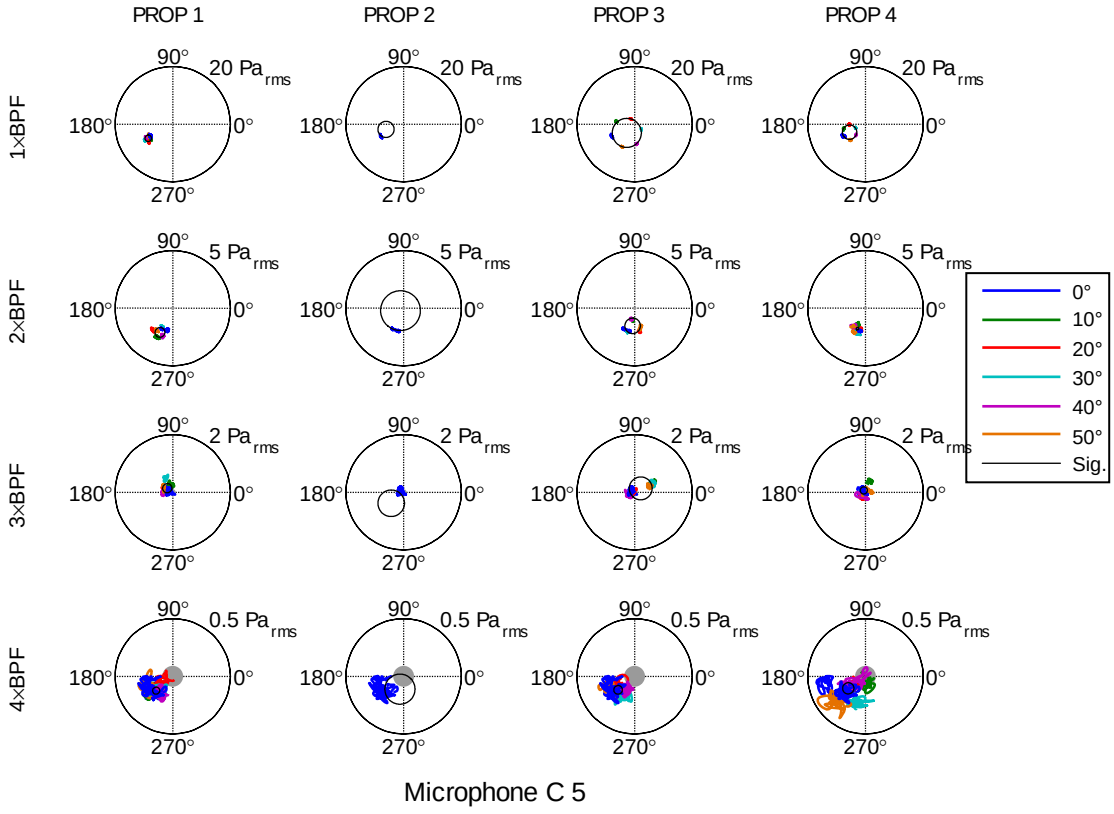

Figure G.13 Effect of separately clocking the synchrophase angle of each propeller on the amplitude and phase of the harmonic components measured with Mic. C 5.

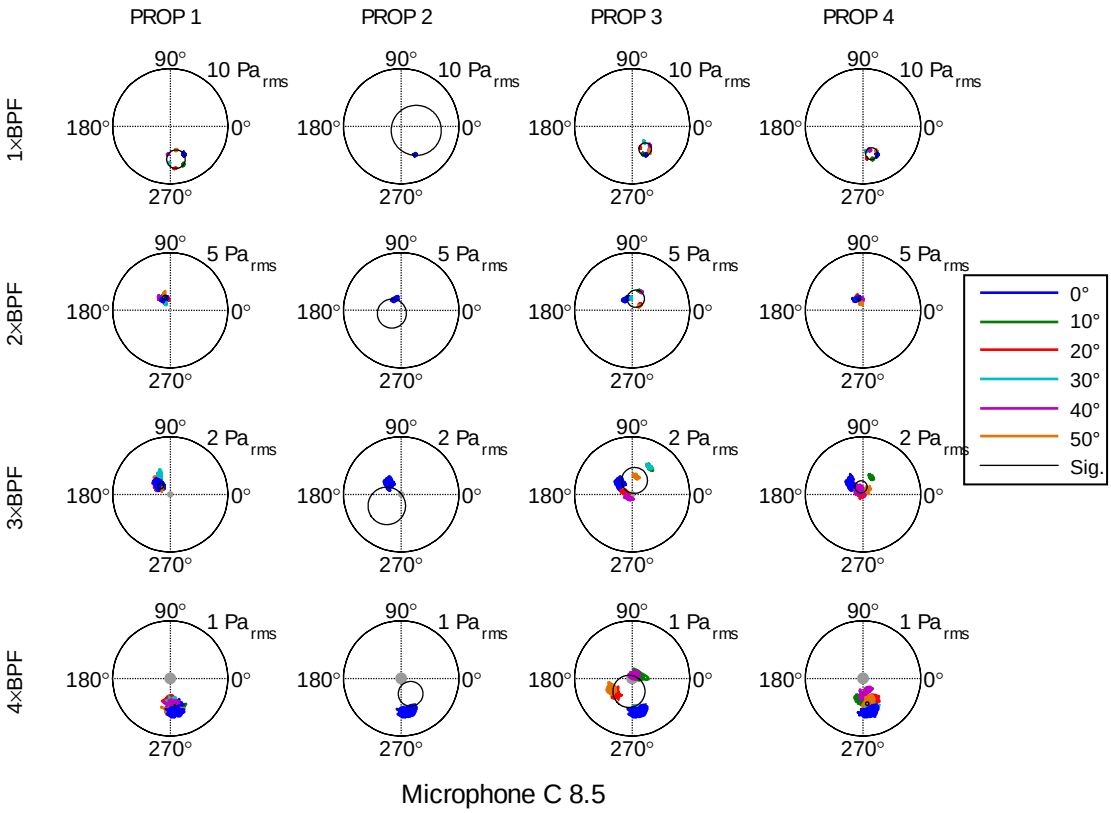

Figure G.14 Effect of separately clocking the synchrophase angle of each propeller on the amplitude and phase of the harmonic components measured with Mic. C 8.5.

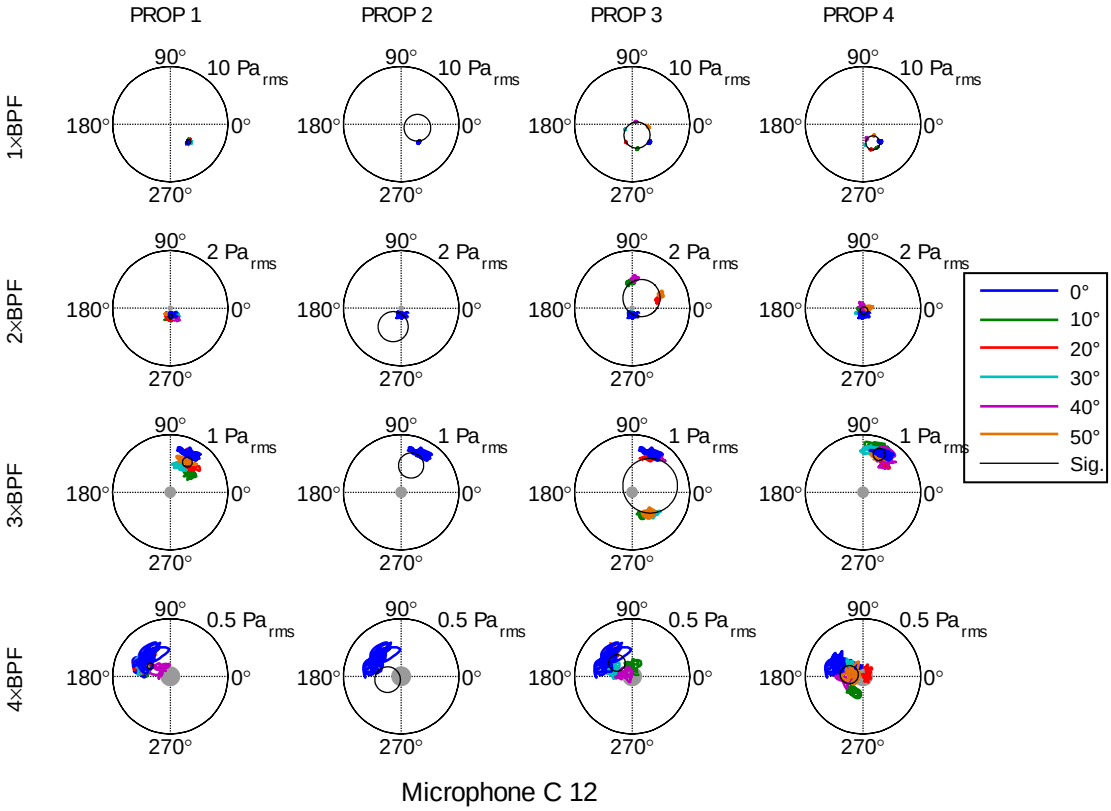

Figure G.15 Effect of separately clocking the synchrophase angle of each propeller on the amplitude and phase of the harmonic components measured with Mic. C 12.

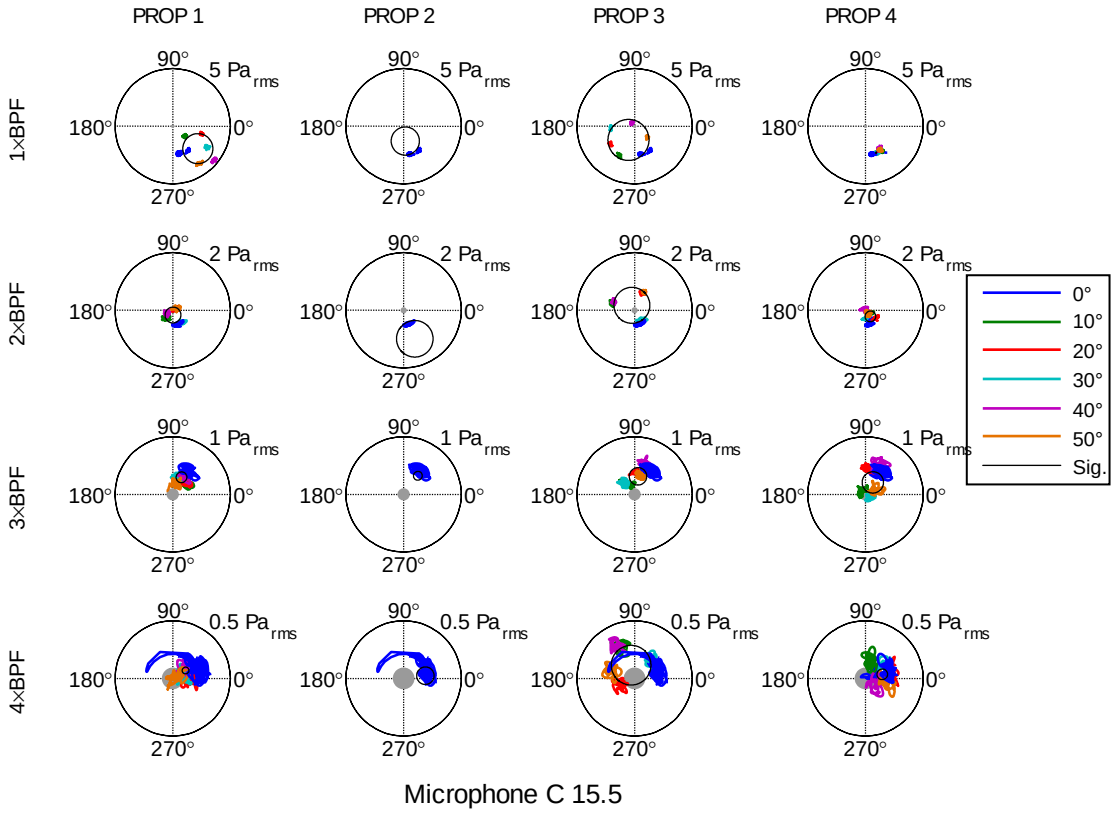

Figure G.16 Effect of separately clocking the synchrophase angle of each propeller on the amplitude and phase of the harmonic components measured with Mic. C 15.5, Trial 1.

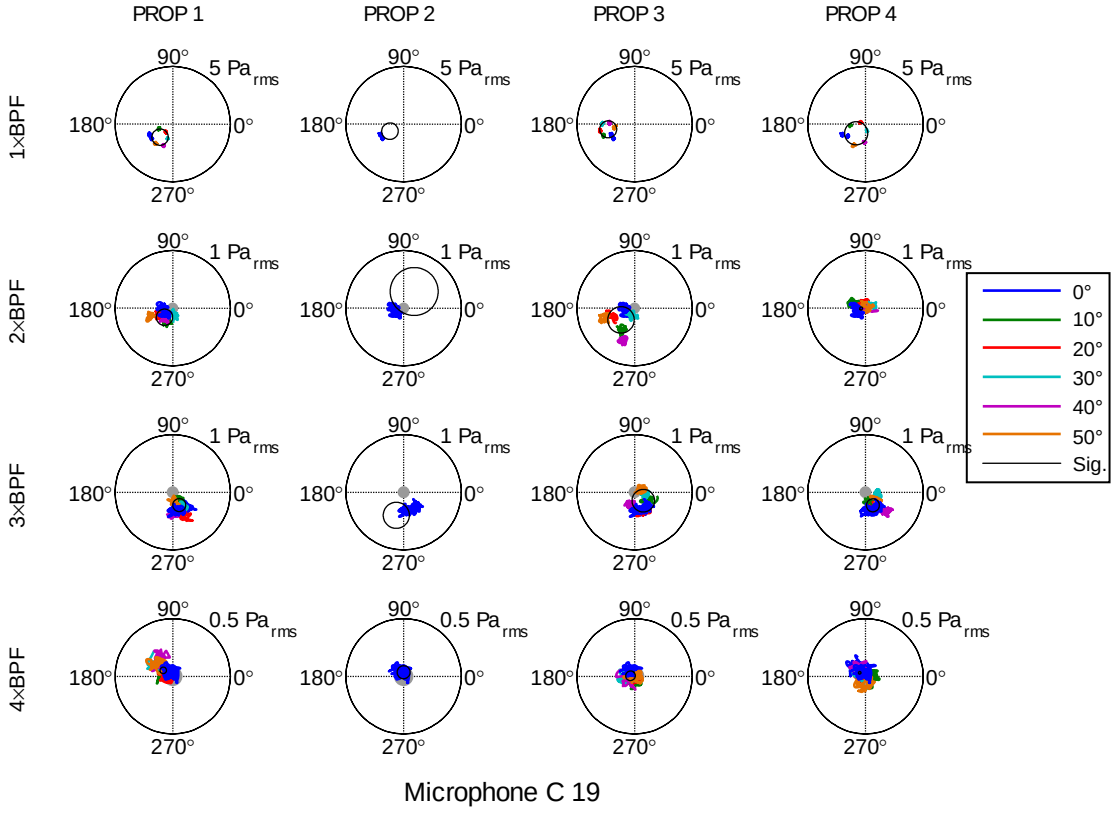

Figure G.17 Effect of separately clocking the synchrophase angle of each propeller on the amplitude and phase of the harmonic components measured with Mic. C 19.

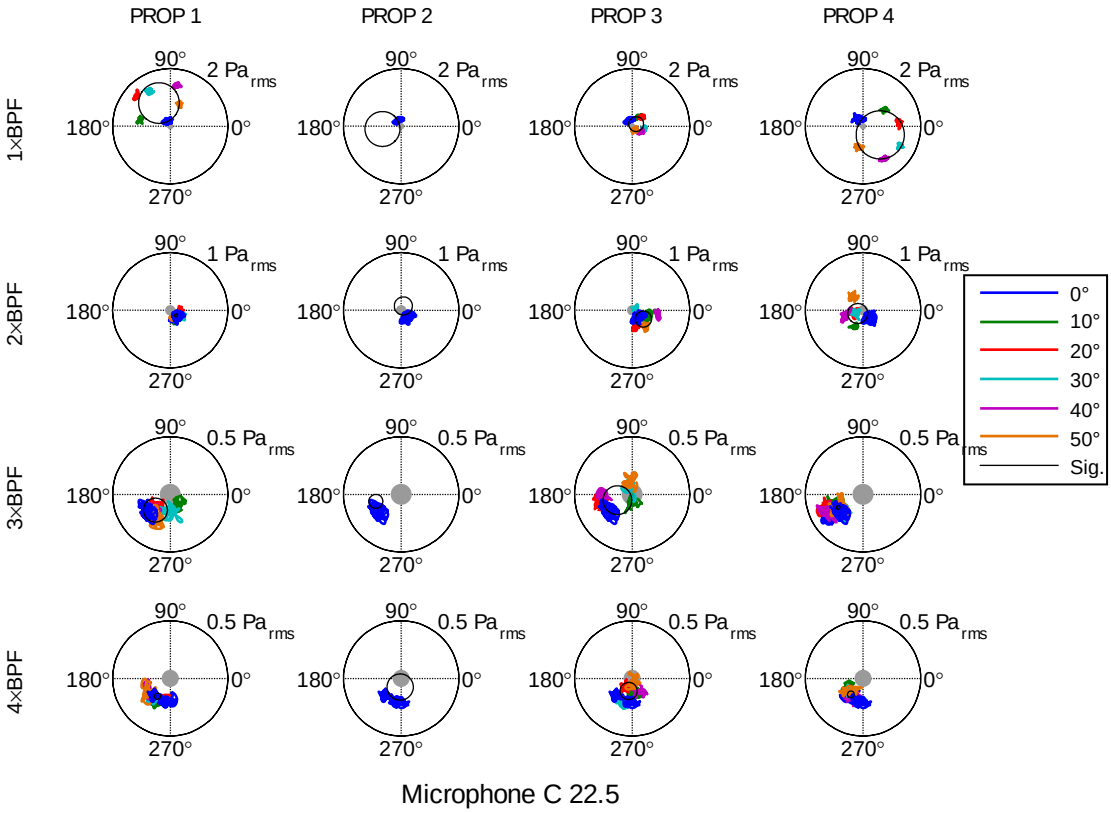

Figure G.18 Effect of separately clocking the synchrophase angle of each propeller on the amplitude and phase of the harmonic components measured with Mic. C 22.5.

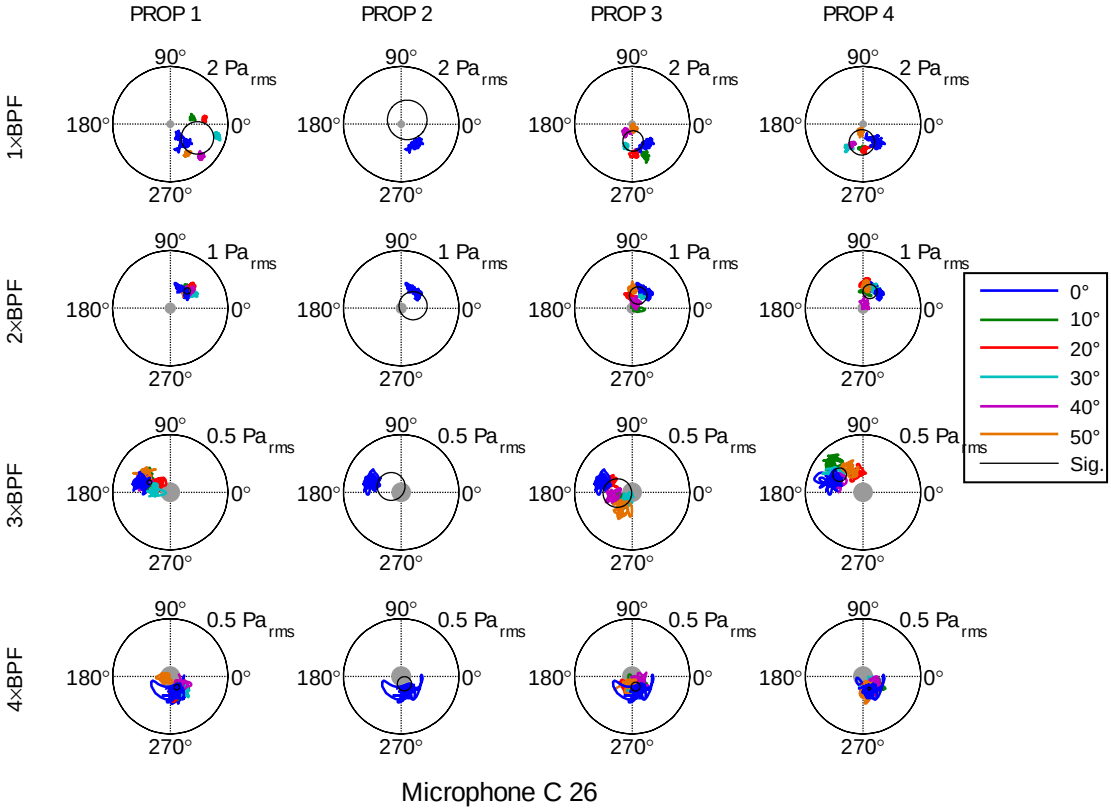

Figure G.19 Effect of separately clocking the synchrophase angle of each propeller on the amplitude and phase of the harmonic components measured with Mic. C 26.

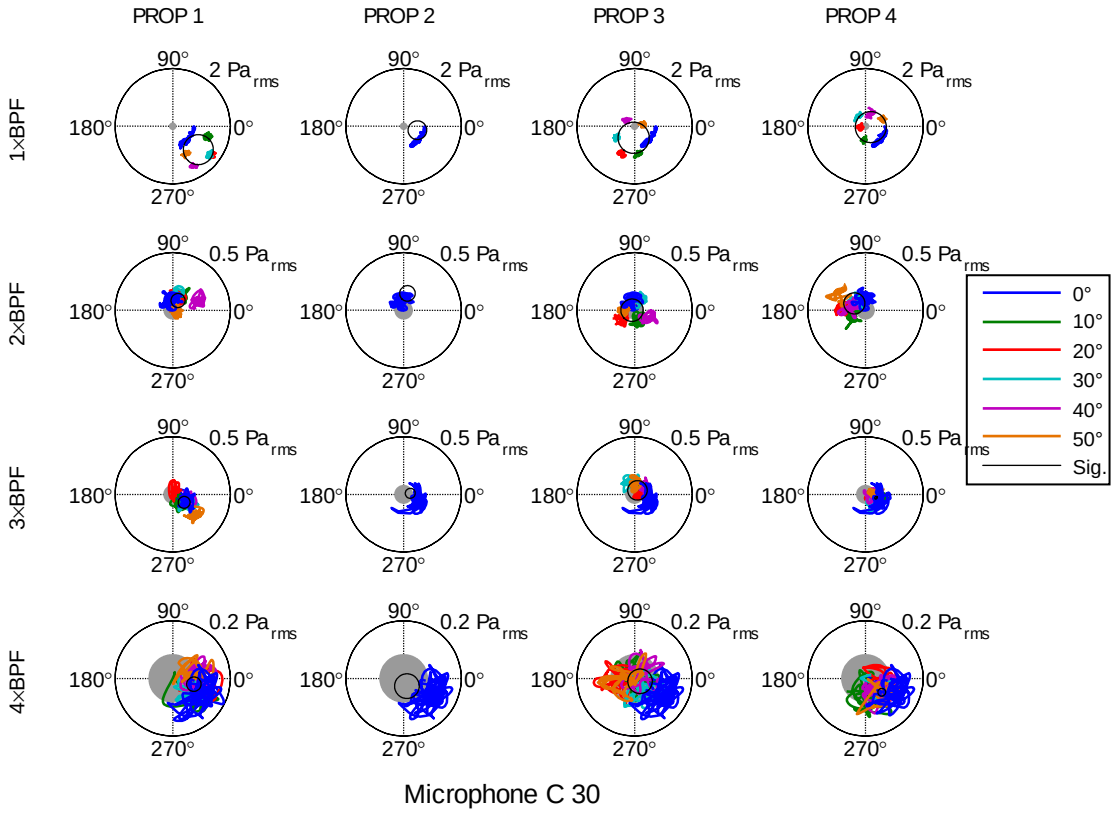

Figure G.20 Effect of separately clocking the synchrophase angle of each propeller on the amplitude and phase of the harmonic components measured with Mic. C 30.

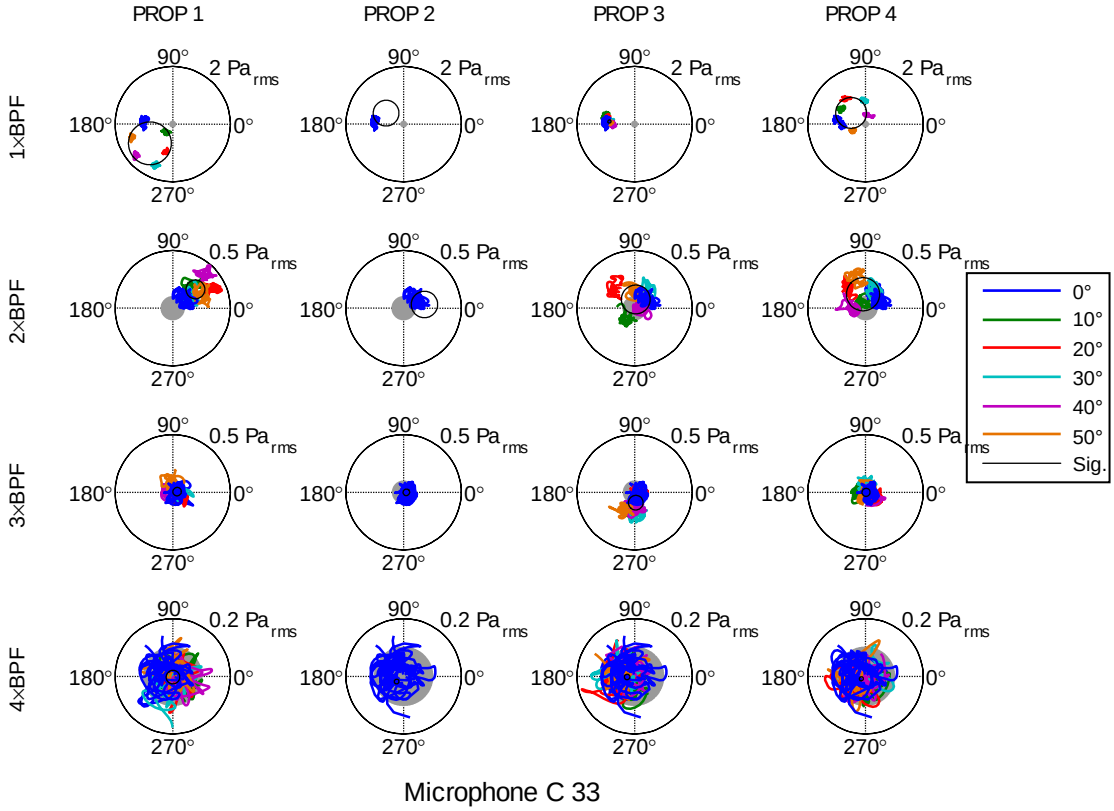

Figure G.21 Effect of separately clocking the synchrophase angle of each propeller on the amplitude and phase of the harmonic components measured with Mic. C 33.

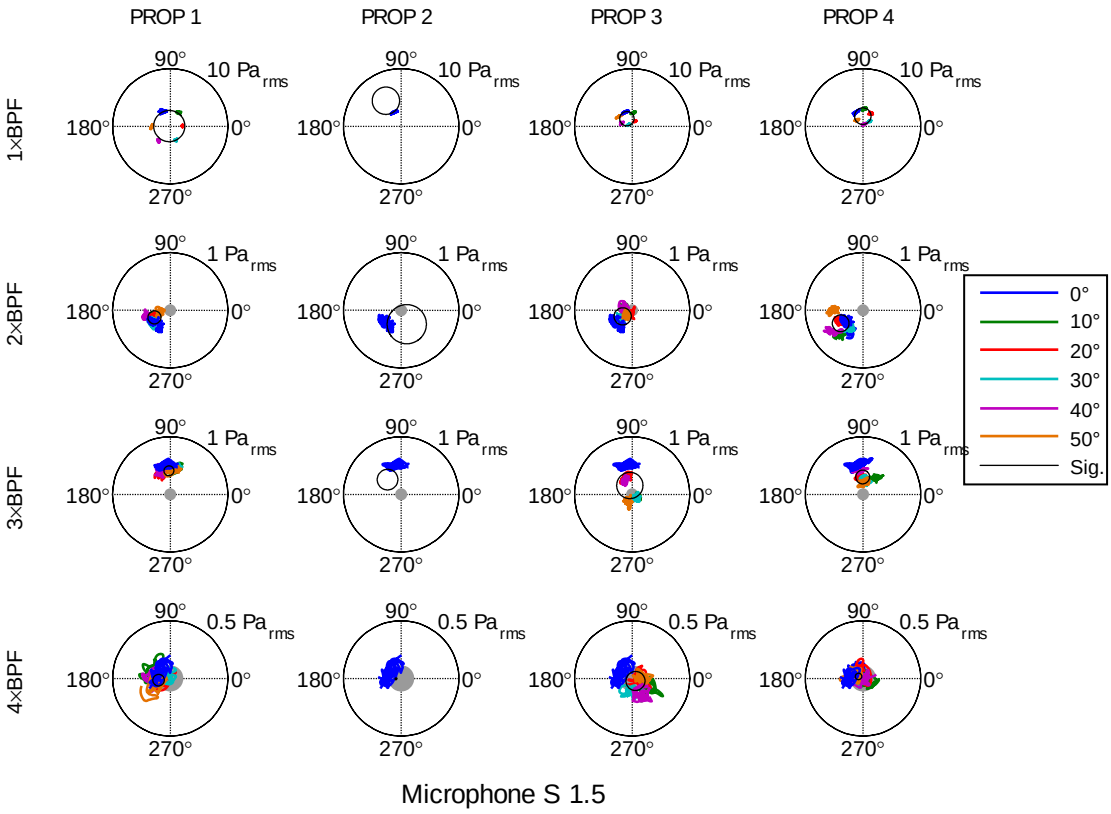

Figure G.22 Effect of separately clocking the synchrophase angle of each propeller on the amplitude and phase of the harmonic components measured with Mic. S 1.5.

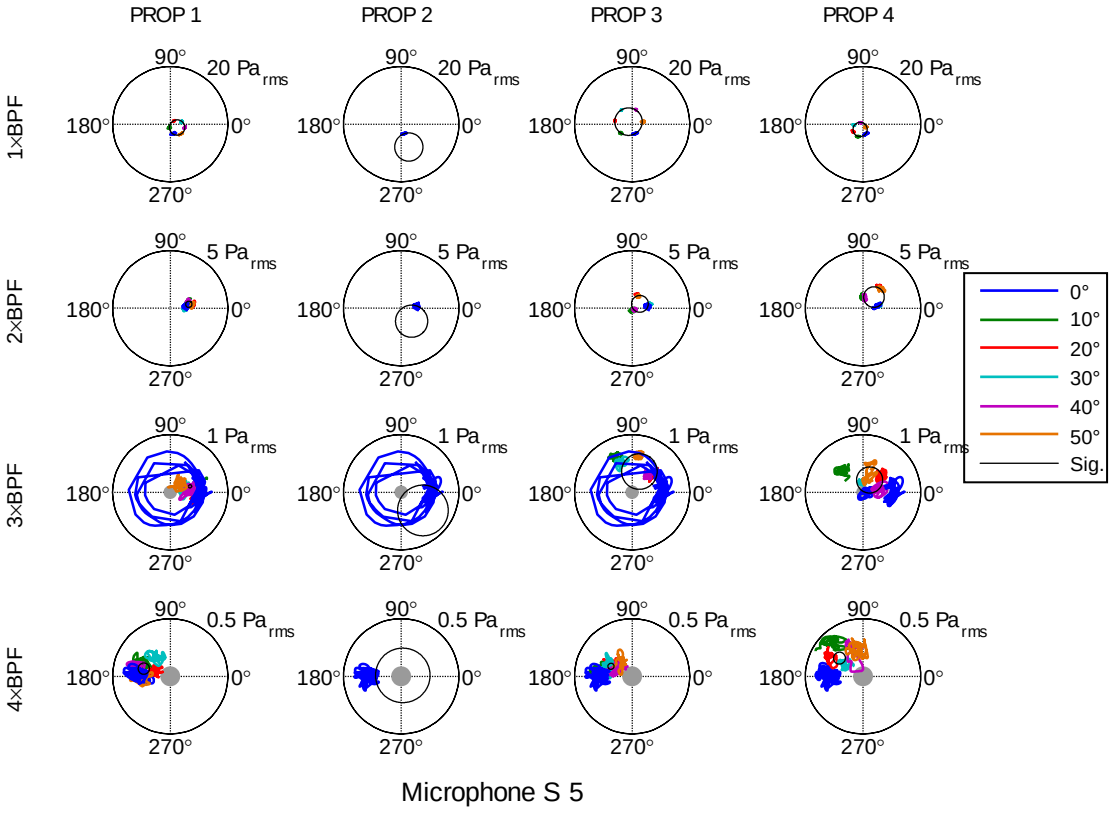

Figure G.23 Effect of separately clocking the synchrophase angle of each propeller on the amplitude and phase of the harmonic components measured with Mic. S 5.

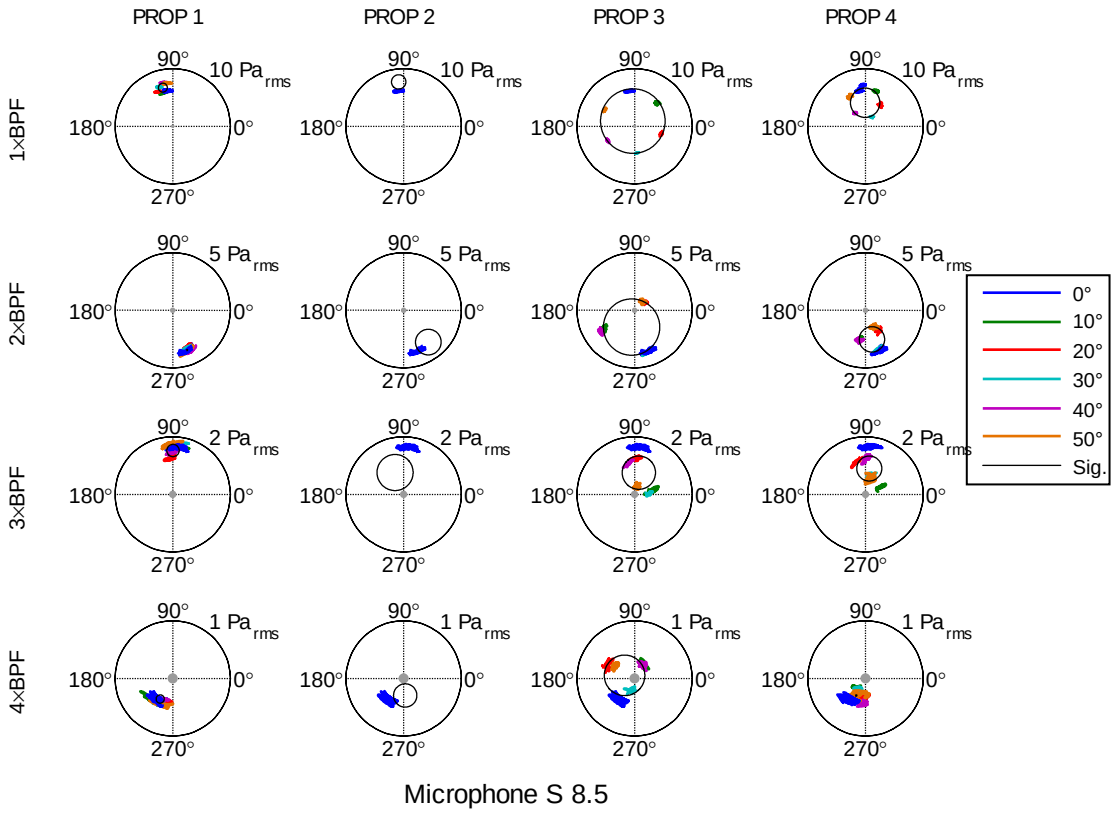

Figure G.24 Effect of separately clocking the synchrophase angle of each propeller on the amplitude and phase of the harmonic components measured with Mic. S 8.5.

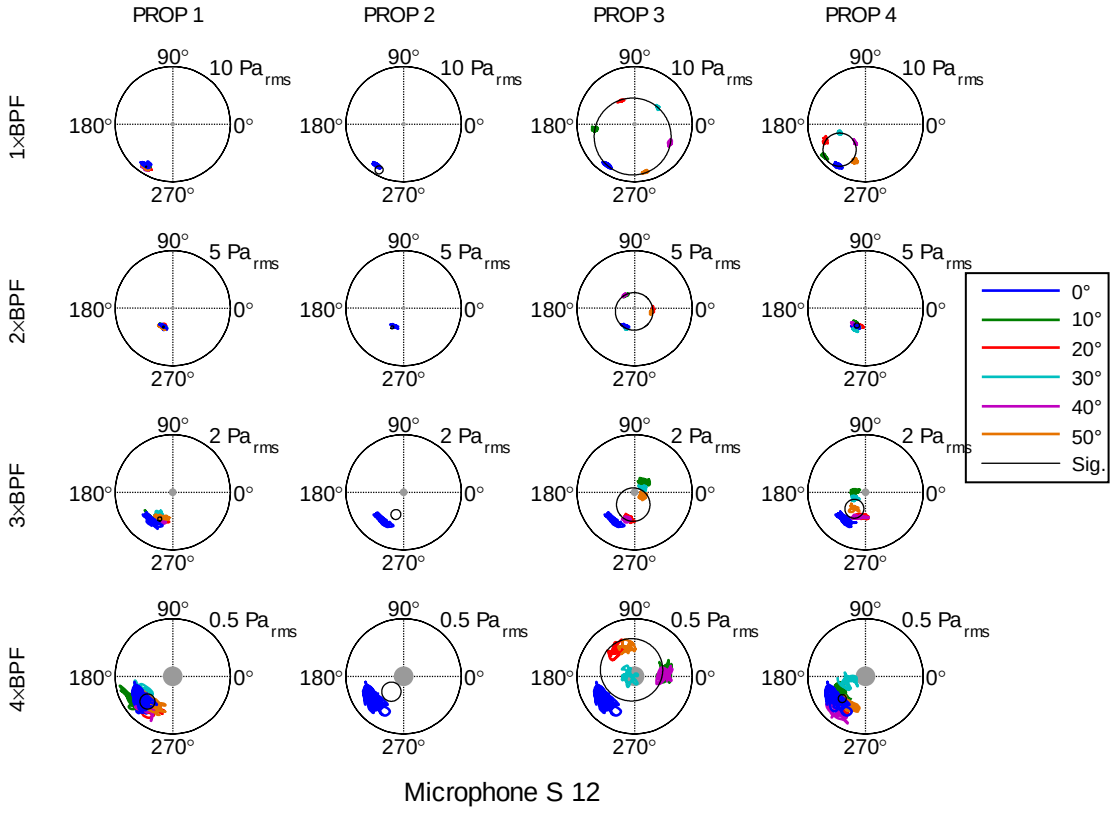

Figure G.25 Effect of separately clocking the synchrophase angle of each propeller on the amplitude and phase of the harmonic components measured with Mic. S 12.

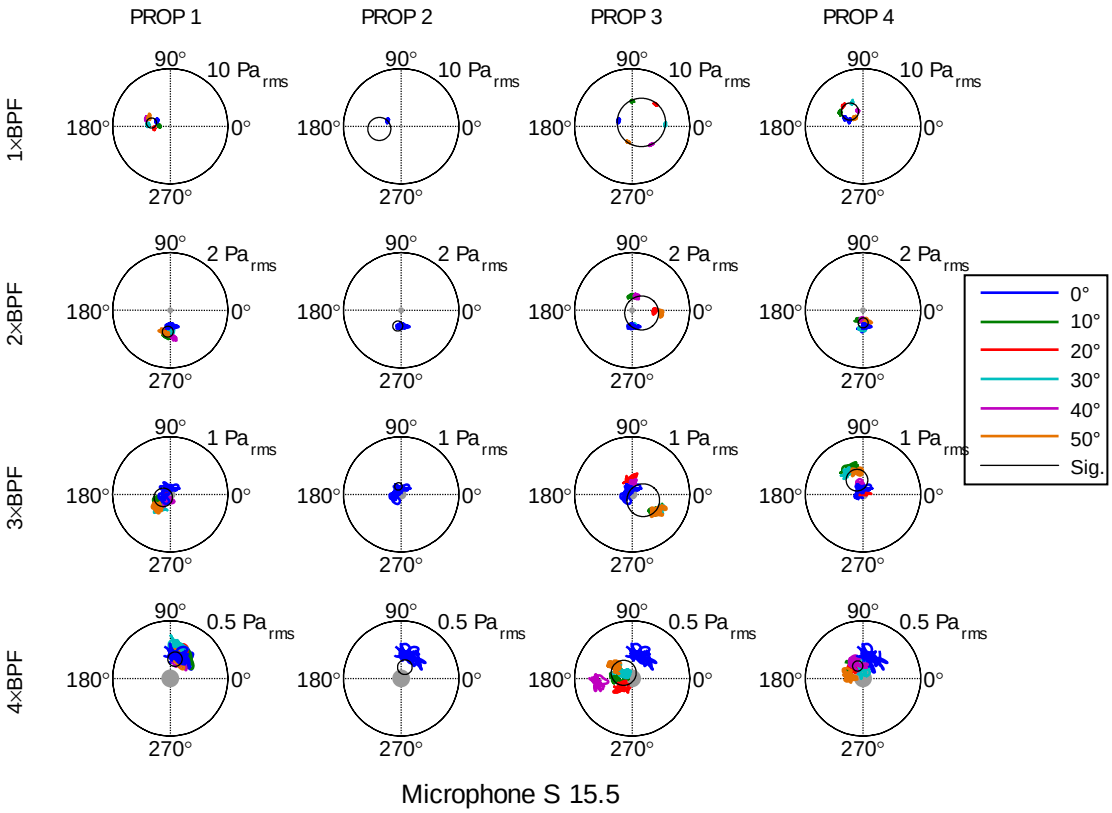

Figure G.26 Effect of separately clocking the synchrophase angle of each propeller on the amplitude and phase of the harmonic components measured with Mic. S 15.5.

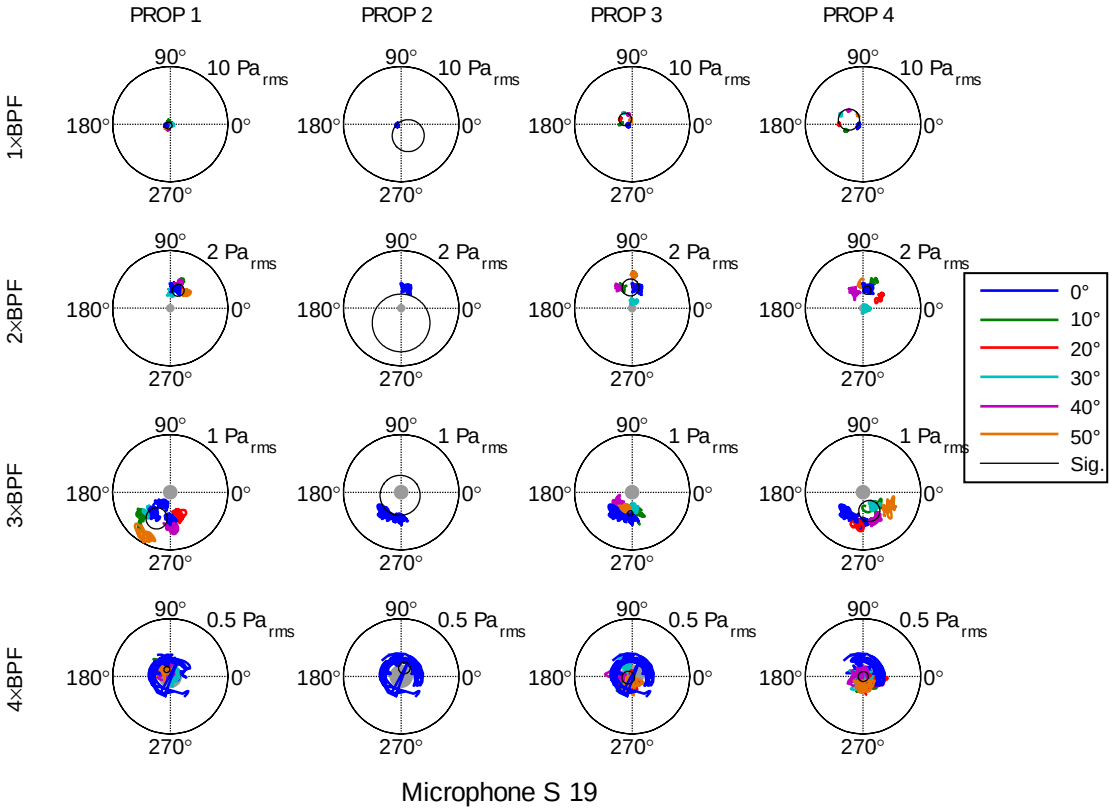

Figure G.27 Effect of separately clocking the synchrophase angle of each propeller on the amplitude and phase of the harmonic components measured with Mic. S 19.

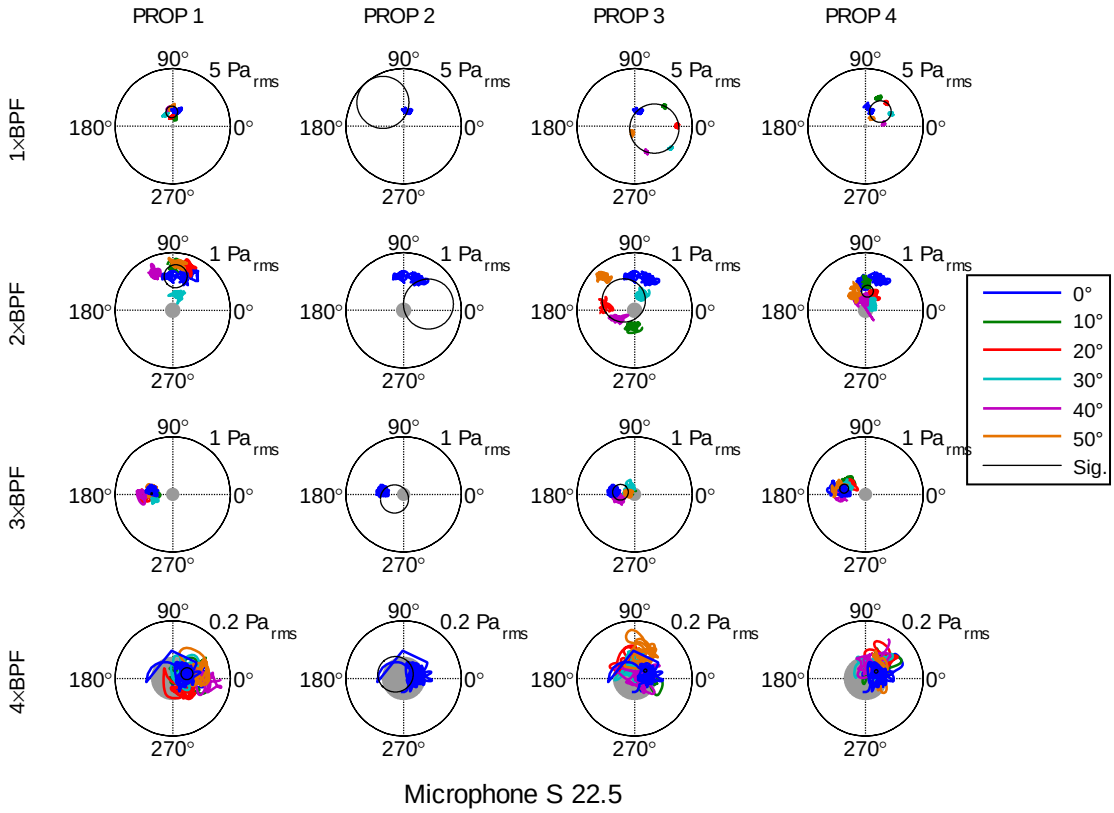

Figure G.28 Effect of separately clocking the synchrophase angle of each propeller on the amplitude and phase of the harmonic components measured with Mic. S 22.5.

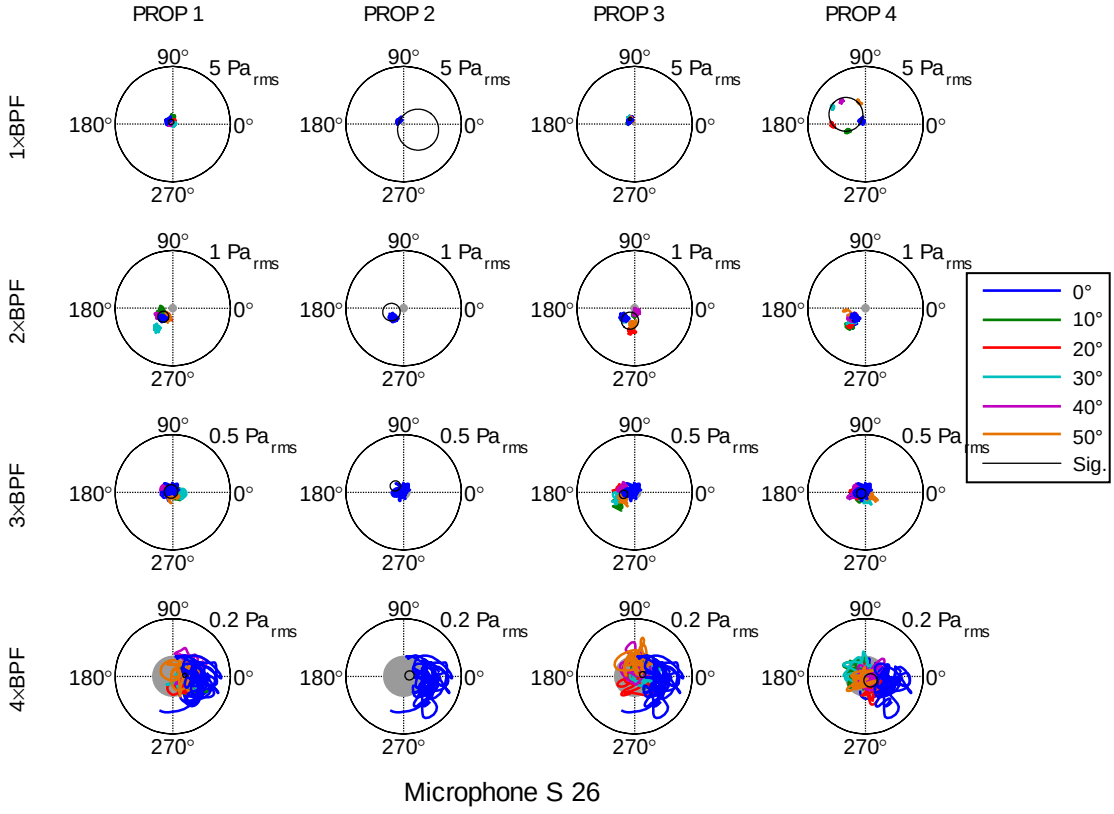

Figure G.29 Effect of separately clocking the synchrophase angle of each propeller on the amplitude and phase of the harmonic components measured with Mic. S 26.

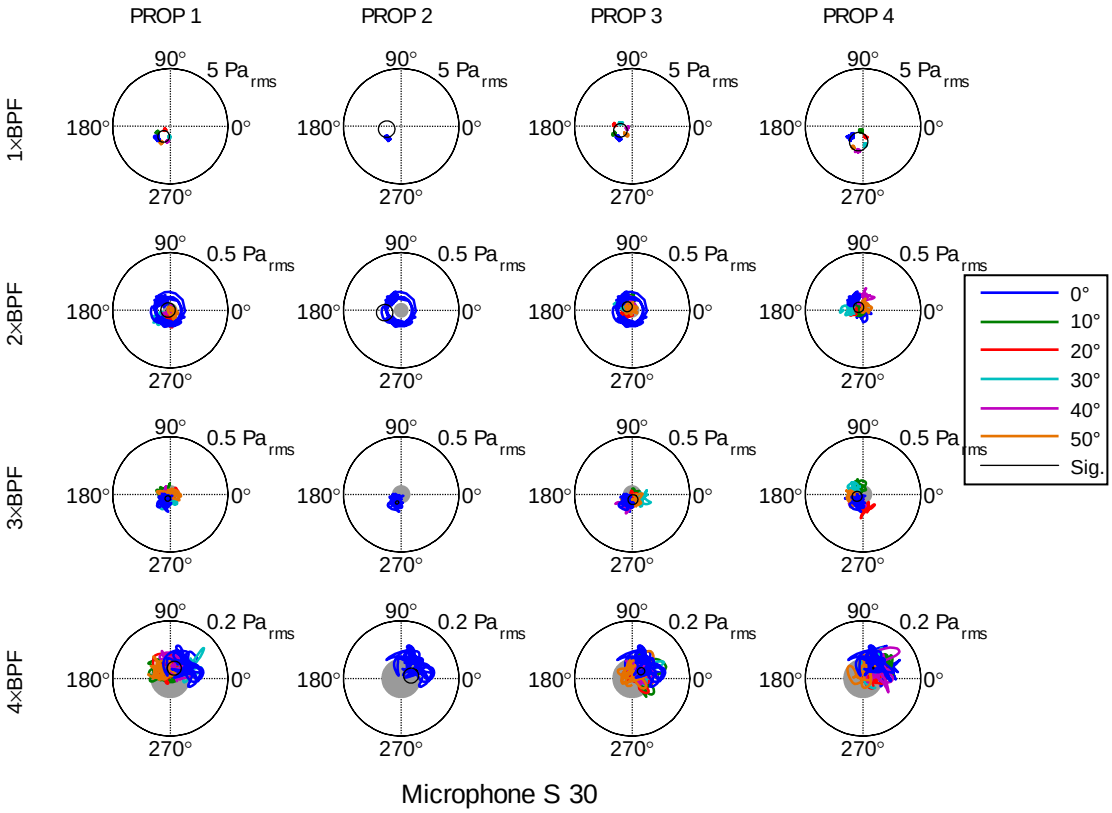

Figure G.30 Effect of separately clocking the synchrophase angle of each propeller on the amplitude and phase of the harmonic components measured with Mic. S 30.

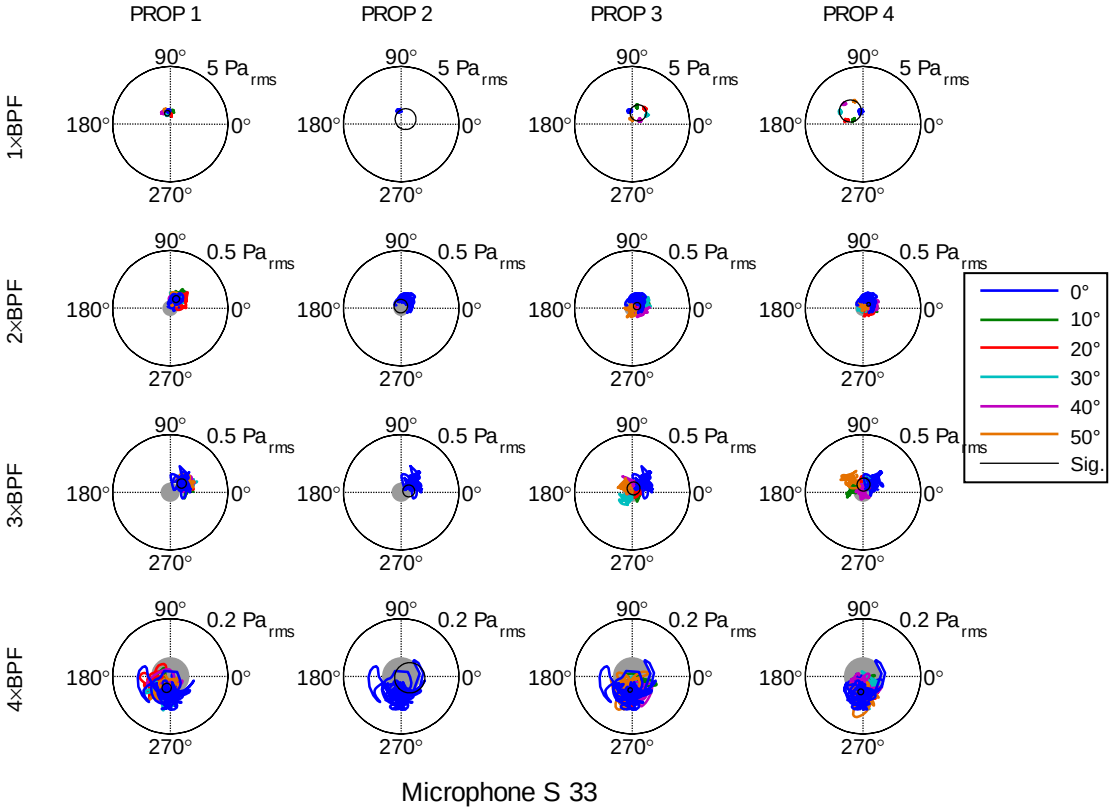

Figure G.31 Effect of separately clocking the synchrophase angle of each propeller on the amplitude and phase of the harmonic components measured with Mic. S 33.

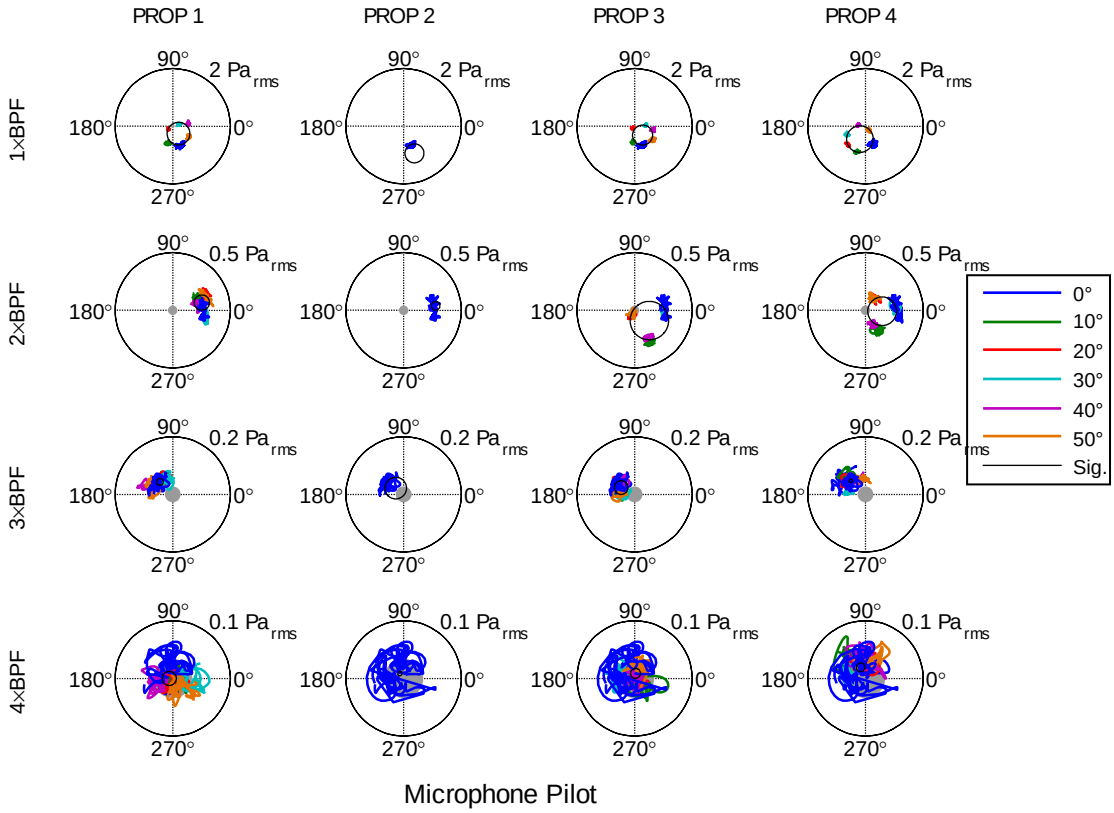

Figure G.32 Effect of separately clocking the synchrophase angle of each propeller on the amplitude and phase of the harmonic components measured with Pilot Mic..

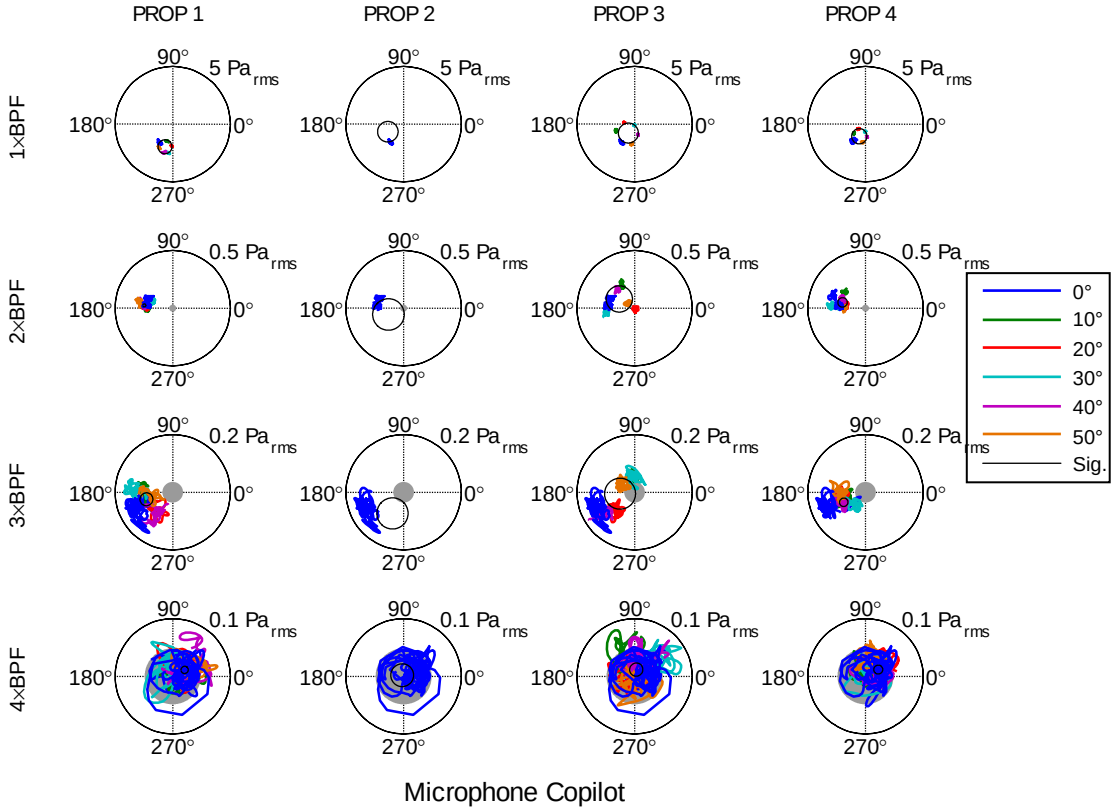

Figure G.33 Effect of separately clocking the synchrophase angle of each propeller on the amplitude and phase of the harmonic components measured with Co-Pilot Mic..

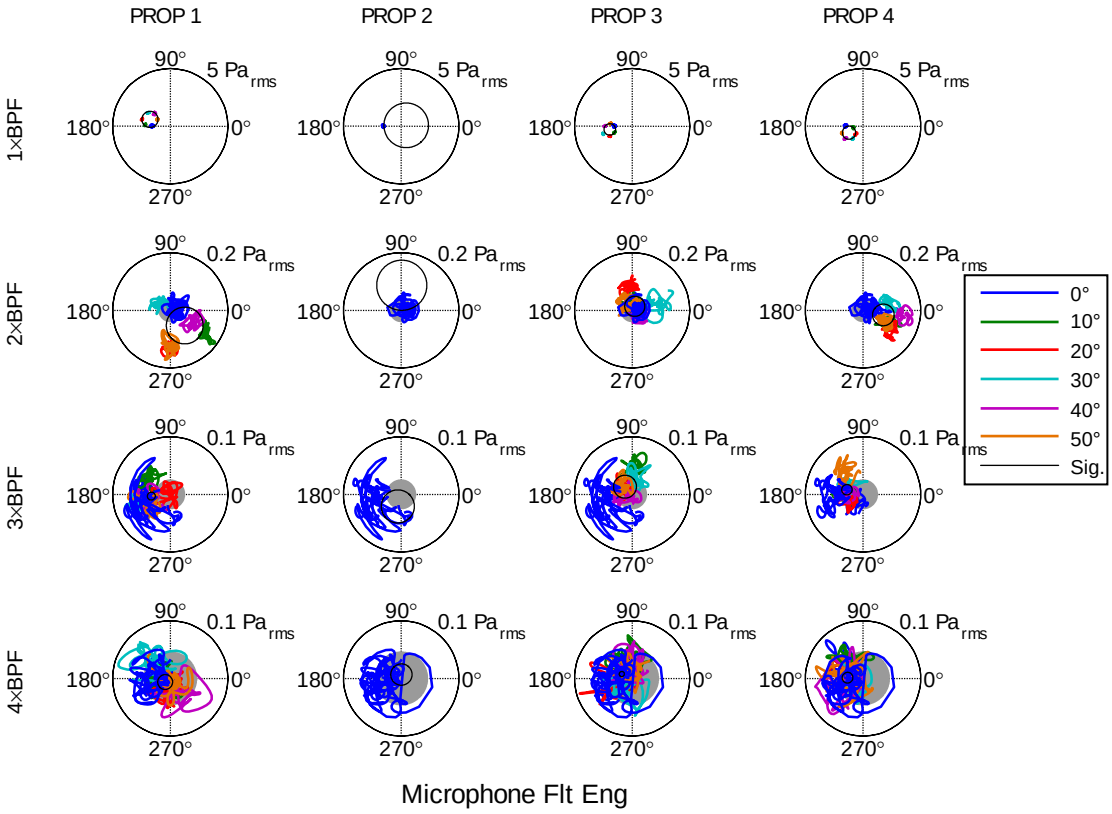

Figure G.34 Effect of separately clocking the synchrophase angle of each propeller on the amplitude and phase of the harmonic components measured with Flt Eng. Mic.

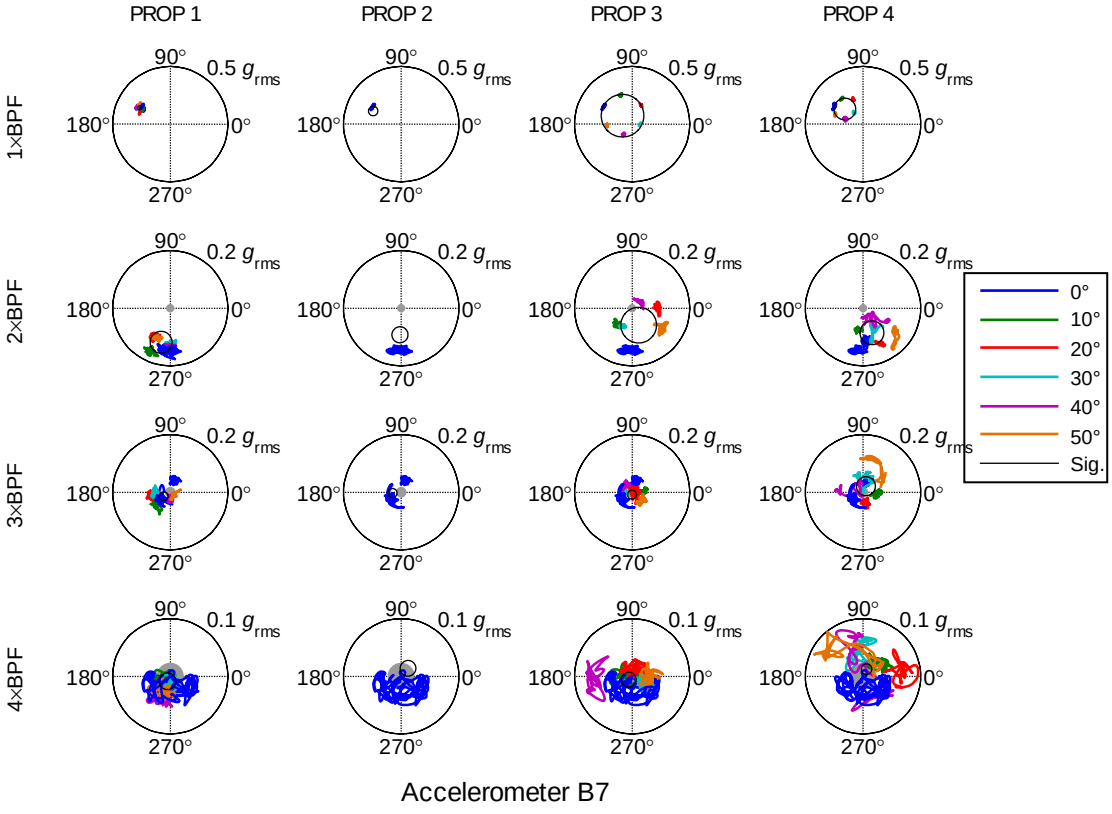

Figure G.35 Effect of separately clocking the synchrophase angle of each propeller on the amplitude and phase of the harmonic components measured with Accel. B7.

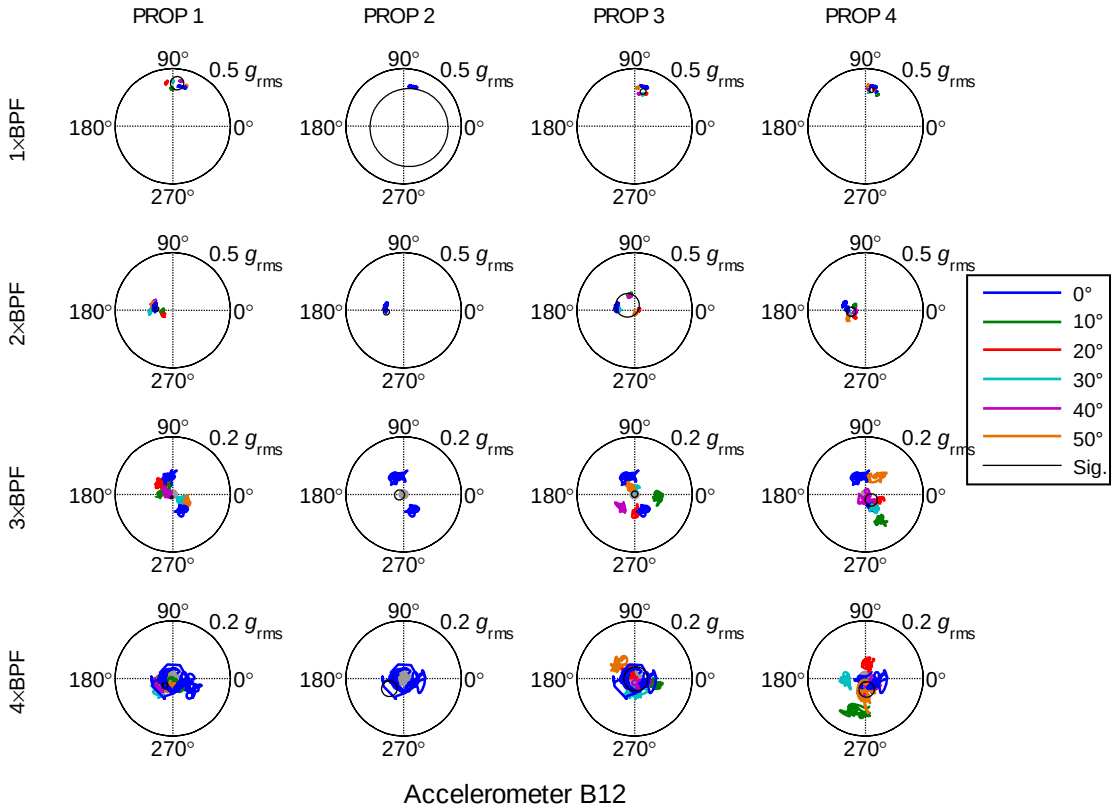

Figure G.36 Effect of separately clocking the synchrophase angle of each propeller on the amplitude and phase of the harmonic components measured with Accel. B12.

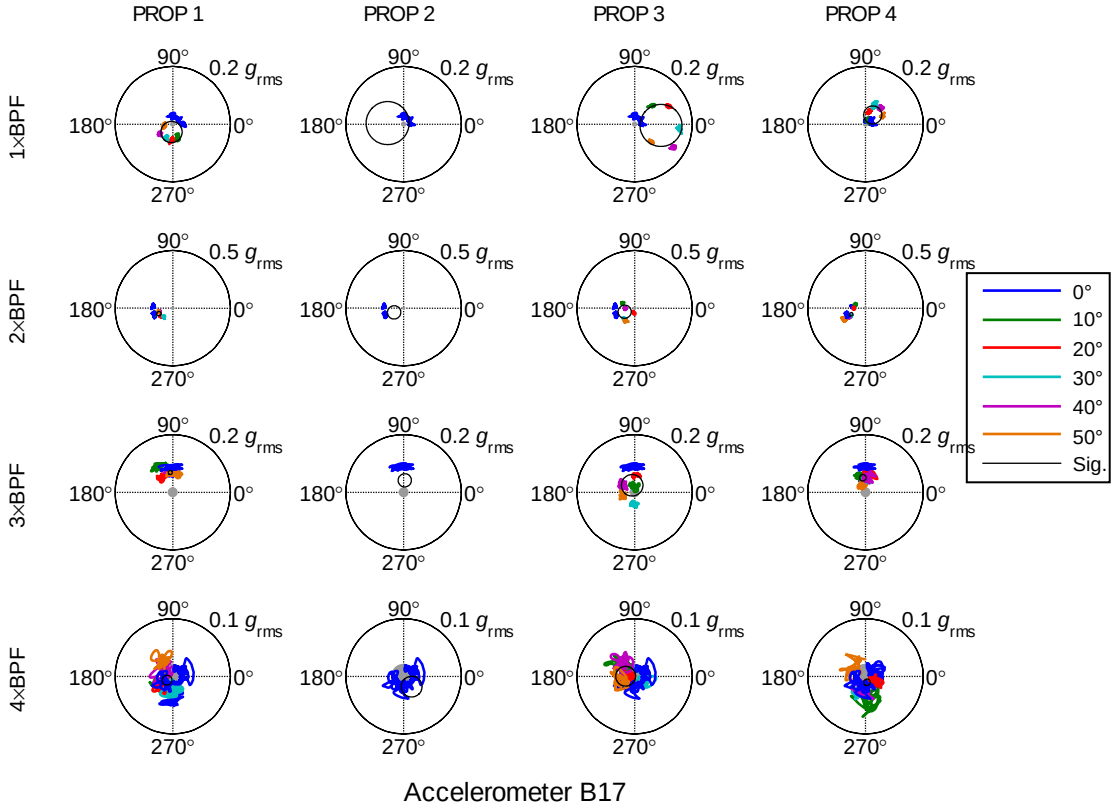

Figure G.37 Effect of separately clocking the synchrophase angle of each propeller on the amplitude and phase of the harmonic components measured with Accel. B17.

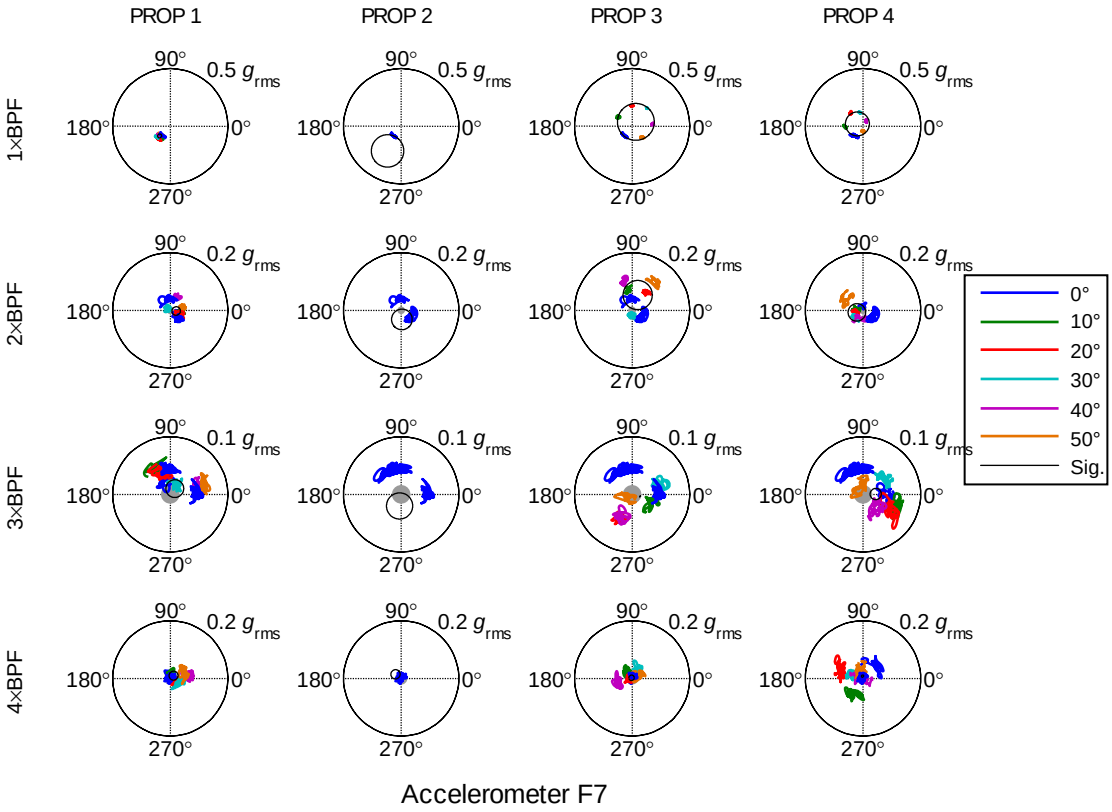

Figure G.38 Effect of separately clocking the synchrophase angle of each propeller on the amplitude and phase of the harmonic components measured with Accel. F7.

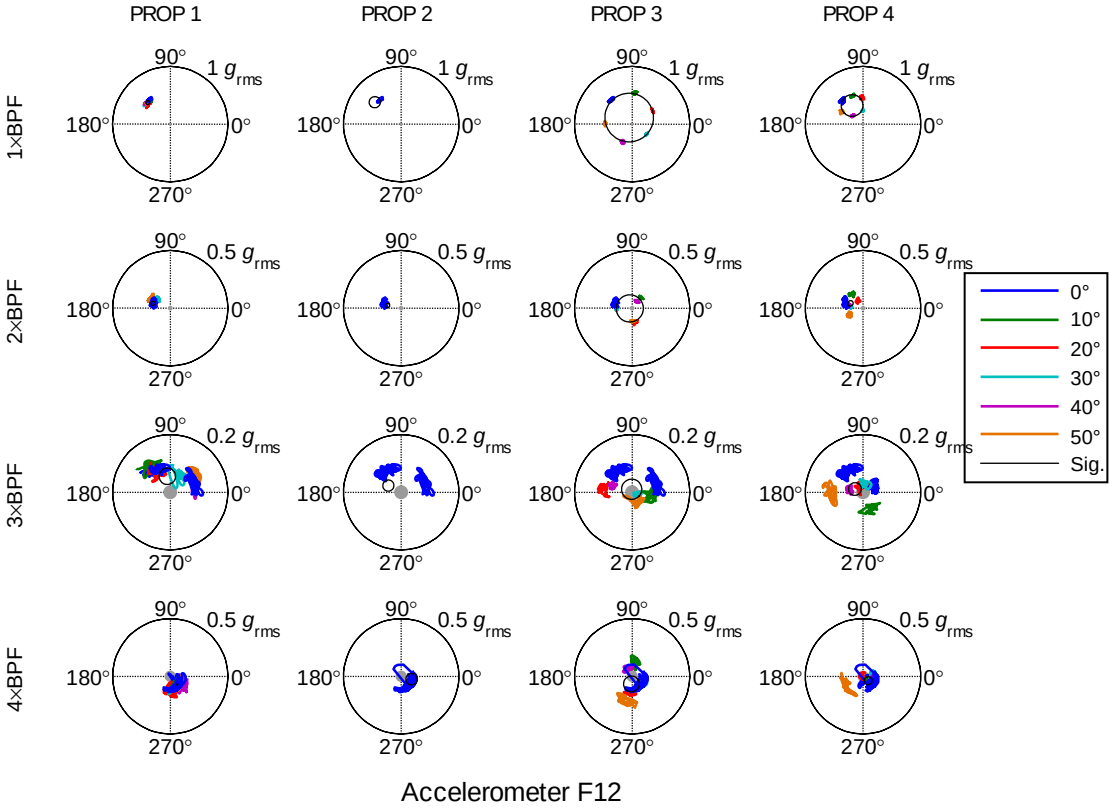

Figure G.39 Effect of separately clocking the synchrophase angle of each propeller on the amplitude and phase of the harmonic components measured with Accel. F12.

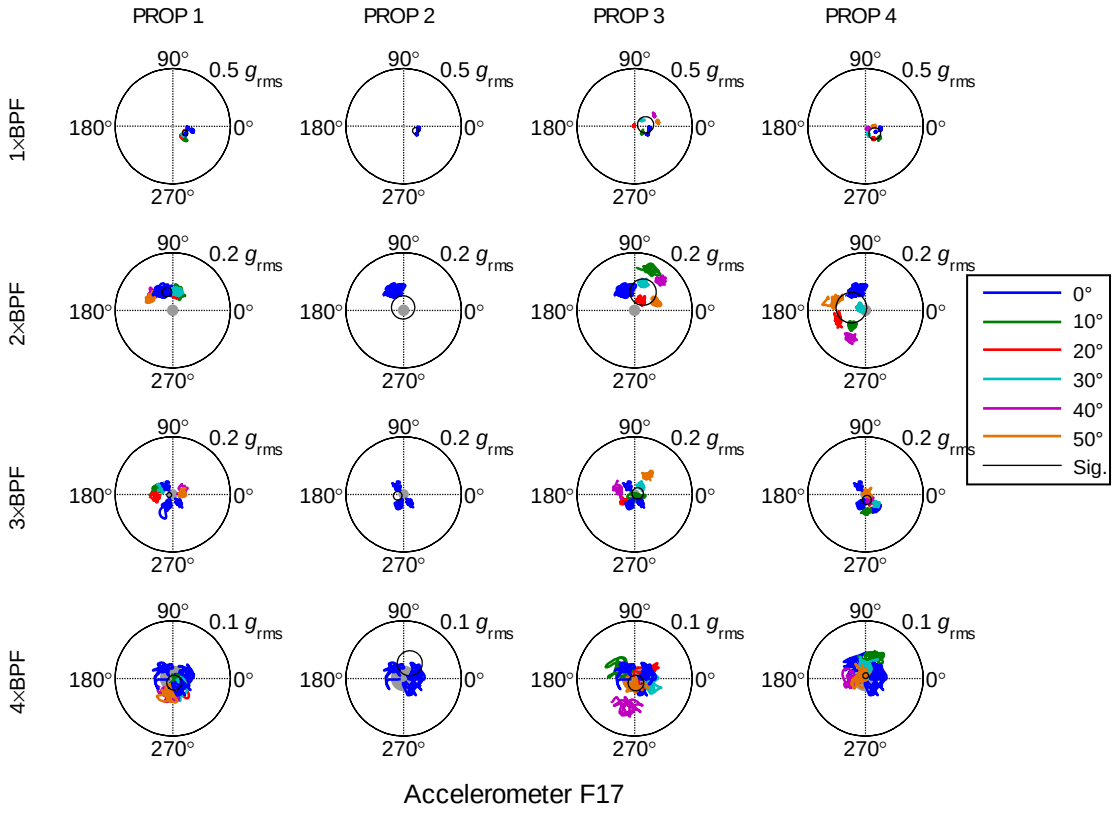

Figure G.40 Effect of separately clocking the synchrophase angle of each propeller on the amplitude and phase of the harmonic components measured with Accel. F17.

Appendix H. AP-3C Predicted Sound and Vibration Levels

Table H.1 AP-3C measured BPF levels for default synchrophase angles.

Serial	Synchrophase Angles	Max. SPL (dB re 20μPa)	Avg. SPL (dB re 20μPa)	Min. SPL (dB re 20μPa)	Max. Accel. (dB re 1 g_{rms})	Avg. Accel. (dB re 1 g_{rms}))	Min. Accel. (dB re 1 g_{rms}))
1	Default Angles	98.7	91.1	79.0	−23.4	−28.2	−36.4
2	Default Angles	97.5	90.3	69.9	−23.8	−28.9	−39.0
3	Default Angles	96.1	90.0	75.7	−24.4	−29.2	−35.2
4	Default Angles	98.4	90.5	74.2	−22.3	−28.2	−41.5
5	Default Angles	98.1	90.8	37.3	−22.4	−28.7	−46.6
6	Default Angles	96.5	89.3	72.9	−22.3	−28.4	−47.7
7	Default Angles	95.7	90.0	70.8	−21.2	−27.3	−38.2
8	Default Angles	102.3	94.1	77.5	−20.6	−27.0	−35.0
9	Default Angles	97.6	90.8	70.2	−20.9	−27.4	−37.4
10	Default Angles	101.6	93.4	70.5	−19.8	−26.4	−38.3
11	Default Angles	101.9	95.7	69.0	−18.2	−25.0	−35.1
12	Default Angles	98.4	91.5	75.9	−20.5	−27.2	−45.0
13	Default Angles	101.0	94.9	79.4	−19.7	−25.1	−33.7
14	Default Angles	105.6	98.1	81.0	−20.8	−25.1	−30.8
15	Default Angles	109.6	101.2	75.3	−19.4	−21.5	−30.8
16	Default Angles	101.0	95.3	79.3	−19.6	−24.7	−34.8
17	Default Angles	102.9	96.9	84.8	−20.0	−24.9	−31.5
18	Default Angles	106.8	99.6	85.2	−19.7	−22.7	−30.3
19	Default Angles	100.9	95.0	68.9	−19.9	−26.2	−35.7
20	Default Angles	102.8	97.5	82.3	−20.3	−24.8	−28.6
21	Default Angles	105.9	99.4	72.8	−18.6	−21.5	−27.7
22	Default Angles	101.1	95.8	70.1	−20.9	−25.3	−42.6
23	Default Angles	102.4	97.1	54.8	−20.7	−24.8	−30.6
24	Default Angles	105.1	98.4	71.5	−20.4	−22.8	−33.3
25	Default Angles	99.8	91.2	73.2	−21.9	−27.4	−40.1
26	Default Angles	99.2	90.9	77.3	−22.7	−28.2	−39.3
27	Default Angles	98.4	91.5	73.6	−22.5	−27.7	−39.2
28	Default Angles	97.3	90.4	66.3	−21.7	−28.2	−47.5

Table H.2 AP-3C predicted BPF levels for default synchrophase angles.

Serial	Synchrophase Angles	Max. SPL (dB re 20μPa)	Avg. SPL (dB re 20μPa)	Min. SPL (dB re 20μPa)	Max. Accel. (dB re 1 g_{rms})	Avg. Accel. (dB re 1 g_{rms}))	Min. Accel. (dB re 1 g_{rms}))
1	Default Angles	99.8	92.5	78.3	−21.7	−26.4	−33.3
2	Default Angles	99.3	92.4	74.4	−21.8	−26.3	−31.2
3	Default Angles	99.0	91.9	81.5	−22.1	−26.6	−33.5
4	Default Angles	99.7	92.5	71.6	−20.9	−26.3	−35.2
5	Default Angles	100.1	93.6	62.6	−20.5	−26.6	−37.7
6	Default Angles	99.5	91.6	76.4	−20.5	−26.4	−43.5
7	Default Angles	100.9	94.2	73.8	−19.6	−25.3	−31.9
8	Default Angles	103.4	96.2	78.4	−18.5	−24.2	−29.5
9	Default Angles	100.8	93.4	78.3	−19.2	−25.3	−29.8
10	Default Angles	103.6	96.3	71.9	−17.4	−23.9	−35.6
11	Default Angles	105.1	98.3	76.7	−16.7	−23.4	−34.7
12	Default Angles	102.8	94.4	78.3	−18.5	−24.8	−39.9
13	Default Angles	104.3	96.7	72.7	−18.1	−23.1	−29.0
14	Default Angles	107.6	100.2	89.5	−19.1	−23.3	−42.6
15	Default Angles	110.9	103.3	87.8	−16.1	−19.1	−26.3
16	Default Angles	104.2	96.5	84.6	−17.5	−22.3	−32.6
17	Default Angles	105.7	98.6	85.0	−18.0	−22.4	−28.9
18	Default Angles	109.3	101.6	77.1	−17.0	−20.3	−29.1
19	Default Angles	103.8	96.6	64.6	−17.8	−23.7	−32.7
20	Default Angles	106.1	99.3	83.7	−18.0	−22.6	−27.5
21	Default Angles	109.4	101.4	79.9	−16.8	−19.3	−24.9
22	Default Angles	104.3	98.0	71.0	−18.4	−23.4	−34.7
23	Default Angles	105.2	98.6	77.0	−18.2	−23.0	−30.5
24	Default Angles	108.5	100.6	80.2	−18.5	−20.2	−29.8
25	Default Angles	102.0	93.8	78.3	−19.1	−24.9	−41.3
26	Default Angles	102.1	94.5	82.0	−19.5	−24.8	−31.4
27	Default Angles	101.4	94.0	74.5	−19.7	−25.0	−36.6
28	Default Angles	100.7	94.4	73.4	−18.7	−24.5	−35.7

Table H.3 AP-3C synchrophase angles and BPF levels for the highest predicted average over all microphones of the SPL at the BPF.

Serial	Synchrophase Angles	Max. SPL (dB re 20μPa)	Avg. SPL (dB re 20μPa)	Min. SPL (dB re 20μPa)	Max. Accel. (dB re 1 g_{rms})	Avg. Accel. (dB re 1 g_{rms}))	Min. Accel. (dB re 1 g_{rms}))
1	(−44°,−38°,0°,−30°)	107.8	99.6	84.7	−21.8	−25.5	−54.4
2	(42°,−38°,0°,−32°)	108.9	100.4	78.9	−21.3	−24.0	−48.0
3	(42°,−42°,0°,−30°)	107.9	99.6	64.9	−22.0	−25.0	−46.7
4	(42°,−36°,0°,−32°)	107.6	100.1	71.3	−21.3	−25.2	−54.1
5	(44°,−38°,0°,−34°)	109.1	101.4	68.6	−20.2	−23.8	−41.1
6	(42°,−36°,0°,−32°)	108.7	101.2	82.7	−21.6	−23.9	−37.2
7	(−44°,−40°,0°,−30°)	111.4	103.0	80.4	−24.2	−28.4	−36.9
8	(38°,40°,0°,−32°)	112.5	104.2	78.0	−25.5	−29.6	−37.2
9	(−40°,−30°,0°,−30°)	107.8	100.9	78.2	−19.7	−23.8	−33.5
10	(−38°,−38°,0°,−26°)	111.8	104.1	70.6	−19.7	−26.0	−40.3
11	(−38°,−42°,0°,−22°)	114.6	106.2	86.3	−19.4	−24.6	−37.5
12	(−28°,−30°,0°,−20°)	108.8	102.0	85.0	−18.6	−24.4	−34.5
13	(−26°,−34°,0°,−16°)	111.7	103.9	74.8	−16.9	−23.0	−29.7
14	(−32°,−38°,0°,−18°)	114.0	106.1	78.8	−14.8	−21.8	−42.5
15	(−20°,−32°,0°,−10°)	116.0	108.5	74.2	−13.3	−17.3	−21.5
16	(−22°,−22°,0°,−16°)	110.5	103.5	78.4	−16.3	−21.0	−31.8
17	(−16°,−22°,0°,−10°)	111.5	104.4	83.7	−14.7	−20.2	−40.9
18	(−16°,−28°,0°,−8°)	113.9	106.8	83.2	−13.0	−17.9	−28.9
19	(−14°,−16°,0°,−14°)	109.0	102.7	83.1	−15.9	−20.7	−28.8
20	(−10°,−20°,0°,−8°)	111.1	104.1	83.9	−14.9	−19.8	−33.4
21	(−6°,−20°,0°,−6°)	112.0	105.2	82.8	−13.4	−17.4	−25.0
22	(−6°,−10°,0°,−12°)	109.1	102.4	90.6	−13.3	−17.1	−26.6
23	(−6°,−22°,0°,−4°)	110.6	103.0	80.3	−14.7	−17.7	−32.2
24	(0°,−16°,0°,−6°)	108.9	102.9	86.3	−14.5	−20.2	−27.5
25	(NaN°,20°,0°,−30°)	103.8	98.3	81.0	−22.3	−25.4	−39.8
26	(NaN°,−44°,0°,−30°)	107.9	99.6	79.3	−22.0	−24.7	−36.6
27	(NaN°,−34°,0°,−28°)	107.6	99.5	78.1	−19.8	−23.4	−36.9
28	(NaN°,−38°,0°,−32°)	107.3	99.7	72.1	−18.5	−22.4	−38.1

Table H.4 AP-3C optimum synchrophase angles and BPF levels for the lowest predicted average over all microphones of the SPL at the BPF.

Serial	Synchrophase Angles	Max. SPL (dB re 20μPa)	Avg. SPL (dB re 20μPa)	Min. SPL (dB re 20μPa)	Max. Accel. (dB re 1 g_{rms})	Avg. Accel. (dB re 1 g_{rms}))	Min. Accel. (dB re 1 g_{rms}))
1	(30°,−6°,0°,14°)	96.8	91.1	81.8	−24.0	−26.4	−31.2
2	(−14°,−28°,0°,20°)	95.1	90.3	78.0	−23.9	−29.4	−36.8
3	(10°,−20°,0°,16°)	96.2	90.7	73.1	−25.5	−29.5	−39.5
4	(−10°,−28°,0°,20°)	97.6	90.0	80.7	−24.9	−27.8	−44.0
5	(−18°,38°,0°,12°)	96.3	91.8	83.2	−25.3	−29.1	−37.8
6	(40°,2°,0°,16°)	97.1	91.1	80.4	−20.6	−26.5	−51.9
7	(2°,−34°,0°,20°)	97.5	91.5	71.9	−22.5	−27.5	−39.7
8	(−4°,−42°,0°,18°)	98.0	90.5	70.7	−22.3	−26.5	−35.7
9	(−16°,44°,0°,16°)	94.7	90.2	81.1	−22.3	−28.4	−38.6
10	(24°,−20°,0°,22°)	97.0	91.6	70.0	−19.1	−24.4	−37.0
11	(24°,−26°,0°,26°)	101.4	94.8	74.1	−18.0	−24.1	−40.7
12	(−10°,36°,0°,22°)	96.6	91.4	82.6	−22.9	−25.1	−39.2
13	(−34°,12°,0°,22°)	101.4	94.6	77.9	−17.2	−23.7	−33.4
14	(−38°,−2°,0°,30°)	104.2	96.6	69.0	−15.8	−21.0	−28.1
15	(−34°,−6°,0°,36°)	106.0	99.8	82.8	−15.4	−21.9	−32.5
16	(−10°,40°,0°,26°)	97.1	93.3	71.0	−17.1	−21.3	−29.8
17	(−24°,22°,0°,30°)	101.4	95.2	85.2	−20.1	−24.1	−31.4
18	(−32°,0°,0°,36°)	102.4	96.7	80.6	−16.6	−23.3	−37.4
19	(−12°,38°,0°,26°)	98.2	92.4	75.4	−20.1	−24.5	−30.5
20	(−22°,12°,0°,38°)	99.8	94.5	72.5	−19.6	−25.1	−35.2
21	(−26°,4°,0°,40°)	101.1	95.1	75.3	−19.2	−23.5	−39.1
22	(−4°,−40°,0°,26°)	97.4	91.5	81.5	−19.8	−25.8	−52.5
23	(−14°,34°,0°,32°)	97.7	93.4	77.4	−19.5	−24.1	−34.6
24	(−22°,6°,0°,40°)	100.9	95.1	72.5	−19.2	−23.1	−31.3
25	(NaN°,−36°,0°,16°)	100.7	92.6	60.1	−25.1	−28.3	−31.0
26	(NaN°,−30°,0°,18°)	97.0	92.2	76.9	−23.0	−27.8	−44.3
27	(NaN°,12°,0°,18°)	99.6	93.7	79.3	−20.4	−25.5	−38.1
28	(NaN°,−24°,0°,18°)	96.9	91.6	61.3	−22.2	−27.6	−36.5

Table H.5 AP-3C optimum synchrophase angles and BPF levels for the lowest predicted average over the seat & table microphones (H1–H12, T1) of the SPL at the BPF.

Serial	Synchrophase Angles	Max. SPL (dB re 20μPa)	Avg. SPL (dB re 20μPa)	Min. SPL (dB re 20μPa)	Max. Accel. (dB re 1 g_{rms})	Avg. Accel. (dB re 1 g_{rms}))	Min. Accel. (dB re 1 g_{rms}))
1	(12°,−18°,0°,8°)	100.8	92.6	75.8	−26.0	−28.1	−35.4
2	(4°,−18°,0°,10°)	101.3	92.6	62.1	−24.7	−28.7	−37.6
3	(6°,−22°,0°,6°)	100.8	92.4	76.5	−27.2	−29.3	−41.9
4	(−4°,−26°,0°,10°)	102.4	92.0	72.1	−25.2	−29.3	−50.5
5	(−10°,−38°,0°,12°)	98.7	92.8	78.8	−25.5	−28.9	−39.3
6	(−4°,−28°,0°,12°)	103.0	92.9	67.0	−26.4	−29.9	−40.2
7	(−6°,−36°,0°,20°)	98.4	92.3	81.8	−23.2	−28.2	−39.2
8	(−10°,−44°,0°,18°)	97.6	91.2	64.0	−23.1	−26.6	−36.1
9	(−12°,−42°,0°,12°)	99.4	91.0	63.4	−20.9	−27.6	−49.4
10	(8°,−32°,0°,18°)	99.5	92.8	80.0	−20.7	−26.0	−39.9
11	(−4°,42°,0°,22°)	103.5	96.4	74.9	−17.8	−24.5	−46.6
12	(4°,−38°,0°,22°)	99.5	92.2	81.3	−19.9	−24.4	−34.0
13	(−4°,40°,0°,24°)	102.6	96.4	84.0	−19.1	−22.8	−29.9
14	(−6°,34°,0°,24°)	106.6	99.8	81.3	−15.2	−19.5	−27.9
15	(26°,−34°,0°,30°)	110.9	102.6	86.1	−13.2	−19.3	−31.4
16	(18°,−28°,0°,22°)	103.3	94.4	85.9	−17.2	−21.1	−32.5
17	(20°,−34°,0°,26°)	105.4	97.3	83.1	−16.5	−21.5	−35.8
18	(28°,−32°,0°,30°)	107.8	99.8	79.4	−14.3	−19.9	−30.2
19	(20°,−28°,0°,24°)	103.5	94.1	77.2	−19.9	−23.4	−36.7
20	(16°,−36°,0°,28°)	104.9	97.5	81.0	−15.9	−21.4	−29.4
21	(24°,−34°,0°,28°)	107.7	100.2	78.9	−14.6	−17.9	−31.5
22	(22°,−24°,0°,24°)	102.1	94.2	81.8	−18.4	−23.3	−41.2
23	(8°,−36°,0°,32°)	102.9	96.3	82.3	−17.0	−20.7	−38.1
24	(26°,−32°,0°,30°)	106.1	98.4	81.5	−13.1	−17.7	−34.2
25	(NaN°,−28°,0°,8°)	101.3	93.5	77.5	−23.6	−27.1	−36.7
26	(NaN°,−30°,0°,4°)	103.3	94.9	71.4	−22.6	−26.8	−40.2
27	(NaN°,−26°,0°,8°)	101.6	94.9	74.6	−23.3	−26.2	−39.0
28	(NaN°,−28°,0°,10°)	101.5	92.6	79.7	−21.3	−27.4	−48.5

Table H.6 AP-3C optimum synchrophase angles and BPF levels for the lowest predicted average over the grab-rail microphones (G1–G8) of the SPL at the BPF.

Serial	Synchrophase Angles	Max. SPL (dB re 20μPa)	Avg. SPL (dB re 20μPa)	Min. SPL (dB re 20μPa)	Max. Accel. (dB re 1 g_{rms})	Avg. Accel. (dB re 1 g_{rms}))	Min. Accel. (dB re 1 g_{rms}))
1	(−34°,2°,0°,20°)	98.1	92.2	77.9	−22.0	−25.4	−30.3
2	(−14°,−28°,0°,24°)	96.4	90.6	66.3	−23.2	−28.6	−37.8
3	(−34°,16°,0°,14°)	98.8	92.1	78.0	−21.7	−25.8	−33.9
4	(−12°,−22°,0°,26°)	97.2	91.0	77.9	−23.2	−26.1	−33.6
5	(−26°,26°,0°,8°)	99.5	92.4	78.2	−21.9	−27.1	−36.5
6	(−40°,18°,0°,12°)	99.0	91.5	74.6	−20.5	−26.2	−44.3
7	(−26°,22°,0°,8°)	99.2	92.7	82.3	−20.0	−25.1	−38.5
8	(8°,−34°,0°,18°)	97.2	91.3	79.1	−21.3	−26.4	−38.9
9	(−18°,42°,0°,16°)	95.1	90.2	79.9	−23.1	−28.6	−36.8
10	(26°,−20°,0°,22°)	96.6	91.8	74.5	−19.1	−24.4	−36.7
11	(32°,−18°,0°,28°)	102.5	95.0	80.9	−19.3	−24.1	−35.5
12	(−30°,16°,0°,18°)	98.8	92.3	72.4	−18.4	−24.3	−52.8
13	(−40°,8°,0°,20°)	101.3	94.8	78.6	−16.5	−23.6	−34.1
14	(−40°,−4°,0°,26°)	104.7	96.8	75.5	−15.2	−21.1	−28.5
15	(−32°,0°,0°,34°)	106.7	99.9	77.3	−15.1	−22.1	−31.1
16	(−22°,32°,0°,24°)	98.4	93.6	82.6	−18.2	−22.4	−29.7
17	(−26°,22°,0°,28°)	101.7	95.2	86.4	−19.9	−24.1	−31.6
18	(−30°,0°,0°,36°)	102.5	96.7	82.8	−16.6	−23.2	−37.6
19	(−18°,36°,0°,24°)	98.2	92.6	74.9	−20.9	−25.0	−30.0
20	(−22°,6°,0°,38°)	100.6	94.8	79.1	−19.0	−24.2	−36.0
21	(−24°,4°,0°,40°)	101.2	95.2	77.8	−19.2	−23.4	−35.6
22	(−8°,−44°,0°,26°)	97.6	91.6	78.7	−20.6	−26.4	−43.1
23	(−14°,2°,0°,−44°)	101.5	94.9	74.9	−18.0	−23.1	−37.6
24	(−18°,2°,0°,40°)	101.9	95.5	76.6	−18.3	−21.8	−28.4
25	(NaN°,22°,0°,10°)	102.4	93.9	81.2	−19.2	−25.1	−45.1
26	(NaN°,26°,0°,8°)	102.7	94.2	80.9	−20.1	−25.2	−38.0
27	(NaN°,20°,0°,14°)	100.8	93.8	72.1	−20.0	−25.2	−39.2
28	(NaN°,−18°,0°,22°)	97.6	92.0	74.0	−22.9	−27.2	−39.2

Table H.7 AP-3C optimum synchrophase angles and BPF levels for the lowest predicted average over the forward-seat microphones (H1–H5) of the SPL at the BPF.

Serial	Synchrophase Angles	Max. SPL (dB re 20μPa)	Avg. SPL (dB re 20μPa)	Min. SPL (dB re 20μPa)	Max. Accel. (dB re 1 g_{rms})	Avg. Accel. (dB re 1 g_{rms}))	Min. Accel. (dB re 1 g_{rms}))
1	(6°,−26°,0°,8°)	101.1	93.1	72.4	−24.8	−29.5	−49.8
2	(8°,−22°,0°,12°)	99.1	91.9	57.4	−24.3	−29.6	−41.6
3	(10°,−24°,0°,10°)	99.2	91.4	73.2	−25.9	−29.5	−49.6
4	(20°,−20°,0°,14°)	97.7	91.8	74.9	−25.2	−29.6	−49.7
5	(22°,−24°,0°,16°)	101.9	93.7	57.4	−25.5	−27.9	−47.6
6	(26°,−18°,0°,16°)	99.3	92.5	65.6	−24.2	−28.4	−37.3
7	(20°,−24°,0°,18°)	99.1	92.3	78.8	−23.0	−26.7	−39.7
8	(18°,−30°,0°,16°)	98.6	92.8	70.7	−21.1	−26.4	−53.6
9	(14°,−32°,0°,22°)	101.0	94.4	69.4	−17.7	−25.2	−41.4
10	(10°,−36°,0°,16°)	99.7	92.5	77.1	−21.1	−26.4	−35.5
11	(8°,−40°,0°,24°)	103.4	95.5	80.4	−17.2	−24.2	−40.7
12	(16°,−34°,0°,24°)	100.4	92.0	76.2	−18.7	−23.9	−34.7
13	(−10°,28°,0°,42°)	104.3	98.0	78.1	−22.8	−25.4	−30.6
14	(−18°,18°,0°,44°)	107.7	99.9	75.8	−15.8	−20.4	−27.2
15	(0°,32°,0°,44°)	108.9	103.3	80.4	−14.6	−20.6	−32.5
16	(24°,−28°,0°,28°)	103.2	94.3	78.9	−17.3	−20.7	−30.3
17	(4°,40°,0°,40°)	105.5	97.4	76.0	−18.4	−22.1	−30.6
18	(−6°,30°,0°,38°)	106.0	99.7	80.2	−16.9	−21.2	−30.5
19	(24°,−30°,0°,32°)	102.8	94.4	77.8	−19.7	−22.4	−33.3
20	(−44°,−10°,0°,40°)	103.1	96.3	65.8	−17.9	−22.2	−36.6
21	(−32°,−2°,0°,38°)	101.8	95.5	78.7	−18.5	−22.1	−37.0
22	(40°,−18°,0°,32°)	102.3	94.1	78.9	−17.1	−21.8	−32.6
23	(4°,44°,0°,44°)	104.2	96.3	77.7	−17.9	−22.7	−35.2
24	(−8°,24°,0°,44°)	104.6	96.3	79.2	−19.0	−22.5	−29.5
25	(NaN°,−28°,0°,12°)	101.0	93.0	79.8	−23.8	−27.8	−43.2
26	(NaN°,−30°,0°,10°)	100.2	93.2	81.3	−23.0	−27.7	−44.4
27	(NaN°,−30°,0°,10°)	101.2	94.6	74.7	−22.6	−26.6	−47.3
28	(NaN°,−30°,0°,12°)	100.0	92.0	75.1	−21.7	−27.7	−47.2

Table H.8 AP-3C optimum synchrophase angles and BPF levels for the lowest predicted average over the mid-seat microphones (H6–H10) of the SPL at the BPF.

Serial	Synchrophase Angles	Max. SPL (dB re 20μPa)	Avg. SPL (dB re 20μPa)	Min. SPL (dB re 20μPa)	Max. Accel. (dB re 1 g_{rms})	Avg. Accel. (dB re 1 g_{rms}))	Min. Accel. (dB re 1 g_{rms}))
1	(34°,0°,0°,8°)	97.9	91.9	75.6	−22.0	−25.4	−30.2
2	(20°,−8°,0°,4°)	100.7	92.7	70.9	−22.1	−25.8	−32.2
3	(22°,0°,0°,10°)	97.3	91.6	70.2	−21.7	−26.7	−31.9
4	(−4°,−24°,0°,8°)	103.2	92.8	66.7	−24.2	−28.7	−43.2
5	(−18°,42°,0°,8°)	98.2	92.5	81.9	−25.9	−29.8	−54.4
6	(14°,−18°,0°,6°)	102.2	93.5	79.2	−22.2	−26.6	−32.8
7	(8°,−26°,0°,16°)	97.7	92.6	78.7	−23.5	−26.5	−35.6
8	(−6°,−40°,0°,18°)	97.7	91.2	68.2	−22.5	−26.5	−36.6
9	(2°,−20°,0°,10°)	104.0	94.9	74.7	−19.0	−23.9	−37.8
10	(20°,−16°,0°,18°)	100.9	93.7	77.6	−18.7	−23.6	−36.1
11	(8°,−36°,0°,22°)	102.7	96.1	81.5	−17.4	−24.2	−42.2
12	(20°,−18°,0°,24°)	99.7	94.0	81.0	−18.9	−23.4	−41.7
13	(32°,−16°,0°,26°)	101.0	95.5	80.9	−18.4	−23.3	−44.5
14	(30°,−18°,0°,26°)	105.0	99.0	84.2	−15.5	−20.3	−33.5
15	(30°,−24°,0°,30°)	110.0	102.3	75.4	−14.4	−19.3	−33.6
16	(26°,−10°,0°,24°)	102.9	95.7	70.8	−18.0	−22.2	−41.0
17	(26°,−16°,0°,28°)	105.1	98.4	79.2	−18.6	−21.8	−55.3
18	(40°,−10°,0°,34°)	106.2	98.8	76.0	−15.9	−21.2	−34.9
19	(26°,−10°,0°,26°)	102.7	95.4	79.4	−18.1	−23.2	−47.5
20	(−24°,38°,0°,28°)	103.6	96.2	77.4	−18.4	−24.6	−46.0
21	(44°,4°,0°,36°)	106.8	99.4	75.6	−16.7	−21.9	−32.4
22	(4°,−28°,0°,22°)	99.9	94.0	82.7	−18.3	−23.2	−33.3
23	(18°,−16°,0°,34°)	105.0	98.0	63.9	−16.3	−20.1	−34.3
24	(18°,−28°,0°,30°)	106.0	99.0	80.0	−13.1	−17.7	−40.5
25	(NaN°,−2°,0°,8°)	100.7	94.2	54.8	−20.1	−24.6	−31.8
26	(NaN°,−10°,0°,4°)	103.2	95.5	77.1	−20.8	−24.0	−30.1
27	(NaN°,8°,0°,14°)	100.0	93.8	77.6	−20.0	−25.2	−38.6
28	(NaN°,−24°,0°,4°)	104.2	94.7	77.7	−20.3	−25.7	−36.7

Table H.9 AP-3C optimum synchrophase angles and BPF levels for the lowest predicted average over the rear seat & table mics (H11–H12, T1) of the SPL at the BPF.

Serial	Synchrophase Angles	Max. SPL (dB re 20μPa)	Avg. SPL (dB re 20μPa)	Min. SPL (dB re 20μPa)	Max. Accel. (dB re 1 g_{rms})	Avg. Accel. (dB re 1 g_{rms}))	Min. Accel. (dB re 1 g_{rms}))
1	(−26°,−40°,0°,−4°)	104.9	96.8	71.8	−28.2	−31.7	−36.1
2	(−34°,−38°,0°,0°)	105.2	96.0	74.7	−26.9	−29.5	−38.0
3	(−16°,−34°,0°,0°)	104.1	95.3	80.3	−28.5	−31.6	−41.2
4	(−12°,−30°,0°,0°)	105.3	95.1	71.6	−24.2	−29.5	−43.7
5	(−42°,30°,0°,−36°)	108.4	99.8	78.8	−23.1	−27.3	−36.4
6	(−30°,44°,0°,2°)	104.8	95.4	79.4	−31.1	−34.4	−40.7
7	(34°,22°,0°,−12°)	107.5	98.4	66.0	−20.5	−24.4	−32.4
8	(−22°,−42°,0°,4°)	107.6	99.0	78.5	−24.5	−28.5	−35.5
9	(26°,14°,0°,28°)	105.7	97.4	75.7	−19.1	−25.7	−34.5
10	(−6°,−22°,0°,0°)	109.4	101.4	57.9	−15.9	−22.9	−47.0
11	(−20°,−34°,0°,24°)	109.1	102.1	82.3	−20.4	−25.8	−40.0
12	(30°,14°,0°,42°)	107.0	98.8	73.1	−20.4	−25.4	−32.9
13	(0°,0°,0°,−10°)	110.3	101.9	75.0	−14.7	−21.1	−41.2
14	(10°,4°,0°,−40°)	110.1	103.5	79.8	−14.9	−18.3	−33.5
15	(4°,−4°,0°,2°)	113.9	107.2	86.7	−12.0	−17.2	−25.4
16	(10°,0°,0°,−14°)	108.5	101.5	77.2	−15.3	−20.6	−33.0
17	(20°,6°,0°,28°)	107.7	100.8	65.5	−15.0	−21.3	−30.3
18	(2°,−2°,0°,10°)	112.8	105.6	78.5	−12.0	−18.2	−31.3
19	(12°,−22°,0°,−16°)	107.7	101.3	78.2	−17.3	−21.8	−38.9
20	(18°,2°,0°,0°)	109.5	102.8	58.2	−14.4	−20.9	−34.3
21	(4°,−2°,0°,2°)	112.7	104.7	76.3	−13.5	−17.9	−36.9
22	(32°,−6°,0°,−6°)	107.5	100.8	72.6	−15.7	−19.3	−31.0
23	(16°,−4°,0°,−10°)	109.3	101.6	59.9	−15.3	−20.9	−32.2
24	(32°,10°,0°,−32°)	108.3	100.0	73.6	−14.8	−19.3	−28.9
25	(NaN°,−32°,0°,−6°)	104.3	96.1	73.3	−21.9	−25.0	−35.4
26	(NaN°,−30°,0°,−4°)	105.8	96.9	80.4	−21.8	−25.4	−36.3
27	(NaN°,−34°,0°,2°)	103.2	96.2	81.5	−22.1	−25.6	−49.2
28	(NaN°,−26°,0°,14°)	99.5	91.8	72.5	−21.8	−27.6	−39.5

Table H.10 AP-3C optimum synchrophase angles and BPF levels for the lowest predicted average over the seat-rail accelerometers (S1–S7) of the acceleration at the BPF.

Serial	Synchrophase Angles	Max. SPL (dB re 20μPa)	Avg. SPL (dB re 20μPa)	Min. SPL (dB re 20μPa)	Max. Accel. (dB re 1 g_{rms})	Avg. Accel. (dB re 1 g_{rms}))	Min. Accel. (dB re 1 g_{rms}))
1	(−16°,−40°,0°,−4°)	104.2	96.5	75.6	−27.4	−32.7	−39.7
2	(−14°,−40°,0°,0°)	104.5	95.5	75.0	−28.1	−33.8	−50.0
3	(−18°,−40°,0°,4°)	102.4	94.2	78.2	−27.7	−33.2	−43.5
4	(−26°,42°,0°,−12°)	106.8	97.2	80.8	−29.4	−34.4	−41.9
5	(−42°,44°,0°,6°)	103.5	96.4	84.0	−30.9	−33.7	−39.7
6	(−30°,−42°,0°,6°)	103.7	94.8	82.4	−34.1	−36.0	−41.7
7	(−34°,−42°,0°,6°)	107.1	98.7	78.2	−28.9	−33.1	−42.7
8	(−42°,34°,0°,−32°)	112.0	103.4	82.1	−27.2	−32.0	−36.7
9	(−30°,42°,0°,16°)	99.3	92.8	77.9	−25.4	−29.5	−34.8
10	(−42°,36°,0°,−26°)	111.8	103.2	75.1	−28.6	−32.1	−36.3
11	(−40°,28°,0°,−26°)	113.5	104.9	90.1	−24.2	−29.2	−40.6
12	(−32°,34°,0°,−34°)	108.2	100.1	84.9	−26.4	−29.8	−34.6
13	(−32°,24°,0°,−34°)	109.3	101.3	84.6	−26.5	−29.2	−40.0
14	(−40°,30°,0°,−14°)	113.7	104.8	72.6	−25.7	−28.3	−32.9
15	(−24°,12°,0°,−44°)	108.0	101.7	87.6	−18.4	−23.6	−37.7
16	(−30°,28°,0°,−40°)	107.6	99.6	87.9	−24.3	−27.2	−37.4
17	(−28°,32°,0°,40°)	104.5	98.2	84.1	−23.4	−26.4	−39.3
18	(−24°,16°,0°,42°)	105.9	98.6	69.7	−19.6	−24.3	−36.7
19	(−28°,32°,0°,36°)	101.8	95.7	80.1	−22.6	−26.0	−31.1
20	(−26°,24°,0°,38°)	102.2	95.9	76.2	−21.7	−26.4	−33.7
21	(−24°,18°,0°,40°)	103.0	96.9	80.3	−21.3	−26.6	−50.1
22	(−12°,36°,0°,28°)	100.0	92.6	82.3	−24.1	−27.4	−34.5
23	(−22°,22°,0°,34°)	101.5	94.0	76.9	−21.6	−25.4	−30.7
24	(−20°,28°,0°,−38°)	105.3	98.2	84.6	−23.4	−28.1	−55.2
25	(NaN°,−26°,0°,22°)	100.4	93.1	80.1	−24.1	−28.7	−36.0
26	(NaN°,−38°,0°,12°)	98.4	92.6	82.1	−23.1	−28.3	−58.0
27	(NaN°,−24°,0°,22°)	100.2	94.1	76.6	−23.8	−27.4	−36.3
28	(NaN°,−34°,0°,12°)	99.1	92.0	77.8	−22.0	−27.8	−40.6

Appendix I. C-130J-30 Predicted Sound and Vibration Levels for Trial 1

The tables below show the maxima, minima and average levels at the BPF from the sensors available in each flight. Note that the low-sound-pressure predictions for Flights 1 and 2, and the low-floor-vibration predictions for Flight 3 are not reliable due to the small number of microphones/accelerometers (6) in these respective cases.

Table I.1 C-130J-30 predicted BPF levels for the default synch. angles, Flt 1, Trial 1.

Serial	Synchrophase Angles	Max SPL (dB re 20μPa)	Avg SPL (dB re 20μPa)	Min SPL (dB re 20μPa)	Max Floor Vib (dB re 1grms)	Avg Floor Vib (dB re 1grms)	Min Floor Vib (dB re 1grms)
1.0	Default Angles	110.2	104.7	95.5	−11.4	−18.9	−40.6
2.0	Default Angles	111.5	107.0	95.9	−10.3	−17.3	−41.9
3.0	Default Angles	115.4	110.7	100.7	−7.6	−14.4	−33.1
4.1	Default Angles	112.0	107.3	94.6	−9.9	−16.1	−38.1
4.2	Default Angles	115.1	110.7	96.8	−8.0	−14.3	−41.0
4.3	Default Angles	116.6	111.9	99.2	−7.7	−13.6	−33.6
5.1	Default Angles	112.6	108.2	82.3	−8.1	−15.3	−35.5
5.2	Default Angles	115.0	110.8	91.8	−7.1	−14.1	−49.9
5.3	Default Angles	116.4	112.1	97.7	−7.5	−13.7	−31.8
6.1	Default Angles	112.9	109.1	89.8	−7.7	−15.3	−40.8
6.2	Default Angles	114.8	111.0	94.1	−7.7	−14.6	−38.7
6.3	Default Angles	115.4	111.6	93.9	−7.6	−14.4	−32.6
7.3	Default Angles	115.7	111.5	89.5	−9.1	−15.1	−31.0

Table I.2 C-130J-30 predicted BPF levels for the default synch. angles, Flt 2, Trial 1.

Serial	Synchrophase Angles	Max SPL (dB re 20μPa)	Avg SPL (dB re 20μPa)	Min SPL (dB re 20μPa)	Max Floor Vib (dB re 1grms)	Avg Floor Vib (dB re 1grms)	Min Floor Vib (dB re 1grms)
1.0	Default Angles	108.1	106.3	99.4	−10.1	−18.2	−40.2
2.0	Default Angles	110.0	107.7	99.4	−9.7	−17.1	−44.4
3.0	Default Angles	112.9	110.2	101.8	−9.1	−15.5	−46.7
4.1	Default Angles	110.3	107.8	98.4	−8.1	−16.3	−40.7
4.2	Default Angles	111.8	109.4	100.5	−8.0	−15.4	−48.2
4.3	Default Angles	112.1	109.5	101.9	−8.0	−14.7	−35.1
5.1	Default Angles	109.5	107.1	93.5	−8.7	−16.9	−42.1
5.2	Default Angles	110.9	108.4	95.8	−7.9	−15.7	−52.9
5.3	Default Angles	111.2	108.5	99.4	−9.9	−15.4	−32.2
5.4	Default Angles	113.3	109.8	100.7	−7.2	−14.1	−28.6
6.1	Default Angles	110.0	107.4	93.0	−8.2	−16.4	−63.3
6.2	Default Angles	110.5	107.6	94.9	−9.0	−16.1	−37.1
6.3	Default Angles	110.4	107.9	97.4	−10.5	−16.0	−36.9
6.4	Default Angles	111.8	109.0	96.3	−8.5	−15.1	−33.1
7.3	Default Angles	109.7	107.4	92.8	−10.9	−16.3	−47.6

Table I.3 C-130J-30 predicted BPF levels for the default synch. angles, Flt 3, Trial 1.

Serial	Synchrophase Angles	Max SPL (dB re 20μPa)	Avg SPL (dB re 20μPa)	Min SPL (dB re 20μPa)	Max Floor Vib (dB re 1grms)	Avg Floor Vib (dB re 1grms)	Min Floor Vib (dB re 1grms)
1.0	Default Angles	114.0	104.7	83.4	−10.9	−14.4	−25.1
2.0	Default Angles	115.2	104.8	85.5	−13.7	−16.1	−29.7
3.0	Default Angles	117.5	108.5	90.7	−6.5	−10.5	−20.1
4.1	Default Angles	115.0	106.1	85.9	−7.4	−12.1	−23.2
4.2	Default Angles	116.2	107.2	88.7	−6.3	−10.5	−21.6
4.3	Default Angles	116.8	107.5	93.3	−8.0	−12.0	−20.3
5.1	Default Angles	115.1	106.0	76.1	−7.3	−11.6	−24.5
5.2	Default Angles	116.2	107.0	85.4	−5.8	−10.0	−20.4
5.3	Default Angles	116.2	107.9	90.1	−5.1	−9.3	−19.9
5.4	Default Angles	116.9	108.1	85.5	−3.4	−8.2	−16.3
6.1	Default Angles	115.5	106.2	83.5	−6.3	−9.8	−30.4
6.2	Default Angles	115.8	106.5	85.1	−5.7	−9.5	−34.1
6.3	Default Angles	116.0	107.0	88.2	−4.7	−9.0	−27.8
7.1	Default Angles	115.4	105.5	81.8	−7.2	−10.2	−32.9
7.2	Default Angles	115.7	105.8	86.3	−7.1	−10.2	−33.0
7.3	Default Angles	116.7	106.9	77.9	−5.9	−9.5	−29.9
10.0	Default Angles	116.1	107.5	91.4	−5.1	−9.6	−18.7

Table I.4 C-130J-30 synchrophase angles and BPF levels for the highest predicted average over all microphones of the SPL at the BPF, Flight 1, Trial 1.

Serial	Synchrophase Angles	Max SPL (dB re 20μPa)	Avg SPL (dB re 20μPa)	Min SPL (dB re 20μPa)	Max Floor Vib (dB re 1grms)	Avg Floor Vib (dB re 1grms)	Min Floor Vib (dB re 1grms)
1.0	(41°,0°,38°,59°)	111.9	107.7	94.9	−12.8	−19.0	−34.6
2.0	(36°,0°,35°,53°)	113.0	109.3	95.2	−10.6	−17.5	−39.5
3.0	(26°,0°,33°,44°)	117.2	113.1	95.5	−6.8	−14.7	−43.8
4.1	(28°,0°,39°,49°)	115.4	111.0	92.3	−7.9	−16.6	−40.8
4.2	(23°,0°,37°,43°)	117.7	113.5	88.1	−7.5	−14.8	−46.5
4.3	(19°,0°,35°,41°)	119.3	114.7	92.9	−6.9	−14.3	−49.1
5.1	(23°,0°,39°,47°)	116.1	112.1	88.6	−9.1	−15.8	−33.9
5.2	(20°,0°,37°,43°)	118.0	113.8	89.5	−7.7	−14.4	−36.5
5.3	(19°,0°,35°,40°)	119.0	114.7	95.2	−5.9	−13.4	−35.7
6.1	(22°,0°,40°,45°)	117.4	113.2	87.8	−8.1	−14.8	−36.4
6.2	(17°,0°,39°,42°)	118.7	114.3	94.0	−6.1	−13.4	−38.4
6.3	(12°,0°,39°,42°)	118.9	114.5	89.1	−5.9	−13.6	−40.0
7.3	(18°,0°,38°,37°)	119.6	114.9	94.1	−4.2	−11.9	−38.9

Table I.5 C-130J-30 synchrophase angles and BPF levels for the highest predicted average over all microphones of the SPL at the BPF, Flight 2, Trial 1.

Serial	Synchrophase Angles	Max SPL (dB re 20μPa)	Avg SPL (dB re 20μPa)	Min SPL (dB re 20μPa)	Max Floor Vib (dB re 1grms)	Avg Floor Vib (dB re 1grms)	Min Floor Vib (dB re 1grms)
1.0	(41°,0°,26°,45°)	108.4	106.5	99.9	−10.5	−18.1	−34.9
2.0	(39°,0°,27°,45°)	110.6	107.9	99.1	−10.7	−17.3	−44.4
3.0	(31°,0°,29°,40°)	114.1	110.9	97.3	−9.3	−15.8	−47.0
4.1	(29°,0°,36°,46°)	111.7	109.3	94.4	−10.6	−17.3	−48.4
4.2	(30°,0°,33°,42°)	113.5	110.6	98.5	−9.3	−15.7	−40.8
4.3	(23°,0°,31°,38°)	114.6	111.2	98.6	−7.2	−14.5	−38.2
5.1	(28°,0°,37°,46°)	111.8	109.2	92.0	−10.5	−17.1	−42.8
5.2	(22°,0°,39°,47°)	115.0	111.1	91.5	−8.0	−15.6	−38.2
5.3	(19°,0°,35°,39°)	115.1	111.1	98.1	−7.3	−14.7	−43.4
5.4	(17°,0°,32°,31°)	116.7	112.4	101.9	−3.8	−12.0	−33.0
6.1	(21°,0°,40°,46°)	113.3	110.2	95.7	−8.7	−16.0	−41.5
6.2	(19°,0°,40°,45°)	114.1	111.1	93.6	−8.6	−15.7	−36.7
6.3	(19°,0°,37°,38°)	113.7	110.5	97.9	−6.9	−14.4	−39.0
6.4	(16°,0°,35°,33°)	116.3	112.5	100.1	−4.2	−12.4	−36.3
7.3	(17°,0°,40°,40°)	114.8	111.7	97.1	−6.2	−13.9	−38.5

Table I.6 C-130J-30 synchrophase angles and BPF levels for the highest predicted average over all microphones of the SPL at the BPF, Flight 3, Trial 1.

Serial	Synchrophase Angles	Max SPL (dB re 20μPa)	Avg SPL (dB re 20μPa)	Min SPL (dB re 20μPa)	Max Floor Vib (dB re 1grms)	Avg Floor Vib (dB re 1grms)	Min Floor Vib (dB re 1grms)
1.0	(45°,0°,28°,54°)	115.3	105.5	90.5	−11.3	−14.4	−23.5
2.0	(9°,0°,29°,54°)	115.1	106.4	72.4	−8.6	−12.2	−22.3
3.0	(34°,0°,26°,40°)	117.6	108.7	88.2	−6.0	−10.3	−18.4
4.1	(45°,0°,25°,38°)	114.9	106.1	82.8	−7.2	−12.0	−23.4
4.2	(33°,0°,29°,39°)	116.5	107.6	83.6	−6.4	−10.5	−19.5
4.3	(18°,0°,34°,41°)	117.7	109.5	82.5	−3.7	−8.7	−14.3
5.1	(37°,0°,27°,39°)	115.5	106.2	79.5	−7.3	−11.6	−25.9
5.2	(21°,0°,34°,41°)	115.9	107.6	77.0	−6.0	−10.3	−19.0
5.3	(23°,0°,31°,37°)	116.9	108.9	84.7	−4.0	−8.9	−22.9
5.4	(19°,0°,25°,29°)	118.8	110.1	90.5	−1.4	−7.0	−16.5
6.1	(23°,0°,36°,42°)	116.4	107.5	84.1	−5.9	−9.5	−25.2
6.2	(20°,0°,33°,37°)	116.6	108.3	84.6	−4.4	−8.8	−33.4
6.3	(19°,0°,32°,35°)	116.9	108.7	84.8	−3.4	−8.1	−28.1
7.1	(19°,0°,36°,39°)	116.4	107.5	81.9	−5.9	−9.2	−30.7
7.2	(17°,0°,36°,38°)	117.0	108.3	86.3	−4.5	−8.4	−30.4
7.3	(11°,0°,30°,28°)	118.8	110.2	80.0	−1.7	−6.6	−24.7
10.0	(20°,0°,28°,34°)	117.3	109.0	84.4	−3.1	−8.6	−22.0

Table I.7 C-130J-30 optimum synchrophase angles and BPF levels for the lowest predicted average over all microphones of the SPL at the BPF, Flight 1, Trial 1.

Serial	Synchrophase Angles	Max SPL (dB re 20μPa)	Avg SPL (dB re 20μPa)	Min SPL (dB re 20μPa)	Max Floor Vib (dB re $1g_{rms}$)	Avg Floor Vib (dB re $1g_{rms}$)	Min Floor Vib (dB re $1g_{rms}$)
1.0	(13°,0°,3°,52°)	97.1	94.6	89.9	−15.8	−23.8	−53.2
2.0	(6°,0°,1°,43°)	96.2	93.3	89.3	−15.0	−22.3	−37.8
3.0	(58°,0°,59°,35°)	99.3	95.4	83.7	−14.0	−20.8	−39.8
4.1	(2°,0°,4°,41°)	97.0	91.5	85.0	−15.7	−22.6	−40.4
4.2	(54°,0°,3°,35°)	100.8	95.5	72.2	−14.0	−20.4	−35.3
4.3	(52°,0°,1°,32°)	102.5	97.3	87.0	−13.1	−20.9	−46.5
5.1	(55°,0°,5°,39°)	99.6	93.9	81.6	−15.1	−22.0	−37.4
5.2	(55°,0°,8°,48°)	101.0	96.2	81.9	−15.1	−21.1	−40.1
5.3	(55°,0°,7°,47°)	103.0	98.9	84.4	−13.1	−20.2	−35.6
6.1	(53°,0°,12°,49°)	101.0	97.6	74.5	−14.6	−21.3	−40.7
6.2	(54°,0°,11°,50°)	100.4	97.3	78.1	−11.4	−19.1	−34.7
6.3	(52°,0°,11°,52°)	102.3	99.1	88.3	−10.9	−18.6	−39.2
7.3	(48°,0°,5°,29°)	105.7	100.4	89.2	−11.4	−19.0	−42.2

Table I.8 C-130J-30 optimum synchrophase angles and BPF levels for the lowest predicted average over all microphones of the SPL at the BPF, Flight 2, Trial 1.

Serial	Synchrophase Angles	Max SPL (dB re 20μPa)	Avg SPL (dB re 20μPa)	Min SPL (dB re 20μPa)	Max Floor Vib (dB re 1grms)	Avg Floor Vib (dB re 1grms)	Min Floor Vib (dB re 1grms)
1.0	(16°,0°,58°,55°)	94.6	92.0	84.4	−16.9	−24.7	−51.5
2.0	(11°,0°,55°,41°)	96.0	93.3	90.6	−14.9	−23.1	−39.9
3.0	(5°,0°,58°,39°)	98.8	95.8	85.5	−17.7	−22.1	−36.1
4.1	(3°,0°,2°,38°)	98.8	96.2	82.8	−15.7	−22.0	−45.3
4.2	(59°,0°,60°,35°)	100.1	95.5	84.0	−14.8	−19.9	−42.8
4.3	(58°,0°,59°,35°)	99.6	95.9	88.6	−16.0	−22.5	−42.7
5.1	(60°,0°,5°,42°)	100.6	96.6	78.4	−16.1	−22.7	−35.7
5.2	(57°,0°,3°,37°)	99.8	95.1	86.5	−16.1	−21.5	−33.1
5.3	(56°,0°,5°,43°)	99.3	97.1	79.3	−14.3	−21.3	−46.2
5.4	(54°,0°,2°,36°)	102.5	98.8	79.9	−11.5	−18.4	−44.2
6.1	(55°,0°,8°,43°)	98.4	95.7	88.2	−15.5	−21.9	−35.2
6.2	(53°,0°,10°,48°)	99.7	97.0	88.5	−12.3	−20.0	−34.6
6.3	(51°,0°,8°,42°)	101.6	97.5	86.1	−13.6	−20.7	−44.0
6.4	(50°,0°,6°,39°)	103.1	99.7	87.4	−8.8	−16.8	−31.3
7.3	(49°,0°,11°,45°)	101.9	98.2	88.0	−11.9	−19.2	−33.3

Table I.9 C-130J-30 optimum synchrophase angles and BPF levels for the lowest predicted average over all microphones of the SPL at the BPF, Flight 3, Trial 1.

Serial	Synchrophase Angles	Max SPL (dB re 20μPa)	Avg SPL (dB re 20μPa)	Min SPL (dB re 20μPa)	Max Floor Vib (dB re $1g_{rms}$)	Avg Floor Vib (dB re $1g_{rms}$)	Min Floor Vib (dB re $1g_{rms}$)
1.0	(13°,0°,50°,40°)	107.9	100.5	80.8	−17.4	−21.6	−35.0
2.0	(22°,0°,55°,38°)	108.3	101.8	81.5	−12.5	−17.6	−27.7
3.0	(4°,0°,51°,32°)	107.7	101.6	79.4	−11.9	−17.9	−30.8
4.1	(6°,0°,53°,30°)	106.2	99.6	77.4	−14.5	−20.4	−35.3
4.2	(2°,0°,51°,27°)	105.6	100.2	84.1	−11.2	−17.7	−34.5
4.3	(57°,0°,57°,34°)	107.5	102.1	83.4	−10.1	−15.9	−40.2
5.1	(4°,0°,52°,27°)	105.3	98.7	79.4	−13.7	−19.2	−26.2
5.2	(57°,0°,51°,23°)	105.2	100.0	86.5	−10.0	−16.7	−27.3
5.3	(56°,0°,53°,25°)	107.0	100.5	84.4	−10.1	−16.3	−28.6
5.4	(50°,0°,47°,17°)	109.7	103.0	84.2	−9.3	−15.0	−28.4
6.1	(57°,0°,51°,22°)	105.0	99.6	75.4	−11.5	−17.3	−23.1
6.2	(54°,0°,51°,21°)	105.8	100.3	79.1	−9.2	−15.5	−26.4
6.3	(53°,0°,52°,21°)	106.9	101.1	76.4	−9.6	−16.3	−22.9
7.1	(52°,0°,54°,23°)	105.6	99.9	76.1	−9.8	−16.3	−26.1
7.2	(50°,0°,50°,19°)	106.2	100.3	83.4	−10.2	−16.8	−27.0
7.3	(43°,0°,48°,11°)	109.7	103.0	67.3	−7.2	−13.7	−29.2
10.0	(54°,0°,47°,19°)	106.4	100.3	86.9	−10.4	−16.6	−29.1

Table I.10 C-130J-30 optimum synchrophase angles and BPF levels for the lowest predicted average over the main cabin mics of the SPL at the BPF, Flight 1, Trial 1.

Serial	Synchrophase Angles	Max SPL (dB re 20μPa)	Avg SPL (dB re 20μPa)	Min SPL (dB re 20μPa)	Max Floor Vib (dB re 1grms)	Avg Floor Vib (dB re 1grms)	Min Floor Vib (dB re 1grms)
1.0	(13°,0°,4°,52°)	97.8	94.7	92.1	−15.5	−23.5	−50.8
2.0	(8°,0°,1°,44°)	95.6	93.4	90.1	−15.1	−22.5	−37.3
3.0	(58°,0°,59°,35°)	99.3	95.4	83.7	−14.0	−20.8	−39.8
4.1	(2°,0°,5°,42°)	97.3	91.6	80.3	−15.4	−22.5	−41.0
4.2	(54°,0°,3°,35°)	100.8	95.5	72.2	−14.0	−20.4	−35.3
4.3	(53°,0°,1°,32°)	102.2	97.3	87.1	−13.4	−21.1	−44.5
5.1	(56°,0°,5°,40°)	98.8	93.9	81.1	−15.5	−22.2	−37.2
5.2	(56°,0°,9°,51°)	99.6	96.3	84.3	−14.2	−20.8	−40.5
5.3	(57°,0°,7°,48°)	103.0	99.0	86.8	−12.7	−19.9	−34.2
6.1	(55°,0°,12°,50°)	100.6	97.7	78.8	−14.3	−21.1	−42.4
6.2	(56°,0°,11°,51°)	100.5	97.5	81.4	−11.0	−18.8	−34.8
6.3	(53°,0°,11°,52°)	102.6	99.1	88.8	−10.9	−18.6	−38.7
7.3	(49°,0°,10°,44°)	104.3	100.4	81.6	−8.8	−16.9	−35.0

Table I.11 C-130J-30 optimum synchrophase angles and BPF levels for the lowest predicted average over the main cabin mics of the SPL at the BPF, Flight 2, Trial 1.

Serial	Synchrophase Angles	Max SPL (dB re 20μPa)	Avg SPL (dB re 20μPa)	Min SPL (dB re 20μPa)	Max Floor Vib (dB re 1grms)	Avg Floor Vib (dB re 1grms)	Min Floor Vib (dB re 1grms)
1.0	(16°,0°,58°,54°)	93.8	92.1	87.2	−16.6	−24.7	−46.2
2.0	(12°,0°,56°,44°)	96.5	93.3	90.5	−15.3	−23.4	−36.6
3.0	(8°,0°,59°,41°)	99.1	96.2	87.8	−18.4	−22.4	−36.9
4.1	(7°,0°,2°,38°)	98.4	96.5	84.6	−16.7	−22.4	−41.7
4.2	(4°,0°,60°,35°)	99.8	96.2	77.2	−15.0	−19.9	−42.8
4.3	(1°,0°,59°,35°)	100.5	96.3	91.9	−16.5	−22.8	−37.2
5.1	(6°,0°,5°,43°)	100.1	97.1	81.1	−17.3	−22.8	−33.8
5.2	(59°,0°,3°,37°)	99.3	95.2	88.5	−16.6	−21.7	−33.8
5.3	(58°,0°,5°,43°)	99.9	97.3	84.4	−14.4	−21.4	−44.5
5.4	(59°,0°,2°,36°)	104.5	99.5	89.7	−11.3	−18.4	−37.6
6.1	(59°,0°,8°,43°)	100.0	96.2	91.6	−15.7	−22.0	−34.0
6.2	(56°,0°,10°,49°)	100.9	97.3	91.1	−11.9	−19.8	−34.3
6.3	(55°,0°,8°,43°)	103.1	97.9	89.4	−13.1	−20.5	−42.2
6.4	(55°,0°,5°,38°)	104.6	100.2	83.2	−8.6	−16.7	−31.2
7.3	(52°,0°,11°,46°)	102.8	98.5	90.3	−11.4	−18.9	−32.1

Table I.12 C-130J-30 optimum synchrophase angles and BPF levels for the lowest predicted average over the main cabin mics of the SPL at the BPF, Flight 3, Trial 1.

Serial	Synchrophase Angles	Max SPL (dB re 20μPa)	Avg SPL (dB re 20μPa)	Min SPL (dB re 20μPa)	Max Floor Vib (dB re 1grms)	Avg Floor Vib (dB re 1grms)	Min Floor Vib (dB re 1grms)
1.0	(13°,0°,50°,40°)	107.9	100.5	80.8	−17.4	−21.6	−35.0
2.0	(47°,0°,42°,30°)	110.0	102.0	79.9	−12.8	−18.7	−25.2
3.0	(4°,0°,51°,32°)	107.7	101.6	79.4	−11.9	−17.9	−30.8
4.1	(6°,0°,53°,29°)	106.0	99.6	78.9	−14.3	−20.3	−36.1
4.2	(2°,0°,51°,27°)	105.6	100.2	84.1	−11.2	−17.7	−34.5
4.3	(57°,0°,57°,35°)	107.6	102.1	81.6	−10.0	−15.9	−44.7
5.1	(4°,0°,52°,27°)	105.3	98.7	79.4	−13.7	−19.2	−26.2
5.2	(57°,0°,51°,22°)	105.8	100.0	87.2	−9.9	−16.6	−26.8
5.3	(56°,0°,53°,25°)	107.0	100.5	84.4	−10.1	−16.3	−28.6
5.4	(50°,0°,47°,17°)	109.7	103.0	84.2	−9.3	−15.0	−28.4
6.1	(57°,0°,51°,22°)	105.0	99.6	75.4	−11.5	−17.3	−23.1
6.2	(54°,0°,51°,21°)	105.8	100.3	79.1	−9.2	−15.5	−26.4
6.3	(53°,0°,52°,21°)	106.9	101.1	76.4	−9.6	−16.3	−22.9
7.1	(52°,0°,53°,22°)	105.6	99.9	76.4	−9.7	−16.2	−28.3
7.2	(50°,0°,50°,19°)	106.2	100.3	83.4	−10.2	−16.8	−27.0
7.3	(43°,0°,48°,11°)	109.7	103.0	67.3	−7.2	−13.7	−29.2
10.0	(54°,0°,47°,19°)	106.4	100.3	86.9	−10.4	−16.6	−29.1

Table I.13 C-130J-30 optimum synchrophase angles and BPF levels for the lowest predicted average over the flight deck mics of the SPL at the BPF, Flight 1, Trial 1.

Serial	Synchrophase Angles	Max SPL (dB re 20μPa)	Avg SPL (dB re 20μPa)	Min SPL (dB re 20μPa)	Max Floor Vib (dB re 1grms)	Avg Floor Vib (dB re 1grms)	Min Floor Vib (dB re 1grms)
1.0	(9°,0°,5°,12°)	106.8	101.2	79.9	−16.3	−23.5	−46.9
2.0	(4°,0°,53°,51°)	106.6	102.5	71.7	−15.7	−22.4	−44.2
3.0	(55°,0°,55°,37°)	104.5	101.1	78.6	−14.7	−21.3	−49.8
4.1	(49°,0°,55°,45°)	110.4	105.9	73.6	−12.0	−20.7	−41.4
4.2	(45°,0°,52°,35°)	112.3	107.7	82.3	−11.2	−19.2	−33.8
4.3	(45°,0°,53°,35°)	112.3	107.7	73.6	−11.1	−19.6	−50.3
5.1	(51°,0°,41°,38°)	114.4	109.3	83.5	−9.9	−16.1	−38.5
5.2	(46°,0°,54°,36°)	111.5	106.9	79.4	−12.3	−19.7	−38.0
5.3	(44°,0°,51°,29°)	112.3	107.6	76.7	−12.1	−19.6	−38.7
6.1	(41°,0°,51°,36°)	114.1	109.6	86.6	−10.0	−17.3	−36.5
6.2	(45°,0°,49°,31°)	114.1	109.5	87.3	−10.6	−17.3	−41.9
6.3	(41°,0°,48°,27°)	113.8	109.2	78.9	−10.3	−17.3	−35.5
7.3	(55°,0°,39°,21°)	117.0	112.5	81.6	−7.6	−14.6	−32.5

Table I.14 C-130J-30 optimum synchrophase angles and BPF levels for the lowest predicted average over the flight deck mics of the SPL at the BPF, Flight 2, Trial 1.

Serial	Synchrophase Angles	Max SPL (dB re 20μPa)	Avg SPL (dB re 20μPa)	Min SPL (dB re 20μPa)	Max Floor Vib (dB re $1g_{rms}$)	Avg Floor Vib (dB re $1g_{rms}$)	Min Floor Vib (dB re $1g_{rms}$)
1.0	(14°,0°,3°,14°)	103.1	98.5	78.2	−17.7	−23.9	−48.9
2.0	(7°,0°,2°,16°)	104.4	100.4	79.3	−12.9	−20.1	−39.4
3.0	(59°,0°,5°,12°)	108.4	104.5	84.9	−8.5	−16.7	−31.7
4.1	(60°,0°,1°,34°)	100.3	96.9	81.2	−14.1	−21.4	−43.8
4.2	(55°,0°,12°,16°)	108.9	105.0	83.3	−6.5	−15.4	−33.8
4.3	(54°,0°,57°,31°)	102.0	97.2	86.7	−15.7	−22.3	−47.0
5.1	(56°,0°,16°,26°)	107.9	104.6	78.6	−7.5	−16.8	−44.8
5.2	(53°,0°,7°,34°)	106.0	99.9	85.6	−10.6	−19.0	−29.2
5.3	(49°,0°,2°,58°)	108.2	103.5	83.2	−9.0	−15.9	−40.5
5.4	(48°,0°,46°,20°)	110.1	106.5	86.9	−12.0	−17.1	−37.3
6.1	(51°,0°,31°,26°)	111.6	107.4	83.9	−7.0	−15.4	−34.7
6.2	(49°,0°,37°,25°)	111.2	107.1	89.5	−9.4	−15.6	−33.5
6.3	(46°,0°,36°,17°)	111.3	107.6	92.1	−9.5	−16.0	−34.8
6.4	(45°,0°,32°,3°)	111.8	108.1	84.5	−11.8	−16.1	−32.9
7.3	(44°,0°,36°,19°)	111.7	107.8	90.6	−8.8	−14.9	−40.0

Table I.15 C-130J-30 optimum synchrophase angles and BPF levels for the lowest predicted average over the flight deck mics of the SPL at the BPF, Flight 3, Trial 1.

Serial	Synchrophase Angles	Max SPL (dB re 20μPa)	Avg SPL (dB re 20μPa)	Min SPL (dB re 20μPa)	Max Floor Vib (dB re 1grms)	Avg Floor Vib (dB re 1grms)	Min Floor Vib (dB re 1grms)
1.0	(17°,0°,50°,37°)	107.2	100.7	79.9	−17.9	−21.9	−29.6
2.0	(16°,0°,52°,35°)	109.0	101.9	76.8	−11.5	−16.7	−27.7
3.0	(2°,0°,53°,32°)	108.0	101.8	87.3	−11.3	−17.2	−28.0
4.1	(56°,0°,23°,38°)	114.2	105.9	79.3	−7.4	−12.4	−20.8
4.2	(47°,0°,16°,32°)	114.2	106.7	81.8	−6.2	−10.6	−20.8
4.3	(56°,0°,49°,26°)	110.1	102.9	80.9	−10.6	−14.4	−35.2
5.1	(53°,0°,25°,35°)	114.1	105.8	77.4	−6.8	−11.5	−22.2
5.2	(49°,0°,22°,33°)	115.4	107.1	81.1	−4.9	−9.5	−19.4
5.3	(54°,0°,49°,24°)	106.2	101.1	80.8	−9.7	−15.9	−26.7
5.4	(48°,0°,9°,3°)	113.7	106.7	84.8	−2.2	−7.6	−18.5
6.1	(47°,0°,21°,37°)	114.7	105.9	52.9	−6.2	−10.0	−26.5
6.2	(42°,0°,20°,29°)	115.1	107.2	84.2	−4.0	−8.6	−23.3
6.3	(39°,0°,17°,28°)	115.1	107.5	86.3	−3.7	−8.5	−22.7
7.1	(42°,0°,21°,32°)	114.9	106.0	75.1	−6.5	−9.9	−41.9
7.2	(53°,0°,9°,28°)	112.0	104.1	81.7	−8.0	−12.6	−37.4
7.3	(39°,0°,8°,19°)	114.5	106.7	82.1	−3.9	−9.1	−28.5
10.0	(45°,0°,24°,18°)	114.1	106.8	85.5	−4.0	−9.1	−26.2

Table I.16 C-130J-30 synchrophase angles and BPF levels for the highest predicted average over all floor accelerometers of the vibration at the BPF, Flight 1, Trial 1.

Serial	Synchrophase Angles	Max SPL (dB re 20μPa)	Avg SPL (dB re 20μPa)	Min SPL (dB re 20μPa)	Max Floor Vib (dB re 1grms)	Avg Floor Vib (dB re 1grms)	Min Floor Vib (dB re 1grms)
1.0	(42°,0°,28°,50°)	111.5	106.7	97.2	−11.2	−18.3	−34.8
2.0	(37°,0°,27°,46°)	112.8	108.6	96.2	−10.5	−17.0	−41.2
3.0	(34°,0°,25°,36°)	116.6	111.7	97.9	−6.8	−14.0	−33.0
4.1	(51°,0°,29°,38°)	112.9	107.9	93.9	−9.6	−15.8	−41.9
4.2	(39°,0°,29°,37°)	116.5	111.9	96.4	−7.5	−13.9	−45.0
4.3	(41°,0°,26°,32°)	117.3	112.2	99.4	−6.7	−12.9	−37.1
5.1	(38°,0°,30°,37°)	114.5	109.7	72.9	−7.8	−14.8	−38.0
5.2	(39°,0°,28°,32°)	116.1	111.4	89.8	−6.1	−13.3	−39.3
5.3	(30°,0°,25°,28°)	117.5	112.7	99.3	−5.4	−12.2	−41.8
6.1	(30°,0°,29°,31°)	115.1	110.8	91.4	−5.9	−13.5	−35.5
6.2	(24°,0°,29°,31°)	116.7	112.8	96.5	−5.7	−12.6	−42.9
6.3	(31°,0°,28°,28°)	116.0	111.9	96.6	−5.2	−12.6	−38.5
7.3	(18°,0°,28°,24°)	117.8	113.7	92.8	−3.9	−11.1	−40.5

Table I.17 C-130J-30 synchrophase angles and BPF levels for the highest predicted average over all floor accelerometers of the vibration at the BPF, Flight 2, Trial 1.

Serial	Synchrophase Angles	Max SPL (dB re 20μPa)	Avg SPL (dB re 20μPa)	Min SPL (dB re 20μPa)	Max Floor Vib (dB re 1grms)	Avg Floor Vib (dB re 1grms)	Min Floor Vib (dB re 1grms)
1.0	(1°,0°,27°,48°)	107.0	105.4	101.1	−9.2	−17.4	−39.4
2.0	(4°,0°,24°,42°)	109.8	106.8	100.5	−8.0	−16.4	−35.3
3.0	(52°,0°,19°,28°)	112.2	108.9	99.0	−6.6	−14.9	−38.7
4.1	(52°,0°,24°,34°)	110.2	107.4	96.1	−6.9	−15.9	−53.2
4.2	(45°,0°,20°,26°)	111.3	108.0	97.1	−5.9	−14.8	−32.7
4.3	(45°,0°,17°,20°)	111.9	108.1	100.3	−4.6	−13.3	−30.4
5.1	(47°,0°,23°,28°)	109.1	106.1	88.1	−7.1	−16.3	−36.6
5.2	(48°,0°,23°,27°)	111.0	107.3	91.4	−5.8	−14.6	−39.0
5.3	(39°,0°,21°,21°)	111.3	108.0	100.5	−5.9	−13.7	−29.9
5.4	(46°,0°,20°,19°)	114.6	110.0	100.4	−5.5	−11.7	−25.8
6.1	(34°,0°,25°,26°)	110.4	107.3	96.8	−6.2	−14.8	−36.6
6.2	(31°,0°,25°,24°)	110.4	107.4	99.9	−6.2	−14.0	−46.4
6.3	(29°,0°,24°,22°)	111.7	109.0	100.2	−6.2	−13.5	−33.9
6.4	(26°,0°,18°,13°)	111.8	109.1	105.0	−3.9	−11.2	−33.4
7.3	(17°,0°,29°,25°)	112.7	110.2	99.8	−6.7	−13.0	−34.0

Table I.18 C-130J-30 synchrophase angles and BPF levels for the highest predicted average over all floor accelerometers of the vibration at the BPF, Flight 3, Trial 1.

Serial	Synchrophase Angles	Max SPL (dB re 20μPa)	Avg SPL (dB re 20μPa)	Min SPL (dB re 20μPa)	Max Floor Vib (dB re 1grms)	Avg Floor Vib (dB re 1grms)	Min Floor Vib (dB re 1grms)
1.0	(52°,0°,25°,46°)	114.6	105.3	80.0	*10.9	*14.1	*26.3
2.0	(12°,0°,32°,56°)	114.8	106.3	72.6	*8.4	*12.1	*22.9
3.0	(32°,0°,21°,31°)	117.0	108.4	76.6	*5.4	*10.0	*20.0
4.1	(45°,0°,25°,35°)	114.6	106.1	74.3	*7.0	*12.0	*23.5
4.2	(45°,0°,22°,29°)	114.9	106.9	82.0	*5.6	*10.1	*21.3
4.3	(10°,0°,28°,21°)	116.6	108.2	83.5	*2.1	*7.9	*20.9
5.1	(45°,0°,27°,36°)	114.9	106.0	74.0	*6.9	*11.4	*24.1
5.2	(46°,0°,23°,29°)	115.2	107.1	81.6	*4.7	*9.4	*19.8
5.3	(45°,0°,22°,26°)	115.0	108.0	87.2	*3.7	*8.5	*22.1
5.4	(48°,0°,19°,21°)	116.2	108.7	92.2	*0.9	*6.6	*16.7
6.1	(37°,0°,29°,34°)	116.1	106.9	86.1	*5.8	*9.2	*31.9
6.2	(43°,0°,21°,22°)	114.3	107.2	76.3	*3.4	*8.2	*21.2
6.3	(38°,0°,25°,27°)	116.1	108.0	68.1	*3.1	*7.7	*24.2
7.1	(30°,0°,31°,33°)	116.5	107.2	81.3	*5.7	*8.9	*31.0
7.2	(19°,0°,34°,36°)	117.2	108.3	88.4	*4.6	*8.3	*30.2
7.3	(18°,0°,29°,25°)	118.9	110.1	92.3	*1.9	*6.6	*23.3
10.0	(58°,0°,21°,25°)	114.5	108.0	87.3	*2.7	*8.2	*23.6

Table I.19 C-130J-30 optimum synchrophase angles and BPF levels for the lowest predicted average over all floor accels of the vibration at the BPF, Flight 1, Trial 1.

Serial	Synchrophase Angles	Max SPL (dB re 20μPa)	Avg SPL (dB re 20μPa)	Min SPL (dB re 20μPa)	Max Floor Vib (dB re 1grms)	Avg Floor Vib (dB re 1grms)	Min Floor Vib (dB re 1grms)
1.0	(36°,0°,7°,7°)	106.8	100.9	86.1	−17.8	−25.4	−52.3
2.0	(19°,0°,2°,59°)	105.0	98.9	80.4	−18.8	−24.5	−44.8
3.0	(4°,0°,1°,46°)	104.5	99.0	74.8	−15.4	−22.0	−46.0
4.1	(11°,0°,5°,49°)	102.1	96.9	73.1	−18.4	−23.5	−38.8
4.2	(11°,0°,60°,39°)	109.4	103.7	91.7	−17.3	−22.5	−39.4
4.3	(6°,0°,1°,38°)	108.8	102.7	87.7	−18.2	−23.5	−41.4
5.1	(16°,0°,55°,27°)	107.9	103.7	92.3	−17.2	−23.6	−44.7
5.2	(10°,0°,57°,31°)	109.1	104.2	85.3	−16.8	−23.1	−35.7
5.3	(3°,0°,56°,30°)	109.0	103.7	83.8	−16.1	−22.9	−40.0
6.1	(1°,0°,60°,32°)	105.2	101.8	92.4	−15.9	−23.1	−33.4
6.2	(55°,0°,59°,31°)	106.2	102.3	89.5	−15.3	−21.6	−42.3
6.3	(55°,0°,60°,30°)	106.6	102.2	91.7	−14.9	−22.0	−43.7
7.3	(39°,0°,59°,23°)	108.6	104.5	80.6	−13.4	−20.1	−36.0

Table I.20 C-130J-30 optimum synchrophase angles and BPF levels for the lowest predicted average over all floor accels of the vibration at the BPF, Flight 2, Trial 1.

Serial	Synchrophase Angles	Max SPL (dB re 20μPa)	Avg SPL (dB re 20μPa)	Min SPL (dB re 20μPa)	Max Floor Vib (dB re $1g_{rms}$)	Avg Floor Vib (dB re $1g_{rms}$)	Min Floor Vib (dB re $1g_{rms}$)
1.0	(32°,0°,2°,2°)	101.8	97.6	87.9	−21.6	−26.7	−42.5
2.0	(30°,0°,59°,50°)	101.5	98.4	92.1	−19.7	−25.9	−44.7
3.0	(21°,0°,48°,27°)	105.7	103.7	99.3	−18.5	−24.1	−41.4
4.1	(21°,0°,52°,30°)	107.4	103.2	89.1	−19.1	−24.1	−36.1
4.2	(19°,0°,45°,20°)	107.5	104.9	96.4	−16.3	−22.4	−31.8
4.3	(7°,0°,53°,29°)	104.1	100.9	93.5	−18.1	−23.9	−35.4
5.1	(15°,0°,53°,27°)	106.4	101.8	88.8	−20.7	−24.9	−51.0
5.2	(7°,0°,55°,28°)	104.4	101.2	93.7	−19.5	−22.5	−33.8
5.3	(59°,0°,59°,32°)	103.3	99.1	87.1	−17.4	−22.8	−31.3
5.4	(57°,0°,59°,31°)	103.5	99.7	94.3	−12.9	−18.6	−30.7
6.1	(4°,0°,57°,29°)	104.0	101.5	95.4	−17.7	−23.1	−40.3
6.2	(10°,0°,54°,24°)	107.6	104.5	96.7	−16.4	−21.7	−54.3
6.3	(55°,0°,58°,28°)	102.9	101.4	92.3	−16.3	−23.0	−35.0
6.4	(4°,0°,46°,12°)	111.5	108.2	100.0	−12.2	−18.6	−38.1
7.3	(52°,0°,1°,29°)	103.3	100.7	90.3	−15.5	−21.9	−33.4

Table I.21 C-130J-30 optimum synchrophase angles and BPF levels for the lowest predicted average over all floor accels of the vibration at the BPF, Flight 3, Trial 1.

Serial	Synchrophase Angles	Max SPL (dB re 20μPa)	Avg SPL (dB re 20μPa)	Min SPL (dB re 20μPa)	Max Floor Vib (dB re 1grms)	Avg Floor Vib (dB re 1grms)	Min Floor Vib (dB re 1grms)
1.0	(26°,0°,49°,36°)	107.7	101.4	79.1	−17.5	−22.1	−33.1
2.0	(37°,0°,59°,40°)	109.7	102.5	67.9	−13.8	−19.8	−39.1
3.0	(14°,0°,49°,29°)	109.8	102.9	84.7	−13.4	−19.1	−30.0
4.1	(11°,0°,55°,33°)	106.1	99.9	57.8	−14.6	−20.8	−35.5
4.2	(10°,0°,52°,28°)	107.7	101.0	84.9	−12.0	−18.4	−33.0
4.3	(57°,0°,56°,34°)	107.4	102.1	83.7	−10.2	−16.0	−41.0
5.1	(10°,0°,55°,31°)	105.7	99.4	75.2	−14.4	−19.9	−26.0
5.2	(8°,0°,55°,30°)	107.6	101.8	82.1	−11.6	−18.1	−29.1
5.3	(7°,0°,55°,30°)	109.4	102.4	83.6	−11.7	−17.8	−26.0
5.4	(1°,0°,51°,22°)	111.2	104.7	82.6	−11.4	−16.5	−34.0
6.1	(4°,0°,55°,26°)	107.1	100.6	81.4	−12.7	−18.4	−23.8
6.2	(3°,0°,57°,30°)	107.7	101.7	84.2	−10.2	−16.7	−23.0
6.3	(3°,0°,55°,26°)	108.9	102.6	85.0	−11.2	−17.6	−25.0
7.1	(2°,0°,56°,24°)	108.1	101.4	77.3	−11.2	−17.3	−23.7
7.2	(60°,0°,55°,23°)	108.4	101.9	78.2	−11.8	−18.2	−28.5
7.3	(56°,0°,55°,20°)	111.9	104.9	83.8	−10.1	−15.9	−32.0
10.0	(5°,0°,50°,22°)	109.3	102.2	78.3	−11.4	−17.4	−25.3

Appendix J. Other Publications

Other publications resulting from this work are listed in chronological order below:

Blunt, D. M. & Rebbechi, B. (2005) C-130 Cargo Space Vibration Reduction. Paper presented at *Parari 2005, 7th Explosive Ordnance Symposium*, Melbourne, Australia, 8-10 Nov 2005.

Blunt, D. M. & Rebbechi, B. (2006) An investigation into active synchrophasing for cabin noise and vibration reduction in propeller aircraft. Paper presented at *Active 2006*, Adelaide, Australia, 18-20 September.

Blunt, D. M. & Rebbechi, B. (2007) Propeller Synchrophase Angle Optimisation Study. Paper presented at *13th AIAA/CEAS Aeroacoustics Conference (28th AIAA Aeroacoustics Conference)*, Rome, Italy, 21-23 May.

Blunt, D. M. (2010) C-130J-30 Propeller Synchrophase Angle Optimisation. Research Report, DSTO-RR-0348, Defence Science and Technology Organisation, Australia.

Blunt, D. M. (2010) AP-3C Propeller Synchrophase Angle Optimisation. Research Report, DSTO-RR-0355, Defence Science and Technology Organisation.

Blunt, D. M. (2010) Aircraft Propeller Synchrophase Angle Opimisation for Lower Cabin Noise and Vibration. Paper presented at *The 17th International Congress on Sound and Vibration (ICSV 17)*, Cairo, 18-22 July 2010.